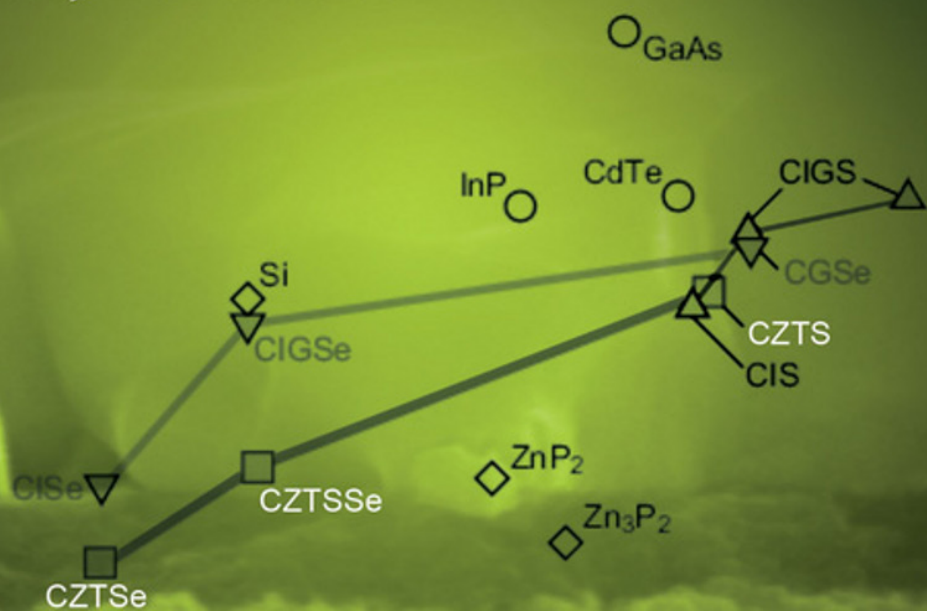


# Copper Zinc Tin Sulfide-Based Thin Film Solar Cells

*Edited by* **Kentaro Ito**



**WILEY**



# **Copper Zinc Tin Sulfide-Based Thin-Film Solar Cells**





# **Copper Zinc Tin Sulfide-Based Thin-Film Solar Cells**

Edited by

KENTARO ITO

*Shinshu University, Nagano, Japan*

**WILEY**

This edition first published 2015  
© 2015 John Wiley & Sons, Ltd

*Registered Office*

John Wiley & Sons Ltd, The Atrium, Southern Gate, Chichester, West Sussex, PO19 8SQ, United Kingdom

For details of our global editorial offices, for customer services and for information about how to apply for permission to reuse the copyright material in this book please see our website at [www.wiley.com](http://www.wiley.com).

The right of the author to be identified as the author of this work has been asserted in accordance with the Copyright, Designs and Patents Act 1988.

All rights reserved. No part of this publication may be reproduced, stored in a retrieval system, or transmitted, in any form or by any means, electronic, mechanical, photocopying, recording or otherwise, except as permitted by the UK Copyright, Designs and Patents Act 1988, without the prior permission of the publisher.

Wiley also publishes its books in a variety of electronic formats. Some content that appears in print may not be available in electronic books.

Designations used by companies to distinguish their products are often claimed as trademarks. All brand names and product names used in this book are trade names, service marks, trademarks or registered trademarks of their respective owners. The publisher is not associated with any product or vendor mentioned in this book.

**Limit of Liability/Disclaimer of Warranty:** While the publisher and author have used their best efforts in preparing this book, they make no representations or warranties with respect to the accuracy or completeness of the contents of this book and specifically disclaim any implied warranties of merchantability or fitness for a particular purpose. It is sold on the understanding that the publisher is not engaged in rendering professional services and neither the publisher nor the author shall be liable for damages arising herefrom. If professional advice or other expert assistance is required, the services of a competent professional should be sought

The advice and strategies contained herein may not be suitable for every situation. In view of ongoing research, equipment modifications, changes in governmental regulations, and the constant flow of information relating to the use of experimental reagents, equipment, and devices, the reader is urged to review and evaluate the information provided in the package insert or instructions for each chemical, piece of equipment, reagent, or device for, among other things, any changes in the instructions or indication of usage and for added warnings and precautions. The fact that an organization or Website is referred to in this work as a citation and/or a potential source of further information does not mean that the author or the publisher endorses the information the organization or Website may provide or recommendations it may make. Further, readers should be aware that Internet Websites listed in this work may have changed or disappeared between when this work was written and when it is read. No warranty may be created or extended by any promotional statements for this work. Neither the publisher nor the author shall be liable for any damages arising herefrom.

*Library of Congress Cataloging-in-Publication Data*

Copper zinc tin sulphide-based thin film solar cells / edited by K. Ito.

pages cm

Includes bibliographical references and index.

ISBN 978-1-118-43787-2 (cloth)

1. Photovoltaic cells--Materials. 2. Solar cells--Materials. 3. Copper-zinc alloys. 4. Thin film devices.

I. Ito, K. (Kentaro)

TK8322.C67 2014

621.31'244--dc23

2014021351

A catalogue record for this book is available from the British Library.

Set in 10/12pt Times by SPi Publisher Services, Pondicherry, India

# Contents

<i>Preface</i>	ix
<i>List of Contributors</i>	xi
<b>Part I Introduction</b>	<b>1</b>
<b>1 An Overview of CZTS-Based Thin-Film Solar Cells</b>	<b>3</b>
<i>Kentaro Ito</i>	
1.1 Introduction	3
1.2 The Photovoltaic Effect	4
1.3 In Pursuit of an Optimal Semiconductor for Photovoltaics	22
1.4 Conclusions	36
Acknowledgements	37
References	37
<b>2 Market Challenges for CZTS-Based Thin-Film Solar Cells</b>	<b>43</b>
<i>Arnulf Jäger-Waldau</i>	
2.1 Introduction	43
2.2 Compound Thin-Film Technologies and Manufacturing	45
2.3 Challenges for CZTS Solar Cells in the Market	49
2.4 Conclusion	51
References	51
<b>Part II The Physics and Chemistry of Quaternary Chalcogenide Semiconductors</b>	<b>53</b>
<b>3 Crystallographic Aspects of <math>\text{Cu}_2\text{ZnSnS}_4</math> (CZTS)</b>	<b>55</b>
<i>Susan Schorr</i>	
3.1 Introduction: What Defines a Crystal Structure?	55
3.2 The Crystal Structure of CZTS	57
3.3 Point Defects in CZTS and the Role of Stoichiometry	68
3.4 Differentiation between Intergrown Kesterite- and Stannite-Type Phases: A Simulation Approach	71
3.5 Summary	72
References	73
<b>4 Electronic Structure and Optical Properties from First-Principles Modeling</b>	<b>75</b>
<i>Clas Persson, Rongzhen Chen, Hanyue Zhao, Mukesh Kumar and Dan Huang</i>	
4.1 Introduction	75
4.2 Computational Background	77
4.3 Crystal Structure	80
4.4 Electronic Structure	82

4.5	Optical Properties	97
4.6	Summary	101
	Acknowledgements	102
	References	102
<b>5</b>	<b>Kesterites: Equilibria and Secondary Phase Identification</b>	<b>107</b>
	<i>Dominik M. Berg and Phillip J. Dale</i>	
5.1	Introduction	107
5.2	Chemistry of the Kesterite Reaction	108
5.3	Phase Identification	116
	Acknowledgements	128
	References	128
<b>6</b>	<b>Growth of CZTS Single Crystals</b>	<b>133</b>
	<i>Akira Nagaoka and Kenji Yoshino</i>	
6.1	Introduction	133
6.2	Growth Process	134
6.3	Properties of CZTS Single Crystals	141
6.4	Conclusion	145
	Acknowledgements	146
	References	146
<b>7</b>	<b>Physical Properties: Compiled Experimental Data</b>	<b>149</b>
	<i>Sadao Adachi</i>	
7.1	Introduction	149
7.2	Structural Properties	150
7.3	Thermal Properties	152
7.4	Mechanical and Lattice Dynamic Properties	157
7.5	Electronic Energy-Band Structure	162
7.6	Optical Properties	169
7.7	Carrier Transport Properties	170
	References	176
<b>Part III</b>	<b>Synthesis of Thin Films and Their Application to Solar Cells</b>	<b>181</b>
<b>8</b>	<b>Sulfurization of Physical Vapor-Deposited Precursor Layers</b>	<b>183</b>
	<i>Hironori Katagiri</i>	
8.1	Introduction	183
8.2	First CZTS Thin-Film Solar Cells	184
8.3	ZnS as Zn-Source in Precursor	184
8.4	Influence of Absorber Thickness	187
8.5	New Sulfurization System	188
8.6	Influence of Morphology	189
8.7	Co-Sputtering System with Annealing Chamber	190
8.8	Active Composition	191
8.9	CZTS Compound Target	192
8.10	Conclusions	201
	References	201

<b>9</b>	<b>Reactive Sputtering of CZTS</b>	<b>203</b>
	<i>Charlotte Platzer-Björkman, Tove Ericson, Jonathan Scragg and Tomas Kubart</i>	
9.1	Introduction	203
9.2	The Reactive Sputtering Process	205
9.3	Properties of Sputtered Precursors	206
9.4	Annealing of Sputtered Precursors	214
9.5	Device Performance	215
9.6	Summary	217
	References	217
<b>10</b>	<b>Coevaporation of CZTS Films and Solar Cells</b>	<b>221</b>
	<i>Thomas Unold, Justus Just and Hans-Werner Schock</i>	
10.1	Introduction	221
10.2	Basic Principles	221
10.3	Process Variations	227
	Acknowledgements	236
	References	236
<b>11</b>	<b>Synthesis of CZTS<sub>Se</sub> Thin Films from Nanocrystal Inks</b>	<b>239</b>
	<i>Charles J. Hages and Rakesh Agrawal</i>	
11.1	Introduction	239
11.2	Nanocrystal Synthesis	241
11.3	Nanocrystal Characterization	249
11.4	Sintering	251
11.5	Conclusion	264
	References	264
<b>12</b>	<b>CZTS Thin Films Prepared by a Non-Vacuum Process</b>	<b>271</b>
	<i>Kunihiko Tanaka</i>	
12.1	Introduction	271
12.2	Sol-Gel Sulfurization Method	272
12.3	Preparation of CZTS Thin Films by Sol-Gel Sulfurization Method	274
12.4	Chemical Composition Dependence	279
12.5	H <sub>2</sub> S Concentration Dependence	282
12.6	CZTS Solar Cell Prepared by Non-vacuum Processes	284
	References	285
<b>13</b>	<b>Growth of CZTS-Based Monograins and Their Application to Membrane Solar Cells</b>	<b>289</b>
	<i>Enn Mellikov, Mare Altosaar, Marit Kauk-Kuusik, Kristi Timmo, Dieter Meissner, Maarja Grossberg, Jüri Krustok and Olga Volobujeva</i>	
13.1	Introduction	289
13.2	Monograin Powder Growths, Basics of the Process	291
13.3	Influence of Chemical Etching on the Surface Composition of Monograins	295
13.4	Thermal Treatment of CZTS-Based Monograins	298

13.5	Optoelectronic Properties of CZTS-Based Monograins and Polycrystals	300
13.6	Conclusion	306
	References	306
<b>Part IV</b>	<b>Device Physics of Thin-Film Solar Cells</b>	<b>311</b>
<b>14</b>	<b>The Role of Grain Boundaries in CZTS-Based Thin-Film Solar Cells</b>	<b>313</b>
	<i>Joel B. Li and Bruce M. Clemens</i>	
14.1	Introduction	313
14.2	CIGSe and CdTe Solar Cells	314
14.3	CZTS-Based Thin-Film Solar Cells	318
14.4	Conclusion	327
	References	328
<b>15</b>	<b>CZTS-Based Thin-Film Solar Cells Prepared via Coevaporation</b>	<b>335</b>
	<i>Byungha Shin, Talia Gershon and Supratik Guha</i>	
15.1	Introduction	335
15.2	Preparation of CZTS and CZTSe Absorbers	337
15.3	Fundamental Properties of Coevaporated CZTS and CZTSe Absorbers	338
15.4	Device Characteristics of Full-Sulfide CZTS Thin-Film Solar Cells	348
15.5	Device Characteristics of Full-Selenide CZTSe Thin-Film Solar Cells	354
15.6	Summary	358
	References	358
<b>16</b>	<b>Loss Mechanisms in Kesterite Solar Cells</b>	<b>363</b>
	<i>Alex Redinger and Susanne Siebentritt</i>	
16.1	Introduction	363
16.2	Current State-of-the-Art CZTS-Based Thin-Film Solar Cells	364
16.3	Dominant Recombination Path	366
16.4	Band-Gap Variations	372
16.5	Series Resistance and its Relation to $V_{oc}$ Losses	376
16.6	Conclusion	381
	Acknowledgements	382
	References	382
<b>17</b>	<b>Device Characteristics of Hydrazine-Processed CZTSSe</b>	<b>387</b>
	<i>Oki Gunawan, Tayfun Gokmen and David B. Mitzi</i>	
17.1	Introduction	387
17.2	Device Characteristics	389
17.3	Summary	406
	Acknowledgements	407
	References	408
	<b>Subject Index</b>	<b>413</b>

# Preface

The most cost-effective route to solar cell fabrication was unlocked by utilizing thin-film technology. The first research papers on this type of cell date back to the 1960s. The semiconductor thin film consisting of a II-VI or I-III-VI<sub>2</sub> compound is normally used in the solar cell as an optical absorber with the thickness of microns. It is prepared on a low-cost substrate such as a glass plate, a metal sheet, or a plastic sheet. It was found in the late 1980s that the thin film of quaternary compound Cu<sub>2</sub>ZnSnS<sub>4</sub> also has a suitable energy band and exhibits a photovoltaic effect. In this book we deal with the multinary compound semiconductors which belong to the tetragonal crystal system and have the optimal band gap for photovoltaics: the quaternary sulfide, its alloy, and a selenide. The chemical formulae of the latter are represented as Cu<sub>2</sub>ZnSn(S<sub>x</sub>Se<sub>1-x</sub>)<sub>4</sub> and Cu<sub>2</sub>ZnSnSe<sub>4</sub>. The purpose of this book is to describe current development of thin-film solar cells, from the viewpoint of device performance and absorber processing. We also describe the physical and chemical properties of these compounds, which are considered to play an important role in determining the efficiency of the solar cells.

In the mid-1970s, Professor A. G. Milnes of Carnegie Institute of Technology visited our University in Nagano to speak on the subject of solar cells. At that time he was a visiting scholar at the Tokyo Institute of Technology. He stressed the importance of cost in producing solar cells, and predicted that photovoltaics would not be of any practical use if the cost was higher than the threshold value (equal to ten cents per watt). He made numerous references to this threshold in his talk. He was interested in developing a low-cost GaAs solar cell which is grown epitaxially on a mono-crystalline substrate, a substrate which could be made reusable by detaching it many times from the epitaxial layer using selective chemical etching. Around that time, the efficiency of a GaAs solar cell was 22% while that of a CdTe thin-film solar cell was 8%. Although his concept is indirectly connected to the recent development of a GaAs solar cell, the efficiency of which has approximately reached the theoretical upper limit, it has not been applied to low-cost solar cells because the large-area mono-crystals are not available. By taking account of the rise in electricity rates (Consumer Price Index) during the past four decades, his threshold has to be upgraded to 45 (54) cents per watt at present. It is interesting to note that this converted threshold is only 1.5 times lower than the price of CdTe thin-film solar modules in 2013, as shown in Chapter 2. Despite polycrystalline nature, cost-effective performances of thin-film solar cells are preferable to those of mono-crystalline solar cells.

Multinary compound semiconductors have an absorption coefficient  $>10^4 \text{ cm}^{-1}$  due to the direct nature of the band gap. Films of thickness 1  $\mu\text{m}$  can absorb almost all the photons in the solar spectrum of wavelength shorter than near-infrared wavelengths, and operate as efficient photocurrent suppliers. The direct band gap is within an optimal range for solar cells, that is, 1.0–1.5 eV. The theoretical upper limit of efficiency for the solar cells is estimated to be 32–34%. There is still room for improvement in the present cell performance

via a high-quality absorber layer and the optimization of device structure. Since all the chemical elements of the compound are Earth-abundant, the material cost of the absorber can be much lowered in comparison to the II-VI or I-III-VI<sub>2</sub> thin-film solar modules in which the absorbers are composed of rare elements such as Te and In.

For the sake of simplicity, the chemical formulae are often abbreviated by replacing copper, zinc, tin, sulfur, and selenium with C, Z, T, S, and Se, respectively, and the suffixes are omitted. Photovoltaic devices which consist of these compounds are referred to as CZTS-based thin-film solar cells.

In the first chapter of Part I it is described how the concept for CZTS-based thin-film solar cells is derived from the physical principle of photovoltaics and also from the viewpoint of abundant natural resources. In the second chapter, their prospects are discussed by reviewing recent advances in producing thin-film solar modules, among which CdTe modules exhibit a learning curve pointing at price \$US 0.7 per peak watt.

In the first chapter of Part II, it is described that the principal structure type of CZTS is kesterite, and the existence of some antisite point defects in the compound is demonstrated by neutron diffraction. Relatively small electron mass and high optical efficiency of the multinary compounds are deduced from theoretical studies of the energy band structure and complex dielectric function, respectively. We learn how CZTS is in thermal equilibrium with volatile sulfur and tin sulfide at growth temperatures, and that the existence of secondary phases in CZTS should be identified using specific analyses. Bulk CZTS single crystals are grown by solution growth, and their transport property is evaluated by Hall measurements. Physical properties of Cu<sub>2</sub>-II-IV-VI<sub>4</sub> compounds are systematically compiled such that their data can provide useful information for the design of thin-film solar cells.

Various processes involved in the preparation of high-quality absorbers for solar cells are introduced in Part III. Study of thin-film CZTS solar cells reveals that a Cu-poor and Zn-rich absorber – prepared by sulfurizing a precursor – is required for the improvement of cell efficiency. Disordered CZTS thin films are first sputter-deposited from metal targets in a residual vapor pressure of H<sub>2</sub>S and are then annealed in sulfur vapor. After coevaporation techniques are elucidated to grow thin-film compounds, their application to CZTS-based thin-film solar cells are reviewed. CZTSe thin films are prepared by annealing the precursor in Se vapor, which is formed by coating a substrate with the ink composed of CZTS nanocrystals. CZTS thin films are prepared by oxidation and subsequent sulfurization of an oxyhydrate precursor which is coated by the sol-gel method. Mono-grain crystallites of the CZTS-based compounds are grown by a flux method and they are arranged in a mono-grain layer to make solar cells.

Part IV is on the device physics of thin-film solar cells. According to the microscopic observation by SKPM and conductive AFM, the enhanced minority carrier collection takes place at the grain boundaries of multinary compounds. The efficiency of CZTS-based thin-film solar cells fabricated by coevaporation and annealing is at least partly correlated with the defect density in the absorber. The device characteristics of the thin-film solar cells are reviewed, and the high series resistance in them is considered attributable to such a secondary phase as ZnSe. Using the hydrazine pure-solution approach, a CZTSSe thin-film solar cell with 12.6% efficiency is obtained. The possible effect of band tailing on the open-circuit voltage is discussed.

We are indebted to Ms Sarah Keegan, Ms Emma Strickland and Ms Rebecca Stubbs for their assistance with manuscript preparation.



# List of Contributors

**Sadao Adachi**, *Division of Electronics and Informatics, Gunma University, Japan*

**Rakesh Agrawal**, *School of Chemical Engineering, Purdue University, USA*

**Mare Altosaar**, *Department of Materials Science, Tallinn University of Technology, Estonia*

**Dominik M. Berg**, *Institute of Energy Conversion, University of Delaware, USA*

**Rongzhen Chen**, *Department of Materials Science and Engineering, Royal Institute of Technology, Sweden*

**Bruce M. Clemens**, *Department of Materials Science & Engineering, Stanford University, USA*

**Phillip J. Dale**, *Laboratory for Energy Materials, Université du Luxembourg, Luxembourg*

**Tove Ericson**, *Department for Engineering Sciences, Uppsala University, Sweden*

**Talia Gershon**, *IBM Thomas J. Watson Research Center, USA*

**Tayfun Gokmen**, *IBM Thomas J. Watson Research Center, USA*

**Maarja Grossberg**, *Department of Materials Science, Tallinn University of Technology, Estonia*

**Supratik Guha**, *IBM Thomas J. Watson Research Center, USA*

**Oki Gunawan**, *IBM Thomas J. Watson Research Center, USA*

**Charles J. Hages**, *School of Chemical Engineering, Purdue University, USA*

**Dan Huang**, *Department of Materials Science and Engineering, Royal Institute of Technology, Sweden*

**Kentaro Ito**, *Department of Electrical and Electronic Engineering, Shinshu University, Japan*

**Arnulf Jäger-Waldau**, *European Commission, Joint Research Centre, Italy*

**Justus Just**, *Helmholtz Centre Berlin for Materials and Energy, Germany*

**Hironori Katagiri**, *Department of Electrical and Electronic Systems Engineering, Nagaoka National College of Technology, Japan*

**Marit Kauk-Kuusik**, *Department of Materials Science, Tallinn University of Technology, Estonia*

**Jüri Krustok**, *Department of Materials Science, Tallinn University of Technology, Estonia*

**Tomas Kubart**, *Department for Engineering Sciences, Uppsala University, Sweden*

**Mukesh Kumar**, *Department of Materials Science and Engineering, Royal Institute of Technology, Sweden*

**Joel B. Li**, *Department of Electrical Engineering, Stanford University, USA*

**Dieter Meissner**, *Department of Materials Science, Tallinn University of Technology, Estonia*

**Enn Mellikov**, *Department of Materials Science, Tallinn University of Technology, Estonia*

**David B. Mitzi**, *IBM Thomas J. Watson Research Center, USA*

**Akira Nagaoka**, *Department of Applied Physics and Electronic Engineering, University of Miyazaki, Japan*

**Clas Persson**, *Department of Physics, University of Oslo, Norway; Department of Materials Science and Engineering, Royal Institute of Technology, Sweden*

**Charlotte Platzer-Björkman**, *Department for Engineering Sciences, Uppsala University, Sweden*

**Alex Redinger**, *Laboratory for Photovoltaics, University of Luxembourg, Luxembourg*

**Hans-Werner Schock**, *Helmholtz Centre Berlin for Materials and Energy, Germany*

**Susan Schorr**, *Helmholtz Centre Berlin for Materials and Energy, Germany; Institute of Geological Sciences, Freie Universitaet Berlin, Germany*

**Jonathan Scragg**, *Department for Engineering Sciences, Uppsala University, Sweden*

**Byungha Shin**, *IBM Thomas J. Watson Research Center, USA; Department of Materials Science and Engineering, Korea Advanced Institute of Science and Technology, Daejeon, Republic of Korea*

**Susanne Siebentritt**, *Laboratory for Photovoltaics, University of Luxembourg, Luxembourg*

**Kunihiko Tanaka**, *Department of Electrical Engineering, Nagaoka University of Technology, Japan*

**Kristi Timmo**, *Department of Materials Science, Tallinn University of Technology, Estonia*

**Thomas Unold**, *Helmholtz Centre Berlin for Materials and Energy, Germany*

**Olga Volobujeva**, *Department of Materials Science, Tallinn University of Technology, Estonia*

**Kenji Yoshino**, *Department of Applied Physics and Electronic Engineering, University of Miyazaki, Japan*

**Hanyue Zhao**, *Department of Materials Science and Engineering, Royal Institute of Technology, Sweden*

# **Part I**

## **Introduction**



# 1

## An Overview of CZTS-Based Thin-Film Solar Cells

*Kentaro Ito*

*Department of Electrical and Electronic Engineering, Shinshu University,  
1-17-4 Wakasato, Nagano 380-8553, Japan*

### 1.1 Introduction

This book deals with the thin-film solar cell with optical absorber layer composed of the copper-zinc-tin-sulphide-based quaternary semiconductor represented by chemical formula  $\text{Cu}_2\text{ZnSnS}_4$  or related compound semiconductors. Throughout this book, we abbreviate the quaternary compound as CZTS. The concept of CZTS thin-film solar cells is based on the following principles. The compound semiconductor meets two necessary conditions for efficient solar cells. One is the direct nature of the band gap and the other is its width within a certain optimal range for photovoltaic cells. Because the pre-factor of absorption coefficient for the CZTS thin film is large enough the layer of just micron thickness is able to absorb sunlight sufficiently, and the use of it as an absorber does not have any damaging effects on photocurrents. The probability of radiative recombination in the film is able to exceed that of non-radiative recombination if both absorption and emission of photons are caused by an allowed direct transition of carriers between valence and conduction bands without any intermediaries such as crystal defects and phonons. It is therefore possible for cell efficiency to approach the theoretical limit if Shockley–Read–Hall-type recombination centers, which play a role in bypassing the direct recombination, are diminished and at the same time a device structure to confine excited electrons in the CZTS base layer is implemented. The CZTS semiconductor is potential candidate material for terawatt (TW) -scale

photovoltaic energy conversion: a fractional amount of the elemental constituents produced annually is sufficient to fabricate CZTS thin-film solar cells which can supply renewable energy on a scale comparable to the world's electricity consumption. The multiplicity of the compound is advantageous in designing the semiconductor material for photovoltaic devices, because we can control its physical properties depending on a substitution of the cation or anion included in the fundamental tetrahedron for another cation or anion and we can also avoid the undesirable use of rare or toxic elements. The incomplete (9%) substitution of sulfur for selenium is a typical example, which has lead to the achievement of alloy thin-film solar cells with over 10% efficiency [1, 2].

The physics of the photovoltaic effect are described in Section 1.2, including: the spectral irradiance of solar radiation and the influence of the Earth's atmosphere on it; the upper limit of conversion efficiency of a single-junction solar cell which is evaluated on the basis of a detailed balance model; an optimal range of energy band gaps for photovoltaic energy conversion; optical absorption in semiconductor thin films and the estimation of the thickness of the absorber layer required for an efficient thin-film solar cell; and important roles of semiconductor p-n (positive or negative) homo- and hetero-junctions in the photovoltaic effect. In Section 1.3 we describe the pursuit of an optimal semiconductor for photovoltaic applications which have a band gap within the optimal range. The history of the thin-film solar cell is first discussed, including studies on some mono-crystalline semiconductor materials and their photovoltaic applications and the development of a chalcopyrite-type thin-film solar cell for comparison. We then describe how the concept of CZTS technology originated. Finally, we describe our synthesis and characterization of the CZTS absorber and n-type buffer layers to conclude the chapter.

## 1.2 The Photovoltaic Effect

### 1.2.1 Solar Radiation

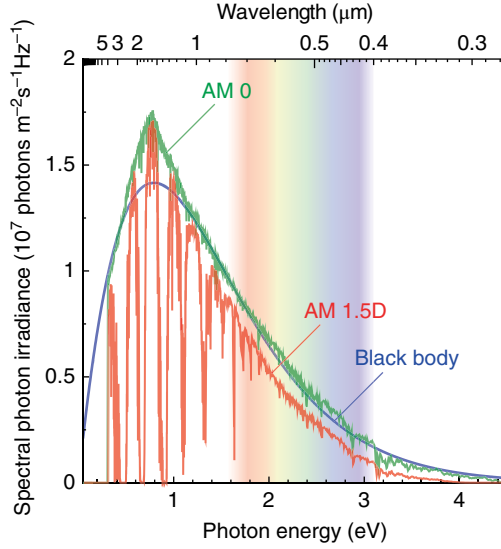
#### 1.2.1.1 Extra-terrestrial Radiation

At the core of the Sun, nuclear fusion of hydrogen releases massive heat. The Sun is surrounded by a thin atmosphere which consists mostly of hydrogen atoms. This is the so-called photosphere that absorbs the heat and emits electromagnetic radiation into outer space with almost the same spectral radiation as that of a black body in thermal equilibrium at a high temperature  $T_s$ . According to Planck's formula, the power emitted per unit projected area of the black body into a unit solid angle per unit frequency interval is given by the spectral irradiance  $L_\nu(T_s)$ , defined

$$L_\nu(T_s) = \frac{2h\nu^3}{c^2} \frac{1}{\exp(h\nu / k_B T_s) - 1} \quad (1.1)$$

where  $\nu$  is the frequency of radiation,  $c$  is the light speed,  $h$  is the Plank constant, and  $k_B$  is the Boltzmann constant. The photon energy of electromagnetic oscillation at frequency  $\nu$  is given by  $h\nu$ . The solid angle  $\Omega_s$  of the Sun (in steradians) which is seen from the Earth is calculated as:

$$\Omega_s = \frac{\pi r^2}{R^2} = 6.79 \times 10^{-5} \quad (1.2)$$



**Figure 1.1** Spectral photon irradiance of AM0, AM1.5D and black body radiation. For color details, please see color plate section

where  $r$  is the radius of the Sun (i.e.  $6.96 \times 10^5$  km) and  $R$  is the mean orbital radius of the Earth rotating around the Sun (i.e.  $1.496 \times 10^8$  km).

The spectral photon irradiance which is defined by the number  $N_\nu(T_s)$  of incident photons per square meter per second per Hertz arriving at the top of the Earth's atmosphere is therefore expressed:

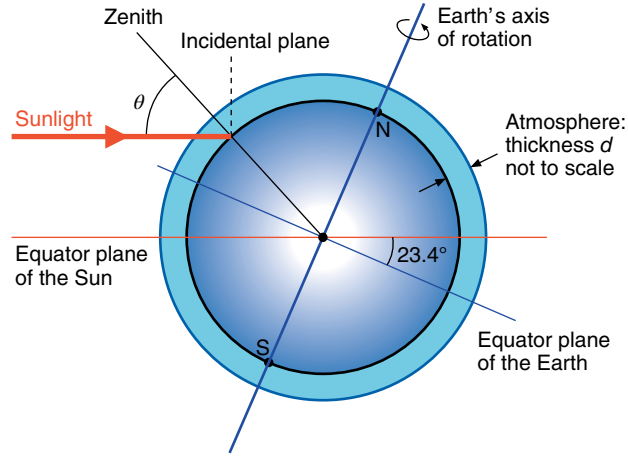
$$N_\nu(T_s) = \frac{\Omega_s L_\nu(T_s)}{h\nu}. \quad (1.3)$$

The smooth curve shown in Figure 1.1 is the theoretical plot of  $N_\nu(T_s)$  versus photon energy  $h\nu$ , evaluated by substituting the effective temperature  $T_s$  of the photosphere (which is assumed to be 5772 K) into Equation (1.3). The accuracy of this assumption is confirmed in Figure 1.1 as the theoretical curve for the electromagnetic wave emitted from a black body at  $T_s$  agrees quite well with the observed spectra of extra-terrestrial radiation in photon energy of 1.15–1.72 eV. The two curves also cross at 3.11 and 0.44 eV. The latter spectra are derived from those of AM0 radiation measured as a function of wavelength [3]. However, there is a significant difference in peak irradiance between the two curves.

The total power of electromagnetic radiation which is perpendicularly incident on a unit area is called the solar constant  $C_s$  and is thus defined by:

$$C_s = \int_0^\infty h\nu N_\nu(T_s) d\nu = \Omega_s \int_0^\infty L_\nu(T_s) d\nu = \frac{r^2 \sigma T_s^4}{R^2}, \quad (1.4)$$

where  $\sigma$  is the Stefan-Boltzmann constant equal to  $5.67 \times 10^{-8} \text{ W m}^{-2} \text{ K}^{-4}$ . The effective surface temperature  $T_s$  ( $= 5772$  K) of the Sun is determined such that the theoretical value



**Figure 1.2** Schematic path length of sunlight through the atmosphere, given by  $d/\cos\theta$

of  $C_s$  given by Equation (1.4) agrees with the solar constant  $1.3608 \text{ kW m}^{-2}$ , which was recently measured by NASA's Solar Radiation and Climate Experiment Satellite [4].

#### 1.2.1.2 Terrestrial Radiation

Figure 1.2 depicts how solar radiation reaches the Earth's surface after passing through the atmosphere of effective thickness  $d$  ( $=8.4 \text{ km}$ ). The radiation is assumed to be perpendicularly incident on a planar solar cell inclined by the solar zenith angle  $\theta$  (the angle between the local zenith and the line of the sight from that place to the Sun). The light pathlength  $s$  given by  $d/\cos\theta$  depends both on time and place on the Earth. The index air mass (AM), which is proportional to the pathlength  $s$ , is defined:

$$\text{AM} = \frac{s}{d} \approx \frac{1}{\cos\theta}. \quad (1.5)$$

Since the AM is equal to the light pathlength  $s$  normalized to the thickness  $d$ , the extra-terrestrial radiation described above is often referred to as "AM0 radiation". Figure 1.1 shows the standard reference spectra of AM1.5D and AM0 rays together with black body radiation as a function of photon energy [3]. The AM1.5D rays are directly incident with a zenith angle  $\theta$  of  $48.2^\circ$ . The total incident power  $P_i$  which is evaluated by integrating  $h\nu N_\nu(T_s)$  for the AM1.5D spectra over the whole photon energy range amounts to  $0.90 \text{ kW m}^{-2}$ , that is, 34% of AM0 radiation is absorbed and scattered by the atmosphere.

The total power directly incident on the Earth's surface  $I_D$  is estimated as:

$$I_D = 2\pi C_s R_E^2 \int_0^{\pi/2} \tau_a \sin\theta \cos\theta d\theta \quad (1.6)$$

where  $R_E$  is the radius of the Earth ( $6.4 \times 10^3 \text{ km}$ ),  $\theta$  is the zenith angle between the vertical at a place on the Earth and the direct light beam from the Sun, and  $\tau_a$  is the optical transmittance of the atmosphere which is experimentally determined by [5]:



$$\tau_a = 0.7^{AM^{0.678}}. \quad (1.7)$$

According to Equations (1.5–1.7),  $I_D$  is estimated as  $0.30\pi R_E^2 C_S = 1.04 \times 10^{17} \text{ W}$ . If this amount is accumulated during one year, its total is equivalent to 50,000 times the recent annual world electricity consumption of 20 PWh. This wide margin could be reduced by 3–4 orders of magnitude when we take into account the scarcity of the land available for module installation, the limitation imposed on solar cell efficiency, climate conditions and the peak demand of electricity. However, the margin thus modified still indicates that photovoltaic technology is an effective means of coping with the limiting supplies of fossil fuel in the foreseeable future.

The validity of Equation (1.7) can be approximately confirmed in the following. When the air mass is equal to 1.5, the transparency of the atmosphere given by Equation (1.7) takes a value of 0.63. The absorbance of the atmosphere is therefore estimated as 37%, which is comparable to the above-mentioned absorption loss of extra-terrestrial radiation in the atmosphere.

Despite the disturbance due to the surrounding atmosphere, the photon irradiance of AM1.5D radiation exhibits a peak at the same photon energy of about 0.77 eV as that of AM0 sunlight. The horizontal axis for the curve shown in Figure 1.1 represents the photon energy in electron-volts, which is converted to Joules if multiplied by electronic charge  $q$ . Since the wavelength of the photon is given by  $c/\nu$  (see the upper horizontal axis of the figure), the peak photon energy corresponds to  $1.6 \mu\text{m}$  which falls within a near-infrared range. The spectral sensitivity of the retina does not match this peak, however; instead it has evolved to cover the shorter-wavelength range in which solar irradiance is hardly weakened by the Earth's atmosphere.

In Figure 1.1 there are several distinct bands in which the photons are absorbed by the atmosphere. A narrow band which appears at 1.63 eV is due to absorption by oxygen molecules. Water vapor is mainly responsible for optical absorption in the atmosphere at the low photon energy range of 0.46–1.7 eV. In this molecule there are two chemical bonds as expressed by H-O-H. Their vibration has numerous quantized states, which can be excited by photons. Their optical absorption bands are always broad and often strong compared with that of oxygen molecules. For example, the absorption band which is centered around 0.90 eV, denoted  $\Omega$ , is assigned to a combined vibration mode associated with symmetric stretching and bending of the bonds [6]. We later refer to the case where optical absorption bands of water vapor have a significant influence on the efficiency of a solar cell.

## 1.2.2 Upper Limit of Conversion Efficiency in a Single-Junction Solar Cell

One of the most important criteria for solar cell materials is the band gap of semiconductors. We explain analytically why it may be of a direct nature and within a certain range of energy. It should be stressed that the compound of CZTS with which this book deals has an optimal direct energy gap. We define the absorber material as ideal if it possesses a direct band gap within the optimal range and, at the same time, is completely free from any sort of non-radiative recombination of carriers. In the strict sense of the word, mono-crystalline Si as an absorber could not be ideal because its band gap is of an indirect nature despite the fact that it has an optimal band gap of 1.12 eV. We discuss the silicon solar cell for comparison in Section 1.2.5.

Based on the detailed balance model which holds thermodynamically between the Sun's radiation and light emission from a solar cell, Shockley and Queisser first predicted the

efficiency limit of a single junction solar cell, which was later called the SQ limit [7]. An extended version of their theory was reported by Yablonovitch *et al.* [8]. It was assumed that incident photons whose energy is higher and slightly lower than the band gap  $E_g$  are capable of exciting an electron and a hole which eventually recombine to emit a photon spontaneously. Both groups of authors incorporated the idealistic assumption that the mobility of carriers is infinitely large.

In a p-type semiconductor at thermal equilibrium there are a lot of free holes with concentration  $p_0$  which is approximately equal to the density of doped acceptor impurities, giving rise to the p-type conductivity. The hole concentration  $p_0$  is given by

$$p_0 = N_v \exp\left(-\frac{E_F - E_v}{k_B T_c}\right) \quad (1.8)$$

where  $N_v$  is the density of states of a valence band,  $E_v$  is the energy level at the top of the band,  $E_F$  is the Fermi level and  $T_c$  is the ambient temperature [9]. As the acceptor density increases,  $E_F$  tends towards  $E_v$ . In addition, there is a very small amount of free electrons with concentration  $n_0$  given by

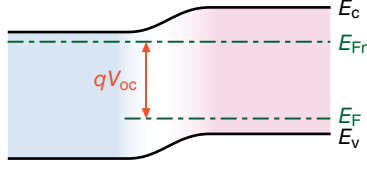
$$n_0 = N_c \exp\left(-\frac{E_c - E_F}{k_B T_c}\right) \quad (1.9)$$

where  $N_c$  is the density of states of a conduction band and  $E_c$  is the energy level at the bottom of the band. The product  $p_0 n_0$  is independent of both the type and the density of impurities, since  $E_c - E_v$  is the forbidden band gap  $E_g$  of the semiconductor, that is, an intrinsic property. The square root of the product is therefore referred to as intrinsic concentration, denoted  $n_i$  and defined:

$$n_i = \sqrt{n_0 p_0} = \sqrt{N_c N_v} \exp\left(-\frac{E_g}{2k_B T_c}\right). \quad (1.10)$$

When the cell consisting of a planar pn-junction is excited by solar radiation, an open-circuit voltage  $V_{oc}$  appears between the p-type and the n-type semiconductors. The open-circuit condition corresponds to the steady state of a thermodynamic system comprising the Sun, Earth and a solar cell. In this state the production rate of entropy reaches a minimum and a chemical potential difference  $qV_{oc}$  arises at the semiconductor pn-junction. We make several assumptions, including: the planar junction with a unit area emits light within a hemisphere as a Lambertian source and hence reflects light completely at a rear electrode; and the cell is in thermal equilibrium at 298 K. Here we will simply assume that solar radiation with photon energy  $h\nu \geq E_g$  excites the cell to emit black body radiation, but that of  $h\nu < E_g$  does not. The quasi-Fermi level  $E_{Fn}$  for electrons in the p-type semiconductor moves upwards by  $qV_{oc}$  in reference to the Fermi level  $E_F$  (see Fig. 1.3). As long as the cell is in thermal equilibrium, and hence not illuminated by solar radiation, the Fermi level  $E_F$  is constant everywhere. However, the minority carrier concentration  $n$  increases due to solar radiation as follows:

$$n = \frac{n_i^2}{p_0} \exp\left(\frac{E_{Fn} - E_F}{k_B T_c}\right) = \frac{n_i^2}{p_0} \exp\left(\frac{qV_{oc}}{k_B T_c}\right). \quad (1.11)$$



**Figure 1.3** Band diagram of the *pn*-junction that is of open-circuit and illuminated by sunlight

The concentration of photo-excited excess electrons ( $n-n_0$ ) is equal to that of photo-excited excess holes ( $p-p_0$ ) because they are produced in pairs. This amount is much smaller than the majority carrier (hole) concentration  $p_0$  in thermal equilibrium when the p-type semiconductor of a solar cell is taken into account. In contrast, this amount ( $n-n_0$ ) exceeds the minority carrier (electron) concentration  $n_0$  at thermal equilibrium, as expressed by the exponential factor of  $\exp(qV_{oc}/k_B T_c)$  in the right-hand side of Equation (1.11). The excited electrons diffuse from the vicinity of the n-type emitter towards the right edge of the semiconductor. In the idealistic solar cell, the diffusion length of minority carriers is infinitely large. If the right surface of the p-type absorber has an extremely low recombination velocity, which a back surface field might bring about, the quasi-Fermi level  $E_{Fn}$  would be almost constant throughout the region.

The number of photons emitted from the cell increases by the same factor as above and should balance the incident photons which are able to contribute to the re-emission of radiation. We therefore obtain:

$$\eta_r \int_0^{2\pi} d\varphi \int_0^{\pi/2} \cos\theta \sin\theta d\theta \int_{E_g/h}^{\infty} \frac{L_v(T_c)}{h\nu} d\nu = \exp\left(\frac{qV_{oc}}{k_B T_c}\right) \int_{E_g/h}^{\infty} N_v(T_s) d\nu \quad (1.12)$$

where  $\theta$  is the zenith angle between an emitted light flux and the direction perpendicular to the cell in a spherical coordinate system,  $\varphi$  is the azimuth angle of the flux,  $L_v(T_c)$  is the spectral irradiance that is re-emitted from the cell and is considered equal to blackbody radiation at  $T_c$ , and  $N_v(T_s)$  is either the measured or the theoretical spectrum of solar photon irradiance. The radiative recombination efficiency  $\eta_r$  for re-emission is defined as follows. The radiative (non-radiative) recombination probability per unit time is equal to the inverse of radiative (non-radiative) recombination lifetime  $\tau_r$  ( $\tau_{nr}$ ). Since total probability of recombination of minority carriers is equal to the sum of the radiative recombination probability and the non-radiative recombination probability,  $\eta_r$  is defined:

$$\eta_r \equiv \frac{1/\tau_r}{1/\tau} = \frac{1/\tau_r}{1/\tau_r + 1/\tau_{nr}} = \frac{1}{1 + \tau_r/\tau_{nr}} \quad (1.13)$$

where  $\tau$  is the total lifetime. The lifetime  $\tau_r$  is given by  $\phi/Bp_0$  where  $B$  is the bimolecular recombination coefficient due to band-to-band recombination and  $\phi$  is the photon recycling factor, that is, the inverse probability of the photon escape through the boundaries of the optical absorber without re-absorption [10, 11]. The factor  $\phi$  is larger than 1 as long as there is enough space for re-emitted photons to excite electron-hole pairs in the absorber.

Lifetime  $\tau_{nr}$  is usually governed by crystal defects such as impurities. According to the simplified Shockley–Read–Hall (SRH) model,  $\tau_{nr}$  is given by the reciprocal of the product of the density  $N_t$  of recombination centers, their capture cross-section  $\sigma_n$  and the thermal velocity  $v_{th}$  of electrons [12]. When  $p_0$  is very high, Auger recombination prevails so that the non-radiative lifetime is inversely proportional to the square of  $p_0$  [13].

Equation (1.12) can be rearranged to yield

$$V_{oc} = \frac{k_B T_c}{q} \ln \left( \frac{\eta_r J_{sc}}{J_0} \right) \quad (1.14)$$

where  $J_{sc}$  is the short-circuit current density given by Equation (1.15) and  $J_0$  is defined by Equation (1.16):

$$J_{sc} = q \int_{E_g/h}^{\infty} N_v(T_s) dv \quad (1.15)$$

$$J_0 = \frac{2\pi q k_B^3 T_c^3}{h^3 c^2} \sum_{m=1}^{\infty} \left[ \frac{1}{m} \left( \frac{E_g}{k_B T_c} \right)^2 + \frac{2}{m^2} \left( \frac{E_g}{k_B T_c} \right) + \frac{2}{m^3} \right] \exp \left( -\frac{m E_g}{k_B T_c} \right). \quad (1.16)$$

Energy band gap  $E_g$  would be much larger than thermal energy  $k_B T_c$  ( $\approx 0.026$  eV) if we take the energy range of  $E_g$  (c. 1 eV) suitable for a solar cell into consideration. Each term in Equation (1.16) is a rapidly decreasing function of integer  $m$ . To evaluate the theoretical performance of solar cells, we later use an equation which is approximated only by the first term (i.e.  $m=1$ ).

If the cell is kept at thermal equilibrium in the dark,  $J_{sc}$  and  $V_{oc}$  should decrease to zero. This inevitable relation could not be seen if we use Equation 1.14 which is derived by neglecting the strict conservation law that the total number of photons incident both from the Sun and the Earth's atmosphere balances that of re-emitted photons. By taking account of this, a strict expression for  $V_{oc}$  is

$$V_{oc} = \frac{k_B T_c}{q} \ln \left( \frac{\eta_r J_{sc} + J_0}{J_0} \right). \quad (1.17)$$

The open-circuit voltage increases with the radiative recombination efficiency  $\eta_r$ . In a real solar cell there might be a photonic loss due to the non-radiative recombination of carriers via crystal defects which leads to a decrease in  $V_{oc}$ . There might also be an optical loss at the rear surface of the cell. These unfavorable circumstances lead to a degradation of efficiency.

The fill factor (FF) of a solar cell is empirically determined by [14]:

$$FF = \frac{q V_{oc} - k_B T_c \ln[(q V_{oc} / k_B T_c) + 0.72]}{q V_{oc} + k_B T_c}. \quad (1.18)$$

If the solar cell is short-circuited, the current density  $J_{sc}$  can be obtained from the cell as given by Equation (1.15). The value of  $J_{sc}$  in a non-idealistic solar cell is less than that given

by Equation (1.15) above because the minority carriers generated in the semiconductor are not collected completely; they are partly lost due to their short diffusion length before arriving at the interface of the pn-junction (see Section 1.2.5). An optical loss due to reflection of solar radiation at the incident surface also causes a decrease in  $J_{sc}$ .

The efficiency  $\eta$  of the solar cell is defined as the product of the open-circuit voltage  $V_{oc}$ , short-circuit current density  $J_{sc}$  and fill factor FF, divided by the incident power  $P_i$  of solar radiation, that is:

$$\eta = \frac{V_{oc} J_{sc} FF}{P_i}. \quad (1.19)$$

The cell efficiency is calculated under various illumination conditions according to the above equations in the following section.

### 1.2.3 Optimal Band Gap for Solar Cells

The spectral absorbance  $A_\nu$  of the Earth's atmosphere at  $h\nu$  is defined as the natural logarithm of AM1.5D irradiance divided by AM0 irradiance. Based on the Beer–Lambert law, we first scrutinize the absorbance which is caused by the two processes predominant in a high-energy range of photons:

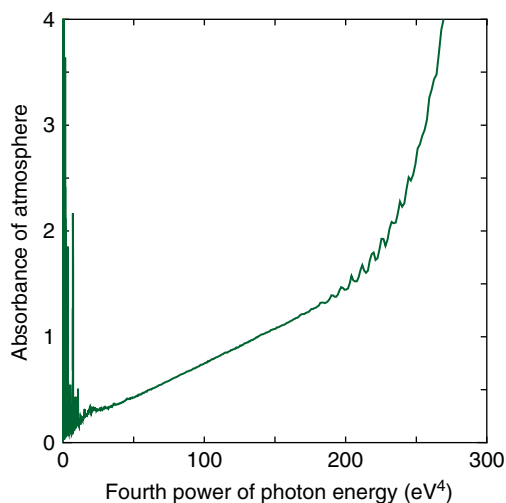
$$A_\nu \equiv \ln \left( \frac{L_{\nu, AM0}}{L_{\nu, AM1.5D}} \right) = s(\sigma_R \rho_R + \sigma_o \rho_o) = n_L (\sigma_R \xi_R + \sigma_o \xi_o), \quad (1.20)$$

where  $\rho$  is the density of gas molecules responsible for preventing rays from reaching a solar cell both fully and directly,  $\sigma$  is the cross-section of molecules, the subscript R represents air particles contributing to Rayleigh scattering [15], and the subscript o indicates the ozone molecules that absorb photons. The effective path length  $\xi$  in the right-hand side of the equation is equivalent to  $\rho d / n_L \cos\theta$  in which  $n_L$  corresponds to the Loschmidt constant  $2.69 \times 10^{25} \text{ m}^{-3}$ , that is, the density of gas molecules at 273 K and 1013 hPa. The value of  $\xi$  is estimated as 8.4 km and 3.2 mm for air and ozone molecules, respectively.

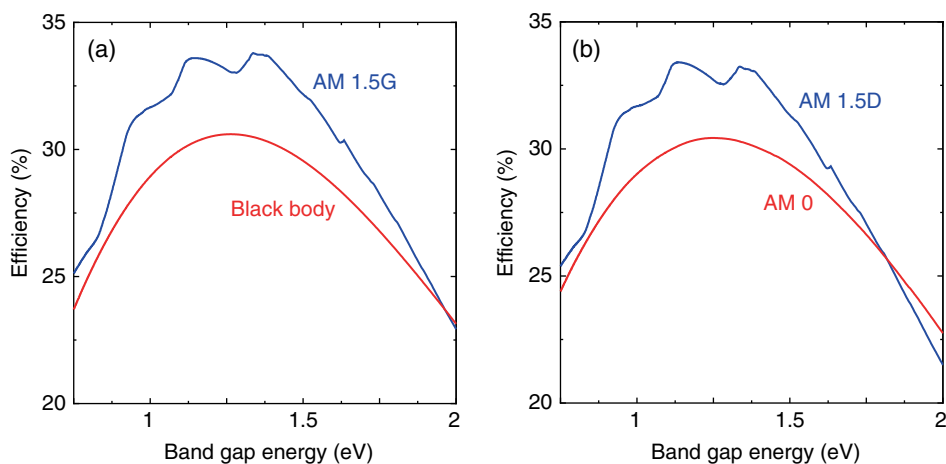
The absorbance is plotted in Figure 1.4 as a function of the fourth power of  $h\nu$ . There is a photon energy region extending from 2.5 to 3.8 eV where the spectral absorbance increases linearly as the fourth power of  $h\nu$  increases, indicating that the extra-terrestrial radiation is scattered by particles in atmospheric air, the diameter of which is much smaller than the related light wavelength [15]. Since the absorbance at  $h\nu = 2.6 \text{ eV}$  is 0.41, the cross-section  $\sigma_R$  of air is estimated as  $1.2 \times 10^{-30} \text{ m}^2$ . This value is 30% higher than that for nitrogen which was observed at the same photon energy in a laboratory [16].

Despite the fact that the effective path length  $\xi_o$  of ozone is extremely small, its absorbance at photon energy higher than 4.1 eV is predominant. A very slightly elevated broad peak of the absorbance curve centered at around 2.06 eV might be superimposed on the absorbance curve due to Rayleigh scattering and coincide with a broad peak of the cross-section  $\sigma_o$  which was observed in laboratory absorption spectra of ozone [17].

We now discuss the effect of the Earth's atmosphere on the efficiency limit. Figure 1.5 shows the theoretical efficiency of a solar cell based on a detailed balance as a function of



**Figure 1.4** Relationship between absorbance of the Earth's atmosphere and the fourth power of photon energy



**Figure 1.5** Theoretical efficiency versus band gap curves of an ideal solar cell under various radiation conditions: (a) AM1.5G and black body radiation; and (b) AM1.5D and AM0 radiation

semiconductor band gap under various radiation conditions at  $T_c = 298$  K. The radiative recombination efficiency  $\eta_r$  is assumed to be equal to 1. In other words, electrons and holes do not recombine non-radiatively, which means  $\tau_r/\tau_{nr} = 0$ . The cell under AM1.5G, AM1.5D and AM0 radiation exhibits the maximum efficiency  $\eta_{\max}$  of 33.8, 33.4 and 30.4% at band gap  $E_{g,\max}$  of 1.34, 1.14 and 1.24 eV, respectively. AM1.5G radiation includes both direct and diffuse radiation. The appearance of double peaks in the former two curves is caused by the third optical absorption band  $\rho\sigma\tau$  due to water vapor.

**Table 1.1** Effects of the Earth's atmosphere on the performance of an ideal solar cell at 298 K. Theoretical calculations for black body radiation at 5772 K are also shown for reference

Solar radiation	$\eta_{\max}$ (%)	$E_{g,\max}$ (eV)	$V_{oc}$ (V)	FF (%)	$J_{sc}$ (A m <sup>-2</sup> )	$E_{g,n}$ (eV)	$E_{g,w}$ (eV)	$P_i$ (kW m <sup>-2</sup> )
AM1.5G	33.8	1.34	1.08	89.0	351	1.06	1.50	1.00
AM1.5D	33.4	1.14	0.89	87.2	387	1.02	1.47	0.90
AM0	30.4	1.24	0.99	88.2	469	0.99	1.56	1.35
Black body	30.6	1.26	1.02	88.4	462	1.02	1.55	1.36

The curve for the cell illuminated by blackbody radiation at 5772 K is also included in the figure for reference. As far as solar cells are concerned, the black-body radiation is almost equivalent to AM0. Abrams *et al.* showed that  $\eta_{\max} = 29.83\%$  and  $E_{g,\max} = 1.34$  eV using a different formulation for black body radiation and the two characteristic values of  $T_s = 6000$  K and  $T_c = 300$  K [18]. Shockley and Queisser showed much earlier that  $\eta_{\max} = 30\%$  and  $E_{g,\max} = 1.1$  eV by adopting these characteristic temperatures [7]. The latter value (1.1 eV) is significantly lower than that calculated by the former authors and implied that the silicon crystal, an indirect semiconductor, could be the most suitable material for solar cells. If we adopted these two characteristic temperatures instead of  $T_s = 5772$  K and  $T_c = 298$  K (see Table 1.1), this would yield  $\eta_{\max} = 31.03\%$  and  $E_{g,\max} = 1.304$  eV. The small discrepancies between the estimations made by Abrams *et al.* and the current authors are due to a difference in approximations used.

The characteristic parameters under these four types of radiation are summarized in Table 1.1. The band gap which makes it possible for cell efficiency to exceed 95% of the maximum efficiency  $\eta_{\max}$  ranges from the narrow end  $E_{g,n}$  of 1.06 eV to the wide end  $E_{g,w}$  of 1.50 eV under AM1.5G. It is quite interesting that CZTS and an alloy,  $\text{Cu}_2\text{ZnSn}(\text{S},\text{Se})_4$  (abbreviated as CZTSSe), possess the band gaps within this range. The values of  $E_{g,\max}$ ,  $E_{g,n}$  and  $E_{g,w}$  shown above agree very well with those reported by Yablonovitch *et al.* [8]. Under AM1.5D,  $E_{g,\max}$  and  $E_{g,w}$  are significantly smaller than under AM0, indicating that the photon number in high-energy spectra is decreased by Rayleigh scattering. The significant blue shift of  $E_{g,\max}$ , which is theoretically predicted above when solar radiation is switched from AM1.5D to AM1.5G, is solely due to this scattering. The band gap of 1.56 eV is still optimal for extra-terrestrial applications of a solar cell, but not for terrestrial applications. Since high-energy photons scattered by air can be partly incident on a solar cell under AM1.5G, cell efficiency with a band gap wider than 1.1 eV is always higher than that under AM1.5D. Consistent with Rayleigh scattering, the relative difference between the two becomes large as the band gap is increased to 3.5 eV.

When a band gap is as wide as 4 eV, incident photons terrestrially available for the excitation of electron-hole pairs are reduced both due to Rayleigh scattering by air and optical absorption by ozone, virtually leading to the loss of the entire photovoltaic effect. If a cell is used under an extra-terrestrial condition, the short-circuit current density would approach zero quite rapidly as  $E_g$  increases further because, under black body radiation, it is defined:

$$J_{sc} = \frac{2qk_B T_s E_g^2 \Omega_s}{h^3 c^2} \exp\left(-\frac{E_g}{k_B T_s}\right). \quad (1.21)$$

As the band gap is decreased from 4 eV however, the efficiency under AM1.5D and AM1.5G rises rather steeply and exceeds that under AM0 radiation. This is explained by the fact that in the former two cases energy loss caused by excess photon energy ( $h\nu - E_g$ ) is smaller than in the latter case, and the contribution of the high-energy photons to total incident power is reduced by the presence of air and ozone. The optical absorption by oxygen molecules and the first two absorption bands due to water vapor do not have any significant effect on efficiency.

As the band gap decreases further, cell efficiency falls because the open-circuit voltage decreases. This tendency is amplified when the band gap falls within the energy range of a strong absorption band due to water vapor: the open-circuit voltage drops rapidly as the dark current increases while the short-circuit current density remains almost constant, resulting in a few dips or cliffs in the  $\eta$  versus  $E_g$  curve. At AM1.5D and AM1.5G the efficiency drops by 5% because of the  $\Omega$  absorption band. Direct sunlight, which is most likely represented by AM1.5D radiation, can be concentrated by lenses or mirrors. Using a 100 $\times$  concentrator, for example, we are able to collect solar radiation as if the distance between the Earth and the Sun were made 10 times shorter. As described in Equations (1.2), (1.3) and (1.15), the solid angle  $\Omega_s$  and  $J_{sc}$  become 100 times larger, and consequently  $V_{oc}$  and FF increase, contributing to the enhancement of cell efficiency. It is desirable to avoid the use of the semiconductor band gap coinciding with an absorption band such as the  $\Omega$  band, particularly when the multi-junction solar cell is designed for a concentrated solar power system. Sağol *et al.* showed that the four-junction solar cell with theoretical efficiency 62% could be limited to 59% at best if the band gap of the bottom cell is between 0.8 and 0.9 eV [19].

If the band gap of a semiconductor approaches zero, and hence the semiconductor becomes a nearly perfect black body kept at  $T_c$ , the open-circuit voltage of the cell based on a detailed balance would exhibit the ultimate open-circuit voltage given by:

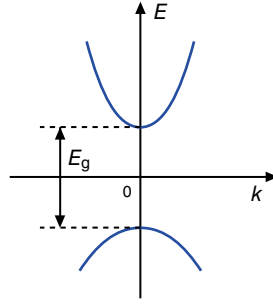
$$V_{oc,u} = \frac{k_B T_c}{q} \ln \left[ \eta_r \left( \frac{r}{R} \right)^2 \left( \frac{T_s}{T_c} \right)^3 + 1 \right]. \quad (1.22)$$

Using the five parameters mentioned before,  $V_{oc,u}$  is evaluated as 3.7 mV. The cell might therefore be useful for measuring the effective temperature of the Sun but is a poor quantum energy converter, with an ultimate efficiency of 0.07%.

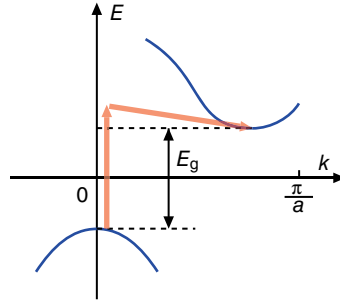
### 1.2.4 Optical Absorption in Semiconductor Thin Films

A semiconductor such as CZTS has the direct forbidden band gap  $E_g$  shown in Figure 1.6. Electrons at the top of the valence band have the maximum energy when their crystal momentum, that is, the wave number  $k$  multiplied by the Planck constant  $h$  divided by  $2\pi$ , is equal to zero. By shedding light on the p-type semiconductor at photon energy of  $E_g$ , the valence electrons are excited from the top of the valence band to the bottom of the conduction band, generating holes in the valence band and an equal amount of minority carriers (electrons) in the conduction band. Since the conservation law of momentum is satisfied in this direct transition, optical absorption proceeds without difficulty. After electrons are injected to the conduction band, they recombine with the majority carriers (holes) to emit light within their short lifetime  $\tau_r$ . The situation is quite different in an indirect gap semiconductor such as Si. Figure 1.7 demonstrates how an electron excited to the conduction





**Figure 1.6** E v. k curve of a direct band gap semiconductor



**Figure 1.7** E v. k curve of an indirect band gap semiconductor

band minimum has a crystal momentum which is nearly equal to  $\pi$  divided by the lattice constant  $a$  of silicon, while a hole in the valence band has momentum equal to zero. In order to fulfill the momentum conservation before and after the indirect transition, the third particle must participate such that a phonon with a wavelength of  $2a$  is emitted: the light wavelength pertaining to solar cells is much longer than  $2a$ . The radiative recombination lifetime  $\tau_r$  is therefore very long in silicon. The high absorption coefficient and the large bimolecular recombination coefficient of a direct gap semiconductor make it easier to enhance the energy conversion efficiency of a thin-film solar cell.

Table 1.2 shows the photovoltaic characteristics of two types of highly efficient solar cell measured at AM1.5G and 298 K. One consists of a thin film of epitaxial lift-off (ELO) GaAs [20, 21] while the other comprises a bulk silicon crystal with a hetero-junction with intrinsic thin layer (HIT) structure [22–25]. The number in parentheses is the ratio of the measured value to the theoretical value calculated under the above conditions and the assumption that  $\tau_r/\tau_{nr}=0$  or  $\tau_{nr}=\infty$ . It should be noted that the former cell achieved 96% of the theoretical open-circuit voltage whereas the latter achieved 85%. The higher achievement ratio in the former could be attributed to the much shorter  $\tau_r$  of GaAs than that of Si. The absorber region of the two solar cells is sandwiched by wide-gap semiconductors, where the hetero-structure is considered effective in reducing the recombination velocity at the interface. Both efficient solar cells share the tendency according to which the open-circuit voltage is a decreasing function of absorber thickness; however, the physics governing each cell is quite different as the discussion in the next section reveals.

**Table 1.2** Device characteristics of GaAs and Si solar cells: a comparison between theoretical and experimental

Absorber	$E_g$ (eV)	$\eta$ (%)	$V_{oc}$ (V)	$J_{sc}$ (A m <sup>-2</sup> )	Sources
Epitaxial GaAs thin film	1.43 direct	28.8 (0.87)	1.122 (0.961)	296.8 (0.938)	Alta Devices
Theoretical		33.2	1.168	316.3	This book
n-type Si single crystal 98 $\mu$ m thick	1.12 indirect	24.7 (0.74)	0.750 (0.854)	395 (0.902)	Panasonic
Theoretical		33.6	0.878	437.8	This book

The absorption coefficient of a direct-gap semiconductor is defined [9, 10]:

$$\alpha = \alpha_0 \sqrt{\frac{h\nu - E_g}{E_g}}. \quad (1.23)$$

Only photons with energy higher than or equal to  $E_g$  can excite the valence electrons and the absorption coefficient increases with photon energy. The absorption coefficient  $\alpha$  at  $h\nu = 2E_g$  is equal to  $\alpha_0$ . According to the van Roosbroeck–Shockley relation for carrier recombination [26], the factor  $\alpha_0$  is proportional to the bimolecular recombination coefficient  $B$ . As discussed in the next section, the higher the value of  $\alpha_0$  the shorter the radiative lifetime, the smaller the dark saturation current density, and hence the higher the open-circuit voltage. If the semiconductor is a thin film of thickness  $t$  whose rear side has a perfect reflector and there is no reflection at the front surface, the intensity  $I$  of light escaping from the front is expressed:

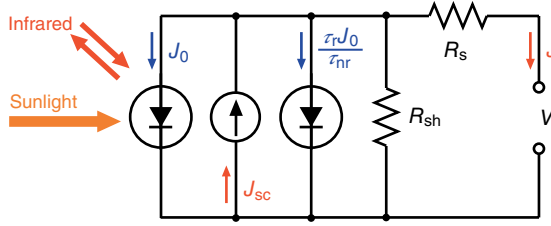
$$I = I_0 \exp(-2\alpha t) \quad (1.24)$$

where  $I_0$  is the intensity of incident light. For example, for a value of  $\alpha_0$  of  $5 \times 10^4 \text{ cm}^{-1}$  and  $h\nu$  of  $1.16E_g$ , with a thickness of  $1.7 \mu\text{m}$  the light intensity absorbed in the film could reach 99.9% of  $I_0$ . This is a rough estimate of the thickness theoretically required for the optical absorber layer of a CZTS thin-film solar cell. In the indirect-gap semiconductor of Si however, the value of  $\alpha_0$  is as small as  $1 \times 10^3 \text{ cm}^{-1}$  and the absorption coefficient is proportional to the square of  $(h\nu - E_g)$ . According to the same estimate as above, a  $130 \mu\text{m}$  thick silicon crystal is required for the absorber.

### 1.2.5 Semiconductor pn-Junctions

As far as the ideal solar cell which works under the principle of detailed balance is concerned, the electric current  $J$  which is supplied from the unit area cell to a load can be expressed:

$$J = J_{sc} - J_d \left[ \exp\left(\frac{qV + qR_s J}{k_B T_c}\right) - 1 \right] - \frac{V + R_s J}{R_{sh}}, \quad (1.25)$$



**Figure 1.8** Equivalent circuit model for an idealized solar cell

where  $V$  is the voltage drop of the load,  $R_s$  is the series resistance,  $R_{sh}$  is the shunt resistance of the diode, and  $J_d$  is the dark current density of the cell, defined

$$J_d = \left( 1 + \frac{\tau_r}{\tau_{nr}} \right) J_0 = \left( 1 + \frac{\phi}{B n_0 \tau_{nr}} \right) J_0. \quad (1.26)$$

Equation (1.25) agrees with Equation (1.17) when  $R_s$  is zero and  $R_{sh}$  is infinite. The equivalent circuit of the cell could therefore be drawn as in Figure 1.8. The circuit model defines  $J_d$  as the saturation current density in the dark which would be obtained if the pn-junction diode is biased backward ( $V < 0$ ) and  $R_{sh}$  is infinitely large. Since solar cells of course operate under forward bias,  $J_d$  actually represents the pre-exponential factor of the forward current at a large bias. The value of  $J_d$  is the sum of two components. One is the current density  $J_0$  which is determined by detailed balance and the other is the component which is proportional to the ratio  $\tau_r/\tau_{nr}$ . This ratio is one of the key parameters in obtaining an ideal solar cell because the smaller the value of the ratio, the higher the open-circuit voltage. In an ideal solar cell,  $\tau_r/\tau_{nr}$  is equal to zero because there is no indirect recombination.

We next discuss whether the detailed balance model may be applied to the ELO thin-film GaAs or the HIT Si solar cell. Consider a device structure whose base is an n-type semiconductor with the electron concentration  $n_0$ . The inherent radiative lifetime  $\tau_r/\phi$  of GaAs (Si) is estimated to be 50 ns (4.2 ms) by assuming that  $n_0$  is  $1 \times 10^{23}$  ( $5 \times 10^{22}$ )  $\text{m}^{-3}$ , and the bimolecular recombination coefficient  $B = 2 \times 10^{-16}$  ( $4.73 \times 10^{-21}$ )  $\text{m}^3 \text{s}^{-1}$ . Using the theoretical dark current density,  $J_0 = 5.6 \times 10^{-18}$  ( $6.1 \times 10^{-13}$ )  $\text{A m}^{-2}$  and experimentally observed  $V_{oc}$  and  $J_{sc}$  of GaAs (Si) solar cells shown in Table 1.2, the ratio of  $\tau_r/\tau_{nr}$  is estimated to be 4.6 (133).

The SRH lifetime in an n-type GaAs double hetero-structure is 63.5 ns [11]. Because this value should be comparable to  $\tau_{nr}$ , the photon recycling factor  $\phi$  is considered equal to 5.9. If the  $J$ - $V$  curve of the GaAs solar cell were governed by carrier diffusion instead of detailed balance, under the no-surface-recombination assumption, the dark saturation current density would be defined [27]:

$$J_0 = \frac{qDp}{L} \tanh\left(\frac{t}{L}\right) = \frac{qn_i^2}{n_0} \sqrt{\frac{D}{\tau}} \tanh\left(\frac{t}{L}\right) \quad (1.27)$$

where  $D$  is the diffusion coefficient of holes to which Einstein's relation  $D = \mu k_B T_c / q$  links hole mobility  $\mu$ ,  $\tau$  is the total recombination lifetime,  $L$  is the diffusion length of holes which is equal to the square root of  $D\tau$ , and  $t$  is the thickness of the absorber layer. If  $L$  is

much smaller than  $t$ , the Shockley equation for a pn-junction diode can be derived from Equation (1.27) since the hyperbolic tangent is nearly equal to one. However,  $L$  is actually larger than  $t$  according to the device parameters cited above.  $J_0$  is therefore defined:

$$J_0 = \frac{qpt}{\tau}. \quad (1.28)$$

The dark current is equivalent to the electric current which would flow if all of the holes accumulated at one edge of the n-type absorber adjacent to the p-type emitter diffuse to the other edge in their lifetime. The value of  $J_0$  calculated as above is  $4 \times 10^{-16} \text{ A m}^{-2}$ , which is two orders of magnitude larger than the theoretical value estimated by assuming the detailed balance model and  $\tau_r/\tau_{nr} = 0$ . The open-circuit voltage of 1.055 V is theoretically deduced from the calculated value of  $J_0$ . The experimentally observed voltage is therefore 0.067 V higher than the theoretical voltage shown in Table 1.2. This amount of discrepancy can never be explained reasonably. If the Shockley equation did hold, the open-circuit voltage would have become even lower ( $\approx 1.00 \text{ V}$ ). The current transport through the ELO GaAs junction is therefore controlled by detailed balance rather than carrier diffusion. The radiative lifetime  $\tau_r$  is proportional to the photon recycling factor  $\phi$ . As the thickness of the absorber layer increases, it is expected that  $\phi$  increases [11] and the open-circuit voltage  $V_{oc}$  decreases. In order to improve  $V_{oc}$  it is important to diminish surface recombination, in which minority carriers recombine via interface states without light emission. At the same time, it is necessary to reduce the re-absorption of photons caused by recycling of the confined photons.

Another issue to be addressed is the question of whether or not the high value of  $\tau_r/\tau_{nr}$  ( $\approx 133$ ) estimated for the Si solar cell on the basis of detailed balance is plausible. Since the absorption coefficient of Si is very low in contrast to a direct semiconductor,  $\phi$  could not become significantly larger than 1. A value of  $\tau_{nr} = 32 \mu\text{s}$ , which could be estimated using the experimental data and Equation (1.26), is too short to be consistent with the SRH lifetime of 0.5–1 ms in the Si crystal used. The detailed balance model is not an appropriate theory to explain why  $V_{oc}$  is improved in the HIT silicon solar cell. According to the device parameters of the cell, the diffusion length (0.9 mm) of holes is much larger than the thickness of the n-type Si base (0.098 mm). Equation (1.28) subsequently holds and the holes carry the dark current from one edge of the base adjacent to a p-type  $a\text{-Si:H}$  layer to the other edge. The open-circuit voltage is therefore:

$$V_{oc} = \frac{k_B T_c}{q} \ln \left( \frac{\tau J_{sc}}{qpt} \right) = \frac{E_g}{q} - \frac{k_B T_c}{q} \ln \left( \frac{q N_c N_v t}{J_{sc} n_0 \tau} \right). \quad (1.29)$$

The open-circuit voltage increases by  $k_B T_c / q$  ( $\approx 25.7 \text{ mV}$  at 298 K) as the thickness  $t$  (lifetime  $\tau$ ) of the absorber crystal decreases (increases) by a factor of 2.72, in crude agreement with experimental data [24, 25]. The performance of this type of solar cell is therefore best explained by diffusion theory in which base thickness is smaller than minority carrier diffusion length.

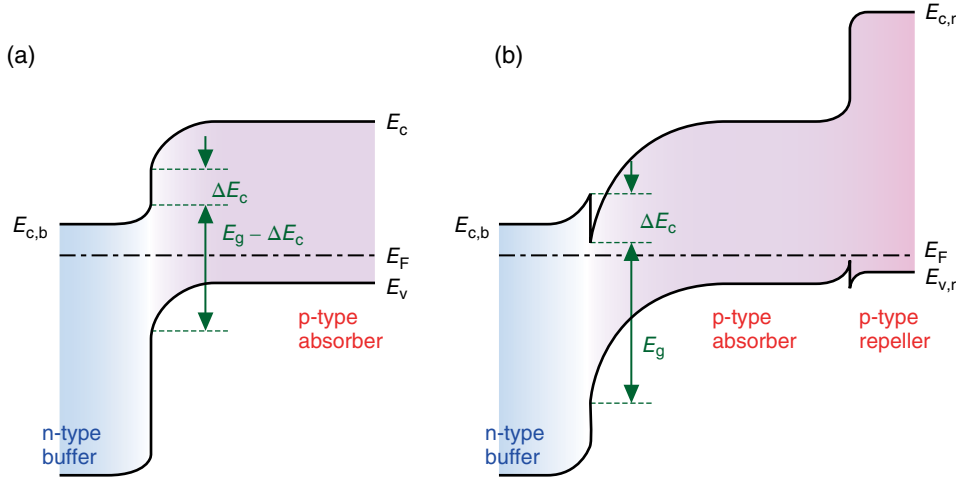
The open-circuit voltage of real solar cells is empirically given by:

$$V_{oc} = \frac{E_a}{q} - \frac{\eta_D k_B T_c}{q} \ln \left( \frac{J_{00}}{J_{sc}} \right). \quad (1.30)$$

Based on earlier discussions we are able to evaluate these parameters for the ideal solar cell: the activation energy as  $E_a = E_g$ , the diode factor as  $\eta_D = 1$ , and the pre-factor  $J_{00}$  of the diode current density as weakly temperature-dependent (see Equations (1.16) and (1.27) or (1.29)). The theoretical difference  $\Delta w$  between  $E_g/q$  and  $V_{oc}$  is a slightly increasing function of  $E_g$  as mentioned below. In the non-ideal solar cell,  $E_a$  is less than  $E_g$  depending on the type of hetero-junction, and  $\eta_D$  is between 1 and 2 depending on recombination mechanism of carriers. Todorov *et al.* reported that a CZTSSe polycrystalline thin-film solar cell with a diode factor  $\eta_D$  of 1.5 exhibits  $E_a$  (=1.06 eV) which is slightly lower than  $E_g$  (=1.13 eV) [1, 2]. The relation  $E_a \approx E_g$  was observed not only in Cu(In,Ga)(S,Se)<sub>2</sub> polycrystalline thin-film solar cells [28] but also in solution-grown mono-crystalline Si solar cells [29].

When the carrier recombination at the space charge region of the junction is predominant and its recombination centers are located in the middle of the energy gap, we have the following relations:  $E_a = E_g$ ,  $\eta_D = 2$  and  $J_{00} = q t_d \sqrt{N_c N_v} N_t \sigma_p v_{th} / 2$  where  $t_d$  is the width of a depletion (space charge) region [30]. This type of current-voltage characteristic was observed experimentally in a junction between p-type Si<sub>0.92</sub>Ge<sub>0.08</sub> and n-type Si in the dark [31]. The alloy layer was grown on the (111) face of the Si substrate. We used liquid-phase epitaxial growth in an alumina crucible containing aluminum as a solvent. The lattice misfit of the junction was 0.34%, giving rise to the dangling bond density of  $5.5 \times 10^{12} \text{ cm}^{-2}$ . The value of  $J_d$  was  $7 \times 10^{-8} \text{ A cm}^{-2}$ , which was two orders of magnitude larger than that of the junction with a misfit equal to 0.01%. The increase in the dark current of the diode is attributable to that in the density  $N_t$  of SRH recombination centers originating from the dangling bonds: the band gap shrinkage due to the alloy is too small ( $\approx 0.03 \text{ eV}$ ) to explain the increase in  $J_d$ .

A photovoltaic device usually contains a metallurgically intimate junction between the p-type semiconductor and the n-type counterpart consisting of the same material. Either one of the semiconductors is heavily doped with shallow impurities such that its spreading resistance is low enough for  $R_s$  to be made negligibly small, and hence fill factor is improved. Since an absorber layer such as CZTS, CZTSSe, CuInS<sub>2</sub> (abbreviated CIS) and Cu(In,Ga)Se<sub>2</sub> (abbreviated CIGSe) can only be obtained as a p-type semiconductor, a different semiconductor with n-type conductivity and wide band gap is utilized to prepare a pn-hetero-junction for photovoltaic applications. Figure 1.9 shows the two types of hetero-junction. In the staggered gap (type II) hetero-junction shown in Figure 1.9(a), photo-excited electrons gain energy due to an energy cliff  $\Delta E_c$ . Electrons recombine with holes at the interface as if the absorber has a narrow band gap of  $E_g - \Delta E_c$ . Therefore,  $qV_{oc}$  extrapolated to 0 K is decreased from  $E_g$  to  $E_a = E_g - \Delta E_c$  when the interface recombination is a predominant mechanism to determine the dark current of the hetero-junction. This band structure is not effective for confining the minority carriers in the absorber, resulting in the decrease of open-circuit voltages. In the straddling gap (type I) hetero-junction shown in Figure 1.9(b) there is an energy spike  $\Delta E_c$  in the conduction band. The minority carriers (electrons) in the p-type absorber layer need energy to move from there to the buffer/window layer. The electrons might recombine with holes via interface states. If we want to reduce the dark current and enhance the open-circuit voltage, we have to reduce the interface state density. One more hetero-junction is implemented on the opposite side so that the conduction band spike of a p-type wide-gap semiconductor, which is equivalent to an electric field accelerating the backward electron motion, can prevent excited electrons from recombining at the hetero-interface.



**Figure 1.9** Band diagram of *pn*-hetero-junction solar cells in thermal equilibrium: (a) staggered (type II) hetero-junction; and (b) straddling (type I) hetero-junction to which one more straddling *pp*<sup>+</sup>-hetero-junction is added to form a double hetero-structure

It is well known that by employing a double hetero-structure the external efficiency of a light-emitting diode can be improved and the threshold current of laser diodes decreased [10]. As depicted in Figure 1.9(b), the iso-type (*pp*) hetero-junction is placed on the opposite side of the aniso-type (*np*) hetero-junction emitter using a high-quality wide-gap semiconductor. Minority carriers, which are electrons in the case of a *p*-type base, could be repelled by the back surface field of the former hetero-junction so that their non-radiative recombination at the interface is avoided. Both minority carriers and photons are confined in the base region because the base region is surrounded by energy barriers and optical media of low refractive index. The beneficial effect of the hetero-structure was verified in a few thin-film solar cells [32]. These cells employ a graded double hetero-structure; on the other hand, ELO technology employs an abrupt double hetero-junction. Very recently Kato *et al.* achieved a 9.2% efficiency CZTS sub-module with aperture area of 14 cm<sup>2</sup> [33]. The CZTS thin film was prepared using the two-step process described in the following section. The open-circuit voltage was 0.708 V; segregation of ZnS at the back surface of the absorber layer was found to be beneficial. Although the specific effect of the segregation remains unknown, it was explained in terms of a back surface field.

If the ratio  $\tau_i/\tau_{nr}$  decreases as non-radiative life time  $\tau_{nr}$  increases, the open-circuit voltage could increase due to relatively infrequent non-radiative recombination in an absorber. In other words, if a dark saturation current density  $(\tau_i/\tau_{nr})J_0$  which is generated by the bypass current source shown in Figure 1.8 decreases, the open-circuit voltage could increase. From this viewpoint, the cell performance could be improved by: (1) employing the absorber layer with an optimal band gap and high bimolecular recombination coefficient, that is, high absorption coefficient; (2) removing the recombination centers from the absorber and its interfaces as far as possible; (3) decreasing the absorber thickness without sacrificing the absorbance of the layer appreciably in order to keep the photon recycling factor low; and (4) increasing the majority carrier concentration without sacrificing SRH/

Auger lifetime appreciably. It should be noted that conditions (1) and (3) in particular are not satisfied if an indirect semiconductor is used. Condition (4) should be optimized at an appropriate doping concentration of shallow impurities. It was found by Redinger and Siebentritt that the total photoluminescence yield is higher for high-quality CZTSe absorbers (Chapter 16). Their finding can be interpreted in terms of re-emission of radiation discussed above, because the re-emission probability increases with a decrease in the density of a defect such as SRH recombination centers.

We consider the case where the monochromatic light flux  $\Phi_0$  of photon energy  $h\nu$  is incident on the top surface of a hetero-junction solar cell [34]. The cell consists of an n-type window (p-type absorber) layer with a thickness of  $t_n$  ( $t_p$ ) and an absorption coefficient of  $\alpha_n$  ( $\alpha_p$ ). Let us place the origin ( $x=0$ ) of the one-dimensional (1D) coordinate system at the pn-hetero-junction interface. The photon flux  $\Phi(x)$  at  $x>0$  in the absorber layer is given by

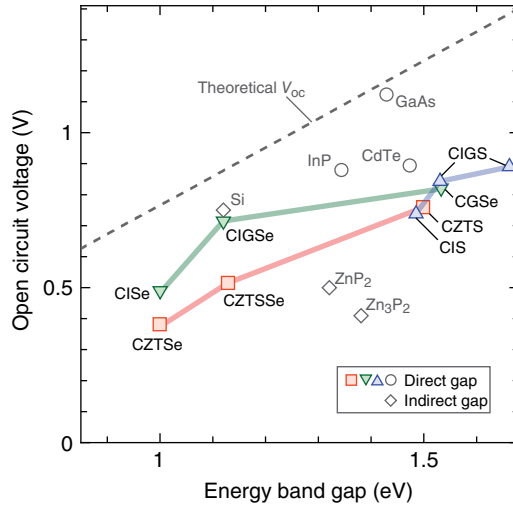
$$\Phi(x) = \Phi_0 \exp(-\alpha_n t_n - \alpha_p x). \quad (1.31)$$

Since the mobility and diffusion length  $L$  of minority carriers are limited in non-idealistic cells, the photons which are absorbed deep inside the thick absorber cannot be easily collected by the junction. By considering that the generation rate of electrons is given by  $\alpha_p \Phi(x)$  and only the fraction  $\exp(-x/L)$  of the minority carriers can contribute to the photo-current, internal quantum efficiency  $\eta_q$  – defined by the ratio of photo-current density to the incident photon flux  $\Phi_0$  multiplied by  $q$ – is given by:

$$\begin{aligned} \eta_q &= \exp(-\alpha_n t_n) \int_0^{t_p} \Phi_0 \exp(-x/L) \exp(-\alpha_n t_n - \alpha_p x) dx / \Phi_0 \\ &= \frac{\alpha_p L}{\alpha_p L + 1} \left[ 1 - \exp\left(-\frac{\alpha_p L t_p + t_p}{L}\right) \right] \exp(-\alpha_n t_n). \end{aligned} \quad (1.32)$$

The internal quantum efficiency  $\eta_q$  is an increasing function of diffusion length  $L$ , absorption coefficient  $\alpha_p$  and absorber thickness  $t_p$ . When photon energy  $h\nu$  is much higher than the energy band gap,  $\eta_q$  is nearly equal to  $\exp(-\alpha_n t_n)$ . To reduce the photon loss in the window layer, particularly in a high-energy range, the window layer must be thin enough and have a wide band gap. On the other hand, it becomes proportional to  $\alpha_p L$  and approaches 0 as  $h\nu$  decreases to the value of band gap. In this case, the carrier scattering by lattice defects such as impurities, vacancies, interstitials and so on reduces the internal quantum efficiency and hence the short-circuit current density. The drawback could be alleviated by the improvement of crystal quality or the passivation of crystal defects. By measuring the internal quantum efficiency at slightly higher photon energy than the band gap, we can evaluate the diffusion length and consequently the quality of the absorber layer.

Figure 1.10 shows the theoretical and experimental relationship between the open-circuit voltage of a solar cell and the band gap of the semiconducting absorber. The values of open-circuit voltages observed among highly efficient solar cells are collected from this chapter and other references [33–38]. The upper curve is the theoretical curve at 298 K under AM1.5G radiation, which is calculated by assuming that the solar cell is ideal ( $\tau_i/\tau_{nr}=0$ ) as described before. With the increase of the band gap within the optimal range (from  $E_{g,n}=1.06$  to  $E_{g,w}=1.50$  eV), the open-circuit voltage is almost linearly increased from 0.823 to 1.237 V and their theoretical difference  $\Delta w$  is slightly increased from 0.239 to 0.268 V. The lower, right



**Figure 1.10** Relation between open-circuit voltage and energy band gap of an ideal photovoltaic cell and various solar cells

middle and left middle line plots represent the relationships for CZTSSe, Cu(In,Ga) $S_2$  (abbreviated CIGS) and CIGSe alloy and related thin-film solar cells, respectively. The first curve shows that the open-circuit voltage of S-lean alloy thin-film solar cells tend to increase with the band gap parallel to the theoretical curve, whereas that of a CZTS thin-film solar cell is lower than expected from this tendency. Wang *et al.* obtained the open-circuit voltage of 0.513 V at a band gap of 1.13 eV in CZTSSe thin-film solar cells [2], which is lower than the theoretical value by 0.374 V as shown in the figure. In contrast, the effect of a cation substitution is quite obvious in the third line plot. The distance between the theoretical curve and the plot is smallest at  $E_g = 1.12$  eV for Ga-lean CIGSe thin-film solar cells. It is difficult to dope p-type CIGSe alloys with shallow donor impurities when the Ga content becomes large [39]. This might be one of the reasons that the difference  $\Delta w$  increases significantly as the band gap increases [34]. Another possible explanation is that the energy spike of the conduction band at the CdS/CIGSe hetero-junction interface becomes too large [40] or tetragonal distortion increases as discussed in the following. The open circles (rhombuses) which are shown in the figure represent direct (indirect) gap semiconductors: they are mono-crystalline InP, GaAs and CdTe (mono-crystalline Si,  $ZnP_2$  and polycrystalline  $Zn_3P_2$ ), in ascending order of band gap.

In the following section, we show how CZTS technology was conceived while pursuing an optimal absorber material for photovoltaics.

### 1.3 In Pursuit of an Optimal Semiconductor for Photovoltaics

#### 1.3.1 Mono-Crystalline Semiconductor with Optimal Band Gap

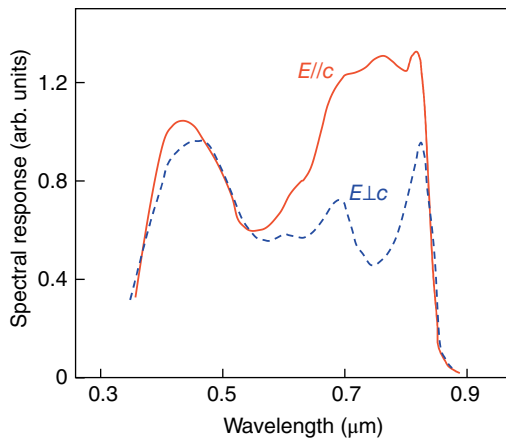
In the late 1960s I was interested in growing InP single crystals for various electronic device applications. The epitaxial layers were prepared by chemical vapor deposition and then the bulk single crystals were grown by a temperature gradient method. All the



non-doped InP crystals had n-type conductivity. I noticed that the point contact diodes which consist of the p-type single crystals doped with Zn or Cd exhibit better rectification than the n-type single crystals in the dark. Since the dark current–voltage curve of a solar cell is directly related to the illuminated curve, it is no accident that the efficient hetero-junction solar cells described in the following section always have p-type absorbers.

#### 1.3.1.1 Zinc Phosphide

Zinc phosphides, which are known to exhibit polymorphism, are semiconducting compounds. Bhushan and Catalano first suggested  $\text{Zn}_3\text{P}_2$  as a promising photovoltaic material because of its “direct” band gap and mineralogically abundant constituents, and derived a solar cell with 6% efficiency using a polycrystalline  $\text{Zn}_3\text{P}_2$  Schottky barrier [41]. However, Kimball *et al.* reported recently that the conduction band edge  $E_c$  of the compound is located at 1.38 eV above the valence band edge  $E_v$  but the electron transition is of indirect nature [42]. They also fabricated solar cells consisting of bulk  $\text{Zn}_3\text{P}_2$  poly-crystals, which exhibited an efficiency of 4.5% and open-circuit voltage of 0.41 V [43, 44]. The earliest report motivated our research and we began the search for new and abundant photovoltaic materials. Our first attempt was to study the photovoltaic effect of monoclinic  $\text{ZnP}_2$  single-crystal platelets [45]. They were grown in a vacuum-sealed quartz ampoule using a two-zone Globar furnace. A hetero-junction was formed between a transparent conductive n-type  $\text{In}_2\text{O}_3$  thin film and the p-type  $\text{ZnP}_2$  crystal. The open-circuit voltage of the hetero-junction was 0.275 V and the saturation current density in the dark was  $6.8 \times 10^{-7} \text{ A cm}^{-2}$ . Känel *et al.* improved the open circuit voltage to 0.5 V using an electrolyte liquid junction [46]. Figure 1.11 shows the spectral photo-response of our hetero-junction. In a wavelength range of c.  $0.76 \mu\text{m}$ , we observed higher photo-response for  $E//c$  (the electric vector  $E$  of plane-polarized light parallel to the  $c$ -axis of the monoclinic crystal) than  $E \perp c$  (that perpendicular to it). This higher response agrees fairly well with the higher absorption coefficient due to an allowed direct band gap which was recently reported by Morozova *et al.* [47]. However, the lowest energy required for the indirect transition of electrons from  $E_v$  to  $E_c$  is



**Figure 1.11** Spectral photo-response of an  $\text{In}_2\text{O}_3/\text{ZnP}_2$  hetero-junction cell

equal to 1.32 eV. The narrow peak observed at 0.83  $\mu\text{m}$  for  $E_{\perp c}$  is most likely due to the excitonic transition in a forbidden direct band gap. The band gaps of the two zinc phosphides are within the optimal range for photovoltaic applications. However, the open-circuit voltages of the cells so far obtained are considerably smaller than those expected from the band gaps (see Figure 1.10); this is perhaps due to the indirect nature of the band gap. Another possibility is that a high interface state density ( $>10^{13} \text{ eV}^{-1} \text{ cm}^{-2}$ ) prevents barrier formation by pinning the surface Fermi level [48]. When discussing the prehistory of his successful unipolar field-effect transistor in Tokyo, Shockley asked the audience whether or not a research work ought to reach its goal straightforwardly. At first he failed in his attempt to replace a vacuum tube with a rudimentary field-effect transistor, since the high-density surface states of a germanium thin film prevented him from determining the conductivity modulation.

### 1.3.1.2 Indium Phosphide and Cadmium Telluride

First we studied the photovoltaic cell consisting of a hetero-junction between n-type CdS and p-type InP [49, 50]. Using vapor transport in a purified hydrogen gas flow, an epitaxial wurtzite CdS layer of about 10  $\mu\text{m}$  thick was deposited on the (111)A surface of mono-crystalline InP. The p-type single crystal was grown by a temperature gradient method developed in our laboratory [51]. The efficiency of the cell was limited to 4.2% due to a too-thick window layer and undesirable solid-state reaction at the hetero-interface. The open-circuit voltage  $V_{oc}$  was 0.400 V. When CdS layers were deposited on the (111)B surface,  $V_{oc}$  was decreased to 0.282 V. The latter layer was identified as a wurtzite crystal with twin faults [52]. The density  $N_t$  of recombination centers originated from the faults probably increased in comparison with the hetero-epitaxy of CdS (0001)/InP (111) A, resulting in the increase of  $J_0$  and subsequently the decrease of  $V_{oc}$ . We also fabricated an  $\text{In}_2\text{O}_3/\text{InP}$  hetero-junction solar cell with 11.6% efficiency [53]. Using reactive evaporation discussed in the following, the n-type  $\text{In}_2\text{O}_3$  window layer 0.2  $\mu\text{m}$  thick was deposited on InP (111)A face. It was later revealed that the cells were heat-resisting up to 500°C in air and had a conversion efficiency of 16.3% when the oxide films were deposited in two steps [54]. An amorphous indium oxide layer 10 nm thick was deposited first. In the next step, a polycrystalline layer about 100 nm thick was deposited on the first layer heated to 200°C [55].

Saito *et al.* fabricated highly efficient hetero-junction solar cells [56]. Their window, buffer and absorber consisted of an atom-beam-sputtered transparent conductive ZnO layer 150 nm thick, a chemical-bath-deposited CdS layer about 100 nm thick and a p-type InP single crystal (acceptor density  $2.3 \times 10^{16} \text{ cm}^{-3}$ ; crystal surface parallel to the (100) plane), respectively. The open-circuit voltage and fill factor of the ZnO/CdS/InP solar cell reached 0.750 V and 0.72, respectively, resulting in 17.4% cell efficiency which is the highest among InP solar cells with no lattice matching. Without the buffer layer, the efficiency deteriorated to 10.6% mainly due to a decrease in short-circuit current and fill factor. This was probably caused by sputter damage to the InP single crystal and the subsequent formation of a dead region because the spectral photo-response decreases with a decrease in wavelength. It is known that the surface of the p-type InP is converted to n-type by the bombardment of high-energy sputter gas particles [57]. It was verified that a wurtzite-type CdS buffer layer is superior to a zinc-blende-type buffer layer as a window material (see

subsection 1.3.2). The former exhibited a decay of the response at the wavelength of 470 nm and the latter at 500 nm. When the thickness of the former CdS buffer layer under the ZnO window layer was increased from 45 to 240 nm, the first derivative of the inverse square of diode capacitance  $C$  with respect to bias voltage  $V$ , that is,  $d(C^{-2})/dV$ , was increased. The donor density in the wurtzite CdS layer is therefore considered to be reduced with an increase in thickness [34]. However, the capacitance of the cell with the zinc-blende-type layer was larger than the former and the first derivative was independent of the thickness. Keaveney *et al.* reported that their pn-homo-junction InP solar cell grown by metal organic chemical vapor deposition (MOCVD) exhibits a record efficiency of 22.0% and an open-circuit voltage of 0.878 V [58]. The inferior performance of the hetero-junction solar cell is likely attributable to a conduction band discontinuity and/or the misfit parameter of 0.31% existing between wurtzite CdS and zinc-blende InP.

Nakazawa *et al.* fabricated the 14.4% efficiency solar cell consisting of a hetero-junction between thin-film n-type  $\text{In}_2\text{O}_3$  and p-type CdTe single crystal [59]. The open-circuit voltage reached 0.892 V, which is the highest  $V_{oc}$  observed to date for CdTe-based cells. The  $\text{In}_2\text{O}_3$  layer of about 100 nm thickness was deposited directly on the (111) surface of the crystal by reactive evaporation of indium in a pure oxygen gas maintained at 0.1 Pa. During deposition the crystal was heated to 200–230°C. The layer exhibited a resistivity of  $6 \times 10^{-4} \Omega \text{ cm}$  and the optical transmittance over 80%. The solar cell was actually a buried pn-homo-junction for the following reasons. It was revealed by the measurement of a capacitance versus voltage curve that the cell has a linear graded junction in which there is an acceptor density gradient of  $3.3 \times 10^{20} \text{ cm}^{-4}$ . The acceptor density of  $6.9 \times 10^{15} \text{ cm}^{-3}$  evaluated at the edge of the depletion region with the thickness of 0.42  $\mu\text{m}$  agreed fairly well with that estimated from a Hall measurement. The spectral photo-response of the cell tended to increase with the wavelength up to 800 nm, indicating that there is a so-called dead region adjacent to the depletion region where the carrier lifetime is quite short. Diffusion of shallow donor-type impurities such as indium from the interface of the hetero-junction can be suggested as a possible reason for the formation of the buried junction. Heavy doping with shallow donors at the top surface of the p-type optical absorber is considered important to the improvement of the open-circuit voltage [34]. It should be noted that the efficient solar cell mentioned above does not need a buffer layer between the window layer and the absorber, in contrast to all the conventional hetero-junction solar cells (except for lattice-matched cells). This is explained by the fact that the reactive evaporation used does not cause any radiation damage to the absorber, as often observed in the case of sputtering.

## 1.3.2 Development of Thin-Film Solar Cells

### 1.3.2.1 History

If the aim is to mass-produce solar modules while consuming the least amount of materials, high-quality semiconducting absorbers must be utilized in *thin-film* form. It is also necessary for them to possess an optimal direct band gap.

The first CdS solar cell was studied using elevated-temperature Cu diffusion to a CdS single crystal. The p-type  $\text{Cu}_{2-x}\text{S}$  thin film thus formed on the crystal surface is believed to act as an optical absorber of the cell while the wide-gap n-type CdS crystal provides a

potential barrier to separate the electrons and holes generated in the absorber layer. A thin-film solar cell based on the same structure was developed with slightly lower efficiency than the single crystal cell. However, the thin-film cell has not been put into practical use until today due to a stability issue [48].

In 1963, Cusano reported 6% efficiency polycrystalline thin-film solar cells consisting of  $\text{Cu}_{2-x}\text{Te}$ -CdTe hetero-junctions [60]. Vapor-reacted n-type CdTe thin films were deposited on CdS:Ga, I conductively coated glass substrate. The p-type  $\text{Cu}_{2-x}\text{Te}$  was formed by treating the film in a warm cuprous ion aqueous solution. In 1969 Andirovich *et al.* reported the thin-film solar cell consisting of a hetero-junction between n-type CdS and p-type CdTe which was deposited on  $\text{SnO}_2$ -coated glass [61]. Although the efficiency of this cell was only 1% at that time, both very-high-efficiency solar cells and commercial thin-film solar modules are based on the same device structure.

In 1974, Wagner *et al.* studied infrared hetero-junction photovoltaic detectors [62]. They consisted of an n-type CdS window layer which was vacuum-deposited on a p-type  $\text{CuInSe}_2$  single crystal. In the following year, the same group reported a solar cell which had the same hetero-structure and exhibited 12% efficiency, a high value at that time [63]. In 1977 Kazmerski *et al.* developed the first thin-film solar cell consisting of  $\text{CuInSe}_2$  with an efficiency of 4–5% [64]. He also reported CIS thin-film homo-junction solar cells with 3% efficiency [65].

In 1978 Konagai *et al.* developed a 13.5% efficiency solar cell consisting of an n-type (Ga,Al)As/p-type GaAs hetero-junction [66]. The epitaxial GaAs film 30  $\mu\text{m}$  thick was deposited on a sacrificial (Al,Ga)As layer which had been grown on a reusable GaAs substrate. The former film was then peeled off from the substrate by etching the latter layer using a selective chemical etchant. The technology is now referred to as epitaxial lift-off (ELO), applied to the fabrication of the highly efficient thin-film solar cell discussed in Section 1.2.4 [20, 21].

Five types of thin-film solar cells achieved efficiency higher than 10%, as listed in Table 1.3. All of these consist of semiconductor thin films with optimal direct band gaps. They were all invented several decades ago (except for the last one) and the first three were brought into commercial use after intensive research and development efforts. Recent progress in CZTS-based thin-film solar cell technology is remarkable, despite the fact that the semiconducting properties of CZTS and its photovoltaic effect were not known of until 1988. As described in Chapter 17, Gunawan and coworkers at IBM Thomas J. Watson Research Center have succeeded in achieving over 10% efficiency CZTSSe thin-film solar cells using solution-based processing in this decade [1, 2].

**Table 1.3** Five absorber layers that have been used for thin-film solar cells with the highest efficiencies. CIGSe, CIGS and CZTSSe are abbreviations for  $\text{Cu}(\text{In,Ga})\text{Se}_2$ ,  $\text{Cu}(\text{In,Ga})\text{S}_2$ , or  $\text{CuInS}_2/\text{CuGaS}_2$  and  $\text{Cu}_2\text{ZnSn}(\text{S,Se})_4$ , respectively

Absorber	CdTe	CIGSe	CIGS	GaAs	CZTSSe
$E_g$ (eV)	1.5	1.12	1.5	1.43	1.13
Efficiency (%)	20.4	20.3	12.9, 13	28.8	12.6
Laboratory	First solar	ZSW	Sulfurcell, Shinshu U.	Alta Devices	IBM Watson Research Center

### 1.3.2.2 CIGS Thin-Film Solar Cells

In 1994, Ogawa *et al.* fabricated the 9.7% efficiency thin-film solar cell consisting of an  $\text{In}_2\text{O}_3/\text{CdS}/\text{CIS}$  hetero-junction [67]. A stacked Cu/In precursor layer was first deposited on a Mo-coated soda-lime glass substrate by vacuum evaporation and, in the next step, sulfurized at  $550^\circ\text{C}$  under the flow of a  $\text{H}_2\text{S}$ -Ar mixture gas. We call this type of preparation a two-step process, distinct from single-step co-evaporation. It was first investigated by Grindle *et al.* [68] and was subsequently employed by Uenishi *et al.* to fabricate a  $\text{ZnO}/\text{CdS}/\text{CIS}$  thin-film solar cell [69]. However, its efficiency was 3.1% at best. In the successful development described above, the absorber layer was etched in a KCN aqueous solution to remove the impurity phase of a copper sulfide from the Cu-rich ternary compound. The CdS buffer layer followed by a sputtered  $\text{In}_2\text{O}_3$  or ZnO window layer was then deposited on the etched thin film. Based on this type of process, a spin-out company called Sulfurcell launched CIS thin-film solar modules onto the market in 2005 after incubation years at Hahn-Meitner Institute [70]. This was the first module which consists of a sulfide absorber and is available commercially.

In 1997, Nakabayashi *et al.* found that the CIS absorber layer alloyed with a small amount of Ga is beneficial in improving efficiency to over 10% [71]. A Ga layer was first deposited on a Mo-coated soda-lime glass substrate. The  $1\text{ }\mu\text{m}$  thick metallic stack with a Cu/In ratio of 1.5 was then deposited on it. The whole precursor was then sulfurized. When the Ga layer was 27 nm thick, we achieved 10.5% efficiency and an open-circuit voltage of 0.717 V. Depth profiling of the film indicated that the content of Ga is highest around the film-substrate interface, which is considered effective to form a back-surface field, and then gradually decreases towards the top surface with the  $[\text{Ga}]/([\text{Ga}] + [\text{In}])$  ratio of 2%. The short-circuit current density and fill factor of a solar cell tended to decrease with increasing thickness of Ga. The long-wavelength cut-off of these cells coincided approximately with that of a cell which did not contain any Ga. The decrease in the short-circuit current density is therefore not due to the band gap widening, but possibly to the presence of secondary phases. Using a precursor consisting of a Cu/In/GaS stack, Ohashi *et al.* clarified that a single-phase CIGS layer can be obtained only if the precursor composition ratio of  $[\text{Ga}]/([\text{Ga}] + [\text{In}])$  is smaller than 0.2 [72]. It was revealed by an XPS depth profile of the alloy layer that the  $[\text{Ga}]/([\text{In}] + [\text{Ga}])$  ratio is nearly equal to zero at the very surface of the layer, but is gradually increased towards the alloy/substrate interface. In 1999 the cell efficiency was further improved to 12.3% using a rapid thermal process [73]. The process could be effective to prevent the growth of hillocks which are composed of an indium-rich compound and might cause the deterioration of cell performance. The dark saturation current density  $J_0$  of the cell was equal to  $5.4 \times 10^{-11} \text{ A cm}^{-2}$ . When the sulfurization process was performed at a low heating rate by means of a conventional electric furnace  $J_0$  was four orders of magnitude higher than the rapid thermal process, which eventually deteriorated the open-circuit voltage. In a review paper we reported the progress in CIS and CIGS thin-film solar cells at the beginning of this century [74]. It was reported by Hashimoto *et al.* that the conduction band offset of a CdS/CIS hetero-junction belongs to that of type-II hetero-junction, that is, an energy cliff  $\Delta E_c$  is formed at the interface [75]. By combining this report with another, in which the value of  $\Delta E_c$  is further increased with the content of Ga [76], one might speculate that the  $V_{oc}$  is decreased with the Ga content. On the contrary, the observed  $V_{oc}$  is enhanced by the addition of Ga, even if the amount is small. The beneficial effects of alloying described above seem to indicate that the non-radiative lifetime of

minority carriers is increased by the back-surface field. Merdes *et al.* reported recently that a cell efficiency of 12.9% was also achieved using the rapid thermal process [38]. The open-circuit voltage was 0.842 V, which is significantly higher than our data.

Goto *et al.* studied the double hetero-structure consisting of a sputtered  $\text{In}_2\text{O}_3$  window, a chemical-bath-deposited (CBD) CdS buffer, a CIS absorber and a thin  $\text{CuGaS}_2$  bottom layer to achieve 13% efficiency [77, 78]. It was found that the hetero-structure is beneficial in improving the performance of the CIS thin-film solar cell. The preparation conditions of the absorber layer were as follows. In the first step, the Ga-Cu stacked precursor layer with a [Cu] to [Ga] ratio of 1.0 and a total thickness of 240 nm was vacuum-evaporated on a Mo-coated soda-lime glass. It was then sulfurized in an  $\text{Ar}/\text{H}_2\text{S}$  mixture gas at 530 °C. The  $\text{CuGaS}_2$  layer thus formed was treated in a KCN solution to remove excess copper sulfides. In the next step, the In-Cu stacked precursor of 1  $\mu\text{m}$  thickness with a [Cu] to [In] ratio of 1.7 was deposited on the sulfide surface. An iso-type (pp) hetero-junction for the rear side of the double hetero-structure was thus formed using the same treatment as described above. This was an attempt to apply the hetero-structure to thin-film solar cells. It was also found that the structure is useful for improving the cell's adhesion to the Mo-coated substrate (the same was also true of a  $\text{Cu}(\text{In},\text{Al})\text{S}_2$  thin-film solar cell [77, 78]).

During our pursuit of photovoltaic materials described in the previous section, up until 1987 we succeeded in achieving highly efficient solar cells using semiconducting compounds containing rare elements such as In and Te. It was noted that the scarcity of the economically extractable minerals limited the power capability of the cells to a level which was much lower than the annual world electricity consumption; the possibility of replacing any of these elements with more-abundant alternatives was considered. A line from Hamlet (which we performed during my High School days) is recalled: "There are more things in heaven and earth, Horatio, than are dreamt of in your philosophy." A novel attempt to employ a quaternary semiconducting compound as an absorber was initiated. This compound can be fabricated by replacing half of the In cations in chalcopyrite CIS with Zn cations, and the other half with Sn cations.

### 1.3.3 CZTS Thin-Film Solar Cells

#### 1.3.3.1 CZTS Absorber Layer

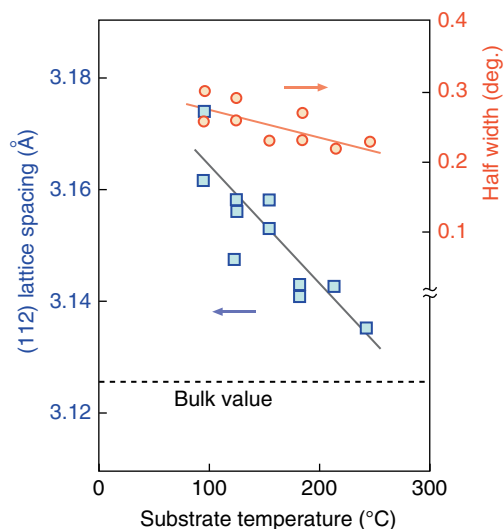
The abbreviation CZTS for the quaternary compound of copper-zinc-tin-sulfide [79] has been used by many researchers in the field. From the viewpoint of both an atomic arrangement and a band gap, the CZTS crystal is analogous to one of chalcopyrite crystals, that is, copper indium disulfide. The kesterite-type CZTS crystal could be easily derived if two indium cations in the tetragonal unit cell of a chalcopyrite-type lattice (one of them is placed in the basal plane and the other on the side line of the unit cell) are substituted for two tin cations, while the other two indium cations (they are placed in the side planes of the unit cell) are substituted for two zinc cations (see Chapter 3). On the other hand, the stannite-type CZTS crystal can be reproduced by a somewhat complicated procedure. The chalcopyrite structure is firstly transformed into a kesterite structure using the same substitution as above. Secondly, tetrahedrons consisting of  $\text{Cu}_2\text{ZnSnS}$  of the kesterite (the sulfur anion is placed at the center of the tetrahedron and surrounded by four cations) are rotated 120 degrees about a Sn-S bond axis. The rotation should be operated clockwise or

counter-clockwise so that every zinc cation can be placed at the corner and the center of the tetragonal unit cell. After the advent of the prototype CZTS thin-film solar cell, another name distinguishing it from the well-known chalcopyrite-type thin-film solar cell was sought; we named it a “stannite”-type cell because Schäfer and Nitsche identified their synthesized CZTS crystal as tetragonal, suggesting that it is isostructural to mineral stannite  $\text{Cu}_2\text{FeSnS}_4$  and is the ordered analog of a zinc-blende structure [80].

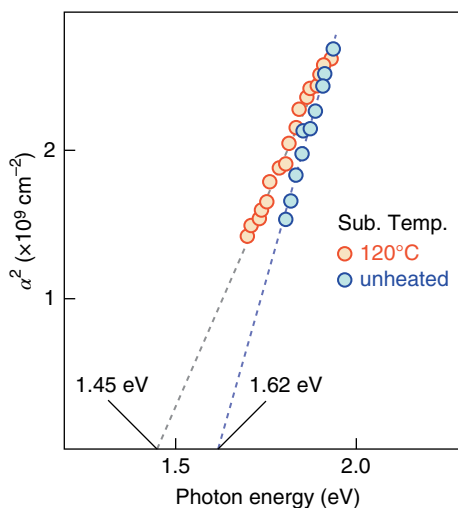
The discovery that a CZTS thin film has an optimum direct band gap of 1.45 eV for solar cells and a high absorption coefficient of  $10^4 \text{ cm}^{-1}$  was made in the laboratory of Shinshu University [81]. These values are almost equivalent to those of CIS. We prepared the first CZTS thin films using atom beam sputtering in which accelerated argon ions, that were neutralized eventually, bombarded a target consisting of the compound. The gas pressure in a sputtering chamber was maintained at 0.2 Pa during deposition. The sputtering target was synthesized as follows. A stoichiometric mixture of the elements with a purity of 99.999% (“five nines” purity) was sealed in a quartz ampoule under vacuum, which was then heated to 1050°C for 2.0 days. The crystals thus obtained exhibited p-type conductivity. They were ground into a fine powder, which was in turn pressed in an aluminum saucer. A Corning 7059 glass slide was used as a substrate, and its temperature was varied from room temperature to 240°C. A CZTS thin film of 0.3–1  $\mu\text{m}$  thickness was deposited on it in 2–6 hours. The deposition rate was decreased with an increase of substrate temperature. The result was probably caused by re-evaporation of a volatile compound or constituent, as agrees with recent findings. Much later, another sulfurization process was employed to prepare CZTS thin films at higher temperatures. The precursor layer was vacuum-sealed in a glass ampoule together with a controlled amount of sulfur powder. The partial pressure of sulfur can be much increased in comparison with the low-rate sputtering and the two-step process, making it difficult for volatile constituents to re-evaporate from the surface of the compound. This method was initially developed for the growth of  $\text{CuAlS}_2$  [82], and later applied to that of CZTS. It was found by Momose *et al.* that the re-evaporation of tin and copper can be suppressed when the vapor pressure of sulfur is kept higher than one atmospheric pressure during growth of CZTS thin films [83]. A solar cell with a 3.7% conversion efficiency has been obtained from the CZTS thin film sulfurized at 590°C for 7 min under a sulfur vapor pressure of 1.5 atm. However, Sn- and Cu-deficient CZTS thin films were formed under the sulfur pressure of 0.1 atm and resulted in lower efficiencies.

Figure 1.12 shows the lattice spacing of (112) plane of the sputter-deposited CZTS evaluated from X-ray diffraction (XRD) and a half width of the (112) peak as a function of substrate temperature. They are decreased with the increase of substrate temperature. The lattice spacing approaches the bulk value shown by a dotted line in the figure. The half width of the peak indicates the enhancement of crystallinity at higher temperatures. The resistivity of the CZTS thin films was decreased from  $4 \times 10^3$  to  $1.3 \Omega \text{ cm}$  as the substrate temperature was increased.

Figure 1.13 shows that in a range of photon energy  $h\nu \geq 1.7 \text{ eV}$  the absorption coefficient of the (112) oriented thin film sputter-deposited at a substrate temperature of 120°C is higher than  $3.8 \times 10^4 \text{ cm}^{-1}$ . The square of the absorption coefficient of the film was increased linearly with photon energy. The direct band gap of the film is therefore evaluated to be 1.45 eV using Equation (1.23). It was in 1988 that the CZTS thin film was verified as being a potential candidate semiconductor for a thin-film solar cell. This compound as an absorber layer material is free from any rare and toxic constituents.



**Figure 1.12** (112) lattice spacing and half width of the X-ray diffraction peak for sputtered CZTS thin films as a function of substrate temperature



**Figure 1.13** Square of the absorption coefficient of sputtered CZTS thin films as a function of photon energy

We also reported the advent of the first CZTS thin-film solar cell [79, 80], which was fabricated using stainless steel as a substrate. The substrate temperature was maintained at 160°C during the sputter deposition. A highly transparent and conductive cadmium-tin oxide (CTO) [84] or indium oxide ( $\text{In}_2\text{O}_3$ ) thin film was used as a window layer. The former was deposited at a substrate temperature of 150°C using the same technique as in the case of the absorber layer, while the latter was deposited using reactive evaporation at a substrate

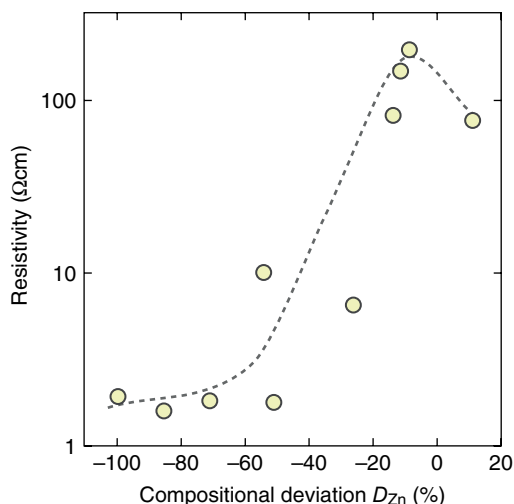


temperature of 200°C. The photovoltaic characteristics of these cells were measured under AM1.5 illumination of a solar simulator. The CTO/CZTS hetero-junction solar cell showed an open-circuit voltage  $V_{oc}$  of 0.165 V, although the short-circuit current was very small. After annealing it in an oxygen flow at 300°C, the  $V_{oc}$  was improved to 0.25 V. The  $\text{In}_2\text{O}_3/\text{CZTS}$  cell exhibited the short-circuit current density of  $1 \text{ mA cm}^{-2}$ , while  $V_{oc}$  is lower than 2 mV. The spectral photo-response of the latter cell was raised steeply at a wavelength of about 300 nm, corresponding to the absorption edge of the  $\text{In}_2\text{O}_3$  thin film. At 880 nm, it exhibited a similar decay to that shown in Figures 1.17 and 1.18, corresponding to the direct band gap of the absorber layer. However, there was an additional response tail extending to the wavelength of about 950 nm, the origin of which could not be identified at that time because the energy band structure of CZTS was not known in detail. It was shown theoretically that in CZTS crystals the most stable phase is a kesterite structure rather than a stannite structure, although the total energy of the former is only 1.3 meV per atom lower than the latter [85]. It is therefore expected that both phases may coexist and it should be relatively easy to grow materials with mixed phases depending on growth conditions. As shown in Chapter 4, the direct energy gap of the kesterite is theoretically 0.14 eV wider than that of the stannite. The long wavelength tail of the response mentioned above may be ascribed to an impurity phase of the stannite structure included in a kesterite matrix. We cannot observe the tail if an absorber layer is prepared at a higher temperature.

In 1988, an attempt to fabricate thin films of CZTS by spray pyrolysis was made in cooperation with Nakayama. Their chemical composition could be controlled by the solute concentration in a spray solution [86]. Since the reaction proceeds under ordinary pressure, re-evaporation of volatile constituents from the film could be suppressed and the use of expensive vacuum systems could be avoided. The solution in a flask was transported to the glass nozzle by compressed air and was then sprayed at a flow rate of  $2.5\text{--}3.0 \text{ mL min}^{-1}$ . A soda-lime glass substrate was placed 15 cm above the nozzle and then heated to  $280\text{--}360^\circ\text{C}$  by nichrome wire. The solution usually consisted of  $\text{CuCl}$ ,  $\text{ZnCl}_2$ ,  $\text{SnCl}_4$  and thiourea dissolved in deionized water, the concentration of which was 20, 10, 10 and  $80 \text{ mmol L}^{-1}$ , respectively. A stoichiometric CZTS thin film could be obtained after annealing the sprayed film at  $550^\circ\text{C}$  in an argon flow containing  $\text{H}_2\text{S}$ . Using this sulfurization process we could enhance the S content of the film from 28% to 38% to the stoichiometric content (50%). The crystal structure of the sprayed CZTS thin film was at first reported to be stannite but was later identified as kesterite by Kamoun *et al.* [87]. We studied the deviation  $D_c$  from stoichiometry defined by the following equation as a function of the zinc concentration in the spray solution:

$$D_c = 100 \frac{y - y_{st}}{y_{st}} (\%) \quad (1.33)$$

where  $D_c$  is defined for each elemental constituent,  $y_{st}$  is the stoichiometric composition of  $\text{Cu}_2\text{ZnSnS}_4$ , and  $y$  is the measured composition of the film. As the zinc concentration in the solution was increased from 2 to  $20 \text{ mmol L}^{-1}$  while the concentrations of the other chemical agents were kept constant as mentioned above, the value of  $D_{\text{Zn}}$  for zinc was increased from  $-88\%$  to  $+12\%$  and those for tin and copper decreased. However, the sulfur composition is approximately stoichiometric independent of the zinc concentration, that is,  $D_s \approx 0\%$ . When the zinc concentration was  $16 \text{ mmol L}^{-1}$ , a stoichiometric CZTS thin film was obtained. Figure 1.14 shows the resistivity of the CZTS thin film as a function of  $D_{\text{Zn}}$ . The



**Figure 1.14** Resistivity of sprayed CZTS thin films as a function of compositional deviation  $D_{Zn}$  of spray solution

resistivity of a single-phase thin film was higher than  $6 \Omega \text{ cm}$ . The highest resistivity of  $200 \Omega \text{ cm}$  was observed when stoichiometry prevails in the film. However, it decreased steeply as the ratio of copper to another metal was increased. The film containing an impurity phase of  $\text{Cu}_2\text{SnS}_3$  exhibited resistivity of a few  $\Omega \text{ cm}$ . CZTS thin films were also prepared from a mixed solvent of water and ethanol. Even without the sulfurization process they had a nearly stoichiometric composition of sulfur (48%). It was revealed by scanning electron microscopy that the cleaved section of the film appears to be smooth and dense when compared to one sprayed without ethanol. The spectral transmittance of two films  $0.72$  and  $0.85 \mu\text{m}$  thick was measured to deduce the absorption coefficient versus photon energy; we estimated the optical band gap to be  $1.46 \text{ eV}$ . This value agrees fairly well with that of the sputter-deposited quaternary thin film as described above.

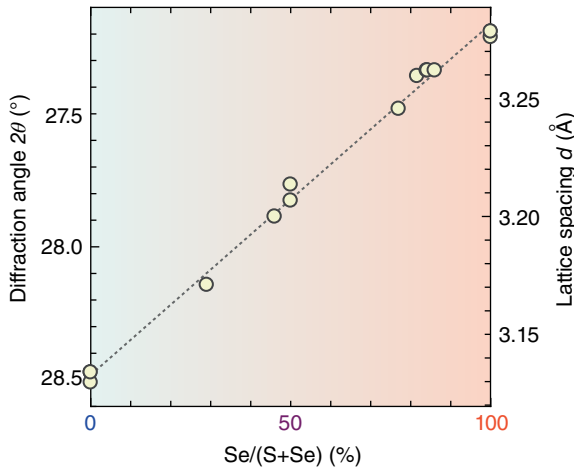
In 1990 I stayed at the University of Stuttgart as a visiting scholar and had an opportunity to present an invited talk on the CZTS thin-film solar cell. A few days later a mineralogist from the audience, Dittrich, visited me to discuss the polymorphism of CZTS. He touched on one more mineralogical form whose pronunciation I could not follow at that time. In 1998 he published a paper on “kesterite” thin-film solar cells utilizing vacuum co-evaporation with his two coauthors [88]. According to a recent private communication, he performed simulations of X-ray powder diffraction patterns for their thin films and could distinguish kesterite from stannite. In 1994 I was invited as a speaker for the conference held in Niigata University. There I talked about solar cells and their thin-film materials including CZTS; Katagiri was among the audience. He and his group in Nagaoka-NCT adopted the two-step process first applied to the CIS absorber. They later replaced evaporation with sputtering for the first step and improved the efficiency of CZTS thin-film solar cells towards  $6.77\%$  by 2008 using a preferential etching treatment of the absorber layer (Chapter 8; [89]).

Momose *et al.* also studied CZTSSe thin-film solar cells. The alloy absorber layer was prepared by the reaction of a metallic precursor layer with elemental sulfur and selenium

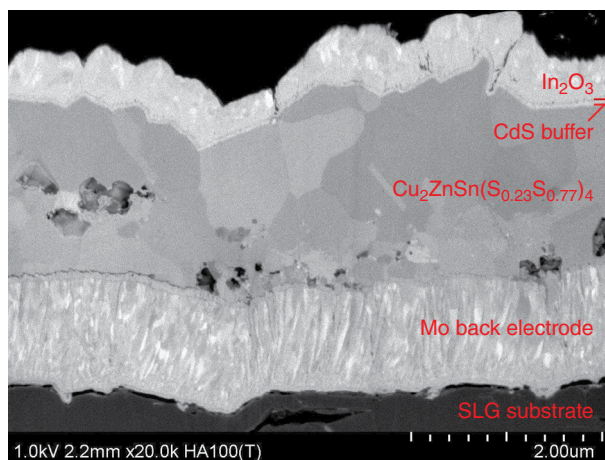
vapor simultaneously [90]. The precursor consisting of a Cu-Zn-Sn stack  $0.65\text{ }\mu\text{m}$  thick was deposited on a soda-lime glass substrate by sputtering. The cationic ratio of it was adjusted as  $[\text{Cu}]/2[\text{Zn}]=0.75$ ,  $[\text{Cu}]/2[\text{Sn}]=0.90$  and  $[\text{Zn}]/[\text{Sn}]=1.2$ . The precursor layers and powders of elemental sulfur and selenium were vacuum-sealed in a glass ampoule. A rapid thermal process was then used to heat it to  $520^\circ\text{C}$  at a high elevation rate of  $310^\circ\text{C min}^{-1}$ . The alloy composition of Se in the thin film could be controlled by the partial vapor pressure of Se in the ampoule during annealing.

Figure 1.15 shows that Vegard's law holds between lattice spacing of (112) planes and  $[\text{Se}]/([\text{S}]+[\text{Se}])$  ratio. The peak intensity of (112) reflection was increased with the ratio, in agreement with the microscopic observation that the grain size of the film is an increasing function of selenium content. Figure 1.16 shows the cross-sectional image of a  $\text{Cu}_2\text{ZnSn}(\text{S}_{0.23}\text{Se}_{0.77})_4$  thin-film solar cell by scanning electron microscopy. We can see crystal grains one micron in diameter, and several voids in some of them. The short-circuit current density was  $31.7\text{ mA cm}^{-2}$  while the open-circuit voltage was equal to  $300\text{ mV}$ . The conversion efficiency of the cell was  $4.22\%$ . The normalized quantum efficiency of the cell is shown in Figure 1.17. The band gap of an absorber can be estimated to be about  $1.09\text{ eV}$ , which is close to the band gap of CZTSe thin film reported by Ahn *et al.* [91]. The other quantum efficiency curve indicates that the threshold photon energy of the cell with the  $[\text{Se}]/([\text{S}]+[\text{Se}])$  ratio of  $0.50$  is  $1.36\text{ eV}$ .

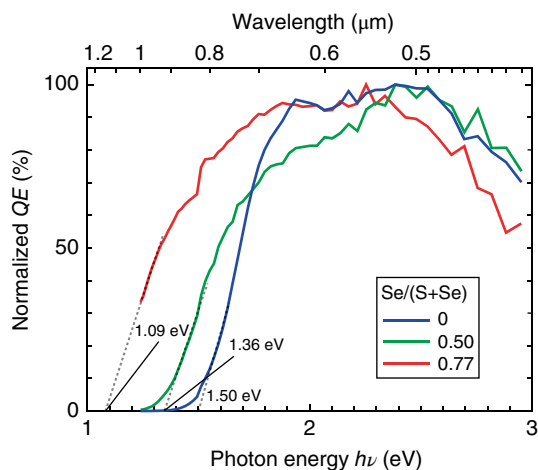
The best cell prepared as described above is obtained at the composition ratio  $x=[\text{S}]/([\text{S}]+[\text{Se}])=0.23$ , while the best one prepared by the hydrazine-based slurry process had an  $x=0.09$  [1, 2]. According to the XRD study on the tetragonal CZTSSe single crystal performed by Levenco *et al.* [92], the ratio of  $c/a$  in which  $c(a)$  is the lattice constant along the  $c(a)$  axis is almost equal to 2, that is,  $1.998(6)$  and  $1.997(5)$ , when  $x$  is equal to  $0.125$  and  $0.25$ , respectively. This means that the tetragonal distortion,  $2-(c/a)$ , almost vanishes at this compositional range. Balboul *et al.* suggested that the highest-efficiency CIGSe thin-film solar cell prepared by co-evaporation can be obtained when the  $c/a$  ratio is made equal to 2 by adjusting the composition as  $[\text{Ga}]/([\text{Ga}]+[\text{In}])=0.2$  [93]. The beneficial effects of



**Figure 1.15** Relation between X-ray diffraction angle  $2\theta$  and composition ratio of  $\text{Se}/(\text{S}+\text{Se})$  in the CZTSSe thin films



**Figure 1.16** Cross-sectional SEM image of an  $\text{In}_2\text{O}_3/\text{CdS}/\text{CZTSSe}$  thin-film solar cell



**Figure 1.17** Normalized spectral quantum efficiency of CZTSSe thin-film solar cells

alloying seem to indicate that the non-radiative lifetime of minority carriers is enhanced by eliminating the tetragonal distortion in the ternary and quaternary compounds.

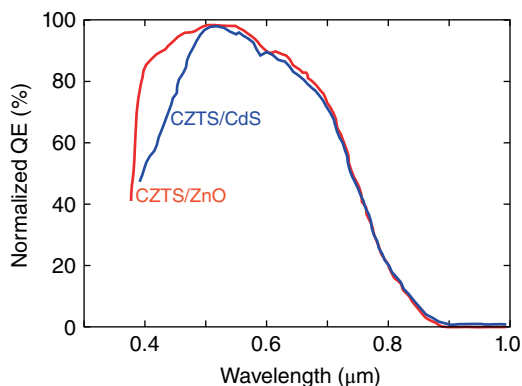
### 1.3.3.2 Buffer Layer

A CZTS-based thin-film solar cell consists of a p-type polycrystalline absorber layer because it cannot be doped with donor-type shallow impurities or defects. Here an n-type semiconductor is needed, which contacts it intimately and subsequently provides the cell with an electric field that separates the electrons and the holes excited by solar radiation. The thin region of the cell is often called a buffer layer because it is placed between a

window layer and the absorber layer. The following are prerequisites for the buffer: its band gap must be wide enough so that sunlight is able to reach the absorber without significant absorption loss in the buffer layer; the pn-hetero-junction must belong to the straddling type with moderate conduction-band spike  $\Delta E_c$ ; the lattice misfit of the hetero-junction must be as small as possible to reduce the dangling bond density; deposition does not damage the surface of the absorber, so the use of sputtering for the deposition is therefore undesirable; and even if the absorber layer has a rough surface, direct contact between the window and the absorber should be avoided (from this point of view, vacuum evaporation of buffer layers is not appropriate).

A chemical-bath-deposited (CBD) CdS thin film is often used as a material suitable for the buffer because it substantially meets the prerequisites mentioned above. The CBD method is inherently a low-temperature process because the layer can be deposited in an aqueous solution of  $\text{CdI}_2$ ,  $\text{NH}_4\text{I}$  and  $\text{SC}(\text{NH}_2)_2$  at about  $80^\circ\text{C}$  [94]. The film has a wurtzite structure with a direct band gap of  $E_g = 2.62\text{ eV}$  as determined using Equation (1.23). The value of  $E_g$  is significantly larger than that of the bulk single crystal ( $2.53\text{ eV}$ ). The widening of  $E_g$  in the former film, which coincides fairly well with a decrease both in the refractive index and lattice constant  $a$ , is beneficial to photovoltaic applications. These properties might be attributed to a micro-crystalline nature of the wurtzite layer. The resistivity of the buffer layer is of the order of  $10^{8-10}\ \Omega\text{ cm}$  in the dark. It decreases by 5 orders of magnitude under illumination. The extensive photoconductivity of the wurtzite CdS layer is possibly related to its low donor density compared with the zinc-blende CdS layer and the resultant long carrier lifetime. Incidentally, the crystal structure of the CBD CdS thin film is dependent on the preparation conditions, although the bulk material tends to crystallize in wurtzite structure. We found that by using a vapor transport reaction, the mono-crystalline film of hexagonal wurtzite CdS can be obtained on the single-crystal substrate of InP with a specific epitaxial relation [52]. However, the CBD CdS thin film synthesized from a chloride solution had zinc-blende structure, a longer bond length and a narrower band gap of  $2.45\text{ eV}$ . In both types of structure each anion (S) is surrounded by four nearest-neighbor cations (Cd) which are located at the corners of a tetrahedron, forming covalent and partially ionic bonds with each other. In the hexagonal wurtzite (cubic zinc-blende) crystal, anions expressed as equal-sized spheres are arranged periodically in hexagonal closed packed (cubic closed packed) sequences, and cations occupy half the alternate tetrahedral voids in each lattice sequence. When a material is synthesized in thin-film form for photovoltaic applications, caution over whether the physical properties and crystal structure are the same as those of a bulk material is required.

To employ the CdS layer as a buffer is not desirable from an environmental point of view. The use of electrical and electronic equipment containing hazardous substances such as cadmium is controlled by the EU's Restriction of Hazardous Substances (RoHS) directive. Htay *et al.* investigated a ZnO thin film as an alternative buffer layer [95], deposited on a CZTS thin film by ultrasonically agitated spray pyrolysis. The deposition temperature was varied from  $300$  to  $400^\circ\text{C}$  and the thickness of the ZnO buffer from  $60$  to  $200\text{ nm}$ . The resistivity of the buffer layer was increased from  $56$  to  $5.3 \times 10^4\ \Omega\text{ cm}$  with the decrease of deposition temperature. When the ZnO buffer layer of about  $60\text{ nm}$  thickness exhibited a resistivity of the order of  $10^3\ \Omega\text{ cm}$ , a thin-film solar cell of  $4.29\%$  efficiency was obtained. The open-circuit voltage of the cell was  $0.65\text{ V}$  and the short-circuit current density was



**Figure 1.18** Normalized spectral quantum efficiency of ZnO/CZTS and CdS/CZTS heterojunction thin-film solar cells

$13.8 \text{ mA cm}^{-2}$ . Figure 1.18 shows the quantum efficiency of ZnO:Al/ZnO/CZTS and  $\text{In}_2\text{O}_3/\text{CdS/CZTS}$  hetero-junction solar cells. The quantum efficiency of the former cell is larger than the latter in a wavelength range shorter than 510 nm. Since the band gap of CBD CdS is narrower than that of ZnO, that is,  $E_g = 3.37 \text{ eV}$ , the absorption in the former buffer layer is not negligible in the short-wavelength range.

## 1.4 Conclusions

The CZTS-based thin-film solar cell is a photovoltaic device that has the potential to provide a considerable amount of low-cost electricity. The energy conversion efficiency of an ideal solar cell consisting of CZTS, which is theoretically calculated by a detailed balance model, is equal to 32%. The next technological target for the CZTS-based thin-film solar cell could be set for the achievement of half the theoretical limit, which is high enough to cut the balance of system cost per peak watt. The pre-factor of the absorption coefficient of CZTS of the order of  $10^4 \text{ cm}^{-1}$  suggests that the solar cell can be produced in thin-film form; the material cost of a solar cell can therefore be drastically reduced by using the Earth-abundant elements.

We have to address a few technological issues before developing CZTS-based thin-film solar modules. The open-circuit voltage of the present cell is much lower than that of an ideal pn-junction. One of the methods to improve the voltage is to remove recombination centers such as SRH-type defects from an absorber layer as far as possible. The modifications of the junction interface to enable doping with shallow donors might enhance the improvement. It is interesting to study whether a double hetero-structure is effective to confine minority carriers in the absorber of the thin-film solar cell. Vacuum processing for the growth of CZTS-based thin films, which requires costly equipment, often leads to the loss of constituents from the compound due to their volatility. From this viewpoint, non-vacuum processes may be advantageous for the production of thin-film solar cells. Required future research is the investigation of how the formation of secondary phases in the quaternary compound can be minimized.

CZTS-based technology is a great challenge. It was once said people of the island of Bensalem dare strive for the concerted betterment of their lives subject to natural conditions [96]. People in the world shall not cease to do so.

## Acknowledgements

I would like to express my gratitude to Prof. Y. Hashimoto at Shinshu University, Dr A. Jäger-Waldau at European Commission, Joint Research Centre, Dr T. Nakazawa and Dr M.T. Htay at Shinshu University for valuable discussions. I would also like to thank Dr N. Momose at Nagano National College of Technology for helpful discussions and assistance in preparing the manuscript.

## References

- [1] Todorov, T.K., Tang, J., Bag, S., Gunawan, O., Gokmen, T., Zhu, Y. & Mitzi, D.B. (2013) Beyond 11% efficiency: Characteristics of state-of-the-art  $\text{Cu}_2\text{ZnSn}(\text{S},\text{Se})_4$  solar cells. *Advanced Energy Materials*, **3**, 34–38.
- [2] Wang, W., Winkler, M.T., Gunawan, O., Gokmen, T., Todorov, T.K., Zhu, Y. & Mitzi, D.B. (2013) Device characteristics of CZTSSe thin-film solar cells with 12.6% efficiency. *Advanced Energy Materials*, published online November 2013, doi: 10.1002/aenm.201301465 (2013).
- [3] NREL (2014) Reference Solar Spectral Irradiance: ASTM G-173. National Renewable Energy Laboratory. Available at <http://redc.nrel.gov/solar/spectra/> (accessed 10 July 2014).
- [4] Kopp, G. & Lean, J. (2011) A new, lower value of total solar irradiance: Evidence and climate significance. *Geophysical Research Letters*, **38**, L01706.
- [5] Meinel, A.B. & Meinel, M.P. (1976) *Applied Solar Energy: An Introduction*. Addison-Wesley Publishing, New York.
- [6] Jacquemoud, S. & Ustin, S.L. (2003) Application of radiative transfer models to moisture content estimation and burned land mapping. *Joint European Association of Remote Sensing Laboratories (EARSel) and GOCF/GOLD-Fire Program*, 4th Workshop on Forest Fires, Ghent University.
- [7] Shockley, W. & Queisser, H.J. (1961) Detailed balance limit of efficiency of  $p$ - $n$  Junction solar cells. *Journal of Applied Physics*, **32**, 510–519.
- [8] Yablonovitch, E., Miller, O. & Kurtz, S. (2012) Strong internal and external luminescence as solar cells approach the Shockley-Queisser Limit. *IEEE Journal of Photovoltaics*, **2**, 303–311.
- [9] Smith, R.A. (1959) *Semiconductors*. Cambridge University Press, Cambridge.
- [10] Schubert, E.F. (2003) *Light-emitting Diodes*. Cambridge University Press, Cambridge.
- [11] Ahrenkiel, R.K. (1992) Measurement of minority-carrier life time by time-resolved photoluminescence. *Solid-State Electronics*, **35**, 239–250.
- [12] Shockley, W. & Read, W.T. (1952) Statistics of the recombinations of holes and electrons. *Physical Review*, **87**, 835–842.
- [13] Lundstrom, M. (2000) *Fundamentals of Carrier Transport*, 2nd edition. Cambridge University Press, Cambridge.
- [14] Green, M.A. (1981) Solar cell fill factors: general graph and empirical expressions. *Solid-State Electronics*, **24**, 788–789.
- [15] Bohren, C.F. & Huffman, D.R. (1983) *Absorption and Scattering of Light by Small Particles*. John Wiley & Sons, New York.
- [16] Snee, M. & Ubachs, W. (2005) Direct measurement of the Rayleigh scattering cross section in various gases, *Journal of Quantitative Spectroscopy & Radiative Transfer*, **92**, 293–310.
- [17] Orphal, J. (2003) A critical review of the absorption cross-sections of  $\text{O}_3$  and  $\text{NO}_2$  in the ultraviolet and visible. *Journal of Photochemistry & Photobiology A: Chemistry*, **157**, 185–209.

- [18] Abrams, Z.R., Gharghi, M., Niv, A., Gladden, C. & Zhang, X. (2012) Theoretical efficiency of 3rd generation solar cells: Comparison between carrier multiplication and down-conversion. *Solar Energy Materials and Solar Cells*, **99**, 308–315.
- [19] Sağol, B.E., Erol, B., Seidel, U., Szabó, N., Schwarzburg, K. & Hannappel, T. (2007) Basic concepts and interfacial aspects of high-efficiency III-V multijunction solar cells. *CHIMIA*, **61**, 775–779.
- [20] Kayes, B.M. (2012) Light management in single junction III-V solar cells, a plenary talk from SPIE Optics+ Photonics 2012.
- [21] Kayes, B.M., Hui, N., Twist, R., Spruytte, S.G., Reinhardt, F., Kizilyalli, I.C. & Higashi, G.S. (2011) *Proceedings of 37th Photovoltaic Specialists Conference*, IEEE, New York, pp. 4–8.
- [22] Fujishima, D., Yano, A., Kinoshita, T., Taguchi, M., Maruyama, E. & Tanaka, M. (2012) An approach for the higher efficiency in the HIT cells. *Panasonic Technical Journal*, **57**, 40–45.
- [23] Taguchi, M., Yano, A., Tohoda, S., Matsuyama, K., Nishiwaki, T., Fujita, K. & Maruyama, E. (2014) 24.7% record efficiency HIT solar cell on thin silicon wafer. *IEEE Journal of Photovoltaics*, **4**, 96–99.
- [24] Mishima, T., Taguchi, M., Sakata, H. & Maruyama, E. (2011) Development status of high-efficiency HIT solar cells. *Solar Energy Materials & Solar Cells*, **95**, 18–21.
- [25] Taguchi, M., Sakata, H., Yoshimine, Y., Maruyama, E., Terakawa, A. & Tanaka, M. (2005) An approach for the higher efficiency in the HIT cells. In *Proceedings of the 31st IEEE Photovoltaic Specialists Conference*, Orlando, FL, USA, 3–7 January, pp. 866–871.
- [26] van Roosbroeck, W. & Shockley, W. (1954) Photon-radiative recombination of electrons and holes in germanium. *Physical Review*, **94**, 1558–1560.
- [27] Hovel, H.J. (1975) Solar cells. In *Semiconductors and Semimetals*, Vol. **11** (eds A.C. Beer & R.K. Willardson), Academic Press, New York.
- [28] Rusu, M., Eisele, W., Würz, R., Ennaoui, A., Lux-Steiner, M.Ch., Niesen, T.P. & Karg, F. (2003) Current transport in ZnO/ZnS/Cu(In,Ga)(S,Se)<sub>2</sub> solar cell. *Journal of Physics and Chemistry of Solids*, **64**, 2037–2040.
- [29] Ito, K. & Kojima, K. (1980) Solution-grown silicon solar cells. *Japanese Journal of Applied Physics*, **19-2**, 37–41.
- [30] Sah, C.T., Noyce, R.N. & Shockley, W. (1957) Carrier generation and recombination in *p-n* junctions and *p-n* junction characteristics. *Proceedings of the IRE*, **45**, 1228–1243.
- [31] Ito, K. (1980) Effect of lattice misfit on *pn* junction characteristics. *Applied Physics Letters*, **36**, 577–579.
- [32] Contreras, M.A., Tuttle, J., Gabor, A., Tennant, A., Ramanathan, K., Asher, S., Franz, A., Keane, J., Wang, L., Scofield, J. & Noufi, R. (1994) High efficiency Cu(In,Ga)Se<sub>2</sub>-based solar cells: processing of novel absorber structures. *Proceedings of the 1st World Conference on Photovoltaic Energy Conversion*, IEEE, New York, pp. 68–75.
- [33] Kato, T., Hiroi, H., Sakai, N., Muraoka, S. & Sugimoto, H. (2012) Characterization of front and back interfaces on Cu<sub>2</sub>ZnSnS<sub>4</sub> thin-film solar cells. *Proceedings of 27th European Photovoltaic Solar Energy Conference and Exhibition*, Frankfurt, pp. 2236–2239.
- [34] Ito, K., Matsumoto, N., Horiuchi, T., Ichino, K., Shimoyama, H., Ohashi, T., Hashimoto, Y., Hengel, I., Beier, J., Klenk, R., Jäger-Waldau, A., Lux-Steiner, M.Ch. (2000) Theoretical model and device performance of CuInS<sub>2</sub> thin film solar cell. *Japanese Journal of Applied Physics*, **39**, 126–136.
- [35] Contreras, M., Mansfield, L., Egaas, B., Li, J., Romero, M., Noufi, R., Rudiger-Voigt, E. & Mannstadt, W. (2011) Improved energy conversion efficiency in wide-bandgap Cu(In,Ga)Se<sub>2</sub> solar cells. In *Proceedings of the 37th IEEE Photovoltaic Specialists Conference*, Seattle, NREL/CP-5200-50669.
- [36] Repins, I., Beall, C., Vora, N., DeHart, C., Kuciauskas, D., Dippo, P., To, B., Mann, J., Hsu, W.C., Goodrich, A. & Noufi, R. (2012) Co-evaporated Cu<sub>2</sub>ZnSnSe<sub>4</sub> films and devices. *Solar Energy Materials and Solar Cells*, **101**, 154–159.
- [37] Repins, I.L., Li, J.V., Kanevce, A., Perkins, C.L., Steirer, K.X., Pankow, J., Teeter, G., Kuciauskas, D., Beall, C., Dehart, C., Carapella, J., Bob, B., Park, J.-S. & Wei, S.-H. (2014) Effects of deposition termination on CZTSe device characteristics. *Thin Solid Films*, in press.



- [38] Merdes, S., Mainz, R., Klaer, J., Meeder, A., Rodriguez-Alvarez, H., Schock, H.W., Lux-Steiner, M.Ch. & Klenk, R. (2011) 12.6% efficient CdS/Cu(In,Ga)S<sub>2</sub>-based solar cell with an open circuit voltage of 879 mV prepared by a rapid thermal process. *Solar Energy Materials and Solar Cells*, **95**, 864–869.
- [39] Persson, C., Zhao, Y.J., Lany, S. & Zunger, A. (2005) *n*-type doping of CuInSe<sub>2</sub> and CuGaSe<sub>2</sub>. *Physical Review B*, **72**, 035211.
- [40] Gloeckler, M. & Sites, J.R. (2005) Efficiency limitations for wide-band-gap chalcopyrite solar cells. *Thin Solid Films*, **480–481**, 241–245.
- [41] Bhushan, M. & Catalano, A. (1981) Polycrystalline Zn<sub>3</sub>P<sub>2</sub> Schottky barrier solar cells. *Applied Physics Letters*, **38**, 39–41.
- [42] Kimball, G.M., Müller, A.M., Lewis, N.S. & Atwater, H.A. (2009) Photoluminescence-based measurements of the energy gap and diffusion length of Zn<sub>3</sub>P<sub>2</sub>. *Applied Physics Letters*, **95**, 112103.
- [43] Kimball, G.M., Lewis, N.S. & Atwater, H.A. (2010) Mg doping and alloying in Zn<sub>3</sub>P<sub>2</sub> heterojunction solar cells. In *Proceedings of 35th Photovoltaic Specialists Conference*, IEEE, New York, pp. 1039–1043.
- [44] Bosco, J.P., Demers, S.B., Kimball, G.M., Lewis, N.S. & Atwater, H.A. (2012) Band alignment of epitaxial ZnS/Zn<sub>3</sub>P<sub>2</sub> heterojunctions. *Journal of Applied Physics*, **112**, 093703.
- [45] Ito, K., Matsuura, Y., Nakazawa, T. & Takenouchi, H. (1981) Photovoltaic effect in monoclinic ZnP<sub>2</sub>. *Japanese Journal of Applied Physics*, **20–2**, 109–112.
- [46] von Känel, H., Hauger, R. & Wachter, P. (1982) Photoelectrochemistry of monoclinic ZnP<sub>2</sub>: A promising new solar cell material. *Solid State Communications*, **43**, 619–621.
- [47] Morozova, V., Marenkin, S., Koshelev, O. & Trukhan, V. (2006) Optical absorption in monoclinic zinc diphosphide. *Inorganic Materials*, **42**, 221–225.
- [48] Bube, R.H. (1998) *Photovoltaic Materials*. Imperial College Press, London.
- [49] Ohsawa, T. & Ito, K. (1974) *n* CdS-*p* InP heterojunctions. *Proceedings of Shin-etsu Meeting of the Institute of Electronics and Communication Engineers*, Japan, Shinshu University, 7–12 October.
- [50] Ito, K. & Ohsawa, T. (1975) Photovoltaic effect at *n* CdS-*p* InP heterojunctions. *Japanese Journal of Applied Physics*, **14**, 1259–1260.
- [51] Ito, K. & Ito, H. (1978) Growth of *p*-type InP single crystals by the temperature gradient method. *Journal of Crystal Growth*, **45**, 248–251.
- [52] Ito, K. & Ohsawa, T. (1977) Epitaxial CdS layers deposited on InP substrates. *Japanese Journal of Applied Physics*, **16**, 11–18.
- [53] Ito, K. & Nakazawa, T. (1979) *n* In<sub>2</sub>O<sub>3</sub>-*p* InP solar cells. *Surface Science*, **86**, 492–497.
- [54] Ito, K. & Nakazawa, T. (1985) Heat-resisting and efficient indium oxide/indium phosphide heterojunction solar cells. *Journal of Applied Physics*, **58**, 2638–2639.
- [55] Ito, K., Nakazawa, T. & Ohsaki, K. (1987) Amorphous to crystalline transition of indium oxide films deposited by reactive evaporation. *Thin Solid Films*, **151**, 215–222.
- [56] Saito, S., Hashimoto, Y. & Ito, K. (1994) Efficient ZnO/CdS/InP heterojunction solar cell. In *Proceedings of 1st World Conference on Photovoltaic Energy Conversion*, IEEE, New York, vol. **2**, pp. 1867–1870.
- [57] Bube, R.H. (1980) Heterojunctions for thin film solar cells. In *Solar Material Science* (ed. L.E. Murr). Academic Press, New York, pp. 585–618.
- [58] Keaveney, C. J., Haven, V. E. & Vernon, S. M. (1990) Emitter structures in MOCVD InP solar cells. In *Proceedings of 21st Photovoltaic Specialists Conference*, IEEE, New York, vol. **1**, pp. 141–144.
- [59] Nakazawa, T., Takamizawa, K. & Ito, K. (1987) High efficiency indium oxide/cadmium telluride solar cells. *Applied Physics Letters*, **50**, 279–280.
- [60] Cusano, D.A. (1963) CdTe solar cells and PV heterojunctions in II-VI compounds. *Solid-State Electronics*, **6**, 217–232.
- [61] Bacewicz, R. (1997) Polycrystalline thin film solar cells. *Opto-Electronic Review*, **5**, 167–173.
- [62] Wagner, S., Shay, J.L., Migliorato, P. & Kasper, H.M. (1974) CuInSe<sub>2</sub>/CdS heterojunction photovoltaic detectors. *Applied Physics Letters*, **25**, 434–435.

- [63] Shay, J.L., Wagner, S. & Kasper, H.M. (1975) Efficient CuInSe<sub>2</sub>/CdS solar cells. *Applied Physics Letters*, **27**, 89–90.
- [64] Kazmerski, L.L., White, E.R., Ayyagari, M.S., Juang, Y.J. & Patterson, R.P. (1977) Growth and characterization of thin-film compound semiconductor photovoltaic heterojunctions. *Journal of Vacuum Science & Technology*, **14**, 65–68.
- [65] Kazmerski, L.L. & Sanborn, G.A. (1977) CuInS<sub>2</sub> thin-film homojunction solar cells. *Journal of Applied Physics*, **48**, 3178–3180.
- [66] Konagai, M., Sugimoto, M. & Takahashi, K. (1978) High-efficiency GaAs thin-film solar-cells by peeled film technology. *Journal of Crystal Growth*, **45**, 277–280.
- [67] Ogawa, Y., Jäger-Waldau, A., Hashimoto, Y. & Ito, K. (1994) In<sub>2</sub>O<sub>3</sub>/CdS/CuInS<sub>2</sub> thin film solar cell with 9.7% efficiency. *Japanese Journal of Applied Physics*, **33**, L1775–L1777.
- [68] Grindle, S.P., Smith, C.W. & Mittleman, S.D. (1979) Preparation and properties of CuInS<sub>2</sub> thin films produced by exposing sputtered Cu-In films to an H<sub>2</sub>S atmosphere. *Applied Physics Letters*, **35**, 24–26.
- [69] Uenishi, S., Tohyama, K. & Ito, K. (1994) Photovoltaic characteristics of thin film CdS/CuInS<sub>2</sub> heterojunctions. *Solar Energy Materials and Solar Cells*, **35**, 231–237.
- [70] Klenk, R. & Lux-Steiner, M.Ch. (2006) Chalcopyrite-based solar cells. In *Thin Film Solar Cells: Fabrication, Characterization and Applications* (eds J. Poortmans & V. Arkhipov). John Wiley & Sons, Chichester.
- [71] Nakabayashi, T., Miyazawa, T., Hashimoto, Y. & Ito, K. (1997) Over 10% efficiency CuInS<sub>2</sub> solar cell. *Solar Energy Materials and Solar Cells*, **49**, 375–381.
- [72] Ohashi, T., Wakamori, M., Hashimoto, Y. & Ito, K. (1998) Cu(In<sub>1-x</sub>Ga<sub>x</sub>)S<sub>2</sub> thin films prepared by sulfurization of precursors consisting of metallic and gallium sulfide layers. *Japanese Journal of Applied Physics*, **37**, 6530–6534.
- [73] Ohashi, T., Hashimoto, Y. & Ito, K. (1999) Cu(In<sub>1-x</sub>Ga<sub>x</sub>)S<sub>2</sub> thin film solar cells with efficiency above 12%, fabricated by sulfurization. *Japanese Journal of Applied Physics*, **38**, L748–L750.
- [74] Ito, K. & Hashimoto, Y. (2001) CuInS<sub>2</sub> thin film solar cells. In *Ternary and Multinary Compounds in the 21st Century* (ed. T. Matsumoto). IPAP Books I, Institute of Pure and Applied Physics, Tokyo, pp. 342–347.
- [75] Hashimoto, Y., Takeuchi, K. & Ito, K. (1995) Band alignment at CdS/CuInS<sub>2</sub> heterojunction. *Applied Physics Letters*, **67**, 980–982.
- [76] Johnson, B., Klaer, J., Vollmer, A., Gorgoi, M., Höpfner, B., Merdes, S. & Lauermann, I. (2012) The development of the Cu(In,Ga)(S,Se)<sub>2</sub> conduction band with changing stoichiometry: a NEXAFS study. In *Proceedings of EMRS*, Strasbourg.
- [77] Goto, H., Hashimoto, Y. & Ito, K. (2004) Efficient thin film solar cell consisting of TCO/CdS/CuInS<sub>2</sub>/CuGaS<sub>2</sub> structure. *Thin Solid Films*, **451–452**, 552–555.
- [78] Inazu, T., Bhandari, R.K., Kadowaki, Y., Hashimoto, Y. & Ito, K. (2005) Cu(In,Al)S<sub>2</sub> thin film solar cell. *Japanese Journal of Applied Physics*, **44**, 1204–1207.
- [79] Ito, K. & Nakazawa, T. (1989) Stannite-type photovoltaic thin films. In *Proceedings of 4th Conference on Photovoltaic Science and Engineering*, Sydney, pp. 341–346.
- [80] Schäfer, W. & Nitsche, R. (1974) Tetrahedral quaternary chalcogenides of the type Cu<sub>2</sub>-II-IV-S<sub>4</sub>(Se)<sub>4</sub>. *Materials Research Bulletin*, **9**, 645–654.
- [81] Ito, K. & Nakazawa, T. (1988) Electrical and optical properties of stannite-type quaternary semiconductor thin films. *Japanese Journal of Applied Physics*, **27**, 2094–2097.
- [82] Bhandari, R.K., Hashimoto, Y. & Ito, K. (2004) CuAlS<sub>2</sub> thin-films prepared by sulfurization of metallic precursors and their properties. *Japanese Journal of Applied Physics*, **43**, 6890–6893.
- [83] Momose, N., Htay, M.T., Yudasaka, T., Igarashi, S., Seki, T., Iwano, S., Hashimoto, Y. & Ito, K. (2011) Cu<sub>2</sub>ZnSnS<sub>4</sub> thin film solar cells utilizing sulfurization of metallic precursor prepared by simultaneous sputtering of metal targets. *Japanese Journal of Applied Physics*, **50**, 01BG09.
- [84] Nakazawa, T. & Ito, K. (1989) Atom-beam sputtering of transparent conductive oxide thin films and their applications to heterojunctions. *Surface Science*, **27**, 753–763.
- [85] Persson, C. (2010) Electronic and optical properties of Cu<sub>2</sub>ZnSnS<sub>4</sub> and Cu<sub>2</sub>ZnSnSe<sub>4</sub>. *Journal of Applied Physics*, **107**, 053710.
- [86] Nakayama, N. & Ito, K. (1996) Sprayed films of stannite Cu<sub>2</sub>ZnSnS<sub>4</sub>. *Applied Surface Science*, **92**, 171–175.

- [87] Kamoun, N., Bouzouita, H. & Rezig, B. (2007) Fabrication and characterization of  $\text{Cu}_2\text{ZnSnS}_4$  thin films deposited by spray pyrolysis technique. *Thin Solid Films*, **515**, 5949–5952.
- [88] Friedlmeier, T.M., Dittrich, H. & Schock, H.W. (1998) Growth and characterization of  $\text{Cu}_2\text{ZnSnS}_4$  and  $\text{Cu}_2\text{ZnSnSe}_4$  thin films for photovoltaic applications. In *Institute of Physics Conference Series*, vol. **152**, Section B, pp. 345–348. Institute of Physics, London.
- [89] Katagiri, H., Jimbo, K., Yamada, S., Kamimura, T., Maw, W.S., Fukano, T., Ito, T. & Motohiro, T. (2008) Enhanced conversion efficiencies of  $\text{Cu}_2\text{ZnSnS}_4$ -based thin film solar cells by using preferential etching technique. *Applied Physics Express*, **1**, 041201.
- [90] Momose, N., Htay, M.T., Sakurai, K., Iwano, S., Hashimoto, Y. & Ito, K. (2012)  $\text{Cu}_2\text{ZnSn}(\text{S}_x\text{Se}_{1-x})_4$  thin film solar cells utilizing simultaneous reaction of a metallic precursor with elemental sulfur and selenium vapor sources. *Applied Physics Express*, **5**, 081201.
- [91] Ahn, S., Jung, S., Gwak, J., Cho, A., Shin, K., Yoon, K., Park, D., Cheong, H. & Hyun, J. (2010) Determination of band gap energy ( $E_g$ ) of  $\text{Cu}_2\text{ZnSnSe}_4$  thin films: On the discrepancies of reported band gap values. *Applied Physics Letters*, **97**, 021905.
- [92] Levenco, S., Dumcenco, D., Wang, Y.P., Huang, Y.S., Ho, C.H., Arushanov, E., Tezlevan, V. & Tiong, K.K. (2012) Influence of anionic substitution on the electrolyte electroreflectance study of band edge transition in single crystal  $\text{Cu}_2\text{ZnSn}(\text{S}_x\text{Se}_{1-x})_4$  solid solutions. *Optical Materials*, **34**, 1362–1365.
- [93] Balboul, M.R., Schock, H.M., Fayak, S.A., Abdel El-Aal, A., Werner, J.H. & Ramadan, A.A. (2008) Correlation of structure parameters of absorber layer with efficiency of  $\text{Cu}(\text{In,Ga})\text{Se}_2$  solar cell. *Applied Physics A*, **92**, 557–563.
- [94] Nakanishi, T. & Ito, K. (1994) Properties of chemical bath deposited CdS thin films. *Solar Energy Materials and Solar Cells*, **35**, 171–178.
- [95] Htay, M.T., Hashimoto, Y., Momose, N., Sasaki, K., Ishiguchi, H., Igarashi, S., Sakurai, K. & Ito, K. (2011) A cadmium-free  $\text{Cu}_2\text{ZnSnS}_4/\text{ZnO}$  heterojunction solar cell prepared by practicable processes. *Japanese Journal of Applied Physics*, **50**, 032301.
- [96] Spedding, J. (1905) Preface to the New Atlantis. In *The Philosophical Works of Francis Bacon* (ed. Robertson, J.M.), Routledge, Oxford.



# 2

## Market Challenges for CZTS-Based Thin-Film Solar Cells

*Arnulf Jäger-Waldau*

*European Commission, Joint Research Centre; Renewable Energy Unit  
Via Enrico Fermi 2749, 21027 Ispra, Italy*

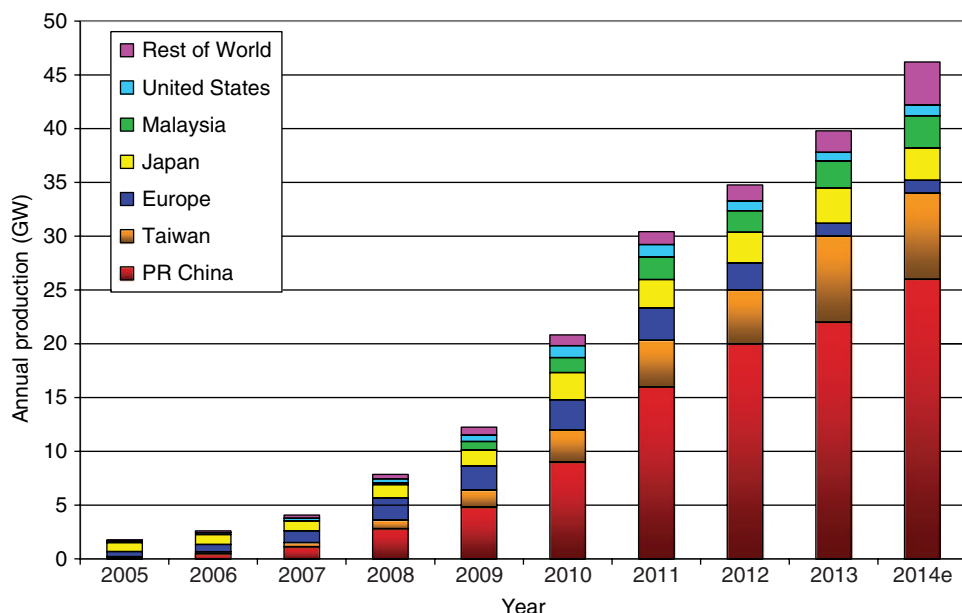
### 2.1 Introduction

Production data for global solar cell production (i.e. for silicon-wafer-based solar cells only the cells or, in the case of thin films, the complete integrated module) in 2013 vary from 38 GW to 43 GW and estimates for 2014 are in the 45–50 GW range. The significant uncertainty in these data is due to the highly competitive market environment, as well as the fact that some companies report shipment figures while others report sales or production figures. 2013 was characterized by a shift in the main markets from Europe to Asia, mainly due to increased demand in China and Japan.

The data presented, collected from stock market reports of listed companies, market reports and colleagues, led to an estimate of 40 GW (Fig. 2.1), representing an increase of about 15% compared to 2012; a similar increase is expected for 2014.

Since 2000, total photovoltaic (PV) production has increased by two orders of magnitude, with annual growth rates of 40–90%. The most rapid growth in annual production over the last five years is observed in Asia, where China and Taiwan together now account for more than 75% of worldwide production.

The existing overcapacity in the solar industry has led to continuous price pressure along the value chain and resulted in a reduction of spot market prices for polysilicon materials, solar wafers and cells, as well as solar modules. Since 2008, PV module prices



**Figure 2.1** World PV Cell/Module Production from 2005 to 2014 (data source: Photon Magazine, PV Activities in Japan, PV News, and own analysis). For color details, please see color plate section

have decreased by 80%; they fell by 20% in 2012 alone, before reductions slowed in 2013 [1]. These rapid price declines are putting all solar companies under enormous pressure and access to fresh capital is key to survival. It is believed that this situation will continue at least until 2015, when the global PV market should exceed 50 GW of new installations.

The change in the market from that of supply-restricted to demand-driven and the resulting overcapacity for solar modules has resulted in the dramatic price reduction of PV systems of more than 50% over the last four years. In 2013 the average system price in Germany for systems smaller than 100 kWp (kilowatt peak) was in the range of € 1.51/Wp (US\$ 1.95/Wp) and below € 1.40/Wp (US\$ 1.82/Wp) at the end of the year [2]. In February 2014 the worldwide average system price for installing residential systems, excluding permit or connection costs, was given as US\$ 1.93/Wp, ranging between US\$ 1.67/Wp (€ 1.29/Wp) in Germany and up to US\$ 2.90/Wp in some other cases [3]. For commercial systems, this price range was given as US\$ 1.22–2.40/Wp [3]. For the total capital expenditure (CAPEX) for a project, which includes projecting and permit costs, the range for all non-tracking PV systems was given as US\$ 1.35–4.33/Wp by Bloomberg New Energy Finance at the beginning of 2014 [4]. The resulting levelized costs of electricity (LCOE) also depend on the solar radiation, fixed operation and maintenance (O&M) costs and the return on equity expectations, which differ from country to country. The overall range is given as 82–329 US\$/MWh [4].

Market predictions for the 2014 PV market vary between 40 GW and 52 GW [5–9] with a consensus value in the 45 GW range. Analysts expect a further increase in 2015, mainly

driven by Asia and new markets in South America. After the solar equipment market contracted from around US\$ 12–13 billion in 2010 to around US\$ 2–2.5 billion in 2013, analysts expect increases of 30–40% for 2014 and 2015. Most of the investment will be used to upgrade existing facilities with more advanced production steps and higher cell efficiencies, but expansion plans, some even in the GW size, were also announced in the second half of 2013.

The high number of new entrants to the field, notably large semiconductor or energy-related companies, has overcompensated for the large number of bankruptcies and companies with idling production lines or even permanent closures of their production facilities. Rapid changes in the sector, with the difficult financing situation on the one hand and an increasing trend towards mergers and acquisition on the other, mean that a reasonable forecast for future capacity developments is highly speculative.

## 2.2 Compound Thin-Film Technologies and Manufacturing

Production of thin-film solar modules reached more than 100 MW per annum for the first time in 2005. Between 2005 and 2009, the compound annual growth rate (CAGR) of thin-film solar module production was beyond that of the overall industry, increasing the market share of thin-film products from 6% in 2005 to 10% in 2007 and to 16–20% in 2009. The temporary silicon shortage during these years and the market entry of turnkey manufacturing equipment suppliers were responsible for this rapid increase of market shares. However, the thin-film share has been decreasing slowly since then. There are a number of reasons for this development. First, the rapid increase in polysilicon production capacity resulted in falling silicon prices. Second, the >150% growth of the PV market in 2010 led to a peak in equipment spending of about US\$ 14 billion in 2011 and the build-up of massive overcapacities. Third, the slower-than-expected ramp-up of the new thin-film manufacturing plants and slower-than-expected efficiency improvements led to a much slower growth of thin-film capacities compared to the silicon-wafer-based technologies. Last but not least, a significant number of start-up companies were not able to establish themselves in the market and disappeared or returned to a research and development (R&D) stage. The companies listed in the following sections are just a selection and do not claim to be complete.

### 2.2.1 Cadmium Telluride

Cadmium telluride (CdTe) has two features that make it appear to be an ideal candidate for thin-film solar cells. It can be deposited with various deposition methods which all result in reasonable quality, and has a direct energy gap at  $E_g = 1.45$  eV, which is within the ideal range for solar energy conversion.

When CdTe is deposited onto substrates above 449°C it condenses stoichiometrically as the stable phase in this regime [10]. These films are in general p-type with carrier concentrations of  $p < 10^{15} \text{ cm}^{-3}$  due to a slight cadmium deficiency. The most common CdTe solar cell structure consists of the n-CdS/p-CdTe hetero-junction, where the CdS is deposited on a transparent conductive oxide (TCO) -coated glass substrate. An important feature of this

type of solar cell is that CdS and CdTe can be deposited with the same deposition technologies. CdTe also allows band gap engineering if additional elements such as mercury (Hg) or manganese (Mn) are added. With increasing mercury content the band gap of  $\text{Cd}_{1-x}\text{Hg}_x\text{Te}$  decreases, whereas the increase of the manganese concentration increases the band gap in  $\text{Cd}_{1-x}\text{Mn}_x\text{Te}$ . The proof of concept for a two-terminal tandem solar cell based on CdMnTe and CdHgTe absorbers was demonstrated by Alvin Compaan in 2004 [11].

The standard techniques to deposit p-type CdTe of good crystalline quality and high electron mobility are: sublimation/condensation (S); close spaced sublimation (CSS), that is, a modification of the first process; chemical spraying (CS); screen printing (SP); chemical vapor deposition (CVD); sputtering; and electro-deposition (ED).

In 2013 major improvements were reported. The top efficiency for a cell achieved at GE Global Research was  $19.6 \pm 0.4\%$  and First Solar achieved  $16.16 \pm 0.5\%$  on a module scale [12].

**First Solar LLC** is one of the few companies worldwide to produce CdTe thin-film modules. The company currently has two manufacturing sites in Perrysburg (USA) and in Kulim (Malaysia), which had a combined capacity of 2.130 GW at the end of 2013. During this year, it is estimated that the company produced between 1.6 and 1.7 GW. Average module efficiency is given as 13.1%, with high-end products up to 14%. In the third quarter of 2013 the company reported production costs of US\$ 0.58/Wp, excluding underutilization and upgrading costs.

In 2012 the company underwent a major restructuring to respond to the changing market conditions. The result was that the company closed their factory in Frankfurt/Oder, Germany and cancelled the expansion planned in Meza (AZ), USA as well as in the Dong Nam Industrial Park, Vietnam.

In 2013 the company acquired GE Global's global cadmium telluride (CdTe) solar intellectual property portfolio after GE postponed the construction of a 400MW factory in 2012. In return, GE became a shareholder of First Solar and the two companies agreed that GE Global Research and First Solar R&D would collaborate on future technology development to further advance CdTe solar technology.

**Calyxo GmbH** was founded as a subsidiary of Q-Cells AG, located in Wolfen, Saxony-Anhalt, Germany. In February 2011, Solar Fields LLC took over the ownership from Q-Cells. In 2008, the company started to manufacture CdTe thin-film solar cells with a pilot 25 MW line and planned an expansion project to 85 MW. The economic and market development resulted in a postponement and technology upgrade. In December 2013 the new 60 MW production line was inaugurated.

**Advanced Solar Power Inc.** is located in Hangzhou Zhejiang Province, China. The company was founded by Professor Wu in 2008. Before returning to China in 2007, he worked at NREL and achieved an efficiency of  $16.5 \pm 0.5\%$  for a device prepared by CSS (CdTe) and chemical bath deposition (CdS) [13] in 2001. In 2011 the company completed its first 25 MW production line and achieved a module efficiency of 11.4% early in 2012.

## 2.2.2 Chalcopyrites

Chalcopyrites with  $\text{Cu(In,Ga)(S,Se)}_2$  are an interesting material system which offer the possibility to tailor the device's band gap – between 1.01 eV for  $\text{CuInSe}_2$  to 1.68 eV for  $\text{CuGaSe}_2$  or 2.4 eV for  $\text{CuGaS}_2$  – by substituting indium with gallium or selenium with sulfur. This renders chalcopyrites not only an interesting material for single-junction



devices, but also provides the possibility of a tandem structure device made from the same class of materials. The use of chalcopyrite solar cells in concentrator applications is being investigated by NREL and other research groups such as the Tokyo Institute of Technology.

Significant progress has not only been made in the basic understanding of the material properties of these devices, but also in the field of large area production of monolithically interconnected modules. The first  $\text{CuInSe}_2/\text{CdS}$  solar cell was realized in the early 1970s at Bell Labs [14]. The incorporation of Ga and/or S to produce  $\text{CuInGa}(\text{Se},\text{S})_2$  (CIGSS) allows a widened band gap and band-gap engineering depending on the composition [15]. A maximum efficiency of 20.8% was demonstrated with CIGS-based solar cells [12, 16] using a double-graded layer of Ga in the absorption layer to realize both high current density and high open-circuit voltage. Commercial module efficiencies are up to 15.7% [12] for  $\text{CuInGaSe}_2$  and 14.6% for  $\text{CuInGa}(\text{SSe})_2$  [17].

**Solar Frontier** is a 100% subsidiary of Showa Shell Sekiyu KK. In 1986, Showa Shell Sekiyu started to import small modules for traffic signals, and started module production in Japan cooperatively with Siemens (now Solar World). The company developed CIS solar cells and completed the construction of the first factory with 20MW capacity in October 2006. Commercial production started in FY 2007. In August 2007, the company announced the construction of a second factory with a production capacity of 60MW to be fully operational in 2009. In July 2008, the company announced they would open a research centre “to strengthen research on CIS solar powered cell technology, and to start collaborative research on mass production technology of the solar modules with Ulvac, Inc.” The aim of this project was to start a new plant in 2011 with a capacity of 900MW. The ramp-up started in February 2011 and, at the end of the year, overall capacity was 980MW. In December 2013 the company announced that a fourth factory would be built in the Tohoku Region with a capacity of 150MW. Production figures for 2013 are estimated to be in the range of 900MW.

**Hanergy Solar Group Ltd.** is a subsidiary of Hanergy Holding Group, which was established as Beijing He Tai He Trade & Development Co. Ltd in 1994. Since then, the company has invested in hydropower projects with a capacity of >6 GW and wind power projects of >130MW. In 2009 the company began its solar activities and its Heyuan Thin Film Solar Module Research Development and Manufacture Base was opened in 2011. In May 2011 the company became a major shareholder of Apollo Solar Energy, an amorphous silicon thin-film and equipment manufacturer. According to the company it had a production capacity of 3 GW based on five amorphous silicon technologies in 2012. In January 2013 Apollo Solar changed the name to Hanergy Solar Group Ltd. In addition to the amorphous silicon-based solar cell manufacturing in China, Hanergy acquired the CIGS manufacturers Solibro GmbH (DE/SE) and Miasolé (USA) in 2012 and Global Solar (USA) in 2013. In January 2014 the company placed two 300MW orders of CIGS turnkey factories, one based on Solibro and another on Miasolé technology [18]. The lines should be operational by the end of 2014 and are the first order of a planned CIGS capacity of 5.25 GW [19].

**Jenn Feng Co. Ltd.** was incorporated in 1975. The company plans and installs solar systems. According to the company, commercial production on their first CIGS 30MW line began in December 2009. The company offers standard and see-through modules for building facades. No current capacity or production figures are given.

**AVANCIS GmbH & Co KG** was founded as a joint venture between Shell and Saint-Gobain in 2006. In 2008, commercial production started in the new factory with an initial annual capacity of 20 MW in Torgau, Germany. In 2009, Saint-Gobain took over the shares of Shell and began the construction of a second CIS factory with a total capacity of 100 MW in Torgau. In October 2010, the company announced a joint venture with Hyundai Heavy Industries (HHI) in Korea for the production of CIS solar cells. The initial production capacity of 100 MW was planned to be operational in 2013, but the project was delayed. In April 2013 the first 20 MW line in Torgau was converted into a research facility and on 1 September 2013 the company temporarily stopped module production without providing any restart date.

**Ascent Solar Technologies Incorporated** was established in 2005 to manufacture CIGS thin-film solar modules with a roll-to-roll process. A 30 MW production line was completed in 2009. In 2011 TFG Radiant Group invested in the company and doubled its share to 41% by early 2012. In January 2014 the company signed a definitive agreement to build a new manufacturing plant under a joint venture with the Municipal Government of Suqian, Jiangsu, China [20].

**HelioVolt** was founded in 2001 with the aim of developing and commercializing its FASST® process for applying CIGS thin-film photovoltaics directly onto conventional construction materials. The company operates a pilot line in Austin, TX and started commercial production in 2011. In September 2011, Korean SK Group invested in the company.

Founded in 2006, **Solo Power Inc.** is a California-based manufacturer of thin-film solar photovoltaic cells and modules based on CIGS. In June 2009, the company received certification under ANSI/UL 1703 standards. In February 2011, the company announced that it had received a conditional commitment from the US Department of Energy (DOE) Loan Programs Office for a US\$ 197 million (€ 152 million) loan guarantee. The company plans to construct a new manufacturing plant which, when completed and at full capacity, is expected to produce approximately 400 MW of thin-film modules annually.

**Stion** was founded in 2006 to manufacture CIGS solar cells and is headquartered in San Jose, CA. In January 2011, the company announced that another 100 MW manufacturing plant would be built in Hattiesburg, MS; it opened in October 2011 and shipped its first modules in March 2012. In December 2011 the company received a substantial equity investment from AVACO and Korean equity funds. According to press reports, Stion will set up a Korean subsidiary and construct a thin-film photovoltaic module factory in the Seongseo Industrial Complex in Daegu, Korea by 2014 [21].

**TSMC Solar** is fully owned by TSMC, one of the largest semiconductor foundries worldwide. The company started their solar business in 2009. In February 2010 they invested in a 20% stake of the silicon manufacturer Motech, Taiwan and added a 21% investment in Stion, USA in June of the same year. The CIGS thin-film plant with a nameplate capacity of 100 MW in Taichung, Taiwan became fully operational in the first quarter of 2012. A second phase is in the planning stage and could bring capacity up to 1 GW by 2015.

### 2.2.3 Kesterites

The photovoltaic effect was discovered in  $\text{Cu}_2\text{ZnSnS}_4$  (CZTS) in 1988 [22] and the family of quaternary stannite-type semiconductor, also known as kesterites, was born. Solar conversion efficiencies of close to 10% were reported in 2010, which was then increased to >11% in 2012 [23, 24].

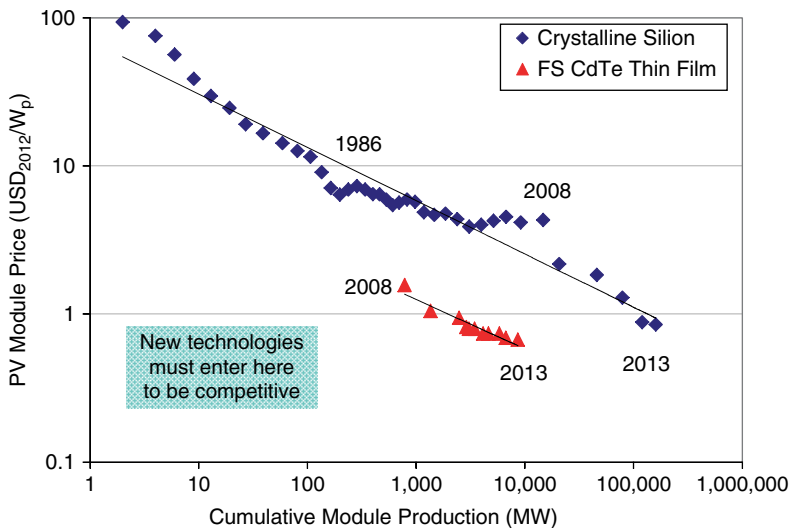
There is an ongoing discussion about whether indium and gallium are available in large enough quantities and at affordable enough prices to move CIGS manufacturing to the multi-gigawatt level needed to develop solar photovoltaic electricity generation into a major electricity source [25–28]. Kesterites are generally seen as one option to avoid the use of some of the elements in question.

No company is yet using kesterites in their manufacturing process but in 2010 IBM, DelSolar, and Solar Frontier partnered to develop the CZTS technology further. In November 2013 Solar Frontier announced that, in joint research with IBM and Tokyo Ohka Kogyo (TOK), the development of a world-record-setting CZTS solar cell with 12.6% energy conversion efficiency [29].

## 2.3 Challenges for CZTS Solar Cells in the Market

The main challenge for each new solar cell technology is the tremendous success of those technologies already in commercial production and the current market situation. Over the last 40 years, module prices have decreased by more than two orders of magnitude. However, the real challenge emerged at the end of 2008 when, after a decade of relatively stable prices, the decrease of module prices accelerated due to the economic situation and the fact that manufacturing capacities grew even faster than the rapid growing markets. During the last five years, average silicon module prices have decreased annually by 15–50% (Fig. 2.2).

Temporary shortages in silicon feedstock between 2004 and 2009, as well as the market entry of companies offering turnkey production lines for thin-film solar cells, led to a massive expansion of investments into thin-film capacities between 2005 and 2009.



**Figure 2.2** Learning curve for crystalline silicon and First Solar CdTe modules (the lines are pure trend lines to guide the eye)

This development resulted in a continuous increase of the market share for thin-film modules until 2009 when it reached almost 20%, mainly driven by the rapid capacity expansion of First Solar.

Since then, the market share of thin films has declined to about 10% and a significant number of companies have ceased operations; many of the business models were only based on the expectation to benefit from the shortage of solar modules, and they were not able to realize the necessary cost reduction through either innovation or benefits of scale.

Despite a number of bankruptcies and companies with idle production lines or even closing down their production permanently, the number of new entrants to the market is still high. Massive capacity increases are once more expected and, if all of them are realized, the worldwide production capacity for solar cells would exceed 80 GW by the end of 2015. With the optimistic market growth expectations (56–62 GW [5, 8]) the planned capacity increases are still above the market growth, even if the massive overcapacities are shrinking. Price pressure will therefore continue, but less brutal than the last few years. Nevertheless, companies in their start-up and expansion phase with limited financial resources and restricted access to capital will continue to fight an uphill battle in the given market environment. In the future, consolidation of the photovoltaic industry will continue and encourage more mergers and acquisitions.

Kesterite solar cells are still in their early development stage; as well as improvement in overall solar cell efficiency, manufacturability of the chosen processes are key to the future success of this technology. The current state of research progress is discussed in this book, describing the hurdles and opportunities for this technology.

As indicated in Figure 2.2, commercial kesterite solar cells will have to enter the mass market at a selling price of US\$ 0.6/Wp with a relatively small production capacity, generating sufficient profit to pay for the necessary capacity expansion to grow fast to compete against the larger companies. The announced industry strategy of China to favor “backbone industrial enterprises” with at least 5 GW of production capacity in 2015 adds pressure to the development of low-cost and sufficiently high-efficiency kesterite solar cells [30].

The two main pathways for kesterite solar cells to enter the market are characterized as follows.

- ***Introduction of kesterite manufacturing to an existing CIGS production plant.*** If kesterite manufacturing can be introduced without major changes to the production process and costs, this could accelerate the necessary capacity increase and manufacturing costs could be decreased through continuous technical improvement and capacity of scale. If this pathway is feasible, smaller quantities of the new product could be made available on the market while reliability and traceability of performance could be established with selected customers and project monitoring at the same time. The new product would also benefit from the already-established distribution and marketing channels.
- ***Paradigm shift and development of a revolutionary new manufacturing process with extreme low costs.*** This pathway could change the way in which solar cells are produced and open new markets. However, to establish the credibility of the new product in terms of performance reliability and the necessary bankability, sufficient funds must be available to support the manufacturing operations during this time period, which could last a few years.

## 2.4 Conclusion

The increase of conventional energy prices has increased the investment attention for renewable energies, in particular photovoltaics, significantly. Thin-film solar cells still offer the possibility of reducing the manufacturing costs considerably; however, considering the increasing maturity of wafer-based production technologies and observed learning curves, newcomers have to enter the game at already very competitive levels. In addition, the entry ticket (i.e. factory size) for thin-film manufacturers to the market is becoming more and more expensive the more the market grows. There is no “winning” technology however, and a viable variety of technology options has to be ensured. To focus on any single technology option now could be a road block in the future. No single solar cell technology can either satisfy worldwide demand or all the different wishes consumers have for the appearance or performance of PV systems.

Kesterite thin-film solar cells still require much research over a wide range of issues, ranging from improvement of the understanding of basic material properties to advanced production technologies and possible market perspectives.

## References

- [1] Liebreich, M. (2013) Scaling up financing to expand the renewables portfolio. Presentation given by Michael Liebreich (CEO), Bloomberg New Energy Finance, at the IEA Renewable Energy Working Party, Paris, 9 April 2013. Available at [http://www.iea.org/media/workshops/2013/scalingupfinancingtoexpandrenewables/2BNEF\\_20130409ParisIEA.pdf](http://www.iea.org/media/workshops/2013/scalingupfinancingtoexpandrenewables/2BNEF_20130409ParisIEA.pdf) (accessed 10 July 2014).
- [2] Ziegler, M. (2014) PV Preisindex. Available at <http://www.photovoltaiik-guide.de/pv-preisindex> (accessed 24 June 2014).
- [3] PVInsights (2014) PVinsights. Available at <http://pvinsights.com/Member/Login.php> (accessed 10 July 2014).
- [4] Bloomberg New Energy Finance (2014) H1 2014 Levelised Cost of Electricity update. Available at <https://www.bnef.com> (accessed 10 July 2014).
- [5] European Photovoltaic Industry Association (2013) Global Market Outlook for Photovoltaics until 2017. Available at [http://www.epia.org/fileadmin/user\\_upload/Publications/GMO\\_2013\\_-\\_Final\\_PDF.pdf](http://www.epia.org/fileadmin/user_upload/Publications/GMO_2013_-_Final_PDF.pdf) (accessed 10 July 2014).
- [6] HIS (2013) Solar Market Predictions for 2014. Available at <http://press.ihs.com/press-release/design-supply-chain/ihs-news-flash-solar-market-predictions-2014#sthash.IsmNLP7q.dpuf> (accessed 10 July 2014).
- [7] Solarbuzz (2013) Strong Growth Forecast for Solar PV Industry in 2014 with Demand Reaching 49 GW. Available at <http://www.solarbuzz.com/news/recent-findings/strong-growth-forecast-solar-pv-industry-2014-demand-reaching-49-gw> (accessed 10 July 2014).
- [8] Deutsche Bank Market Research (2014) 2014 Outlook: Let the Second Gold Rush begin. Available at [https://www.deutschebank.nl/nl/docs/Solar\\_-\\_2014\\_Outlook\\_Let\\_the\\_Second\\_Gold\\_Rush\\_Begin.pdf](https://www.deutschebank.nl/nl/docs/Solar_-_2014_Outlook_Let_the_Second_Gold_Rush_Begin.pdf) (accessed 10 July 2014).
- [9] Bloomberg New Energy Finance (2014) Asia-Pacific: Clean Energy Investment update. Available at <https://www.bnef.com> (accessed 10 July 2014).
- [10] Zanio, K. (1978) *Cadmium Telluride: Material Preparation, Physics, Defects and Application in Semiconductors and Semimetals*, vol. 13. Academic Press, New York.
- [11] Compaan, A. (2004) The status of and challenges in CdTe thin-film solar-cell technology. In *Proceedings of MRS Symposium O on Amorphous and Nanocrystalline Silicon Science and Technology*, Spring 2004, 808.

- [12] Green, M., Emery, K., Hishikawa, Y., Warta, W. & Dunlop, E. (2014) Solar cell efficiency tables (version 43). *Progress in Photovoltaics*, **22**, 1–9.
- [13] Wu, X., Keane, J.C., Dhere, R.G., DeHart, C., Albin, D.S., Duda, A., Gessert, T.A., Asher, S., Levi, D.H. & Sheldon, P. (2001) 16.5%-efficient CdS/CdTe polycrystalline thin-film solar cell. In *Proceedings of 17th European Photovoltaic Solar Energy Conference*, 22–26 October 2001, Munich, Germany, pp 995–1000.
- [14] Wagner, S., Shay, J.L., Migliorato, P. & Kasper, H.M. (1974) CuInSe<sub>2</sub>/CdS heterojunction photovoltaic detectors. *Applied Physics Letters*, **25**, 434.
- [15] Dimmler, B. & Schock, H.W. (1996) Scaling-up of CIS technology for thin-film solar modules. *Progress in Photovoltaics*, **4**(6), 425–433.
- [16] ZSW (2013) Press release 18/2013. Available at <http://www.zsw-bw.de/uploads/media/pi18-2013-ZSW-WorldrecordCIGS.pdf> (accessed 10 July 2014).
- [17] Solar Frontier (2013) Press release. Available at <http://www.solar-frontier.com/eng/news/2013/C020760.html> (accessed 10 July 2014).
- [18] Hanergy Solar (2014) Voluntary announcement. Available at <http://www.hkexnews.hk/listedco/listconews/SEHK/2014/0127/LTN20140127883.pdf> (accessed 10 July 2014).
- [19] Hanergy Solar (2013) Announcement. Available at <http://www.hkexnews.hk/listedco/listconews/SEHK/2013/1101/LTN20131101031.pdf> (accessed 10 July 2014).
- [20] Ascent Solar (2014) Press release. Available at <http://investors.ascentsolar.com/releasedetail.cfm?ReleaseID=816600> (accessed 10 July 2014).
- [21] Korea Times (2012) US solar firm to invest \$320 mil. in Daegu. Available at [http://www.koreatimes.co.kr/www/news/nation/2012/05/113\\_110429.html](http://www.koreatimes.co.kr/www/news/nation/2012/05/113_110429.html) (accessed 10 July 2014).
- [22] Ito, K. & Nakazawa, T. (1988) Electrical and optical properties of stannite-type quaternary semiconductor thin films. *Japanese Journal of Applied Physics*, **27**, 2094.
- [23] Todorov, T. K., Reuter, K.B. & Mitzi, D.B. (2010) High-efficiency solar cell with earth-abundant liquid-processed absorber. *Advanced Materials*, **22**(20), E156.
- [24] Todorov, T. K., Tang, J., Bag, S., Gunawan, O., Gokmen, T., Zhu, Y. & Mitzi, D. B. (2012) Beyond 11% efficiency: characteristics of state-of-the-art Cu<sub>2</sub>ZnSn(S,Se)<sub>4</sub> solar cells. *Advanced Energy Materials*, **3**(1), 34–38.
- [25] Feltrin, A. & Freundlich, A. (2008) Material considerations for terawatt level deployment of photovoltaics *Renewable Energy*, **33**, 180–185.
- [26] Green, M.A. (2009) Estimates of Te and In prices from direct mining of known ores. *Progress in Photovoltaics: Research and Applications*, **17**, 347.
- [27] Wadia, C., Alivisatos, A.P. & Kammen, D.M. (2009) Materials availability expands the opportunity for large-scale photovoltaic deployment. *Environmental Science & Technology*, **43**(6), 2072–2077.
- [28] Candelise, C., Winkler, M. & Gross, R. (2012) Implications for CdTe and CIGS technologies production costs of indium and tellurium scarcity. *Progress in Photovoltaics: Research and Applications*, **20**, 816–831.
- [29] Wang, W., Winkler, M., Gunawan, O., Gokmen, T., Todorov, T., Zhu, Y. & Mitzi, D. (2013) Device characteristics of CZTSSe thin-film solar cells with 12.6% efficiency. *Advanced Energy Materials*, **4**(7), doi: 10.1002/aenm.201301465.
- [30] Ministry of Industry and Information Technology (2012). Issuance of the solar photovoltaic industry, ‘second five development plan’ (in Chinese). Available at <http://www.miit.gov.cn/n11293472/n11293832/n12771663/14473764.html> (accessed 24 June 2014).

# **Part II**

## **The Physics and Chemistry of Quaternary Chalcogenide Semiconductors**





# 3

## Crystallographic Aspects of $\text{Cu}_2\text{ZnSnS}_4$ (CZTS)

*Susan Schorr*

*Helmholtz Centre Berlin for Materials and Energy, Department Crystallography,  
Hahn-Meitner-Platz 1, D-14109 Berlin, Germany  
Freie Universitaet Berlin, Institute of Geological Sciences, Malteserstr. 74-100,  
D-12249 Berlin, Germany*

### 3.1 Introduction: What Defines a Crystal Structure?

The word ‘crystal’ originates from the Greek word for quartz (*krystallos*), as a result of the belief that quartz was just ice which had been petrified by extreme cold.

Crystals are just the forms of the simplest ordered structures; in a crystalline material the atoms (ions) are arranged in a periodic manner in three dimensions. This periodic arrangement shows certain symmetry properties, which are rotational symmetry, mirror symmetry, inversion symmetry, screw rotational symmetry and glide mirror symmetry. The latter two are a coupling of translational and rotational (screw rotational) and translational and mirror symmetry (glide mirror), respectively. Table 3.1 provides an overview of these symmetries (in classical crystals) in addition to the symbols used to indicate the symmetry elements in the international space group notation by Hermann and Mauguin. It should be noted that there exists another space group notation by Schoenflies, which will not be used in this paper. An overview of the crystallographic classification systems (crystal systems, Bravais lattices, space groups) is provided in Table 3.2.

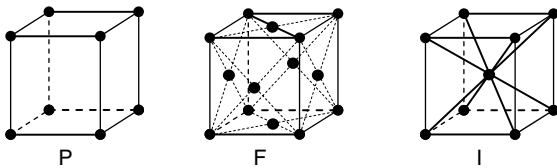
A mathematical model, the Bravais lattice, is applied for an idealized description of the three-dimensional periodic arrangement of atoms (ions). Here lattice points are used to

**Table 3.1** Symmetry, symmetry elements and their symbols

Symmetry (symmetry element)	Symbols (according to the international notation of Hermann–Maugin)
Rotational symmetry (rotational axis)	1, 2, 3, 4, 6
Inversion symmetry	$\bar{1}$
Inversion rotational symmetry (inversion rotational axis)	$\bar{3}, \bar{4}, \bar{6}$
Mirror symmetry (mirror plane)	m
Screw rotational symmetry (screw rotational axis)	$2_1, 3_1, 3_2, 4_1, 4_2, 4_3, 6_1, 6_2, 6_3, 6_4, 6_5$
Glide mirror symmetry (glide mirror plane)	a, b, c, n, d

**Table 3.2** Crystallographic classification systems

Crystallographic coordinate systems (crystal systems)	7 (triclinic, monoclinic, orthorhombic, rhomboedric (trigonal), hexagonal, tetragonal, cubic)
Bravais lattices	14
Space groups (symmetry groups)	230

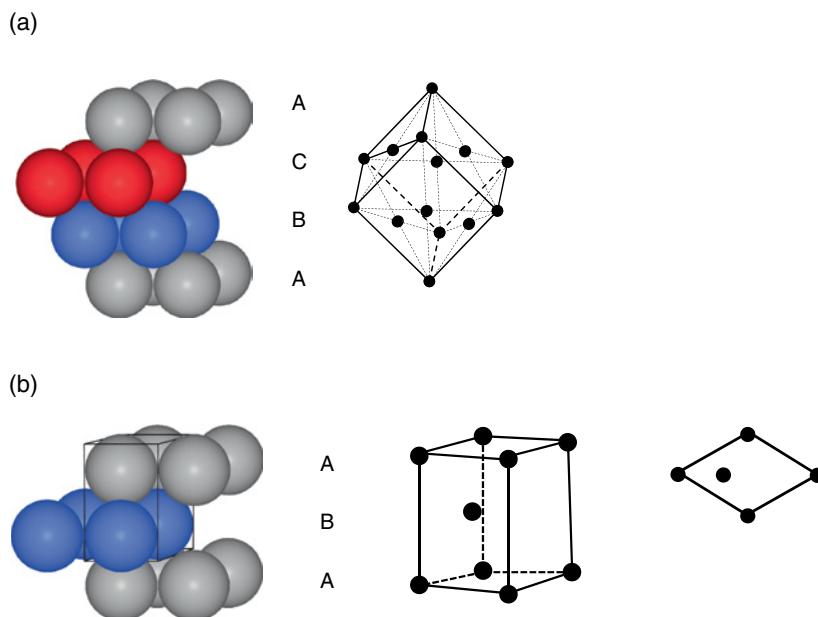


**Figure 3.1** Bravais lattice types: P: primitive; F: face centered; I: body centered (here the Bravais lattices of the cubic crystal system are shown for simplicity)

classify the basic lattice types as primitive, body-centered and face-centered (see Fig. 3.1). These lattice types are referred to as P, F, and I, respectively. These letters are also used in the space group notation to indicate the Bravais lattice type.

There are two closed packed arrays of spheres (representing atoms/ions): the cubic closed packed (ABCABC... stacking sequence) and the hexagonal closed packed (ABAB... stacking sequence) array. They can be described by means of the cubic face-centered Bravais lattice and the hexagonal centered Bravais lattice, respectively (see Fig. 3.2).

The crystal structure is defined in general as a combination of the lattice and the atoms/ions (so-called asymmetric unit) occupying certain sites within the lattice. These sites are indicated by atomic coordinates ( $x, y, z$ ) which are related to a suitable coordinate system which defines the crystallographic unit cell. The unit cell is the smallest building block of the crystal structure and reflects the symmetry of the structure as well as the chemical information on the compound. The latter is described by the value  $Z$ , equivalent to the number of formulae units/unit cell. For the kesterite-type structure as well as for the stannite-type structure, the unit cell contains four copper, two zinc, two tin and eight sulfur atoms. Taking into account the chemical composition  $\text{Cu}_2\text{ZnSnS}_4$ , this results in  $Z=2$ .



**Figure 3.2** (a) Cubic closed packed array of spheres (left) and its representation as cubic face-centered Bravais lattice (right). (b) Hexagonal closed packed array of spheres (left) and its representation as hexagonal-centered Bravais lattice (middle). Right: plan view of the hexagonal centered Bravais lattice

A crystal structure type is therefore defined by the space group, reflecting the symmetry of the atomic arrangement and a certain set of sites (Wyckoff positions) which are occupied by atomic species. The Wyckoff position is named by a number and a letter. The number gives the multiplicity of the site, and the letter is used to number the site within the space group. Often crystal structures are named from minerals or compounds, for which this structure type was determined first.

In reality, this vision of a perfect 3D periodic arrangement of atoms/ions is an ideal one. Every natural crystal has structural defects (point defects, dislocations, and the existence of a surface can be considered as a defect). These defects often influence or even determine the properties of the material in a crucial way.

For further reading on the basics of structural crystallography, textbooks such as *Structure of Materials: An Introduction to Crystallography, Diffraction and Symmetry* by M. De Graef and M. E. McHenry (Oxford University Press, 2012) are recommended.

## 3.2 The Crystal Structure of CZTS

### 3.2.1 Family Tree Structure of Adamantines

There exist two modifications of carbon in which every atom is tetrahedral bonded to four nearest neighbors. The first is diamond, providing the name for the diamond-type structure consisting of two interpenetrating face-centered cubic Bravais lattices and belonging to the space group  $\text{Fd}\bar{3}\text{m}$ . The other less known modification is lonsdaleite, providing the name

**Table 3.3** The system of Adamantine compounds

	$N=2$ (chalcogenides)	$N=3$ (pnictides)
Binary compounds	$A^{\text{II}}X^{\text{VI}}$	$A^{\text{III}}X^{\text{V}}$
Ternary compounds	$A^{\text{I}}B^{\text{III}}X_2^{\text{VI}}$	$A^{\text{II}}B^{\text{IV}}X_2^{\text{V}}$
Quaternary compounds	$A_2^{\text{I}}B^{\text{II}}C^{\text{IV}}X_4^{\text{VI}}$	$A_2^{\text{II}}B^{\text{IV}}C^{\text{V}}X_4^{\text{V}}$

for the lonsdaleite-type structure which is built of two interpenetrating hexagonal-centered lattices, belonging to the space group  $P6_3/mmc$ . These two crystal structures each form the starting point of the structure tree of a compound family, which is based on a tetrahedral coordination and on an ordering of the atomic species on the two interpenetrating lattice types. Chemical phases crystallizing in structures derived from the diamond-type structure or the lonsdaleite-type structure (or a hybrid of the two) are referred to as *Adamantines* [1].

To derive the crystal structures within the Adamantine family tree (Table 3.3), the octet rule of classical chemistry has to be satisfied which ensures that there are four electrons per atom (four-electrons-per-site rule). Nevertheless, some compounds exist which contain vacant cation sites and also lone electron pairs on the corresponding anions, for instance, the so-called vacancy compounds  $\text{CuIn}_3(\text{S}, \text{Se})_5$  and  $\text{CuIn}_3\text{Se}_8$  (the vacancy compound  $\text{CuIn}_3\text{S}_8$  crystallizes in the spinel-type structure; here the indium exists in tetrahedral and also octahedral coordination). It is assumed that vacancies can assist compound formation [1, 2].

Pamplin [1] has derived some empirical basic rules which are valid for Adamantine phases. These state that the two interpenetrating Bravais lattices, from which the structure is built, must both be populated with cations and anions. There is therefore always a cation substructure and an anion substructure. The metals are ordered on defined cation sites, comprising one or more unit cells of the parent structures (diamond or lonsdaleite structure). This led to typical superstructures with lowered symmetries. Moreover, some elements (e.g. Cu, Zn, Si, Ge, Ga, Ag, S, Se, and Te) are often found to be constituents of Adamantine compounds. They prefer tetrahedral coordination due to their tendency for  $sp^3$  bonding.

Binary compounds of the Adamantine family have the general formulae  $A^N X^{8-N}$ , where  $N$  is the group number in the periodic table of elements. They crystallize according to the ionicity of the chemical bonds between A and X in the sphalerite-type structure (which is also referred to as zincblende-type structure) which belongs to the cubic crystal system, or in the wurtzite-type structure which belongs to the hexagonal crystal system. Both cations A and anions X occupy one of the two interpenetrating Bravais lattices each. The transition from the sphalerite- to the wurtzite-type structure, as observed in the temperature-dependent structural phase transition for instance in ZnS, occurs just by changing the stacking sequence from ABCABC to ABAB. This change can be easily realized by stacking faults.

In ternary compounds of the Adamantine family the sites in the Bravais lattice of the cations are occupied by two different cation species A and B, resulting in the general formulae  $A^{N-1}B^{N+1}X_2^{8-N}$ . The both most important representatives are  $A^{\text{I}}B^{\text{III}}X_2^{\text{VI}}$  compounds ( $N=2$ ) and  $A^{\text{II}}B^{\text{IV}}X_2^{\text{V}}$  compounds ( $N=3$ ). Depending on the ionicity of the chemical bonds between A–X and B–X they crystallize in the chalcopyrite-type structure or adopt the  $\beta$ - $\text{NaFeO}_2$ -type structure [3]. The chalcopyrite-type structure belongs to the tetragonal crystal system, whereas the  $\beta$ - $\text{NaFeO}_2$ -type structure belongs to the orthorhombic crystal system. The latter can also be seen as a superstructure of the wurtzite-type structure [3].

**Table 3.4** Crystal structure types within the Adamantine compound family. The crystal system is provided in parentheses, after which the chemical formula of the mineral is provided

	Diamond-type structure	Lonsdaleite-type structure
Binary compounds	Sphalerite structure (cubic), $\text{ZnS}$	Wurtzite structure (hexagonal), $\text{ZnS}$
Ternary compounds	Chalcopyrite structure (tetragonal), $\text{CuFeS}_2$	$\beta$ - $\text{NaFeO}_2$ -type structure (orthorhombic)
Quaternary compounds	Stannite structure (tetragonal), $\text{Cu}_2\text{FeSnS}_4$	Wurtz-stannite structure (orthorhombic)
	Kesterite structure (tetragonal), $\text{Cu}_2\text{ZnSnS}_4$	Wurtz-kesterite structure (monoclinic)

The symmetry of the ternary compounds is therefore reduced with respect to the binary compounds, which is a general aspect within the crystal structure tree.

Quaternary compounds of the Adamantine family can be represented by the general formulae  $\text{A}_2^{N-1}\text{B}^{2N-2}\text{C}^{N+2}\text{X}_4^{8-N}$ . Most important are the  $\text{A}_2^{\text{I}}\text{B}^{\text{II}}\text{C}^{\text{IV}}\text{X}_4^{\text{VI}}$  compounds ( $N=2$ ). They crystallize in the kesterite- or stannite-type structure which belong to the tetragonal crystal system, as well as in the wurtz-kesterite- or wurtz-stannite-type structure, which belong to the monoclinic and orthorhombic crystal system.

An overview of the general formulae of the adamantine compounds is provided in Table 3.4. Table 3.5 lists the definition of the crystal structures of interest; use Table 3.1 to understand the space group symbols used in the definition of several crystal structure types. The atomic species occupy so-called special sites, for instance  $(0, 0, 0)$  or  $(0, \frac{1}{2}, \frac{1}{4})$ , as well as so-called general sites, for example  $(x, x, z)$  or  $(x, y, z)$ . In the latter the value of the atomic coordinates depends on the compound, that is, two different compounds which crystallize in the same structure type have different atomic coordinates. For instance, the anion in the kesterite-type structure occupies a  $(x, y, z)$  position which corresponds to  $(0.7416, 0.7416, 0.6287)$  for  $\text{Cu}_2\text{ZnSnSe}_4$  and  $(0.7538, 0.75993, 0.8769)$  for  $\text{Cu}_2\text{ZnGeSe}_4$  (G. Gurieva, pers. comm., 2012). Illustrations of the different crystal structures are provided in Table 3.6.

All these crystal structures have been determined precisely by single-crystal X-ray diffraction (XRD) and are listed in the International Crystal Structure Database (ICSD). This knowledge can be used to identify Adamantine phases present in bulk or polycrystalline thin-film samples using X-ray powder diffraction (for thin films applying the grazing incidence geometry). The method of Rietveld refinement [4] of powder diffraction data is most suitable for determining structural parameters of the crystalline phases.

### 3.2.2 Kesterite v. Stannite-Type Structure and other Polytypes

For  $\text{A}_2^{\text{I}}\text{B}^{\text{II}}\text{C}^{\text{IV}}\text{X}_4^{\text{VI}}$  compounds, different crystal structure types are discussed in the literature, including the kesterite- and the stannite-type structures, which can be seen as tetragonal superstructures of the sphalerite structure, as well as the wurtz-stannite- and wurtz-kesterite-type structures, which are orthorhombic and monoclinic superstructures of the wurtzite-type structure. The two former structures are discussed in this section.

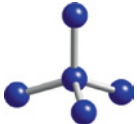
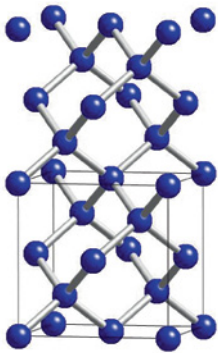
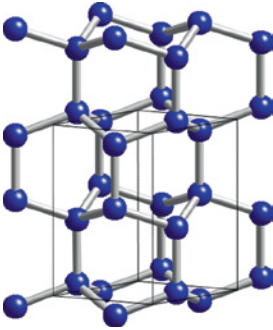
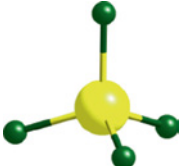
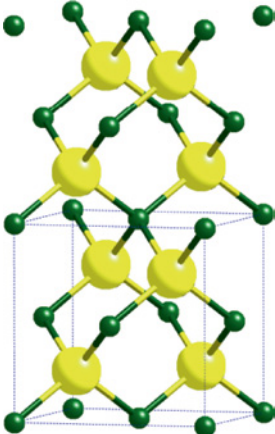
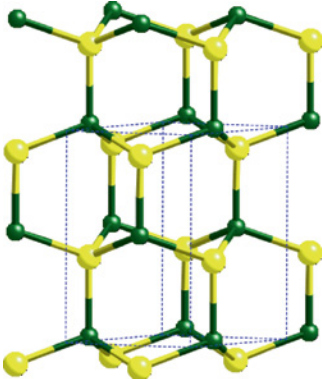

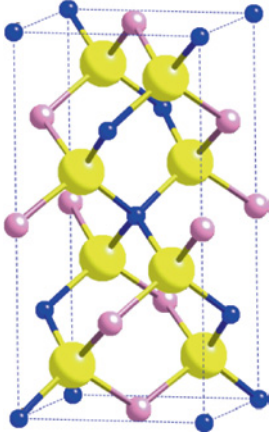
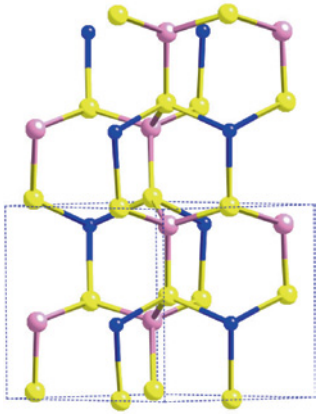
**Table 3.5** Definition of the crystal structure types of interest, based on the (1) diamond-type and (2) lonsdaleite-type structure. Site occupancies by atomic species are only named for chalcogenides

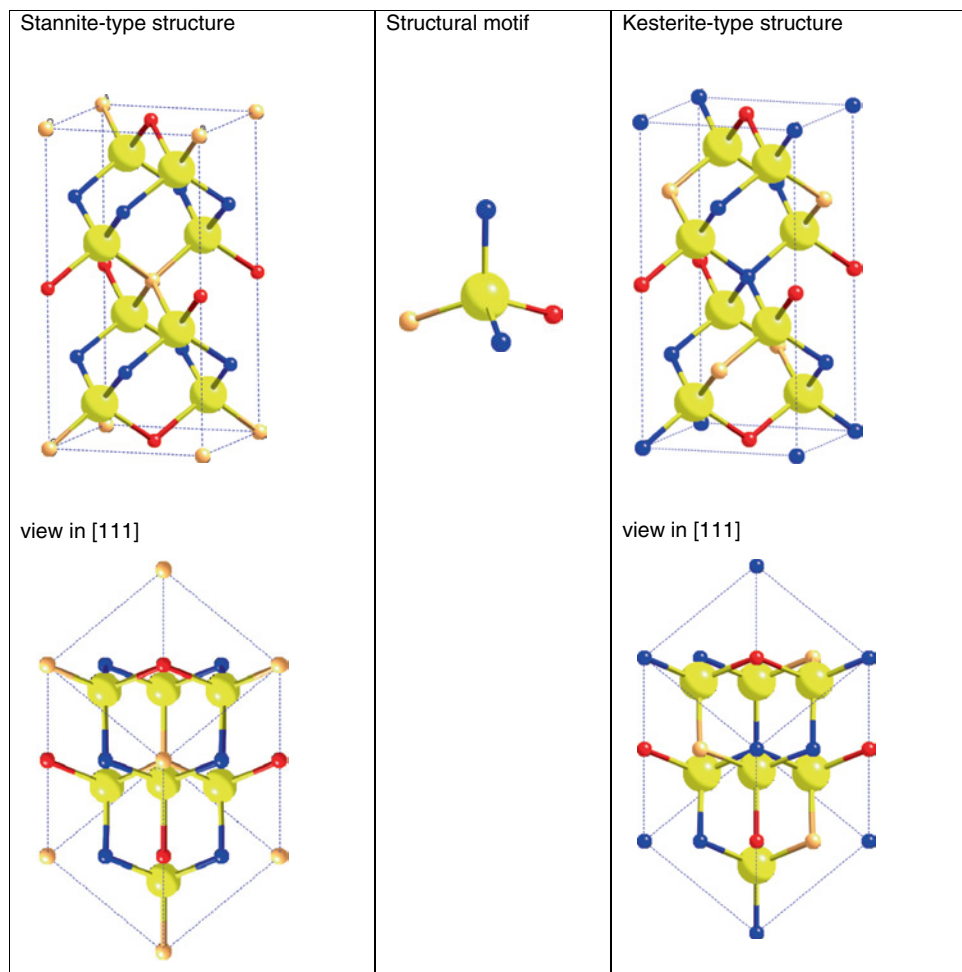
Structure type	Space group	Wyckoff positions and site occupancies
(1) Diamond-type		
Sphalerite	$F\bar{4}3d$	4a: (0, 0, 0) occupied by A <sup>II</sup> 4b: ( $\frac{1}{4}$ , $\frac{1}{4}$ , $\frac{1}{4}$ ) occupied by X <sup>VI</sup>
Chalcopyrite	$\bar{1}42d$	4a: (0, 0, 0) occupied by A <sup>I</sup> 4b: (0, 0, $\frac{1}{2}$ ) occupied by B <sup>III</sup> 8d: ( $x$ , $\frac{1}{4}$ , $\frac{1}{8}$ ) occupied by X <sup>VI</sup>
Stannite [4]	$\bar{1}42m$	2a: (0, 0, 0) occupied by B <sup>II</sup> 4d: (0, $\frac{1}{2}$ , $\frac{1}{4}$ ) occupied by A <sup>I</sup> 2b: ( $\frac{1}{2}$ , $\frac{1}{2}$ , 0) occupied by C <sup>IV</sup> 8g: ( $x$ , $x$ , $z$ ) occupied by X <sup>VI</sup>
Kesterite [5]	$\bar{1}4$	2a: (0, 0, 0) occupied by A <sup>I</sup> 2c: (0, $\frac{1}{2}$ , $\frac{1}{4}$ ) occupied by A <sup>I</sup> 2d: (0, $\frac{1}{2}$ , $\frac{3}{4}$ ) occupied by B <sup>II</sup> 2b: ( $\frac{1}{2}$ , $\frac{1}{2}$ , 0) occupied by C <sup>IV</sup> 8i: ( $x$ , $y$ , $z$ ) occupied by X <sup>VI</sup>
(2) Lonsdaleite-type		
Wurtzite	$P6_3mc$	2b: ( $\frac{1}{3}$ , $\frac{2}{3}$ , $z$ ) occupied by A <sup>II</sup> 2b: ( $\frac{1}{3}$ , $\frac{2}{3}$ , $z$ ) occupied by X <sup>VI</sup>
$\beta$ -NaFeO <sub>2</sub> [3]	$Pna2_1$	4a: ( $x$ , $y$ , $z$ ) occupied by A <sup>I</sup> 4a: ( $x$ , $y$ , $z$ ) occupied by B <sup>III</sup> 4a: ( $x$ , $y$ , $z$ ) occupied by X <sup>VI</sup>
Wurtz-stannite [5]	$Pmn2_1$	2a: (0, $y$ , $z$ ) occupied by B <sup>II</sup> 4b: ( $x$ , $y$ , $z$ ) occupied by A <sup>I</sup> 2a: (0, $y$ , $z$ ) occupied by C <sup>IV</sup> 2a: (0, $y$ , $z$ ) occupied by X <sup>VI</sup> (2 different positions occur) 4b: ( $x$ , $y$ , $z$ ) occupied by X <sup>VI</sup>
Wurtz-kesterite [12]	Pc	2a: ( $x$ , $y$ , $z$ ) occupied by A <sup>I</sup> (4 different positions occur) 2a: ( $x$ , $y$ , $z$ ) occupied by B <sup>II</sup> (2 different positions occur) 2a: ( $x$ , $y$ , $z$ ) occupied by C <sup>IV</sup> (2 different positions occur) 2a: ( $x$ , $y$ , $z$ ) occupied by X <sup>VI</sup> (8 different positions occur)

The quaternary compound Cu<sub>2</sub>ZnSnS<sub>4</sub> is known as the natural mineral kesterite, after which the kesterite-type structure is named. The stannite-type structure is named after the mineral stannite (Cu<sub>2</sub>FeSnS<sub>4</sub>). Both structures are closely related, but show a different cation distribution which leads to different space groups (see Table 3.5). The kesterite-type structure is characterized by alternating cation layers of CuSn, CuZn, CuSn, and CuZn at  $z=0$ ,  $\frac{1}{4}$ ,  $\frac{1}{2}$ , and  $\frac{3}{4}$ , respectively (Fig. 3.3). On the other hand, in the stannite-type structure ZnSn layers alternate with Cu<sub>2</sub> layers (Fig. 3.3). In both structures Sn is located at the same structural site [5]. The sequence of the cation layers in the stannite-type structure is reminiscent of the CuAuI-type cation ordering in CuInS<sub>2</sub>, in which Cu<sub>2</sub> layers alternate with In<sub>2</sub> layers.

Another structural difference is the anion position. In the stannite-type structure the anion lies on the (110) mirror plane on a ( $x$ ,  $x$ ,  $z$ ) position. In the kesterite-type structure the anion occupies a ( $x$ ,  $y$ ,  $z$ ) position; the mirror symmetry therefore vanishes. For Cu<sub>2</sub>ZnSnS<sub>4</sub>, the single-crystal XRD-determined anion position is (0.7560, 0.7566, 0.8722) [5]. It can

**Table 3.6** Crystal structure representations. (See Fig. 3.3 and Section 3.2.3 for the structure of quaternary compounds)

Diamond structure related branch	Structural motif	Lonsdaleite structure related branch
Diamond-type structure (2 unit cells are shown; 1 is indicated)		Lonsdaleite-type structure
		
Sphalerite-type structure (2 unit cells are shown; 1 is indicated)		Wurtzite-type structure
		
Chalcopyrite-type structure		$\beta$ -NaFeO <sub>2</sub> -type structure
		



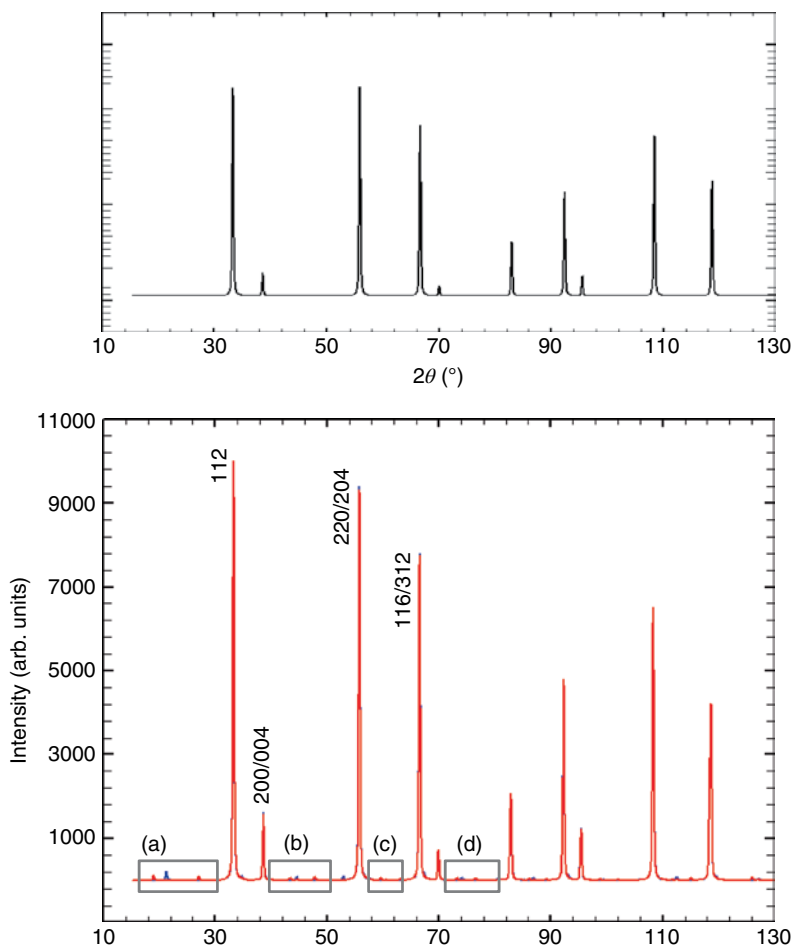
**Figure 3.3** Representations of the stannite and kesterite type structure (blue: Cu, orange: Zn, red: Sn, yellow: S). For color details, please see color plate section

be seen that the difference between  $x$  and  $y$  is very small and almost impossible to determine with high accuracy from powder diffraction data.

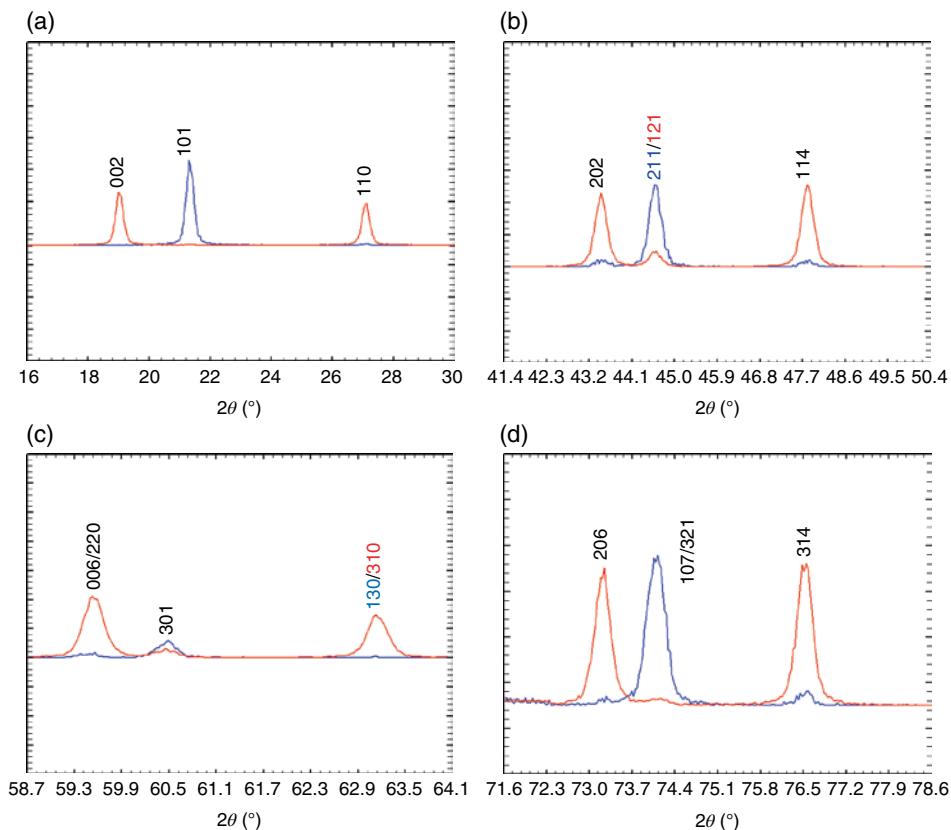
It should be kept in mind however that the same tetrahedral metal coordination (2 Cu, 1 Zn and 1 Sn surrounding each S-atom) is possible in space group  $I\bar{4}$  and  $I\bar{4}2m$ . A clear decision can only be made by a detailed structure analysis for the compound [6]. Figure 3.4 shows a simulated neutron powder diffraction pattern of  $\text{Cu}_2\text{ZnSnS}_4$  in comparison with simulated data for ZnS. It can be seen that the main Bragg peaks for both compounds are the same, which is not surprising due to the structure-superstructure relation between the crystal structures. The difference between the diffraction patterns lies in the additional superstructure reflections occurring for  $\text{Cu}_2\text{ZnSnS}_4$ . These Bragg peaks occur due to the ordered distribution of cations, but they are very low in intensity (see Table 3.7). Measurements with very good statistics are therefore necessary for the structural



refinement procedure. Moreover, it is unsurprising that the grazing incidence XRD pattern of polycrystalline  $\text{Cu}_2\text{ZnSnS}_4$  thin films appears to adopt a sphalerite-type structure, because the superstructure peaks are hard to detect. The strongest superstructure peak is the 101 Bragg peak; it is therefore recommended to start the diffraction measurement at a  $2\theta$  value at which it is suitable to detect that peak. Another feature in the powder diffraction pattern due to the tetragonal symmetry is the so-called tetragonal peak splitting. The Bragg peaks of the parent structure (in this case the cubic sphalerite-type structure) occur in the diffraction pattern of the tetragonal compound CZTS as two peaks. This is due to the lower symmetry of CZTS and the tetragonal unit cell with  $c \neq 2a$  ( $a$ ,  $c$  are the lattice parameters). In the case of CZTS the  $c/2a$  ratio is very close to 1; the tetragonal peak splitting is therefore very small and, in measurements with poor resolution, it gives the impression of only



**Figure 3.4** Simulated neutron powder diffraction pattern ( $\lambda = 1.79 \text{ \AA}$ ) for: ZnS (top) and  $\text{Cu}_2\text{ZnSnS}_4$  (middle) in kesterite- (blue) and stannite- (red) type structure. The four regions (a)–(d) marked in the diffraction pattern of  $\text{Cu}_2\text{ZnSnS}_4$ , indicating the small superstructure reflections. For color details, please see color plate section



**Figure 3.4** (continued)

one Bragg peak at the corresponding  $2\theta$  positions. Moreover it should be noted that the order of the two Bragg peaks, which arise due to the tetragonal peak splitting, changes depending on whether  $c/2a > 1$  or  $< 1$ . In the case of the calculation in Table 3.7,  $c/2a > 1$  and so the order of the Bragg peaks is 004/200, 204/220 and 116/312. If  $c/2a < 1$  then the order is reversed. The same is true for the chalcopyrite-type compound  $\text{Cu}(\text{In,Ga})\text{Se}_2$ . For  $\text{CuInSe}_2$   $c/2a > 1$  whereas for  $\text{CuGaSe}_2$   $c/2a < 1$ ; for a certain Ga content  $c = 2a$  [6, 7]. This pseudo-cubic ratio can also be reached for CZTS, for instance by alloying CZTS with  $\text{CuInS}_2$ . It has been shown that CZTS with an indium content of c. 10% adopts the kesterite-type structure with lattice parameter showing a  $c/2a$  ratio of c. 1 [8].

Due to the very similar atomic form factors of  $\text{Cu}^+$  and  $\text{Zn}^{2+}$  (copper and zinc are neighboring elements in the periodic table), they cannot be distinguished in the data analysis of a conventional XRD diffraction experiment. Their neutron scattering lengths are however different, and so neutron powder diffraction has been applied to solve the question of the cation distribution in  $\text{Cu}_2\text{ZnSnS}_4$  [8, 9]. Figure 3.4 shows a simulated neutron diffraction pattern for CZTS assuming a kesterite- and a stannite-type structure, respectively. It can be seen that the major differences are in the small superstructure reflections.

**Table 3.7** Bragg peaks of ZnS and CZTS: superstructure and tetragonal peak splitting. For the calculation of the  $d$  values, the lattice parameters ZnS:  $a = 5.406 \text{ \AA}$ ; CZTS:  $a = 5.427 \text{ \AA}$ ,  $c = 10.871 \text{ \AA}$  were used. The relative intensities are valid for X-rays ( $\text{CuK}\alpha$  radiation)

ZnS (sphalerite type)			CZTS (kesterite type)			Remark
hkl	$d$ ( $\text{\AA}$ )	$I_{\text{rel}}$	hkl	$d$ ( $\text{\AA}$ )	$I_{\text{rel}}$	
111	3.121	100.00	002	5.435	1.24	Superstructure peak
			101	4.855	4.33	Superstructure peak
			110	3.837	1.47	Superstructure peak
200	2.703	11.88	112	3.135	100.00	Strongest Bragg peak
			103	3.014	2.09	Superstructure peak
			004	2.718	5.05	Tetragonal peak splitting
220	1.911	60.80	200	2.713	10.07	
			202	2.428	1.10	Superstructure peak
			121	2.369	1.15	Superstructure peak
			211	2.369	1.15	Superstructure peak
			114	2.218	<1	Superstructure peak
			105	2.018	<1	Superstructure peak
			123	2.016	<1	Superstructure peak
			213	2.016	<1	Superstructure peak
			204	1.920	36.73	Tetragonal peak splitting
			220	1.919	18.31	
311	1.630	40.83	006	1.811	<1	Superstructure peak
			222	1.809	<1	Superstructure peak
			301	1.784	<1	Superstructure peak
			130	1.716	<1	Superstructure peak
			310	1.716	<1	Superstructure peak
			116	1.638		Tetragonal peak splitting
			312	1.636		

It was shown by neutron powder diffraction analysis that the crystal structure of CZTS and CZTSe powder is the kesterite-type structure [9–11]. Nevertheless, this method cannot be applied to thin films due to the relatively large sample volumes (c.  $1 \text{ cm}^3$ ) necessary for neutron diffraction experiments. Using synchrotron radiation and choosing an appropriate X-ray wavelength that causes an anomalous dispersion effect on the atomic scattering factor of copper, it was possible to determine the crystal structure of CZTS using only a small sample volume [12].

Table 3.8 provides a comparison of lattice parameters for CZTS prepared by different methods and theoretical values. The situation is similar to that in the chalcopyrites: the lattice parameters vary widely due to the varying chemical composition but also probably due to cation disorder (defects).

Table 3.9 shows the total energy (meV/atom) of  $\text{Cu}_2\text{ZnSnS}_4$  in different crystal structures, which was calculated within the density-functional formalism [13]. According to these theoretical studies, based on first-principle calculation, the kesterite-type structure is the ground state structure in  $\text{Cu}_2\text{ZnSnS}_4$ , but the energy difference between the kesterite- and the stannite-type structure is small.

As well as the kesterite- and stannite-type structure, different polytypes based on a tetragonal unit cell are described in the literature [21, 22]. Nevertheless, their total energy is always larger than the energy required for the kesterite-type structure.

**Table 3.8** Lattice parameters for different CZTS samples (powder and thin films). The reference given in “Sample type” refers to the sample preparation and the reference to the lattice parameter determination

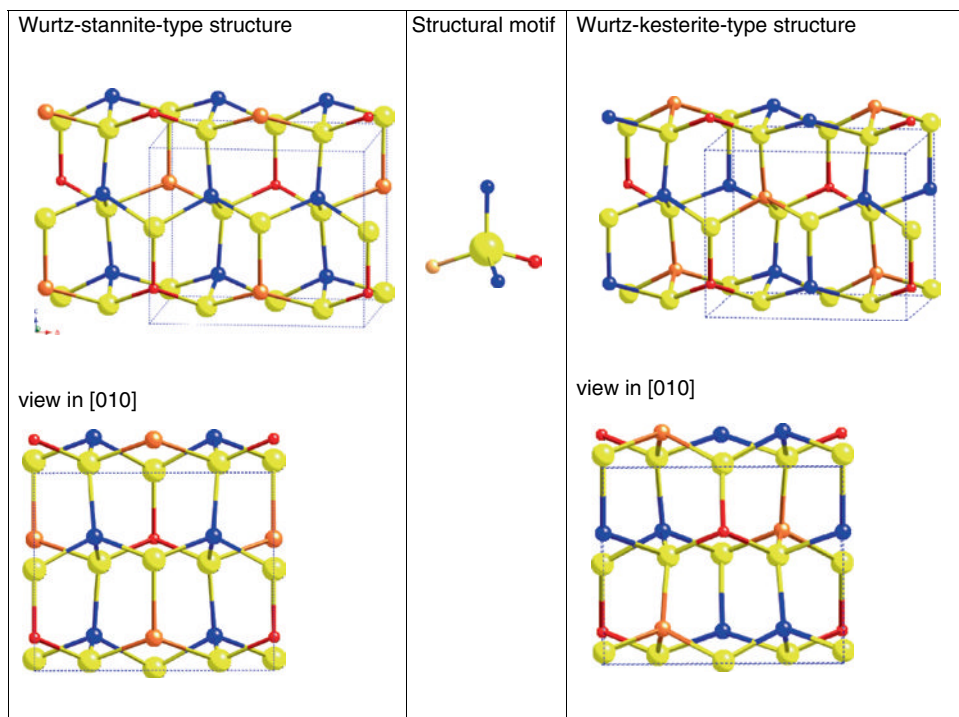
No.	Sample type	Ref.	a (Å)	c (Å)	c/(2a)
1	Single crystal, single-crystal XRD	[13]	5.434 (1)	10.856 (1)	0.9989 (2)
2	Powder sample, grown by solid state reaction, quenched at 750°C, stoichiometric composition, neutron diffraction	[8]	5.428 (2)	10.864 (2)	1.0008 (5)
3	Powder sample (same as no. 2) cooled at 1 K h <sup>-1</sup> to room temperature, stoichiometric composition, neutron diffraction	own work	5.419 (2)	10.854 (2)	1.0015 (4)
4	Powder sample grown by Bridgman technique (Cu/(Zn + Sn) = 1.03; Zn/Sn = 1.07), contains secondary phase ZnS, neutron diffraction	own work	5.434 (2)	10.827 (2)	0.9962 (4)
5	Thin film co-evaporation [14] (Cu/(Zn + Sn) = 0.9; Zn/Sn = 1.0), grazing incidence XRD	own work, [14]	5.431 (2)	10.840 (2)	0.9979 (4)
6	Thin-film spray pyrolysis [15]: Cu/(Zn + Sn) = 1.03; Zn/Sn = 0.97 Cu/(Zn + Sn) = 0.89; Zn/Sn = 0.81 Cu/(Zn + Sn) = 0.92; Zn/Sn = 0.72 grazing incidence XRD	own work, [15]	5.423 (2) 5.428 (2) 5.428 (2)	10.860 (2) 10.829 (2) 10.823 (2)	1.0013 (4) 0.9975 (4) 0.9970 (4)
7	Single crystals Cu/(Zn + Sn) = 0.99; Zn/Sn = 0.90 Cu/(Zn + Sn) = 0.89; Zn/Sn = 1.10 Cu/(Zn + Sn) = 0.79; Zn/Sn = 1.19 Cu/(Zn + Sn) = 0.96; Zn/Sn = 1.08 Cu/(Zn + Sn) = 1.17; Zn/Sn = 0.75 resonant X-ray scattering Theoretical values (see also [20])	[16]      [17–20]	5.4344 (2) 5.4334 (1) 5.4301 (1) 5.4279 (1) 5.4294 (1) 5.465 5.739	10.8382 (6) 10.8311 (2) 10.8222 (2) 10.8289 (3) 10.8391 (2) 10.944 11.389	0.9972 (3) 0.9969 (3) 0.9965 (3) 0.9975 (3) 0.9982 (3) 1.000 0.9923

**Table 3.9** Total energy (meV/atom) in different crystal structures relative to the kesterite type structure [12]

	Kesterite	Stannite	Wurtz-kesterite	Wurtz-stannite
Cu <sub>2</sub> ZnSnS <sub>4</sub>	0.0	2.8	6.0	7.2

**3.2.3 The Wurtz-Stannite- and the Wurtz-Kesterite-Type Structure**

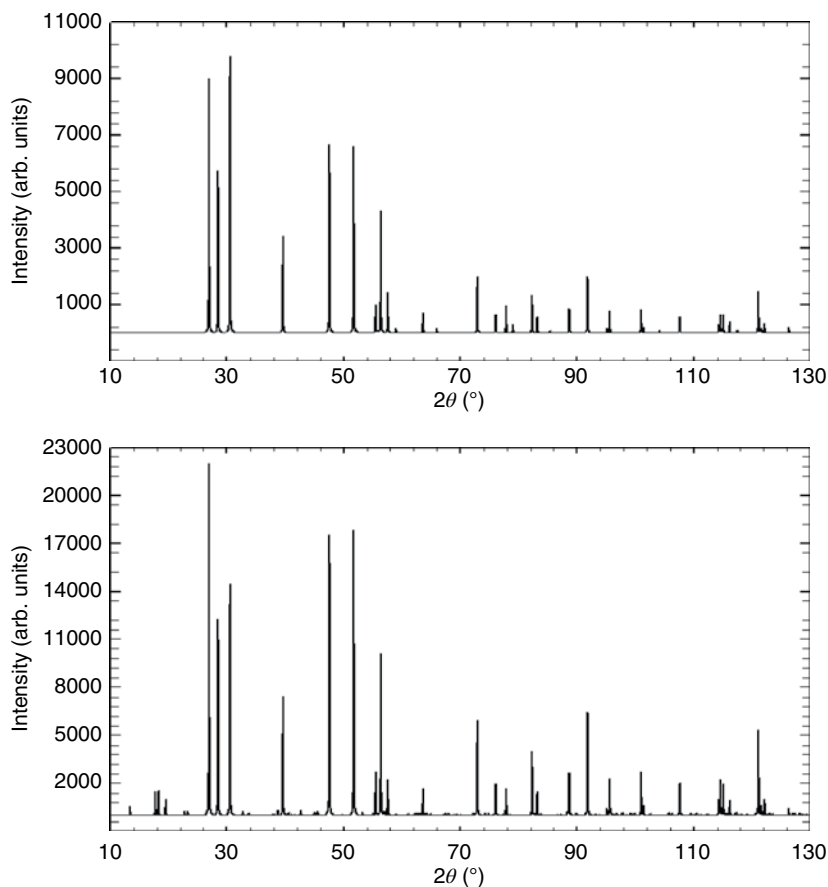
A<sub>2</sub><sup>I</sup>B<sup>II</sup>C<sup>IV</sup>X<sub>4</sub><sup>VI</sup> compounds containing Si as four-valent cation, such as Cu<sub>2</sub>ZnSiS<sub>4</sub>(Se<sub>4</sub>), are reported in the literature to adopt the wurtz-stannite-type structure [6]. This structure type was also reported for CZTSe nanocrystals [23]. Wurtzite-derived structures were also considered for CZTS, and total energy calculations are reported in the literature (see Table 3.9).



**Figure 3.5** Representations of the wurtz-stannite and wurtz-kesterite type structure (blue: Cu, orange: Zn, red: Sn, yellow: S).

The wurtz-stannite- and wurtz-kesterite-type structure (see structure representations in Fig. 3.5) can be derived from the wurtzite-type structure in a similar way as the kesterite- and stannite-type structure is derived from the sphalerite-type structure, that is, by doubling the unit cell of the wurtzite-type structure in the direction of the crystallographic  $c$  axis and introducing three different cations ( $A^I$ ,  $B^{II}$  and  $C^{IV}$ ) in an ordered way. The majority of the reported wurtz-stannite-type structures can be predicted as an orthorhombic superstructure of the wurtzite-type structure with unit cell dimension  $a_{\text{or}} \sim 2a_{\text{w}}$ ,  $b_{\text{or}} \sim \sqrt{3}a_{\text{w}}$  and  $c_{\text{or}} \sim c_{\text{w}}$  (where subscripts or and w represent orthorhombic and wurtzite). Details of these crystal structures can be found in Table 3.5. Note that the same tetrahedral metal coordination (2 Cu, 1 Zn and 1 Sn surrounding each S-atom) is possible in space group  $\text{Pmn}2_1$  and  $\text{Pc}$ . A clear decision can only be made by a detailed structure analysis for the compound.

Because both these structures are related to the wurtzite structure, their diffraction patterns show similar features. Figure 3.6 depicts a simulated X-ray diffraction pattern for ZnS in a wurtzite-type structure and CZTS in a wurtz-stannite-type structure. As for sphalerite and kesterite/stannite-type structures, the main Bragg peaks for both compounds are identical which is due to the structure-superstructure relation between the crystal structures. The difference lies in the additional superstructure reflections occurring for wurtz-stannite-type  $\text{Cu}_2\text{ZnSnS}_4$ . These Bragg peaks occur due to the ordered distribution of cations, but they are very low in intensity.



**Figure 3.6** Simulated X-ray diffraction pattern for wurtzite-type ZnS (top) and wurtz-stannite-type CZTS (bottom). The simulation was performed assuming CuK $\alpha$  radiation

Highly characteristic of these wurtzite-derived structures is the group of three Bragg peaks in the low  $2\theta$  region. In the pattern of wurtzite-type compounds these are three individual reflections, whereas in wurtz-stannite-type compounds a peak splitting of the first and the third Bragg peak within this group occurs (see Table 3.10). Nevertheless, the peak splitting is very small and depends on the ratios of the orthorhombic lattice parameters.

### 3.3 Point Defects in CZTS and the Role of Stoichiometry

Efficiencies of CZTSSe-based thin-film solar cells of higher than 8% are reported in literature for thin films with elemental ratios of Cu/(Zn+Sn)  $\sim$  0.8 and Zn/Sn  $\sim$  1.2 [24–29]. It therefore appears that Cu-poor and Zn-rich growth conditions should yield the highest

**Table 3.10** Bragg peaks of ZnS and CZTS in the lower  $2\theta$  range: orthorhombic peak splitting. For the calculation of the  $d$  values the lattice parameters ZnS:  $a = 3.318 \text{ \AA}$  and  $c = 6.260 \text{ \AA}$ ; CZTS:  $a = 2a_w$ ,  $b = \sqrt{3}b_w$  and  $c = c_w$ . The low-intensity superstructure reflections for the wurtz-stannite type CZTS phase are not shown. The relative intensities are valid for X-rays ( $\text{CuK}\alpha$  radiation)

ZnS (wurtzite type)			CZTS (wurtz-stannite type)			
hkl	$d$ (Å)	$I_{\text{rel}}$	hkl	$d$ (Å)	$I_{\text{rel}}$	Remark
100	3.306	92.37	210	3.3064	100.00	Orthorhombic peak splitting
			020	3.3060	48.01	
002	3.130	59.47	002	3.130	85.00	Orthorhombic peak splitting
101	2.924	100.00	211	2.9236	67.25	
			021	2.9234	32.25	

**Table 3.11** Calculated formation energies (eV) for intrinsic point defects in CZTS under different growth conditions

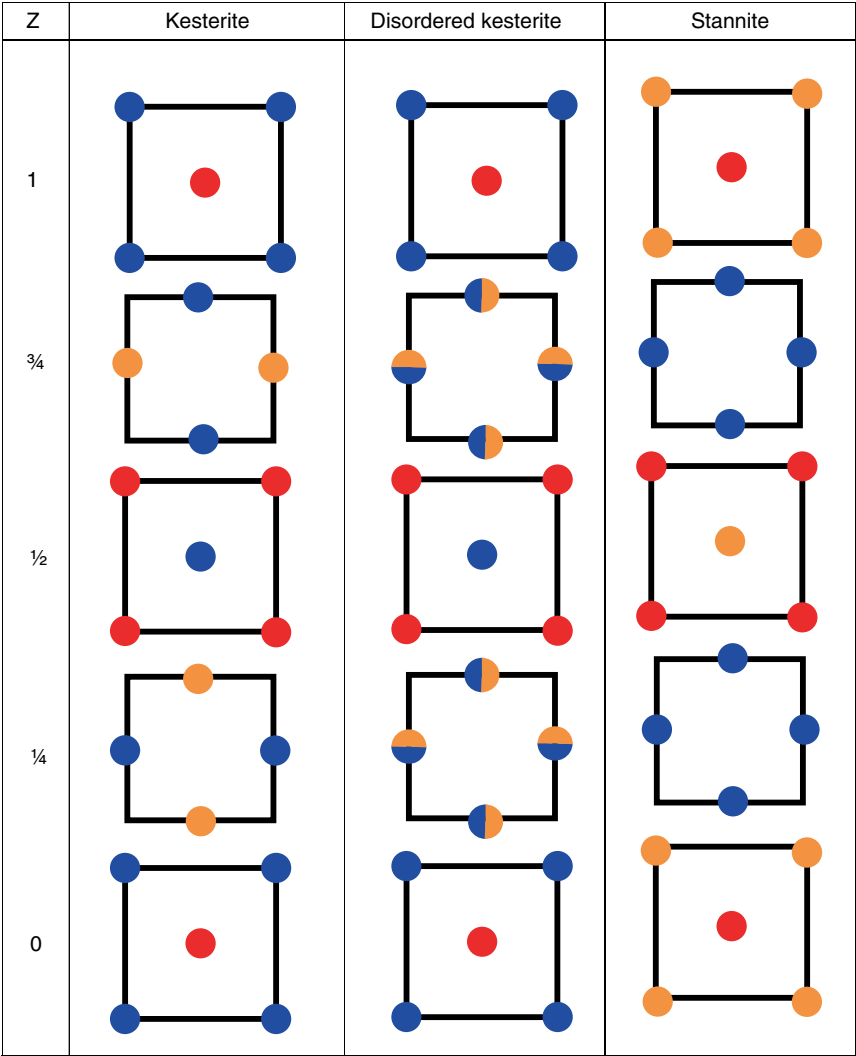
Defect	[32]	Cu-poor conditions [30]
$V_{\text{Cu}}$	0.590	0.21–0.67
$\text{Zn}_{\text{Cu}}$	−0.064 to −0.318	2.43–2.60
$\text{Cu}_{\text{Zn}}$	0.378–0.632	−0.16 to 0.01
$V_{\text{Zn}}$	0.631–0.885	0.39–1.02
$\text{Sn}_{\text{Zn}}$	0.158–0.599	4.11–4.44
$\text{Sn}_{\text{Cu}}$	0.170–0.732	6.54–7.05

device performance. Such compositional ratios represent a strong deviation from stoichiometry and probably indicate the existence of secondary phases, for instance ZnS, or a high population of intrinsic defects. Nevertheless, both possibilities would have a detrimental influence on the solar cell performance; the interplay of intrinsic point defects is therefore complex in CZTS because, despite these apparent problems, the efficiencies are promising.

Several authors report the calculation of the formation energies of defects and defect clusters in CZTS, based on first-principle theory [19, 30–33]. It has been shown that copper vacancies ( $V_{\text{Cu}}$ ) and some defect pairs such as ( $V_{\text{Cu}} + \text{Zn}_{\text{Cu}}$ ) and ( $\text{Cu}_{\text{Zn}} + \text{Zn}_{\text{Cu}}$ ) are easily formed under Cu-poor and Zn-rich conditions [31]. The antisite defect  $\text{Zn}_{\text{Cu}}$  even has a negative formation energy [33]. It has been assumed that  $V_{\text{Cu}}$  but also  $\text{Cu}_{\text{Zn}}$  are the dominant acceptor defects in CZTS [32, 34] which cause the p-type conductivity of the compound. The formation energy of interstitial defects is  $>1 \text{ eV}$  [33]. All donor defects show higher formation energies. An overview of the defect formation energies in CZTS under different growth conditions is provided in Table 3.11.

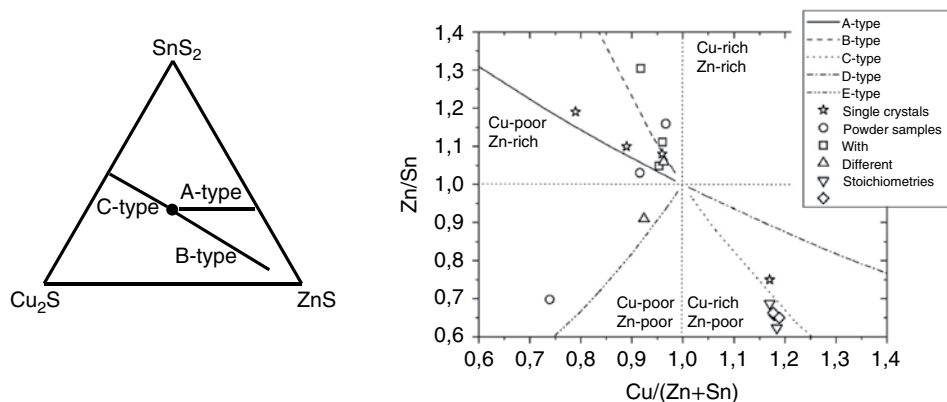
The existence of  $\text{Cu}_{\text{Zn}}$  and  $\text{Zn}_{\text{Cu}}$  antisite defects has been demonstrated experimentally by neutron powder diffraction using stoichiometric bulk samples [9, 10]. It was recently demonstrated that NMR spectroscopy is also sensitive enough to probe this Cu/Zn disorder [35]. Nevertheless, this antisite defect is limited to the 2c and 2d Wyckoff position in the planes at  $z = 1/4$  and  $3/4$ . The other copper site (Wyckoff position 2a) is not influenced

(see Fig. 3.7). If the small difference in the anion position is disregarded, this disordered kesterite may be attributed to the space group  $\bar{1}42m$  with a statistical distribution of copper and zinc on the Wyckoff position 4d. Nevertheless, in this case the remaining copper will occupy the 2a site. It would therefore be not correct to attribute this cation distribution to the stannite-type structure, because this would be in contradiction to the definition of the structure.



**Figure 3.7** View on the a-b-plane of the kesterite-type and the stannite-type structure as well as the disordered kesterite-type structure. The numbers indicate the z value (with respect to the crystallographic c axis) of the corresponding a-b-plane. The anions planes are not shown (blue: Cu; orange: Zn; red: Sn). For color details, please see color plate section





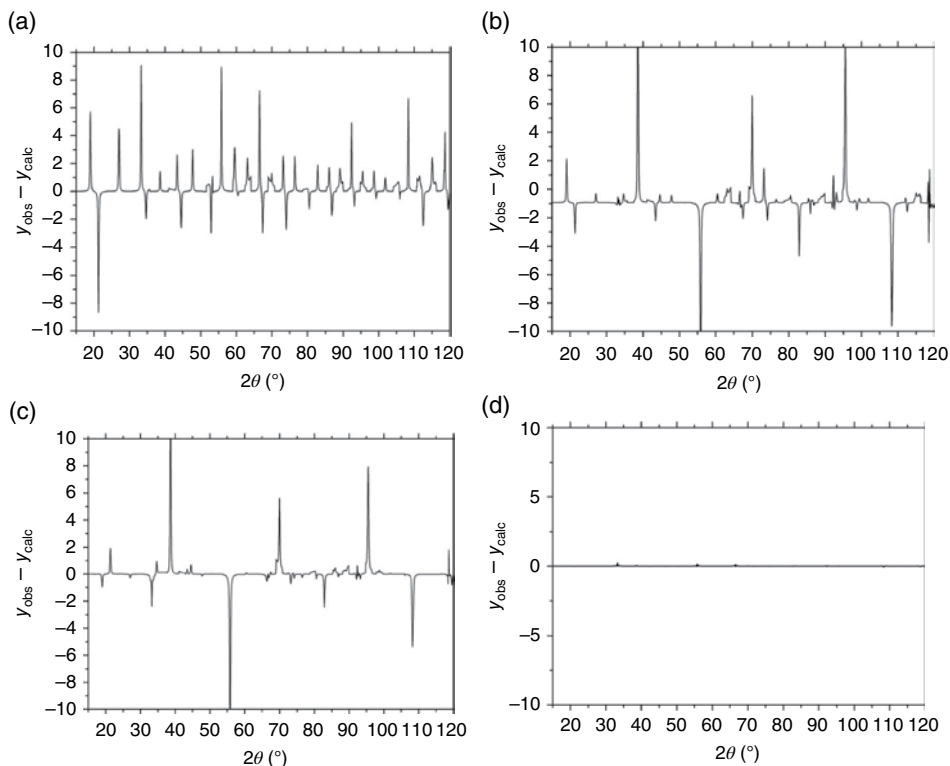
**Figure 3.8** Left: general representation of the cationic substitution types proposed by Choubrac *et al.* [17] in CZTS within the  $\text{Cu}_2\text{S}$ – $\text{SnS}_2$ – $\text{ZnS}$  phase diagram. The point marks stoichiometric CZTS. Right: cationic substitution types with respect to the ratios  $\text{Cu}/(\text{Zn}+\text{Sn})$  and  $\text{Zn}/\text{Sn}$ . The symbols mark the composition of off-stoichiometric CZTS single crystals [17, 18] and powder samples synthesized by solid-state reaction

### 3.3.1 Cationic defect types

Choubrac *et al.* [17] and Lafond *et al.* [18] recommended that the point defects in the form of cationic substitutions are related to the non-stoichiometry in CZTS. Four different types of substitutions were performed, which gave rise to several point defects: for Cu-poor and Zn-rich CZTS the A-type formation of  $\text{V}_{\text{Cu}}$  and  $\text{Zn}_{\text{Cu}}$  the B-type formation of  $\text{Zn}_{\text{Cu}}$  and  $\text{Zn}_{\text{Sn}}$ ; and for Cu-rich and Zn-poor CZTS the C-type formation of  $\text{Cu}_{\text{Zn}}$  and  $\text{Sn}_{\text{Zn}}$  as well as the D-type formation of  $\text{Cu}_{\text{Zn}}$  and  $\text{Cu}_i$ . In Figure 3.8 these cationic substitution types are related to the  $\text{Cu}_2\text{S}$ – $\text{SnS}_2$ – $\text{ZnS}$  ternary phase diagram as well as to the cationic ratios  $\text{Cu}/(\text{Zn}+\text{Sn})$  and  $\text{Zn}/\text{Sn}$ . Four quadrants can be recognized in the latter: Cu-poor/Zn-rich, Cu-rich/Zn-rich, Cu-poor/Zn-poor and Cu-rich/Zn-poor. The lines for off-stoichiometric A-type and B-type CZTS can be found in the quadrant Cu-poor/Zn-rich and for off-stoichiometric C-type and D-type CZTS in the quadrant Cu-rich/Zn-poor. The empirical conditions for high-efficiency CZTS-based thin-film solar cells (Cu-poor and Zn-rich) would correspond to the A-type or B-type substitution mechanism. Nevertheless, CZTS powder samples prepared by solid-state reaction also indicate off-stoichiometric compositions in the quadrant Cu-poor/Zn-poor. E-type CZTS is therefore introduced, connected with the formation of  $\text{V}_{\text{Cu}}$  and  $\text{Sn}_{\text{Zn}}$ .

## 3.4 Differentiation between Intergrown Kesterite- and Stannite-Type Phases: A Simulation Approach

The question may arise if it is possible to recognize the intergrowth of the kesterite- and stannite-type structure. To shed some light on that question, neutron powder diffraction patterns for a fictitious CZTS sample consisting of both phases with a 50:50 share were simulated and subsequently analyzed by the Rietveld method. In the refinement, different models were applied: (i) a single-phase sample with kesterite-type structure; (ii) a single-phase sample with disordered kesterite structure; (iii) a single-phase sample with kesterite-type



**Figure 3.9** Difference lines  $Y_{\text{obs}} - Y_{\text{calc}}$  resulting from the Rietveld refinement of a simulated neutron diffraction pattern ( $\lambda = 1.79 \text{ \AA}$ ) of a fictitious CZTS sample containing a kesterite type and a stannite type phase with a 50:50 share. (a)–(d) represent models (i)–(iv) respectively

relaxed cation site occupancies (i.e. the cation site occupancies have been free parameters for the fitting procedure); and (iv) a sample containing two phases, one with kesterite- and one with stannite-type structure. In Figure 3.9 the difference lines  $Y_{\text{obs}} - Y_{\text{calc}}$  of the refinement procedure are presented. It can be seen that only model (iv) results in a good refinement of the simulated data. It can therefore be concluded that a disordered kesterite can be distinguished from an intergrowth of a kesterite- and a stannite-type phase in CZTS.

### 3.5 Summary

The issues related to the crystal structure of CZTS have been discussed. It is now generally accepted that CZTS as well as CZTSe (single crystals, powder, and thin films) crystallize in the kesterite-type structure, but with a Cu/Zn disorder in the planes at  $z = 0.25$  and  $0.75$  (referred to as “disordered kesterite”). This disorder causes a high concentration of  $\text{Cu}_{\text{Zn}}$  and  $\text{Zn}_{\text{Cu}}$  anti-site defects (concerning the crystallographic sites 2c and 2d), even in stoichiometric compounds. The first experimental evidence for the Cu/Zn disorder and its quantification was given by neutron powder diffraction [9, 10]. The effect was also proved later by anomalous X-ray scattering (resonant X-ray scattering) [17, 18], Raman spectroscopy [36], and NMR

spectroscopy [34]. Using these spectroscopic methods the disorder can be determined qualitatively. Hints of an order–disorder transition at low temperatures have recently been found using Raman spectroscopy [37]. The transition temperature for CZTS was determined as  $T_c = 260 \pm 10^\circ \text{C}$ ; annealing at temperatures lower than this should reduce the Cu/Zn disorder.

This chapter on the crystallographic aspects of CZTS is also intended to remind the reader of the importance of a careful structural analysis. It should however be kept in mind that the same tetrahedral metal coordination (two Cu, one II-, and one IV-element surrounding each S-atom) is possible in space group  $\bar{I}4$  and  $\bar{I}42m$ . A clear decision can only be made by a detailed structural analysis of each compound [6].

## References

- [1] Pamplin, B. (1981) The Adamantine family of compounds. *Progress in Crystal Growth and Characterization of Materials*, **3**, 179–192.
- [2] Stephan, C., Schorr, S., Tovar, M. & Schock, H.-W. (2011) Comprehensive insights into point defect and cluster formation in  $\text{CuInSe}_2$ . *Applied Physics Letters*, **98**, 091906.
- [3] Kühn, G. & Neumann, H. (1987)  $\text{A}^{\text{IV}}\text{B}^{\text{III}}\text{C}_2^{\text{VI}}$ -Halbleiter mit Chalkopyritstruktur. *Zeitschrift für Chemie*, **27**, 197–206.
- [4] Rietveld, H. M. (1969) A profile refinement method for magnetic and nuclear structures. *Journal of Applied Crystallography*, **2**, 65–71.
- [5] Hall, S. R., Szymanski, J. T. & Stewart, J. M. (1978) Kesterite,  $\text{Cu}_2(\text{Zn,Fe})\text{SnS}_4$ , and stannite,  $\text{Cu}_2(\text{Fe,Zn})\text{SnS}_4$ , structurally similar but distinct minerals. *Canadian Mineralogist*, **16**, 131–137.
- [6] Schaefer, W. & Nitzsche, R. (1974) Tetrahedral quaternary chalcogenides of the type  $\text{Cu}_2\text{-II-IV-S}_4(\text{Se}_4)$ . *Materials Research Bulletin*, **9**, 645–654.
- [7] Abou-Ras, D., Caballero, R., Kaufmann, C.A., Nichterwitz, M., Sakurai, K., Schorr, S., Unold, T. & Schock, H.W. (2008) Impact of the Ga concentration in  $\text{CuIn}_{1-x}\text{Ga}_x\text{Se}_2$  solar absorbers on their microstructures. *Physica Status Solidi (RRL)*, **3**, 135–137.
- [8] Schorr, S., Tovar, M., Hoebler, H.-J. & Schock, H.-W. (2009) Structure and phase relations in the  $2(\text{CuInS}_2) - \text{Cu}_2\text{ZnSnS}_4$  solid solution system. *Thin Solid Films*, **517**, 2508–2510.
- [9] Schorr, S., Höbner, H.-J. & Tovar, M. (2007) A neutron diffraction study of the stannite-kesterite solid solution series. *European Journal of Mineralogy*, **19**, 65–73.
- [10] Schorr, S. (2011) The crystal structure of kesterite type compounds: a neutron and X-ray diffraction study. *Solar Energy Materials and Solar Cells*, **95**, 1482–1488.
- [11] Maeda, T., Nakamura, S., Kou, H., Wada, T., Inoue, K. & Yamaguchi, Y. (2009) Technical Digest. Proceedings of European Photovoltaic Solar Energy Conference, PVSEC-19, CIG-O-44.
- [12] Washio, T., Nozaki, H., Fukano, T., Motohiro, T., Jimbo, K. & Katagiri, H. (2011) Analysis of lattice site occupancy in kesterite structure of  $\text{Cu}_2\text{ZnSnS}_4$  films using synchrotron X-ray diffraction. *Journal of Applied Physics*, **110**, 074511.
- [13] Chen, S., Walsh, A., Luo, Y., Yang, J.-H., Gong, X. G. & Wei, S. H. (2010) Wurtzite-derived polytypes of kesterite and stannite quaternary chalcogenide semiconductors. *Physical Review B*, **82**, 195203.
- [14] Bonazzi, P., Bindi, L., Bernardini, G. P. & Menchetti, S. (2003) A model for the mechanism of incorporation of Cu, Fe and Zn in the stannite-kesterite series,  $\text{Cu}_2\text{FeSnS}_4 - \text{Cu}_2\text{ZnSnS}_4$ . *Canadian Mineralogist*, **41**, 639–647.
- [15] Schubert, B.-A., Marsen, B., Cinque, S., Unold, Th., Klenk, R., Schorr, S. & Schock, H.-W. (2011)  $\text{Cu}_2\text{ZnSnS}_4$  thin film solar cells by fast co-evaporation. *Progress in Photovoltaics: Research and Applications*, **19**, 93–96.
- [16] Bruc, L. I., Guc, M., Rusu, M., Sherban, D. A., Simashkevich, A. V., Schorr, S., Izquierdo-Roca, V., Perez-Rodriguez, A. & Arushanov, E. K. (2012) Kesterite thin films obtained by spray pyrolysis. In *Proceedings of 27th EUPVSEC*, 24–28 September 2012, Frankfurt.
- [17] Choubrac, L., Lafond, A., Guillot-Deudon, C., Moelo, Y. & Jobic, S. (2011) Structure flexibility of the  $\text{Cu}_2\text{ZnSnS}_4$  absorber in low-cost photovoltaic cells: from the stoichiometric to the copper-poor compounds. *Inorganic Chemistry*, **51**, 3343–3922.

- [18] Lafond, A., Choubrac, L., Guillot-Deudon, C., Deniard, P. & Jobic, S. (2012) Crystal structures of photovoltaic chalcogenides, an intricate puzzle to solve: the cases of CIGSe and CZTS materials. *Zeitschrift für Anorganische und Allgemeine Chemie*, **638**, 2571–2577.
- [19] Maeda, T., Nakamura, S. & Wada, T. (2011) First principles calculations of defect formation in In-free photovoltaic semiconductors  $\text{Cu}_2\text{ZnSnS}_4$  and  $\text{Cu}_2\text{ZnSnSe}_4$ . *Japanese Journal of Applied Physics*, **50**, 04DP07.
- [20] Zhang, Y., Sun, X., Zhang, P., Yuan, X., Huang, F. & Zhang, W. (2012) Structural properties and quasiparticle band structures of Cu-based quaternary semiconductors for photovoltaic applications. *Journal of Applied Physics*, **111**, 063709.
- [21] Paier, J., Asahi, R., Nagoya, A. & Kresse, G. (2009)  $\text{Cu}_2\text{ZnSnS}_4$  as a potential photovoltaic material: Hartree-Fock density functional theory study. *Physical Review B*, **79**, 115126.
- [22] Ichimura, M. & Nakashima, Y. (2009) Analysis of atomic and electronic structures of  $\text{Cu}_2\text{ZnSnS}_4$  based on first-principles calculation. *Japanese Journal of Applied Physics*, **48**, 090202.
- [23] Lin, X., Kavalakkatt, J., Kornhuber, K., Abou-Ras, D., Schorr, S., Lux-Steiner, M.-C. & Ennaoui, A. (2012) Synthesis of  $\text{Cu}_2\text{Zn}_x\text{Sn}_{1+x/2}\text{Se}_4$  nanocrystals with wurtzite-derived structure. *RSC Advances*, **2**, 9894–9898.
- [24] Todorov, T. K., Reuter, K. B. & Mitzi, D. B. (2010) High-efficiency solar cell with earth-abundant liquid-processed absorber. *Advanced Materials*, **22**, E156.
- [25] Barkhouse, D., Gunawan, O., Gokmen, T., Todorov, T. & Mitzi, D. (2012) Device characteristics of a 10.1% hydrazine-processed  $\text{Cu}_2\text{ZnSn}(\text{Se},\text{S})_4$  solar cell. *Progress in Photovoltaics*, **20**, 6.
- [26] Repins, I., Beall, C., Vora, N., DeHart, C., Kuciauskas, D., Dippo, P., To, B., Mann, J., Hsu, W.-C. & Goodrich, A. (2012) Co-evaporated  $\text{Cu}_2\text{ZnSnSe}_4$  solar cells and devices, *Solar Energy Materials and Solar Cells*, **101**, 154.
- [27] Shin, B., Gunawan, O., Zhu, Y., Bojarczuk, N. A., Chey, S. J. & Guha, S. (2013) Thin film solar cell with 8.4% power conversion efficiency using an earth-abundant  $\text{Cu}_2\text{ZnSnS}_4$  absorber. *Progress in Photovoltaics: Research and Applications*, **21**, 72–76.
- [28] Todorov, T., Gunawan, O., Chey, S. J., de Monsabert, T. G., Prabhakar, A. & Mitzi, D. B. (2011) Progress towards marketable Earth-abundant chalcogenide solar cells. *Thin Solid Films*, **519**, 7378.
- [29] Ericson, T., Scragg, J., Kubart, T., Törndahl, T. & Platzer-Björkman, C. (2013) Annealing behaviour of reactively sputtered precursor films for  $\text{Cu}_2\text{ZnSnS}_4$  solar cells. *Thin Solid Films*, **535**, 22–26.
- [30] Chen, S., Gong, X. G., Walsh, A. & Wei, S.-H. (2010) Defect physics of the kesterite thin-film solar cell absorber  $\text{Cu}_2\text{ZnSnS}_4$ . *Applied Physics Letters*, **96**, 021902.
- [31] Chen, S., Yang, J.-H., Gong, X. G., Walsh, A. & Wei, S.-H. (2010) Intrinsic point defects and complexes in the quaternary kesterite semiconductor  $\text{Cu}_2\text{ZnSnS}_4$ . *Physical Review B*, **81**, 245204.
- [32] Chen, S., Wang, L.-W., Walsh, A., Gong, X. G. & Wei, S.-H. (2012) Abundance of  $\text{Cu}_{\text{Zn}}$  +  $\text{Sn}_{\text{Zn}}$  and  $2\text{Cu}_{\text{Zn}}$  +  $\text{Sn}_{\text{Zn}}$  defect clusters in kesterite. *Applied Physics Letters*, **101**, 223901.
- [33] Nagoya, A., Asahi, R., Wahl, R. & Kresse, G. (2010) Defect formation and phase stability of  $\text{Cu}_2\text{ZnSnS}_4$  photovoltaic material. *Physical Review B*, **81**, 113202.
- [34] Raulot, J. M., Domain, C. & Guillemoles, J. F. (2005) Ab initio investigation of potential indium and gallium free chalcopyrite compounds for photovoltaic application. *Journal of Physics and Chemistry of Solids*, **66**, 2019.
- [35] Choubrac, L., Paris, M., Lafond, A., Guillot-Deudon, C., Roquefelte, X. & Jobic, S. (2013) Multinuclear ( $^{67}\text{Zn}$ ,  $^{119}\text{Sn}$  and  $^{65}\text{Cu}$ ) NMR spectroscopy – an ideal technique to probe the cation ordering in  $\text{Cu}_2\text{ZnSnS}_4$  photovoltaic materials. *Physical Chemistry, Chemical Physics*, **15**, 10722–10725.
- [36] Valakh, M. Y., Kolomys, O. F., Ponomaryov, S. S., Yukhymchuk, V. O., Babichuk, I. S., Izquierdo-Roca, V., Saucedo, E., Perez-Rodriguez, A., Morante, J. R., Schorr, S. & Bodnar, I. V. (2013) Raman scattering and disorder effect in  $\text{Cu}_2\text{ZnSnS}_4$ . *Physica Status Solidi RRL*, **7**, 258–261.
- [37] Scragg, J., Choubrac, L., Lafond, A., Ericson, T. & Platzer-Björkman, C. (2014) A low temperature order-disorder transition in  $\text{Cu}_2\text{ZnSnS}_4$  thin films. *Applied Physics Letters*, **104**, 041911.

# 4

## Electronic Structure and Optical Properties from First-Principles Modeling

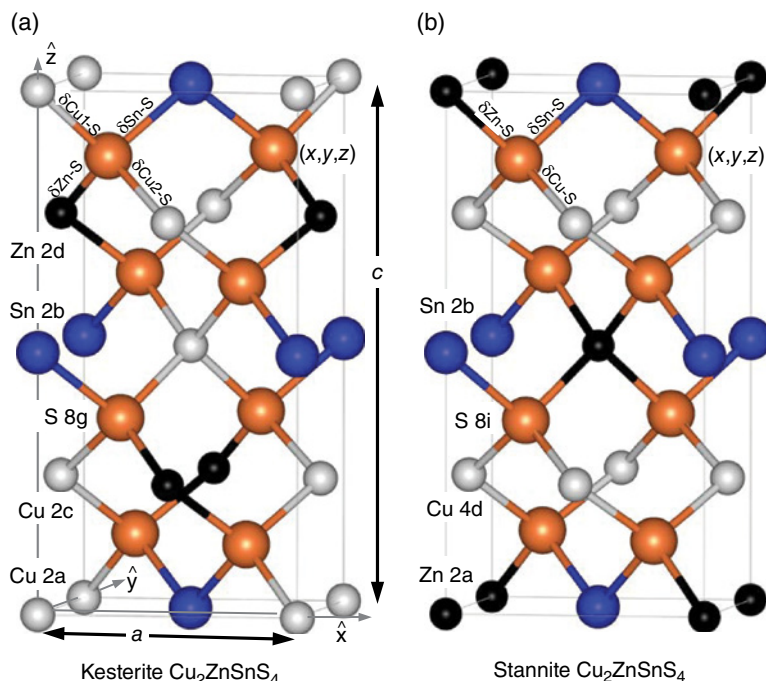
*Clas Persson,<sup>1,2</sup> Rongzhen Chen,<sup>2</sup> Hanyue Zhao,<sup>2</sup> Mukesh Kumar<sup>2</sup>  
and Dan Huang<sup>2</sup>*

*<sup>1</sup>Department of Physics, University of Oslo, P.O. Box 1048 Blindern,  
NO-0316 Oslo, Norway*

*<sup>2</sup>Department of Materials Science and Engineering, Royal Institute of Technology,  
SE-100 44 Stockholm, Sweden*

### 4.1 Introduction

$\text{Cu}_2\text{ZnSnS}_4$  (CZTS) and  $\text{Cu}_2\text{ZnSnSe}_4$  (CZTSe) belong to a very interesting type of materials. These two group-I<sub>2</sub>-II-IV-VI<sub>4</sub> compounds have a similar tetrahedral bonds geometry as traditional group-IV, III-V, and II-VI semiconductors; see Figure 4.1. The compounds obey Lewis' octet rule with eight electrons around each anion atom (S or Se); the four bonds of each anion therefore form together a close valence shell. CZT(S,Se) can be constructed from the binary Zn(S,Se) by replacing two of the four Zn atoms with Cu, and one of the four Zn atom by Sn, whereupon the number of valence electrons is preserved. However, the cubic or hexagonal crystal symmetry of ZnS is thereby lowered to a tetragonal body-centered symmetry with either kesterite  $S_4^2$  or stannite  $D_{2d}^{11}$  crystalline phase, respectively (a third primitive-mixed CuAu-like phase has been modeled, but this phase is not discussed in this chapter). Since CZT(S,Se) have a similar bond geometry as traditional semiconductors, similar material properties as, for instance, Ge, GaAs, and ZnS may be expected.



**Figure 4.1** Conventional unit cells of the (a) kesterite and (b) stannite structures of CZTS. The primitive unit cells involve four Cu atoms, two Zn atoms, two Sn atoms, and eight S atoms. For the kesterite  $S_4^2$  phase, the crystal structures are fully defined by the anion 8g Wyckoff position  $(x, y, z)$ , while for the stannite  $D_{2d}^{11}$  phase the structure is defined by the anion 8i position  $(x, y = x, z)$ . For color details, please see color plate section

This is true to some extent; however, there are fundamental differences between the Cu-based quaternaries and the group-IV, III-V, and II-VI binary semiconductors. First, while the traditional semiconductors have pure bond with  $sp^3$  hybridization, the bonds in CZT(S,Se) also involve Cu- $d$ -anion- $p$  hybridized antibonding states. This weakens the bonds in CZT(S,Se). Second, while the group III-V (group II-VI) semiconductors have three (two) valence  $s$ -like electrons for their cations, Cu in CZTS and CZTSe has only one valence  $s$ -like electron. These two properties imply that the formation energy of Cu vacancies  $V_{Cu}$  is small compared with corresponding cation vacancies in traditional semiconductors. It is therefore relatively easy to grow highly off-stoichiometry materials with Cu-related native defects.

The possibility of forming quaternary-like CZT(S,Se)-type compounds with diamond-like covalent bonds was discussed by Goodman [1] and later by Pamplin [2] over half a century ago. However, the theoretical studies of CZT(S,Se) began as late as 2005 when Raulot *et al.* [3] modeled the crystal structures of semiconductors with Cu-(S,Se) bonds and calculated the electronic structures. This study employed the local density approximation (LDA) within the density functional theory (DFT). The LDA is known to strongly underestimate the fundamental band-gap energy  $E_g$ , but the authors estimated that CZTS and CZTSe have gap energies  $E_g \approx 1.2$  and  $0.9$  eV, respectively. They also predicted that the kesterite phase of both CZTS and CZTSe was more crystalline stable

than their corresponding stannite phase. The work certainly encouraged further DFT-based research on CZT(S,Se).

Since 2009, there have been several DFT-based theoretical studies of CZT(S,Se) that have analyzed the material properties, for example the crystalline and electronic structures, defect properties, and lattice dynamics [4–21]. In our work, we explore the electronic and optical properties of the kesterite and stannite phases of CZTS and CZTSe by means of first-principles modeling [9, 13, 19, 20]. Many fundamental physical properties of semiconductors are governed by the shape of the energy bands near the band edges. We therefore focus on the details in the band edges of the valence band (VB) and the conduction band (CB). We describe and analyze the energy states at the VB maximum (VBM) and at the CB minimum (CBM). The effective masses are calculated by including spin-orbit coupling which strongly affects the hole masses. The band edges are parameterized in order to more accurately describe the energy dispersion in a wider energy region; this is important when investigating material properties that are related to the free carriers, for example the electronic mobility, impacts of scattering, and/or in measurements that involve strong excitation conditions. We also analyze the optical properties of CZT(S,Se), here discussed in terms of the dielectric function and the optical absorption coefficient. The anisotropy of the crystalline structure in CZT(S,Se) is reflected in anisotropic electronic and optical properties of these materials. To describe the properties of these materials, the longitudinal ( $\parallel$ ) direction is defined as the directions along the crystalline (001)  $c$ -axis; see Figure 4.1. The transverse ( $\perp$ ) direction is the plane perpendicular to the longitudinal direction. Moreover, throughout this work energies are referenced to the VBM.

In these investigations, we employ the DFT in conjunction with the Kohn–Sham (KS) equation, utilizing the generalized gradient approximation (GGA) [22–24], the screened hybrid functional [25], and the single-electron excitation GW approach [26], as implemented in the Wien2k [27] and VASP [28, 29] software packages. Note that there are numerous LDA, GGA, and hybrid functionals. There are also several GW methods. All these related methods can generate slightly different results. In the theoretical research on CZT(S,Se) several methods and implementations have been utilized, and it is not surprising to find somewhat deviating results for calculations using similar computational approaches. We therefore very briefly discuss these methods.

## 4.2 Computational Background

In the DFT, the ground-state total energy of a material can be exactly determined uniquely from the density  $n(\mathbf{r})$  of the electrons; the total energy  $E[n]$  is therefore a functional of the density  $n$ . To date however, no explicit expression for this functional exists, and complementary ways to solve the many-electron system have to be generated.

The DFT in conjunction with the KS equation determines the many-electron system by utilizing auxiliary KS orbitals (which are normally Hartree-like functions). Since the 1980s, the KS equation has been extremely successful in describing material systems with a large number of atoms, for instance solids, nanostructures, and large molecules. In employing the DFT, theoreticians are supporting experimental studies analyzing the underlying physics of many-electron systems, but also exploring novel crystal structures and complex molecules.

In the KS equation, the complex part of the electron–electron interactions is treated by the exchange–correlation potential  $V_{xc}(\mathbf{r})$ . The equation implies in principle an exact first-principles modeling (i.e. without external parameters) if the exchange–correlation potential is described exactly. The single-electron KS equation:

$$\left\{ \frac{-\hbar^2 \nabla^2}{2m} + V_{\text{ext}}(\mathbf{r}) + V_{\text{H}}(\mathbf{r}) + V_{xc}(\mathbf{r}) \right\} \psi_{nk}^{\text{KS}}(\mathbf{r}) = E_{nk}^{\text{KS}} \psi_{nk}^{\text{KS}}(\mathbf{r}) \quad (4.1)$$

with

$$n(\mathbf{r}) = \sum_{nk}^{\text{occ.}} \left| \psi_{nk}^{\text{KS}}(\mathbf{r}) \right|^2$$

calculates the ground-state total energy  $E_t$  within the DFT as:

$$E_t[n] = \sum_{nk} E_{nk} - \frac{1}{2} \int V_{\text{H}}(\mathbf{r}) n(\mathbf{r}) d\mathbf{r} + E_{xc}[n] - \int V_{xc}(\mathbf{r}) n(\mathbf{r}) d\mathbf{r} \quad (4.2)$$

Here  $V_{\text{ext}}(\mathbf{r})$  is the external potential including the Coulomb potential from the nuclei, and  $V_{\text{H}}(\mathbf{r})$  is the standard Hartree potential.  $\psi_{nk}^{\text{KS}}(\mathbf{r})$  are the auxiliary KS Hartree-like orbitals, and  $E_{nk}^{\text{KS}}$  are the corresponding single-electron KS energies. The exchange–correlation potential in Equation 4.1 is obtained from the exchange–correlation energy  $E_{xc}[n]$  by  $V_{xc}(\mathbf{r}) = \delta E_{xc}[n] / \delta n(\mathbf{r})$ . The exchange–correlation potential is often divided into the exchange  $V_x(\mathbf{r})$  and correlation  $V_c(\mathbf{r})$  parts as  $V_{xc}(\mathbf{r}) = V_x(\mathbf{r}) + V_c(\mathbf{r})$ .

The total energy  $E_t$  is exact if the unique exchange–correlation energy functional  $E_{xc}[n]$  is exactly generated. To date, the explicit expression of  $E_{xc}[n]$  is unknown and a proper approximation is required. The LDA is a first, rough approximation to the exchange–correlation energy where the exchange–correlation energy  $E_{xc}^{\text{LDA}}[n]$  is locally described in terms of the corresponding known energy for the homogeneous electron gas. Despite its very simplicity, the LDA generates surprisingly accurate total energies and single-electron energies. The second family of approximations is the generalized gradient approximation  $E_{xc}^{\text{GGA}}[n]$  where the gradient of the density is also taken into account to generate the exchange–correlation. Both LDA and GGA describe fairly accurately the total energy of the solid. For example, the LDA normally overbinds (i.e.  $\sim 1\text{--}3\%$  too small lattice constants) and GGA normally underbinds (i.e.  $\sim 1\text{--}3\%$  too large lattice constants).

However, LDA and GGA are approximations that have drawbacks when describing details in the electronic structure. For instance, both methods are known to underestimate the band gap  $E_g$  by typically 50%. In principle, the band-gap energy can be calculated from the total energy  $E_t$  of the  $N$ -electron system:  $E_g = E_t(N+1) + E_t(N-1) - 2E_t(N)$ . However, the gap is in general determined from the KS eigenvalues  $E_{nk}^{\text{KS}}$  at the CBM and VBM. Since  $E_{nk}^{\text{KS}}$  are obtained from auxiliary KS orbitals, it is not evident that the gap energy can be determined from these KS eigenvalues; how accurate the gap energy will be with the exact  $E_{xc}[n]$  is still under discussion. The gap energy therefore contains two uncertainties: the approximation of the exchange–correlation energy and the KS eigenvalues. In addition, experimental band-gap energies are normally obtained via optical excitation and at room temperature, while the DFT is (often) zero-temperature ground-state calculation. Another



problem with the LDA and GGA is that the localization of *d*- and *f*-like states is normally not described accurately; this problem can sometimes be corrected by an on-atom-site local and angular-momentum-dependent Coulomb correction.

Another method of approximating  $E_{xc}[n]$  is to solve the exchange energy exactly within the Hartree–Fock approximation, and then use an approximation for the correlation energy. This exchange-energy method typically generates too-large band-gap energies. A combination of the exchange-energy method with the LDA or GGA may sometimes be preferred. This is the so-called hybrid functional approach, where the exchange energy is mixed in order to empirically obtain better total energies and band-gap energies. There are numerous ways to perform the mixing. In the HSE06 method (by Heyd, Scuseria, and Ernzerhof), defined:

$$E_{xc}^{\text{HSE}} = \alpha E_x^{\text{SR}}(\mu) + (1 - \alpha) E_x^{\text{PBE,SR}}(\mu) + E_x^{\text{PBE,LR}}(\mu) + E_c^{\text{PBE}}, \quad (4.3)$$

the short-range part (SR) of the exact exchange  $E_x^{\text{SR}}$  is mixed with a short-range part of the GGA exchange  $E_x^{\text{PBE,SR}}$  by Perdew, Burke, and Ernzerhof (PBE) [22, 23]. The standard mixing is 25% Hartree–Fock, that is  $\alpha=0.25$ . In addition, the decaying long-ranged part (LR) of the exchange energy is replaced by a corresponding PBE counterpart  $E_x^{\text{PBE,LR}}$ . This is described by the range-separation parameter  $\mu$ , the recommended value for which is 0.2. The correlation part of the electron–electron interaction is obtained from the PBE approximation  $E_c^{\text{PBE}}$ .

The hybrid functionals such as the HSE06 are designed to generate better total energies (e.g. the error in lattice constants is often less than 1–2%) and band-gap energies (the error bar is typically in the order of ~10%). One shall however not expect that the hybrid functionals always predict the very exact band gap energies; see discussion in the previous paragraphs. A problem with the orbital-based hybrid functionals is that they are computationally demanding and that they are more sensitive to parameters such as the basis set and Brillouin zone (BZ)  $\mathbf{k}$ -mesh. For practical purposes these convergence parameters are set to a minimal level, but that may affect the accuracy of the details in the electronic structure.

In order to include excitation, a beyond-DFT approach is normally considered. The GW approximation includes single-electron excitations, and the method better describes the single-electron energies via the self-energy  $\Sigma_{nk}$ ; the single-particle energies are described as quasi-particle energies. In the GW approach, the KS equation is extended to:

$$\left\{ \frac{-\hbar^2 \nabla^2}{2m} + V_{\text{ext}}(\mathbf{r}) + V_{\text{H}}(\mathbf{r}) \right\} \psi_{nk}^{\text{GW}}(\mathbf{r}) + \int \Sigma(\mathbf{r}, \mathbf{r}', E_{nk}^{\text{GW}}) \psi_{nk}^{\text{GW}}(\mathbf{r}') d\mathbf{r}' = E_{nk}^{\text{GW}} \psi_{nk}^{\text{GW}}(\mathbf{r}) \quad (4.4)$$

by including the self-energy operator  $\Sigma(\mathbf{r}, \mathbf{r}', E_{nk}^{\text{GW}})$  that depends on the Green's function  $G(\mathbf{r}, \mathbf{r}', E_{nk}^{\text{GW}} + E)$  and the screened Coulomb potential  $W(\mathbf{r}, \mathbf{r}', E)$ . The GW approach models the single-electron excitation and therefore mimics the experimentally determined single-electron energies better. Since GW is based on orbitals as a basis set, the method is computationally demanding just like the Hartree–Fock-based hybrid functionals. There are actually many approaches to solve the GW approximation, and the different approaches yield often slightly deviating band-gap energies; it is therefore not surprising that different published GW calculations do not generate exactly the same results.

In this work we present results from calculations using the GGA, hybrid functional, and GW; overall, the methods yield qualitatively similar electronic structures and density-of-states (DOS).

To analyze details in the electronic structure, we employ the all-electron and full-potential linearized augmented plane wave (FP-LAPW) method in the Wien2k program package [27]. We choose the GGA potential of Engel and Vosko to analyze the electronic structures of CZTS and CZTSe. This GGA was generated by optimizing the exchange–correlation potential  $V_{xc}$  instead of the corresponding exchange–correlation  $E_{xc}$ , and this implies better KS single-electron energies but less accurate total energies. The band-gap energy is corrected by the GGA in combination with an approximated quasi-particle (QP) method proposed by Bechstedt and Del Sole [30]. Their correction is based on the difference in self-energies obtained from the LDA and the GW approximation. With the QP model, the gap energy is corrected by:

$$\Delta_g = \frac{e^2 q_{TF}}{2\pi\epsilon_0} \int_0^\infty \frac{dt}{1+t^2} \left[ (1-\alpha_p) f(q_{TF} r_A t) + (1+\alpha_p) f(q_{TF} r_B t) \right]^2 \quad (4.5)$$

where

$$f(x) = \frac{3-10x^2+3x^4}{3(1+x^2)^6}; \quad r_A = \frac{a}{4\pi \times 1.6}; \quad r_B = \frac{a}{4\pi \times 1.8},$$

$e$  is the elementary charge,  $q_{TF}$  is the Thomas–Fermi wave number,  $\epsilon_0$  is the static dielectric constant, and  $\alpha_p$  is the polarity of the interatomic interaction [30, 31]. This method has been shown to predict the band-gap energies fairly accurately [32, 33], and with this GGA method we can analyze the electronic structure with very high numerical accuracy of the energies and symmetry of the eigenfunctions. The notation of the symmetry of the eigenfunction, that is, the irreducible representations, is according to Koster *et al.* [34].

We also present the band-gap energies, the DOS, and the optical response functions calculated by the HSE06 and the GW approaches in the VASP package, employing the projector augmented wave (PAW) method [28, 29]. For the screened HSE06 hybrid functional we use the standard mixing of exchange  $\alpha=0.25$ , and the recommended range-separation parameter of  $\mu=0.2$ . For the partially self-consistent GW calculation the Green's function  $G(\mathbf{r}, \mathbf{r}', E_{nk}^{GW} + E)$  is updated, while the screened Coulomb potential  $W(\mathbf{r}, \mathbf{r}', E)$  is kept fixed. This approach is denoted  $GW_0$ .

It is worth mentioning that the KS equation above describes a non-relativistic Schrödinger-like equation. In practice, however, the core electrons are calculated from the relativistic Dirac equation. The semi-core and valence electrons are calculated by the scalar-relativistic equation that includes also the mass-velocity correction and the Darwin interaction. The spin–orbit interaction  $-i\hbar^2 \boldsymbol{\sigma} [\nabla V(\mathbf{r}, t) \times \nabla] / 4m^2 c^2$  is included as a second-order perturbation.

### 4.3 Crystal Structure

(The section is reprinted with permission from [9]. Copyright 2010, American Institute of Physics.) In Figure 4.1, the kesterite and stannite crystalline structures are presented for CZTS. Kesterite phase with space group  $S_4^2$  ( $I\bar{4}$ ; space group no. 82) has in its conventional unit cell four copper atoms on the Wyckoff positions  $2a$  and  $2c$ , two zinc atoms on

position  $2d$ , two tin atoms on position  $2b$  (all four cation positions have  $S_4$  point-group symmetry), and eight sulfur atoms on the  $8g$  position (point group  $C_1$ ). The anion  $8g$  position is fully defined with the position  $(x, y, z)$ , and each anion S-atom therefore has four inequivalent bonds  $\delta_{x-s}$  to the cations  $X=\text{Cu}(1)$ ,  $\text{Cu}(2)$ ,  $\text{Zn}$ , and  $\text{Sn}$ . The cation positions all have  $S_4$  point-group symmetry, and S positions have  $C_1$  symmetry. The stannite phase with space group  $D_{2d}^{11}$  ( $I\bar{4}2m$ ; no. 121) has four equivalent Cu atoms on the Wyckoff  $4d$  position (with  $S_4$  point-group symmetry), two Zn atoms on  $2a$ , two Sn atoms on  $2b$  (both Zn and Sn have  $D_{2d}$  symmetry) and eight S atoms on the  $8i$  position (point group  $C_s$ ). In this structure, the anion  $8i$  position is defined by the position  $(x, y=x, z)$ , and each S-atom therefore has three inequivalent bonds  $\delta_{x-s}$  to the cations  $X=\text{Cu}$ ,  $\text{Zn}$ , and  $\text{Sn}$ . The kesterite and stannite phases differ only by the positions of the Zn atoms and half of the Cu atoms, but the bond characters are the same where each S is surrounded by two Cu, one Zn, and one Sn. The ideal structures of both kesterite and stannite (i.e. when all bond lengths are equal as in binary analogue) are obtained for a ratio  $c/a=2$  of the lattice constants, and with an anion atom positioned at  $(x, y, z)=(3/4, 3/4, 7/8)$ . The discussion above also holds for the crystalline structure of CZTSe.

The lattice constants are obtained by minimizing the total energy with respect to the primitive lattice vectors, whereas the ion positions are obtained by minimizing the forces on each atom. Relaxation with the screened hybrid functional HSE06 results in slightly too-large unit cells compared with the experimental data (Table 4.1). On the other hand, the LDA tends to overbind and the relaxed cell volumes are somewhat smaller than the measured values [35–39]. However, both HSE06 and LDA generate a value of the  $c/a$  ratio that is very close to 2 for all four compounds. The lattice parameters of CZTS (and CZTSe) are only slightly larger than its binary cubic analogue ZnS (and ZnSe) which has a measured lattice constant of  $a=5.41$  (5.67) Å. From the calculated total energy difference  $\Delta E_t = E_t(\text{stannite}) - E_t(\text{kesterite})$  the most stable phase is found to be the kesterite structure for both the S- and the Se-based compounds. This is accordance with most of the recent experimental data [36, 38, 40, 41], but the stannite phase can also be grown [37, 39, 42–44]. However, the total energy of kesterite CZTS is only  $\sim 50$  meV/cell (i.e.  $\sim 3$  meV/atom) lower than the corresponding stannite structure. Similarly, the total energy of the kesterite CZTSe is  $\sim 64$  meV/cell (i.e.  $\sim 4$  meV/atom) lower than their stannite structure. This indicates that the kesterite phase will be formed under equilibrium growth conditions but since the total energy, lattice parameters, and bonds of kesterite and stannite are very similar (Table 4.1), both phases may exist; it is most likely rather easy to grow materials with mixed phases depending on growth method and growth conditions. This may also partly explain the existence of disorder structure with more random distribution of the Cu and Zn on the cation positions [45]. Moreover, the total energy  $E_t$  increases slowly with respect to variations of the ratio  $c/a$ , and this ratio may therefore differ slightly in differently grown samples. However, even if  $c/a$  is allowed to vary moderately, it is found that the kesterite structure has the lowest total energy.

Because  $c/a$  is  $\sim 2$ , the position of the anions are roughly at the ideal position with  $(x, y, z)=(3/4, 3/4, 7/8)$ . This is in agreement with structural characterization by Hall *et al.* [35]. The bond lengths follow clear trends. The differences in the cation–anion bond lengths in kesterite and stannite phases are small, at most 0.02 Å, and the bond lengths of Cu(1)–anion and Cu(2)–anion are very similar. CZTS has roughly 0.10–0.15 Å shorter bonds than CZTSe, which is of course due to the  $\sim 0.3$  Å smaller lattice constants. However, the main

**Table 4.1** Crystal structure parameters of kesterite and stannite phases of CZTS and CZTSe. The lattice volumes from the HSE06 calculation are, as expected, somewhat larger than from the corresponding LDA results (in brackets). Overall, the theoretical crystal parameters are in agreement with available experimental data [35–39]. The anion position (x, y, z) is given in fractions of the lattice vectors.  $\delta_{\text{X-anion}}$  represents the bond length between the cation X and the anion. The difference in the total energy  $\Delta E_t$  (in units of meV per primitive cell) indicates that kesterite is the most stable ground state structure

	$\text{Cu}_2\text{ZnSnS}_4$		$\text{Cu}_2\text{ZnSnSe}_4$	
	Kesterite	Stannite	Kesterite	Stannite
Space group	$S_4^2$	$D_{2d}^{11}$	$S_4^2$	$D_{2d}^{11}$
$a$ (Å)	5.440 (5.326) 5.467 <sup>a</sup> , 5.448 <sup>b</sup> 5.321 <sup>c</sup> 5.427 <sup>d</sup> , 5.428 <sup>e</sup>	5.450 (5.325) 5.458 <sup>a</sup> , 5.438 <sup>b</sup> 5.318 <sup>c</sup> , 5.436 <sup>f</sup>	5.732 (5.605) 5.763 <sup>a</sup> , 5.604 <sup>c</sup> 5.68 <sup>g</sup>	5.738 (5.604) 5.762 <sup>a</sup> , 5.603 <sup>c</sup> 5.681 <sup>f</sup> , 5.688 <sup>h</sup>
$c/a$	2.002 (2.002) 1.998 <sup>a</sup> , 1.999 <sup>b</sup> 2.001 <sup>c</sup> , 2.003 <sup>d</sup> , 2.002 <sup>e</sup>	1.996 (1.996) 2.008 <sup>a</sup> , 2.012 <sup>b</sup> 2.004 <sup>c</sup> , 1.996 <sup>f</sup>	1.992 (1.998) 1.996 <sup>a</sup> , 1.999 <sup>c</sup> , 2.00 <sup>g</sup>	1.996 (2.000) 2.000 <sup>a</sup> , 2.000 <sup>c</sup> , 1.996 <sup>f</sup> , 1.993 <sup>h</sup>
Anion position				
x	0.758 (0.760) 0.755 <sup>c</sup> , 0.756 <sup>d</sup>	0.755 (0.760) 0.755 <sup>c</sup>	0.761 (0.761) 0.757 <sup>c</sup>	0.755 (0.761) 0.757 <sup>c</sup> , 0.759 <sup>h</sup>
y	0.745 (0.769) 0.764 <sup>c</sup> , 0.757 <sup>d</sup>	x	0.745 (0.771) 0.767 <sup>c</sup>	x
z	0.877 (0.870) 0.872 <sup>c</sup> , 0.872 <sup>d</sup>	0.869 (0.865) 0.867 <sup>c</sup>	0.878 (0.869) 0.871 <sup>c</sup>	0.868 (0.864) 0.865 <sup>c</sup> , 0.871 <sup>g</sup>
$\delta_{\text{Cu(1)-anion}}$ (Å)	2.325 (2.295)	2.325 (2.292)	2.438 (2.395)	2.439 (2.390)
$\delta_{\text{Cu(2)-anion}}$ (Å)	2.330 (2.294)	2.325 (2.292)	2.448 (2.392)	2.438 (2.390)
$\delta_{\text{Zn-anion}}$ (Å)	2.349 (2.349)	2.365 (2.357)	2.473 (2.458)	2.494 (2.466)
$\delta_{\text{Sn-anion}}$ (Å)	2.416 (2.473)	2.422 (2.475)	2.559 (2.606)	2.565 (2.607)
$\Delta E_t$ (meV/cell)	0 (0)	50 (11)	0 (0)	64 (27)

<sup>a</sup>Chen *et al.* [4], GGA potential; <sup>b</sup>Paier *et al.* [5], HSE06 potential; <sup>c</sup>Gürel *et al.* [14], LDA; <sup>d</sup>Hall *et al.* [35]; <sup>e</sup>Schorr *et al.* [36]; <sup>f</sup>Hahn *et al.* [37]; <sup>g</sup>Babu *et al.* [38]; <sup>h</sup>Olekseyuk *et al.* [39]

origin to the smaller cell volume and the shorter bond lengths is that S has a roughly 0.15 Å smaller covalent radius compared with Se. All cation–anion bonds in CTZS will therefore be ~0.15 Å shorter than their corresponding bond lengths in CZTSe.

## 4.4 Electronic Structure

The electronic band structures for the kesterite and stannite phases of CZTS and CZTSe are generated by the all-electron FP-LAPW method [27] using the GGA plus an onsite Coulomb interaction  $U_d$  for the Cu- $d$  states. The correction of the  $d$ -like states has a modest impact on the main electronic structure, but it localizes the Cu- $d$  and lowers the VBM by the order of ~0.1 eV [33, 46]. Spin-orbit interaction is included in the calculations. The band-gap energy is estimated from the GGA calculation in combination with the QP method. We also present the band-gap energies calculated by the HSE06 and  $\text{GW}_0$  approaches. The three methods

yield roughly the same values, and we therefore estimate the gap energies to be  $E_g \approx 1.5$  eV for CZTS and  $E_g \approx 1.0$  eV for CZTSe. We have also found that the band-gap energy of the kesterite  $\text{Cu}_2\text{ZnSn}(\text{S}_{1-x}\text{Se}_x)_4$  alloy varies fairly linearly [20].

#### 4.4.1 Band Energies

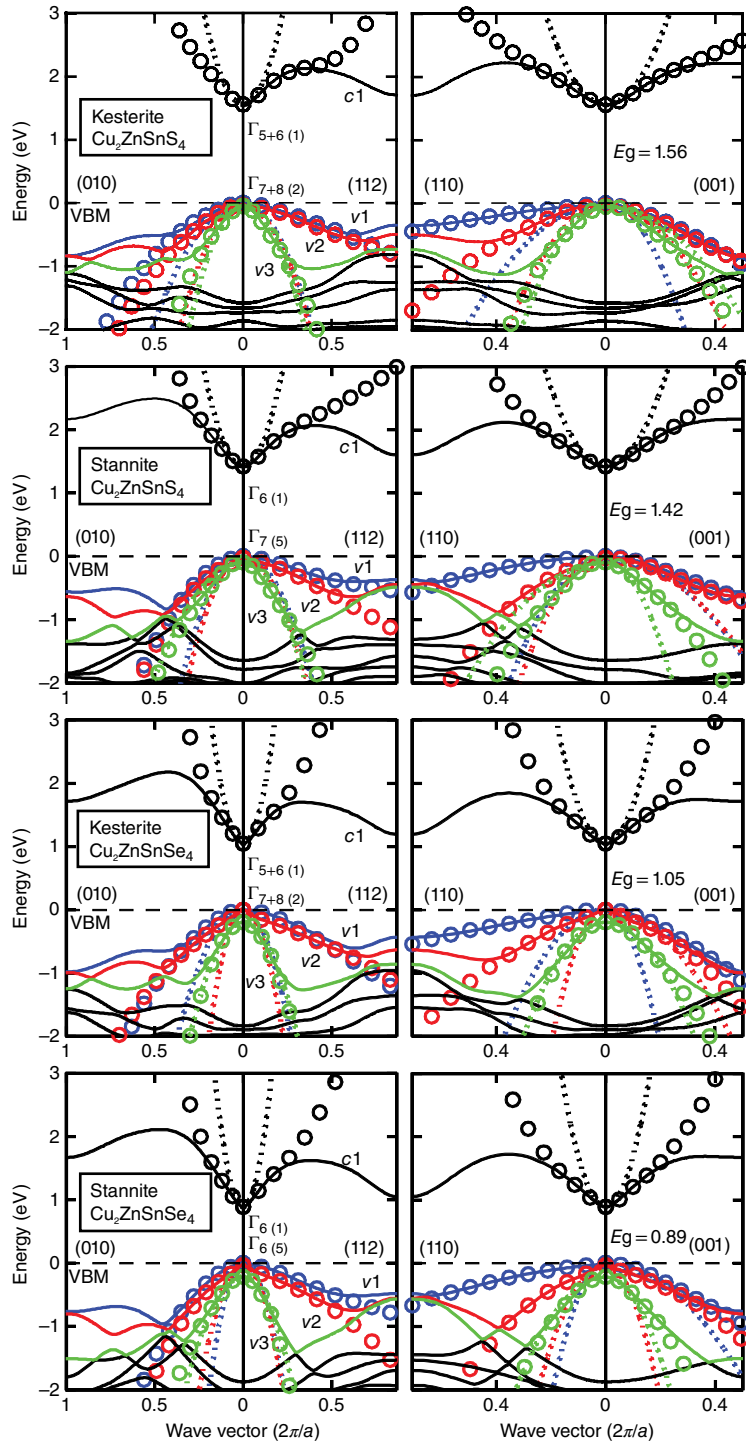
In Figure 4.2 (solid lines), the calculated band structures of kesterite and stannite CZT(S,Se) are presented along four main symmetry directions. Overall, the electronic structures are similar to the traditional group-IV, III-V, and II-VI semiconductors [47], and they are also comparable to the band structures of  $\text{Cu}(\text{In,Ga})(\text{S,Se})_2$  [48]. All four compounds are direct-gap semiconductors. With the GGA + QP, the  $\Gamma$ -point band-gap energy is  $E_g = 1.56, 1.42, 1.05$ , and  $0.89$  eV for kesterite CZTS, stannite CZTS, kesterite CZTSe, and stannite CZTSe, respectively. Corresponding band-gap values from the HSE06 calculation are  $1.47, 1.27, 0.90$ , and  $0.70$  eV, and the gap values from the  $\text{GW}_0$  calculation are  $1.57, 1.40, 0.72$ , and  $0.85$  eV. We expect that the HSE06 generates slightly underestimated gap energies. However, our results are in agreement with other calculated data and available experimental results (Table 4.2). This indicates that  $E_g \approx 1.5$  eV in CZTS and  $E_g \approx 1.0$  eV in CZTSe. The gap energies for the S-based compounds are therefore  $\sim 0.5$  eV larger than for the corresponding Se-based compounds, which is comparable to the trend in  $\text{Cu}(\text{In,Ga})(\text{S,Se})_2$  and  $\text{Zn}(\text{S,Se})$ . The calculated results agree well with band-gap determination by various measurement techniques [49–60]. Moreover, we have found that the band-gap energy of the kesterite  $\text{Cu}_2\text{ZnSn}(\text{S}_{1-x}\text{Se}_x)_4$  alloy varies fairly linearly as a function of the Se content  $x$  [20] with  $E_g = 1.47, 1.30, 1.17, 1.01$ , and  $0.90$  eV for  $x=0, 1/4, 1/2, 3/4$ , and  $1$ , using the HSE06 potential. This linear relation is in agreement with diffuse reflectance and transmittance measurements by Gao *et al.* [52], photoluminescence by Haight *et al.* [56], and absorption analysis by He *et al.* [57].

**Table 4.2** Crystal field split  $\Delta_{\text{cf}}$ , spin–orbit split-off energy  $\Delta_{\text{so}}$ , and band-gap energies  $E_g$  obtained from the GGA + QP, the HSE06, and the beyond-DFT GW approaches. The standard HSE06 approach (with  $\alpha=0.25$  and  $\mu=0.2$ ) is expected to slightly underestimate the gap energies in these compounds.

	$\text{Cu}_2\text{ZnSnS}_4$		$\text{Cu}_2\text{ZnSnSe}_4$	
	Kesterite	Stannite	Kesterite	Stannite
$\Delta_{\text{cf}}$ GGA + QP (meV)	–36	84	–7	68
$\Delta_{\text{so}}$ GGA + QP (meV)	–27	24	198	220
$E_g$ at $\Gamma$ -point (eV)				
GGA + QP	1.56	1.42	1.05	0.89
HSE06	1.47	1.27	0.90	0.70
$\text{GW}_0$	1.57	1.40	0.72	0.85
Other HSE06	$1.50^a, 1.487^b,$ $1.52^c$	$1.38^a, 1.295^b,$ $1.27^c$	$0.96^a, 0.94^c$	$0.82^a, 0.75^c$
Other GW	$1.64^c, 1.65^d$	$1.33^c, 1.40^d$	$1.02^c, 1.08^d$	$0.87^c$
Expt.	$1.45^e, 1.5^f, 1.51^g, 1.5^h, 1.45^i$		$1.05^g, 1.0^j, 0.95^k, 0.96^l, 0.96^m$	

<sup>a</sup>Chen *et al.* [4]; <sup>b</sup>Paier *et al.* [5]; <sup>c</sup>Botti [15]; <sup>d</sup>Zhang *et al.* [16]; <sup>e</sup>Ito *et al.* [49, 50]; <sup>f</sup>Kamoun *et al.* [51]; <sup>g</sup>Gao *et al.* [52];

<sup>h</sup>Tanaka *et al.* [44]; <sup>i</sup>Patel *et al.* [54]; <sup>j</sup>Ahn *et al.* [55]; <sup>k</sup>Haight *et al.* [56]; <sup>l</sup>He *et al.* [57]; <sup>m</sup>Repins *et al.* [58].



**Figure 4.2** The electronic band structure  $E_j(\mathbf{k})$  of the kesterite and stannite structures of CZTS and CZTSe along four symmetry directions. The energy refers to the VBM (dashed lines). The spin-orbit interaction is included, but the index of the bands ( $j=v1, v2, v3$ , and  $c1$ ) refers to spin-independent bands where  $c1$  represents the lowest CB and  $v1$  represents the topmost VB. The solid lines are the data from GGA/FP-LAPW calculations, the circles show the results from the full band parameterization, and the dotted lines represent the parabolic band approximation. For color details, please see color plate section.

The  $\Gamma$  point has  $S_4$  point-group symmetry in the kesterite structure and  $D_{2d}$  point-group symmetry in the stannite structure. The CBMs of all four compounds have  $\Gamma_1$  symmetry in the single-group irreducible representation (not considering the spin-orbit coupling). The corresponding double-group representation (including the spin-orbit interaction) of the CBM is  $\Gamma_{5+6}$  for the kesterite phase and  $\Gamma_6$  for the stannite phase. The VBMs of both kesterite CZTS and CZTSe have  $\Gamma_2$  symmetry for the single group and  $\Gamma_{7+8}$  for the double group. The VBMs of both stannite CZTS and CZTSe have  $\Gamma_5$  symmetry for the single group. With the spin-orbit interaction, the VBM of stannite CZTS has  $\Gamma_7$  symmetry while stannite CZTSe has  $\Gamma_6$  symmetry. In Figure 4.2 we present both the single-group (in brackets) and the double-group representations.

One obvious difference between CZT(S,Se) and the traditional semiconductors is that the lowest CB in CZT(S,Se) is not degenerate at the BZ edge. The reason for this is that CZT(S,Se) has a low crystalline symmetry. Since the lowest CB is not degenerate with the second CB, the lowest CB has relatively flat band dispersion. The indirect band gaps are therefore small. In kesterite CZTS, stannite CZTS, kesterite CZTSe, and stannite CZTSe, respectively, the indirect-gap energies are 2.2, 2.2, 1.7, and 1.7 eV for the CBM at the  $(0,1,0)=(0,0,1)$  BZ edge, and the energies are 1.7, 1.6, 1.2, and 1.1 eV for the CBM at the  $(1,1,2)=(1,1,0)$  BZ edge. The indirect gap is therefore only  $\sim 0.2$  eV larger than the fundamental band-gap energy  $E_g$ .

Moreover, also the topmost VB is relatively flat. In combination with a flat CB, the direct energy gaps are small for  $\mathbf{k}$ -points away from the  $\Gamma$ -point. In kesterite CZTS, stannite CZTS, kesterite CZTSe, and stannite CZTSe, respectively, the direct-gap energies are 3.0, 2.7, 2.7, and 2.4 eV at the  $(0,1,0)$  BZ edge, and 2.1, 2.0, 1.6, and 1.5 eV at the  $(1,1,2)$  BZ edge. The flat CB and VB dispersions are more pronounced in CZT(S,Se) compared to corresponding bands in chalcopyrite  $\text{Cu}(\text{In,Ga})(\text{S,Se})_2$  compounds [48]. Flat-energy dispersions of the CB and VB imply a larger DOS near the band edges, and therefore a possibility of a stronger optical absorption. The disadvantage is however that the effective mass is often larger when the whole band is flat, and this may affect the electronic transport properties.

Close to the  $\Gamma$ -point CBM and  $\Gamma$ -point VBM, the energy bands of CZT(S,Se) can be described by parabolic (i.e. ellipsoidal) energy dispersion of the form:

$$E_j^{\text{pb}}(\mathbf{k}) = E_j(\mathbf{0}) \pm \left[ \frac{\tilde{k}_x^2 + \tilde{k}_y^2}{m_j^\perp} + \frac{\tilde{k}_z^2}{m_j^\parallel} \right] \quad (4.6)$$

where

$$\tilde{k}_\alpha^2 = \frac{\hbar^2 k_\alpha^2}{2e}, \quad \alpha = x, y, z,$$

and  $e$  is the value of the elementary charge to yield data in electronvolt (eV) unit. The positive and negative sign represents the CB and VBs, respectively, and  $m_j^\perp$  and  $m_j^\parallel$  are the effective masses in the vicinity of the  $\Gamma$ -point. The calculated effective masses are presented in the following section. The ellipsoidal shape of the energy bands is only valid near the CBM and VBM. This is obvious from Figure 4.2, where the dotted lines represent the parabolic approximation of the band dispersions.

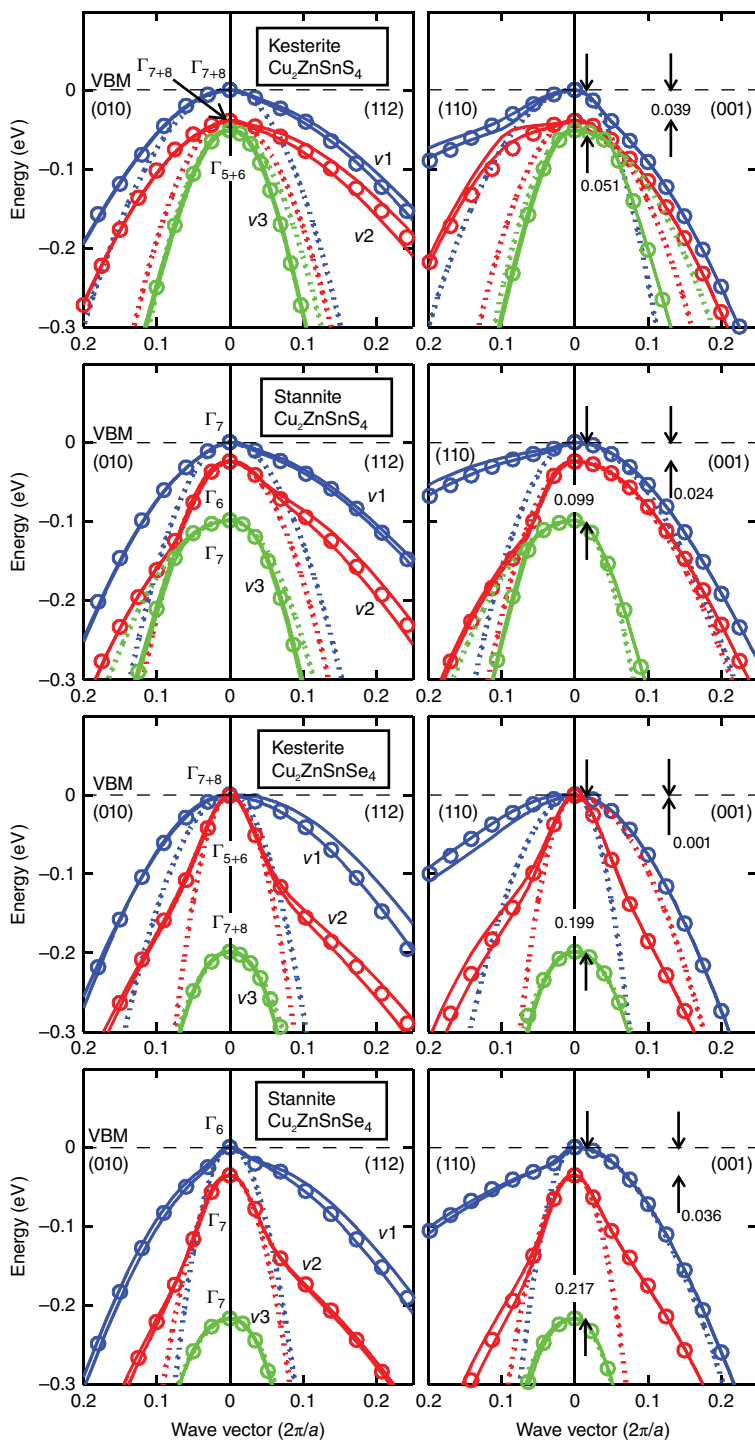
The calculations demonstrate that the energy dispersion of the VBs of both CZTS and CZTSe are anisotropic in the range of energy region from 0 to about  $-1$  eV; see Figure 4.2. The topmost VB has a dispersive energy band near the VBM, but it is rather flat away from the  $\Gamma$ -point. Comparing the band dispersion for the two uppermost VBs in the different directions, the energy at the BZ edges  $(1/2, 1/2, 1)$  and  $(1/2, 1/2, 0)$  is around  $-0.5$  eV, whereas the energy at  $(0, 1/2, 0)$  and  $(0, 0, 1/2)$  is around  $-1.0$  eV. Furthermore, below  $-1$  eV, there is one obvious difference between CZT(S,Se) and traditional semiconductors [47]. CZT(S,Se) has, similar to  $\text{Cu(In,Ga)(S,Se)}_2$ , several energetically rather localized bands that are associated with the Cu-*d*-like states.

The close-up figure (Figure 4.3) of the electronic structure around the VBM reveals that the three uppermost VBs are also non-parabolic very close to the  $\Gamma$ -point and for energies already at  $-0.01$  eV. The main reason for this non-parabolicity is the coupling between the three bands in combination with the crystal field and the spin-orbit coupling that split degeneracies at the  $\Gamma$ -point. The sign of the crystal-field split  $\Delta_{\text{cf}}$  is defined by the order of the VB states when spin-orbit coupling is neglected, and a negative  $\Delta_{\text{cf}}$  implies that the single state is above the twofold degenerate state. The kesterite phase therefore has a negative crystal field, whereas the stannite phase has a positive crystal field. The crystal-field split energy is  $\Delta_{\text{cf}} \approx -0.04, 0.08, -0.01$ , and  $0.07$  eV in kesterite CZTS, stannite CZTS, kesterite CZTSe, and stannite CZTSe, respectively. The crystal-field split of the stannite phase is therefore larger ( $\Delta_{\text{cf}} \approx 70$  meV) than for the kesterite phase, indicating a stronger anisotropy of the ionicity. The spin-orbit interaction further reduces the degeneracy of the otherwise twofold degenerate VB state at the  $\Gamma$ -point. For the kesterite phase, the spin-orbit interaction generates the split  $\Gamma_{3+4} \otimes D_{1/2} \Rightarrow \Gamma_{5+6} \oplus \Gamma_{7+8}$  and changes the symmetry  $\Gamma_2 \otimes D_{1/2} \Rightarrow \Gamma_{7+8}$ . For the stannite phase it splits  $\Gamma_5 \otimes D_{1/2} \Rightarrow \Gamma_6 \oplus \Gamma_7$  and changes the symmetry  $\Gamma_4 \otimes D_{1/2} \Rightarrow \Gamma_7$ . The spin-orbit split-off energy is  $\Delta_{\text{so}} \approx 0.02$  eV for CZTS and  $\sim 0.20$  eV in CZTSe, according to the corresponding results for  $\text{Cu(In,Ga)(S,Se)}_2$  [48]. The lighter S-atom therefore implies roughly 10 times smaller  $\Delta_{\text{so}}$  compared to the Se atom.

The value of the spin-orbit coupling cannot be determined exactly from the energies of the VB states because there is an additional coupling between the three topmost bands. That is, due to group theoretical symmetries, the VBs away from the  $\Gamma$ -point are not allowed to cross; the bands are therefore constrained in their ordering and the spin-orbit interaction is not allowed to freely split the energy bands. Moreover, from our test calculations with the HSE06 potential, the values of the spin-orbit split is about 10–20% larger than in these GGA+QP calculations.

The irreducible representations of the three uppermost VBs at the  $\Gamma$ -point demonstrate that the four compounds have some differences; see Figures 4.2 and 4.3. For the kesterite phase, both CZTS and CZTSe have  $\Gamma_{7+8}$  symmetry for the topmost VB. However, whereas CZTS has  $\Gamma_{7+8}$  symmetry also for the second VB and  $\Gamma_{5+6}$  symmetry for the third VB, CZTSe has the opposite ordering of these two VBs. Moreover, for the stannite phase there is a different type of dissimilarity. Both stannite CZTS and CZTSe have  $\Gamma_7$  symmetry for the third VB. However, whereas CZTS has  $\Gamma_7$  symmetry for the topmost VB and  $\Gamma_6$  symmetry for the second VB, CZTSe has the opposite ordering of these two uppermost VBs. All together, the four compounds have rather different symmetry characteristics of their three uppermost VBs. However, these dissimilarities do not have much of an impact on the overall electronic structure (Figure 4.2). All four compounds have very anisotropic VB





**Figure 4.3** A close-up of Figure 4.2 near the VBM, demonstrating that the uppermost VBs are very non-parabolic. For color details, please see color plate section

dispersion. Also, it is clearly seen how the second VB couples to the third VBs at about 0.1–0.2 eV below the VBM.

Due to the coupling between the three bands, the energy dispersions are very non-parabolic. The parabolic approximation (Equation (4.6)) is therefore only valid in the vicinity of the  $\Gamma$ -point. This approximation has to be extended in order to better describe the energies of the band edges, so that the energy dispersion away from the  $\Gamma$ -point can also be analyzed. For traditional semiconductors, with twofold degenerate  $sp^3$ -like VBM, the energy dispersion can be modeled rather accurately by the standard  $\mathbf{k}\cdot\mathbf{p}$  approximation [61–63]. However, for CZTS and CZTSe the energy bands of VBM also involve Cu- $d$ -Se- $p$  antibonding-like states, and the crystal field as well as the spin-orbit coupling generates rather complex energy dispersions that are anisotropic and non-parabolic. The standard  $\mathbf{k}\cdot\mathbf{p}$  approximation is therefore not sufficient. Instead, we extend the  $\mathbf{k}\cdot\mathbf{p}$  expressions with higher-order terms and with lower band symmetries by choosing the form:

$$\begin{aligned}
 E_j(\mathbf{k}) = E_j^{\text{pb}}(\mathbf{k}) + E_j^0 + \Delta_{j,1} & \left( \delta_{j,1}^2 \left( \frac{\tilde{k}_x^4 + \tilde{k}_y^4}{m_0^2} \right) + \delta_{j,2}^2 \left( \frac{\tilde{k}_x^2 \tilde{k}_y^2}{m_0^2} \right) + 1 \right)^{1/2} \\
 & + \Delta_{j,2} \left( \delta_{j,3}^3 \left( \frac{\tilde{k}_x^6 + \tilde{k}_y^6}{m_0^3} \right) + \delta_{j,4}^3 \left( \frac{\tilde{k}_x^2 \tilde{k}_y^4 + \tilde{k}_x^4 \tilde{k}_y^2}{m_0^3} \right) + 1 \right)^{1/3} \\
 & + \Delta_{j,3} \left( \delta_{j,5}^2 \left( \frac{\tilde{k}_z^4}{m_0^2} \right) + 1 \right)^{1/2} + \Delta_{j,4} \left( \delta_{j,6}^3 \left( \frac{\tilde{k}_z^6}{m_0^3} \right) + 1 \right)^{1/3} + \Delta_{j,5} \left( \delta_{j,7}^2 \left( \frac{\tilde{k}_x^2 \tilde{k}_z^2 + \tilde{k}_y^2 \tilde{k}_z^2}{m_0^2} \right) + 1 \right)^{1/2} \\
 & + \Delta_{j,6} \left( \delta_{j,8}^3 \left( \frac{\tilde{k}_x^4 \tilde{k}_z^2 + \tilde{k}_y^4 \tilde{k}_z^2}{m_0^3} \right) + \delta_{j,9}^3 \left( \frac{\tilde{k}_x^2 \tilde{k}_z^4 + \tilde{k}_y^2 \tilde{k}_z^4}{m_0^3} \right) + \delta_{j,10}^3 \left( \frac{\tilde{k}_x^2 \tilde{k}_y^2 \tilde{k}_z^2}{m_0^3} \right) + 1 \right)^{1/3}, \quad (4.7)
 \end{aligned}$$

where the parameterized energy bands  $E_j(\mathbf{k})$  represent an average of the two spinor states  $\psi_j^\sigma(\mathbf{k})$  where  $\sigma = \downarrow$  and  $\uparrow$ . This is a reasonable approach because, due to the time-reversal symmetry, there exists a spin-down state for each spin-up state (i.e.  $E_j^\downarrow(-\mathbf{k}) = E_j^\uparrow(\mathbf{k})$ ) and this makes the material overall spin-independent. Each  $\mathbf{k}$ -dependent term in Equation (4.7) describes a parabolic dispersion, but the higher-order terms affect the dispersion for the long wave vectors away from the  $\Gamma$ -point. The terms together therefore describe local effects at the  $\Gamma$ -point such as the crystal field and the spin-orbit coupling, and also the anisotropy of the bands away from the  $\Gamma$ -point. Whereas the CBs of both CZTS and CZTSe are rather isotropic and parabolic, the complex VB energy dispersions require many fitting parameters. These fitting parameters are presented in Table 4.3.

We verify that the parameterized energy dispersions (circles in Figures 4.2 and 4.3) are suitable for describing the energy bands down to about 0.5 eV below the VBM for the three uppermost VBs, and about 0.5 eV above the CBM for the lowest CB. Despite the fact that the VBs have a complex character, the parameterization can fairly accurately follow the curvatures in this energy region. The parameterized band structures are therefore considerably improved compared to the parabolic approximation which is valid to only  $\sim 0.01$  eV below the VBM.

**Table 4.3** Parameters that describe the energy dispersions  $E_j(\mathbf{k})$  of the lowest CB and the three uppermost VBs; see Equation (4.7)

j =	Cu <sub>2</sub> ZnSnS <sub>4</sub>						Cu <sub>2</sub> ZnSnSe <sub>4</sub>									
	Kesterite			Stannite			Kesterite			Stannite						
	c1	v1	v2	v3	c1	v1	v2	v3	c1	v1	v2	v3	c1	v1	v2	v3
E <sub>j</sub> (0) (eV)	1.56	0	0.039	0.051	1.42	0	0.024	0.099	1.05	0	0.001	0.199	0.89	0	0.036	0.217
m <sub>j</sub> <sup>⊥</sup> (m <sub>0</sub> )	0.18	0.71	0.35	0.26	0.17	0.33	0.27	0.73	0.08	0.33	0.09	0.24	0.06	0.09	0.15	0.29
m <sub>j</sub> <sup>  </sup> (m <sub>0</sub> )	0.20	0.22	0.52	0.76	0.18	0.84	0.88	0.17	0.08	0.09	0.50	0.28	0.06	0.66	0.09	0.15
E <sub>j</sub> <sup>0</sup> (eV)	-0.9015	-0.2833	-1.448	-0.4022	0.6792	-0.3973	-0.7537	-0.5605	0.2528	-0.5595	-0.3250	-0.6676	0.4321	-0.7027	-0.2290	0.1446
Δ <sub>j1</sub> (10 <sup>-3</sup> eV)	-389.7	162.7	1.720	-0.3360	-270.0	11.24	-37.89	399.8	-51.27	3.680	124.1	293.3	-49.88	26.71	160.7	275.4
Δ <sub>j2</sub> (10 <sup>-3</sup> eV)	-3.912	-81.48	136.3	129.6	-2.867	19.46	125.8	-156.5	-135.4	116.7	180.7	-27.47	-151.8	68.18	-9.518	-40.49
Δ <sub>j3</sub> (10 <sup>-3</sup> eV)	-527.1	42.24	1424	280.4	-383.7	6.247	738.3	298.4	-250.5	478.2	159.3	379.7	-286.5	591.4	73.52	253.7
Δ <sub>j4</sub> (10 <sup>-3</sup> eV)	-5.705	197.3	16.46	-84.79	-4.120	251.6	-62.41	3.112	-3.678	1.165	-0.7860	-27.84	-8.921	-0.6350	89.71	-12.34
Δ <sub>j5</sub> (10 <sup>-3</sup> eV)	-27.10	4.543	-131.8	-10.10	-40.01	199.8	220.4	-261.7	-11.82	-40.33	-159.7	-49.96	-2.023	101.7	25.25	-979.9
Δ <sub>j6</sub> (10 <sup>-3</sup> eV)	1855	-41.97	1.649	87.38	21.45	-91.07	-230.5	277.4	199.9	0.04600	21.42	99.89	67.05	-84.63	-110.7	359.0
δ <sub>j1</sub> (eV <sup>-1</sup> )	8.726	20.25	982.2	1042	11.90	165.5	47.88	12.46	108.6	421.2	78.35	12.33	184.1	360.5	55.49	12.85
δ <sub>j2</sub> (eV <sup>-1</sup> )	14.98	19.47	1842	7323	21.10	425.8	174.4	22.00	168.5	1205	116.0	18.48	272.2	615.2	94.42	16.97
δ <sub>j3</sub> (eV <sup>-1</sup> )	250.2	30.15	3.482	16.41	357.3	7.959	35.85	30.97	25.61	4.888	3.723	70.45	27.63	4.670	375.3	54.24
δ <sub>j4</sub> (eV <sup>-1</sup> )	377.1	0.06851	0.03354	27.52	491.7	0.05103	75.25	59.31	40.83	2.730	1.953	147.5	44.43	0.01546	712.0	107.2
δ <sub>j5</sub> (eV <sup>-1</sup> )	6.689	83.57	0.823	16.50	9.535	43.65	1.731	11.37	28.65	2.061	48.57	9.112	30.80	1.971	130.4	19.49
δ <sub>j6</sub> (eV <sup>-1</sup> )	190.3	2.281	45.86	56.80	242.9	2.329	4.273	280.8	854.3	8158	8819	62.65	625.7	90.27	7.479	99.96
δ <sub>j7</sub> (eV <sup>-1</sup> )	74.04	579.4	2.242	303.4	210.2	7.918	65.68	55.84	328.8	5.376	31.80	94.75	2146	98.14	285.2	24.56
δ <sub>j8</sub> (eV <sup>-1</sup> )	1.196	57.34	71.72	0.6072	172.7	14.15	45.22	31.00	4.735	7563	64.18	50.65	20.06	100.4	48.08	51.62
δ <sub>j9</sub> (eV <sup>-1</sup> )	0.9985	0.3192	634.3	39.68	277.6	1.501	54.42	47.76	0.03787	8099	298.8	25.97	15.03	99.30	26.09	0.000
δ <sub>j10</sub> (eV <sup>-1</sup> )	0.000	47.82	797.6	60.01	294.5	2.682	26.80	59.56	13.05	7243	280.1	55.61	18.10	0.000	48.22	44.42

To further demonstrate the non-parabolic nature of the band dispersion, we utilize the parameterized energy bands and plot the constant energy surfaces of the three uppermost VBs in kesterite CZTS (Figure 4.4). In the figure, the left column represents the constant energy surface at  $E = -1$  meV, that is, at the vicinity of the  $\Gamma$ -point (i.e. 1 meV below the VBM), whereas the right column represent the constant energy surface at  $E = -200$  meV, away from the  $\Gamma$ -point. The energy bands are highly ellipsoidal shaped close to the VBM at the  $\Gamma$ -point, and in this region the effective mass tensor can describe the energy dispersion accurately. For the topmost VB, it can be observed that the heavier transverse mass ( $m_{v1}^{\perp} = 0.71 m_0$ ) compared to the longitudinal mass ( $m_{v1}^{\parallel} = 0.22 m_0$ ) implies that the energy surface becomes a flat ellipsoid, whereas for the second VB the lighter transverse mass ( $m_{v2}^{\perp} = 0.35 m_0$ ) compared to the longitudinal mass ( $m_{v2}^{\parallel} = 0.52 m_0$ ) generates a tall ellipsoidal-shaped energy surface.

#### 4.4.2 Effective Masses

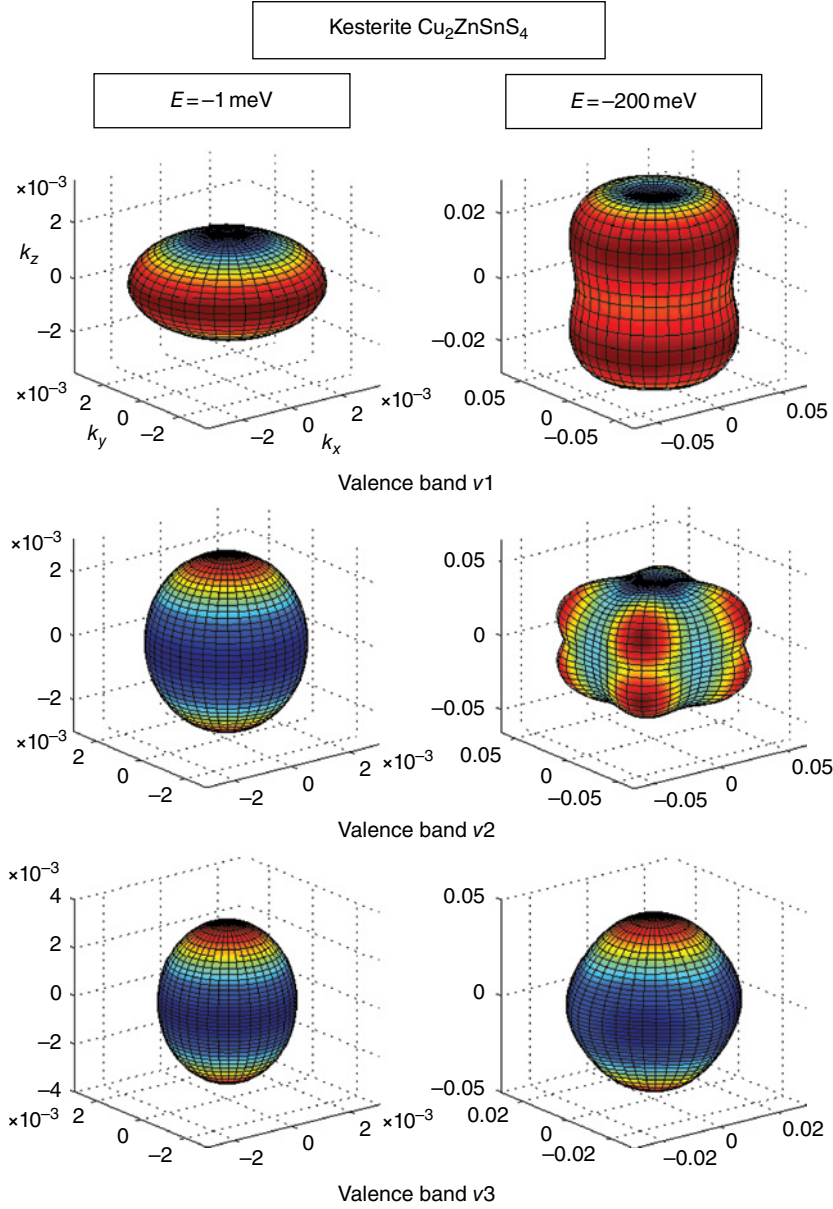
The effective electronic mass is a fundamental quantity of semiconductors used in numerous analyses of experiments and theoretical modeling. Motions of the electrons in the CBs and the holes in the VB are represented by the effective masses. The electronic mass is defined from the electronic bands structure, and can be experimentally determined through a correlation with other parameters in processes involving the motion of the electrons.

The electronic mass describes the response of an electron in the conduction to an applied electric field. The effective electronic masses are defined through the tensor  $1/m(\mathbf{k})$ , defined:

$$\frac{1}{m(\mathbf{k})_{\alpha\beta}} = \pm \frac{\partial^2 E_j(\mathbf{k}) / \partial k_{\alpha} \partial k_{\beta}}{\hbar^2} \quad (4.8)$$

where the plus/minus sign is associated with the electrons and holes, respectively. When determining the effective masses, it is crucial to have a very high accuracy of the band energies. This is especially true for the effective hole masses, for which the crystal field and the spin-orbit interaction split the energy bands near the VBM and thereby generate very non-parabolic band curvatures. We therefore determine the effective masses from the FP-LAPW electronic energies at the vicinity of the  $\Gamma$ -point, using the Engel and Vosko GGA potential and taking into account the spin-orbit coupling. We have shown that this potential generates accurate effective masses for traditional semiconductor materials [32, 64].

For CZT(S,Se), the diagonalized mass tensor has components in the transverse and longitudinal directions. Furthermore, although CZT(S,Se) are primarily covalent semiconductors, the compounds also have an ionic character. When the cations and anions vibrate, the longitudinal optical (LO) phonons will therefore build up an electric field along the direction of the vibrations. The charged electrons and holes interact with this field, and this interaction is known as the polaron effect. The interaction makes the electrons and holes move somewhat slower in the material, and the effect can therefore be regarded as a change in the effective masses. This effective polaron mass  $m^p$  includes the electron-phonon



**Figure 4.4** Constant energy surfaces  $S_i(E)$  of kesterite CZTS for the energies  $E = -1 \text{ meV}$  below the VBM (left column) and  $E = -200 \text{ meV}$  (right column). The  $\mathbf{k}$ -mesh is in the unit  $2\pi/a$ . Notice the different scales on the  $\mathbf{k}$ -axis. This figure demonstrates that the three uppermost VBs are very anisotropic away from the  $\Gamma$ -point. For color details, please see color plate section

interactions, and the mass is estimated from the LO phonon energies  $\hbar\omega_{\text{LO}}$  and the dielectric constants  $\epsilon_0$  and  $\epsilon_\infty$  which characterize the ionicity of the material:

$$m^p \approx \frac{m}{1 - \alpha/6} \quad (4.9)$$

where  $\alpha$  is the Fröhlich constant, defined:

$$\alpha = \frac{e^2 \sqrt{2m\omega_{\text{LO}}/\hbar}}{8\pi\epsilon_0 \hbar \omega_{\text{LO}}} \left( \frac{1}{\epsilon_\infty} - \frac{1}{\epsilon_0} \right).$$

In this model, harmonic oscillations of the ions, interactions only with the long-wave-length phonons with constant frequency  $\omega_{\text{LO}}$ , non-degenerate bands, and the effective mass approximation [65, 66] are all assumed. In our calculations of the polaron masses, we use  $\omega_{\text{LO}} = 330 \text{ cm}^{-1}$  for CZTS and  $200 \text{ cm}^{-1}$  for CZTSe. These frequencies are average values calculated from the Born effective charges, and the values agree with recent lattice dynamic modeling [12, 14, 21]. Moreover, the kesterite and stannite phases are found to have similar frequencies. This implies the phonon energies  $\hbar\omega_{\text{LO}} \approx 41$  and  $25 \text{ meV}$  for CZTS and CZTSe, respectively, which are relatively small energies of the optical phonons. The values of the dielectric constants are presented in Section 4.5.1.

The calculated effective polaron masses  $m^p$  of CZT(S,Se) are presented in Table 4.4. The values for the corresponding bare masses are given in brackets. The effective electron masses are very isotropic for both CZTS and CZTSe, and the values are relatively small:  $m_{c1} \approx 0.20m_0$  and  $0.07m_0$ , respectively. The kesterite phase has somewhat larger electron masses compared to the corresponding stannite phase, but the absolute difference is less than  $0.02m_0$ .

**Table 4.4** The effective polaron masses for the electrons ( $m_{c1}$ ) and for the holes ( $m_{v1}$ ,  $m_{v2}$ , and  $m_{v3}$ ); the values in brackets show the corresponding bare masses. The spin-orbit interaction is included in the calculation. These values describe the parabolic energy dispersions of the bands in the very vicinity of the  $\Gamma$ -point

	$\text{Cu}_2\text{ZnSnS}_4$		$\text{Cu}_2\text{ZnSnSe}_4$	
	Kesterite	Stannite	Kesterite	Stannite
$m_{c1}^\perp (m_0)$	0.19 (0.18)	0.18 (0.17)	0.08 (0.08)	0.06 (0.06)
$m_{c1}^\parallel (m_0)$	0.21 (0.20)	0.19 (0.18)	0.08 (0.08)	0.06 (0.06)
$m_{v1}^\perp (m_0)$	0.76 (0.71)	0.37 (0.33)	0.34 (0.33)	0.10 (0.09)
$m_{v1}^\parallel (m_0)$	0.24 (0.22)	0.88 (0.84)	0.09 (0.09)	0.68 (0.66)
$m_{v2}^\perp (m_0)$	0.37 (0.35)	0.30 (0.27)	0.09 (0.09)	0.16 (0.15)
$m_{v2}^\parallel (m_0)$	0.57 (0.52)	0.92 (0.88)	0.52 (0.50)	0.09 (0.09)
$m_{v3}^\perp (m_0)$	0.28 (0.26)	0.81 (0.73)	0.25 (0.24)	0.31 (0.29)
$m_{v3}^\parallel (m_0)$	0.83 (0.76)	0.18 (0.17)	0.29 (0.28)	0.16 (0.15)

Since the effective base masses of the CB electrons are below  $0.20m_0$ , and the Fröhlich constant depends on the square-root of  $m$ , the correction due to the polaron coupling is small for the CB electrons (only  $\sim 0.01m_0$ ). One noticeable difference is that the effective electron mass of CZTS is roughly 2.5 times larger than the corresponding mass of CZTSe. Of course, in absolute values the difference is of the order  $\sim 0.1m_0$  but this difference might be possible to detect experimentally. The main reason for a larger mass in the S-based compounds is that the lowest CB is flatter with weaker energy dispersion at the  $\Gamma$ -point. This effect is related to the wider band gap for CZTS compared with CZTSe. The CZTS compounds have effective electron bare mass of  $\sim 0.19m_0$  and the CZTSe compounds have effective electron mass of  $\sim 0.07m_0$ . CZTS therefore has similar electron bare mass as  $\text{CuInS}_2$  ( $m_{c1} \approx 0.17m_0$ ) and  $\text{ZnSe}$  ( $m_{c1} \approx 0.14m_0$ ), whereas CZTSe has similar electron mass as for instance  $\text{CuInSe}_2$  ( $m_{c1} \approx 0.08m_0$ ) and  $\text{GaAs}$  ( $m_{c1} \approx 0.07m_0$ ) [47, 48].

The values of the hole masses are much more diverging for the four compounds, and the main reason for this are the differences in the crystal-field split and the spin-orbit interaction; see Figure 4.3. It is worth mentioning that since all VBs are split at the  $\Gamma$ -point, the VBs cannot be described as heavy-hole, light-hole, spin-orbit split-off bands. Instead, we use the notation  $m_{v1}$ ,  $m_{v2}$ , and  $m_{v3}$  to represent the masses of the three uppermost VBs. The anisotropy of the effective hole masses is strong in all four compounds, except for  $m_{v3}$  in stannite CZTSe. For both CZTS and CZTSe, the topmost VB of the kesterite compounds with  $\Delta_{cf} < 0$  has a large transverse hole mass (i.e.  $m_{v1}^\perp / m_{v1}^\parallel \approx 3 > 1$ ) whereas an opposite relation holds (i.e.  $m_{v1}^\perp / m_{v1}^\parallel \approx 1/3 < 1$ ) for the stannite phase with  $\Delta_{cf} > 0$ . The mass values of the three topmost VBs are however below  $1.0m_0$  for all four compounds, and the energy dispersions of the VBs are therefore rather broad in CZT(S,Se) down to about at least 0.5 eV below the VBM where the strong Cu- $d$  character has a strong impact on the band dispersion; see Figure 4.2.

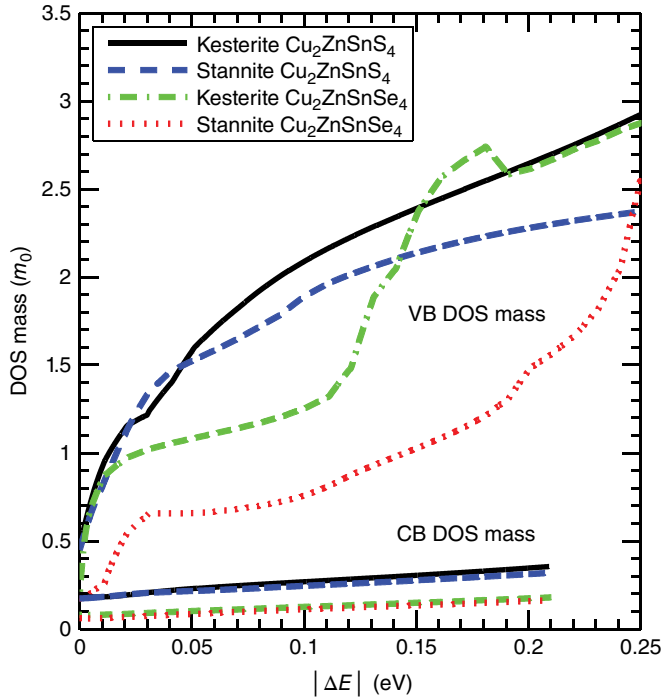
Overall, we find that the S-based compounds have larger effective masses compared to the corresponding Se-based compounds. It may therefore be expected that the carriers in CZTS have a somewhat weaker response to an applied electric field compared to CZTSe, at least for a moderate applied electric field. Furthermore, the effective hole masses in Table 4.4 are only valid in a region near the  $\Gamma$ -point. In order to analyze the electronic transport in these materials, the non-parabolicity of the energy dispersion therefore has to be considered; see Equation (4.7). Also, it is important to take the anisotropy into account for single-crystal-like materials.

It is important to distinguish the so-called DOS mass from the electronic mass. While the electronic mass describes the response of the electron to an applied field, the DOS mass is a parameter that describes the DOS, the band filling, and the quasi-Fermi level. Very close to the  $\Gamma$ -point, the DOS mass of the CB and the VB follows the ellipsoidal expressions  $m_c^{\text{DOS}} = (m_{c1}^\perp m_{c1}^\perp m_{c1}^\parallel)^{1/3}$  and  $m_v^{\text{DOS}} = (m_{v1}^\perp m_{v1}^\perp m_{v1}^\parallel)^{1/3}$ , respectively. These expressions are therefore valid for very low concentrations of free carriers in the CB and VBs, and the corresponding quasi-Fermi energies are  $E_{F,c}^* = \hbar^2 (3\pi n^{2/3} / 2m_c^{\text{DOS}})$  and  $E_{F,v}^* = \hbar^2 (3\pi p^{2/3} / 2m_v^{\text{DOS}})$  for the free electron concentration  $n$  and hole concentration  $p$ . However, for moderate to heavy band filling of carriers, the ellipsoidal expressions are not valid and a full description of the band dispersion has to be taken into account. This means that one cannot use the  $\Gamma$ -point effective mass values to describe the band filling and the quasi-Fermi energies. However, in order to utilize standard expressions for describing band filling, we define an energy-dependent DOS mass  $m_{v/c}^{\text{DOS}}(E)$  as:

$$g_{v/c}(E) = \sum_j g_j(E) = \frac{1}{2\pi^2} \left( \frac{2m_{v/c}^{\text{DOS}}(E)}{\hbar^2} \right)^{3/2} \sqrt{|E - E_{v1/c1}(\mathbf{0})|} \quad (4.10)$$

where the full DOS  $g_{v/c}(E)$  of the CB and VB are determined from the parameterized band structure in Equation (4.7). With the parameterized bands to describe the DOS, the energy-dependent DOS masses  $m_{v/c}^{\text{DOS}}(E)$  include the non-parabolicity and anisotropy of the energy bands to about 0.5 eV above CBM and 0.5 eV below VBM. Note that the total DOS  $g_v(E)$  is obtained by a summation over the three uppermost VBs;  $g_v(E)$  is therefore the total DOS of the VBs and  $m_v^{\text{DOS}}(E)$  describes how these three bands are filled by free holes. In the non-equilibrium state, the quasi-Fermi energies are  $E_{F,v}^* = E$  where  $E < E_{v1}(\mathbf{0}) = 0$  for holes in the VBs and  $E_{F,c}^* = E$  where  $E > E_{c1}(\mathbf{0}) = E_g$  for electrons in the CB. We therefore define  $|\Delta E|$  as the energy difference  $E_{F,c}^* - E_{c1}(\mathbf{0})$  for  $E > E_g$  and  $E_{v1}(\mathbf{0}) - E_{F,v}^*$  for  $E < 0$ .  $|\Delta E|$  therefore describes the band-filling effect on the quasi-Fermi energies.

In Figure 4.5, we present the DOS masses for the CB and the VBs as functions of the energy  $|\Delta E|$ . For very small energies  $|\Delta E|$ , the DOS masses are equal to the ellipsoidal expressions  $(m_{c1}^\perp m_{c1}^\perp m_{c1}^\parallel)^{1/3}$  and  $(m_{v1}^\perp m_{v1}^\perp m_{v1}^\parallel)^{1/3}$ . In this region the CB DOS mass  $m_c^{\text{DOS}}(E) \approx 0.2m_0$



**Figure 4.5** The DOS mass  $m_{v/c}^{\text{DOS}}(E)$  of the VBs and the CB in CZTS and CZTSe. This energy-dependent mass generates fairly accurate quasi-Fermi energies  $E_{F,v}^*$  and  $E_{F,c}^*$  as functions of the carrier concentration.  $|\Delta E|$  is the energy difference  $E_{F,c}^* - E_{c1}(\mathbf{0})$  for the CB and  $E_{v1}(\mathbf{0}) - E_{F,v}^*$  for the VBs.



and  $0.1m_0$  for CZTS and CZTSe, respectively. One also observes that the VB DOS mass of stannite CZTSe is small:  $m_v^{\text{DOS}}(E) \approx 0.2m_0$ . This is because stannite CZTSe has a very small transverse component of the effective hole mass:  $m_{v1}^{\perp} = 0.09m_0$ . With an increase of  $|\Delta E|$ , all DOS masses increase as function of  $|\Delta E|$ . That demonstrates that the energy bands become more flat away from the  $\Gamma$ -point. The CB DOS mass increases only slightly as a function of  $|\Delta E|$ , because the CB is fairly parabolic in energy range  $|\Delta E|=0-0.2\text{ eV}$ , that is, from  $E_g$  to  $E_g+0.2\text{ eV}$ . However, the value of the CB DOS mass is increased by a factor of  $\sim 2$  when energy is  $E_g+0.2\text{ eV}$ . For example, the CB DOS mass for kesterite CZTS is  $\sim 0.19m_0$  in the vicinity of the CBM (i.e.  $|\Delta E| \approx 0$ ), but is increased to  $\sim 0.36m_0$  for the energy  $0.2\text{ eV}$  above the CBM ( $|\Delta E|=0.2\text{ eV}$ ).

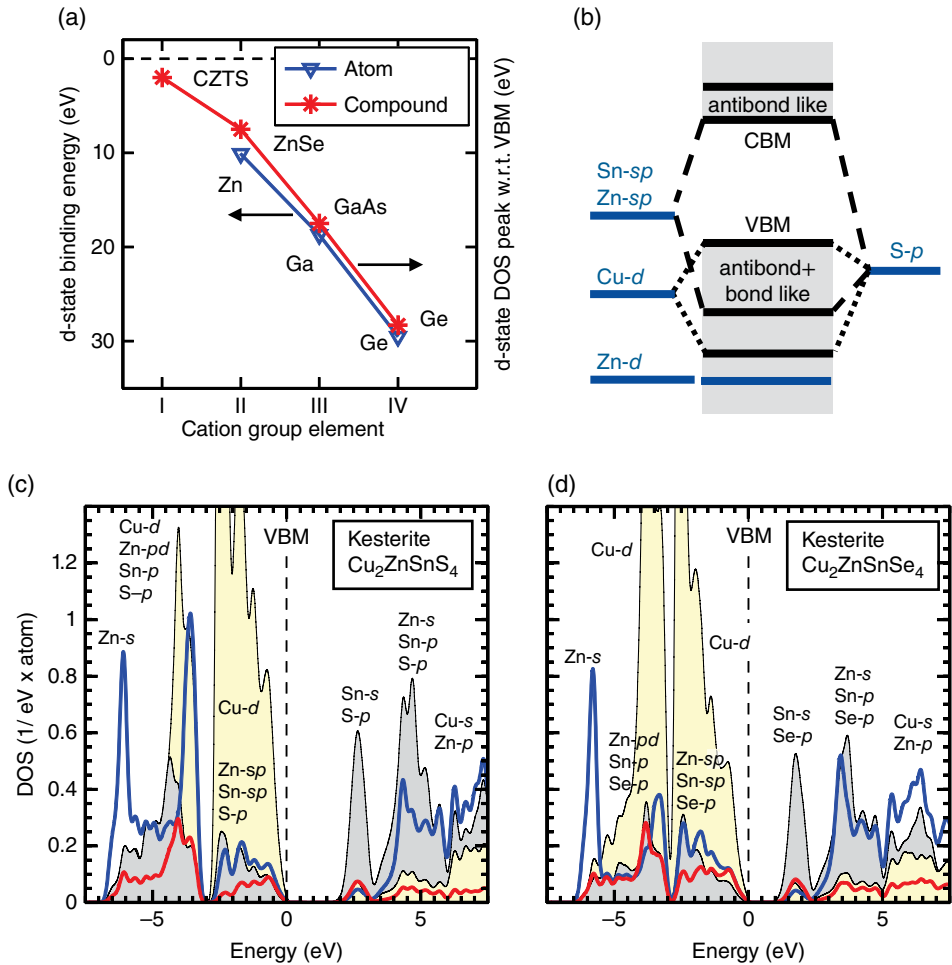
For the VBs, however, the VB DOS mass changes significantly when  $|\Delta E|$  increases. The main reason is that the crystal field and the spin-orbit coupling split the energy bands at the  $\Gamma$ -point, and this generates non-parabolic band dispersion. For example, the VB DOS mass of kesterite CZTS is  $\sim 0.48m_0$  in the vicinity of VBM (i.e.  $|\Delta E| \approx 0$ ), but the value reaches  $\sim 1.0m_0$  when the energy is only  $50\text{ meV}$  below the VBM ( $|\Delta E| \approx 0.05\text{ eV}$ ) and  $\sim 2.0m_0$  when the energy is only  $0.1\text{ eV}$  below the VBM.

The VB DOS masses are directly related to the band structure in Figure 4.3. For both kesterite and stannite CZTS all three uppermost VBs couple in the energy region  $0$  to  $-0.15\text{ eV}$  since both  $\Delta_{\text{cf}}$  and  $\Delta_{\text{so}}$  are small. This generates a rather complex energy band dispersion, and CZTS therefore has a strong change in their VB DOS mass. For both kesterite and stannite CZTSe, the VB DOS masses are more stable than CZTS in the energy region  $|\Delta E|=0.01-0.10\text{ eV}$ . This is explained by the energy split of second and third VBs. In the energy region  $-0.01$  to  $-0.15\text{ eV}$ , the band dispersions of the second and third VBs are fairly parabolic which thereby generate a stable VB DOS mass. Furthermore, kesterite and stannite CZTS have more constant VB DOS mass than CZTSe for the energies  $|\Delta E| > 0.15\text{ eV}$  because this energy is below both the crystal-field split and the spin-orbit split-off energies in CZTS, and VBs are relatively parabolic below  $0.15\text{ eV}$ .

#### 4.4.3 Density-of-States

The atom-resolved DOS of kesterite CZTS and CZTSe (Figure 4.6) are calculated by the partially self-consistent and frequency-dependent  $\text{GW}_0$  method. The kesterite and stannite phases have similar tetrahedral bond geometries where each anion atom is surrounded by two Cu atoms, one Zn, and one Sn atom. The DOS of the stannite phase is therefore very similar to that of the kesterite phase [9], and not presented in the figure. Moreover, from the figure it is obvious that CZTS and CZTSe have comparable DOS, though the DOS of the CBs in CZTS is energetically  $\sim 0.5\text{ eV}$  higher due to the large energy gap. Overall however, all four CZT(S,Se) compounds have very comparable DOS.

One obvious difference between CZT(S,Se) and the traditional group-IV, III-V, and II-VI semiconductors is the strong Cu- $d$  contribution in the VB DOS of CZT(S,Se). Normally, the cation  $d$ -like states do not influence the semiconductor properties because for the group-IV materials (e.g. Ge and Sn), the cation  $d$ -like states are  $\sim 25\text{ eV}$  below the VBM and for group-III-V materials (e.g. GaAs and InN) the  $d$ -like states are  $\sim 18\text{ eV}$  below the VBM. For the group-II-VI semiconductors (e.g. ZnSe and ZnO) the cation  $d$ -like states affect the DOS at about  $6-8\text{ eV}$  below the VBM by hybridizing with the anion  $p$ -like states [67]. For CZT(S,Se) with very shallow Cu energy states, the Cu  $3d^{10}$ -like states will



**Figure 4.6** (a) Energy levels of the cation  $d$ -like states in sole atoms and in binary compounds. (b) Schematic illustration of the band edges in CZTS. Atomic and angular-momentum resolved DOS of kesterite (c) CZTS and (d) CZTSe; the corresponding stannite phases have very similar DOS [9]. The DOS distributions are presented with a 70 meV Lorentzian broadening. Reprinted with permission from [9]. Copyright 2010, American Institute of Physics

hybridize with the anion  $p$ -like states in a broad energy range of the VBs, and thereby influence the DOS also near the VBM. Thus, the fully occupied  $3d^{10}$ -like states dominate the VB DOS in CZT(S,Se).

In Figure 4.6, the angular-momentum-dependent contribution to the DOS is indicated. The DOS can be understood by comparing the energy dispersion with the electronic structure in Figure 4.2. The flat and energetically localized VBs about at about  $-1$  eV in Figure 4.2 are associated with the Cu  $d$ -like bands. These states generate strong Cu  $d$ -like VB DOS which is an advantage for high optical activity. The upper region of the VB DOS also contains Zn- $p$  and Sn- $sp$  bonded with the anion  $p$ -like states.

The energetically lower region of the CB DOS (at about 2–3 eV) primarily contains Sn-*s* and anion *p*-like states. In the higher energy region (4–6 eV) the DOS also involves Zn-*s* and Sn-*p* antibonded with the anion-*p*. For even higher energies (6–8 eV), Cu-*s* and Zn-*p* also become important. The strong Sn-*s* DOS for the low CB DOS (i.e. at 2–3 eV) is very significant for the CZT(S,Se) compounds. From Figure 4.2, it can be observed that this DOS peak arises from the lowest CB which is localized in the narrow energy region around 1.5 eV above the CBM. This pronounced Sn-*s* DOS character is also different from the chalcopyrite Cu(In,Ga)(S,Se)<sub>2</sub>. These chalcopyrites have higher crystalline symmetry, and thereby the lowest CB is degenerate with higher-lying CBs at the BZ edge, which in turn generates a broader DOS character of the CBs. In CZT(S,Se) however, the lowest CB is separated from the higher energy bands and is therefore more localized in energy. Due to this localized CB in CZT(S,Se), the energy position of the Sn-*s*–anion-*p* DOS peak can be expected to vary in energy by alloying on the Sn-site with other group-IV elements (e.g. Ge). The band-gap energy can therefore be tailored by cation alloying for an optimized optical efficiency of the materials.

## 4.5 Optical Properties

The optical properties are analyzed in terms of the complex dielectric function  $\epsilon(\omega) = \epsilon_1(\omega) + i\epsilon_2(\omega)$  and the absorption coefficient  $\alpha(\omega)$ , using the results from the GW<sub>0</sub> calculations as discussed in the previous section. As a complement, the dielectric constants from the HSE06 calculations are also presented.

### 4.5.1 Dielectric Function

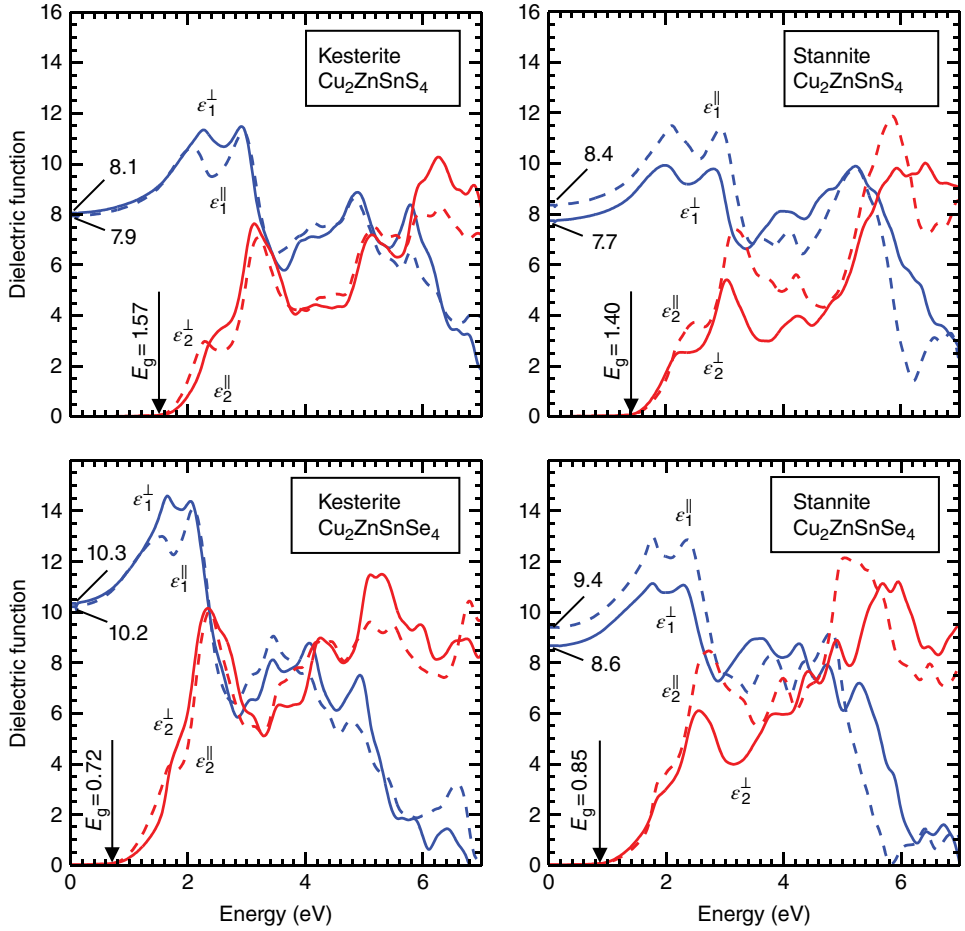
The dielectric function describes the response of the material when the charge density is changed. The dielectric function is also an important property for describing the screening of the charges in the material near dopants, defects, and for other structural perturbations of the crystal. The imaginary part of the dielectric functions is calculated from the linear response in the long wavelength limit ( $\lambda_q = 2\pi/q \rightarrow \infty$ ) through [68]:

$$\epsilon_2^{\alpha\beta}(\omega) = \lim_{q \rightarrow 0} \frac{4\pi^2 e^2}{\Omega q^2} \sum_{c,v,\mathbf{k}} 2w_{\mathbf{k}} \delta(E_c(\mathbf{k}) - E_v(\mathbf{k}) - \hbar\omega) \times \langle u_c(\mathbf{k} + \mathbf{e}_\alpha \mathbf{q}) | u_v(\mathbf{k}) \rangle \langle u_c(\mathbf{k} + \mathbf{e}_\beta \mathbf{q}) | u_v(\mathbf{k}) \rangle^* \quad (4.11)$$

The real part of the dielectric function is obtained via the Kramers–Kronig transformation relation:

$$\epsilon_1^{\alpha\beta}(\omega) = 1 + \frac{2}{\pi} P \int_0^\infty \frac{\omega' \epsilon_2^{\alpha\beta}(\omega')}{\omega'^2 - \omega^2 + i\eta} d\omega' \quad (4.12)$$

where  $u_j(\mathbf{k})$  is the cell periodic part of the wave function,  $\Omega$  is the volume of the primitive cell,  $w_{\mathbf{k}}$  is the weight of the  $\mathbf{k}$ -points, and  $\mathbf{e}_\alpha$  is the unit vector in the Cartesian coordinates.  $P$  is the principal value and  $\eta$  is an infinitesimally small number. Experimentally, the



**Figure 4.7** The dielectric function  $\epsilon(\omega) = \epsilon_1(\omega) + i\epsilon_2(\omega)$  of CZTS and CZTSe. The dielectric response is divided into the transverse ( $\perp$ ; solid lines) and longitudinal ( $\parallel$ ; dashed lines) contributions.

high-frequency dielectric constant  $\epsilon_\infty$  is determined typically in the mid-gap region, that is  $\epsilon_\infty \approx \epsilon_1(0 < \hbar\omega < E_g)$ . In our theoretical modeling, we determine  $\epsilon_\infty$  from the dielectric function at  $\epsilon_1(\hbar\omega=0)$  when the electron-optical phonon coupling is excluded and also complementary at  $\epsilon_1(\hbar\omega=E_g/2)$ . The static dielectric function  $\epsilon_0$  is calculated from the Born effective charges, taking into account the ionic contribution.

The dielectric response function is directly related to the joint DOS (i.e. the Dirac-delta function in Equation (4.11)), and the electronic band structure is the main underlying property for analyzing the polarization response. Therefore, and because all four compounds have similar DOS, their dielectric response spectra are expected to be similar. In Figure 4.7, the real part  $\epsilon_1(\omega)$  and the imaginary part  $\epsilon_2(\omega)$  are depicted, demonstrating that the spectra are qualitatively similar for the four compounds. Also, the dielectric functions are also comparable to those of  $\text{Cu}(\text{In,Ga})(\text{S,Se})_2$  [13].

**Table 4.5** Static  $\epsilon_0$  and high-frequency  $\epsilon_\infty$  dielectric constants in the transverse and longitudinal directions. The results are from the  $GW_0$  calculations, and the values in brackets are the corresponding HSE06 results. The static dielectric constant is determined from a contribution via the Born effective charges with the PBE potential

	$\text{Cu}_2\text{ZnSnS}_4$		$\text{Cu}_2\text{ZnSnSe}_4$	
	Kesterite	Stannite	Kesterite	Stannite
$\epsilon_0^\perp$	11.2 (9.4)	12.2 (10.7)	13.1 (10.3)	12.4 (11.5)
$\epsilon_0^\parallel$	12.5 (10.9)	10.2 (8.4)	13.4 (11.0)	11.5 (10.3)
$\epsilon_\infty^\perp$	8.1 (6.3)	7.7 (6.2)	10.3 (7.4)	8.6 (7.7)
$\epsilon_\infty^\parallel$	7.9 (6.3)	8.4 (6.6)	10.2 (7.7)	9.4 (8.2)

The calculated dielectric constants are presented in Table 4.5. The difference in the static and high-frequency constants is  $\epsilon_0 - \epsilon_\infty \approx 12 - 9 = 3$  which indicates a moderate ionicity. For kesterite CZTS, stannite CZTS, kesterite CZTSe, and stannite CZTSe, the average static values are  $\epsilon_0 = (2\epsilon_0^\perp + \epsilon_0^\parallel)/3 = 11.6, 11.5, 13.2,$  and  $12.1$ , respectively. The corresponding average high-frequency values are  $\epsilon_\infty = (2\epsilon_\infty^\perp + \epsilon_\infty^\parallel)/3 = 8.0, 7.9, 10.3,$  and  $8.7$  at  $\hbar\omega = 0$ , and  $8.2, 8.2, 10.5,$  and  $9.0$  at  $\hbar\omega = E_g/2$ . The mid-gap values are therefore about 0.2–0.3 larger than the zero-frequency values. Moreover, the values from the HSE06 calculations (values in brackets in the table) are somewhat smaller than the corresponding  $GW_0$  results.

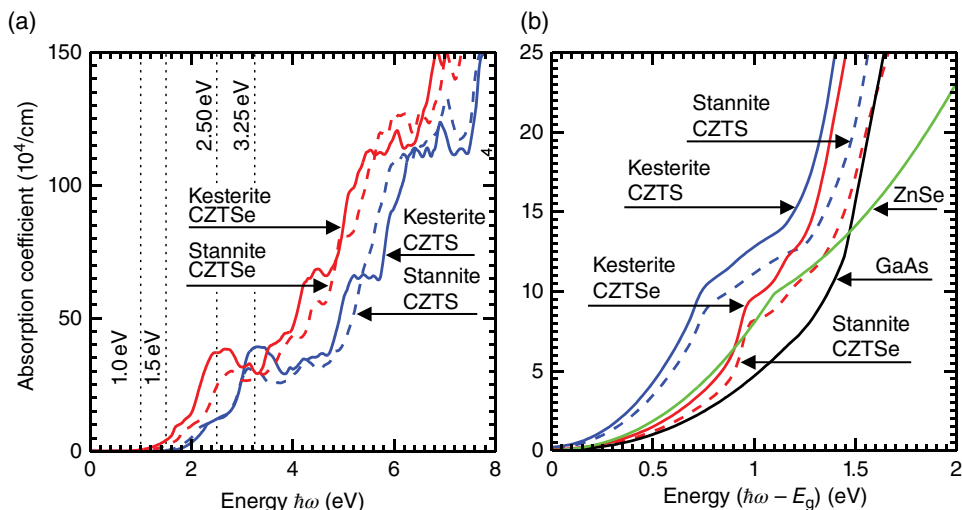
Note that the two kesterite and stannite phases have comparable dielectric constants, both for CZTS and CZTSe. The S-based compounds have slightly smaller dielectric constants compared with the Se-based compounds. This is consistent with the relation between the energy gap and the dielectric response: large band-gap energy implies small dielectric constant. However, the difference in the dielectric constants between CZTS and CZTSe is relatively small. Also, all four compounds show a distinct  $\epsilon_2(\omega)$  peak at about  $\sim 3.0$  eV for CZTS and  $\sim 2.5$  eV for CZTSe. The energy difference of 0.5 eV between CZTS and CZTSe is equal to the difference in the band-gap energy, and the peak therefore appears  $\sim 1.5$  eV above  $E_g$  for both CZTS and CZTSe. This peak is associated with the Sn-like CB in the DOS at the  $(0,1,0)=(0,0,1)$  BZ edges; see Figure 4.6. The peak has been identified to be Cu-3d to Sn-5s transitions for CZTSe by Choi *et al.* [69].

Although the four compounds have similar spectra, there are clear differences in the anisotropy in both the real and the imaginary part. At the band gap energy  $\hbar\omega \approx E_g$ , the two stannite phase show stronger anisotropy with  $\epsilon_2^\perp(\omega) > \epsilon_2^\parallel(\omega)$  compared with the kesterite phase that in addition exhibits  $\epsilon_2^\perp(\omega) < \epsilon_2^\parallel(\omega)$ . This is a consequence of the stronger and positive crystal field in the stannite phase. At the energy region  $\hbar\omega = E_g$  to  $E_g + 1$  eV, however, the opposite anisotropy appears with  $\epsilon_2^\perp(\omega) < \epsilon_2^\parallel(\omega)$  for stannite and  $\epsilon_2^\perp(\omega) > \epsilon_2^\parallel(\omega)$  for kesterite. This anisotropy is also reflected in the real part of the dielectric function. The stannite phase has a stronger anisotropy of the high-frequency dielectric constant with  $\epsilon_\infty^\perp < \epsilon_\infty^\parallel$ . The difference is  $\sim 0.7$ , and it is perhaps possible to detect this property experimentally for single-crystal-like films. We therefore propose that polarization-dependent optical characterization together with determination of the crystal-field split-off energy  $\Delta_{\text{cf}}$  can be a complementary support for analyzing the crystalline structure of the CZTS and CZTSe films.

### 4.5.2 Absorption Coefficient

The optical absorption coefficient is determined directly from the complex dielectric function through the relation  $\varepsilon_1^{\alpha\beta}(\omega)^2 + \varepsilon_2^{\alpha\beta}(\omega)^2 = [\varepsilon_1^{\alpha\beta}(\omega) + \alpha^{\alpha\beta}(\omega)^2 c^2 / 2\omega^2]^2$ , where  $c$  is the speed of light. In Figure 4.8, the average absorption coefficient  $\alpha(\omega) = [2\alpha^\perp(\omega) + \alpha^\parallel(\omega)]/3$  is presented. Since the absorption is related to the dielectric response function, the character of  $\varepsilon_2(\omega)$  is reflected in  $\alpha(\omega)$ . For instance, the  $\varepsilon_2(\omega)$  peak at about  $\sim 3.0$  eV for CZTS and  $\sim 2.5$  eV for CZTSe is seen also in  $\alpha(\omega)$ , which corresponds to the DOS peak of the CB  $\text{Sn-5}s$  at  $\sim 3.25$  and  $\sim 2.50$  eV, respectively; these energies are indicated by dotted vertical lines in the figure. Overall, the four compounds have a similar absorption spectra, considering that the band-gap energy is  $\sim 0.5$  eV larger in CZTS compared with CZTSe. The absorption coefficient is relatively large for high photon energies ( $>10^5 \text{ cm}^{-1}$  at  $\hbar\omega > E_g + 1 \text{ eV}$ ).

A clear onset to absorption occurs at the band-gap energies  $\sim 1.5$  eV for CZTS and  $\sim 1.0$  eV for CZTSe, and there are therefore no symmetry-forbidden transition rules that suppress excitations across the band edges. Instead, the absorption is relatively strong for energies near the onset of absorption. This is clearly seen in Figure 4.8(b) where we present  $\alpha(\omega)$  where the energy scale is shifted by  $\hbar\omega - E_g$ . With this energy scale, the optical efficiency can be better compared for materials with different band-gap energies. In the energy region  $\hbar\omega - E_g = 0$  to  $1.5$  eV, the CZTS has higher absorption than CZTSe. This is according to the more flat band CB of CZTS with a large CB mass; see Figure 4.3 and Table 4.4. In the energy region  $\hbar\omega - E_g = 0$  to  $0.8$  eV, CZTS has roughly twice as large absorption coefficient.



**Figure 4.8** (a) Absorption coefficients  $\alpha(\omega)$  as a function of photon energy  $\hbar\omega$  for CZTS and of CZTSe. The optical absorption is generated from the dielectric function (see Fig. 4.7), and the spectra are presented with a Lorentzian broadening of  $0.1 \text{ eV}$ . The dotted lines at  $1.0$  and  $1.5 \text{ eV}$  indicate the band-gap energies, while the dotted lines at  $2.50$  and  $3.25 \text{ eV}$  represent the small energy gap in the conduction band region (Figs 4.6(c) and (d)). (b) Close-up of  $\alpha(\omega)$  of CZT(S,Se), GaAs, and ZnSe where the energy scale is shifted by  $E_g$  in order to compare the absorption for materials with difference band gaps.

The kesterite phase has slightly higher absorption compared with the stannite phase, partly because both the CB and VB DOS masses are larger in the kesterite phase. In Figure 4.8(b), we also compare the optical efficiency of CZT(S,Se) with two traditional semiconductors, namely GaAs (with  $m_{cl} \approx 0.07 m_0$ ) and ZnSe ( $m_{cl} \approx 0.2 m_0$ ). It can be observed that these semiconductors have comparable absorption as CZTSe in the low energy region ( $\hbar\omega - E_g = 0$  to 0.8 eV) and thus lower absorption compared with CZTS. Overall, the absorption in CZTS is roughly twice that in GaAs and ZnSe.

## 4.6 Summary

To summarize, the electronic structure, density-of-states, and optical response functions of the four CZT(S,Se) are overall very comparable. However, there are distinct differences in the details in the band structure of the band edges. The band structures of the VBs in particular are very non-parabolic and anisotropic. We have therefore demonstrated that it is important to accurately describe these band edges in order to analyze properties that are related to the free carrier concentrations, for instance in studies of electronic transport and/or measurements that involve strong excitation conditions.

The four compounds have different energy splitting of the uppermost VBs, and this effect generates different anisotropy and characters of the optical response functions. The dissimilarity in the dielectric functions between the kesterite and the stannite structures might be possible to detect experimentally in high-quality films, and this can complement analysis of the crystalline structure of CZT(S,Se).

Comparing CZT(S,Se) with traditional binary semiconductors with similar tetrahedral bond symmetry, the electronic structures are comparable but there is a major dissimilarity with respect to the cation energy states. The energetically shallow Cu *d*-like VB states in CZT(S,Se) generate a strong VB DOS and thereby a high optical efficiency in the visible light region with  $\alpha(\omega) > 10^5 \text{ cm}^{-1}$  at  $\hbar\omega > E_g + 1 \text{ eV}$ . In the low-energy region, the absorption in CZTS is roughly twice as large as in GaAs and ZnSe.

Comparing CZT(S,Se) with chalcopyrite  $\text{Cu}(\text{In,Ga})(\text{S,Se})_2$ , both these types of semiconductors have strong Cu *d*-like VB states DOS and thus their electronic structure and optical absorption spectra are similar. Kesterite CZTS has somewhat larger absorption coefficients in the low-energy region near the band-gap energy, partly due to a larger effective electron mass. The main advantage of CZT(S,Se) over  $\text{Cu}(\text{In,Ga})(\text{S,Se})_2$  is of course that the material is In-free. However, the  $\text{CuIn}_{1-x}\text{Ga}_x\text{Se}_2$  alloy has a smaller effective electron mass compared with CZT(S,Se) considering materials with equal band-gap energies. A material with smaller mass is preferable for high electronic transport of the minority carriers (i.e. the electrons) in *p*-type materials. Moreover, CZT(S,Se) and chalcopyrite  $\text{Cu}(\text{In,Ga})(\text{S,Se})_2$  have similar and low formation energies of the Cu vacancies  $V_{\text{Cu}}$  [20]. This is advantageous in the growth of the material, but can be an obstacle for the electronic transport through and near the *pn*-junction device. It is well known that  $2V_{\text{Cu}} + \text{In}_{\text{Cu}}$  complexes in  $\text{Cu}(\text{In,Ga})(\text{S,Se})_2$  make it easy to grow materials with high variation of the  $[\text{Cu}]/[(\text{In,Ga})]$  ratio. The analogue to this three-atom complex in CZT(S,Se) is the two-atom defect  $V_{\text{Cu}} + \text{Zn}_{\text{Cu}}$ . The formation energy of the  $V_{\text{Cu}} + \text{Zn}_{\text{Cu}}$  and  $\text{Cu}_{\text{Zn}} + \text{Zn}_{\text{Cu}}$  defects has been calculated by Chen *et al.* to be very low [10]; this defect is therefore as important in CZT(S,Se) as  $2V_{\text{Cu}} + \text{In}_{\text{Cu}}$  is in  $\text{Cu}(\text{In,Ga})(\text{S,Se})_2$ . Huang *et al.* [19] have demonstrated the presence of larger defect

clusters in Cu-poor CZT(S,Se), which in turn stabilizes the band-gap energy. Furthermore, since CZT(S,Se) has three types of cation atoms with a different number of valence electrons, there are several shallow and deep native defects in CZT(S,Se).

Nevertheless, the In-free CZT(S,Se) compounds have sufficiently small effective electron mass and high optical efficiency. By anion alloying, the band-gap energy of  $\text{Cu}_2\text{ZnSn}(\text{S}_{1-x}\text{Se}_x)_4$  can be varied almost linearly from  $\sim 1.5$  eV (for  $x=0$ ) to  $\sim 1.0$  eV ( $x=1$ ) which is utilized to tailor and optimize the optical properties of the material. By cation alloying, the change in the band-edge of the lowest Sn  $s$ -like CB can be an alternative way of optimizing the material.

## Acknowledgements

This work is supported by the Swedish Energy Agency (STEM), the Swedish Research Council (VR), the China Scholarship Council (CSC), the Swedish Institute (SI), and the Erasmus Mundus ECW scholarship program India4EU. Special thanks are due to Yingfang He, Alphonsa Lourduoss, and Danielle Edvardsson at KTH International Relations. We acknowledge access to high-performance computing resources at NSC and HPC2N centers through SNIC/SNAC and Matter network.

## References

- [1] Goodman, C. H. L. (1958) The prediction of semiconducting properties in inorganic compounds. *Journal of Physics and Chemistry of Solids*, **6**, 305–314.
- [2] Pamplin, B. R. (1964) A systematic method of deriving new semiconducting compounds by structural analogy. *Journal of Physics and Chemistry of Solids*, **25**, 675–684.
- [3] Raulot, J. M., Domain, C. & Guillemoles, J. F. (2005) Ab initio investigation of potential indium and gallium free chalcopyrite compounds for photovoltaic application. *Journal of Physics and Chemistry of Solids*, **66**, 2019–2023.
- [4] Chen, S., Gong, X. G., Walsh, A. & Wei, S. H. (2009) Crystal and electronic band structure of  $\text{Cu}_2\text{ZnSnX}_4$  (X=S and Se) photovoltaic absorbers: First-principles insights. *Applied Physics Letters*, **94**, 041903-1-3.
- [5] Paier, J., Asahi, R., Nagoya, A. & Kresse, G. (2009)  $\text{Cu}_2\text{ZnSnS}_4$  as a potential photovoltaic material: A hybrid Hartree-Fock density functional theory study. *Physical Review B*, **79**, 115126-1-8.
- [6] Chen, S., Gong, X. G., Walsh, A. & Wei, S. H. (2009) Electronic structure and stability of quaternary chalcogenide semiconductors derived from cation cross-substitution of II-VI and I-III-VI<sub>2</sub> compounds. *Physical Review B*, **79**, 165211-1-10.
- [7] Ichimura, M. & Nakashima, Y. (2009) Analysis of atomic and electronic structures of  $\text{Cu}_2\text{ZnSnS}_4$  based on first-principle calculation. *Japanese Journal of Applied Physics*, **48**, 090202-1-3.
- [8] Nakamura, S., Maeda, T. & Wada, T. (2009) Electronic structure of stannite-type  $\text{Cu}_2\text{ZnSnSe}_4$  by first-principles calculations. *Physica Status Solidi C*, **6**, 1261–1265.
- [9] Persson, C. (2010) Electronic and optical properties of  $\text{Cu}_2\text{ZnSnS}_4$  and  $\text{Cu}_2\text{ZnSnSe}_4$ . *Journal of Applied Physics*, **107**, 053710-1-8.
- [10] Chen, S., Yang, J. H., Gong, X. G., Walsh, A. & Wei, S. H. (2010) Intrinsic point defects and complexes in the quaternary kesterite semiconductor  $\text{Cu}_2\text{ZnSnS}_4$ . *Physical Review B*, **81**, 245204-1-10.
- [11] Nagoya, A., Asahi, R., Wahl, R. & Kresse, G. (2010) Defect formation and phase stability of  $\text{Cu}_2\text{ZnSnS}_4$  photovoltaic material. *Physical Review B*, **81**, 113202-1-4.



- [12] Amiri, N. B. M. & Postnikov, A. (2010) Electronic structure and lattice dynamics in kesterite-type  $\text{Cu}_2\text{ZnSnSe}_4$  from first-principles calculations. *Physical Review B*, **82**, 205204-1-8.
- [13] Zhao, H. & Persson, C. (2011) Optical properties of  $\text{Cu}(\text{In,Ga})\text{Se}_2$  and  $\text{Cu}_2\text{ZnSn}(\text{S,Se})_4$ . *Thin Solid Films*, **519**, 7508–7512.
- [14] Gürel, T., Semik, C. & Çağın, T. (2011) Characterization of vibrational and mechanical properties of quaternary compounds  $\text{Cu}_2\text{ZnSnS}_4$  and  $\text{Cu}_2\text{ZnSnSe}_4$  in kesterite and stannite structures. *Physical Review B*, **84**, 205201-1-7.
- [15] Botti, S., Kammerlander, D. & Marques, M. A. L. (2011) Band structures of  $\text{Cu}_2\text{ZnSnS}_4$  and  $\text{Cu}_2\text{ZnSnSe}_4$  from many-body methods. *Applied Physics Letters*, **98**, 241915-1-3.
- [16] Zhang, Y., Yuan, X., Sun, X., Shih, B. C., Zhang, P. & Zhang, W. (2011) Comparative study of structural and electronic properties of Cu-based multinary semiconductors. *Physical Review B*, **84**, 075127-1-9.
- [17] Maeda, T., Nakamura, S. & Wada, T. (2011) First-principles calculations of vacancy formation in In-free photovoltaic semiconductor  $\text{Cu}_2\text{ZnSnSe}_4$ . *Thin Solid Films*, **519**, 7513–7516.
- [18] He, X. & Shen, H. (2011) First-principles study of elastic and thermo-physical properties of kesterite-type  $\text{Cu}_2\text{ZnSnS}_4$ . *Physica B*, **406**, 4604–4607.
- [19] Huang, D. & Persson, C. (2013) Band gap change induced by defect complexes in  $\text{Cu}_2\text{ZnSnS}_4$ . *Thin Solid Films*, **535**, 265–269.
- [20] Kumar, M., Zhao, H. & Persson, C. (2013) Cation vacancies in the alloys compounds of  $\text{Cu}_2\text{ZnSn}(\text{S}_{1-x}\text{Se}_x)_4$  and  $\text{CuIn}(\text{S}_{1-x}\text{Se}_x)_2$ . *Thin Solid Films*, **535**, 318–321.
- [21] Khare, A., Himmetoglu, B., Johnson, M., Norris, D. J., Cococcioni, M. & Aydil, E. S. (2012) Calculation of the lattice dynamics and Raman spectra of copper zinc tin chalcogenides and comparison to experiments. *Journal of Applied Physics*, **111**, 083707-1-9.
- [22] Perdew, J. P., Burke, K. & Ernzerhof, M. (1996) Generalized gradient approximation made simple. *Physical Review Letters*, **77**, 3865–3868.
- [23] Perdew, J. P., Chevary, J. A., Vosko, S. H., Jackson, K. A., Pederson, M. R., Singh, D. J. & Fiolhais, C. (1992) Atoms, molecules, solids, and surfaces: Applications of the generalized gradient approximation for exchange and correlation. *Physical Review B*, **46**, 6671–6687.
- [24] Engel, E. & Vosko, S. H. (1993) Exact exchange-only potentials and the virial relation as microscopic criteria for generalized gradient approximations. *Physical Review B*, **47**, 13164–13174.
- [25] Heyd, J., Scuseria, G. E. & Ernzerhof, M. (2003) Hybrid functionals based on a screened Coulomb potential. *Journal of Chemical Physics*, **118**, 8207–8215.
- [26] Shishkin, M. & Kresse, G. (2006) Implementation and performance of frequency-dependent GW method within PAW framework. *Physical Review B*, **74**, 035101-1-13.
- [27] Blaha, P., Schwarz, K., Madsen, G. K. H., Kvasnicka, D. & Luitz, J. (2001) Wien2k. An augmented plane wave + local orbitals program for calculating crystal properties, ISBN 3-9501031-1-2.
- [28] Kresse, G. & Furthmüller, J. (1996) Efficient iterative schemes for *ab initio* total-energy calculations using a plane-wave basis set. *Physical Review B*, **54**, 11169–11186.
- [29] Kresse, G. & Joubert, D. (1999) From ultrasoft pseudopotentials to the projector augmented-wave method. *Physical Review B*, **59**, 1758–1775.
- [30] Bechstedt, F. & Del Sole, R. (1998) Analytical treatment of band-gap underestimates in the local-density approximation. *Physical Review B*, **38**, 7710–7716.
- [31] Harrison, W. A. (1980) *Electronic Structure and the Properties of Solids*. Freeman, San Francisco.
- [32] Persson, C., Ferreira da Silva, A., Ahuja, R. & Johansson, B. (2001) Effective electronic masses in wurtzite and zinc-blende GaN and AlN. *Journal of Crystal Growth*, **231**, 397–406.
- [33] Persson, C., Platzer-Björkman, C., Malmström, J., Törndahl, T. & Edoff, M. (2006) Strong valence-band offset bowing of  $\text{ZnO}_{1-x}\text{S}_x$  enhances *p*-type nitrogen doping of ZnO-like alloys. *Physical Review Letters*, **97**, 146403-1-4.
- [34] Koster, G. F., Dimmock, J. O., Wheeler, R. G. & Statz, H. (1963) *Properties of the Thirty-Two Point Groups*. MIT Press, Cambridge MA.
- [35] Hall, S. R., Szymanski, J. T. & Stewart, J. M. (1978) Kesterite,  $\text{Cu}_2(\text{Zn,Fe})\text{SnS}_4$ , and stannite,  $\text{Cu}_2(\text{Fe,Zn})\text{SnS}_4$ , structurally similar but distinct minerals. *Canadian Mineralogist*, **16**, 131–137.

- [36] Schorr, S., Hoebler, H. -J. & Tovar, M. (2007) A neutron diffraction study of the stannite-kersterite solid solution series. *European Journal of Mineralogy*, **19**, 65–73.
- [37] Hahn, H. & Schulze, H. (1965) Quaternary germanium and tin chalcogenides. *Naturwissenschaften*, **52**, 426.
- [38] Babu, G. S., Kumar, Y. B. K., Bhaskar, P. U. & Raja, V. S. (2008) Effect of post-deposition annealing on the growth of  $\text{Cu}_2\text{ZnSnS}_4$  thin films for a solar cell absorber layer. *Semiconductor Science and Technology*, **23**, 085023-1-12.
- [39] Olekseyuk, I. D., Gulay, L. D., Dydychak, I. V., Piskach, L. V., Parasyuk, O. V. & Marchuk, O. V. (2002) Single crystal preparation and crystal structure of the  $\text{Cu}_2\text{Zn}/\text{Cd,Hg}/\text{SnSe}_4$  compounds. *Journal of Alloys and Compounds*, **340**, 141–145.
- [40] Katagiri, H., Saitoh, K., Washio, T., Shinohara, H., Kurumadani, T. & Miyajima, S. (2001) Development of thin film solar cell based on  $\text{Cu}_2\text{ZnSnS}_4$  thin films. *Solar Energy Materials and Solar Cells*, **65**, 141–148.
- [41] Seol, J. -S., Lee, S. -Y., Lee, J. -C., Nam, H. -D. & Kim, K. -H. (2003) Electrical and optical properties of  $\text{Cu}_2\text{ZnSnS}_4$  thin films prepared by rf magnetron sputtering process. *Solar Energy Materials and Solar Cells*, **75**, 155–162.
- [42] Nitsche, R., Sargent, D. F. & Wild, P. (1967) Crystal growth of quaternary  $1_{246}_4$  chalcogenides by iodine vapor transport. *Journal of Crystal Growth*, **1**, 52–53.
- [43] Matsushita, H., Maeda, T., Katsui, A. & Takizawa, T. (2000) Thermal analysis and synthesis from the melts of Cu-based quaternary compounds  $\text{Cu-III-IV-VI}_4$  and  $\text{Cu}_2\text{-II-IV-VI}_4$  (II=Zn, Cd; III=Ga, In; IV=Ge, Sn; VI=Se). *Journal of Crystal Growth*, **208**, 416–422.
- [44] Tanaka, T., Nagatomo, T., Kawasaki, D., Nishio, M., Guo, Q., Wakahara, A., Yoshida, A. & Ogawa, H. (2005) Preparation of  $\text{Cu}_2\text{ZnSnS}_4$  thin films by hybrid sputtering. *Journal of Physics and Chemistry of Solids*, **66**, 1978–1981.
- [45] Schorr, S. (2007) Structural aspects of adamantine like multinary chalcogenides. *Thin Solid Films*, **515**, 5985–5991.
- [46] Persson, C. & Zunger, A. (2005) A compositionally-induced valence-band offset at the grain boundary of polycrystalline chalcopyrites creates a hole barrier. *Applied Physics Letters*, **87**, 211904-1-3.
- [47] Madelung, O. (ed) (1996) *Semiconductor: Basic Data*, 2nd Edition, Springer, Berlin.
- [48] Persson, C. (2008) Anisotropic hole-mass tensor of  $\text{CuIn}_{1-x}\text{Ga}_x(\text{Se,S})_2$ : presence of free carriers narrows the energy gap. *Applied Physics Letters*, **93**, 072106-1-3.
- [49] Ito, K. & Nakazawa, T. (1988) Electrical and optical properties of stannite-type quaternary semiconductor thin films. *Japanese Journal of Applied Physics*, **27**, 2094–2097.
- [50] Nakayama, N. & Ito, K. (1996) Sprayed films of stannite  $\text{Cu}_2\text{ZnSnS}_4$ . *Applied Surface Science*, **92**, 171–175.
- [51] Kamoun, N., Bouzouita, H. & Rezig, B. (2007) Fabrication and characterization of  $\text{Cu}_2\text{ZnSnS}_4$  thin films deposited by spray pyrolysis technique. *Thin Solid Films*, **515**, 5949–5952.
- [52] Gao, F., Yamazoe, S., Maeda, T., Nakanishi, K. & Wada, T. (2012) Structural and optical properties of In-free  $\text{Cu}_2\text{ZnSn}(\text{S,Se})_4$  solar cell materials. *Japanese Journal of Applied Physics*, **51**, 10NC29-1-5.
- [53] Tanaka, K., Fukui, Y., Moritake, N. & Uchiki, H. (2011) Chemical composition dependence of morphological and optical properties of  $\text{Cu}_2\text{ZnSnS}_4$  thin films deposited by sol-gel sulfurization and  $\text{Cu}_2\text{ZnSnS}_4$  thin film solar cell efficiency. *Solar Energy Materials and Solar Cells*, **95**, 838–842.
- [54] Patel, M., Mukhopadhyay, I. & Ray, A. (2012) Structural, optical and electrical properties of spray-deposited CZTS thin films under a non-equilibrium growth condition. *Journal of Physics D: Applied Physics*, **45**, 445103-1-10.
- [55] Ahn, S., Jung, S.H., Gwak, J.Y., Cho, A., Shin, K., Yoon, K., Park, D.Y., Cheong, H. & Yun, J.H. (2010) Determination of band gap energy ( $E_g$ ) of  $\text{Cu}_2\text{ZnSnSe}_4$  thin films: On the discrepancies of reported band gap values. *Applied Physics Letters*, **97**, 021905-1-3.
- [56] Haight, R., Barkhouse, A., Gunawan, O., Shin, B., Copel, M., Hopstaken, M. & Mitzi, D. B. (2011) Band alignment at the  $\text{Cu}_2\text{ZnSn}(\text{S}_x\text{Se}_{1-x})_4/\text{CdS}$  interface. *Applied Physics Letters*, **98**, 253502-1-3.

- [57] He, J., Sun, L., Chen, S., Chen, Y., Yang, P. & Chu, J. (2012) Composition dependence of structure and optical properties of  $\text{Cu}_2\text{ZnSn}(\text{S,Se})_4$  solid solutions: An experimental study. *Journal of Alloys and Compounds*, **511**, 129–132.
- [58] Repins, I., Beall, C., Vora, N., DeHart, C., Kuciauskas, D., Dipbo, P., To, B., Mann, J., Hsu, W.C., Goodrich, A. & Noufi, R. (2012) Co-evaporated  $\text{Cu}_2\text{ZnSnSe}_4$  films and devices. *Solar Energy Materials and Solar Cells*, **101**, 154–159.
- [59] Jimbo, K., Kimura, R., Kamimura, T., Yamada, S., Maw, W. S., Araki, H., Oishi, K. & Katagiri, H. (2007)  $\text{Cu}_2\text{ZnSnS}_4$ -type thin film solar cells using abundant materials. *Thin Solid Films*, **515**, 5997–5999.
- [60] Ennaoui, A., Lux-Steiner, M., Weber, A., Abou-Ras, D., Kötschau, I., Schock, H.-W., Schurr, R., Hölzing, A., Jost, S., Hock, R., Voß, T., Schulze, J. & Kirbs, A. (2009)  $\text{Cu}_2\text{ZnSnS}_4$  thin film solar cells from electroplated precursors: Novel low-cost perspective. *Thin Solid Films*, **517**, 2511–2514.
- [61] Luttinger, J.M. & Kohn, W. (1955) Motion of electrons and holes in perturbed periodic fields. *Physical Review*, **97**, 869–883.
- [62] Dresselhaus, G., Kip, A.F. & Kittel, C. (1955) Cyclotron resonance of electrons and holes in silicon and germanium crystals. *Physical Review*, **98**, 368–384 (1955).
- [63] Kane, E.O. (1956) Energy band structure in p-type germanium and silicon. *Journal of Physics and Chemistry of Solids*, **1**, 82–99.
- [64] Persson, C. & Mirbt, S. (2006) Improved electronic structure and optical properties of sp-hybridized semiconductors using LDA+U. *Brazilian Journal of Physics*, **36**, 447–450.
- [65] Devreese, J. T. (ed.) (1972) *Polarons in Ionic Crystals and Polar Semiconductors*. North-Holland, Amsterdam.
- [66] Persson, C., Lindefelt, U. & Sernelius, B. E. (1999) Doping-induced effects on the band structure in n-type 3C, 2H, 4H, 6HSiC, and Si. *Physical Review B*, **60**, 16479–16493.
- [67] Persson, C., Dong, C. L., Vayssieres, L., Augustsson, A., Schmitt, T., Mattesini, M., Ahuja, R., Nordgren, J., Chang, C. L., Ferreira da Silva, A. & Guo, J.-H. (2006) X-ray absorption and emission spectroscopy of ZnO nanoparticles and highly oriented ZnO microrod arrays. *Microelectronics Journal*, **37**, 686–689.
- [68] Gajdoš, M., Hummer, K., Kresse, G., Furthmüller, J. & Bechstedt, F. (2006) Linear optical properties in the PAW methodology. *Physical Review B*, **73**, 045112-1-9.
- [69] Choi, S. G., Zhao, H.Y., Persson, C., Perkins, C. L., Donohue, A.L., To, B., Norman, A. G., Li, J. & Repins, I. L. (2012) Dielectric function spectra and critical-point energies of  $\text{Cu}_2\text{ZnSnSe}_4$  from 0.5 to 9.0 eV. *Journal of Applied Physics*, **111**, 033506-1-6.



# 5

## Kesterites: Equilibria and Secondary Phase Identification

*Dominik M. Berg<sup>1</sup> and Phillip J. Dale<sup>2</sup>*

*<sup>1</sup>Institute of Energy Conversion, University of Delaware, 451 Wyoming Rd,  
Newark, DE, 19716, USA*

*<sup>2</sup>Laboratory for Energy Materials, Université du Luxembourg, 41, rue du Brill,  
L-4422, Belvaux, Luxembourg*

### 5.1 Introduction

Efficient thin-film polycrystalline CZTSe-based photovoltaic devices require a single-phase kesterite absorber. Secondary phases such as  $\text{Cu}_2\text{SnSe}_3$  can reduce cell open-circuit voltage [1], while ZnSe can reduce photocurrent [2, 3]. The challenge then is to grow kesterite material free of detrimental secondary phases; however, this is a problem for two reasons: (1) growth of single-phase CZTSSe semiconductor is difficult; and (2) determination of phase purity using only standard laboratory tools is also difficult. These two important themes are explored in the following section.

Single-phase kesterite material can be difficult to obtain due to relatively low thermal stability of the compound under typical synthesis conditions [4] coupled with a relatively narrow single-phase region [5]. The key to understanding the synthesis and thermal stability of the kesterite lies with the governing chemical equilibria, the steady-state conditions of processing, and the mass-transfer mechanisms. Once the equilibrium theory of chemical reactions is appreciated, solutions to the apparent problem of kesterite thermal stability are immediately forthcoming. In Section 5.2, the equilibrium behavior of the kesterite during annealing is demonstrated, and the underlying chemical reasons are examined. A review of

chemical equilibrium is given first. The consequences for the synthesis of the pure semiconductor are explained, and a new simple synthesis route for the kesterite is illustrated.

Once a thin film having the approximate desired chemical composition is synthesized, the next step is to determine the phases present. The relatively narrow single-phase region of kesterite means that secondary phases should be expected [5]. CZTSSe consists of three metals and up to two chalcogens, so the number of possible secondary phases is large. A further complication is that several of the phases, including CZTSSe itself, have a variety of polymorphs. In Section 5.3 the identification of secondary phases are discussed in terms of common laboratory equipment as well as synchrotron-based methods. To illustrate the difficulty in identifying secondary phases a quantitative case study of the ability of X-ray diffraction and single-wavelength Raman scattering to discriminate ZnS and  $\text{Cu}_2\text{SnS}_3$  from a  $\text{Cu}_2\text{ZnSnS}_4$  phase is presented. It will be shown that the discrimination of small amounts of secondary phases is extremely difficult using standard laboratory tools. A discussion on the current best practice for identifying secondary phases is initiated. Finally, a collection of methods to remove secondary phases through wet chemical etchants as available in literature is provided and compared.

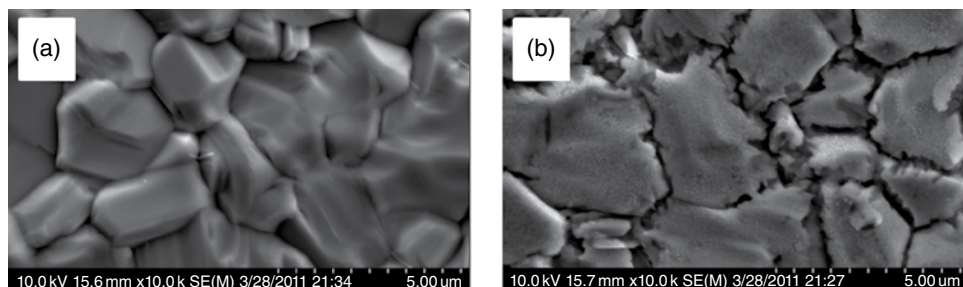
These two seemingly disparate areas of CZTSSe equilibria reactions and secondary phase detection have been investigated using the flexible synthesis tools of electrodeposition and annealing (EDA). In this chapter we discuss the kesterite sulfide system in particular, but exactly the same considerations apply for the selenide and mixed chalcogen systems. Importantly, the findings shown here are not limited to EDA but are material properties independent of the fabrication route, and therefore are relevant all research in the field of kesterite synthesis.

## 5.2 Chemistry of the Kesterite Reaction

This section examines the chemistry of the kesterite formation and decomposition reactions using the theory of chemical equilibria. It begins with a brief overview of solid–gas equilibrium reactions. Evidence will then be given to show that equilibrium theory applies to the kesterite reaction, and some reasons will be discussed for its relative lower thermal stability compared to the related semiconductor  $\text{Cu}(\text{In,Ga})\text{Se}_2$ . Finally, the consequences of the *kesterite equilibrium* are discussed in terms of synthetic strategies to maximize the kesterite phase.

### 5.2.1 Chemical Equilibrium

Thin-film semiconductor absorber layers are produced typically at elevated temperatures such as 500–600°C. The purpose of elevated-temperature synthesis is to supply sufficient energy for solid-state chemical reactions, grow grains, remove defects to grain boundaries, and insert volatile species from the gas phase into the solid phase. Empirically it is found for CZTSSe and for  $\text{Cu}(\text{In,Ga})\text{Se}_2$  that volatile chalcogen species should be supplied in the gas phase during any high-temperature processing step to produce high-quality films, defined by overall chemical homogeneity, lateral uniformity, and dense grain packing. To visibly illustrate the detrimental effect of not supplying the relevant chalcogen (selenium in this case) even on a seemingly “stable” semiconductor such as  $\text{Cu}(\text{In,Ga})\text{Se}_2$ , the following



**Figure 5.1** Scanning electron micrographs of co-evaporated  $\text{Cu(In,Ga)Se}_2$  (a) before and (b) after thermal treatment at  $550^\circ\text{C}$  under vacuum for 8 hours. Reproduced with permission from [6]. Copyright © 2012, John Wiley and Sons Ltd

experiment was conducted. A co-evaporated  $\text{Cu(In,Ga)Se}_2$  absorber layer, capable of forming a 17% efficient device, was post-annealed for eight hours at  $550^\circ\text{C}$  in vacuum; micrographs of the layer before and after annealing are shown in Figure 5.1.

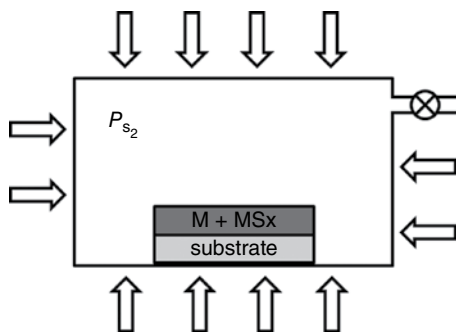
The micrographs reveal more space between the grains after annealing, with development of jagged grain boundaries. Analysis of the composition of both films shows that the vacuum-annealed film has 8% less selenium than before annealing. To explain these observations and to lay the foundations for understanding the relative thermal stability of the CZTSSe phases we consider solid–gas equilibrium thermodynamics. For a more general and deeper look at chemical equilibria, the reader is referred to related works [7, 8].

To give a concrete example of the reaction scenario we consider a thin film of a metal binary chalcogenide, such as  $\text{ZnS}$ , located on top of an inert substrate inside an annealing chamber which is uniformly heated and contains a fixed partial pressure of sulfur,  $P_{\text{S}_2}$ . (Sulfur, like selenium, has many polymeric allotropes and in the gas phase there is a complex compositional relationship between them depending on the temperature and pressure. Here it is only considered that sulfur exists as  $\text{S}_2$ , which is a reasonable assumption at low pressures and high temperatures.) The idealized annealing chamber is completely sealed except for a valve which can be opened or closed to allow gas exchange as shown in Figure 5.2.

The metal sulfide (MS) is formed by the reaction of the sulfur vapor ( $\text{S}_2$ ) with the metal film (M):



The total conversion of the metal to the metal sulfide is not in fact guaranteed and the extent of the reaction (how far the reaction proceeds in converting reactants into products) depends primarily on which metal is being reacted, on the temperature, and on the partial pressure of sulfur gas in the chamber. The reaction is also reversible, meaning that some or even the entire product can break down into the reactants depending on the conditions in the chamber. Such a reaction which can proceed forwards and backwards is reversible, and is known as an equilibrium reaction. The equilibrium is indicated by the double arrow in the reaction equation. When the reaction is finished, the concentrations of the products and the reactants are constant with time, and their ratio is defined as the equilibrium constant  $K$ . Thus at equilibrium there will always be some metal *and* metal chalcogenide species



**Figure 5.2** Idealized annealing apparatus, consisting of a sealed chamber allowing no chemical species to leave or enter except via the valve. Inside the chamber, a thin film consisting of metal and metal sulfide sits on an inert substrate. The arrows indicate a uniform heat field surrounding the chamber and  $P_{S_2}$  indicates a certain partial pressure of sulfur

co-existing together in the same film, as well as a certain vapor pressure of chalcogen in the atmosphere. The relative quantities of each phase depend on the magnitude of the equilibrium constant. Equilibrium can only be achieved if no chemical species are allowed to be added or removed; for a true equilibrium the reaction must be sealed away from all influences of the outside world. If the reaction favors the product formation then  $K > 1$ , and if it favors the reactant side then  $K < 1$ . For known chemical species the magnitude of  $K$  can be calculated from the following relationship:

$$K = \exp(-\Delta G_r / RT) \quad (5.2)$$

where  $\Delta G_r$  is the difference in Gibbs free energy between the products and reactants of the reaction,  $T$  is the temperature, and  $R$  is the molar gas constant. The  $\Delta G_r$  of a particular reaction reflects the favorability of this reaction. If  $\Delta G_r$  is negative then some chemical energy is transformed into free available energy, while if  $\Delta G_r$  is positive then extra energy is required to drive the reaction. The Gibbs free energy itself consists of an enthalpy term and an entropy term. If the number of chemical bonds remains constant, the enthalpy term mostly reflects any difference in bond strengths between the products and reactants while the entropy term reflects the difference in the number of ways that the atoms can be arranged in their respective crystal structures.

Considering the metal-sulfur reaction again, to obtain the metal chalcogenide, that is,  $K > 1$ ,  $\Delta G_r$  for the reaction must be negative. The equilibrium lies strongly on the product side if  $\Delta G_r$  is large and negative and  $T$  is small. In this case the amount of remaining metal in the film will be low, and the amount of metal chalcogenide will be high. Also for large negative  $\Delta G_r$  the vapor pressure of sulfur required to drive the reaction to the product side will be low. In general,  $\Delta G_r$  values tend to become more positive as the temperature is raised and  $K$  is therefore reduced. Heating the system therefore moves the equilibrium to the left-hand side, that is, to the reactant side. This is an example of perturbing the overall position of the reaction. The system may also be perturbed by the addition of extra sulfur gas through the valve of the annealing apparatus, for example (see Fig. 5.2). The addition of extra chalcogen momentarily changes the ratio of products to reactants. The system will



try to restore the thermodynamic value of  $K$ . In this case, the added extra gas will react with some proportion of the remaining metal, thus reducing the metal and gas concentrations. This is an example of the Le Chatelier principle [8]. Conversely, if we open the valve for a short time some of the sulfur gas will escape, reducing the partial pressure of sulfur in the annealing chamber. To compensate for this, some of the metal sulfide will decompose to form metal and sulfur to maintain a constant equilibrium position.

Returning to the example of high-temperature processing of  $\text{Cu(In,Ga)Se}_2$  under vacuum depicted in Figure 5.1, this situation is comparable to that of having left the valve open and of deliberately evacuating all the chalcogen gas. Selenium vapor is constantly being extracted by the vacuum pump and the metal chalcogenide, or in this case the multinary metal chalcogenide ( $\text{Cu(In,Ga)Se}_2$ ), is constantly releasing selenium in an effort to maintain the equilibrium vapor pressure of selenium. This then explains why the thermally treated sample had 8% less selenium than the starting material. The experiment thus illustrates that even  $\text{Cu(In,Ga)Se}_2$  can be made to decompose if its equilibrium is perturbed. The following general question then arises for the synthesis of solid compounds which are in equilibrium with gas phase species: how large is this effect under certain annealing conditions? This addresses the question of *stability*.

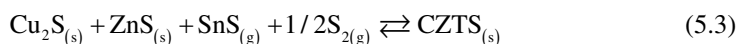
The word “stable” is a relative term. It means that the compound exists and does not decompose under the used experimental conditions. If the experimental conditions are changed, an increase in temperature for example, a compound may become “unstable” or break down into constituent species. As we have seen above, the stability of a material depends on the equilibrium constant  $K$ , which in turn depends on  $\Delta G_R$  and temperature. If  $\Delta G_R$  is large and negative then only a low partial pressure of chalcogen in the annealing chamber is required to maintain  $K$ , and therefore not much metal chalcogenide needs to decompose to release the chalcogen in the event that chalcogen is being removed from the chamber. Comparatively, a binary chalcogenide with a large negative  $\Delta G_R$  will be less prone to decomposition than another with a small value of  $\Delta G_R$  at higher temperatures and/or lower partial pressures of chalcogen. One practical way to avoid the decomposition of a metal chalcogen during annealing is then to supply excess volatile species.

So far the discussion has centered on a binary compound, but the kesterite is a multinary compound. If a multinary compound  $\text{ABS}_2$  exists under certain conditions, it must by definition be more stable than the two binary phases which it could be made out of, for example  $\text{A}_2\text{S}$  and  $\text{B}_2\text{S}_3$ . Another way of saying this is that the free energy of reaction for the ternary compound from the two binary compounds is negative. The consequence of this lower free energy is that when the ternary compound is annealed at elevated temperatures a lower partial pressure of chalcogen is required to stop its decomposition than would be necessary for the binary species. As will be seen, the situation can become more complicated if the multinary compound decomposes to additional volatile phases.

Having covered the preliminaries, we have seen that solid–gas reactions are of an equilibrium nature; in order to maximize the product or to stop the product from decomposing, a high partial pressure of the reactive gas should be maintained. The stability of the material with respect to gas species loss from its structure at a fixed temperature depends how far the equilibrium reaction is to the product side or, in other words, it depends on the magnitude of the Gibbs free energy of reaction. Finally, a multinary compound should be more stable with respect to the constituent binaries. In the next section the relative stability of the kesterite system is explored with reference to the theoretical considerations made here.

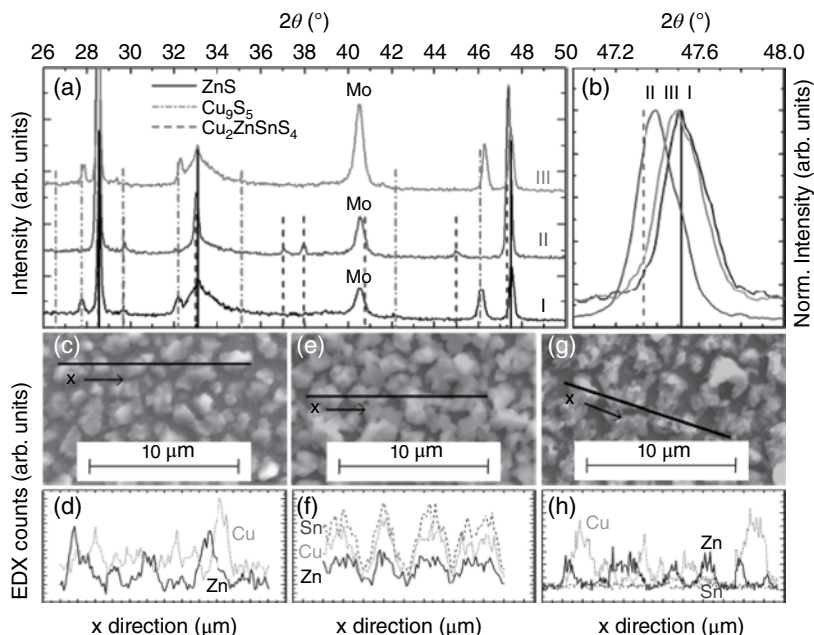
### 5.2.2 Proof of the Kesterite Chemical Equilibrium

In this section proof of the chemical equilibrium of the kesterite formation reaction is given, and it will be shown that the kesterite is in equilibrium with not one but two gas phase species. Early experimental work on the annealing of CZTS precursor layers indicated that the annealed films contained less tin than the precursor [9]. Weber *et al.* observed that films  $\text{Cu}_2\text{SnS}_3$  and  $\text{SnS}_2$  also lost tin after a thermal annealing step, and assigned the tin loss in all cases to the loss of volatile  $\text{SnS}$  [4]. Coincidentally, in our laboratory we observed that heating a zinc-rich copper alloy in the presence of sulfur (without any intentional introduction of tin) resulted in a majority  $\text{ZnS}$  phase with a minority kesterite phase! As kesterite can only be formed when tin is present, a volatile tin species, namely  $\text{SnS}$ , must have been present in our annealing chamber from previously annealing CZTS layers. Based on this evidence the following equilibrium reaction was proposed [10]:



To prove the hypothesis we prepared a thin film containing the solid phases of the left-hand side of the reaction (step I) and then provided the gas phases in large excess (step II) in a nearly closed environment to push the reaction as far to the right-hand side as possible in accordance with Le Chatelier's principle. After confirming that the film now only contained the product on the right-hand side of the reaction, the reversibility of the reaction was confirmed by providing conditions to return the reaction back to the starting products on the left-hand side (step III). The experimental evidence takes the form of energy-dispersive x-ray spectroscopy (EDX) line scans, scanning electron micrographs, and X-ray diffraction data (Fig. 5.3). All heating steps were carried out at 550°C.

Cu/Zn stacks were electrodeposited onto a molybdenum substrate in the molar proportion of 2:1 and annealed with sulfur to form a film containing a mixture of  $\text{Cu}_{2-x}\text{S}$  and  $\text{ZnS}$  as evidenced by the x-ray diffractogram in Figure 5.3(a), pattern I. EDX line scans in Figure 5.3(c) and (d) show that the chemical signals of Cu and Zn are not correlated, meaning that there is no compound formation between copper and zinc as expected. At this stage the first two components of the left-hand side of the reaction are prepared. The mixed  $\text{Cu}_{2-x}\text{S}$ - $\text{ZnS}$  sample was then annealed in an almost-sealed environment in the presence of excess sulfur and  $\text{SnS}$  gas, thus pushing Reaction (5.3) to the right-hand side. In this case the X-ray diffractogram of the resulting sample (see pattern II in Fig. 5.3(a)) shows the presence of the unique kesterite reflexes, indicating that kesterite had formed, and the absence of  $\text{Cu}_{2-x}\text{S}$  reflexes. Furthermore, a closer inspection of the diffractogram at 47–48 degrees (Fig. 5.3(b)) shows a shift from the cubic  $\text{ZnS}$  position to the kesterite position. An EDX line scan (Fig. 5.3(e) and (f)) shows that all the metal atoms in the CZTS are correlated with one another, demonstrating that there is no phase segregation. It is therefore shown that CZTS had been made, and that Reaction (5.3) is far to the right-hand side within the detection limits of the techniques used (see Section 5.3 on secondary phase identification). To prove that the reaction is reversible, the kesterite sample was heated in the absence of the gas phase species under vacuum for six hours, and as the diffractogram (pattern III) and chemical line scans show in Figure 5.3(a), (b), (g), (h), the film reverts back to  $\text{Cu}_{2-x}\text{S}$  and  $\text{ZnS}$  with a complete loss of tin.



**Figure 5.3** Experimental data for the three steps taken to show the kesterite equilibrium where (I) is the precursor consisting of  $\text{Cu}_{2-x}\text{S}$  and  $\text{ZnS}$ , (II) is the annealed precursor film consisting of  $\text{Cu}_2\text{ZnSnS}_4$ , and (III) is the vacuum-annealed  $\text{Cu}_2\text{ZnSnS}_4$  showing extreme tin loss. (a) X-ray diffractograms of the thin films at stages I–III; (b) a close-up of the diffractograms at  $2\theta$  equal to 47–48°; (c, e, g) SEM images of steps I–III; and (d, f, h) EDX line scans of stages I–III

The above experiment shows that, under typical thin-film annealing conditions, the position of the CZTS reaction can be changed from the left- to the right-hand side by controlling the partial pressures of both gas phase species. Under the same harsh annealing conditions of 550°C and vacuum,  $\text{Cu(In,Ga)Se}_2$  lost 8% selenium while CZTS lost all its tin and was decomposed to  $\text{Cu}_{2-x}\text{S}$  and  $\text{ZnS}$ . This experiment demonstrates the relatively low stability of CZTS as compared to  $\text{Cu(In,Ga)Se}_2$  for the same annealing conditions.

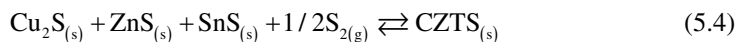
In summary, the importance of controlling the partial pressure of the chalcogen and the tin chalcogenide during thermal processing of kesterite absorber layers is demonstrated. In order to maximize the amount of kesterite produced and to avoid tin loss and thus secondary phase formation, excess tin chalcogenide and chalcogen should be supplied. The underlying reasons for the low stability of the kesterite are discussed in the next section.

### 5.2.3 Kesterite Equilibrium

The previous section showed that CZTS could be formed when S and SnS were present in the gas phase along with  $\text{Cu}_{2-x}\text{S}$  and  $\text{ZnS}$  solid phases. However, in the absence of S and SnS in the gas phase, the  $\text{Cu}_{2-x}\text{ZnSnS}_4$  decomposed to form  $\text{Cu}_{2-x}\text{S}$  and  $\text{ZnS}$ . This showed that CZTS is in fact in equilibrium with two gas phase species. The details of the kesterite equilibria are explored further below. It is instructive to understand why two gas phase species

are involved. The following discussion is based on a kinetic study of Scragg *et al.* [11] and a thermodynamic analysis by Scragg, Dale *et al.* [6]

Chemical equilibria are in fact dynamical at the atomic and molecular level; in other words, at equilibrium both forward and backward reactions are still occurring but at the same rate, so that there are no net changes in the concentration of products or reactants. The kesterite equilibrium reaction (Reaction (5.3)) can be broken down into two steps, first:



and second:



Due to the dynamic equilibrium small amounts of CZTS are always forming and decomposing meaning that, at any given time, there will always be a small amount of binary sulfides and sulfur, given by the equilibrium constant  $K$ . As discussed previously, sulfur is a volatile gas at typical annealing temperatures and therefore must be supplied in excess at all times to keep the reaction to the product side. Copper and zinc sulfides are not volatile species at these temperatures, but tin monosulfide is [12]. Due to the chemical equilibrium small amounts exist at any given time, and these small amounts have the opportunity to evaporate. It is for this reason that SnS should also be present in the atmosphere, in order to saturate it, and why the kesterite decomposition is irreversible in the absence of SnS. Scragg *et al.* [11] showed in a detailed kinetic analysis of the kesterite equilibria reaction that S and SnS are both required, and in fact that there is a critical product of S and SnS concentrations which is necessary to avoid the decomposition of CZTS.

One question arising from this analysis is why is Sn(II)S present at all on the reactant side, when it could also be Sn(IV)S<sub>2</sub>? This question comes about as on the product side for CZTS, the tin has a +4 oxidation state [13] while on the reactant side, the tin has a +2 oxidation state. To answer this question we have to look at the ease of reduction (gain of electrons) of the metal species. Consider a perfect CZTS lattice in which, for whatever reason, some sulfur is removed. The sulfur in the lattice has the oxidation state (-II) but will leave in the gas phase with oxidation state (0). Hence each sulfur atom must leave two electrons behind as it leaves the lattice. As more sulfur vacancies are created, the lattice becomes anion deficient. As this process proceeds beyond the stable composition, that is, if the number of anion deficiencies exceeds the stable vacancy threshold, the CZTS lattice will decompose into other more stable compounds. Due to the condition of mass balance, these more stable compounds must contain the same amount of metal cations and sulfur anions as were in the CZTS lattice before it decomposed. In CZTS the metals have oxidation states Cu(I), Zn(II), and Sn(IV) [13]. For the metals to keep these oxidation states when they form the breakdown compounds, they must be associated with the correct number of sulfur atoms which have oxidation state (-II), that is, Cu<sub>2</sub>S, ZnS, and SnS<sub>2</sub>. However, mass balance must be respected, so the reduced number of sulfur atoms must be accounted for and also the extra electrons given up by the sulfur which had evaporated. Most likely one or more of the metals must change oxidation state to balance the remaining number of anions, such as that given by Reaction (5.6):



(Note that this equation is simplified; Sn(IV) actually passes via an intermediate reaction to Sn(II) [12].) Lowering oxidation state means that less sulfur is required to form a compound with the metal. For the metals in question it is energetically easiest for Sn to lower its oxidation state than either of Cu or Zn. When sulfur is lost from the CZTS lattice, the structure therefore decomposes to  $\text{Cu}_2(\text{I})\text{S}$ ,  $\text{Zn}(\text{II})\text{S}$ , and  $\text{Sn}(\text{II})\text{S}$ . In this case the Sn(II) S requires only one sulfur atom per metal atom instead of the two sulfur atoms per metal atom when Sn had the +4 oxidation state. SnS can also then be lost to the gas phase (via Reaction (5.5)) if there is an insufficient partial pressure of SnS in the annealing atmosphere. Interestingly, theoretical calculations show that it is energetically easier to create chalcogen vacancies in CZTS than in  $\text{Cu}(\text{In,Ga})\text{Se}_2$  [14–17] for the same annealing conditions. These calculations agree with the chemical explanation for the lower observed thermal stability of CZTS [6].

In summary, it was shown that CZTS can only be formed if sufficient partial pressures of S and SnS are present in the gas phase due to the relative volatility of both species. Presence of only one or the other is insufficient to stabilize CZTS. These conclusions are also valid for the kesterite selenide system.

### 5.2.4 Consequences of the Kesterite Equilibrium

At elevated temperatures, CZTS bulk is in equilibrium with a decomposing surface where two phases exist, namely sulfur and tin sulfide, in their own solid–vapor equilibrium as was demonstrated in the preceding sections. Due to the volatility of these two species at elevated temperatures, care in equipment and experimental procedures must be taken to avoid their significant loss.

For the synthesis of thin films with the maximum content of CZTS, one need only follow the principles laid out by Le Chatelier [8] to minimize or completely stop the loss of tin and sulfur during any high-temperature annealing process. This means that sulfur and tin sulfide must be provided in excess in the gas phase to keep the reaction over to the CZTS product side. Below several examples are given where thin films of CZTS(e) have been successfully made and completed into working photovoltaic devices following these principles.

Synthesis methods can be broadly split into: (1) equilibrium, that is, working in a sealed chamber with sufficient partial pressures of sulfur and tin sulfide; and (2) non-equilibrium conditions, that is, having a sink for the volatile species such as a cold wall or vacuum pump.

1. Equilibrium conditions are easily obtained in a sealed quartz tube. An example of this is given in the literature, where metallic precursors were annealed with elemental sulfur [18]. During annealing the sulfur reacts with the precursors to form metallic binary sulfides and then subsequently the kesterite. SnS is released from the thin film until the saturation partial pressure of SnS in the atmosphere is achieved. The amount of SnS loss from the films is then simply proportional to the volume of the tube. Normally the SnS loss to the atmosphere reduces the amount of tin in the film by a negligible amount due to the limited volume of the tube.

2. Non-equilibrium conditions range in severity from a leaky graphite box to a cold wall inside a vacuum chamber. To avoid substantial tin loss, two approaches may be taken or even combined. The first approach (2a) is thermodynamic and the second approach (2b) is kinetic.
  - 2(a) The thermodynamic approach is simply to supply or compensate for the loss of volatile species. Scragg *et al.* demonstrated, as discussed earlier, that both S and SnS are required, and that it is the product of their concentrations which is critical. Examples in the literature of this thermodynamic approach include adding sulfur and tin sulfide to a leaky graphite box which enabled devices of 5.4% efficiency compared to 0% percent in the absence of tin sulfide [10]. For comparison using co-evaporation, many times more flux of Se is required for CZTSe than for Cu(In,Ga)Se<sub>2</sub> as well as the use of excess tin [19]. Extra SnS(e) may also be supplied in excess either in the bulk of the film [20] or by a thin film on the surface [21].
  - 2(b) Kinetically, SnS and S loss may be limited by providing a diffusion-limiting step such as by annealing in a high background pressure of inert gas [4, 22]. The high background pressure slows the movement of the volatile species which reduces the rate of loss, and increases the partial pressure of volatile species above the thin film. Another kinetic approach not yet demonstrated in the literature would be to anneal for short times and to etch off any resulting surface secondary phases, which is the subject of Section 5.3.

Finally, a very simple low-cost approach can be taken for the formation of the CZTS semiconductor simply due to the fact that there are two volatile gas phase species. As already outlined in Section 5.2.2 a simple Cu-Zn alloy can be annealed in the presence of sulfur and tin sulfide to form CZTS. Preliminary device power conversion efficiencies of 2% have been achieved with this approach in our lab [22].

A last consequence of the thermal instability of the kesterite is its likely reaction with the back metal contact, usually molybdenum. Theoretical calculations predicted that Cu<sub>2</sub>ZnSnS<sub>4</sub> reacts with Mo to form MoS<sub>2</sub> and thus the kesterite must break down into its component species [6]. The experimental proof of this reaction was found by careful microscopy studies [23, 24]. To avoid or limit this detrimental reaction at the back surface, new and more stable contacts are required.

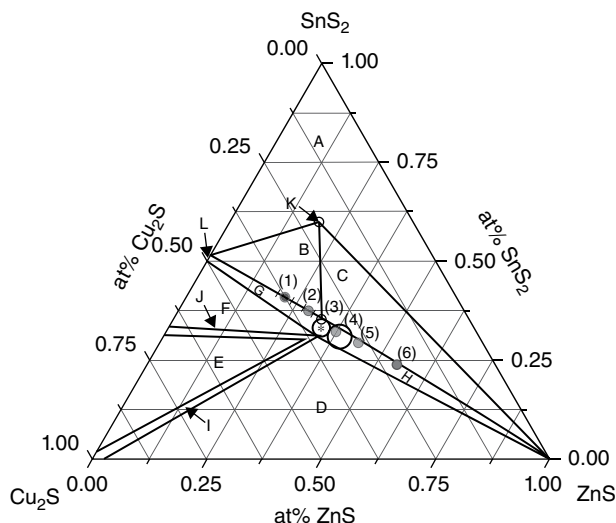
### 5.2.5 Summary

Cu<sub>2</sub>ZnSnS<sub>4</sub> is in equilibrium with its smaller binary compound building blocks. The apparent low thermal stability of Cu<sub>2</sub>ZnSnS<sub>4</sub> compared to Cu(In,Ga)Se<sub>2</sub> arises principally from the fact that it is in equilibrium with two volatile species rather than one, namely sulfur and tin sulfide. To produce the maximum amount of CZTS phase possible, it is therefore recommended to carry out any thermal treatments in the presence of sufficient partial pressures of sulfur and tin sulfide.

## 5.3 Phase Identification

### 5.3.1 Motivation for Secondary Phase Identification

The issue of secondary phase detection and identification as well as suggestions on how to remove undesired phases is the topic of this section. In the previous section, the importance of equilibria during the synthesis of Cu<sub>2</sub>ZnSn(S/Se)<sub>4</sub> (CZTSSe) was discussed. Specifically



**Figure 5.4** Pseudo-ternary phase diagram of the Cu-Zn-Sn-S system at 400°C [5]. The indicated regions contain the following phases: \*  $\text{Cu}_2\text{ZnSnS}_4$  ( $\alpha$ ); A:  $\beta + \text{SnS}_2 + \text{Cu}_2\text{SnS}_3 + \text{ZnS}$ ; B:  $\alpha + \text{Cu}_2\text{SnS}_3 + \beta$ ; C:  $\alpha + \text{ZnS} + \beta$ ; D:  $\alpha + \text{Cu}_2\text{S} + \text{ZnS}$ ; E:  $\alpha + \text{Cu}_4\text{SnS}_4 + \text{Cu}_2\text{S}$ ; F:  $\alpha + \text{Cu}_4\text{SnS}_4 + \text{Cu}_2\text{SnS}_3$ ; G:  $\alpha + \text{Cu}_2\text{SnS}_3$ ; H:  $\alpha + \text{ZnS}$ ; I:  $\alpha + \text{Cu}_2\text{S}$ ; J:  $\alpha + \text{Cu}_4\text{SnS}_4$ ; K:  $\text{Cu}_2\text{ZnSn}_3\text{S}_8$  ( $\beta$ ); L:  $\text{Cu}_2\text{SnS}_3$ . The larger circle indicates the position of the optimal compositional ratio of  $\text{Zn/Sn} = 1.2$ , and  $\text{Cu}/(\text{Zn} + \text{Sn}) = 0.9$  for high-efficiency solar cells [41]. The points (1) to (6) indicate the compositional positions of the areas of interest in the quantitative secondary phase analysis. Reprinted from [5] and [41]. With permission from Elsevier

for the formation of single-phase CZTSSe, certain thermodynamic conditions such as temperature and partial pressures of the volatile species ( $\text{S/Se}_2$  and  $\text{SnS/Se}$ ) have to be met in order to keep the equilibrium position of the formation reaction on the  $\text{Cu}_2\text{ZnSn(S/Se)}_4$  side. In Figure 5.4, the pseudo-ternary phase diagram of the CZTS system (based on the results of Olekseyuk *et al.* [5]) indicates the relatively small existence region for single-phase CZTS (a maximum 1–2 at% deviation in composition [25]) as well as the composition regions for the various possible secondary phases for typical annealing conditions at around 500–550°C. Due to this narrow single phase region in the Cu-Zn-Sn-S/Se system, the formation of such secondary phases can either originate from an initially non-optimal film composition that lies outside the single-phase region, or from a film with initially optimal composition that breaks down due to non-controlled equilibria conditions during the formation process (as previously discussed in Section 5.2). A narrow single-phase region therefore means that there is little tolerance for cation deficiencies, as opposed to the case of  $\text{CuInSe}_2$  where a Cu deficiency of up to 8% from stoichiometry is allowed [26]. Secondary phases are therefore very likely to form out of one or more excess cations. Due to the multiple constituents in the Cu-Zn-Sn-S/Se system and the possibility of multiple metal oxidation states, the formation of a large number of secondary phases (binary as well as ternary phases) is possible. The most common secondary phases in the Cu-Zn-Sn-S/Se system are also listed in Table 5.1.

Depending on their position in the film as well as on their electro-optical properties, secondary phases are considered harmful to the solar cell device performance [37]. As an

**Table 5.1** Most common secondary phases in the Cu-Zn-Sn-S/Se system

Compound	Band gap (eV)	References	Compound	Band gap (eV)	References
$\text{Cu}_2\text{ZnSnS}_4$	1.5	[25]	$\text{Cu}_2\text{ZnSnSe}_4$	1.0	[25]
$\text{Cu}_2\text{SnS}_3$	0.9	[27]	$\text{Cu}_2\text{SnSe}_3$	0.8	[28]
$\text{ZnS}$	3.7	[29]	$\text{ZnSe}$	2.7	[29]
$\text{SnS}_2$	~2.5	[30]	$\text{SnSe}_2$	1.0–1.6	[31]
$\text{SnS}$	1.0 indirect, 1.3 direct	[32,33]	$\text{SnSe}$	1.3	[34]
$\text{Cu}_2\text{S}$	1.2	[35]	$\text{Cu}_2\text{Se}$	1.2	[36]

example, high-band-gap secondary phases can possibly cause a high series resistance when situated at the back contact or can act as a barrier to the charge carriers when situated at the pn-junction, while low-band-gap materials at the pn-junction are usually responsible for a decrease in open-circuit voltage [37].

Comparing the composition of the best-performing solar cells published so far [38–40], it is interesting to note that the composition of the absorber layers are typically Zn-rich and hence lie in a region of the phase diagram (assuming its validity for thin-film synthesis) that would suggest the presence of ZnS/Se as a secondary phase (see large circle in Fig. 5.4); its presence is not discussed, however. This is an indication that, even in the best devices so far, secondary phases are present and perhaps indicates that their full potential has not yet been reached. In order to improve the device performance, it is therefore important to detect and identify the presence and the position of the secondary phases within the film. Having identified these phases, the synthesis process can be altered to avoid the secondary phases or make them easily removable. In the following we will use examples from our own data on CZTS where possible, and reference literature data for CZTSe.

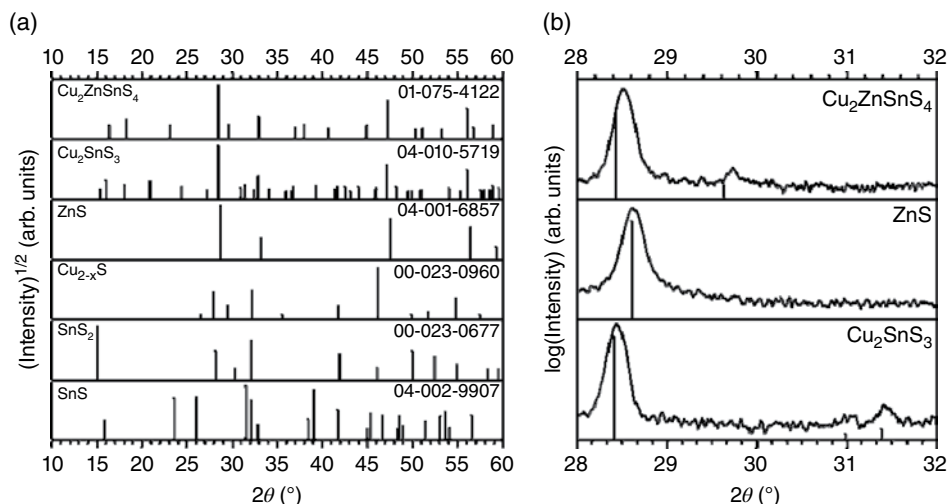
### 5.3.2 Identification of Secondary Phases

Standard laboratory techniques such as X-ray diffraction, Raman spectroscopy, and room temperature photoluminescence can *directly* identify secondary phases. Lateral or depth-resolved chemical information from electron- or wavelength dispersive X-ray spectroscopy coupled with scanning electron microscopy or transmission electron microscopy, secondary ion mass spectrometry, Auger electron spectroscopy, X-ray photoemission spectroscopy, or atom probe tomography (APT) can *indirectly* infer the presence of secondary phases where chemical segregation is observed. Where an X-ray synchrotron (non-standard laboratory technique) is available, X-ray absorption spectroscopy (XAS) has proven useful in identifying and quantifying secondary phases [42, 43]. In this section, the advantages and disadvantages of all these techniques for secondary phase detection are discussed by way of example for the Cu-Zn-Sn-S system. As secondary phases can be situated at the front side, back side, and inside the bulk material of the film [22, 24, 44], the application of the different techniques with respect to their information depth is also discussed.

#### 5.3.2.1 X-ray Diffraction (XRD)

X-ray diffraction gives information about the crystal structure and the lattice constants of the phases present throughout the whole depth of the film by measuring the angular dependent diffraction pattern of X-rays incident on the sample. If desired, the information depth





**Figure 5.5** (a) Position of the XRD reflections of the most common secondary phases according to the ICDD database (PDF numbers given in figure). (b) Restricted experimental XRD pattern showing only the  $2\theta$  range close to the (112)-peak of Cu<sub>2</sub>ZnSnS<sub>4</sub>, the (111)-peak of ZnS, and the (131)-peak of monoclinic Cu<sub>2</sub>SnS<sub>3</sub>. The vertical lines indicate the theoretical position of the reflections according to the ICDD database

can be varied to a certain extent by varying the X-ray incident angle. On a basic level, an XRD pattern of a pure phase can be used as a unique “fingerprint” for this phase since the pattern is a convolution of lattice geometry, size, as well as scattering cross-section of the atoms in the phase. In Figure 5.5(a), literature values of these ‘fingerprints’ for Cu<sub>2</sub>ZnSnS<sub>4</sub> as well as the most likely secondary phases in the Cu-Zn-Sn-S system are shown. From these data, it can be seen that SnS, SnS<sub>2</sub>, and Cu<sub>2-x</sub>S should all be discernible from CZTS without difficulty as their diffraction peaks/fingerprints differ significantly in their angular positions. In literature, this has already been shown for the cases of Cu<sub>2-x</sub>S [45–50], for SnS [51], and SnS<sub>2</sub> [51, 52]. For the identification and discrimination of ZnS and Cu<sub>2</sub>SnS<sub>3</sub> from CZTS, it is commonly reported as being “difficult” or even “impossible” to discern Cu<sub>2</sub>SnS<sub>3</sub> and ZnS from CZTS as their crystal structure and lattice parameters, and hence their XRD-fingerprints, are too similar [34, 45, 53–56].

In the PhD work of Berg [22], this statement was investigated quantitatively by forming two samples with a phase gradient along the tie-line between Cu<sub>2</sub>SnS<sub>3</sub>, through Cu<sub>2</sub>ZnSnS<sub>4</sub>, to ZnS (see Fig. 5.4). For this, Cu and Zn were electrodeposited onto two Mo-coated substrates and the two samples were subsequently annealed in the presence of SnS and elemental sulfur, forming mostly Cu<sub>2</sub>SnS<sub>3</sub> together with CZTS on the Zn-poor sample and ZnS together with CZTS in the Zn-rich sample. Six points along both samples were subsequently investigated structurally and for composition using grazing incidence XRD and energy-dispersive X-ray spectroscopy. Correlating the obtained composition for the six different positions with the phase diagram shown in Figure 5.4 (see points (1) to (6)) allowed the theoretical phase composition to be calculated. Table 5.2 shows the expected phase composition calculated from the measured composition ratios for each of the six points.

**Table 5.2** Quantitative results of the presence of secondary phases from the Rietveld Refinement analysis for the six positions of interest (see Figure 5.4). Expected results are based on chemical compositions from EDX analysis

Position on gradient samples	(1)	(2)	(3)	(4)	(5)	(6)
Secondary phase	Cu <sub>2</sub> SnS <sub>3</sub>	Cu <sub>2</sub> SnS <sub>3</sub>	Cu <sub>2</sub> SnS <sub>3</sub>	ZnS	ZnS	ZnS
Measured Zn/Sn	0.50	0.70	0.85	1.05	1.35	2.15
Measured Cu/Sn	1.75	1.75	1.80	1.80	1.80	1.75
Expected by composition	50 ± 7%	28 ± 2%	15 ± 2%	7 ± 10%	27 ± 9%	53 ± 2%
Obtained by refinement	5%	0%	0%	0%	18%	34%

The objective is then to try and discern from the obtained XRD patterns the relative amounts of CZTS and secondary phases. Possible basic analyses include measuring the relative magnitudes of the unique Cu<sub>2</sub>SnS<sub>3</sub> and Cu<sub>2</sub>ZnSnS<sub>4</sub> peaks (see Fig. 5.5b), or analyzing a change in peak position or FWHM of the main peaks at around 28.5°. However, none of these methods allowed a sufficient discrimination of the ZnS or Cu<sub>2</sub>SnS<sub>3</sub> from Cu<sub>2</sub>ZnSnS<sub>4</sub>, as the unique peaks of the Cu<sub>2</sub>SnS<sub>3</sub> phase were not discernible for less than 50% of Cu<sub>2</sub>SnS<sub>3</sub> and the FWHM did not increase significantly even for large amounts (50%) of ZnS or Cu<sub>2</sub>SnS<sub>3</sub>. Rietveld refinement methods were therefore used, which take into account information from the whole diffractogram including relative peak height and shape. Each XRD pattern has been refined multiple times with respect to the lattice constants, the peak shape, the temperature coefficients, etc., as well as with and without the presence of secondary phases. It was therefore assumed that the films do not consist of a layered structure, but are intimately mixed. The numbers for the best refinements obtained (on the basis of minimization of a goodness-of-fit parameter,  $R_{\text{Bragg}}$ ) are listed in Table 5.2. From these results, it could be concluded that X-ray diffraction together with refinements analyses cannot be used to discern less than around 10% of ZnS from Cu<sub>2</sub>ZnSnS<sub>4</sub> and less than around 30% of Cu<sub>2</sub>SnS<sub>3</sub> from Cu<sub>2</sub>ZnSnS<sub>4</sub>. Hence, the quantitative study could prove what was predicted in the literature, namely that XRD is not a suitable tool to discern small amounts of secondary phases from Cu<sub>2</sub>ZnSnS<sub>4</sub> [22]. However, by detecting the presence of the unique CZTS-peak (see Fig. 5.5b) at around 29.6°, X-ray diffraction is still a useful tool to investigate whether CZTS is present.

In the case of selenide kesterite, Vora *et al.* recently published their results on secondary phase identification in a phase-impure CZTSe sample [57]. Comparable to the CZTS case, their results show that neither ZnSe nor Cu<sub>2</sub>SnSe<sub>3</sub> are discernable from CZTSe using XRD. At the same time, in order to identify Cu<sub>2-x</sub>Se and Sn-Se phases, XRD was shown to be a useful tool.

### 5.3.2.2 Raman Spectroscopy

Raman spectroscopy is a non-destructive technique used to gain information about the phonon behavior of the crystal lattice by looking at the frequency shift of the in-elastically scattered light from the near surface of the sample. Due to the fact that different crystal phases have different vibrational behaviors, the measured Raman shifts of different phases

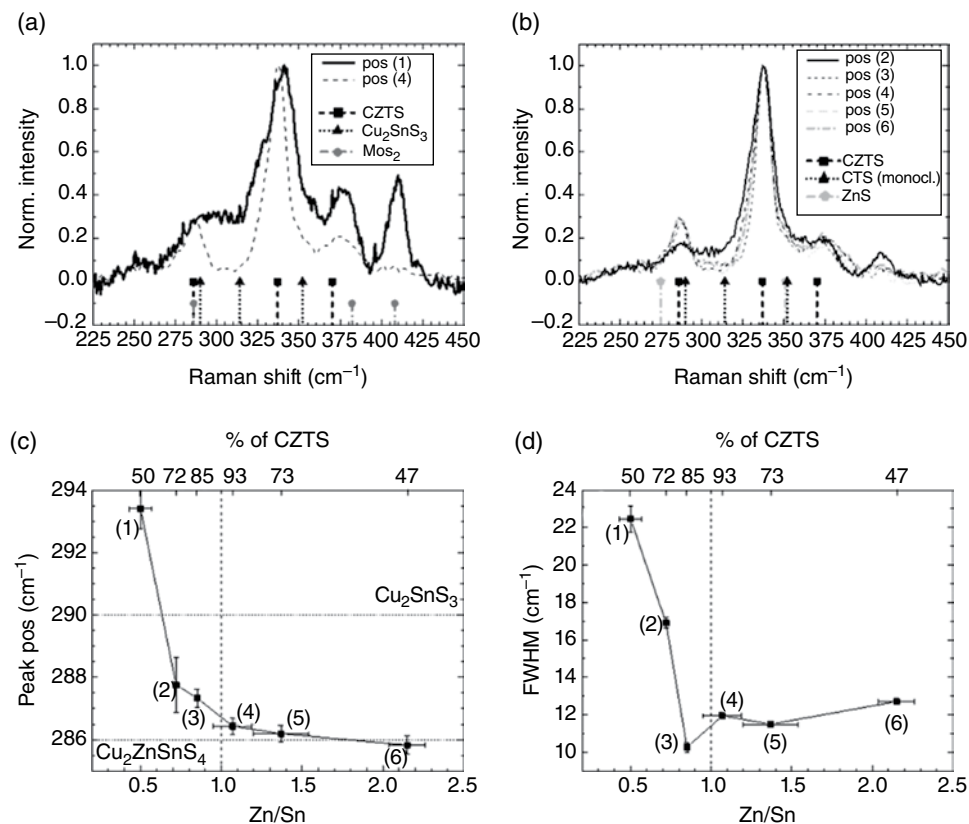
are mostly unique and can be seen as fingerprints for the respective phases. This provides the possibility of detecting different phases in a sample.

Raman spectroscopy is an optical technique where the interaction volume in the sample depends on the excitation wavelength, the sample band gap, and its absorption coefficient. Typically, excitations in the visible regime (488 nm, 532/514 nm, and 633 nm [53]) are used to analyze the samples. Since CZTS has a high absorption coefficient in this wavelength range, the information depth for Raman measurements is of the order 100 nm or smaller (the exact depth of information for the respective excitation wavelengths can be calculated using Beer-Lambert's law and assuming an intensity drop of  $1/e$  for the entering and exiting light). It is therefore a very surface-sensitive technique. Furthermore, it is important to bear in mind the different Raman excitation efficiencies of an incoming photon onto a smaller- or larger-band-gap semiconductor compared to energy of the incoming photon. While the Raman efficiency is small for a photon with an energy smaller than the band gap (below resonant case), the Raman efficiency is large for a photon with an energy larger than the band gap of the semiconductor (above resonant case).

It has been suggested [53] that single-wavelength (typically green excitation such as 514.5 nm and 532 nm) Raman spectroscopy can be used to discern  $\text{Cu}_2\text{SnS}_3$  and ZnS from CZTS, as their Raman fingerprints differ significantly from one another as listed in Table 5.3. At the same time however, there have been reported cases where samples with non-stoichiometric composition were referred to as “single phase” or as “free of secondary phases” simply because green excitation Raman (besides XRD investigations) did not show any sign of a secondary phase [49, 52, 62–64]. In the PhD work of Berg [22], a quantitative investigation was performed to see whether single-wavelength Raman spectroscopy was a suitable tool to sufficiently discern small amounts of ZnS or  $\text{Cu}_2\text{SnS}_3$  from  $\text{Cu}_2\text{ZnSnS}_4$ . In order to do so, six points (see Fig. 5.4) on the two samples with a deliberate phase gradient were investigated with green excitation single-wavelength Raman spectroscopy. The obtained Raman spectra are shown in Figure 5.6(a) and (b). Moreover, the spectra were analyzed in terms of the change in FWHM (Fig. 5.6(d)) of the mode at around  $330\text{ cm}^{-1}$ , and in terms of a shift in peak position (Fig. 5.6(c)) of the mode at around  $290\text{ cm}^{-1}$ . By comparing the six obtained spectra qualitatively, it can be seen that their general modal behavior looks very much like that expected for CZTS and does not change significantly, even though in sample position (1) and (6) at least 50% of the sample consists of  $\text{Cu}_2\text{SnS}_3$ .

**Table 5.3** Main Raman modes for  $\text{Cu}_2\text{ZnSnS}_4$ ,  $\text{Cu}_2\text{SnS}_3$ , and ZnS phases as published in the literature. The reference indicated with \* should be interpreted with care, as the cubic  $\text{Cu}_2\text{SnS}_3$  phase is indicated as a high-temperature phase according to [58] while the sample in reference [53] was prepared at low temperatures

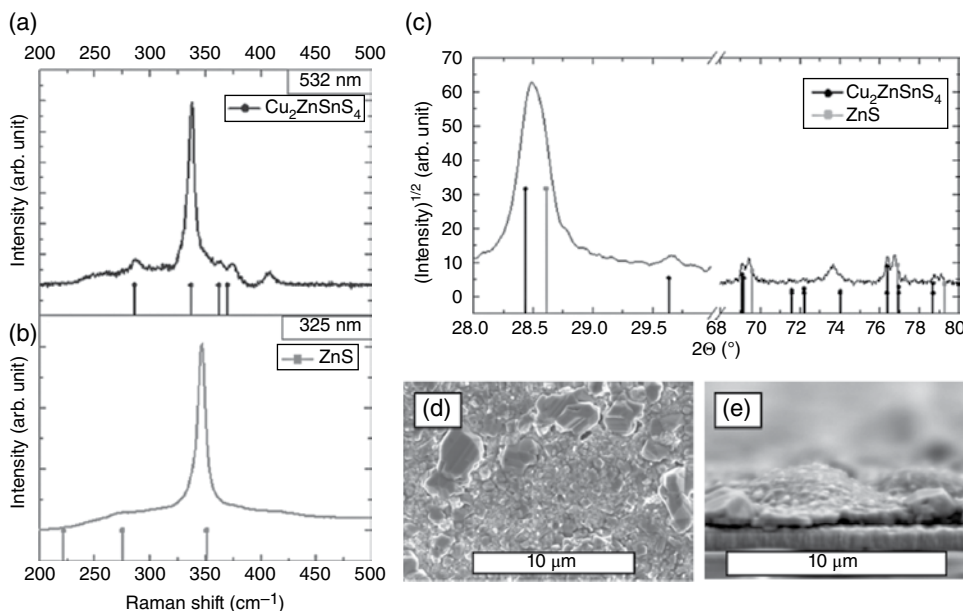
	Raman modes ( $\text{cm}^{-1}$ )	References
$\text{Cu}_2\text{ZnSnS}_4$	66, 83, 97, 143, 166, 252, 272, <b>287</b> , <b>337</b> , 347, 353	[59]
Monocl. $\text{Cu}_2\text{SnS}_3$	290, <b>352</b>	[60]
Tetr. $\text{Cu}_2\text{SnS}_3$	297, <b>337</b> , <b>352</b>	[53]
Cubic $\text{Cu}_2\text{SnS}_3^*$	267, <b>303</b> , <b>356</b>	[53]*
ZnS	219, 275, <b>351</b>	[61]



**Figure 5.6** Normalized Raman spectra of (a) positions (1) and (4) and (b) positions (2) to (6), to visualize the change of pattern shape. The vertical lines indicate the positions of the respective Raman modes as taken from literature. (c) Change in peak position of the ternary 290 cm<sup>-1</sup> mode to the 286 cm<sup>-1</sup> mode of CZTS. (d) Variation of the FWHM of the mode at 337 cm<sup>-1</sup> with respect to the Zn/Sn ratio

and ZnS, respectively. This already gives an indication of the difficulty of discerning secondary phases from CZTS. After conducting peak fitting analysis, the change in peak position and FWHM were analyzed. The results are shown in Figure 5.6(b) and (d), respectively. In both figures, it can be seen that the peak positions and FWHM do change significantly for points (1) to (3). At the same time, in between points (4) to (6) there is no significant change observable. Assuming that all phases are distributed evenly in the film, it can be concluded from these results that Cu<sub>2</sub>SnS<sub>3</sub> cannot be discerned with single-wavelength Raman spectroscopy (532 and 514 nm) if less than 30% of the phase is present, while ZnS is indiscernible.

The assumption in the above analysis that Cu<sub>2</sub>SnS<sub>3</sub> and ZnS are distributed evenly throughout the film typically does not hold. In the case where Cu<sub>2</sub>SnS<sub>3</sub> is in excess, chemical depth profiles for samples prepared in a similar manner show a lack of zinc near the top surface, meaning copper and tin are in excess. This leads to the assumption that in fact



**Figure 5.7** Raman spectra of Zn-rich sample using (a) 532 nm and (b) 325 nm excitation wavelength. \* represents a contribution of MoS<sub>2</sub>. (c) XRD pattern of Zn-rich sample. (d) SEM top-view image of Zn-rich sample. (e) Cross-sectional image of Zn-rich sample where the two large grains (left and right) are related to CZTS and the small grains (in the middle) to ZnS phases

Cu<sub>2</sub>SnS<sub>3</sub> is on the surface [22], strengthening the argument that Cu<sub>2</sub>SnS<sub>3</sub> is hard to discern by green excitation Raman spectroscopy in the presence of CZTS. In the case where ZnS is in excess, its presence has been reported at the front as well as the back interface of the absorber layer [44]. To prove that ZnS is indiscernible from CZTS with a green excitation laser, a sample consisting of 90% ZnS and 10% CZTS has been prepared and characterized. The XRD pattern of the film clearly shows the presence of ZnS (Fig. 5.7c) while green excitation Raman spectroscopy simply shows the presence of the 10% kesterite phase (Fig. 5.7a).

In summary, these results show that the identification of secondary phases in the sulfide kesterite system is much more difficult than currently assumed in the literature, and therefore leads to the question of to what extent the published XRD and Raman data concerning secondary phases have to be re-interpreted. For the selenide kesterite system, Raman spectroscopy has recently been proven to be useful to qualitatively discern the presence of ZnSe [55, 57] from CZTSe.

As a solution to the difficulty of discerning ZnS from CZTS, Fontané *et al.* suggested the use of multiple-wavelength Raman spectroscopy [44]. In their work, they showed that ZnS-resonant UV excitation makes it possible to detect ZnS secondary phases in a mixed ZnS-CZTS containing sample. The idea behind their approach is to use resonant-Raman excitations for the individually expected secondary phases, in order to increase the Raman efficiency for the individual phases. In an example of this, Figure 5.7(b) shows UV-light-excited Raman measurements performed on a Zn-rich sample with 90% ZnS phase. This

result clearly shows the presence of a ZnS phase and provides evidence for its presence at the surface of the film, as UV-excited Raman spectroscopy is even more surface sensitive than using green light excitation. Due to the high surface sensitivity of Raman spectroscopy, Fontané *et al.* also suggested the combination of multiple wavelength Raman spectroscopy with a sputtering technique (AES, or SIMS, or XPS with Raman) [44] in order to obtain information about the depth-resolved position of the secondary phases.

In conclusion, Raman spectroscopy can be a useful tool to identify secondary phases, but only if multiple wavelength excitation measurements are performed. Furthermore, combining Raman spectroscopy with depth-profiling techniques allows the possibility of gaining information about the depth distribution of the secondary phases. Single-wavelength Raman spectroscopy measurements should however be interpreted with caution.

### 5.3.2.3 *Room-temperature Photoluminescence (RT-PL)*

Photoluminescence is a non-destructive and reasonably fast technique which detects the photo-induced luminescence of electronic transitions in a semiconductor material. Due to the fact that different semiconductor phases have different band gaps and defect states, and hence difference transitions, the luminescence coming from a certain phase is fairly unique and can be seen as a fingerprint for this particular phase. Measuring the photo-induced luminescence of a material can therefore be useful to detect different phases in a film.

An example has been given where RT-PL, using a green light excitation, was used to detect ZnSe within a  $\text{Cu}_2\text{ZnSnSe}_4$  thin film [65]. In their work, Djemour *et al.* measured RT-PL maps on a very-ZnSe-rich sample (64 mol%) and correlated the results to Raman spectroscopy measurements (using two excitation wavelengths of 457.9 nm and 514.5 nm) performed on the very same areas on the sample. Spatially correlating ZnSe-richer and -poorer areas, as determined by Raman spectroscopy maps, the PL-RT results picked up a broad peak at 1.20–1.32 eV which the authors correlated to a defect luminescence peak from ZnSe. It was concluded that RT-PL mapping can be useful to detect ZnSe in a  $\text{Cu}_2\text{ZnSnSe}_4$  film [65].

### 5.3.2.4 *Indirect Analysis Techniques*

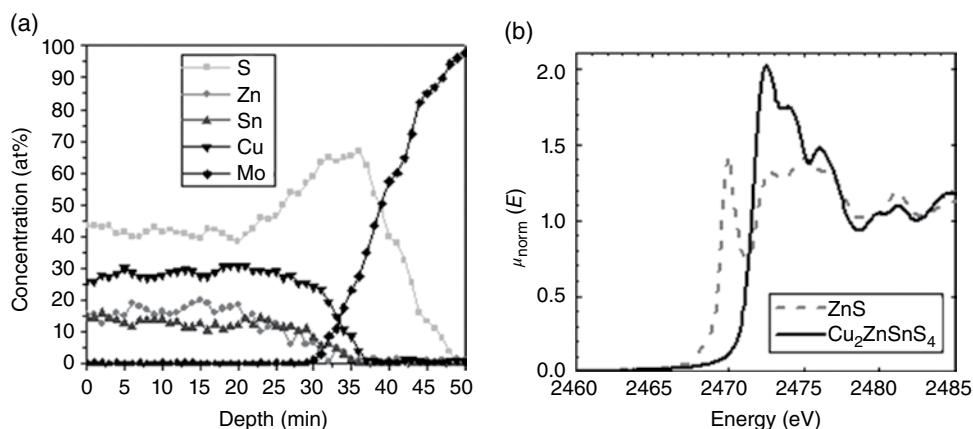
As well as detecting secondary phases directly, chemical-composition-related techniques with depth-dependent resolution offer the possibility of obtaining indications of the presence of secondary phases in an indirect manner. Commonly used techniques are, for example, secondary ion mass spectrometry (SIMS) [1, 55, 66], X-ray photoemission spectroscopy (XPS) [51], energy- or wavelength-dispersive X-ray spectroscopy (EDX/WDX) in combination with scanning electron microscopy (SEM) [47, 57] or transmission electron microscopy (TEM) [67], and Auger electron spectroscopy (AES) [22, 44] depth-profiling techniques. Recently, the technique of atom probe tomography has also been shown to be useful in detecting secondary phases [68].

Vora *et al.* show how low-energy settings of 2 keV for scanning electron microscopy can be used to enhance the contrast of Zn-rich bright spots that indicate the presence of ZnSe phases [57]. The cross-sectional imaging mode has been used to identify the depth position of the ZnSe phase. In order to prove that the bright spots are correlated to ZnSe phases, a combination of the obtained SEM image with compositional investigations such as EDX has been used. Similarly, Wätjen *et al.* have used the combination of TEM and EDX

mapping to detect Zn-S, Cu-S, and Sn-S phases near the  $\text{Cu}_2\text{ZnSnS}_4/\text{Mo}$  interface of a thinly sliced specimen prepared by a focused ion beam [67]. Careful EDX line scans across darker and brighter spots helped to indicate the presence of ZnSe phases. Redinger *et al.* [10] showed that EDX mapping is a useful tool to identify different phase regions. SEM top-view images were overlaid by EDX maps and, by defining a color for each metal, an overlay of the colors allowed phase segregation to be observed. For example ZnS appeared green,  $\text{Cu}_2\text{SnS}_3$  violet, and  $\text{Cu}_2\text{ZnSnS}_4$  appeared white in the work of Redinger *et al.* [10]. The advantage of this technique is that it can be performed with almost any SEM/EDX machine. Furthermore, it gives laterally resolved indications of the presence of secondary phases for top-view images, and it can be used to give depth-resolved secondary phase information in a cross-section mode. The disadvantage of this technique is that it requires the secondary phases to be of a minimum volume and well separated.

The destructive technique of atom probe tomography is a microscopy technique that provides 3D atom-by-atom imaging with a combination of spatial and chemical resolution. For this, layers of atoms are successively evaporated from a specimen by application of electric pulses and subsequently detected by a time-of-flight mass spectroscopy. Computer methods are used to rebuild a three-dimensional view of the sample with atomic resolution. This technique has been proven to be successful in detecting small ZnSe-rich domains in  $\text{Cu}_2\text{ZnSnSe}_4$  thin films [68]. The advantage of this technique is its atomic resolution; the disadvantages however are the long sample preparation time and the small specimen volume. The latter point is important, as it implies that the specimen of interest has to be chosen carefully.

As example of a depth-profiling technique, Figure 5.8(a) shows an AES depth profile of a CZTS layer grown by co-evaporation and annealing [44]. It can be seen that, throughout most of the film, the sample consists of a CZTS layer while at the back interface between CZTS and Mo, a  $\text{MoS}_2$  secondary phase can be assumed as the S signal increases dramatically, while those of Cu, Zn, and Sn drop.



**Figure 5.8** (a) Secondary phase identification using Auger electron spectroscopy depth profiling. Reprinted with permission from [44]. Copyright 2011, AIP Publishing LLC. (b) XANES spectra at the sulfur K-edge ( $\mu_{\text{norm}}(E)$ ) of CZTS and ZnS normalized to an edge step of 1. Reprinted with permission from [42]. Copyright 2011, AIP Publishing LLC

Combining typical composition data with such depth profiles offers the possibility of indirectly identifying secondary phases. It is therefore recommended to analyze the samples with more than one technique. The disadvantage, however, is that it is difficult to quantify the amount of a secondary phase, especially when these secondary phases are hidden within the bulk of the film.

#### 5.3.2.5 Synchrotron-Based Analysis Techniques

As a source of highly intense X-rays with tunable energies, synchrotron radiation opens up a larger range of analytical techniques that can be useful to analyze the sample in terms of secondary phases than is possible with standard lab techniques. One of these techniques is X-ray absorption spectroscopy (XAS). When X-rays hit the sample, the electric field of the incident X-rays interact with the electrons bound in an atom and the incident radiation is absorbed, transmitted, or scattered. By tuning the photon energy to a range where atomic core electrons can be excited, information about the bonding energy of the electrons in an atom, and hence about the local chemical environment of the atom itself, can be obtained. There are three main regions in a typical XAS spectrum: the so called X-ray absorption near-edge structure (XANES); the near-edge X-ray absorption fine structure (NEXAFS); and the extended X-ray absorption fine structure (EXAFS). For the quantitative identification of secondary phases in the Cu-Zn-Sn-S system, XANES has proven to be a useful tool [42, 43]. In XANES the distinguishing feature between each of the secondary phases and the kesterite is the initial absorption edge. As the absorption edge for CZTS is different from that of other secondary phases (as shown for ZnS in Fig. 5.8(b)), it is possible to determine the amounts of a secondary phase (e.g. ZnS) in a mixed sample with CZTS by de-convoluting the absorption edge measured on the mixed sample with respect to contributions from, for example, ZnS and CZTS [42]. This has been demonstrated for the quantification of ZnS in a CZTS sample by Just *et al.* and it has been predicted that, by using XANES investigations, it is possible to discern ZnS from CZTS down to 3% by volume [42].

The advantage of this technique is clearly that even small amounts of a secondary phase can be identified. The disadvantages are that it is time consuming and it does not provide the position of the secondary phase within the film.

### 5.3.3 Removal of Secondary Phases

Secondary phases can appear at the back surface, in the bulk, and on the surface. Removal and minimization of secondary phases at the back and bulk require improved synthesis methods. However, those on the surface can be removed by wet chemical etching.

In Cu(In,Ga)Se<sub>2</sub> research, KCN etching is useful for removing undesired Cu<sub>x</sub>Se<sub>y</sub> phases [69]. In the field of kesterite research, this has been confirmed in several publications [1, 45, 50, 70]. In recent developments, Fairbrother *et al.* [70] and Mousel *et al.* [1] have shown independently that HCl is a suitable selective etchant for ZnS/Se phases. Furthermore, HCl has been suggested to slowly etch SnS in addition to ZnS/Se [70]. In the study of Mousel *et al.*, it has additionally been shown that the etchant Br<sub>2</sub>-MeOH is suitable to remove Cu<sub>2</sub>SnSe<sub>3</sub> [1, 71]. In a recent study of López-Marino *et al.*, several etchants were tested to remove ZnSe [72]; KMnO<sub>4</sub> in H<sub>2</sub>SO<sub>4</sub> was selected as the most effective route to remove ZnSe.



**Table 5.4** Conditions for secondary phase etching as taken from literature

Compound	Etchant	Conditions	References
$\text{Cu}_2\text{SnSe}_3$ $\text{ZnS}/\text{Se}$	$\text{Br}_2$ -MeOH	1 min, 0.02 M $\text{Br}_2$ -MeOH	[1]
	HCl	5 min, 75°C, 10% V/V HCl	[70]
$\text{Cu}_x(\text{S}/\text{Se})_y$		1 min, 37 wt% HCl	[1]
	$\text{KMnO}_4$	3 min, 0.01 M + 1 M $\text{H}_2\text{SO}_4$	[72]
	KCN	30 s, 5 wt% KCN	[1]

The advantage of such etching procedures is that individual secondary phases can be removed selectively after the formation reaction has been performed. Note however that only those phases that can be accessed from the surface can be removed. Phases at the back interface and those within the bulk of the material are not easily removable. It is therefore suggested to change the formation process such that the growth of single-phase material is possible.

Table 5.4 lists the etching conditions for the removal of  $\text{ZnS}/\text{Se}$ ,  $\text{Cu}_x\text{Se}_y$ , and  $\text{Cu}_2\text{SnSe}_3$  phases, as taken from the literature.

### 5.3.4 Summary

It has been shown that the identification of secondary phases and their discrimination from CZTSSe is difficult. While XRD has been shown to be a useful tool to identify and discern Sn-S/Se and Cu-S/Se phases from CZTSSe, the identification and discrimination of  $\text{ZnS}/\text{Se}$  and  $\text{Cu}_2\text{Sn}(\text{S}/\text{Se})_3$  from CZTSSe in general is not straightforward. In the case of sulfide kesterite, it could be shown that XRD cannot be used to discern less than 10% of ZnS from CZTS, while  $\text{Cu}_2\text{SnS}_3$  is even more difficult to discern. Only careful XRD measurements in a grazing incidence mode comparing results from different incident angles can give a slight indication of the position of the secondary phases within the depth of the film.

By using single-wavelength Raman spectroscopy with a green light excitation, it was shown that less than 30% of  $\text{Cu}_2\text{SnS}_3$  could not be discerned from CZTS, while ZnS was completely indiscernable. In combination with the XRD results, this shows that  $\text{Cu}_2\text{SnS}_3$  is very hard to discern from  $\text{Cu}_2\text{ZnSnS}_4$ . Multiple-wavelength resonant Raman spectroscopy has however been proven to be a useful tool for the discrimination of ZnS from CZTS. In the case of selenide kesterite, single-wavelength Raman spectroscopy has qualitatively been proven useful for the discrimination of ZnSe from  $\text{Cu}_2\text{ZnSnSe}_4$ . As Raman spectroscopy is surface sensitive however, a combination of obtaining Raman spectra with depth-profile techniques is especially interesting, as the in-depth position of the secondary phases can be evaluated.

So far, the most promising tool to identify small amounts of secondary phases is XANES. The disadvantage however is that it does not allow a high sample throughput as the analysis is time consuming and requires access to a synchrotron.

In the absence of a synchrotron, the best method of obtaining indications of the presence of secondary phases is to combine results from compositional, morphological, structural, and other techniques, especially depth-profiling techniques, as secondary phases can be distributed at the front side, the back side, and within the bulk of the thin-film material.

Using low energy settings for SEM imaging or thinly sliced specimens for TEM, both in combination with careful EDX investigations, can be extremely useful.

The use of atom probe tomography to detect small domains of secondary phases is very promising, yet limited. As well as the small specimen volume and hence the localized information gained, this technique allows a fairly low throughput as the specimen preparation and the analysis are fairly time consuming. Furthermore, this technique is not commonly available.

In general, most of the secondary phase investigations reported in the literature focused on pure sulfide kesterite. The XRD data of selenide kesterites have been qualitatively shown to be similar to those of ZnSe and  $\text{Cu}_2\text{SnSe}_3$ . The quaternary shares similar lattice spacings with the binary and the ternary, and yet the effectiveness of single-wavelength Raman spectroscopy in the selenide case is certainly different, due to the smaller band gap and hence higher Raman efficiency of ZnSe. Quantitative studies have yet to be performed. The option of removing undesired secondary phases by a selective etch has also been discussed. A KCN-etch removes Cu-S/Se phases, HCl has been shown to selectively remove ZnS/Se and SnS phases, a  $\text{Br}_2$ -MeOH etch can be useful to remove the  $\text{Cu}_2\text{SnSe}_3$  phases, and  $\text{KMnO}_4$  in  $\text{H}_2\text{SO}_4$  has been shown to etch ZnSe. As etchants typically remove only surface phases, from a secondary phase minimization viewpoint it is recommended to grow as close to single phase as possible. To do so, carefully controlling the equilibrium conditions during the CZTSSe formation reaction is advised.

## Acknowledgements

The authors would like to thank the following people for their technical support and fruitful discussions: Yasuhiro Aida, Johannes Fischer, Alex Redinger, Thomas Schuler, Susanne Siebentritt, and Maxime Thevenin. We also thank Douglas Bishop, Diego Colombara, Brian McCandless, Thomas Mangan, and Jonathan Scragg for proofreading the manuscript. The authors acknowledge the Fonds National de la Recherche du Luxembourg (ATTRACT Fellowship Grant 07/06).

## References

- [1] Mousel, M., Redinger, A., Djemour, R., Arasimowicz, M., Valle, N., Dale, P. & Siebentritt, S. (2013) HCl and  $\text{Br}_2$ -MeOH etching of  $\text{Cu}_2\text{ZnSnSe}_4$  polycrystalline absorbers. *Thin Solid Films*, **535**, 83–87.
- [2] Wätjen, J. T., Engman, J., Edoff, M. & Platzer-Björkman, C. (2012) Direct evidence of current blocking by ZnSe in  $\text{Cu}_2\text{ZnSnSe}_4$  solar cells. *Applied Physics Letters*, **100**(17), 3.
- [3] Colombara, D., Robert, E. V. C., Crossay, A., Taylor, A., Guennou, M., Arasimowicz, M., Malaquias, J. C. B., Djemour, R. & Dale, P. J. (2014) Quantification of surface ZnSe in  $\text{Cu}_2\text{ZnSnSe}_4$ -based solar cells by analysis of the spectral response. *Solar Energy Materials and Solar Cells*, **123**, 220–227.
- [4] Weber, A., Mainz, R. & Schock, H. W. (2010) On the Sn loss from thin films of the material system Cu-Zn-Sn-S in high vacuum. *Journal of Applied Physics*, **107**(1), 013516.
- [5] Oleksyuk, I. D., Dudchak, I. V. & Piskach, L. V. (2004) Phase equilibria in the  $\text{Cu}_2\text{S}$ -ZnS-SnS<sub>2</sub> system. *Journal of Alloys and Compounds*, **368**(1–2), 135–143.
- [6] Scragg, J. J., Dale, P. J., Colombara, D. & Peter, L. M. (2012) Thermodynamic Aspects of the Synthesis of Thin-Film Materials for Solar Cells. *ChemPhysChem*, **13**(12), 3035–3046.

- [7] Price, G. (1998) *Thermodynamics of Chemical Processes*. Oxford University Press, Oxford.
- [8] Atkins, P. (1994) *Physical Chemistry*, 5th Edition. Oxford University Press, Oxford.
- [9] Weber, A., Krauth, H., Perl, S., Schubert, B., Kotschau, I., Schorr, S. & Schock, H. W. (2009) Multi-stage evaporation of  $\text{Cu}_2\text{ZnSnS}_4$  thin films. *Thin Solid Films*, **517**(7), 2524–2526.
- [10] Redinger, A., Berg, D. M., Dale, P. J. & Siebentritt, S. (2011) The consequences of kesterite equilibria for efficient solar cells. *Journal of American Chemical Society*, **133**(10), 3320–3323.
- [11] Scragg, J. J., Ericson, T., Kubart, T., Edoff, M. & Platzer-Björkman, C. (2011) Chemical insights into the instability of  $\text{Cu}_2\text{ZnSnS}_4$  films during annealing. *Chemistry of Materials*, **23**(20), 4625–4633.
- [12] Piacente, V., Foglia, S. & Scardala, P. (1991) Sublimation study of the tin sulfides  $\text{SnS}_2$ ,  $\text{Sn}_2\text{S}_3$  and  $\text{SnS}$ . *Journal of Alloys and Compounds*, **177**(1), 17–30.
- [13] Di Benedetto, F., Bernardini, G. P., Borri, D., Lottermoser, W., Tippelt, G. & Amthauer, G. (2005) Fe-57- and Sn-119-Mössbauer study on stannite ( $\text{Cu}_2\text{FeSnS}_4$ )-kesterite ( $\text{Cu}_2\text{ZnSnS}_4$ ) solid solution. *Physics and Chemistry of Minerals*, **31**(10), 683–690.
- [14] Chen, S. Y., Yang, J. H., Gong, X. G., Walsh, A. & Wei, S. H. (2010) Intrinsic point defects and complexes in the quaternary kesterite semiconductor  $\text{Cu}_2\text{ZnSnS}_4$ . *Physical Review B*, **81**(24), 10.
- [15] Maeda, T., Nakamura, S. & Wada, T. (2011) First-principles calculations of vacancy formation in In-free photovoltaic semiconductor  $\text{Cu}_2\text{ZnSnSe}_4$ . *Thin Solid Films*, **519**(21), 7513–7516.
- [16] Oikkonen, L. E., Ganchenkova, M. G., Seitsonen, A. P. & Nieminen, R. M. (2011) Vacancies in  $\text{CuInSe}_2$ : new insights from hybrid-functional calculations. *Journal of Physics: Condensed Matter*, **23**(42), 013516.
- [17] Guillemoles, J. F. (2000) Stability of  $\text{Cu(In,Ga)Se}_2$  solar cells: a thermodynamic approach. *Thin Solid Films*, **361**, 338–345.
- [18] Ahmed, S., Reuter, K. B., Gunawan, O., Guo, L., Romankiw, L. T. & Deligianni, H. (2011) A high efficiency electrodeposited  $\text{Cu}_2\text{ZnSnS}_4$  solar cell. *Advanced Energy Materials*, **2**(2), 253–259.
- [19] Repins, I., Beall, C., Vora, N., DeHart, C., Kuciauskas, D., Dippo, P., To, B., Mann, J., Hsu, W. C., Goodrich, A. & Noufi, R. (2012) Co-evaporated  $\text{Cu}_2\text{ZnSnSe}_4$  films and devices. *Solar Energy Materials and Solar Cells*, **101**, 154–159.
- [20] Guo, Q., Ford, G. M., Yang, W. C., Walker, B. C., Stach, E. A., Hillhouse, H. W. & Agrawal, R. (2010) Fabrication of 7.2% efficient CZTSSe solar cells using CZTS nanocrystals. *Journal of American Chemical Society*, **132**(49), 17384–17386.
- [21] Redinger, A., Mousel, M., Djemour, R., Gutay, L., Valle, N. & Siebentritt, S. (2014)  $\text{Cu}_2\text{ZnSnSe}_4$  thin film solar cells produced via co-evaporation and annealing including a  $\text{SnSe}_2$  capping layer. *Progress in Photovoltaics*, **22**(1), 51–57.
- [22] Berg, D. M. (2012) Kesterite equilibrium reaction and the discrimination of secondary phases from  $\text{Cu}_2\text{ZnSnS}_4$ . PhD thesis, University of Luxembourg, Belval.
- [23] Scragg, J. J., Kubart, T., Wätjen, J. T., Ericson, T., Linnarsson, M. K. & Platzer-Björkman, C. (2013) Effects of back contact instability on  $\text{Cu}_2\text{ZnSnS}_4$  devices and processes. *Chemistry of Materials*, **25**(15), 3162–3171.
- [24] Scragg, J. J., Wätjen, J. T., Edoff, M., Ericson, T., Kubart, T. & Platzer-Björkman, C. (2012) A detrimental reaction at the molybdenum back contact in  $\text{Cu}_2\text{ZnSn(S,Se)}_4$  thin-film solar cells. *Journal of American Chemical Society*, **134**(47), 19330–19333.
- [25] Siebentritt, S. & Schorr, S. (2012) Kesterites: a challenging material for solar cells. *Progress in Photovoltaics*, **20**(5), 512–519.
- [26] Stanbery, B. J. (2002) Copper indium selenides and related materials for photovoltaic devices. *Critical Reviews in Solid State and Materials Science*, **27**(2), 73–117.
- [27] Berg, D. M., Djemour, R., Gutay, L., Zoppi, G., Siebentritt, S. & Dale, P. J. (2012) Thin film solar cells based on the ternary compound  $\text{Cu}_2\text{SnS}_3$ . *Thin Solid Films*, **520**(19), 6291–6294.
- [28] Marcano, G., Rincon, C., de Chabaud, L. M., Bracho, D. B. & Perez, G. S. (2001) Crystal growth and structure, electrical, and optical characterization of the semiconductor  $\text{Cu}_2\text{SnSe}_3$ . *Journal of Applied Physics*, **90**(4), 1847–1853.

- [29] Yu, P. Y. & Cardonna, M. (2003) *Fundamentals of Semiconductors*. Springer, Berlin, Heidelberg, New York.
- [30] Lin, Y. T., Shi, J. B., Chen, Y. C., Chen, C. J. & Wu, P. F. (2009) Synthesis and Characterization of Tin Disulfide (SnS<sub>2</sub>) Nanowires. *Nanoscale Research Letters*, **4**(7), 694–698.
- [31] Sava, F., Lorinczi, A., Popescu, M., Socol, G., Axente, E., Mihailescu, I. N. & Nistor, M. (2006) Amorphous SnSe(2) films. *Journal of Optoelectronics and Advanced Materials*, **8**(4), 1367–1371.
- [32] Vidal, J., Lany, S., d’Avezac, M., Zunger, A., Zakutayev, A., Francis, J. & Tate, J. (2012) Band-structure, optical properties, and defect physics of the photovoltaic semiconductor SnS. *Applied Physics Letters*, **100**(3), 032104.
- [33] Sinsermsuksakul, P., Heo, J., Noh, W., Hock, A. S. & Gordon, R. G. (2011) Atomic layer deposition of tin monosulfide thin films. *Advanced Energy Materials*, **1**(6), 1116–1125.
- [34] Franzman, M. A., Schlenker, C. W., Thompson, M. E. & Brutchey, R. L. (2010) Solution-phase synthesis of SnSe nanocrystals for use in solar cells. *Journal of American Chemical Society*, **132**(12), 4060.
- [35] Liu, G. M., Schulmeyer, T., Brotz, J., Klein, A. & Jaegermann, W. (2003) Interface properties and band alignment of Cu<sub>2</sub>S/CdS thin film solar cells. *Thin Solid Films*, **431**, 477–482.
- [36] Kashida, S., Shimosaka, W., Mori, M. & Yoshimura, D. (2003) Valence band photoemission study of the copper chalcogenide compounds, Cu<sub>2</sub>S, Cu<sub>2</sub>Se and Cu<sub>2</sub>Te. *Journal of Physics and Chemistry of Solids*, **64**(12), 2357–2363.
- [37] Siebentritt, S. (2013) Why are kesterite solar cells not 20% efficient? *Thin Solid Films*, **535**, 1–4.
- [38] Barkhouse, D. A. R., Gunawan, O., Gokmen, T., Todorov, T. K. & Mitzi, D. B. (2011) Device characteristics of a 10.1% hydrazine-processed Cu<sub>2</sub>ZnSn(Se,S)<sub>4</sub> solar cell. *Progress in Photovoltaics*, **20**(1), 6–11.
- [39] Todorov, T. K., Tang, J., Bag, S., Gunawan, O., Gokmen, T., Zhu, Y. & Mitzi, D. B. (2012) Beyond 11% efficiency: characteristics of state-of-the-art Cu<sub>2</sub>ZnSn(S,Se)<sub>4</sub> solar cells. *Advanced Energy Materials*, **3**, 34–38.
- [40] Wang, W., Winkler, M. T., Gunawan, O., Gokmen, T., Todorov, T. K., Zhu, Y. & Mitzi, D. B. (2013) Device characteristics of CZTSSe thin-film solar cells with 12.6% efficiency. *Advanced Energy Materials*, **4**, 1301465.
- [41] Katagiri, H., Jimbo, K., Maw, W. S., Oishi, K., Yamazaki, M., Araki, H. & Takeuchi, A. (2009) Development of CZTS-based thin film solar cells. *Thin Solid Films*, **517**(7), 2455–2460.
- [42] Just, J., Luzenkirchen-Hecht, D., Frahm, R., Schorr, S. & Unold, T. (2011) Determination of secondary phases in kesterite Cu<sub>2</sub>ZnSnS<sub>4</sub> thin films by x-ray absorption near edge structure analysis. *Applied Physics Letters*, **99**(26), 3.
- [43] Bär, M., Schubert, B. A., Marsen, B., Wilks, R. G., Blum, M., Krause, S., Pookpanratana, S., Zhang, Y., Unold, T., Yang, W., Weinhardt, L., Heske, C. & Schock, H. W. (2012) Cu<sub>2</sub>ZnSnS<sub>4</sub> thin-film solar cell absorbers illuminated by soft x-rays. *Journal of Materials Research*, **27**(8), 1097–1104.
- [44] Fontané, X., Calvo-Barrio, L., Izquierdo-Roca, V., Saucedo, E., Perez-Rodriguez, A., Morante, J. R., Berg, D. M., Dale, P. J. & Siebentritt, S. (2011) In-depth resolved Raman scattering analysis for the identification of secondary phases: Characterization of Cu<sub>2</sub>ZnSnS<sub>4</sub> layers for solar cell applications. *Applied Physics Letters*, **98**(18), 3.
- [45] Schubert, B. A., Marsen, B., Cinque, S., Unold, T., Klenk, R., Schorr, S. & Schock, H. W. (2011) Cu<sub>2</sub>ZnSnS<sub>4</sub> thin film solar cells by fast coevaporation. *Progress in Photovoltaics*, **19**(1), 93–96.
- [46] Liu, F. Y., Zhang, K., Lai, Y. Q., Li, J., Zhang, Z. A. & Liu, Y. X. (2010) Growth and characterization of Cu<sub>2</sub>ZnSnS<sub>4</sub> thin films by DC reactive magnetron sputtering for photovoltaic applications. *Electrochemical and Solid-State Letters*, **13**(11), H379–H381.
- [47] Salome, P. M. P., Malaquias, J., Fernandes, P. A., Ferreira, M. S., Leitao, J. P., da Cunha, A. F., Gonzalez, J. C., Matinaga, F. N., Ribeiro, G. M. & Viana, E. R. (2011) The influence of hydrogen in the incorporation of Zn during the growth of Cu<sub>2</sub>ZnSnS<sub>4</sub> thin films. *Solar Energy Materials and Solar Cells*, **95**(12), 3482–3489.

- [48] Yoo, H. & Kim, J. (2010) Growth of  $\text{Cu}_2\text{ZnSnS}_4$  thin films using sulfurization of stacked metallic films. *Thin Solid Films*, **518**(22), 6567–6572.
- [49] Yoo, H., Kim, J. H. & Zhang, L. X. (2012) Sulfurization temperature effects on the growth of  $\text{Cu}_2\text{ZnSnS}_4$  thin film. *Current Applied Physics*, **12**(4), 1052–1057.
- [50] Fernandes, P. A., Salome, P. M. P. & da Cunha, A. F. (2009) Precursors' order effect on the properties of sulfurized  $\text{Cu}_2\text{ZnSnS}_4$  thin films. *Semiconductor Science and Technology*, **24**(10), 7.
- [51] Platzer-Björkman, C., Scragg, J., Flammersberger, H., Kubart, T. & Edoff, M. (2012) Influence of precursor sulfur content on film formation and compositional changes in  $\text{Cu}_2\text{ZnSnS}_4$  films and solar cells. *Solar Energy Materials and Solar Cells*, **98**, 110–117.
- [52] Shin, S. W., Pawar, S. M., Park, C. Y., Yun, J. H., Moon, J. H., Kim, J. H. & Lee, J. Y. (2011) Studies on  $\text{Cu}_2\text{ZnSnS}_4$  (CZTS) absorber layer using different stacking orders in precursor thin films. *Solar Energy Materials and Solar Cells*, **95**(12), 3202–3206.
- [53] Fernandes, P. A., Salome, P. M. P. & da Cunha, A. F. (2011) Study of polycrystalline  $\text{Cu}_2\text{ZnSnS}_4$  films by Raman scattering. *Journal of Alloys and Compounds*, **509**(28), 7600–7606.
- [54] Mitzi, D. B., Gunawan, O., Todorov, T. K., Wang, K. & Guha, S. (2011) The path towards a high-performance solution-processed kesterite solar cell. *Solar Energy Materials and Solar Cells*, **95**(6), 1421–1436.
- [55] Redinger, A., Hones, K., Fontane, X., Izquierdo-Roca, V., Saucedo, E., Valle, N., Perez-Rodriguez, A. & Siebentritt, S. (2011) Detection of a ZnSe secondary phase in coevaporated  $\text{Cu}_2\text{ZnSnSe}_4$  thin films. *Applied Physics Letters*, **98**(10), 3.
- [56] Salome, P. M. P., Fernandes, P. A. & da Cunha, A. F. (2009) Morphological and structural characterization of  $\text{Cu}_2\text{ZnSnSe}_4$  thin films grown by selenization of elemental precursor layers. *Thin Solid Films*, **517**(7), 2531–2534.
- [57] Vora, N., Blackburn, J., Repins, I., Beall, C., To, B., Pankow, J., Teeter, G., Young, M. & Noufi, R. (2012) Phase identification and control of thin films deposited by co-evaporation of elemental Cu, Zn, Sn, and Se. *Journal of Vacuum Science and Technology A*, **30**(5), 051201.
- [58] Moh, G. H. (1975) Tin-containing mineral systems *Chemie der Erde*, **34**(1), 1–61.
- [59] Dimitrievska, M., Fairbrother, A., Fontané, X., Jawhari, T., Izquierdo-Roca, V., Saucedo, E. & Pérez-Rodríguez, A. (2014) Multiwavelength excitation Raman scattering study of polycrystalline kesterite  $\text{Cu}_2\text{ZnSnS}_4$  thin films. *Applied Physics Letters*, **104**(2), 021901.
- [60] Berg, D. M., Djemour, R., Gutay, L., Siebentritt, S., Dale, P. J. & Fontané, X., Izquierdo-Roca, V. & Perez-Rodriguez, A. (2012) Raman analysis of monoclinic  $\text{Cu}_2\text{SnS}_3$  thin films. *Applied Physics Letters*, **100**(19), 192103.
- [61] Brafman, O. & Mitra, S. (1968) Raman effect in wurtzite- and zinc-blende-type ZnS single crystals. *Physical Review B*, **171**(3), 931.
- [62] Fella, C. M., Uhl, A. R., Romanyuk, Y. E. & Tiwari, A. N. (2012)  $\text{Cu}_2\text{ZnSnSe}_4$  absorbers processed from solution deposited metal salt precursors under different selenization conditions. *Physica Status Solidi A: Applications and Materials*, **209**(6), 1043–1048.
- [63] Ilari, G. M., Fella, C. M., Ziegler, C., Uhl, A. R., Romanyuk, Y. E. & Tiwari, A. N. (2012)  $\text{Cu}_2\text{ZnSnSe}_4$  solar cell absorbers spin-coated from amine-containing ether solutions. *Solar Energy Materials and Solar Cells*, **104**, 125–130.
- [64] Yoo, H. & Kim, J. (2010) Comparative study of  $\text{Cu}_2\text{ZnSnS}_4$  film growth. *Solar Energy Materials and Solar Cells*, **95**(1), 239–244.
- [65] Djemour, R., Mousel, M., Redinger, A., Gutay, L., Crossay, A., Colombara, D., Dale, P. J. & Siebentritt, S. (2013) Detecting ZnSe secondary phase in  $\text{Cu}_2\text{ZnSnSe}_4$  by room temperature photoluminescence. *Applied Physics Letters*, **102**(22), 222108.
- [66] Redinger, A., Berg, D. M., Dale, P. J., Djemour, R., Gütay, L., Eisenbarth, T., Valle, N. & Siebentritt, S. (2011) Route toward high-efficiency single-phase  $\text{Cu}_2\text{ZnSn(S,Se)}_4$  thin-film solar cells: Model experiments and literature review. *IEEE Journal of Photovoltaics*, **1**(2), 200–206.
- [67] Wätjen, J. T., Scragg, J. J., Ericson, T., Edoff, M. & Platzer-Björkman, C. Secondary compound formation revealed by transmission electron microscopy at the  $\text{Cu}_2\text{ZnSnS}_4/\text{Mo}$  interface. *Thin Solid Films*, **535**, 31–34.

- [68] Schwarz, T., Cojocaru-Miredin, O., Choi, P., Mousel, M., Redinger, A., Siebentritt, S. & Raabe, D. (2013) Atom probe study of  $\text{Cu}_2\text{ZnSnSe}_4$  thin-films prepared by co-evaporation and post-deposition annealing. *Applied Physics Letters*, **102**(4), 042101.
- [69] Hashimoto, Y., Kohara, N., Negami, T., Nishitani, M. & Wada, T. (1996) Surface characterization of chemically treated  $\text{Cu}(\text{In,Ga})\text{Se}_2$  thin films. *Japanese Journal of Applied Physics Part 1*, **35**(9A), 4760–4764.
- [70] Fairbrother, A., Garcia-Hemme, E., Izquierdo-Roca, V., Fontané, X., Pulgarin-Agudelo, F. A., Vigil-Galan, O., Perez-Rodriguez, A. & Saucedo, E. (2012) Development of a selective chemical etch to improve the conversion efficiency of Zn-rich  $\text{Cu}_2\text{ZnSnS}_4$  solar cells. *Journal of American Chemical Society*, **134**(19), 8018–8021.
- [71] Timmo, K., Altosaar, M., Raudoja, J., Grossberg, M., Danilson, M., Volobujeva, O. & Mellikov, E. (2010) In *Chemical Etching of  $\text{Cu}_2\text{ZnSn}(\text{S,Se})_4$  Monograin Powder*, Conference Record of the IEEE Photovoltaic Specialists Conference, Honolulu, HI, Honolulu, pp 1982–1985.
- [72] López-Marino, S., Sánchez, Y., Placidi, M., Fairbrother, A., Espindola-Rodríguez, M., Fontané, X., Izquierdo-Roca, V., López-García, J., Calvo-Barrio, L., Pérez-Rodríguez, A. & Saucedo, E. (2013) ZnSe etching of Zn-rich  $\text{Cu}_2\text{ZnSnSe}_4$ : An oxidation route for improved solar-cell efficiency. *Chemistry: A European Journal*, **19**(44), 14814–14822.

# 6

## Growth of CZTS Single Crystals

*Akira Nagaoka and Kenji Yoshino*

*Department of Applied Physics and Electronic Engineering, University of Miyazaki,  
1-1 Gakuenkibanadai-nishi, 889-2192 Miyazaki, Japan*

### 6.1 Introduction

At the present time the majority of solar cells are produced based on silicon crystal, followed by semiconductor thin films (see Chapter 2). A Cu(In, Ga)Se<sub>2</sub> (CIGS) thin-film solar cell exhibits better performance than conventional compound semiconductor solar cells as its efficiency reaches as high as 20.8% [1]. However, the existence of indium and gallium in the Earth's crust is limited while worldwide demand for ITO (indium-tin oxide) touch-sensitive displays is increasing. Finding a substitute for In and Ga in CIGS has therefore become an important issue. A Cu<sub>2</sub>ZnSnS<sub>4</sub> (CZTS) polycrystalline thin film has been proposed as a candidate material to replace the CIGS (Cu(In,Ga)S<sub>2</sub>) optical absorber layer. CZTS has a high absorption coefficient of over 10<sup>4</sup> cm<sup>-1</sup> and optical direct band-gap energy of 1.4–1.5 eV, which makes it suitable for applications in thin-film solar cell devices [2–5]. With regard to CZTS solar cell devices, a conversion efficiency of 8.4% has been achieved [6]. This value has even been exceeded by the related selenium-containing compound Cu<sub>2</sub>ZnSn(S,Se)<sub>4</sub> (CZTSSe) with a record efficiency of 12.6% [7].

Improvement of CZTS solar cells requires better understanding of the fundamental properties of the material itself, as well as that of physical parameters that have a major impact on characteristics of the solar cells. Theoretical knowledge of optical properties [5], band structure [8, 9], and intrinsic point defects of the quaternary semiconductor [8, 10] have been reported using first-principles calculations. On the other hand, there are few reports from the experimental side, for which the optoelectronic and growth properties of polycrystalline

CZTS thin-films have been measured [11–15]. However, in order to obtain more accurate and reliable knowledge on CZTS properties, it is necessary to investigate CZTS bulk single crystals. So far few studies on CZTS bulk single crystals have been performed because it is difficult to grow most multinary compounds such as CZTS and CIGS, which should be grown through a solid-state transition during the cooling process. General melt growth is therefore not suitable for CZTS bulk single crystal. Furthermore, the single crystal, which is grown by iodine transport methods over long periods of time, is quite small and irregularly shaped. In this chapter we therefore focus on the solution growth of single crystals, which is possible below melting point. We describe the solution growth process of CZTS bulk single crystals and the fundamental physical properties from an experimental viewpoint.

## 6.2 Growth Process

For preparation of bulk crystals, knowledge of phase diagrams is indispensable. The phase diagram for ternary I–III–VI<sub>2</sub> chalcopyrite compounds has usually been investigated along the I<sub>2</sub>VI–III<sub>2</sub>VI<sub>3</sub> pseudobinary system [16]. The growth mechanisms of Cu–III–VI<sub>2</sub> chalcopyrite compounds (e.g. CuInSe<sub>2</sub>, CuGaSe<sub>2</sub>) show a solid-state transition or a peritectic reaction from the melts during cooling process. For the Cu<sub>2</sub>Se–In<sub>2</sub>Se<sub>3</sub> pseudobinary system, CuInSe<sub>2</sub> crystals are grown through a solid-state phase transition from the zinc-blende structure [16]. For Cu<sub>2</sub>Se–Ga<sub>2</sub>Se<sub>3</sub> pseudobinary system, a peritectic point exists at temperature 1030°C below the melting point of the stoichiometric CuGaSe<sub>2</sub> [17]. While Ag–III–VI<sub>2</sub> chalcopyrite compounds (e. g. AgGaSe<sub>2</sub>, AgGaS<sub>2</sub>) crystals are directly grown by cooling from their stoichiometric melts, the compositions of the obtained crystals deviate from stoichiometry due to incongruent melting [18, 19].

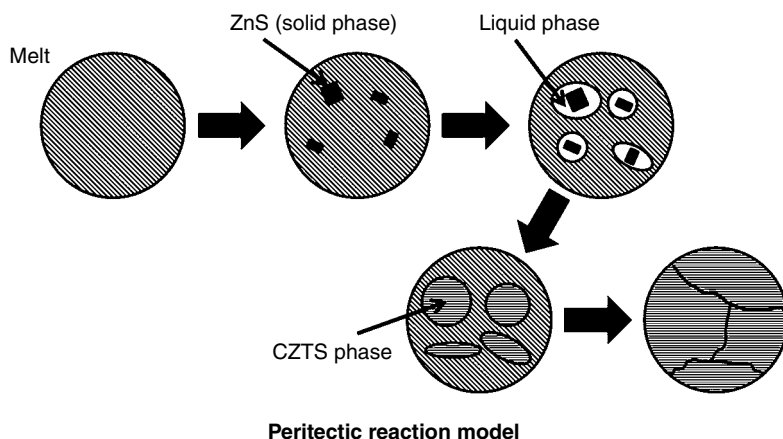
Currently, there are few publications on the quaternary compound CZTS phase diagram. Olekseyuk *et al.* reported on the Cu<sub>2</sub>S–ZnS–SnS<sub>2</sub> pseudoternary system. In particular, the growth mechanism of CZTS crystal was interpreted by the Cu<sub>2</sub>SnS<sub>3</sub>–ZnS pseudobinary system [20]. The quaternary compound CZTS is grown at 1253 K (980°C) by the peritectic reaction (ZnS solid phase + liquid phase  $\Rightarrow$  CZTS phase); the composition of the peritectic point is ZnS 12.5 mol%. Figure 6.1 depicts the peritectic growth process for CZTS at the peritectic point. As the high-temperature melt is cooled gradually, a ZnS solid phase is crystallized. When cooled further, the ZnS solid phase reacts with a surrounding liquid phase, and CZTS phases are synthesized.

### 6.2.1 Flux Method

Single-crystal growth is usually divided into three types of method: liquid phase, solid phase, and vapor phase. The solid and vapor phase methods are not suitable for large single-crystal growth. Furthermore, the liquid phase method is divided into melt growth and solution growth. As mentioned at the start of Section 6.2, melt growth is not suitable for CZTS single-crystal growth. We have therefore selected the flux method, which is one of the solution growth methods. The advantage of the flux method is that single crystals can be grown below melting point. On the other hand, the disadvantage is the difficulty of solvent selection and the existence of a secondary phase during growth.

Selection of solvent is most important because of its decisive role in growing. The properties desired for a solvent include: (1) high solubility of solute; (2) low melting point; (3) low





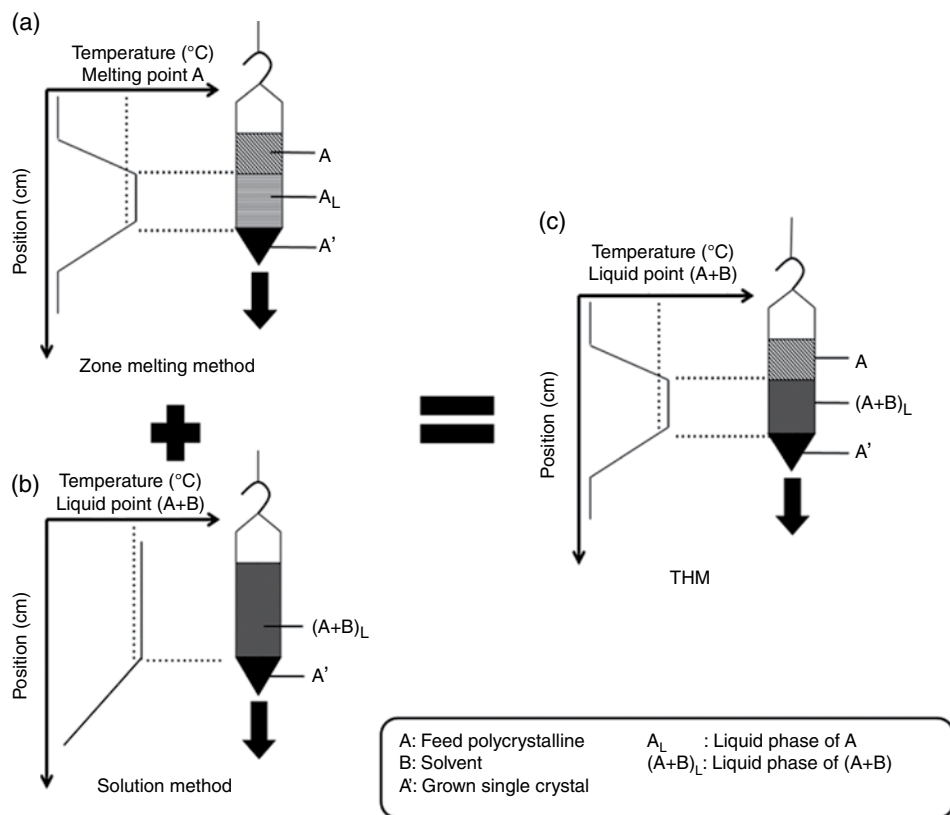
**Figure 6.1** Peritectic growth process for CZTS at the peritectic point

viscosity; (4) amount of evaporation is low; (5) only objective crystals are crystallized; (6) inactive even when it is incorporated as impurities into crystal; (7) low toxicity; and (8) safety.

An optimum solvent is selected while considering all the required properties; requirements (1)–(6) are particularly important. From the recent viewpoint of global environmental protection, both (7) and (8) should be also taken into consideration.

### 6.2.2 Traveling Heater Method (THM)

The traveling heater method (THM) is a growth technique in which the zone method of melt growth is applied to the solution growth, and is very useful for growing fairly large crystals and especially for growing alloy crystals with compositional uniformity. Figure 6.2 depicts schematic diagrams of bulk crystal growth. The zone melting method depicted in Figure 6.2(a) is used for the growth of high-purity crystal. A feed polycrystalline (A) is melted into the zone ( $A_L$ ), the temperature of which is higher than the melting point. The grown single crystal ( $A'$ ) is located at the lower portion of the melt zone. Figure 6.2(b) shows the schematic diagram for bulk crystal growth, that is, solution Bridgman growth which is one of the solution methods. A feed polycrystalline (A) and a solvent (B) are inserted into a quartz ampoule, and the ampoule is then heated to form a solution ( $A+B$ )<sub>L</sub> by dissolution of feed polycrystalline into solvent completely. The single crystal ( $A'$ ) is grown from the solution ( $A+B$ )<sub>L</sub> by moving to the low-temperature zone, where the solution is in supersaturation. The growth temperature is lower than the melting point of feed polycrystalline (A). The growth temperature and composition of the grown crystal ( $A'$ ) change during the process however, because the concentration of the feed polycrystalline (A) dissolved in the solution decreases as the growth proceeds. Figure 6.2(c) depicts THM, where the melt ( $A_L$ ) of the zone melting method in Figure 6.2(a) is replaced with a solution ( $A+B$ )<sub>L</sub> of solute (A) and solvent (B). Part of the feed polycrystalline (A) dissolves in the zone, as the maximum temperature is set at the melting point of solution ( $A+B$ )<sub>L</sub>. When the quartz ampoule charged with solute (A) and solvent (B) is moved downwards in the temperature gradient region, a single crystal ( $A'$ ) is grown from the zone solution ( $A+B$ )<sub>L</sub>, and as much feed polycrystalline (A) as grown single crystal ( $A'$ ) dissolves at the upper part of



**Figure 6.2** Schematic diagrams of bulk crystal growth

zone. The concentration of grown crystal and liquid temperature are therefore kept constant during THM growth.

Advantages of THM growth include the following:

1. Growth temperature is low compared to that of melt growth, in which crystals are grown through a solid transition from melt during cooling.
2. Growth rate is fast in comparison with the vapor transport method, which can also be used to grow single crystal below melting point.
3. Because the concentration and temperature of the zone solution can be kept constant during the growth process, a bulk single crystal with a uniform composition can be grown.

The THM growth technique has been applied to the single-crystal growth of I–III–VI<sub>2</sub> chalcopyrite compounds [21–29]. Table 6.1 provides a list of Cu–III–VI<sub>2</sub> chalcopyrite compounds for solution growth.

#### 6.2.2.1 Preparation

Indium (In) was used as solvent for THM growth of Cu–III–VI<sub>2</sub> chalcopyrite compounds because of a constituent element, low melting point and high solubility. However, it has been observed that a miscibility gap exists in the liquid state of both CuGaS<sub>2</sub>–In and

**Table 6.1** List for solution growth of Cu-III-VI<sub>2</sub> chalcopyrite compounds

Feed Polycrystalline	Solvent	Growth mechanism	Melting point (°C)	Ref.
CuInSe <sub>2</sub>	In	Phase transition	986	[21]
	CuSe			[22]
CuInS <sub>2</sub>	In	Phase transition	1050	[23]
	Cu <sub>2</sub> Se (Zone melt)	Peritectic reaction	1090	[24]
CuGaS <sub>2</sub>	In	Incongruent	1250	[25]
	In			[26]
	CuI			[27]
	Sn			[28]
	Pb			[28]
AgGaS <sub>2</sub>	PbCl <sub>2</sub>	Direct	1040	[29]

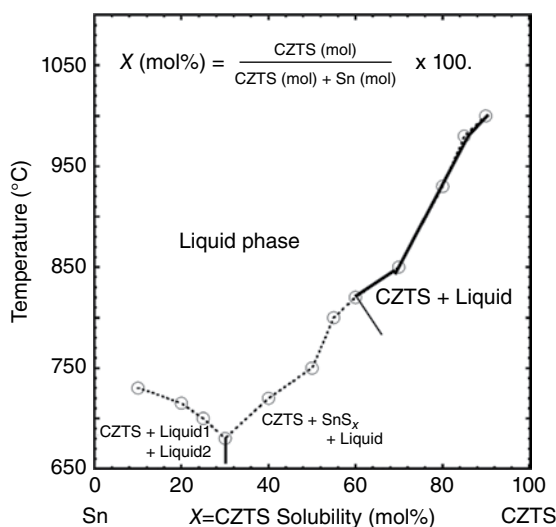
CuInS<sub>2</sub>-In pseudobinary systems [30, 31]. It is therefore important to investigate optimum solvent and CZTS-solvent pseudobinary system in order to achieve high-quality bulk single crystals.

We selected tin (Sn) as a solvent for CZTS single-crystal growth because of a constituent element, low melting point and high solubility. We describe the CZTS-Sn pseudobinary system in the following, in particular the existence of a region of miscibility gap in the liquid state.

Polycrystalline CZTS solute was grown by the melting method. Prescribed amounts of elemental copper, zinc, tin, and sulfur corresponding to the composition of stoichiometric CZTS were charged into a carbon-coated quartz ampoule. The grades of copper, tin, and sulfur were 5N and that of zinc was 6N. The ampoule charged with the elements was sealed off after evacuation to a pressure of 10<sup>-6</sup> Torr. The ampoule was then inserted into a vertical furnace, heated to 1100°C at a low rate of about 100–200°C h<sup>-1</sup>, and kept at this temperature for 24 h. The ampoule was then cooled in the air. Polycrystalline CZTS solute and Sn solvent were inserted into a quartz ampoule. The prescribed ratio of X, calculated as follows, was varied between 10 and 90 mol%:

$$X(\text{mol}\%) = \frac{\text{CZTS}(\text{mol})}{\text{CZTS}(\text{mol}) + \text{Sn}(\text{mol})} \times 100. \quad (6.1)$$

The ampoule was sealed off after evacuation to a pressure of 10<sup>-6</sup> Torr. The sealed ampoule was heated up to 1100°C at a rate of 200°C h<sup>-1</sup> for complete reaction and homogenization in a vertical furnace and kept at this temperature for 24 h. The ampoule was then pulled out from the vertical furnace and quenched in water. After the quenching, the ampoule was placed in a transparent furnace. The liquid was visually observed during a cycle of slow heating and cooling in steps of 10°C, and was held at each temperature for 5 h. The accuracy of the temperature was ±10°C. In order to check the existence of two liquid phases along the liquid curve, the CZTS-Sn solution prepared as above was heated to the determined liquid temperature at a rate of 200°C h<sup>-1</sup> in the vertical furnace. After that temperature was held for 24 h, the ampoule was pulled out from the vertical furnace and then quenched in water. A cross-section was cut from the synthesized ingot, from which the phase was visually inspected. The phase and composition were determined by the powder X-ray diffraction (XRD).



**Figure 6.3** Phase diagram of CZTS-Sn pseudobinary system

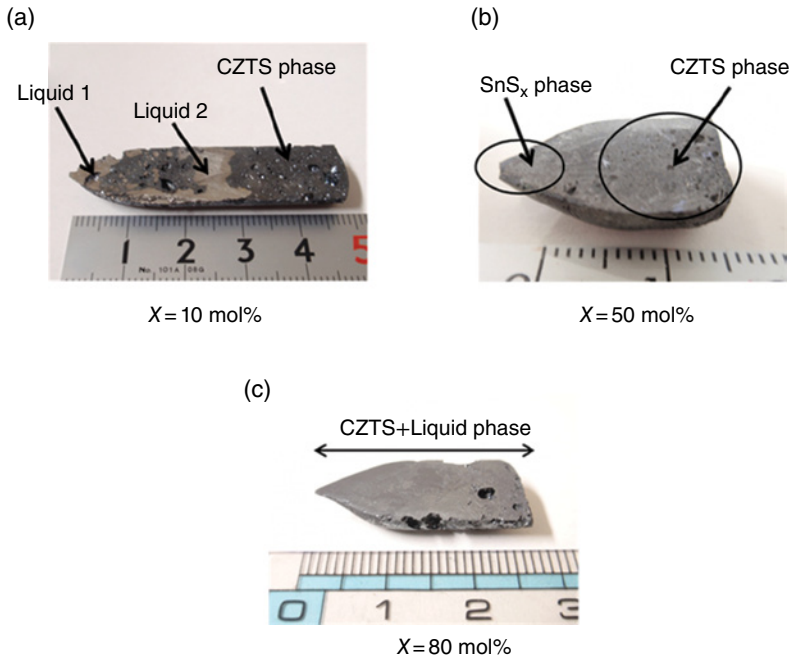
The phase diagram of CZTS-Sn pseudobinary system is depicted in Figure 6.3 [32]. There exists a miscibility gap in the saturated Sn solution. A cross-section of the synthesized ingots quenched in water is shown in Figure 6.4 [33].

There exists a miscibility gap at less than  $X=60$  mol% Sn solutions. The Sn solution saturated with CZTS solutes with  $X < 30$  mol% is separated into a CZTS phase and two liquid phases. Two clearly separated liquid phases can be observed in Figure 6.4(a). A Sn solution with  $30 \text{ mol\%} < X < 60 \text{ mol\%}$  is also separated into two phases: one is a CZTS phase and the other a  $\text{SnS}_x$  phase as shown in Figure 6.4(b).

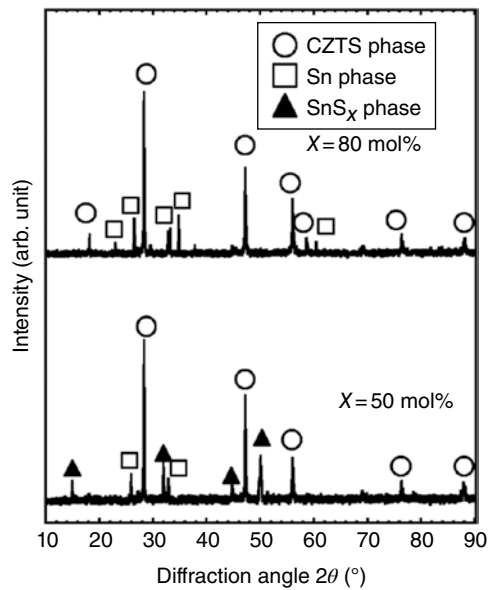
The single phase (CZTS<sub>x</sub> phase + liquid phase) of a Sn solution with  $X > 60$  mol% can be seen from Figure 6.4(c). Figure 6.5 shows the powder XRD patterns for solutions with  $X=50$  and  $X=80$  mol% [32]. The XRD pattern of  $X=80$  mol% at a single-phase region is composed of the peaks from the CZTS compound and Sn solvent; however, that of  $X=50$  mol% at a two-phase region includes peaks from the  $\text{SnS}_x$  compound. The grown crystals from a Sn solution with  $X < 60$  mol% always become polycrystalline, because the densities of Sn and  $\text{SnS}_x$  are higher than those of CZTS ( $=4.404 \text{ g cm}^{-3}$ , as determined from the value of CZTS single crystal). They tend to solidify at the bottom of the ampoule and disturb the single-crystal growth. In order to obtain a single crystal from Sn solution containing stoichiometric CZTS solute, the growth temperature and solution concentration should be kept between 820 and 980°C and  $> 60 \text{ mol\%}$ , respectively (the double line region in Fig. 6.3).

#### 6.2.2.2 THM Growth

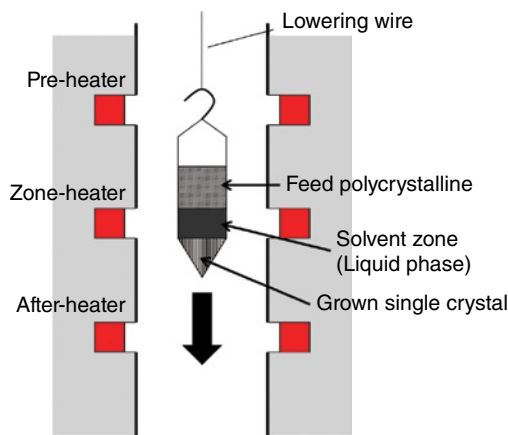
Figure 6.6 depicts the THM furnace, which is a vertical furnace with three coil heaters [34]. The pre-heater which keeps the temperature of the upper part of the ampoule tens of degrees lower than the zone heater was used to prevent deposition of gaseous species such as sulfur or tin sulfide on the inner wall of the ampoule. For the growth, a carbon-coated



**Figure 6.4** Synthesized ingots ( $X = 10, 50$  and  $80 \text{ mol\%}$ ) quenched from each liquid temperature



**Figure 6.5** Powder XRD patterns for solutions with  $X = 50, 80 \text{ mol\%}$



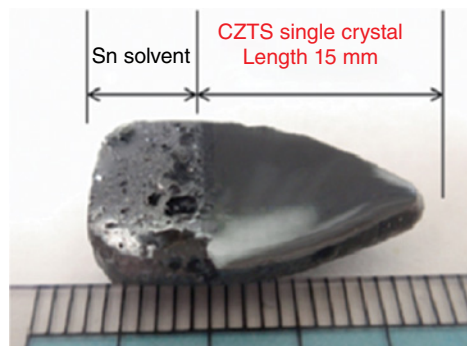
**Figure 6.6** Schematic of THM furnace

(a)



CZTS single crystal ingot

(b)



CZTS single crystal cross-section

**Figure 6.7** Photographs of a (a) CZTS single crystal ingot and (b) cross-section of ingot

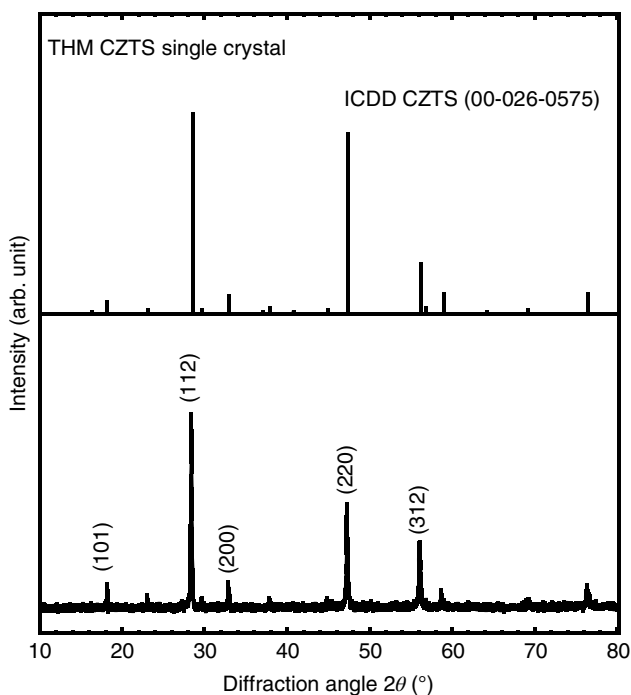
quartz ampoule of 10 mm diameter was used. The role of carbon coating is to prevent contamination from quartz ampoule and adhesion of grown crystal to quartz ampoule. A polycrystalline ingot of 10–15 g for the feed and Sn for the zone solvent was inserted into the ampoule. After evacuation to a pressure of  $10^{-6}$  Torr, the ampoule was sealed off and was then placed in the THM furnace. The maximum temperature (zone-heater temperature) was set to a temperature where the Sn solution became a single liquid phase, and the temperature gradient at the point of growth was about tens of degrees per centimeter. The growth was normally performed by lowering the ampoule at a speed of 4–5 mm day<sup>-1</sup>.

The optimum growth condition of CZTS single crystal is to use a 70 mol% solution and to keep the growth temperature at 900°C. This temperature is set 50°C higher than the liquidus temperature on the basis of the data shown in Figure 6.3. Figure 6.7 shows the photographs of a (a) CZTS single-crystal ingot and (b) cross-section of another ingot. The grain boundary was invisible. The obtained single crystal is 10 mm in diameter and 25 mm in length; the end portion is the remaining Sn solvent zone.

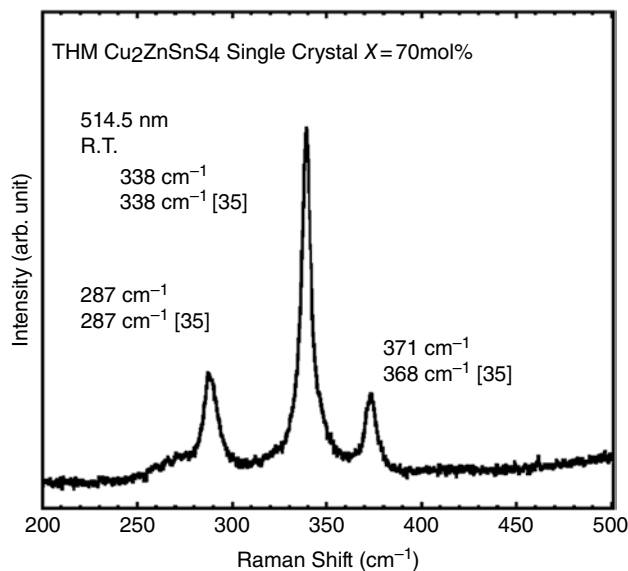
## 6.3 Properties of CZTS Single Crystals

### 6.3.1 Structural Properties

The CZTS single-crystal structure was examined by powder XRD and Raman spectroscopy measurement. Figure 6.8 shows the powder XRD pattern of the CZTS single crystal [32]. It is difficult to identify the CZTS single phase based on the XRD measurement because the peaks of CZTS corresponded well to those of ZnS. We therefore carried out the Raman measurement to evaluate the CZTS single phase. All the XRD peaks, namely the (112) peak at  $2\theta=28.53^\circ$ , (220) peak at  $2\theta=47.33^\circ$ , and (312) peak at  $2\theta=56.18^\circ$ , correspond to the International Centre for Diffraction Data (ICDD) (#00-026-0575). The lattice constants of the  $a$ - and  $c$ -axes are calculated from high-angle XRD peaks, namely the (204) and (312) peaks. The lattice constant of the  $a$ -axis is 5.455 Å and that of the  $c$ -axis is 10.880 Å, both of which correspond well to the reported  $a=5.430$  Å and  $c=10.850$  Å [20]. Figure 6.9 shows the Raman spectrum of the CZTS single crystal. The Raman peaks were observed at 287 and 338  $\text{cm}^{-1}$  [35] and these correspond well to data for CZTS in the literature [32]. The obvious peak at 371  $\text{cm}^{-1}$  is observed in the CZTS single crystal, which closely matches the CZTS polycrystalline thin-film peak at 368  $\text{cm}^{-1}$  [32]. The strongest peak at 338  $\text{cm}^{-1}$  is attributed to the  $A_1$  symmetry and is related to the vibration of the S atoms in CZTS [36]. The ZnS peaks, which would be at 218, 295, 386, 422, and 448  $\text{cm}^{-1}$ , are not observed [37]. Furthermore, other possible secondary phases, for example copper sulfide compounds and tin sulfide compounds, are not observed [14]. It can therefore be concluded that, according to XRD and Raman measurements, the CZTS single phase is obtained.



**Figure 6.8** Powder XRD pattern of the CZTS single crystal



**Figure 6.9** Raman spectra of the CZTS single crystal

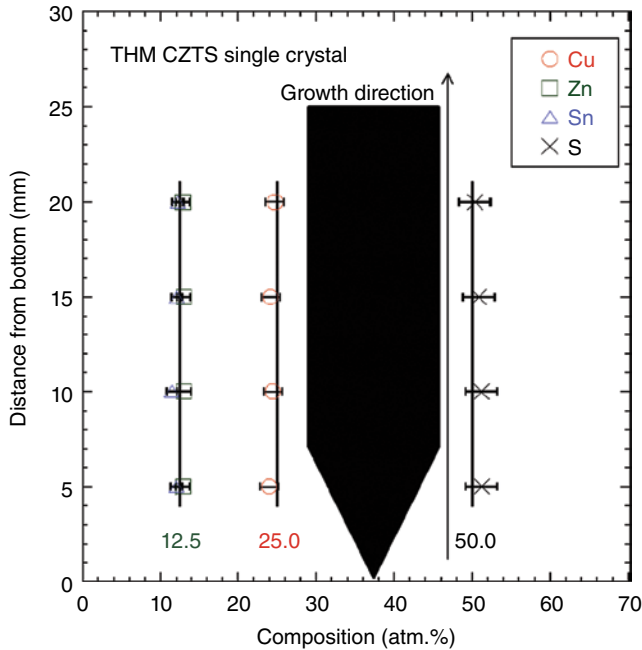
### 6.3.2 Compositional Properties

The composition of the CZTS single crystal was estimated by electron probe microanalysis (EPMA) along the growth direction. The CZTS single-crystal wafers were cut from the growth tip portion at 5 mm intervals except for the end region. Figure 6.10 shows the composition of the single crystal along the growth direction which is estimated by EPMA with an accuracy of 1%. It can clearly be seen that the composition is homogeneous along the growth direction, and has a stoichiometric ratio of CZTS. The compositions of CZTS single crystals are found to be slightly Cu-poor, Zn-rich, Sn-poor and S-rich from the stoichiometric ratio. Table 6.2 lists the detailed composition of CZTS single crystals. The composition ratios are found to be  $0.96 < \text{Cu}/(\text{Zn}+\text{Sn}) < 0.99$  and  $1.05 < \text{Zn}/\text{Sn} < 1.14$ , respectively. Through first-principles calculations, Maeda *et al.* reported that Cu vacancies are easily formed under Cu-poor, Zn-rich, and S-rich conditions in kesterite-type CZTS [38]. Furthermore, it has been shown that Cu on Zn antisites ( $\text{Cu}_{\text{Zn}}$ ) and Cu vacancies ( $\text{V}_{\text{Cu}}$ ) were the dominant intrinsic point defects in CZTS [8, 10]. The  $\text{Cu}_{\text{Zn}}$  with the lowest formation energy gives rise to an acceptor level with activation energy of 0.12 eV, while the  $\text{V}_{\text{Cu}}$  gives rise to an acceptor level with activation energy of 0.02 eV. In this composition range, i.e., the Cu-poor, Zn-rich and S-rich region, high-efficiency CZTS thin-film solar cells were achieved [39]. It is therefore assumed that the dominant point defects are related to  $\text{V}_{\text{Cu}}$  and  $\text{Cu}_{\text{Zn}}$ , resulting in p-type conductivity of quaternary crystal.

### 6.3.3 Electrical Properties

Regarding the electrical properties of the single crystal, we measured the temperature dependence of the Hall effect. Hall effect measurements were carried out at 20–300 K under a 0.54 T magnetic field in the Van der Pauw geometry. The compositions of CZTS





**Figure 6.10** Composition of CZTS single crystal estimated by EPMA along the growth direction

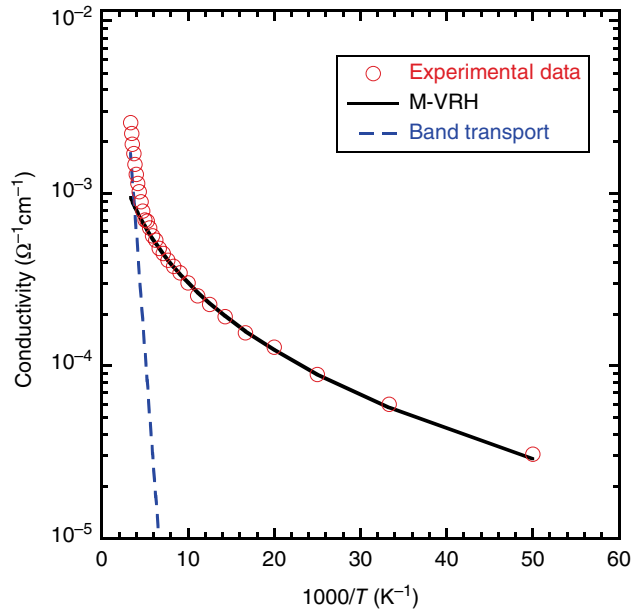
**Table 6.2** The detailed composition of CZTS single crystal

Distance from top (mm)	Cu (at%)	Zn (at%)	Sn (at%)	S (at%)	Cu/(Zn+Sn)	Zn/Sn
5.0	23.94	12.87	12.05	51.20	0.96	1.07
10.0	24.21	13.00	11.46	51.40	0.99	1.14
15.0	24.11	12.99	12.12	50.81	0.96	1.07
20.0	24.70	12.85	12.22	50.32	0.99	1.05

bulk single crystals were analyzed by using EPMA and were found to be within a Cu-poor and Zn-rich range, which is known to lead to high-efficiency CZTS solar cells. The sample dimensions were  $5 \times 5 \times 0.5$  mm and the sample was mechanically polished with  $0.01 \mu\text{m}$   $\text{Al}_2\text{O}_3$  powder. Multiple Au contacts of diameter 1 mm were deposited by evaporation onto the corners of each CZTS bulk single crystal to a thickness of 200 nm.

Based on the Hall effect measurement at 300 K, the carrier concentration, hole mobility, and resistivity of the single crystal are estimated as listed in Table 6.2. The hole carrier concentration  $p$  is equal to  $10^{16}$ – $10^{17} \text{ cm}^{-3}$ , the hole mobility  $\mu_h$  is  $15$ – $35 \text{ cm}^2 \text{ V}^{-1} \text{ s}^{-1}$ , and the resistivity  $\rho \sim 10^2 \Omega \text{ cm}$ . The high-quality CZTS single crystal was most likely obtained because the hole mobility is comparable to that of a p-CuInSe<sub>2</sub> single crystal [40].

The temperature dependence of the Hall effect measurement was performed in order to investigate more detailed electrical properties of CZTS single crystals. The temperature



**Figure 6.11** Temperature dependence of the conductivity in Cu-poor, Zn-rich composition sample ( $[Cu]/([Zn]+[Sn])=0.90$ ,  $[Zn]/[Sn]=1.41$ )

**Table 6.3** Parameter to fit the temperature-dependent conductivity in CZTS single crystal

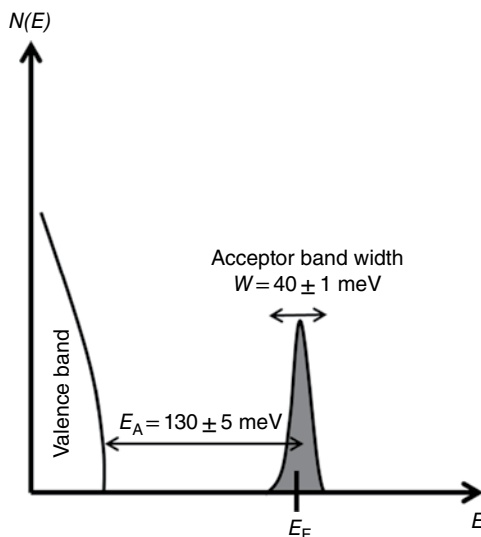
M-VRH (Defect transport)			Band transport	
$\sigma_H$	$T_0$ ( $K \times 10^4$ )	$W$ (meV)	$\sigma_B$	$E_A$ (meV)
0.03	5.08	40.9	0.32	135.3

dependence of the conductivity  $\sigma$  is shown in Figure 6.11 for a CZTS single-crystal sample having a slightly Cu-poor and Zn-rich composition. The conductivity of CZTS is defined as [41]:

$$\sigma(T) = \sigma_H \exp\left(-\left(\frac{T_0}{T}\right)^{1/4}\right) + \sigma_B \exp\left(-\frac{E_A}{k_B T}\right). \quad (6.2)$$

where  $\sigma_H$  and  $\sigma_B$  are pre-factor constants,  $k_B$  is the Boltzmann constant,  $T_0$  is the Mott characteristic temperature, and  $E_A$  is the activation energy associated with thermal conduction process. The fitted parameters are listed in Table 6.3. The first term of Equation (6.2) describes Mott variable range hopping (M-VRH) in three dimensions; the second term may arise from either nearest-neighbor hopping or freeze-out of band carriers to dopants.

At a low temperature below the onset temperature  $T_M=100$  K, the M-VRH is dominant because all samples clearly indicated a linear regime in  $\log \sigma$  with  $T^{-1/4}$  [41]. For  $T_M > 100$  K, the typical thermally activated behavior is dominant because the data were fitted to and in good agreement with a simple Arrhenius plot. The absence of shallow acceptor-like native



**Figure 6.12** Density of states *v.* energy of the acceptor band;  $E_F$  is the Fermi level

defects predicted by the theories discussed previously suggests that freeze-out of holes from the valence band to the native acceptor levels may be responsible. Arrhenius analysis indicated a common thermal activation energy  $E_A = 130 \pm 5 \text{ meV}$  in all samples. The experimentally obtained thermal activation energy  $E_A$  is in good agreement with the calculated transition energy of 120 meV above the valence band maximum for  $\text{Cu}_{\text{Zn}}$  point defects [10]. The acceptor band width parameter  $W$  is defined [42]:

$$W = k_B \left( T_M^3 T_0 \right)^{1/4}. \quad (6.3)$$

We determined the acceptor band width  $W$  at  $T = 100 \text{ K}$  to be  $W = 40 \pm 1 \text{ meV}$ . The simple image of the acceptor band is shown in Figure 6.12 by using the conduction parameters of CZTS given the above [43]. The center level of the acceptor band is 132 meV above the valence band maximum, and is of width 40 meV.

## 6.4 Conclusion

We have described the bulk single-crystal growth of CZTS compound. The THM technique can avoid a peritectic reaction and a solid-state transition, generally encountered during growth process from stoichiometric melt. In order to study CZTS single-crystal growth by THM using a Sn solvent, the phase diagram of the CZTS-Sn pseudobinary system was determined. There exists the miscibility gap in the liquid phase. The Sn solutions saturated with CZTS solutes below c. 30 mol% are separated into two phases (a CZTS phase and a Sn phase). Between 30 and 60 mol%, a CZTS phase and a  $\text{SnS}_x$  phase co-exist. In the CZTS-Sn system, solids in equilibrium with the liquids at a temperature (or “at”)

> 820°C are single-phase CZTS compounds. A CZTS single crystal was grown from an  $X=70$  mol% Sn solution (liquid temperature 850°C) at 900°C by THM, in which the Sn solution saturated with CZTS was a single phase. The powder XRD patterns of the crystals corresponded to the ICDD data. No secondary phase could be observed from Raman and XRD spectra. The results showed that good-quality single-phase CZTS single crystals could be obtained by THM growth. The composition of CZTS single crystals was homogeneous and the stoichiometric ratio of CZTS was found to be slightly Cu-poor, Zn-rich and S-rich. It is therefore assumed that the dominant point defects are related to  $V_{\text{Cu}}$  and  $\text{Cu}_{\text{Zn}}$ , which lead to p-type conduction. On the basis of the CZTS-Sn pseudobinary phase diagram, we determined that suitable THM growth conditions for CZTS single crystals were a Sn solution with  $X=70$  mol% and growth temperature of 900°C. Both hopping through defect states and band transport operate in parallel, with M-VRH dominating at low temperatures and thermal activation from acceptor states into the valence band dominating at higher temperatures. The center level of the acceptor band is 132 meV above the valence band maximum, and is of width 40 meV.

## Acknowledgements

The authors would like to thank Professor Hideto Miyake of Mie University and Professor Tomoyasu Taniyama and Dr Hiroki Taniguchi of Tokyo Institute of Technology for helpful discussions. The first author is supported by JSPS Research Fellowships for Young Scientists.

## References

- [1] Jackson, P., Hariskos, D., Wuerz, R., Wischmann, W., & Powalla, M., (2014) Compositional investigation of potassium doped  $\text{Cu}(\text{In}, \text{Ga})\text{Se}_2$  solar cells with efficiencies up to 20.8%. *Physica Status Solidi RRL*, **8**, 219–222.
- [2] Ito, K. & Nakazawa, T. (1988) Electrical and optical properties of stannite-type quaternary semiconductor thin films. *Japanese Journal of Applied Physics*, **27**, 2094–2097.
- [3] Katagiri, H., Ishigaki, N., Ishida, T. & Saito, K. (2001) Characterization of  $\text{Cu}_2\text{ZnSnS}_4$  thin films prepared by vapor phase sulfurization. *Japanese Journal of Applied Physics*, **40**, 500–504.
- [4] Katagiri, H., Saitoh, K., Washio, T., Shinohara, H., Kurumadani, T. & Miyazima, S. (2001) Development of thin film solar cell based on  $\text{Cu}_2\text{ZnSnS}_4$  thin films. *Solar Energy Materials and Solar Cells*, **65**, 141–148.
- [5] Persson, C. (2010) Electronic and optical properties of  $\text{Cu}_2\text{ZnSnS}_4$  and  $\text{Cu}_2\text{ZnSnSe}_4$ . *Journal of Applied Physics*, **107**, 053710–8.
- [6] Shin, B., Gunawan, O., Zhu, Y., Bojarczuk, N. A., Chey, S. J. & Guha, S. (2013) Thin film solar cell with 8.4% power conversion efficiency using an earth-abundant  $\text{Cu}_2\text{ZnSnS}_4$  absorber. *Progress in Photovoltaics: Research and Applications*, **21**, 72–76.
- [7] Wang, W., Winkler, M.T., Gunawan, O., Gokmen, T., Todorov, T.K., Zhu, Y. & Mitzi, D.B. (2014) Device characteristics of CZTSSe thin-film solar cells with 12.6% efficiency. *Advanced Energy Materials*, **4**, 1301465 1–5.
- [8] Nagoya, A., Asahi, R., Wahl, R. & Kresse, G. (2010) Defect formation and phase stability of  $\text{Cu}_2\text{ZnSnS}_4$  photovoltaic material. *Physical Review B*, **81**, 113202 1–4.
- [9] Chen, S., Walsh, A., Luo, Y., Yang, J. H., Gong, X. G. & Wei, S. H. (2010) Wurtzite-derived polytypes of kesterite and stannite quaternary chalcogenide semiconductors. *Physical Review B*, **82**, 195203 1–8.

- [10] Chen, S., Yang, J. H., Gong, X. G., Walsh, A. & Wei, S. H. (2010) Intrinsic point defects and complexes in the quaternary kesterite semiconductor  $\text{Cu}_2\text{ZnSnS}_4$ . *Physical Review B*, **81**, 245204 1–10.
- [11] Tanaka, K., Moritake, N. & Uchiki, H. (2007) Preparation of  $\text{Cu}_2\text{ZnSnS}_4$  thin films by sulfurizing sol-gel deposited precursors. *Solar Energy Materials and Solar Cells*, **91**, 1199–1201.
- [12] Miyamoto, Y., Tanaka, K., Oonuki, M., Moritake, N. & Uchiki, H. (2008) Optical properties of  $\text{Cu}_2\text{ZnSnS}_4$  thin films prepared by sol-gel and sulfurization method. *Japanese Journal of Applied Physics*, **47**, 596–597.
- [13] Altosaar, M., Raudoja, J., Timmo, K., Danilson, M., Grossberg, M., Krustok, J. & Mellikov, E. (2008)  $\text{Cu}_2\text{Zn}_{1-x}\text{Cd}_x\text{Sn}(\text{Se}_{1-y}\text{S}_y)_4$  solid solutions as absorber materials for solar cells. *Physica Status Solidi*, **205**, 167–170.
- [14] Fernandes, P. A., Salomé, P. M. P. & Gunha, A. F. (2009) Growth and Raman scattering characterization of  $\text{Cu}_2\text{ZnSnS}_4$  thin films. *Thin Solid Films*, **517**, 2519–2523.
- [15] Leitão, J. P., Santos, N. M., Fernandes, P. A., Salomé, P. M. P., da Cunha, A. F., González, J. C., Ribeiro, G. M. & Matinaga, F. M. (2011) Photoluminescence and electrical study of fluctuating potentials in  $\text{Cu}_2\text{ZnSnS}_4$ -based thin films. *Physical Review B*, **84**, 024120–8.
- [16] Rogacheva, E. I. (1996) Phase relations in chalcopyrite materials. *Crystal Research and Technology*, **31**, S 1–10.
- [17] Mikkelsen, J. C. (1981) Ternary phase relations of the chalcopyrite compound  $\text{CuGaSe}_2$ . *Journal of Electronic Materials*, **10**, 541–558.
- [18] Brandt, G. & Krämer, V. (1976) Phase investigations in the silver-gallium-sulphur system. *Materials Research Bulletin*, **11**, 1381–1388.
- [19] Mikkelsen Jr., J. C. (1977)  $\text{Ag}_2\text{Se-Ga}_2\text{Se}_3$  pseudobinary phase diagram. *Materials Research Bulletin*, **12**, 497–502.
- [20] Olekseyuk, I. D., Dudchak, I. V. & Piskach, L. V. (2004) Phase equilibria in the  $\text{Cu}_2\text{S-ZnS-SnS}_2$  system. *Journal of Alloys and Compounds*, **368**, 135–143.
- [21] Baldus, A. & Benz, K. W. (1993) Melt and metallic solution crystal growth of  $\text{CuInSe}_2$ . *Journal of Crystal Growth*, **130**, 37–44.
- [22] Miyake, H., Ohtake, H. & Sugiyama, K. (1995) Solution growth of  $\text{CuInSe}_2$  from  $\text{CuSe}$  solutions. *Journal of Crystal Growth*, **156**, 404–409.
- [23] Hsu, H. J., Yang, M. H., Tang, R. S., Hsu, T. M. & Hwang, H. L. (1984) A novel method to grow large  $\text{CuInS}_2$  single crystals. *Journal of Crystal Growth*, **70**, 427–432.
- [24] Mandel, L., Tomlinson, R. D. & Hampshire, M. J. (1976) The fabrication and doping of single crystals of  $\text{CuGaSe}_2$ . *Journal of Crystal Growth*, **36**, 152–156.
- [25] Sugiyama, K., Kato, H. & Miyake, H. (1989) Growth of  $\text{CuGaSe}_2$  single crystals by the traveling heater method. *Journal of Crystal Growth*, **98**, 610–616.
- [26] Miyake, H. & Sugiyama, K. (1990) Growth of  $\text{CuGaS}_2$  single crystals by traveling heater method. *Japanese Journal of Applied Physics*, **29**, L1859–L1861.
- [27] Miyake, H., Hata, M. & Sugiyama, K. (1994) Solution growth of  $\text{CuGaS}_2$  and  $\text{CuGaSe}_2$  using  $\text{CuI}$  solvent. *Journal of Crystal Growth*, **130**, 383–388.
- [28] Höbner, H. J., Kühn, G. & Tempel, A. (1981) Crystallization of  $\text{CuGaS}_2$  from  $\text{Pb}$  and  $\text{Sn}$  solutions. *Journal of Crystal Growth*, **53**, 451–457.
- [29] Post, E. & Krämer, V. (1993) Crystal growth of  $\text{AgGaS}_2$  by the Bridgman-Stockbarger and travelling heater methods. *Journal of Crystal Growth*, **129**, 485–490.
- [30] Miyake, H., Hayashi, T. & Sugiyama, K. (1993) Preparation of  $\text{CuGa}_x\text{In}_{1-x}\text{S}_2$  alloys from  $\text{In}$  solutions. *Journal of Crystal Growth*, **134**, 174–180.
- [31] Fearheiley, M. L., Dietz, N., Birkholz, M. & Höpfner, C. (1991) Phase relations in the system  $\text{In-CuInS}_2$ . *Journal of Electronic Materials*, **20**, 175–177.
- [32] Nagaoka, A., Yoshino, K., Taniguchi, H., Taniyama, T. & Miyake, H. (2012) Preparation of  $\text{Cu}_2\text{ZnSnS}_4$  single crystals from  $\text{Sn}$  solutions. *Journal of Crystal Growth*, **341**, 38–41.
- [33] Nagaoka, A., Yoshino, K., Taniguchi, H., Taniyama, T., Kakimoto, K. & Miyake, H. (2013) Growth and characterization of  $\text{Cu}_2\text{ZnSnS}_4$  single crystals. *Physica Status Solidi (A)*, **210**, 1328–1331.
- [34] Nagaoka, A., Yoshino, K., Taniguchi, H., Taniyama, T. & Miyake, H. (2011) Growth of  $\text{Cu}_2\text{ZnSnS}_4$  single crystals by traveling heater method. *Japanese Journal of Applied Physics*, **50**, 128001-1-2.

- [35] Wang, K., Gunawan, O., Todorov, T., Shin, B., Chey, S. J., Bojarczuk, N. A., Mtzi, D. & Guha, S. (2010) Thermally evaporated  $\text{Cu}_2\text{ZnSnS}_4$  solar cells. *Applied Physics Letters*, **97**, 143508-1-3.
- [36] Himmrich, M. & Haeuseler, H. (1991) Far infrared studies on stannite and wurtzstannite type compounds. *Spectrochimica Acta*, **47A**, 933–942.
- [37] Cheng, Y. C., Jin, C. Q., Gao, F., Wu, X. L., Zhong, W., Li, S. H. & Chu, P. K. (2009) Raman scattering study of zinc blende and wurtzite  $\text{ZnS}$ . *Journal of Applied Physics*, **106**, 123505-5.
- [38] Maeda, T., Nakamura, S. & Wada, T. (2011) First principles calculations of defect formation in In-free photovoltaic semiconductors  $\text{Cu}_2\text{ZnSnS}_4$  and  $\text{Cu}_2\text{ZnSnSe}_4$ . *Japanese Journal of Applied Physics*, **50**, 04DP07–6.
- [39] Katagiri, H., Jimbo, K., Tahara, M., Araki, H. & Oishi, K. (2009) The influence of the composition ratio on CZTS-based thin film solar cells. *Materials Research Society Symposium Proceedings*, **1165**, 1165-M04-01.
- [40] Irie, T., Endo, S. & Kimura, S. (1979) Electrical properties of p- and n-type  $\text{CuInSe}_2$  single crystals. *Japanese Journal of Applied Physics*, **18**, 1303–1310.
- [41] Mott, N. F. & Davis, E. A. (1971) *Electronic Processes in Non-crystalline Materials*. Clarendon, Oxford.
- [42] Shklovskii, B. I. & Efros, A. L. (1984) *Electronic Properties of Doped Semiconductors*. Springer, Berlin.
- [43] Nagaoka, A., Miyake, H., Taniyama, T., Kakimoto, K. & Yoshino, K. (2013) Correlation between intrinsic defects and electrical properties in the high-quality  $\text{Cu}_2\text{ZnSnS}_4$  single crystal. *Applied Physics Letters*, **103**, 112107 1–4.

# 7

## Physical Properties: Compiled Experimental Data

*Sadao Adachi*

*Division of Electronics and Informatics, Faculty of Science and Technology,  
Gunma University, Kiryu-shi, Gunma 376-8515, Japan*

### 7.1 Introduction

$\text{Cu}_2\text{-II-IV-VI}_4$  quaternary semiconductors have been of interest for many years because of their appearance as naturally occurring minerals and suitable band-gap energies for applications in various solar energy converters (e.g. solar cells [1] and photocatalytic devices for  $\text{H}_2$  evolution [2]). Knowledge of the lattice parameters of semiconductors is very important for growing high-quality heteroepitaxial layers. Provided that minority carrier diffusion lengths exceed typical absorption depths,  $p$ - $n$  or Schottky-barrier junctions make efficient solar energy converters with high collection efficiency, where recombination at the surface is the dominant loss process [3]. If losses in the layer close to the front surface are greater, it is advantageous to replace the emitter layer with a wider band-gap material. Surface recombination can be reduced by introducing window material with a good interface quality to reflect minority carriers away from the surface.

Melting points are one of the most important thermophysical parameters. Thermal conductivities are necessary for the design and analysis of various thermoelectric devices (e.g. Seebeck and Peltier devices). The Raman scattering technique has been popular for detecting some spurious phases in  $\text{Cu}_2\text{-II-IV-VI}_4$  semiconductors. The spurious phases such as  $\text{Cu}_2\text{S}$  and  $\text{Cu}_2\text{Se}$  are not easy to observe by the X-ray diffraction (XRD) method. These

spurious materials are sometimes contained in  $\text{Cu}_2\text{ZnSnS}_4$  (CZTS) [4] and  $\text{Cu}_2\text{ZnSnSe}_4$  (CZTSe) [5]. Information on Raman scattering is therefore required to perform compositional analysis on  $\text{Cu}_2\text{-II-IV-VI}_4$  semiconductors.

The optical response of semiconductors is strongly connected with their electronic energy-band structure. The most direct and perhaps the simplest method for probing the lowest direct and/or indirect energy gaps in semiconductors is to measure their optical absorption spectra. For this purpose, many optical absorption measurements have been performed on  $\text{Cu}_2\text{-II-IV-VI}_4$  semiconductors. Carrier diffusion lengths are shorter, so the solar cell material needs to be a strong optical absorber. Spectroscopic ellipsometry (SE) is an excellent technique for investigating the optical constants of solids. This technique has recently been applied to some of the  $\text{Cu}_2\text{-II-IV-VI}_4$  semiconductors over a wide spectral range [6–8].

In the case of very short diffusion lengths, it may be necessary to use extended built-in electric fields to aid carrier collection. This may be the case for  $\text{Cu}_2\text{-II-IV-VI}_4$  solar cells, where *p-i-n* or MIS (metal–insulator–semiconductor) structures are preferred. At this stage, high resistive  $\text{Cu}_2\text{-II-IV-VI}_4$  layers ( $10^2\text{--}10^4\ \Omega\ \text{cm}$ ) have been demonstrated to provide good conversion efficiency [9].

In this chapter, a set of the material and semiconducting properties of  $\text{Cu}_2\text{-II-IV-VI}_4$  semiconductors are considered. They can be classified into six groups: (1) structural properties; (2) thermal properties; (3) mechanical and lattice vibrational properties; (4) electronic energy-band structures; (5) optical properties; and (6) carrier transport properties. For almost every parameter given in this chapter, different sources give somewhat different values. In this case, we chose values which we believe to be more reliable or we obtain those values by the use of averaging.

## 7.2 Structural Properties

### 7.2.1 Crystal Structure

Figure 7.1 summarizes the crystal symmetry classes for easily or normally grown  $\text{Cu}_2\text{-II-IV-VI}_4$  semiconductors. They crystallize in the tetragonal stannite or kesterite structure or in the orthorhombic wurtz–stannite structure. The stannite and kesterite structures are closely related, but assigned to different space groups –  $\bar{I}4_2m$  (stannite) and  $\bar{I}4$  (kesterite) – due to a different distribution of the cations Cu and II. Each anion (VI) in both structures is surrounded by two Cu, one II, and one IV and every cation is tetrahedrally coordinated by VI.

The stannite and kesterite structures are body-centered tetragonal with  $c \sim 2a$  (pseudocubic). It is very difficult to distinguish these structures. This is due to the fact that the X-ray diffraction (XRD) patterns of these structures differ only slightly in the splitting of high-order peaks, such as (220)/(204) and (116)/(312) which resulted from a slightly different tetragonal distortion ( $c/2a$ ) [10].

The orthorhombic wurtz–stannite cell is a superstructure of the wurtzite cell and belongs to the space group of  $\text{Pmn}2_1$ . As in the stannite and kesterite structures, each anion (VI) in the wurtz–stannite lattice is surrounded by two Cu, one II and one IV and every cation is tetrahedrally coordinated by VI.



			S	Se	Te
Cu <sub>2</sub> -II-IV-VI <sub>4</sub>	Zn	Si	■	■	□
		Ge	▧	□	□
		Sn	□	□	□
	Cd	Si	■	■	□
		Ge	■	▧	□
		Sn	□	□	□
	Hg	Si	■	■	□
		Ge	▧	□	□
		Sn	□	□	□

: Tetragonal  
 : Orthorhombic  
 : Tetragonal or orthorhombic

**Figure 7.1** Summary of easily or normally grown crystal structure for Cu<sub>2</sub>-II-IV-VI<sub>4</sub> semiconductors

### 7.2.2 Lattice Constant and Crystal Density

The lattice in the tetragonal symmetry is defined by the two length parameters  $a$  and  $c$ , and in the orthorhombic symmetry by the three length parameters  $a$ ,  $b$  and  $c$ . In Table 7.1, we list the crystal structure, lattice constant and X-ray crystal density at 300 K for a number of Cu<sub>2</sub>-II-IV-VI<sub>4</sub> semiconductors. These values were experimentally determined.

CZTS and CZTSe usually crystallize in the kesterite and stannite structures, respectively. However, several authors reported that CZTSe can crystallize in the kesterite structure [11, 12]. As understood from Table 7.1, Cu<sub>2</sub>ZnGeS<sub>4</sub>, Cu<sub>2</sub>CdGeSe<sub>4</sub>, and Cu<sub>2</sub>HgGeS<sub>4</sub> crystallize both in the tetragonal and orthorhombic structures. They are observed to be crystallized in the stannite structure at low temperatures and in the wurtz-stannite structure at high temperatures [13–15]. The structural phase transition from the low-temperature modification (stannite) to the high-temperature modification (wurtz-stannite) occurred in Cu<sub>2</sub>CdGeSe<sub>4</sub> at 605°C [16]. Similarly, the tetragonal kesterite → cubic sphalerite phase transition occurred in CZTS at 875°C [17].

Figure 7.2 plots the unit-cell volume  $V_c$  versus molecular weight ( $M$ ) data for Cu<sub>2</sub>-II-IV-VI<sub>4</sub> semiconductors. Here, the unit-cell volume is defined as  $V_c = a^2c$  and  $V_c = abc$  for the tetragonal and orthorhombic structures, respectively. From Figure 7.2, we obtain:

$$V_c = 3.19 \times 10^{-4} M + 0.168 \quad (7.1)$$

where  $M$  is in amu and  $V_c$  is in nm<sup>3</sup>. The lattice constants in alloy semiconductors are known to obey the Vegard rule very well. Figure 7.3 plots the lattice constants  $a$  and  $c$  versus  $x$  data for the Cu<sub>2</sub>ZnGe(S<sub>*x*</sub>Se<sub>*1-x*</sub>)<sub>4</sub> alloy crystallizing in the stannite structure. The same data but those crystallizing in the wurtz-stannite structure are shown in Figure 7.4. The experimental data are taken from Doverspike *et al.* [13]. These data indicate that the Vegard rule is a good approximation for the estimation of lattice parameters in the Cu<sub>2</sub>ZnGe(S<sub>*x*</sub>Se<sub>*1-x*</sub>)<sub>4</sub> alloy, regardless of the crystal structure. The same results have also been obtained for Cu<sub>2</sub>ZnSn(S<sub>*x*</sub>Se<sub>*1-x*</sub>)<sub>4</sub> and Cu<sub>2</sub>CdGe(S<sub>*x*</sub>Se<sub>*1-x*</sub>)<sub>4</sub> alloys [18, 19].

**Table 7.1** Crystal structure, lattice constant and X-ray crystal density for a number of  $\text{Cu}_2\text{-II-IV-VI}_4$  semiconductors at 300 K. o: orthorhombic ( $\text{Pmn}2_1$ ); t (s): tetragonal (stannite,  $I4_2m$ ); t (k): tetragonal (kesterite,  $I\bar{4}$ )

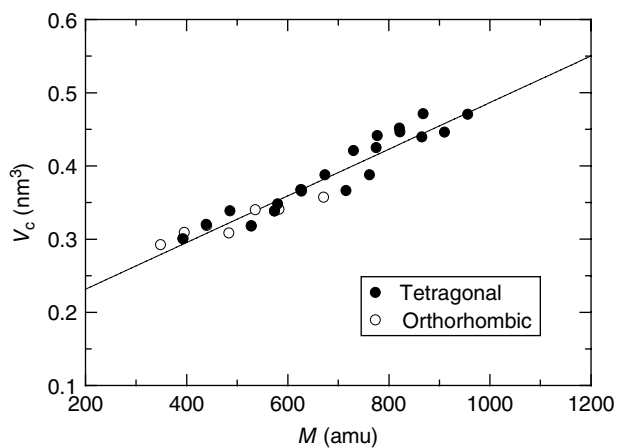
Material	Crystal structure	Lattice constant (nm)			$g$ ( $\text{g cm}^{-3}$ )
		$a$	$b$	$c$	
$\text{Cu}_2\text{ZnSiS}_4$	o	0.7436	0.6398	0.6137	3.968
$\text{Cu}_2\text{ZnSiSe}_4$	o	0.7833	0.6726	0.6450	5.242
$\text{Cu}_2\text{ZnSiTe}_4$	t (s)	0.5972		1.1797	5.770
$\text{Cu}_2\text{ZnGeS}_4$	t (s)	0.5342		1.0513	4.354
	o	0.7507	0.6473	0.6186	4.346
$\text{Cu}_2\text{ZnGeSe}_4$	t (s)	0.5610		1.1047	5.549
$\text{Cu}_2\text{ZnGeTe}_4$	t (s)	0.5977		1.1883	6.067
CZTS	t (k)	0.5430		1.0845	4.564
CZTSe	t (s)	0.5688		1.1341	5.675
$\text{Cu}_2\text{ZnSnTe}_4$	t (s)	0.6088		1.2180	6.044
$\text{Cu}_2\text{CdSiS}_4$	o	0.7606	0.6488	0.6256	4.258
$\text{Cu}_2\text{CdSiSe}_4$	o	0.7860	0.6708	0.6458	5.691
$\text{Cu}_2\text{CdSiTe}_4$	t (s)	0.6110		1.1811	5.860
$\text{Cu}_2\text{CdGeS}_4$	o	0.7704	0.6555	0.6303	4.595
$\text{Cu}_2\text{CdGeSe}_4$	t (s)	0.5749		1.1056	5.707
	o	0.8082	0.6880	0.6596	5.686
$\text{Cu}_2\text{CdGeTe}_4$	t (s)	0.6121		1.1913	6.120
$\text{Cu}_2\text{CdSnS}_4$	t (s)	0.5587		1.0833	4.778
$\text{Cu}_2\text{CdSnSe}_4$	t (s)	0.5831		1.1394	5.778
$\text{Cu}_2\text{CdSnTe}_4$	t (s)	0.6198		1.2256	6.127
$\text{Cu}_2\text{HgSiS}_4$	o	0.7661	0.6501	0.6186	5.218
$\text{Cu}_2\text{HgSiSe}_4$	o	0.7968	0.6818	0.6571	6.248
$\text{Cu}_2\text{HgSiTe}_4$	t (s)	0.6092		1.1831	6.551
$\text{Cu}_2\text{HgGeS}_4$	t (s)	0.5487		1.0543	5.530
	o	0.7683	0.6544	0.6318	5.526
$\text{Cu}_2\text{HgGeSe}_4$	t (s)	0.5745		1.1093	6.496
$\text{Cu}_2\text{HgGeTe}_4$	t (s)	0.6114		1.1928	6.783
$\text{Cu}_2\text{HgSnS}_4$	t (s)	0.5576		1.0871	5.646
$\text{Cu}_2\text{HgSnSe}_4$	t (s)	0.5827		1.1415	6.531
$\text{Cu}_2\text{HgSnTe}_4$	t (s)	0.6191		1.2263	6.760

## 7.3 Thermal Properties

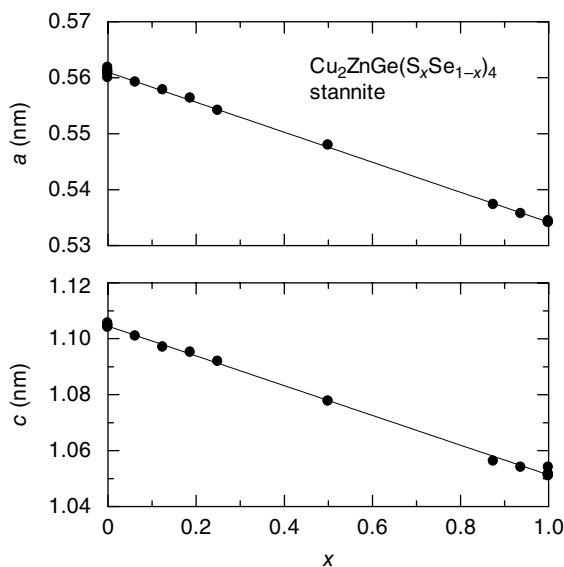
### 7.3.1 Melting Point

We list in Table 7.2 the melting point  $T_m$  for a number of  $\text{Cu}_2\text{-II-IV-VI}_4$  semiconductors at normal pressure. The experimental data were gathered from various sources. In Table 7.2,  $\text{Cu}_2\text{ZnSiS}_4$  has the highest  $T_m$  value 1396 K, which is much lower than that of Si (1687 K) but is slightly higher than that of CdTe (1365 K) [20]. Figure 7.5 also plots the melting point  $T_m$  versus atomic mass  $M$  data for these semiconductors. The solid line represents the least-squares fit with the following relation:

$$T_m = 1752 - 1.065M \quad (7.2)$$

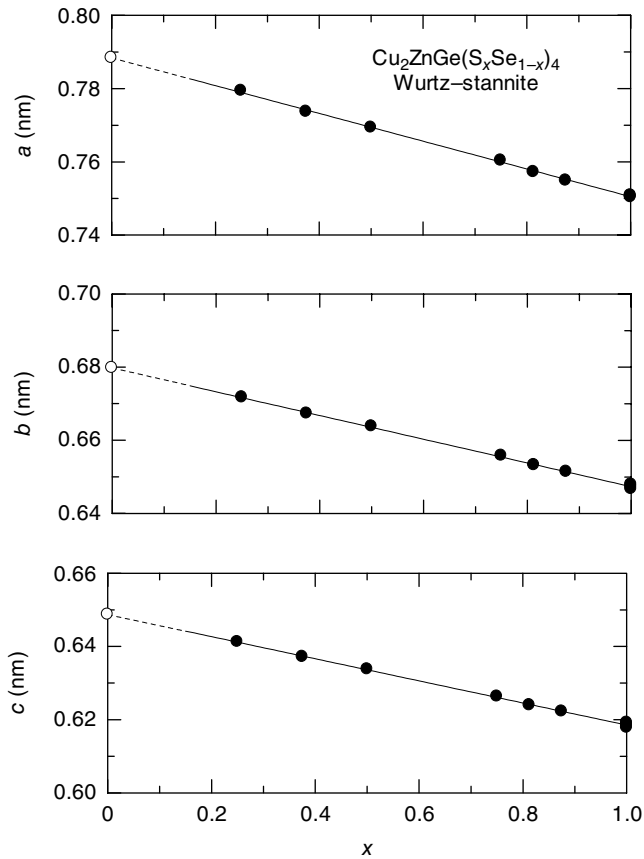


**Figure 7.2** Effective unit-cell volume  $V_c$  versus molecular weight  $M$  for  $\text{Cu}_2\text{-II-IV-VI}_4$  semiconductors. The solid line represents the calculated result using Equation (7.1)



**Figure 7.3** Lattice constants,  $a$  and  $c$ , versus composition  $x$  for  $\text{Cu}_2\text{ZnGe}(\text{S}_x\text{Se}_{1-x})_4$  alloy crystallizing in the stannite structure. The experimental data are taken from Doverspike et al. [13]

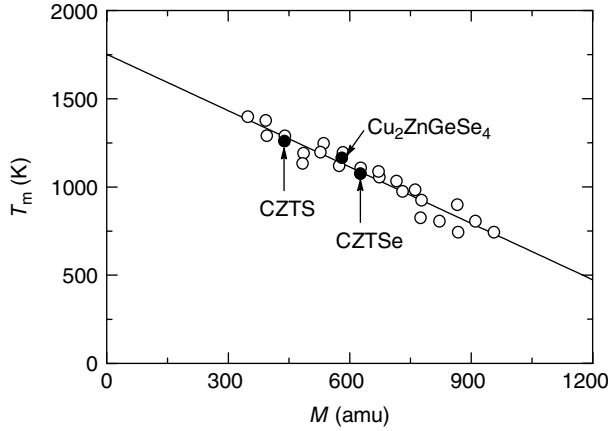
where  $T_m$  is in degrees Kelvin. The higher melting point is observed to reflect lower atomic mass, that is, shorter interatomic bond length (see Fig. 7.2) in the  $\text{Cu}_2\text{-II-IV-VI}_4$  chalcogenide system.



**Figure 7.4** Lattice constants  $a$ ,  $b$ , and  $c$ , versus composition  $x$  for  $\text{Cu}_2\text{ZnGe}(\text{S}_x\text{Se}_{1-x})_4$  alloy crystallizing in the wurtz-stannite structure. The experimental data are taken from Doverspike et al. [13]

**Table 7.2** Melting point and thermal conductivity  $\kappa$  (at 300 K) for a number of  $\text{Cu}_2\text{-II-IV-VI}_4$  semiconductors

Material	Melting point (K)	$\kappa$ ( $\text{W m}^{-1} \text{K}^{-1}$ )	Material	Melting point (K)	$\kappa$ ( $\text{W m}^{-1} \text{K}^{-1}$ )
$\text{Cu}_2\text{ZnSiS}_4$	1396		$\text{Cu}_2\text{CdGeTe}_4$	805	
$\text{Cu}_2\text{ZnSiSe}_4$	1246		$\text{Cu}_2\text{CdSnS}_4$	1190	
$\text{Cu}_2\text{ZnSiTe}_4$	973		$\text{Cu}_2\text{CdSnSe}_4$	1054	2.79 [23]
$\text{Cu}_2\text{ZnGeS}_4$	1376		$\text{Cu}_2\text{CdSnTe}_4$	743	
$\text{Cu}_2\text{ZnGeSe}_4$	1163	3.21 [25]	$\text{Cu}_2\text{HgSiS}_4$	1132	
$\text{Cu}_2\text{ZnGeTe}_4$	823		$\text{Cu}_2\text{HgSiSe}_4$	1086	
CZTS	1259	4.72 [22]	$\text{Cu}_2\text{HgSiTe}_4$	898	
CZTSe	1074	4.26 [22]	$\text{Cu}_2\text{HgGeS}_4$	1195	
$\text{Cu}_2\text{CdSiS}_4$	1289		$\text{Cu}_2\text{HgGeSe}_4$	1032	
$\text{Cu}_2\text{CdSiSe}_4$	1194		$\text{Cu}_2\text{HgGeTe}_4$	805	
$\text{Cu}_2\text{CdSiTe}_4$	923		$\text{Cu}_2\text{HgSnS}_4$	1118	
$\text{Cu}_2\text{CdGeS}_4$	1288		$\text{Cu}_2\text{HgSnSe}_4$	983	
$\text{Cu}_2\text{CdGeSe}_4$	1107		$\text{Cu}_2\text{HgSnTe}_4$	743	



**Figure 7.5** Melting point  $T_m$  versus atomic mass  $M$  for  $\text{Cu}_2\text{-II-IV-VI}_4$  semiconductors. The solid line represents the calculated result using Equation (7.2)

### 7.3.2 Thermal Conductivity

Thermal conductivity  $\kappa$  or resistivity  $W (= \kappa^{-1})$  results from interactions between phonons and from the scattering of phonons by crystalline imperfections (lattice thermal conductivity) and also from interactions between phonons and electrons (electronic thermal conductivity). In the case of semiconductor alloys an additional contribution, which is the result of a random distribution of constituent atoms in sublattice sites, must be taken into consideration. In metals and doped semiconductors, the electronic thermal conductivity  $\kappa_e$  and electrical conductivity  $\sigma$  are related by the Wiedemann–Frantz–Lorenz law  $\kappa_e = L\sigma T$ , where  $L$  and  $T$  are the Lorenz number and lattice temperature, respectively.

Thermal conductivity in  $\text{Cu}_2\text{-II-IV-VI}_4$  semiconductors has been investigated theoretically [21] and experimentally [22–28]. Table 7.2 lists the experimental  $\kappa$  values determined at 300 K of several  $\text{Cu}_2\text{-II-IV-VI}_4$  semiconductors [22, 23, 25]. Figure 7.6 also plots the  $\kappa$  versus crystal density  $g$  data together with those for group-IV, III–V, and II–VI semiconductors [20]. The solid line shows the result of the least-squares fit as follows:

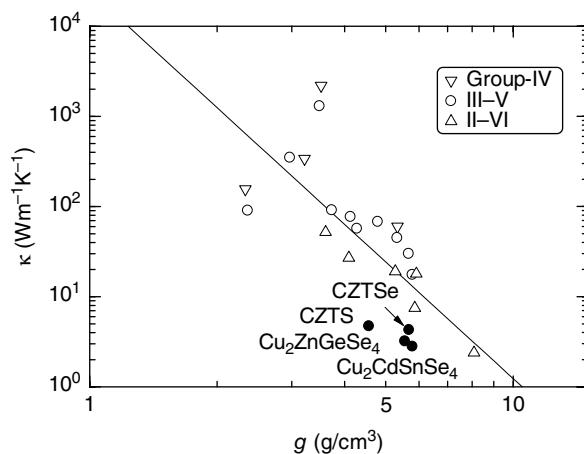
$$\kappa = 2.45 \times 10^4 g^{-4.3} \quad (7.3)$$

where  $g$  is in  $\text{g cm}^{-3}$  and  $\kappa$  is in  $\text{W m}^{-1} \text{K}^{-1}$ . One can easily expect that the smaller  $\kappa$  values of  $\text{Cu}_2\text{-II-IV-VI}_4$  come from their poorer crystalline qualities.

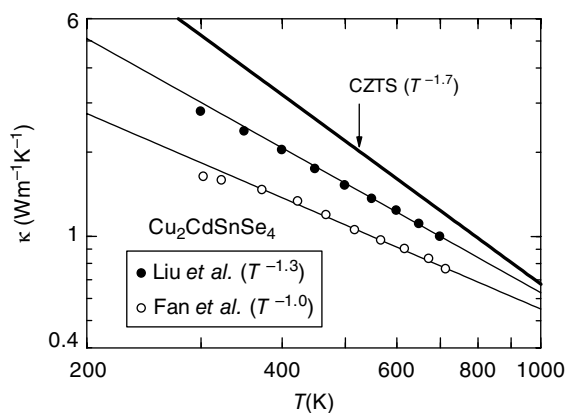
We show in Figure 7.7 the  $\kappa$  value as a function of temperature  $T$  for  $\text{Cu}_2\text{CdSnSe}_4$  measured by Liu *et al.* [23] and Fan *et al.* [24]. In most semiconductors, the thermal conductivity as a function of  $T$  can be expressed [20]:

$$\kappa(T) = AT^n. \quad (7.4)$$

The light solid lines in Figure 7.7 show the results of the least-squares fit using Equation (7.4). The experimental data of CZTS [22] were also analyzed using Equation (7.4) and shown in Figure 7.7 by the heavily solid line. The fit-determined  $A$  and  $n$  values for some  $\text{Cu}_2\text{-II-IV-VI}_4$  semiconductors are summarized in Table 7.3.



**Figure 7.6** Thermal conductivity  $\kappa$  versus crystal density  $g$  for  $\text{Cu}_2\text{-II-IV-VI}_4$  semiconductors, together with those for group-IV, III-V, and II-VI semiconductors. The solid line shows the calculated result using Equation (7.3)

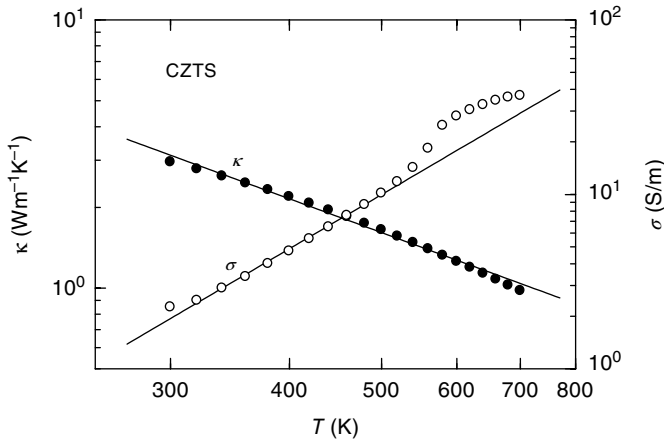


**Figure 7.7** Thermal conductivity  $\kappa$  as a function of temperature  $T$  for  $\text{Cu}_2\text{CdSnSe}_4$  measured by Liu *et al.* [23] and Fan *et al.* [24]. The solid lines represent the calculated results using Equation (7.4). The fitted result using Equation (7.4) for CZTS [22] is also shown by the heavy solid line

Figure 7.8 shows the temperature dependence of  $\kappa$  for CZTS measured by Yang *et al.* [26]. The solid line shows the result calculated using Equation (7.4) with  $A = 5200$  and  $n = -1.3$  ( $\kappa$  in  $\text{W m}^{-1} \text{K}^{-1}$ ). The temperature dependence of the electrical conductivity  $\sigma$  for this chalcogenide is also plotted in Figure 7.8 and can be written as  $\sigma(T) = 2.3 \times 10^{-8} T^{3.2} \text{ S m}^{-1}$ . The Wiedemann–Frantz–Lorenz law gives the expression  $\kappa_e(T)/\sigma(T) = LT$ ; however, the plots in Figure 7.8 yield  $\kappa_e(T)/\sigma(T) = 2.3 \times 10^{-11} T^{-4.5}$ . It can therefore be considered that the thermal conductivity of CZTS is characterized by the lattice thermal conduction, that is, it is determined by the scattering of phonons by crystalline imperfections and phonons (i.e. phonon–phonon scattering) but not by the phonon–electron scattering.

**Table 7.3** Empirical equation (Equation (7.4)) for the thermal conductivity  $\kappa$  as a function of temperature  $T$  for some  $\text{Cu}_2\text{-II-IV-VI}_4$  semiconductors ( $\kappa$  in  $\text{W m}^{-1} \text{K}^{-1}$ )

Material	$A$	$n$	$T$ (K)
CZTS [22]	85000	-1.7	300–700
CZTSe [22]	740	-0.9	300–700
$\text{Cu}_2\text{CdSnSe}_4$ [23]	5000	-1.3	300–700
$\text{Cu}_2\text{CdSnSe}_4$ [24]	550	-1.0	300–700



**Figure 7.8** Thermal conductivity  $\kappa$  and electrical conductivity  $\sigma$  versus temperature  $T$  for CZTS measured by Yang et al. [26]. The solid lines represent the results calculated using  $\kappa(T) = 5.2 \times 10^3 T^{-1.3} \text{ W m}^{-1} \text{K}^{-1}$  and  $\sigma(T) = 2.3 \times 10^{-8} T^{3.2} \text{ S m}^{-1}$

## 7.4 Mechanical and Lattice Dynamic Properties

### 7.4.1 Microhardness

To the best of our knowledge, no experimental data on the elastic properties of  $\text{Cu}_2\text{-II-IV-VI}_4$  semiconductors have been reported to date. However, we can find several experimental data on the microhardness of such chalcogenide semiconductors. The microhardness test has been used for a long time as a simple means of characterizing the mechanical behavior of solids. Table 7.4 lists the microhardness  $H$  determined for  $\text{Cu}_2\text{-II-IV-VI}_4$  semiconductors [29–34].

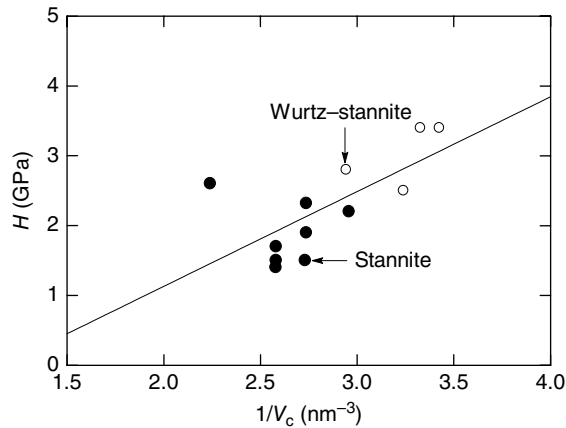
Figure 7.9 shows  $H$  (in GPa) versus inverse unit-cell volume ( $V_c^{-1}$  in  $\text{nm}^{-3}$ ) data for  $\text{Cu}_2\text{-II-IV-VI}_4$  semiconductors (see  $V_c$  in Fig. 7.2). It has been shown [20] that for some group-IV, III-V, and II-VI semiconductors the  $H$  versus  $V_c^{-1}$  plots exhibit a linear relationship. The solid line represents the least-squares fit with the relation:

$$H = 1.4 V_c^{-1} - 1.6. \quad (7.5)$$

The linear relationship between  $H$  and  $V_c^{-1}$  can also be recognized in Figure 7.9.

**Table 7.4** Microhardness of some  $\text{Cu}_2\text{-II-IV-VI}_4$  semiconductors at 300 K. w-s: wurtz-stannite; s: stannite; m: monoclinic

Material	Crystal structure	Microhardness (GPa)	Reference
$\text{Cu}_2\text{ZnSiS}_4$	w-s	3.4	[30]
$\text{Cu}_2\text{ZnSiSe}_4$	w-s	2.8	[30]
$\text{Cu}_2\text{ZnGeS}_4$	w-s	3.4	[30]
$\text{Cu}_2\text{CdSiS}_4$	w-s	2.5	[30]
$\text{Cu}_2\text{CdGeSe}_4$	s	2.32	[29]
	s	1.9	[32]
$\text{Cu}_2\text{CdGeTe}_4$	s	2.6	[33]
$\text{Cu}_2\text{CdSnS}_4$	s	2.2	[34]
$\text{Cu}_2\text{CdSnSe}_4$	s	1.5	[32]
	s	1.7	[34]
$\text{Cu}_2\text{CdSnTe}_4$	m	2.1	[34]
$\text{Cu}_2\text{HgGeSe}_4$	s	1.5	[31]
$\text{Cu}_2\text{HgSnSe}_4$	s	1.4	[31]



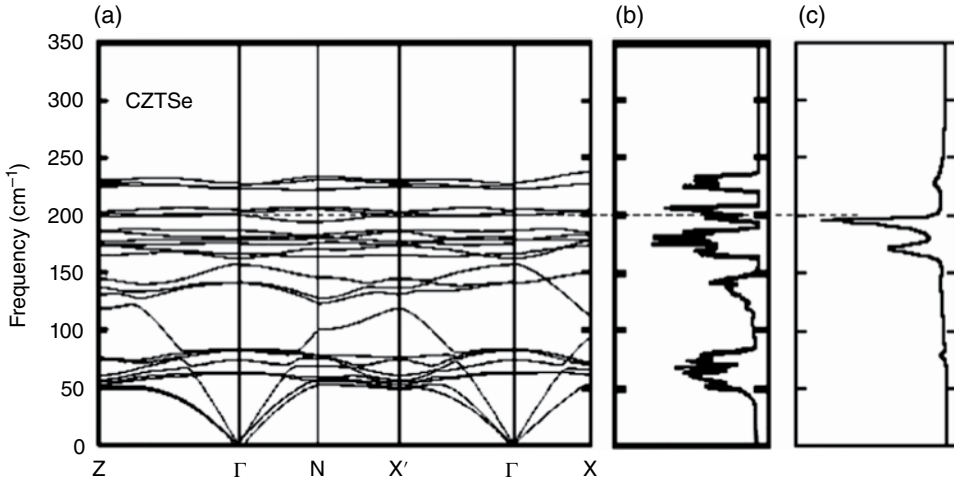
**Figure 7.9** Microhardness  $H$  versus inverse unit-cell volume ( $V_c^{-1}$ ) for  $\text{Cu}_2\text{-II-IV-VI}_4$  semiconductors. The stannite and wurtz-stannite data are represented by the solid and open circles, respectively. The solid line represents the calculated result using Equation (7.5)

### 7.4.2 Long-Wavelength Phonon Frequency

Due to the multinary nature of  $\text{Cu}_2\text{-II-IV-VI}_4$  semiconductors, there may coexist traces of secondary phases with fewer types of hetero-polar bonds. For example, we can expect secondary phases such as  $\text{Cu}_3\text{SnSe}_4$ ,  $\text{Cu}_2\text{SnSe}_3$ ,  $\text{Cu}_2\text{Se}$ ,  $\text{CuSe}$ ,  $\text{ZnSe}$ ,  $\text{SnSe}_2$ ,  $\text{SnSe}$  and elemental Se in CZTSe. This makes phase identification using XRD very difficult. To more exactly confirm secondary phases in  $\text{Cu}_2\text{-II-IV-VI}_4$  semiconductors, Raman scattering studies have been extensively performed.

Figures 7.10(a) and 10(b) show the phonon dispersion and density-of-states (DOS) curves along the principal symmetry directions of CZTSe, respectively. These curves were calculated using a density functional theory by Khare *et al.* [35]. The Raman spectrum measured at 300 K by Altosaar *et al.* [36] is also shown in Figure 7.10(c).





**Figure 7.10** (a) Phonon dispersion curve. (b) Phonon-DOS curve. (a) and (b) Reprinted with permission from [35]. Copyright 2012, AIP Publishing LLC. (c) Room-temperature Raman spectrum for CZTSe. Reproduced with permission from [36]. Copyright © 2008, John Wiley and Sons Ltd

The theoretical phonon-DOS curve increases when  $\nabla_{\mathbf{q}} \nu(\mathbf{q}) \rightarrow 0$  (critical points) for one of the various branches, and this happens predominantly when  $\mathbf{q}$  for that branch reaches a zone boundary, where  $\nu$  and  $\mathbf{q}$  represent the phonon frequency and wavenumber, respectively. In the primitive cell, if there are  $N$  different types of atoms either of differing mass or ordering in space,  $3N$  vibrational modes will result. Three of these branches, namely the acoustic branches, will disappear at the zone center  $\Gamma$ . The group analysis of stannite-type structure ( $N = 6$ ) at the zone center for the optical modes is represented:

$$\Gamma = 2A_1 + A_2 + 2B_1 + 4B_2 + 6E. \quad (7.6)$$

Among these vibrational modes, 14  $A_1$ ,  $B_1$ ,  $B_2$  and  $E$  modes are Raman active and 10  $B_2$  and  $E$  modes are IR active.

The  $A_1$  mode in CZTSe originates from the vibrations of the Se (VI) atom surrounded by the other atoms at rest in the lattice, and this mode is generally expected to be the dominant peak in the Raman spectra of stannite materials. Similarly, the Raman-active  $A$  ( $A_1$ ) mode is expected to be the dominant peak in the Raman spectra of kesterite and wurtz-stannite materials. In CZTSe, the  $A_1$ -mode peak is observed at c. 195  $\text{cm}^{-1}$  (see Fig. 7.10(c)).

Table 7.5 summarizes the optical phonon frequencies observed in the Raman spectra of some tetragonal  $\text{Cu}_2\text{-II-IV-S}_4$  and  $\text{Cu}_2\text{-II-IV-Se}_4$  semiconductors at 300 K [24, 37]. There have been many Raman data reported on CZTS and CZTSe. The values for these semiconductors listed in Table 7.5 are therefore obtained by averaging such experimental data. Table 7.6 also summarizes the Raman frequencies observed at 300 K in the wurtz-stannite semiconductors  $\text{Cu}_2\text{ZnSiS}_4$  and  $\text{Cu}_2\text{ZnSiSe}_4$ , together with their symmetry assignments. The experimental data are taken from Levchenko *et al.* [38]. The strongest Raman peaks ( $A_1$ ) observed in these compounds were at 391  $\text{cm}^{-1}$  ( $\text{Cu}_2\text{ZnSiS}_4$ ) and 222  $\text{cm}^{-1}$  ( $\text{Cu}_2\text{ZnSiSe}_4$ ).

**Table 7.5** Raman frequencies in some tetragonal  $\text{Cu}_2\text{-II-IV-S}_4$  and  $\text{Cu}_2\text{-II-IV-Se}_4$  semiconductors at 300 K

Kesterite	Frequency ( $\text{cm}^{-1}$ )		
	A	A	B/E
CZTS <sup>a</sup>	287	338	369
Stannite	$A_1$	$A_1$	$B_2$
$\text{Cu}_2\text{CdSnS}_4$ [37]	279	329	358
$\text{Cu}_2\text{HgSnS}_4$ [37]	283	318	
CZTSe <sup>a</sup>	172	195	232
$\text{Cu}_2\text{CdSnSe}_4$ [24]	170	191	231

\*Averaged or recommended values.

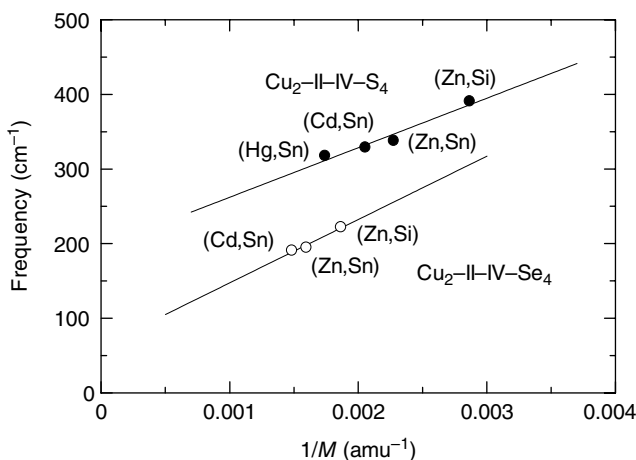
**Table 7.6** Optical phonon frequencies observed in the Raman spectra of orthorhombic  $\text{Cu}_2\text{ZnSiS}_4$  and  $\text{Cu}_2\text{ZnSiSe}_4$  at 300 K [38]

$\text{Cu}_2\text{ZnSiS}_4$	$\text{Cu}_2\text{ZnSiSe}_4$	Symmetry assignment
178		$A_1$ or $B_1$ or $B_2$
213		$A_1$ or $B_1$ or $B_2$
239		$A_1$ or $B_1$ or $B_2$
278		$A_2$
289		$A_1$
333	167	$A_1$
340	178	$A_1$
391	222	$A_1$
	384	$A_2$
498	404	$B_1$ or $B_2$
540	442	$B_1$ or $B_2$

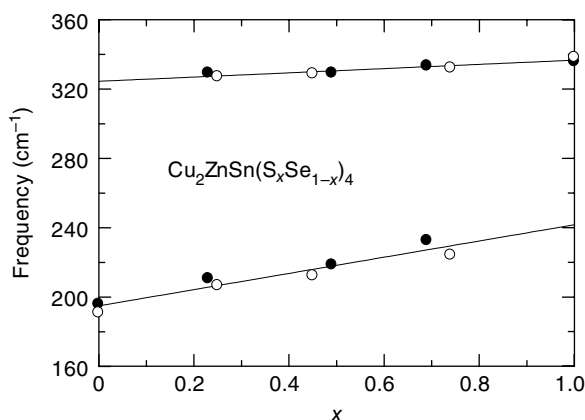
Figure 7.11 shows the dominant Raman peak frequencies plotted as a function of inverse atomic mass  $1/M$  for some  $\text{Cu}_2\text{-II-IV-VI}_4$  semiconductors. The Raman data were taken from Tables 7.5 and 7.6. It is evident from Figure 7.11 that the A- and  $A_1$ -mode frequencies can be classified into two groups:  $\text{Cu}_2\text{-II-IV-S}_4$  and  $\text{Cu}_2\text{-II-IV-Se}_4$ . This can be easily understood from the fact that, as mentioned before, the dominant A- and  $A_1$ -mode frequencies are mainly determined by the vibrations of the anion atom surrounded by the other atoms (Cu, II and IV) at rest in the  $\text{Cu}_2\text{-II-IV-VI}_4$  lattice. More exactly, the A- and  $A_1$ -mode frequencies can be given by [18]:

$$\nu = \sqrt{\frac{2\alpha_{\text{Cu-VI}} + \alpha_{\text{Zn-VI}} + \alpha_{\text{Sn-VI}}}{M_{\text{VI}}}} \quad (7.7)$$

where  $\alpha_{\text{X-VI}}$  (X = Cu, II or IV) is the bond-stretching force constant related to the interaction between the nearest neighbors (X-VI) and  $M_{\text{VI}}$  is the mass of anion atom (VI).



**Figure 7.11** Dominant Raman peak frequencies plotted as a function of inverse atomic mass  $1/M$  for  $\text{Cu}_2\text{-II-IV-VI}_4$  semiconductors. The S- and Se-based compound data are plotted by the solid and open circles, respectively



**Figure 7.12** A- and  $A_1$ -mode frequencies as a function of composition  $x$  for  $\text{Cu}_2\text{ZnSn}(\text{S}_x\text{Se}_{1-x})_4$  alloy at 300 K. The experimental data are taken from He *et al.* [18] and Grossberg *et al.* (open circles) [39]. The solid lines show the calculated results using Equation (7.9)

Equation (7.7) promises that the smaller  $M_{\text{VI}}$  compounds have the higher  $\nu$  values. The atomic masses of S and Se are 32.066 and 78.96, respectively.

The A- and  $A_1$ -mode frequencies in  $\text{Cu}_2\text{ZnSn}(\text{S}_x\text{Se}_{1-x})_4$  as a function of  $x$  are shown in Figure 7.12. The experimental data are taken from He *et al.* [18] and Grossberg *et al.* [39]. A number of models have been proposed to explain the so-called multi-mode behavior in solid solutions. Of these different models, the modified random-element-isodisplacement (MREI) model appears to be the most successful [40]. In the MREI model, if an alloy  $\text{AB}_x\text{C}_{1-x}$  has the relation

$$M_B < \mu_{\text{AC}} \quad (7.8)$$

it exhibits two-mode behavior. Here,  $\mu_{AC}^{-1} = M_A^{-1} + M_C^{-1}$  is the reduced mass of the material AC. The opposite is true for the one-mode behavior. In other words, for an alloy to exhibit two-mode behavior it must have one substituting element whose mass is smaller than the reduced mass of the compound formed by the other two elements. Given the masses of the end members, the MREI model can predict whether an alloy will show one- or two-mode behavior and also the dependence of the optical phonon frequencies on  $x$ .

In Figure 7.12, the  $\text{Cu}_2\text{ZnSn}(\text{S}_x\text{Se}_{1-x})_4$  alloy exhibits clear two-mode behavior. Setting  $A = \text{Cu}_2\text{ZnSn}$  ( $M_A = 2M_{\text{Cu}} + M_{\text{Zn}} + M_{\text{Sn}}$ ), we can regard  $\text{Cu}_2\text{ZnSn}(\text{S}_x\text{Se}_{1-x})_4$  as a pseudobinary alloy of the form of  $\text{AB}_x\text{C}_{1-x}$  with  $B = \text{S}_4$  and  $C = \text{Se}_4$ . The mass criterion of Equation (7.8) indicates that the alloy will exhibit two-mode behavior, in agreement with that observed in Figure 7.12. The solid lines in Figure 7.12 represent the least-squares fits, with the relations:

$$\nu = 324.5 + 12.2x \quad (7.9a)$$

$$\nu = 194.9 + 46.8x \quad (7.9b)$$

for the CZTS and CZTSe modes, respectively, where  $\nu$  is in  $\text{cm}^{-1}$ .

## 7.5 Electronic Energy-Band Structure

### 7.5.1 Electronic Energy-Band Diagram

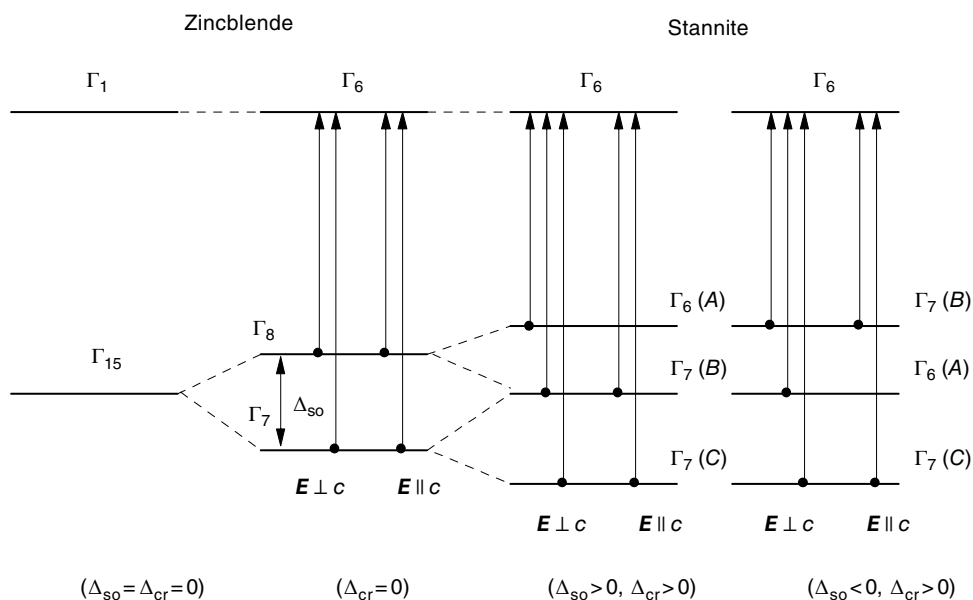
We show in Figure 7.13 the conduction-band and valence-band structures at  $\mathbf{k} = 0$  ( $\Gamma$ ) of tetragonal  $\text{Cu}_2\text{-II-IV-VI}_4$  semiconductors, together with those of a zinc-blende semiconductor with  $\Delta_{\text{so}} = \Delta_{\text{cr}} = 0$  eV and  $\Delta_{\text{cr}} = 0$  eV ( $\Delta_{\text{so}} \neq 0$  eV), where  $\Delta_{\text{so}}$  and  $\Delta_{\text{cr}}$  are the spin-orbit and crystal-field splitting parameters, respectively. Figures 7.13(a) and (b) correspond to those for the stannite and kesterite semiconductors, respectively. The spin-orbit interaction splits the  $\Gamma_{15}$  triplet state into the doublet ( $\Gamma_8$ ) and singlet ( $\Gamma_7$ ) states. The  $\Gamma_6$  ( $\Gamma_5 + \Gamma_6$ ) conduction band in Figure 7.13(a) (Fig. 7.13(b)) is predominantly  $s$ -like in wave function character. The combination effect of both the spin-orbit and crystal-field perturbations in the stannite (kesterite) lattice splits the  $p$ -like  $\Gamma_8$  and  $\Gamma_7$  valence bands into  $\Gamma_6$  (A) [ $\Gamma_5 + \Gamma_6$  (A)],  $\Gamma_7$  (B) [ $\Gamma_7 + \Gamma_8$  (B)], and  $\Gamma_7$  (C) [ $\Gamma_7 + \Gamma_8$  (C)] states, while the wave function for each band may be written as a linear combination of  $p_x$ ,  $p_y$ , and  $p_z$  and spin function. The corresponding dipole transitions between the valence and conduction bands are shown in Figure 7.13 by the vertical arrows.

Figure 7.14 shows the conduction-band and valence-band structures at  $\mathbf{k} = 0$  ( $\Gamma$ ) of a wurtz-stannite  $\text{Cu}_2\text{-II-IV-VI}_4$  semiconductor, together with those of zinc-blende and wurtzite semiconductors. Note that the band structure in Figure 7.14(c) is the critical energy-band diagram at  $\Delta_{\text{so}} \rightarrow 0$  eV of the wurtzite lattice. The corresponding dipole-transition selection rules in these semiconductors are shown in Figures 7.14(b)–(d) by the vertical arrows.

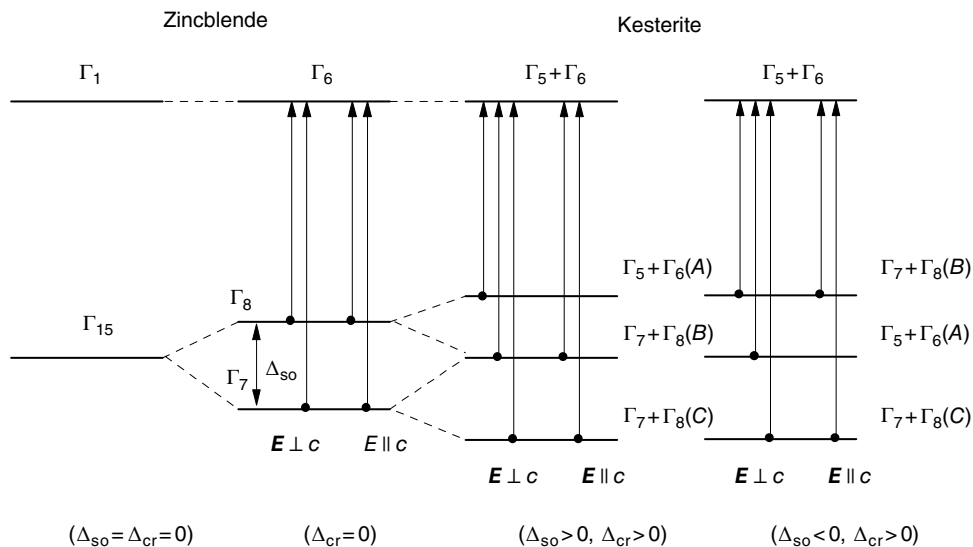
### 7.5.2 Band-Gap Energy: Room-Temperature Value

As evidenced from Figures 7.13 and 7.14, all the  $\text{Cu}_2\text{-II-IV-VI}_4$  semiconductors are optically anisotropic. However, no detailed experiments to determine the band-gap energies in these anisotropic semiconductors have been performed using polarized lights, except for

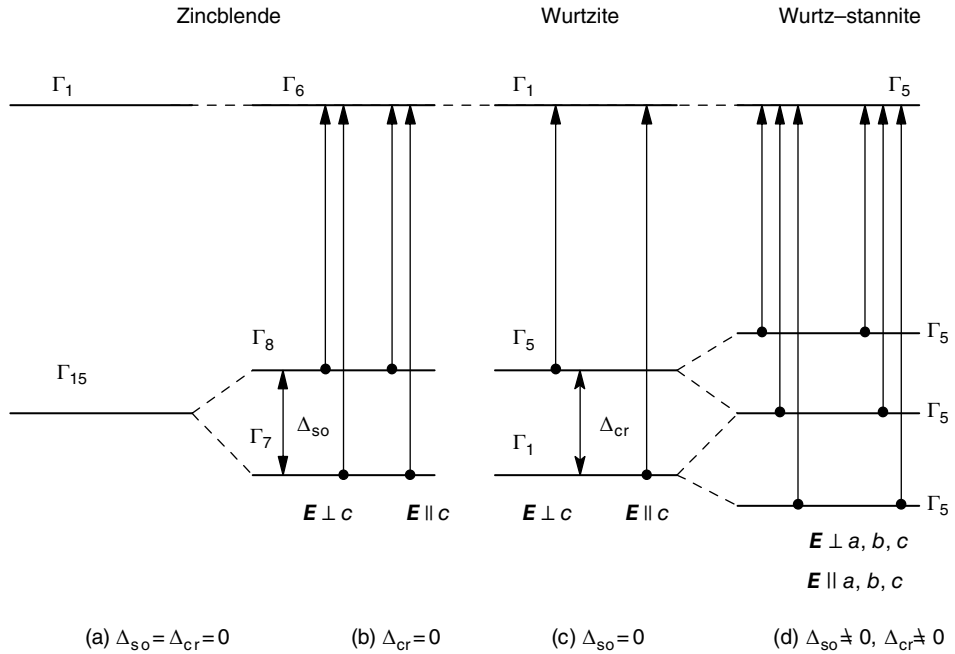
(a)



(b)



**Figure 7.13** Conduction-band and valence-band structures at  $\mathbf{k} = 0$  ( $\Gamma$ ) of (a) stannite and (b) kesterite  $\text{Cu}_2\text{-II-IV-VI}_4$  semiconductors, together with those of a zinc-blende semiconductor. The dipole-transition selection rules are indicated by the vertical arrows



**Figure 7.14** Conduction-band and valence-band structures at  $\mathbf{k} = 0$  ( $\Gamma$ ) of a wurtz-stannite  $\text{Cu}_2\text{-II-IV-VI}_4$  semiconductor, together with those of zinc-blende and wurtzite semiconductors. Note that the wurtzite diagram shown in (c) is the critical case of  $\Delta_{so} \rightarrow 0$  eV ( $\Delta_{cr} \neq 0$  eV). The dipole-transition selection rules are indicated by the vertical arrows

$\text{Cu}_2\text{ZnSiS}_4$ ,  $\text{Cu}_2\text{ZnSiSe}_4$ , and  $\text{Cu}_2\text{ZnGeS}_4$  [41–45]. We summarize in Table 7.7 the lowest indirect and direct band-gap energies ( $E_g$ ) of a number of  $\text{Cu}_2\text{-II-IV-VI}_4$  semiconductors obtained at 300 K [6, 30–32, 42, 44, 46–48]. Several authors reported the  $E_g$  values of “stannite” CZTS [49, 50]. Their averaged value is also listed in Table 7.7.

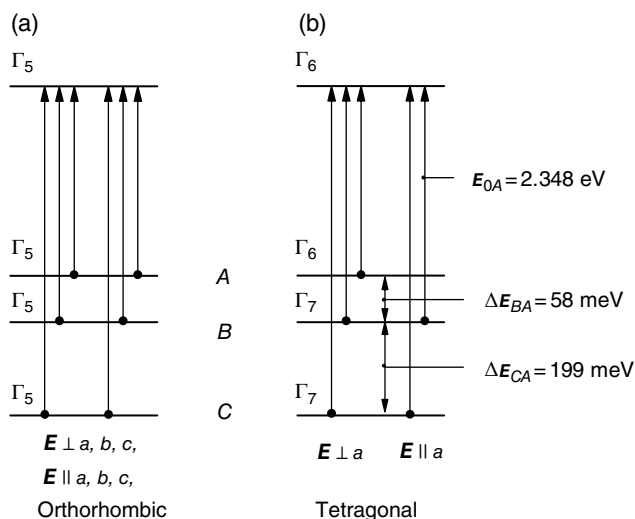
Levcenco *et al.* [41, 44] investigated the band-edge excitonic transitions in orthorhombic  $\text{Cu}_2\text{ZnSiS}_4$  single crystals using polarization-dependent modulation spectroscopy. Analyzing their data, we can obtain the energy-band diagram for  $\text{Cu}_2\text{ZnSiS}_4$  to be given in Figure 7.14(c) ( $\Delta_{so} \sim 0$  meV and  $\Delta_{cr} \sim 90$  meV). Levcenco *et al.* [44] also performed a polarization-dependent electrolyte electroreflectance study on orthorhombic  $\text{Cu}_2\text{ZnSiSe}_4$  single crystals. The lattice constants of  $\text{Cu}_2\text{ZnSiSe}_4$  are  $a = 0.7833$  nm,  $b = 0.6726$  nm and  $c = 0.6450$  nm (Table 7.1). Assuming  $b \approx c$ , this compound can be regarded as a tetragonal material with an optically anisotropic axis in the  $a$  direction. It may then become possible to use the quasicubic model [51] in the band-structure analysis of this material. The valence-band splitting energies reported by Levcenco *et al.* [44] are  $\Delta E_{BA} = 58$  meV and  $\Delta E_{CA} = 199$  meV, as shown in Figure 7.15. These splitting energies yield the spin-orbit and crystal-field parameters of  $\Delta_{so} = 108$  meV and  $\Delta_{cr} = 207$  meV, respectively. Finally, the following optical-transition strength ratio is obtained from the quasicubic model [51]:

$$P_{0A\perp}^2 : P_{0B\perp}^2 : P_{0C\perp}^2 : P_{0A\parallel}^2 : P_{0B\parallel}^2 : P_{0C\parallel}^2 = 1.00 : 0.93 : 0.07 : 0.00 : 0.14 : 1.86. \quad (7.10)$$

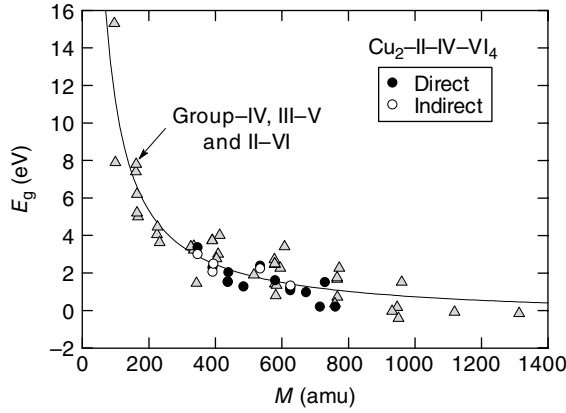
**Table 7.7** Lowest indirect (ID) and direct (D) band-gap energies at 300 K for some  $\text{Cu}_2\text{-II-IV-VI}_4$  semiconductors; w-s: wurtz-stannite; s: stannite; k: kesterite

Material	Crystal structure	$E_g$ (eV)	ID or D
$\text{Cu}_2\text{ZnSiS}_4$	w-s	2.97 [42]	ID
		3.32 [42]	D
$\text{Cu}_2\text{ZnSiSe}_4$	w-s	2.20 [30]	ID
		2.348 [44]	D
$\text{Cu}_2\text{ZnSiTe}_4$	s	1.47 [47]	
$\text{Cu}_2\text{ZnGeS}_4$	s	2.25 [6]	D
	w-s	2.02*	ID
$\text{Cu}_2\text{ZnGeSe}_4$	s	1.57*	D
	k	1.49*	D
CZTS	s	1.50*	D
	s	1.11*	D
CZTSe	k	1.05 [48]	D
	w-s	2.45 [30]	ID
$\text{Cu}_2\text{CdSiS}_4$	w-s	2.00*	
$\text{Cu}_2\text{CdGeS}_4$	w-s	1.29 [32]	ID
$\text{Cu}_2\text{CdGeSe}_4$	s	1.20 [46]	D
	w-s	1.24*	D
$\text{Cu}_2\text{CdSnS}_4$	s	0.94*	D
$\text{Cu}_2\text{HgGeSe}_4$	s	0.16 [31]	D
$\text{Cu}_2\text{HgSnSe}_4$	s	0.17 [31]	D

\*Averaged or recommended value.

**Figure 7.15** (a) Orthorhombic (wurtz-stannite) and (b) tetragonal energy-band diagrams. In (b), the basal axis is in the  $a$  direction. The energy values in (b) correspond to those reported by Levchenko et al. [44] for  $\text{Cu}_2\text{ZnSiSe}_4$ . The dipole-transition selection rules are indicated by the vertical arrows

The above equation predicts that no optical transition occurs in  $\text{Cu}_2\text{ZnSiSe}_4$  between the A-valence and conduction bands for  $E \parallel a$  polarization (Fig. 7.15). The lowest band-gap energy  $E_g$  for  $E \perp a$  should then be smaller than that for  $E \parallel a$ .



**Figure 7.16** Band-gap energy  $E_g$  versus molecular weight  $M$  for  $\text{Cu}_2\text{-II-IV-VI}_4$  semiconductors. The solid line represents the calculated result using Equation (7.11)

Figure 7.16 shows the  $E_g$  versus molecular weight ( $M$ ) plots for  $\text{Cu}_2\text{-II-IV-VI}_4$  semiconductors at 300 K. The  $E_g$  values of group-IV, III-V, and II-VI semiconductors are also plotted by multiplying their  $M$  values by 4 [20]. This is because the total number of valence electrons per molecule of these tetrahedral semiconductors is 8 (octet rule), while that of  $\text{Cu}_2\text{-II-IV-VI}_4$  is 32 ( $= 1 \times 2 + 2 + 4 + 6 \times 4$ ). The solid line in Figure 7.16 shows the least-squares fit with the relation:

$$E_g = \frac{1.15 \times 10^3}{M} - 0.41 \quad (7.11)$$

where  $M$  is in amu and  $E_g$  is in eV.

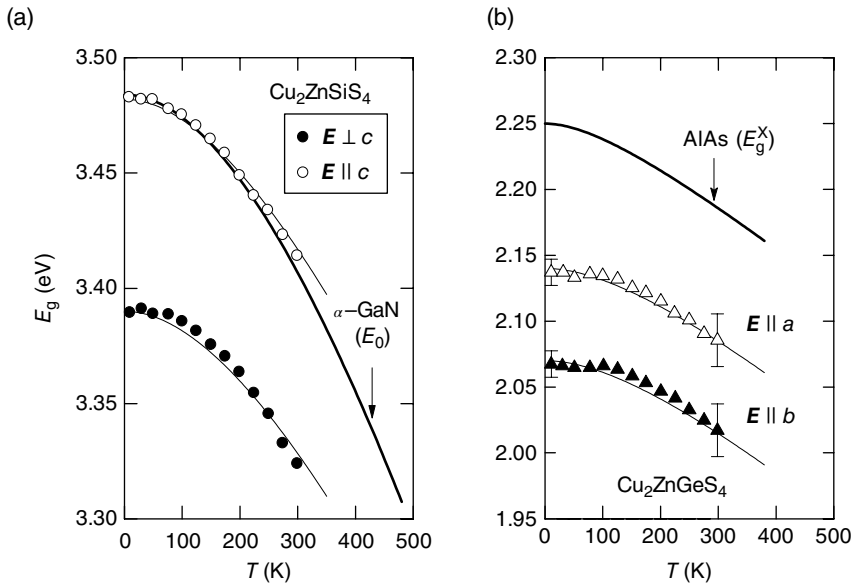
### 7.5.3 Band-Gap Energy: Temperature Dependence

Several authors reported the temperature dependences of the lowest indirect and direct band-gap energies in some  $\text{Cu}_2\text{-II-IV-VI}_4$  semiconductors [41, 43, 45, 52]. Figure 7.17(a) shows the lowest direct band-gap energies for  $E \perp c$  and  $E \parallel c$  in  $\text{Cu}_2\text{ZnSiS}_4$  as a function of temperature  $T$ . The experimental data were obtained by means of piezoreflectance spectroscopy at  $T = 10\text{--}300$  K with the normal of the basal plane along (210) and the long edge of the crystal platelet parallel to the  $c$  axis [41]. The solid lines represent the calculated results using the Varshni equation [20]:

$$E_g(T) = E_g(0) - \frac{\alpha T^2}{T + \beta}. \quad (7.12)$$

The fit-determined  $E_g(0)$ ,  $\alpha$  and  $\beta$  values are listed in Table 7.8. The lowest direct band-gap energies  $E_g(T)$  for  $\alpha\text{-GaN}$  are also plotted and fitted using Equation 7.12 with  $E_g(0) = 3.484$  eV,  $\alpha = 1.28 \times 10^{-3}$  eV  $\text{K}^{-1}$  and  $\beta = 1190$  K [20].





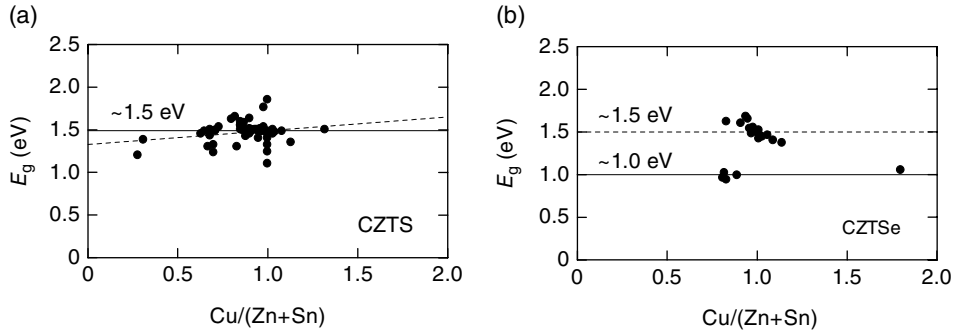
**Figure 7.17** (a) Direct band-gap energies  $E_g$  for  $E \perp c$  and  $E \parallel c$  in  $\text{Cu}_2\text{ZnSiS}_4$  as a function of temperature  $T$  [41]. (b) Indirect band-gap energies  $E_g$  versus  $T$  for wurtz–stannite  $\text{Cu}_2\text{ZnGeS}_4$  [45]. In (a), the normal of the basal plane is along  $(210)$  and the long edge of the crystal platelet is parallel to the  $c$  axis. The solid lines in (a) and (b) show the results calculated using Equation (7.12) (see also Table 7.8)

**Table 7.8** Empirical equation (Equation (7.12)) for the lowest indirect (ID) and direct (D) band-gap energy variations of some  $\text{Cu}_2\text{-II-IV-VI}_4$  semiconductors

Material	$E_g(0)$	$\alpha$ ( $10^{-4}$ eV $\text{K}^{-1}$ )	$\beta$ (K)	Comment	Reference
$\text{Cu}_2\text{ZnSiS}_4$	2.99	4	350	ID, $E \perp c$	[43]
	3.10	4	290	ID, $E \parallel c$	[43]
	3.390	5	380	D, $E \perp c$	[41]
	3.482	5	350	D, $E \parallel c$	[41]
$\text{Cu}_2\text{ZnSiSe}_4^*$	2.15	5	270	ID, $E \perp c$	[43]
	2.20	4	260	ID, $E \parallel c$	[43]
$\text{Cu}_2\text{ZnGeS}_4$	2.07	4	350	ID, $E \parallel a$	[45]
	2.14	4	330	ID, $E \parallel b$	[45]
CZTS	1.64	10	340	D	[52]

\*The normal of the basal plane is along  $(210)$  and the long edge of the crystal platelet is parallel to the  $c$  axis.

Figure 7.17(b) shows the lowest indirect band-gap energy versus  $T$  data for wurtz–stannite  $\text{Cu}_2\text{ZnGeS}_4$  along with the calculated results of Equation (7.12) (see also Table 7.8). The experimental data were obtained from polarization-dependent optical absorption measurements at  $T = 10\text{--}300$  K [45]. The heavy solid line in Figure 7.17(b) also shows the temperature dependence of the lowest indirect band-gap energy  $E_g^X(T)$  for AlAs calculated using Equation (7.12) with  $E_g^X(0) = 2.25$  eV,  $\alpha = 3.6 \times 10^{-4}$  eV  $\text{K}^{-1}$  and  $\beta = 204$  K [20]. In Figure 7.17, the Varshni expression (7.12) is found to successfully explain the temperature



**Figure 7.18** Direct band-gap energies  $E_g$  versus  $\text{Cu}/(\text{Zn}+\text{Sn})$  atomic ratio observed at 300 K for (a) CZTS and (b) CZTSe. The experimental data are gathered from various sources

dependence of the band-gap energies not only in the III–V semiconductors but also in the  $\text{Cu}_2\text{--II--IV--VI}_4$  semiconductors.

#### 7.5.4 Effect of Chemical Composition

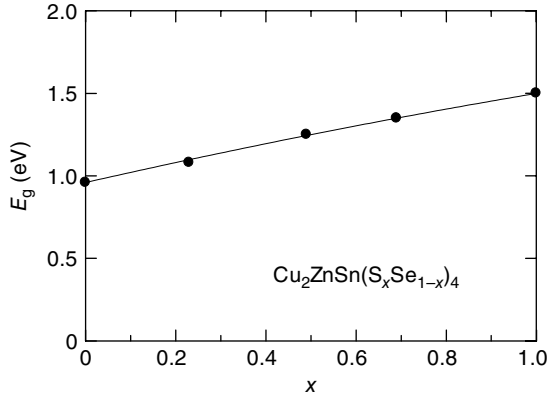
The lowest direct band-gap energies  $E_g$  versus  $\text{Cu}/(\text{Zn}+\text{Sn})$  atomic ratio observed at 300 K in CZTS and CZTSe are shown in Figures 7.18(a) and (b), respectively. The experimental data are gathered from various sources. The solid lines in Figures 7.18(a) and (b) indicate the values of  $E_g \approx 1.5$  and  $\approx 1.0$  eV, respectively. In Figure 7.18(a), CZTS shows a tendency of very slight increase in  $E_g$  with increasing  $\text{Cu}/(\text{Zn}+\text{Sn})$  ratio (dashed line). The same plots but for CZTSe (Fig. 7.18(b)) show no clear relation between the  $E_g$  and  $\text{Cu}/(\text{Cu}+\text{Sn})$  values. The data in Figure 7.18(b) can be classified into two different  $E_g$  groups of c. 1.0 eV (solid line) and c. 1.5 eV (dashed line). Note that  $E_g = 1.11$  eV cited in Table 7.7 (CZTSe) was obtained by averaging numerous values from the literature; most of those studies gave no information on the chemical composition or stoichiometry of the examined samples, however. It is well known that the Se-based chalcogenides have smaller band-gap energies than the S-based chalcogenides (e.g. ZnSe and ZnS have  $E_g$  values of 2.721 and 3.726 eV, respectively [20]). CZTSe should therefore have  $E_g \approx 1.0$  eV rather than  $E_g \approx 1.5$  eV.

#### 7.5.5 Alloy Semiconductor

The composition dependence of the lowest direct band-gap energy for the  $\text{Cu}_2\text{ZnSn}(\text{S}_x\text{Se}_{1-x})_4$  alloy has been studied by several authors [18, 53]. We show in Figure 7.19 the results reported by He *et al.* [18]. The experimental data were obtained from optical absorption measurements of the samples with  $x = 0, 0.23, 0.49, 0.69$ , and 1.0 at 300 K. Traditionally, composition variation of the band-gap energy in an alloy of the form  $\text{AB}_x\text{C}_{1-x}$  is written as

$$E_g(x) = xE_g(\text{AB}) + (1-x)E_g(\text{AC}) + x(1-x)c \quad (7.13)$$

where  $c$  is known as a bowing parameter. The parameters in Equation (7.13) determined by He *et al.* were  $E_g(\text{CZTS}) = 1.5$  eV,  $E_g(\text{CZTSe}) = 0.96$  eV, and  $c = 0.08$  eV (upward bowing). The experimental data obtained by Levchenko *et al.* [53] also showed quadratic dependence on  $x$  with



**Figure 7.19** Composition dependence of the lowest direct band-gap energy for  $\text{Cu}_2\text{ZnSn}(\text{S}_x\text{Se}_{1-x})_4$  alloy. The experimental data were measured by He et al. [18] at 300 K. The solid line shows the result calculated using Equation (7.13)

$E_g(\text{CZTS}) = 1.46 \text{ eV}$ ,  $E_g(\text{CZTSe}) = 0.94 \text{ eV}$ , and  $c = -0.19 \text{ eV}$  (downward bowing). Theoretically, Chen *et al.* [54] predicted  $c = -0.07$  or  $-0.10 \text{ eV}$  from first-principles calculations.

## 7.6 Optical Properties

### 7.6.1 Refractive Index

Optical absorption measurements have been commonly used to determine the fundamental absorption edges of  $\text{Cu}_2\text{-II-IV-VI}_4$  semiconductors. Determination of the optical constants above the fundamental absorption edge becomes increasingly difficult, since the real and imaginary parts of the complex dielectric function ( $\epsilon^* = \epsilon_1 + i\epsilon_2$ ) or complex refractive index ( $n^* = n + ik$ ) can no longer be measured independently. The majority of data on the optical constants above the fundamental absorption edge have been derived from normal-incidence reflectivity measurements over a wide spectral range, and the subsequent calculation of the phase shift by means of the Kramers–Kronig relations. SE has recently been used as an advantageous technique to obtain the fundamental optical spectra of solids.

To the best of our knowledge, no normal-incidence reflectivity measurement has been performed on  $\text{Cu}_2\text{-II-IV-VI}_4$  semiconductors to date. However, there have been several SE measurements on  $\text{Cu}_2\text{ZnGeS}_4$  [6], CZTS [7], and CZTSe [8] carried out. The refractive indices  $n(E)$  in the transparent region of the semiconductors can be obtained by extrapolating the SE  $n(E)$  data using the first-order Sellmeier equation [20]:

$$n(\lambda)^2 = \epsilon_1(\lambda) = A + \frac{B\lambda^2}{\lambda^2 - C^2}. \quad (7.14)$$

Using Equation (7.14), we determined the Sellmeier parameters to be  $A = 2.30$ ,  $B = 4.00$ , and  $C^2 = 0.125 \mu\text{m}^2$  for  $\text{Cu}_2\text{ZnGeS}_4$ ,  $A = 3.10$ ,  $B = 3.85$ , and  $C^2 = 0.220 \mu\text{m}^2$  for CZTS and

$A = 6.80$ ,  $B = 2.30$ , and  $C^2 = 0.660 \mu\text{m}^2$  for CZTSe. As  $\lambda \rightarrow \infty$ , the electronic contribution to the dielectric constant approaches a limiting value  $\epsilon_\infty$ , the high-frequency dielectric constant. The values for  $\epsilon_\infty$ , which can be obtained from Equation (7.14) by setting  $\epsilon_\infty = A+B$ , are 6.30 for  $\text{Cu}_2\text{ZnGeS}_4$ , 6.95 for CZTS, and 9.10 for CZTSe.

Tables 7.9 and 7.10 present the room-temperature SE data of  $\epsilon^* = \epsilon_1 + i\epsilon_2$ ,  $n^* = n + ik$ ,  $\alpha$  (absorption coefficient), and  $R$  (normal-incidence reflectivity) for CZTS [7] and CZTSe [8], respectively, together with the Sellmeier  $n$  values ( $E = 0.2\text{--}0.6$  eV for CZTS;  $0.2\text{--}0.4$  eV for CZTSe). It has been shown [6] that such optical spectra can be successfully interpreted by a simplified model of the interband transitions [20].

## 7.6.2 Optical Absorption Coefficient

Figure 7.20 shows the optical absorption spectra  $\alpha(E)$  of  $\text{Cu}_2\text{ZnGeS}_4$ , CZTS, and CZTSe, together with those of crystalline-Si ( $c\text{-Si}$ ), amorphous-Si ( $a\text{-Si}$ ), and CdTe which are known to be important materials for photovoltaics. The  $\alpha(E)$  data for  $\text{Cu}_2\text{ZnGeS}_4$ , CZTS, and CZTSe were obtained from the SE data [6–8] (see also Tables 7.9 and 7.10). The  $c\text{-Si}$ ,  $a\text{-Si}$ , and CdTe data were taken from Adachi [55]. Several sharp peaks observed at  $E > 3$  eV in  $c\text{-Si}$  and CdTe are due to the interband critical-point structures [20].

The absorption length of a photovoltaic material is a useful quantity. It is defined as the inverse of  $\alpha$ , that is,  $\alpha^{-1}$ . At visible wavelengths, most semiconductors in Figure 7.20 have absorption lengths of less than one micron. This means that only a few microns of material are needed to absorb virtually all of the light. Only  $c\text{-Si}$ , which is an indirect band-gap semiconductor, has an absorption length of tens of microns, so that films of thickness tens or hundreds of microns are needed for good absorption.

## 7.7 Carrier Transport Properties

### 7.7.1 Electrical Conductivity

Table 7.11 summarizes the electrical properties reported in the literature for various  $\text{Cu}_2\text{--II--IV--VI}_4$  semiconductors. As understood from this table, all these semiconductors showed p-type conduction. The electrical resistivity largely varied from insulating ( $\text{Cu}_2\text{ZnSiS}_4$ ) to highly conductive ( $1 \times 10^{-3} \Omega \text{ cm}$ ; CZTSe).

The electrical resistivity  $\rho$  versus  $\text{Cu}/(\text{Zn}+\text{Sn})$  atomic ratio plots for CZTS are shown in Figure 7.21. The experimental data are gathered from various sources. Unfortunately, we can find no clear relation between  $\rho$  and  $\text{Cu}/(\text{Zn}+\text{Sn})$  ratio for CZTS. However, several authors obtained results that indicate that  $\rho$  decreases with increasing  $\text{Cu}/(\text{II}+\text{IV})$  atomic ratio for some  $\text{Cu}_2\text{--II--IV--VI}_4$  semiconductors ( $\text{Cu}_{2+x}\text{Zn}_{1-x}\text{GeSe}_4$  [25], CZTS [56, 57], CZTSe [5], and  $\text{Cu}_{2+x}\text{Cd}_{1-x}\text{SnSe}_4$  [23]). An example of  $\text{Cu}_{2+x}\text{Cd}_{1-x}\text{SnSe}_4$  is shown in Figure 7.22 [23]. In  $\text{Cu}_2\text{--II--IV--VI}_4$  compounds, the Cu content is known to play an important role in determining film resistivity rather than other factors.  $\text{Cu}_2\text{Se}$  is a semi-metallic p-type material. Tanaka *et al.* [5] reported that the higher  $p$  concentration and lower  $\rho$  value observed at higher  $\text{Cu}/(\text{Zn}+\text{Sn})$  ratios of CZTSe are due to the presence of  $\text{Cu}_2\text{Se}$  phase in their deposited films. This consideration was supported by the fact that the Raman peak in  $\text{Cu}_2\text{Se}$  at  $c. 260 \text{ cm}^{-1}$  is observed only in the low-resistive CZTSe samples. Interestingly, CZTS with  $\text{Cu}/(\text{Cu}+\text{Sn})$  ratios less than 1.0 and  $\text{Zn}/\text{Sn}$  ratios larger than 1.0 led to higher

**Table 7.9** Optical constants of CZTS at 300 K

$E$ (eV)	$\epsilon_1$	$\epsilon_2$	$n$	$k$	$\alpha$ (cm <sup>-1</sup> )	$R$
0.2	6.972		2.640			0.203
0.3	7.000		2.646			0.204
0.4	7.040		2.653			0.205
0.5	7.093		2.663			0.206
0.6	7.159		2.676			0.208
0.7	7.234		2.690			0.210
0.8	7.256		2.694			0.210
0.9	7.321		2.706			0.212
1.0	7.473		2.734			0.216
1.1	7.698	0.019	2.775	0.003	$3.84 \times 10^2$	0.221
1.2	7.939	0.180	2.818	0.032	$3.88 \times 10^3$	0.227
1.3	8.112	0.451	2.849	0.079	$1.04 \times 10^4$	0.231
1.4	8.179	0.786	2.863	0.137	$1.95 \times 10^4$	0.234
1.5	8.129	1.093	2.858	0.191	$2.91 \times 10^4$	0.234
1.6	8.020	1.310	2.841	0.231	$3.74 \times 10^4$	0.233
1.7	7.905	1.433	2.823	0.254	$4.38 \times 10^4$	0.231
1.8	7.843	1.530	2.814	0.272	$4.96 \times 10^4$	0.230
1.9	7.811	1.644	2.810	0.293	$5.63 \times 10^4$	0.230
2.0	7.811	1.761	2.812	0.313	$6.35 \times 10^4$	0.231
2.1	7.824	1.895	2.817	0.336	$7.16 \times 10^4$	0.233
2.2	7.838	2.068	2.824	0.366	$8.17 \times 10^4$	0.234
2.3	7.816	2.263	2.824	0.401	$9.34 \times 10^4$	0.236
2.4	7.773	2.489	2.823	0.441	$1.07 \times 10^5$	0.237
2.5	7.708	2.731	2.818	0.485	$1.23 \times 10^5$	0.239
2.6	7.607	2.929	2.807	0.522	$1.38 \times 10^5$	0.240
2.7	7.476	3.086	2.790	0.553	$1.51 \times 10^5$	0.239
2.8	7.338	3.191	2.769	0.576	$1.64 \times 10^5$	0.238
2.9	7.204	3.243	2.748	0.590	$1.73 \times 10^5$	0.236
3.0	7.089	3.251	2.728	0.596	$1.81 \times 10^5$	0.234
3.1	7.019	3.227	2.715	0.594	$1.87 \times 10^5$	0.233
3.2	6.998	3.203	2.711	0.591	$1.92 \times 10^5$	0.232
3.3	7.000	3.175	2.710	0.586	$1.96 \times 10^5$	0.232
3.4	7.048	3.175	2.718	0.584	$2.01 \times 10^5$	0.232
3.5	7.130	3.228	2.735	0.590	$2.09 \times 10^5$	0.235
3.6	7.253	3.309	2.759	0.600	$2.19 \times 10^5$	0.238
3.7	7.408	3.455	2.791	0.619	$2.32 \times 10^5$	0.243
3.8	7.540	3.712	2.823	0.657	$2.53 \times 10^5$	0.250
3.9	7.615	4.059	2.850	0.712	$2.82 \times 10^5$	0.256
4.0	7.599	4.460	2.865	0.779	$3.16 \times 10^5$	0.263
4.1	7.504	4.868	2.868	0.849	$3.53 \times 10^5$	0.268
4.2	7.343	5.233	2.860	0.915	$3.90 \times 10^5$	0.273
4.3	7.128	5.527	2.841	0.973	$4.24 \times 10^5$	0.276
4.4	6.881	5.790	2.817	1.028	$4.58 \times 10^5$	0.279
4.5	6.597	6.061	2.789	1.087	$4.96 \times 10^5$	0.282
4.6	6.276	6.325	2.756	1.148	$5.35 \times 10^5$	0.285
4.7	5.965	6.531	2.721	1.200	$5.72 \times 10^5$	0.288
4.8	5.647	6.702	2.684	1.248	$6.08 \times 10^5$	0.290
4.9	5.326	6.832	2.645	1.292	$6.42 \times 10^5$	0.292
5.0	4.974	6.919	2.598	1.332	$6.75 \times 10^5$	0.294
5.1	4.599	6.988	2.546	1.372	$7.10 \times 10^5$	0.296
5.2	4.238	7.043	2.496	1.411	$7.44 \times 10^5$	0.298
5.3	3.906	7.067	2.448	1.444	$7.76 \times 10^5$	0.299

(continued)

**Table 7.9** (continued)

$E$ (eV)	$\epsilon_1$	$\epsilon_2$	$n$	$k$	$\alpha$ (cm <sup>-1</sup> )	<b>R</b>
5.4	3.578	7.041	2.395	1.470	$8.05 \times 10^5$	0.300
5.5	3.260	6.963	2.340	1.488	$8.30 \times 10^5$	0.300
5.6	2.972	6.840	2.284	1.498	$8.50 \times 10^5$	0.299
5.7	2.726	6.665	2.228	1.496	$8.64 \times 10^5$	0.296
5.8	2.514	6.494	2.177	1.492	$8.77 \times 10^5$	0.293
5.9	2.341	6.336	2.133	1.486	$8.89 \times 10^5$	0.290
6.0	2.211	6.240	2.101	1.485	$9.03 \times 10^5$	0.289
6.1	2.052	6.179	2.069	1.493	$9.23 \times 10^5$	0.289
6.2	1.813	6.104	2.022	1.509	$9.49 \times 10^5$	0.291
6.3	1.537	6.010	1.967	1.527	$9.76 \times 10^5$	0.293
6.4	1.272	5.907	1.912	1.544	$1.00 \times 10^6$	0.296

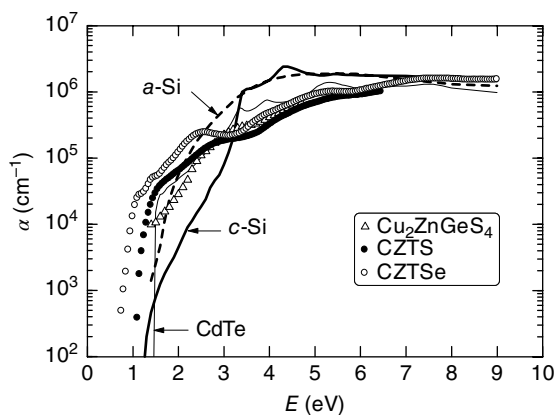
**Table 7.10** Optical constants of CZTSe at 300 K

$E$ (eV)	$\epsilon_1$	$\epsilon_2$	$n$	$k$	$\alpha$ (cm <sup>-1</sup> )	<b>R</b>
0.2	9.140		3.023			0.253
0.3	9.193		3.032			0.254
0.4	9.270		3.045			0.256
0.5	9.372		3.061			0.258
0.6	9.404		3.067			0.258
0.7	9.537		3.088			0.261
0.8	9.838	0.080	3.137	0.013	$1.03 \times 10^3$	0.267
0.9	10.37	0.290	3.221	0.045	$4.11 \times 10^3$	0.277
1.0	10.77	0.848	3.284	0.129	$1.31 \times 10^4$	0.285
1.1	10.61	1.449	3.264	0.222	$2.47 \times 10^4$	0.284
1.2	10.42	1.524	3.237	0.235	$2.86 \times 10^4$	0.281
1.3	10.57	1.691	3.261	0.259	$3.42 \times 10^4$	0.284
1.4	10.51	2.115	3.258	0.325	$4.61 \times 10^4$	0.285
1.5	10.38	2.218	3.241	0.342	$5.20 \times 10^4$	0.284
1.6	10.51	2.301	3.260	0.353	$5.72 \times 10^4$	0.286
1.7	10.64	2.690	3.287	0.409	$7.05 \times 10^4$	0.291
1.8	10.67	3.062	3.299	0.464	$8.47 \times 10^4$	0.294
1.9	10.76	3.408	3.321	0.513	$9.89 \times 10^4$	0.298
2.0	10.78	3.963	3.336	0.594	$1.20 \times 10^5$	0.303
2.1	10.61	4.617	3.330	0.693	$1.48 \times 10^5$	0.307
2.2	10.22	5.149	3.290	0.782	$1.75 \times 10^5$	0.308
2.3	9.569	5.567	3.212	0.866	$2.02 \times 10^5$	0.305
2.4	8.936	5.782	3.129	0.924	$2.25 \times 10^5$	0.301
2.5	8.370	5.750	3.043	0.945	$2.39 \times 10^5$	0.294
2.6	7.796	5.433	2.941	0.924	$2.43 \times 10^5$	0.282
2.7	7.426	4.955	2.859	0.866	$2.37 \times 10^5$	0.269
2.8	7.397	4.566	2.836	0.805	$2.29 \times 10^5$	0.262
2.9	7.556	4.313	2.851	0.756	$2.22 \times 10^5$	0.260
3.0	7.751	4.119	2.875	0.716	$2.18 \times 10^5$	0.259
3.1	8.036	4.015	2.917	0.688	$2.16 \times 10^5$	0.262
3.2	8.285	4.007	2.957	0.677	$2.20 \times 10^5$	0.266
3.3	8.604	4.139	3.013	0.687	$2.30 \times 10^5$	0.273
3.4	9.038	4.383	3.089	0.709	$2.45 \times 10^5$	0.283
3.5	9.340	4.855	3.152	0.770	$2.73 \times 10^5$	0.293
3.6	9.445	5.565	3.194	0.871	$3.18 \times 10^5$	0.304

(continued)

**Table 7.10** (continued)

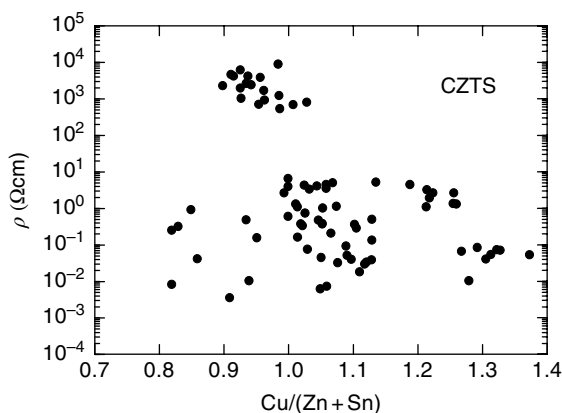
$E$ (eV)	$\varepsilon_1$	$\varepsilon_2$	$n$	$k$	$\alpha$ (cm <sup>-1</sup> )	<b>R</b>
3.7	9.283	6.164	3.196	0.964	$3.62 \times 10^5$	0.310
3.8	9.062	6.622	3.185	1.040	$4.01 \times 10^5$	0.315
3.9	8.785	7.080	3.168	1.118	$4.42 \times 10^5$	0.319
4.0	8.486	7.405	3.142	1.178	$4.78 \times 10^5$	0.322
4.1	8.256	7.623	3.122	1.221	$5.07 \times 10^5$	0.324
4.2	7.930	7.882	3.091	1.275	$5.43 \times 10^5$	0.327
4.3	7.663	8.184	3.072	1.332	$5.81 \times 10^5$	0.331
4.4	7.510	8.545	3.073	1.390	$6.20 \times 10^5$	0.336
4.5	7.234	8.942	3.061	1.461	$6.66 \times 10^5$	0.343
4.6	6.835	9.343	3.034	1.540	$7.18 \times 10^5$	0.349
4.7	6.226	9.626	2.974	1.618	$7.71 \times 10^5$	0.354
4.8	5.624	9.780	2.907	1.682	$8.19 \times 10^5$	0.357
4.9	5.009	9.850	2.834	1.738	$8.63 \times 10^5$	0.360
5.0	4.359	9.840	2.750	1.789	$9.07 \times 10^5$	0.363
5.1	3.787	9.713	2.666	1.822	$9.42 \times 10^5$	0.364
5.2	3.177	9.457	2.564	1.844	$9.72 \times 10^5$	0.363
5.3	2.602	9.139	2.460	1.857	$9.98 \times 10^5$	0.362
5.4	2.351	8.785	2.392	1.836	$1.01 \times 10^6$	0.357
5.5	2.188	8.383	2.329	1.800	$1.00 \times 10^6$	0.349
5.6	2.131	7.998	2.281	1.753	$9.95 \times 10^5$	0.341
5.7	2.231	7.731	2.267	1.705	$9.85 \times 10^5$	0.332
5.8	2.277	7.645	2.264	1.688	$9.93 \times 10^5$	0.329
5.9	2.403	7.730	2.291	1.687	$1.01 \times 10^6$	0.330
6.0	2.387	7.850	2.301	1.706	$1.04 \times 10^6$	0.333
6.1	2.147	7.957	2.279	1.746	$1.08 \times 10^6$	0.339
6.2	1.918	8.068	2.259	1.785	$1.12 \times 10^6$	0.346
6.3	1.699	8.148	2.239	1.820	$1.16 \times 10^6$	0.351
6.4	1.479	8.169	2.211	1.847	$1.20 \times 10^6$	0.355
6.5	1.210	8.110	2.169	1.869	$1.23 \times 10^6$	0.359
6.6	0.866	8.084	2.121	1.906	$1.28 \times 10^6$	0.366
6.7	0.585	8.059	2.082	1.936	$1.32 \times 10^6$	0.371
6.8	0.379	8.074	2.057	1.963	$1.35 \times 10^6$	0.377
6.9	0.087	8.053	2.018	1.996	$1.40 \times 10^6$	0.383
7.0	-0.345	7.932	1.949	2.035	$1.44 \times 10^6$	0.393
7.1	-0.751	7.739	1.874	2.065	$1.49 \times 10^6$	0.401
7.2	-1.015	7.513	1.812	2.073	$1.51 \times 10^6$	0.406
7.3	-1.344	7.222	1.732	2.084	$1.54 \times 10^6$	0.413
7.4	-1.667	6.846	1.640	2.087	$1.57 \times 10^6$	0.421
7.5	-1.767	6.517	1.579	2.064	$1.57 \times 10^6$	0.421
7.6	-1.945	6.174	1.505	2.052	$1.58 \times 10^6$	0.426
7.7	-2.035	5.823	1.438	2.025	$1.58 \times 10^6$	0.427
7.8	-2.054	5.516	1.384	1.993	$1.58 \times 10^6$	0.427
7.9	-2.083	5.211	1.328	1.961	$1.57 \times 10^6$	0.427
8.0	-2.071	4.953	1.284	1.929	$1.56 \times 10^6$	0.425
8.1	-2.011	4.736	1.252	1.892	$1.55 \times 10^6$	0.421
8.2	-1.958	4.471	1.209	1.849	$1.54 \times 10^6$	0.417
8.3	-1.937	4.244	1.168	1.817	$1.53 \times 10^6$	0.416
8.4	-1.866	4.122	1.153	1.788	$1.52 \times 10^6$	0.411
8.5	-1.836	4.030	1.139	1.770	$1.53 \times 10^6$	0.409
8.6	-1.819	3.884	1.111	1.748	$1.52 \times 10^6$	0.408
8.7	-1.820	3.748	1.083	1.730	$1.53 \times 10^6$	0.409
8.8	-1.770	3.630	1.065	1.704	$1.52 \times 10^6$	0.406
8.9	-1.741	3.527	1.047	1.684	$1.52 \times 10^6$	0.404
9.0	-1.774	3.486	1.034	1.686	$1.54 \times 10^6$	0.407



**Figure 7.20** Optical absorption spectra  $\alpha(E)$  of  $\text{Cu}_2\text{ZnGeS}_4$ , CZTS, and CZTSe at 300 K, together with those of c-Si, a-Si, and CdTe. The absorption coefficients for  $\text{Cu}_2\text{ZnGeS}_4$ , CZTS, and CZTSe are obtained from the SE data [6–8] (see also Tables 7.9 and 7.10). The  $\alpha(E)$  data for c-Si, a-Si, and CdTe are taken from Adachi [55]

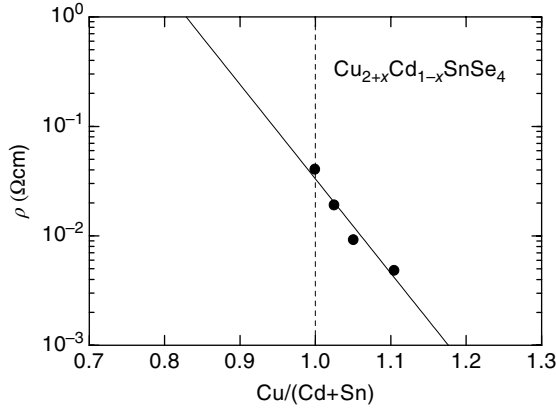
**Table 7.11** Electrical conductivity type, carrier mobility and resistivity for some  $\text{Cu}_2\text{-II-IV-VI}_4$  semiconductors; w-s: wurtz-stannite; s: stannite

Material	Conductivity type	Mobility ( $\text{cm}^2 \text{V}^{-1} \text{s}^{-1}$ )	Resistivity ( $\Omega\text{cm}$ )
$\text{Cu}_2\text{ZnSiS}_4$			Insulating
$\text{Cu}_2\text{ZnSiSe}_4$			$2 \times 10^3 - 3 \times 10^4$
$\text{Cu}_2\text{ZnGeS}_4$	<i>p</i>		$1 - 1.6 \times 10^4$ (w-s)
$\text{Cu}_2\text{ZnGeSe}_4$	<i>p</i>	2–3	$2 \times 10^{-3} - 0.9$
CZTS	<i>p</i>	0.1–35	$3.4 \times 10^{-3} - 600$
CZTSe	<i>p</i>	1.6–39.7	$1 \times 10^{-3} - 9.1$
$\text{Cu}_2\text{CdSiS}_4$			48
$\text{Cu}_2\text{CdGeS}_4$	<i>p</i>	10–15	$40 - 2.5 \times 10^3$
$\text{Cu}_2\text{CdGeSe}_4$	<i>p</i>	1–117	0.5–0.9 (s)
	<i>p</i>		0.1 (w-s)
$\text{Cu}_2\text{CdSnS}_4$	<i>p</i>		0.5
$\text{Cu}_2\text{CdSnSe}_4$	<i>p</i>	5–32	0.02–0.1
$\text{Cu}_2\text{HgGeSe}_4$	<i>p</i>	13	0.3
$\text{Cu}_2\text{HgSnSe}_4$	<i>p</i>	333	0.02

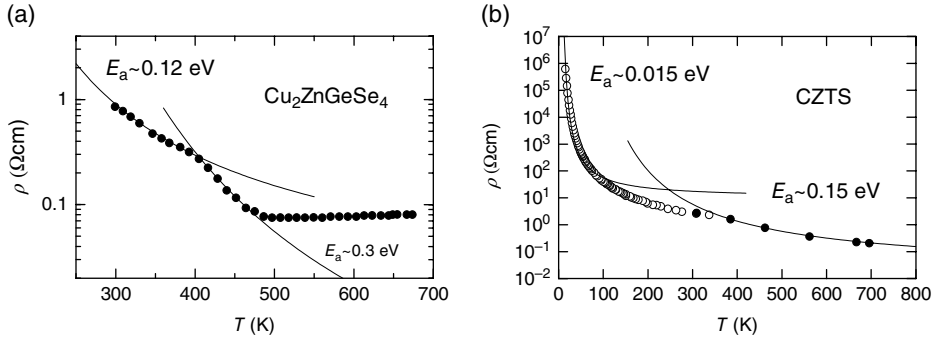


**Figure 7.21** Electrical resistivity  $\rho$  versus  $\text{Cu}/(\text{Zn}+\text{Sn})$  atomic ratio for CZTS at 300 K. The experimental data are gathered from various sources





**Figure 7.22** Electrical resistivity  $\rho$  versus  $\text{Cu}/(\text{Zn}+\text{Sn})$  atomic ratio for  $\text{Cu}_{2+x}\text{Cd}_{1-x}\text{SnSe}_4$  at 300 K. The experimental data are taken from Liu et al. [23]



**Figure 7.23** Electrical resistivity  $\rho$  versus temperature  $T$  for (a)  $\text{Cu}_2\text{ZnGeSe}_4$  [25] and (b) CZTS [22, 58]. The solid lines in (a) and (b) represent the Arrhenius fit results

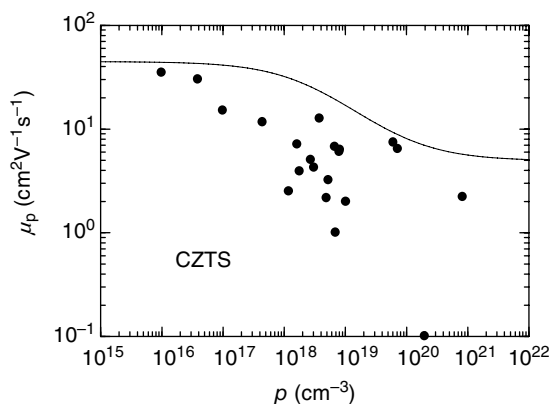
photovoltaic efficiency [9]. Determining whether such non-stoichiometry is essential for obtaining high-efficiency CZTS devices would be an interesting and important area of future research.

Figure 7.23 shows the resistivity  $\rho$  versus temperature  $T$  plots for (a)  $\text{Cu}_2\text{ZnGeSe}_4$  [25] and (b) CZTS [22, 58]. The low-temperature electrical conduction observed at  $T < 50$  K in CZTS is due to the hopping mechanism [58], while those observed in  $\text{Cu}_2\text{ZnGeSe}_4$  and CZTS ( $T > 300$  K) are due to thermally activated hole transport with activation energies of  $E_a \approx 0.12\text{--}0.3$  eV.

### 7.7.2 Hole Mobility

The low-field hole Hall mobility  $\mu$  as a function of free-hole concentration  $p$  can be empirically expressed [20]:

$$\mu(p) = \mu_{\min} + \frac{\mu_{\max} - \mu_{\min}}{1 + (p/p_{\text{ref}})^\alpha} \quad (7.15)$$



**Figure 7.24** Low-field hole Hall mobility  $\mu$  as a function of free-hole concentration  $p$  for CZTS at 300 K. The experimental data are gathered from various sources. The solid line shows the result calculated using Equation (7.15)

where all the fitting parameters are non-negative. Here,  $p_{\text{ref}}$  is a fitting parameter with the aim of achieving dominantly hole–hole scattering at that concentration. This equation implies that, at very low  $p$  concentration,  $\mu$  approaches  $\mu_{\text{max}}$ .

The highest hole  $\mu$  value reported for CZTS is  $35 \text{ cm}^2 \text{ V}^{-1} \text{ s}^{-1}$  ( $p \approx 10^{16}–10^{17} \text{ cm}^{-3}$ ) [59]. Figure 7.24 shows the hole Hall mobilities plotted versus hole concentration  $p$  at 300 K for CZTS. The experimental data are gathered from various sources. The solid line shows the calculated result using Equation (7.15) with  $\mu_{\text{max}} = 45 \text{ cm}^2 \text{ V}^{-1} \text{ s}^{-1}$ ,  $\mu_{\text{min}} = 5 \text{ cm}^2 \text{ V}^{-1} \text{ s}^{-1}$ ,  $p_{\text{ref}} = 3 \times 10^{18} \text{ cm}^{-3}$  and  $\alpha = 0.7$ . We also obtained the best-fit parameters for CZTSe to be  $\mu_{\text{max}} = 55 \text{ cm}^2 \text{ V}^{-1} \text{ s}^{-1}$ ,  $\mu_{\text{min}} = 8 \text{ cm}^2 \text{ V}^{-1} \text{ s}^{-1}$ ,  $p_{\text{ref}} = 2 \times 10^{18} \text{ cm}^{-3}$  and  $\alpha = 1.4$  in Equation (7.15). The highest  $\mu$  value reported for CZTSe at 300 K was c.  $40 \text{ cm}^2 \text{ V}^{-1} \text{ s}^{-1}$  with  $p \approx 2 \times 10^{17} \text{ cm}^{-3}$  [60].

## References

- [1] Ito, K. & Nakazawa, T. (1988) Electrical and optical properties of stannite-type quaternary semiconductor thin films. *Japanese Journal of Applied Physics*, **27**, 2094–2097.
- [2] Tsuji, I., Shimodaira, Y., Kato, H., Kobayashi, H. & Kudo, A. (2010) Novel stannite-type complex sulfide photocatalysts  $A_2^{\text{I}}\text{-Zn-A}^{\text{IV}}\text{-S}_4$  ( $A^{\text{I}}=\text{Cu}$  and  $\text{Ag}$ ;  $A^{\text{IV}}=\text{Sn}$  and  $\text{Ge}$ ) for hydrogen evolution under visible-light irradiation. *Chemistry of Materials*, **22**, 1402–1409.
- [3] Nelson, J. (2003) *The Physics of Solar Cells*. Imperial College Press, London.
- [4] Fernandes, P. A., Salomé, P. M. P. & da Cunha, A. F. (2010)  $\text{Cu}_x\text{SnS}_{x+1}$  ( $x=2, 3$ ) thin films grown by sulfurization of metallic precursors deposited by dc magnetron sputtering. *Physica Status Solidi C*, **7**, 901–904.
- [5] Tanaka, T., Sueishi, T., Saito, K., Guo, Q., Nishio, M., Yu, K. M. & Walukiewicz, W. (2012) Existence and removal of  $\text{Cu}_2\text{Se}$  second phase in coevaporated  $\text{Cu}_2\text{ZnSnSe}_4$  thin films. *Journal of Applied Physics*, **111**, 053522-1–4.
- [6] León, M., Levchenko, S., Serna, R., Gurieva, G., Nateprov, A., Merino, J. M., Friedrich, E. J., Filat, U., Schorr, S. & Arushanov, E. (2010) Optical constants of  $\text{Cu}_2\text{ZnGeS}_4$  bulk crystals. *Journal of Applied Physics*, **108**, 093502-1–5.
- [7] Li, J., Du, H., Yarbrough, Y., Norman, A., Jones, K., Teeter, G., Terry, Jr., F. L. & Levi, D. (2012) Spectral optical properties of  $\text{Cu}_2\text{ZnSnS}_4$  thin film between 0.73 and 6.5 eV. *Optics Express*, **20**, A327–A332.

- [8] Choi, S. G., Zhao, H. Y., Persson, C., Perkins, C. L., Donohue, A. L., To, B., Norman, A. G., Li, J. & Repins, I. L. (2012) Dielectric function spectra and critical-point energies of  $\text{Cu}_2\text{ZnSnSe}_4$  from 0.5 to 9.0 eV. *Journal of Applied Physics*, **111**, 033506-1–6.
- [9] Tanaka, K., Oonuki, M., Moritake, N. & Uchiki, H. (2009)  $\text{Cu}_2\text{ZnSnS}_4$  thin film solar cells prepared by non-vacuum processing. *Solar Energy Materials and Solar Cells*, **93**, 583–587.
- [10] Guo, Q., Hillhouse, H. W. & Agrawal, R. (2009) Synthesis of  $\text{Cu}_2\text{ZnSnS}_4$  nanocrystal ink and its use for solar cells. *Journal of the American Chemical Society*, **131**, 11672–11673.
- [11] Babu, G. S., Kumar, Y. B. K., Bhaskar, P. U. & Raja, V. S. (2008) Effect of post-deposition annealing on the growth of  $\text{Cu}_2\text{ZnSnSe}_4$  thin films for a solar cell absorber layer. *Semiconductor Science and Technology*, **23**, 085023-1–12.
- [12] Gao, F., Yamazoe, S., Maeda, T. & Wada, T. (2012) Structural study of Cu-deficient  $\text{Cu}_{2(1-x)}\text{ZnSnSe}_4$  solar cell materials by X-ray diffraction and X-ray absorption fine structure. *Japanese Journal of Applied Physics*, **51**, 10NC28-1–4.
- [13] Doverspike, K., Dwight, K. & Wold, A. (1990) Preparation and characterization of  $\text{Cu}_x\text{ZnGeS}_{4-y}\text{Se}_y$ . *Chemistry of Materials*, **2**, 194–197.
- [14] Gulay, L. D., Romanyuk, Y. E. & Parasyuk, O. V. (2002) Crystal structures of low- and high-temperature modifications of  $\text{Cu}_2\text{CdGeSe}_4$ . *Journal of Alloys and Compounds*, **347**, 193–197.
- [15] Parasyuk, O. V., Gulay, L. D., Romanyuk, Y. E. & Oleksyuk, I. D. (2002) Phase diagram of the quasi-binary  $\text{Cu}_2\text{GeS}_3$ – $\text{HgS}$  system and crystal structure of the LT-modification of the  $\text{Cu}_2\text{HgGeS}_4$  compound. *Journal of Alloys and Compounds*, **334**, 143–146.
- [16] Quintero, E., Tovar, R., Quintero, M., Delgado, G. E., Morocoima, M., Caldera, D., Ruiz, J., Mora, A. E., Briceño, M. & Fernandez, J. L. (2007) Lattice parameter values and phase transitions for the  $\text{Cu}_x\text{Cd}_{1-x}\text{Mn}_z\text{GeSe}_4$  and  $\text{Cu}_2\text{Cd}_{1-z}\text{Fe}_z\text{GeSe}_4$  alloys. *Journal of Alloys and Compounds*, **432**, 142–148.
- [17] Schorr, S. & Gonzalez-Aviles, G. (2009) In-situ investigation of the structural phase transition in kesterite. *Physica Status Solidi A*, **206**, 1054–1058.
- [18] He, J., Sun, L., Chen, S., Chen, Y., Yang, P. & Chu, J. (2012) Composition dependence of structure and optical properties of  $\text{Cu}_2\text{ZnSn}(\text{S},\text{Se})_4$  solid solutions: An experimental study. *Journal of Alloys and Compounds*, **511**, 129–132.
- [19] Marushko, L. P., Piskach, L. V., Parasyuk, O. V., Oleksyuk, I. D., Volkov, S. V. & Pekhnyo, V. I. (2009) The reciprocal system  $\text{Cu}_2\text{GeS}_3 + 3\text{CdSe} \rightleftharpoons \text{Cu}_2\text{GeSe}_3 + 3\text{CdS}$ . *Journal of Alloys and Compounds*, **473**, 94–99.
- [20] Adachi, S. (2005) *Properties of Group-IV, III–V and II–VI Semiconductors*. John Wiley & Sons Ltd, Chichester.
- [21] Gürel, T., Sevik, C. & Çağın, T. (2011) Characterization of vibrational and mechanical properties of quaternary compounds  $\text{Cu}_2\text{ZnSnS}_4$  and  $\text{Cu}_2\text{ZnSnSe}_4$  in kesterite and stannite structures. *Physical Review B*, **84**, 205201-1–7.
- [22] Liu, M.-L., Huang, F.-Q., Chen, L.-D. & Chen, I.-W. (2009) A wide-band-gap p-type thermoelectric material based on quaternary chalcogenides of  $\text{Cu}_2\text{ZnSnQ}_4$  ( $Q=\text{S},\text{Se}$ ). *Applied Physics Letters*, **94**, 202103-1–3.
- [23] Liu, M.-L., Chen, I.-W., Huang, F.-Q. & Chen, L.-D. (2009) Improved thermoelectric properties of Cu-doped quaternary chalcogenides of  $\text{Cu}_2\text{CdSnSe}_4$ . *Advanced Materials*, **21**, 3808–3812.
- [24] Fan, F.-J., Yu, B., Wang, Y.-X., Zhu, Y.-L., Liu, X.-J., Yu, S.-H. & Ren, Z. (2011) Colloidal synthesis of  $\text{Cu}_2\text{CdSnSe}_4$  nanocrystals and hot-pressing to enhance the thermoelectric figure-of-merit. *Journal of the American Chemical Society*, **133**, 15910–15913.
- [25] Zeier, W. G., LaLonde, A., Gibbs, Z. M., Heinrich, C. P., Panthöfer, M., Snyder, G. J. & Tremel, W. (2012) Influence of a nano phase segregation on the thermoelectric properties of the p-type doped stannite compound  $\text{Cu}_{2+x}\text{Zn}_{1-x}\text{GeSe}_4$ . *Journal of the American Chemical Society*, **134**, 7147–7154.
- [26] Yang, H., Jauregui, L. A., Zhang, G., Chen, Y. P. & Wu, Y. (2012) Nontoxic and abundant copper zinc tin sulfide nanocrystals for potential high-temperature thermoelectric energy harvesting. *Nano Letters*, **12**, 540–545.

- [27] Ibáñez, M., Zamani, R., LaLonde, A., Cadavid, D., Li, W., Shavel, A., Arbiol, J., Morante, J. R., Gorsse, S., Snyder, G. J. & Cabot, A. (2012)  $\text{Cu}_2\text{ZnGeSe}_4$  nanocrystals: Synthesis and thermoelectric properties. *Journal of the American Chemical Society*, **134**, 4060–4063.
- [28] Ibáñez, M., Cadavid, D., Zamani, R., Carcía-Castelló, N., Izquierdo-Roca, V., Li, W., Fairbrother, A., Prades, J. D., Shavel, A., Arbiol, J., Pérez-Rodríguez, A., Morante, J. R. & Cabot, A. (2012) Composition control and thermoelectric properties of quaternary chalcogenide nanocrystals: The case of stannite  $\text{Cu}_2\text{CdSnSe}_4$ . *Chemistry of Materials*, **24**, 562–570.
- [29] Zhukov, E. G., Mkrtchyan, S. A., Dovletov, K., Melikdzhanyan, A. G., Kalinnikov, V. T. & Ashirov, A. (1984) The  $\text{Cu}_2\text{GeSe}_3$ – $\text{CdSe}$  system. *Russian Journal of Inorganic Chemistry*, **29**, 1087–1088.
- [30] Yao, G.-G., Shen, H.-S., Honig, E. D., Kershaw, R., Dwight, K. & Wold, A. (1987) Preparation and characterization of the quaternary chalcogenides  $\text{Cu}_2\text{B(II)C(IV)X}_4$  [B(II)=Zn, Cd; C(IV)=Si, Ge; X=S, Se]. *Solid State Ionics*, **24**, 249–252.
- [31] Mkrtchyan, S. A., Dovletov, K., Zhukov, É. G., Melikdzhanyan, A. G. & Nuryev, S. (1988) Electrophysical properties of  $\text{Cu}_2\text{A}^{\text{II}}\text{B}^{\text{IV}}\text{Se}_4$ . *Inorganic Materials*, **24**, 932–934.
- [32] Konstantinova, N. N., Medvedkin, G. A., Polyshina, I. K., Rud', Y. V., Smirnova, A. D., Sokolova, V. I. & Tairov, M. A. (1989) Optical and electric properties of  $\text{Cu}_2\text{CdSnSe}_4$  and  $\text{Cu}_2\text{CdGeSe}_4$ . *Inorganic Materials*, **25**, 1223–1226.
- [33] Oleksyuk, I. D., Piskach, L. V. & Sysa, L. V. (1996) The  $\text{Cu}_2\text{GeTe}_3$ – $\text{CdTe}$  system and the structure of the compound  $\text{Cu}_2\text{CdGeTe}_4$ . *Russian Journal of Inorganic Chemistry*, **41**, 1356–1358.
- [34] Oleksyuk, I. D. & Piskach, L. V. (1997) Phase equilibria in the  $\text{Cu}_2\text{SnX}_3$ – $\text{CdX}$  (X=S, Se, Te) systems. *Russian Journal of Inorganic Chemistry*, **42**, 274–276.
- [35] Khare, A., Himmetoglu, B., Cococcioni, M. & Aydil, E. S. (2012) First principles calculation of the electronic properties and lattice dynamics of  $\text{Cu}_2\text{ZnSn}(\text{S}_{1-x}\text{Se}_x)_4$ . *Journal of Applied Physics*, **111**, 123704-1–8.
- [36] Altosaar, M., Raudoja, J., Timmo, K., Danilson, M., Grossberg, M., Krustok, J. & Mellikov, E. (2008)  $\text{Cu}_2\text{Zn}_{1-y}\text{Cd}_y\text{Sn}(\text{S}_{1-y}\text{Se}_y)_4$  solid solutions as absorber materials for solar cells. *Physica Status Solidi A*, **205**, 167–170.
- [37] Himmrich, M. & Haeuseler, H. (1991) Far infrared studies on stannite and wurtzstannite type compounds. *Spectrochimica Acta A*, **47**, 933–942.
- [38] Levenco, S., Dumcenco, D. O., Wang, Y. P., Wu, J. D., Huang, Y. S., Arushanov, E., Tezlevan, V. & Tiong, K. K. (2012) Photoluminescence and Raman scattering characterization of  $\text{Cu}_2\text{ZnSiQ}_4$  (Q=S, Se) single crystals. *Optical Materials*, **34**, 1072–1076.
- [39] Grossberg, M., Krustok, J., Raudoja, J., Timmo, K., Altosaar, M. & Raadik, T. (2011) Photoluminescence and Raman study of  $\text{Cu}_2\text{ZnSn}(\text{Se}_x\text{S}_{1-x})_4$  monograins for photovoltaic applications. *Thin Solid Films*, **519**, 7403–7406.
- [40] Adachi, S. (2009) *Properties of Semiconductor Alloys: Group-IV, III–V and II–VI Semiconductors*. John Wiley & Sons Ltd, Chichester.
- [41] Levenco, S., Dumcenco, D., Huang, Y. S., Arushanov, E., Tezlevan, V., Tiong, K. K. & Du, C. H. (2010) Temperature-dependent study of the band-edge excitonic transitions of  $\text{Cu}_2\text{ZnSiS}_4$  single crystals by polarization-dependent piezorefectance. *Journal of Alloys and Compounds*, **506**, 46–50.
- [42] Levenco, S., Dumcenco, D., Huang, Y. S., Arushanov, E., Tezlevan, V., Tiong, K. K. & Du, C. H. (2010) Near band edge anisotropic optical transitions in wide band gap semiconductor  $\text{Cu}_2\text{ZnSiS}_4$ . *Journal of Applied Physics*, **108**, 073508-1–5.
- [43] Levenco, S., Dumcenco, D., Huang, Y. S., Arushanov, E., Tezlevan, V., Tiong, K. K. & Du, C. H. (2011) Absorption-edge anisotropy of  $\text{Cu}_2\text{ZnSiQ}_4$  (Q=S, Se) quaternary compound semiconductors. *Journal of Alloys and Compounds*, **509**, 4924–4928.
- [44] Levenco, S., Dumcenco, D., Huang, Y. S., Arushanov, E., Tezlevan, V., Tiong, K. K. & Du, C. H. (2011) Polarization-dependent electrolyte electroreflectance study of  $\text{Cu}_2\text{ZnSiS}_4$  and  $\text{Cu}_2\text{ZnSiSe}_4$  single crystals. *Journal of Alloys and Compounds*, **509**, 7105–7108.
- [45] Levenco, S., Dumcenco, D., Huang, Y. S., Tiong, K. K. & Du, C. H. (2011) Anisotropy of the spectroscopy properties of the wurtzite-stannite  $\text{Cu}_2\text{ZnGeS}_4$  single crystals. *Optical Materials*, **34**, 183–188.

- [46] Matsushita, H., Maeda, T., Katsui, A. & Takizawa, T. (2000) Thermal analysis and synthesis from the melts of Cu-based quaternary compounds Cu–III–IV–VI<sub>4</sub> and Cu<sub>2</sub>–II–IV–VI<sub>4</sub> (II=Zn, Cd; III=Ga, In; IV=Ge, Sn; VI=Se). *Journal of Crystal Growth*, **208**, 416–422.
- [47] Matsushita, H., Ichikawa, T. & Katsui, A. (2005) Structural, thermodynamical and optical properties of Cu<sub>2</sub>–II–IV–VI<sub>4</sub> quaternary compounds. *Journal of Material Science*, **40**, 2003–2005.
- [48] Salomé, P. M. P., Fernandes, P. A., da Cunha, A. F., Leitão, J. P., Malaquias, J., Weber, A., González, J. C. & da Silva, M. I. N. (2010) Growth pressure dependence of Cu<sub>2</sub>ZnSnSe<sub>4</sub> properties. *Solar Energy Materials and Solar Cells*, **94**, 2176–2180.
- [49] Zhang, J., Shao, L., Fu, Y. and Xie, E. (2006) Cu<sub>2</sub>ZnSnS<sub>4</sub> thin films prepared by sulfurization of ion beam sputtered precursor and their electrical and optical properties. *Rare Metals*, **25**, Special Issue, 315–319.
- [50] Zhou, Z., Wang, Y., Xu, D. & Zhang, Y. (2010) Fabrication of Cu<sub>2</sub>ZnSnS<sub>4</sub> screen printed layers for solar cells. *Solar Energy Materials and Solar Cells*, **94**, 2042–2045.
- [51] Kawashima, T., Adachi, S., Miyake, H. & Sugiyama, K. (1998) Optical constants of CuGaSe<sub>2</sub> and CuInSe<sub>2</sub>. *Journal of Applied Physics*, **84**, 5202–5209.
- [52] Sarswat, P. K. & Free, M. L. (2012) A study of energy band gap versus temperature for Cu<sub>2</sub>ZnSnS<sub>4</sub> thin films. *Physica B*, **407**, 108–111.
- [53] Levenco, S., Dumcenco, D., Wang, Y. P., Huang, Y. S., Ho, C. H., Arushanov, E., Tezlevan, V. & Tiong, K. K. (2012) Influence of anionic substitution on the electrolyte electroreflectance study of band edge transitions in single crystal Cu<sub>2</sub>ZnSn(S<sub>x</sub>Se<sub>1-x</sub>)<sub>4</sub> solid solutions. *Optical Materials*, **34**, 1362–1365.
- [54] Chen, S., Walsh, A., Yang, J.-H., Gong, X. G., Sun, L., Yang, P.-X., Chu, J.-H. & Wei, S.-H. (2011) Compositional dependence of structural and electronic properties of Cu<sub>2</sub>ZnSn(S,Se)<sub>4</sub> alloys for thin film solar cells. *Physical Review B*, **83**, 125201-1–5.
- [55] Adachi, S. (1999) *Optical Constants of Crystalline and Amorphous Semiconductors: Numerical Data and Graphical Information*. Kluwer Academic Press, Boston.
- [56] Nakayama, N. & Ito, K. (1996) Sprayed films of stannite Cu<sub>2</sub>ZnSnS<sub>4</sub>. *Applied Surface Science*, **92**, 171–175.
- [57] Katagiri, H., Ishigaki, N., Ishida, T. & Saito, K. (2001) Characterization of Cu<sub>2</sub>ZnSnS<sub>4</sub> thin films prepared by vapor phase sulfurization. *Japanese Journal of Applied Physics*, **40**, 500–504.
- [58] Leitão, J. P., Santos, N. M., Fernandes, P. A., Salomé, P. M. P., da Cunha, A. F., González, J. C., Ribeiro, G. M. & Matinaga, F. M. (2011) Photoluminescence and electrical study of fluctuating potentials in Cu<sub>2</sub>ZnSnS<sub>4</sub>-based thin films. *Physical Review B*, **84**, 024120-1–8.
- [59] Nagaoka, A., Yoshino, K., Taniguchi, H., Taniyama, T. & Miyake, H. (2012) Preparation of Cu<sub>2</sub>ZnSnS<sub>4</sub> single crystals from Sn solutions. *Journal of Crystal Growth*, **341**, 38–41.
- [60] Wibowo, R. A., Lee, E. S., Munir, B. & Kim, K. H. (2007) Pulsed laser deposition of quaternary Cu<sub>2</sub>ZnSnSe<sub>4</sub> thin films. *Physica Status Solidi A*, **204**, 3373–3379.



# **Part III**

## **Synthesis of Thin Films and Their Application to Solar Cells**





# 8

## Sulfurization of Physical Vapor-Deposited Precursor Layers

*Hironori Katagiri*

*Nagaoka National College of Technology, 888 Nishikatahai, Nagaoka, 940-8532 Japan*

### 8.1 Introduction

Development of the fabrication process of CZTS thin films is necessary to utilize CZTS as an absorber of thin-film solar cells. There are already several publications describing methods of preparation of CZTS thin films. In the field of physical vapor deposition, they include sulfurization of precursors [1, 2], co-evaporation followed by annealing [3], single-step co-evaporation [4–6], pulsed laser deposition [7, 8], and others. Each method has its own individual features. Taking into account the large scale of industrial solar cell production, a two-stage process of sulfurization of physical vapor-deposited precursor layers would have a great advantage. This process consists of precursor fabrication and sulfurization. In 1996, we successfully fabricated a CZTS thin film on a soda-lime glass (SLG) substrate by electron beam (EB) evaporation followed by a sulfurization technique. As a result, an open-circuit voltage of 400 mV and a conversion efficiency of 0.66% were obtained by making a thin-film solar cell structure of SLG/Mo/CZTS/CdS/AZO for the first time [9]. To improve the conversion efficiency, many experiments have been conducted since then. In the late 1990s, the authors focused on stoichiometric CZTS films to characterize their properties. From our present viewpoint, this is considered as one of the reasons why the conversion efficiency was so limited. In fact, our study performed after 2003 revealed that in order to obtain high conversion efficiency cells, CZTS with the off-stoichiometric composition, namely Cu-poor and Zn-rich composition, is preferable to the stoichiometric CZTS. To clarify the existence of such active composition ranges in more

detail, a co-sputtering system was utilized in our laboratory. In this chapter, sulfurization of physical vapor-deposited precursor layers is discussed.

## 8.2 First CZTS Thin-Film Solar Cells

Table 8.1 shows the processes for preparing CZTS thin films and photovoltaic properties of CZTS thin-film solar cells obtained from 1995 to 2008 in our laboratory [9–15]. In Process 1, CZTS films were fabricated by sulfurization of electron beam (EB) evaporated precursors. These precursors consisted of SLG/(Mo)/Zn/Sn/Cu structure and the stacking order was fixed in this process. Each stacked precursor thickness was 160 nm for Zn, 230 nm for Sn, and 180 nm for Cu. The substrate temperature was kept at 150°C in the first stage of precursor deposition, and then CZTS was obtained through a heat treatment in a  $N_2+H_2S$  atmosphere. In this process, a concentration of  $H_2S$  in the reactive gas was kept at 5 vol%. The highest temperature of this heat treatment was limited to 500°C because a tubular furnace with Pyrex glass was used in this experiment. The substrate temperature was elevated to 300°C from room temperature at a rate of 20°C min<sup>-1</sup> and then to 500°C at a rate of either 10°C min<sup>-1</sup> or 2°C min<sup>-1</sup>. The retention time at the highest temperature was either 1 hour or 3 hours. After the heat treatment, the temperature was lowered to 300°C at a rate of 2°C min<sup>-1</sup> and the furnace was then cooled naturally.

From XRD measurements of the CZTS absorber, we confirmed that the peak strength due to secondary phases decreases when the retention time is lengthened and the temperature ramp-up rate is lowered. Under the same condition, the slope of the absorption coefficient versus photon energy curve near the fundamental absorption edge, around 1.5 eV, becomes steeper according to the optical measurement of the film. These results indicate that the crystallinity of CZTS thin films is improved by long sulfurization. Film composition was determined by electron probe microanalysis (EPMA), and the composition ratios of the CZTS film exhibiting desirable properties in both XRD and optical measurements were Cu/(Zn+Sn)=0.960, Zn/Sn=0.916, and S/Metal=1.03. In the latter expression for the composition ratio, “Metal” refers to the total atomic composition of (Cu+Zn+Sn). For the stoichiometric film, all these ratios have to become equal to 1. In Process 1, it was found that Zn/Sn ratio decreases and Cu/(Zn+Sn) ratio increases by increasing the retention time, implying that the volatile Zn is re-evaporated in the long sulfurization process.

To fabricate a CZTS cell, a CdS buffer layer of 20 nm in thickness was deposited on the CZTS absorber. This was conducted by a chemical bath deposition (CBD) process using Cd sulfate, thiourea, ammonia solution, and de-ionized water in a CBD solution at a temperature of 60°C. An Al-doped ZnO window layer was then deposited by an RF sputtering technique using an AZO (ZnO+Al<sub>2</sub>O<sub>3</sub> : 1 wt%) target. As a result, the first CZTS solar cell with an open-circuit voltage  $V_{oc}$  of 400 mV, a short-circuit current density  $J_{sc}$  of 6.0 mA cm<sup>-2</sup>, a fill factor FF of 0.277, and a conversion efficiency of 0.66% was reported for the first time.

## 8.3 ZnS as Zn-Source in Precursor

Process 1 demonstrated the serious problem that CZTS films do not exhibit strong adhesion with substrates. In Process 2, three methods to improve adhesion were therefore examined. The first was to introduce modified precursors consisting of SLG/(Mo)/ZnS/Sn/Cu.

**Table 8.1** The fabrication processes used and the obtained photovoltaic properties from 1995 to 2008 in our laboratory

		Process 1	Process 2	Process 3	Process 4	Process 5.1	Process 5.2	Process 6
Precursor Fabrication	Method Precursor	EB evaporation Zn/Sn/Cu	EB evaporation ZnS/Sn/Cu	EB evaporation ZnS/Sn(SnS <sub>2</sub> )/Cu	EB evaporation ZnS/Sn/Cu	EB evaporation ZnS/Cu/Sn	EB evaporation 5x(ZnS/SnS <sub>2</sub> /Cu)	Co-sputtering Cu+ZnS+SnS
Sulfurization procedure	Substrate temp. (°C)	150	150	200→400	150	150	200→400	Non-heating
	Sulfurization system	Pyrex glass tube hot-wall-type resistive-wire heater	Quartz glass tube hot-wall-type resistive-wire heater	Quartz glass tube hot-wall-type resistive-wire heater	SUS chamber cold-wall-type lamp heater	SUS chamber cold-wall-type lamp heater	SUS chamber cold-wall-type lamp heater	SUS chamber cold-wall-type SiC heater
	Atmosphere	H <sub>2</sub> S (5 vol%) N <sub>2</sub> -balanced 500°C/1, 3 h	H <sub>2</sub> S (5 vol%) N <sub>2</sub> -balanced 530°C/1+6 h	H <sub>2</sub> S (5 vol%) N <sub>2</sub> -balanced 550°C/1, 3 h	H <sub>2</sub> S (5 vol%) N <sub>2</sub> -balanced 550°C/3 h	H <sub>2</sub> S (5 vol%) N <sub>2</sub> -balanced 520°C/3 h	H <sub>2</sub> S (5 vol%) N <sub>2</sub> -balanced 540°C/1 h	H <sub>2</sub> S (20 vol%) N <sub>2</sub> -balanced 580°C/3 h
Cell fabrication	$T_{\text{sub}}$ /time	20°C min <sup>-1</sup> (to 300°C)	10°C min <sup>-1</sup> (to 200°C)	10°C min <sup>-1</sup> (to 200°C)	10°C min <sup>-1</sup> (to 200°C)	5°C min <sup>-1</sup> (to 520°C)	10°C min <sup>-1</sup> (to 540°C)	5°C min <sup>-1</sup> (to 580°C)
	Rate of temp. change	10, 2°C min <sup>-1</sup> (to 500°C)	2°C min <sup>-1</sup> (to 530°C)	2°C min <sup>-1</sup> (to 550°C)	2°C min <sup>-1</sup> (to 550°C)	2°C min <sup>-1</sup> (to 550°C)	2°C min <sup>-1</sup> (to 550°C)	—
	Buffer layer	2°C min <sup>-1</sup> (to 300°C)	2°C min <sup>-1</sup> (to 300°C)	2°C min <sup>-1</sup> (to 300°C)	2°C min <sup>-1</sup> (to 300°C)	Natural cooling	Natural cooling	5°C min <sup>-1</sup> (to 200°C)
Composition Ratio	Cd-source	CBD-CdS	CBD-CdS	CBD-CdS	CBD-CdS	CBD-CdS	CBD-CdS	CBD-CdS
	Window layer	CdSO <sub>4</sub> AZO (Al <sub>2</sub> O <sub>3</sub> :1wt%) EPMA	CdSO <sub>4</sub> AZO (Al <sub>2</sub> O <sub>3</sub> :1wt%) EPMA	CdSO <sub>4</sub> AZO (Al <sub>2</sub> O <sub>3</sub> :2wt%) EPMA	CdSO <sub>4</sub> AZO (Al <sub>2</sub> O <sub>3</sub> :2wt%) EPMA	CdI <sub>2</sub> AZO (Al <sub>2</sub> O <sub>3</sub> :2wt%) EDS	CdI <sub>2</sub> AZO (Al <sub>2</sub> O <sub>3</sub> :2wt%) EDS	CdI <sub>2</sub> AZO (Al <sub>2</sub> O <sub>3</sub> :2wt%) ICP
	Method Cu/(Zn+Sn)	0.96	0.99	0.936	0.96	0.85	0.73	0.87
	Zn/Sn	0.916	1.01	1.02	1.08	1.03	1.7	1.15

(Continued)

**Table 8.1** (Continued)

	Process 1	Process 2	Process 3	Process 4	Process 5.1	Process 5.2	Process 6
Photovoltaic Properties							
$V_{oc}$ (mV)	400	372	522	530, 659, 582	629	644	662
$J_{sc}$ (mA cm <sup>-2</sup> )	6	8.36	14.1	14.8, 10.3, 15.5	12.5	9.23	15.7
Fill factor	0.277	0.347	0.355	0.46, 0.63, 0.60	0.58	0.66	0.55
Area (cm <sup>2</sup> )	0.187	0.105	0.128	0.16, 0.11, 0.11	0.113	0.113	0.155
Efficiency (%)	0.66	1.08	2.62	3.46, 4.25, 5.45	4.53	3.93	5.74
Remarks	First CZTS solar cell	ZnS as Zn-source in precursor	Influence of absorber thickness	New sulfurization system	Influence of morphology	Multi-period precursor	6.77% with DIW-soaking
References	[9]	[10]	[11]	[12]	[13]	[13]	[14, 15]

The first Zn layer in a precursor was replaced with ZnS. Using ZnS as a Zn-source, we tried to control the volume expansion of precursors during sulfurization. The second improvement was seen by the elevation of sulfurization temperature from 500°C to 530°C. Since we believed that the higher temperature would improve the film quality, we replaced the Pyrex tube with a quartz tube in order to elevate the sulfurization temperature. Finally, we extended the annealing period to 6 hours in a  $N_2$  atmosphere at the same temperature, after a 1 hour sulfurization in reactive gas was completed.

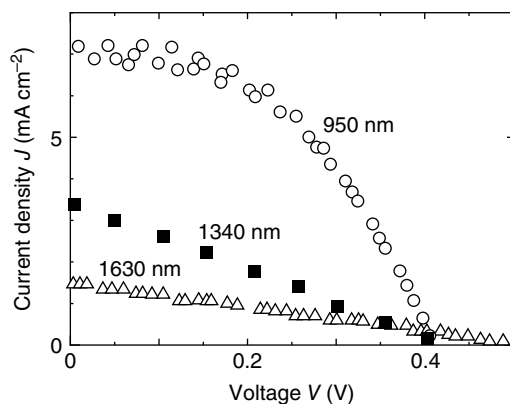
According to scanning electron microscopy (SEM) observations, we could confirm that the grain size was larger than that of Process 1 and there were no voids or cavities between the CZTS films and the substrates. The depth profile estimated by Auger electron spectroscopy (AES) revealed that the CZTS films had a uniform composition [10]. The composition ratios examined by EPMA were  $Cu/(Zn+Sn)=0.990$ ,  $Zn/Sn=1.01$ , and  $S/Metal=1.07$ . We obtained photovoltaic characteristics of  $V_{oc}$  of 372 mV,  $J_{sc}$  of 8.36 mA cm<sup>-2</sup>, FF of 0.347, and a conversion efficiency of 1.08%. From our present viewpoint, the reason that  $V_{oc}$  remained so low is that the composition ratio was set at stoichiometry.

## 8.4 Influence of Absorber Thickness

Process 2 saw the introduction of 7 hours of heat treatment at a constant temperature of 530°C by taking into account the homogeneity seen in the depth profile. However, this lengthy heat treatment was not desirable for the fabrication process of low-cost thin-film solar cells. In Process 3, the sulfurization condition was fixed at 1 hour at 550°C, and the influence of the film thickness on photovoltaic properties was investigated. The structure of precursors was the stacked layers consisting of SLG/Mo/ZnS/Sn/Cu. The thickness ratio of each layer of ZnS, Sn, and Cu were adjusted at 1.00, 0.636, and 0.409 respectively. Three types of precursors were prepared with a total thickness of 300 nm, 450 nm, and 600 nm. By sulfurizing these precursors, CZTS films of 950 nm, 1340 nm, and 1630 nm in thickness were obtained.

Figure 8.1 shows the comparison of  $J$ - $V$  characteristics observed with this experiment. The photovoltaic properties including the conversion efficiency, FF, and  $J_{sc}$  were obviously degraded by the increase in the absorber thickness. We therefore infer that the sulfurization was not sufficient under this condition when the film thickness increased. Considering the stacking order of the precursor SLG/Mo/ZnS/Sn/Cu, there must be a Cu-rich surface layer with low resistivity and a Zn-rich layer with high resistivity near the back contact of Mo for the thicker absorber. Therefore, when the sulfurization condition is not sufficient, the thicker the absorber, the higher the series resistance in the film thickness direction. To fabricate CZTS cells, the sulfurization condition of 1 hour at 550°C should be insufficient because CZTS films of over 1500 nm in thickness are desirable for the absorber layers.

At that point, the aims of our studies were to enhance the adhesion and to suppress the volume expansion at the sulfurization stage. The concentration of S in the precursor was therefore very important. To obtain a CZTS films of high quality and homogeneity, both a slower ramp-up rate and a longer retention time were needed. To fabricate solar cells,  $SnS_2$  was therefore used as a Sn-source in the precursors. Furthermore, the substrate temperature was set as low as 200°C during the evaporation period of ZnS and  $SnS_2$ ; it was then raised to 400°C during the evaporation period of Cu. To enhance the inter-diffusion of elements



**Figure 8.1** Comparison of  $J$ - $V$  characteristics observed by using various absorber thicknesses

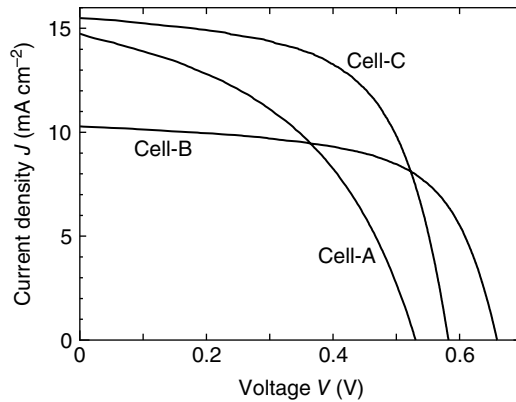
in the precursor, the temperature was kept at 400°C for 1 hour in the same vacuum chamber after the Cu deposition. The sulfurization was conducted for 3 hours at 550°C, and the ramp-up rate and the cooling rate are listed in Table 8.1. Finally, the sputtering target for a window layer changed to AZO ( $\text{ZnO}+\text{Al}_2\text{O}_3$ ; 2 wt%). As a result, the cell properties of  $V_{oc}$  of 522 mV,  $J_{sc}$  of 14.1  $\text{mA cm}^{-2}$ , FF of 0.355, and a conversion efficiency of 2.62% were obtained [11].

## 8.5 New Sulfurization System

In our previous study, the sulfurization system was constructed with a tubular furnace and a rotary pump. Because it was impossible to evacuate to high vacuum in this system, the residual active gas might have degraded the quality of CZTS films. In Process 4, a new sulfurization system constructed with a stainless steel chamber and a turbo molecular pump (TMP) was introduced to eliminate the influence of the residual gas. This was a so-called cold-wall-type furnace, having a lamp heater to elevate the substrate temperature.

Using an EB evaporation system, the stacked precursors of SLG/Mo/ZnS/Sn/Cu were prepared at the substrate temperature of 150°C. The thicknesses of the ZnS, Sn and Cu were 330 nm, 150 nm, and 90 nm, respectively. To obtain the CZTS films, those precursors were sulfurized in a new sulfurization system. In this system, the chamber could be evacuated to a high vacuum of the order  $10^{-4}$  Pa before the sulfurization of the precursor. In Process 3, we confirmed that the sulfurization condition of 1 hour at 550°C was insufficient for the CZTS with thickness over 1000 nm. In Process 4, the sulfurization was conducted for 3 hours at 550°C. As a result, the film thickness of the sulfurized CZTS was about 1400 nm according to the SEM observation and, as revealed by EPMA, the composition ratios of  $\text{Cu}/(\text{Zn}+\text{Sn})$ ,  $\text{Zn}/\text{Sn}$ , and  $\text{S}/\text{Metal}$  were 0.96, 1.08, and 0.92, respectively.

In our previous study the FF had been less than 0.4, so the highest conversion efficiency still remained as low as 2.62%. To improve the conversion efficiency further, we had to increase the FF. In order to form a better pn-junction between a CdS buffer layer and a CZTS thin film, we studied the influence of chemical substances such as Cd-source

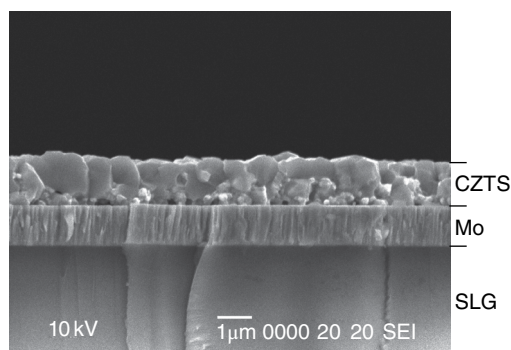


**Figure 8.2**  $J$ - $V$  characteristics of CZTS thin-film solar cells. The solar cells were fabricated by the new sulfurization system which was used in Process 4

dissolved in the CBD solution. Three types of solar cells were fabricated by using CZTS absorbers mentioned above. Figure 8.2 shows the comparison of  $J$ - $V$  characteristics obtained by Process 4. We prepared two cells, Cell A and Cell B, with CdS buffer layers using  $\text{CdSO}_4$  and  $\text{CdI}_2$ , respectively. Photovoltaic properties of  $V_{oc} = 530$  mV,  $J_{sc} = 14.8$  mA  $\text{cm}^{-2}$ , FF = 0.46, and conversion efficiency of 3.46% were observed for Cell A. On the other hand, for Cell B prepared using  $\text{CdI}_2$   $V_{oc} = 659$  mV,  $J_{sc} = 10.3$  mA  $\text{cm}^{-2}$ , FF = 0.63, and a conversion efficiency of 4.25% were obtained. The short-circuit current density had deteriorated in Cell B; however, the open-circuit voltage and the fill factor were improved significantly. In addition, in order to investigate the presence of the Na effect that is commonly known in CIGS, Cell C was fabricated using the substrate  $\text{SLG}/\text{SiO}_2/\text{Mo}/\text{Na}_2\text{S}$  and  $\text{CdI}_2$  was used as a Cd-source in a CBD solution. The short-circuit current density was much improved in Cell C and, as a consequence, the conversion efficiency was increased. Photovoltaic properties of  $V_{oc} = 582$  mV,  $J_{sc} = 15.5$  mA  $\text{cm}^{-2}$ , FF of 0.60, and a conversion efficiency of 5.45% were achieved [12]. From the viewpoint of the shunt resistance estimated from the  $J$ - $V$  characteristics of these three cells, it was confirmed that Cell A prepared by using  $\text{CdSO}_4$  demonstrated the poorest performance. This implies that there would be a difference in the quality of CdS buffer layer corresponding to Cd-source in CBD solution. However, because the thickness of this buffer layer was only a few tens of nanometers, we were not able to evaluate those properties precisely. Furthermore, the origin of the Na effect could not be clarified due to the poor reproducibility in our experiment.

## 8.6 Influence of Morphology

From SEM observations, it was recognized that there were many voids and cavities in CZTS thin films prepared from conventional  $\text{SLG}/\text{Mo}/\text{ZnS}/\text{Sn}/\text{Cu}$  stacked precursors due to the difficulty of making a flat surface of Sn. In fact, the evaporated Sn tended to form a hemispheroid on a flat substrate. In order to improve the morphology of CZTS thin films, the stacking order was changed to  $\text{SLG}/\text{Mo}/\text{ZnS}/\text{Cu}/\text{Sn}$  in Process 5.1. The Sn layer was



**Figure 8.3** Cross-sectional SEM image of SLG/Mo/CZTS. The CZTS thin film was prepared from a multi-layered precursor

deposited as a final layer instead of a middle layer. From this trial, it was confirmed that the morphology of CZTS absorber was much improved according to SEM observations. Photovoltaic properties of  $V_{oc} = 629$  mV,  $J_{sc} = 12.5$  mA cm<sup>-2</sup>, FF = 0.58, and conversion efficiency of 4.53% were obtained, representing the best data without any Na addition at that moment in time.

To improve the morphology of CZTS precursors and to enhance the inter-diffusion of elements in them, a multi-layer type precursor was examined in Process 5.2. Each layer consisted of ZnS/SnS<sub>2</sub>/Cu. We prepared a five-layer precursor on the SLG/Mo substrate and annealed it for 1 hour at 400°C in the same chamber immediately after the evaporation. This precursor was then sulfurized to form a CZTS absorber. The composition ratios of this CZTS absorber determined by energy dispersive spectrometry (EDS) were Cu/(Zn+Sn)=0.73, Zn/Sn=1.7, and S/Metal=1.1. Figure 8.3 shows the cross-section SEM image of SLG/Mo/CZTS. It was confirmed that the grain size was as large as the film thickness and the surface was quite smooth. Using this multi-layered precursor, photovoltaic properties of  $V_{oc} = 644$  mV,  $J_{sc} = 9.23$  mA cm<sup>-2</sup>, FF = 0.66, and a conversion efficiency of 3.93% were obtained. As mentioned above, this CZTS absorber was fairly Zn-rich and Cu-poor. However, their photovoltaic properties were not so degraded as compared with other cells [13]. It was therefore confirmed that both the enhancement of an inter-diffusion of elements in a precursor and the improvement of film morphology are quite important to achieve high conversion efficiency.

## 8.7 Co-Sputtering System with Annealing Chamber

Co-sputtering was one of the most useful methods to enhance the inter-diffusion of elements in a precursor. In Process 6, a mixed-precursor was prepared using a co-sputtering system with annealing chamber. In this system, three 10.6-mm-diameter cathodes with each RF source are set up for three-phase co-sputtering. The targets used were Cu, ZnS, and SnS. The precursor was transported between the sputtering chamber and the annealing chamber without exposure to atmospheric air, as it was considered important to keep the surface of the precursor clean.



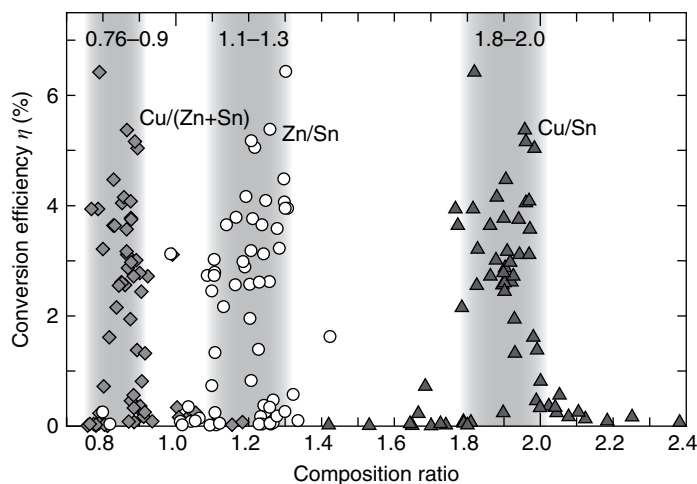
The process was started when the sputtering chamber pressure was of the order  $10^{-4}$  Pa. The parameters of the precursor fabrication were: Ar gas flow rate: 50 sccm; Ar gas pressure: 0.5 Pa; substrate rotation: 20 rpm; pre-sputter time: 3 minutes, no substrate-heating; and typical applied target power: 89–95 W for Cu, 160 W for ZnS, and 100 W for SnS. The prepared precursor could be automatically transferred to the annealing chamber and the chamber was evacuated again to the vicinity of  $10^{-4}$  Pa. The reactive gas of  $N_2+H_2S$  (20 vol%) was flowed to the chamber after closing the main valve. The annealing temperature was elevated from room temperature to  $580^\circ\text{C}$  at the rate of  $5^\circ\text{C min}^{-1}$  and was retained for 3 hours. It was then lowered at the same rate to  $200^\circ\text{C}$  followed by natural cooling. These sulfurization conditions were determined according to the results of the preliminary experiments: using SEM we observed the film morphology and, using inductively coupled plasma atomic emission spectroscopy (ICP-AES), we examined the composition.

In Process 6, all the cells prepared by every RF power for the Cu target showed a conversion efficiency of over 4%. At the RF power of 89 W, photovoltaic properties of  $V_{oc} = 662$  mV,  $J_{sc} = 15.7$  mA  $\text{cm}^{-2}$ , FF = 0.55, and a conversion efficiency of 5.74% were obtained [14]. The composition ratios were  $\text{Cu}/(\text{Zn}+\text{Sn})=0.87$ ,  $\text{Zn}/\text{Sn}=1.15$ , and  $\text{S}/\text{Metal}=1.18$ , which we refer to as the Cu-poor and Zn-rich composition. Furthermore, EPMA measurements revealed that soaking in de-ionized water (DIW) had the effect of preferential etching, which selectively eliminated metal oxide particles in the CZTS layer. By soaking in DIW, a conversion efficiency of 6.77% was achieved [15].

## 8.8 Active Composition

In the characterization of new materials, it would be quite natural for a researcher to intend to form single crystals with stoichiometry. Although we had no expertise in the growth of single crystals, in the early period of this research we attempted to form the stoichiometric CZTS films. All that had to be done was to make a high-quality CZTS film without any defect as far as possible. Solar cells were fabricated using a nearly stoichiometric CZTS film as an absorber layer. We currently believe that the conversion efficiency was low due to focusing our attention on the stoichiometry. After Process 4 (Table 8.1) was researched it was experimentally recognized that, in order to increase the conversion efficiency, off-stoichiometry composition (i.e. Cu-poor and Zn-rich composition of CZTS) is preferable to stoichiometry.

Here we discuss what composition ratio is needed to achieve the high conversion efficiency. Using a co-sputtering system with annealing chamber, we fabricated solar cells with CZTS absorber layers with a wide range of composition ratio ( $\text{Cu}/(\text{Zn}+\text{Sn})$ : 0.75–1.25;  $\text{Zn}/\text{Sn}$ : 0.80–1.35) [16]. As a result, it was confirmed that the highly efficient cells can only be obtained in a relatively narrow region in the compositional map, that is, in the range of Cu-poor and Zn-rich composition. The fabrication procedure was very similar to that of Process 6, though Sn was used in this experiment instead of SnS. In fact, there was a problem with the stability of the sputtering rate of SnS and the concentration of  $H_2S$  was diluted to 5 vol% instead of 20 vol% to reduce the damage caused. The chemical compositions of the films were determined by X-ray fluorescence (XRF) in this experiment. Because XRF is a non-destructive method, solar cells could be fabricated by using the CZTS absorber, the composition of which was determined by XRF in advance. In other words, the

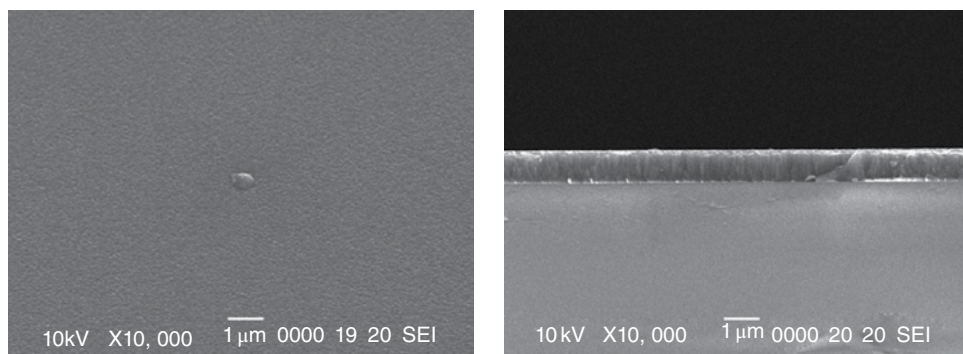


**Figure 8.4** Conversion efficiency of CZTS thin-film solar cells as a function of composition ratio

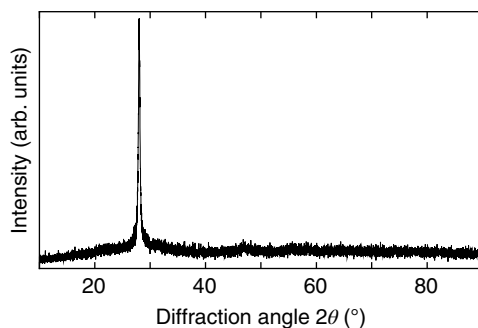
compositional shift of the films after sulfurization could be examined. Figure 8.4 shows the distribution of the conversion efficiency of CZTS thin-film solar cells as a function of the composition ratio. This figure represents the composition ratio of CZTS absorber after sulfurization. It was found that each composition ratio should be restricted to a narrow region if obtaining high conversion efficiency solar cells was the aim. The region could be quantified as 0.76–0.90 for Cu/(Zn+Sn), 1.1–1.3 for Zn/Sn, and 1.8–2.0 for Cu/Sn, referred to as the active composition region.

## 8.9 CZTS Compound Target

If a CZTS compound target can be used, an absorber layer may be formed by a simple single sputtering technique. Considering future expansion in photovoltaics, this simple method has a great advantage. At first, a near-stoichiometric target was examined by using an RF magnetron sputtering system with a 76.2-mm-diameter CZTS compound target. Sputtering conditions were as follows: distance between the target and substrate: 70 mm; applied RF power: 40 W; and substrate rotation: 30 rpm. Because this target was a sulfide compound, we could not apply the high RF power. Sputtering was conducted at the relatively low power of 40 W for 105 min. SEM observations revealed that the as-sputtered film was 1020 nm in thickness. Figure 8.5 shows the SEM images of the as-sputtered film; the surface was quite smooth and the columnar morphology was confirmed. Using XRD of Cu-K $\alpha$  radiation, the crystal structure of the film was examined. Figure 8.6 shows the XRD pattern of the as-sputtered film; from this pattern, we confirm that (112)-oriented polycrystalline film was fabricated successfully with a near-stoichiometric target. Using this as-sputtered film as an absorber the cell structure was fabricated. However, the photovoltaic effect could not be observed at all.



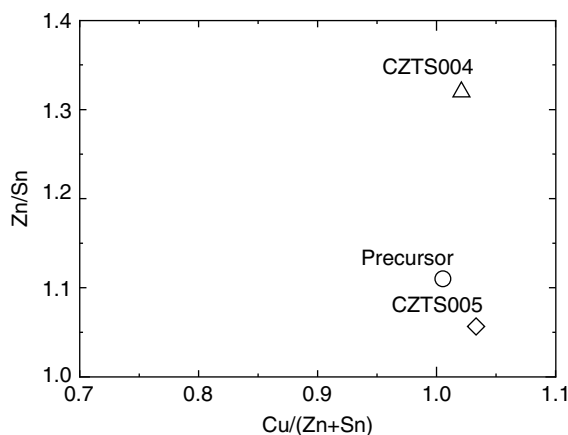
**Figure 8.5** SEM images of as-sputtered film. This sputtering was conducted by using the CZTS compound target



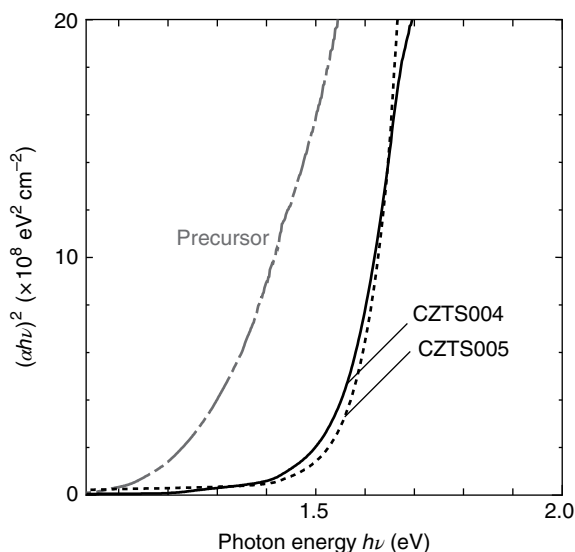
**Figure 8.6** XRD pattern of as-sputtered film

To improve the film properties, heat treatment was conducted for 3 hours at 500°C in both pure  $N_2$  and  $N_2+H_2S$  (5 vol%) atmosphere. During both elevating and cooling periods, the temperature of an electric furnace was changed at the constant rate of  $5^\circ\text{C min}^{-1}$ . Hereafter, we use the term “ $N_2$ -annealing” to refer to heat treatment in pure  $N_2$ , and the term “sulfurization” to refer to heat treatment in  $N_2+H_2S$  (5 vol%). The  $N_2$ -annealed film and sulfurized film were named CZTS004 and CZTS005, respectively. Figure 8.7 shows the change in the composition ratio by both heat treatments. Despite the near-stoichiometric composition of the target, the as-sputtered film had a Zn-rich composition which was designated as a precursor in this figure. In general, this composition change was due to both the density of the compound target and the sputtering condition. The point of CZTS005 in Figure 8.7 shows that there was a small shift of composition ratio towards a Zn-poor region through the sulfurization. However, from the data point of CZTS004, a large increase in Zn/Sn ratio by the  $N_2$ -annealing could be seen. This change was as large as 18%. At the same time, we confirmed that the S/Metal ratio was decreased. We therefore infer that the  $N_2$ -annealing enhanced the sublimation of the Sn-related sulfide compound.

Figure 8.8 shows the comparison of the optical properties of CZTS films. From this figure, the increase of the band-gap energy through both heat treatments was confirmed.

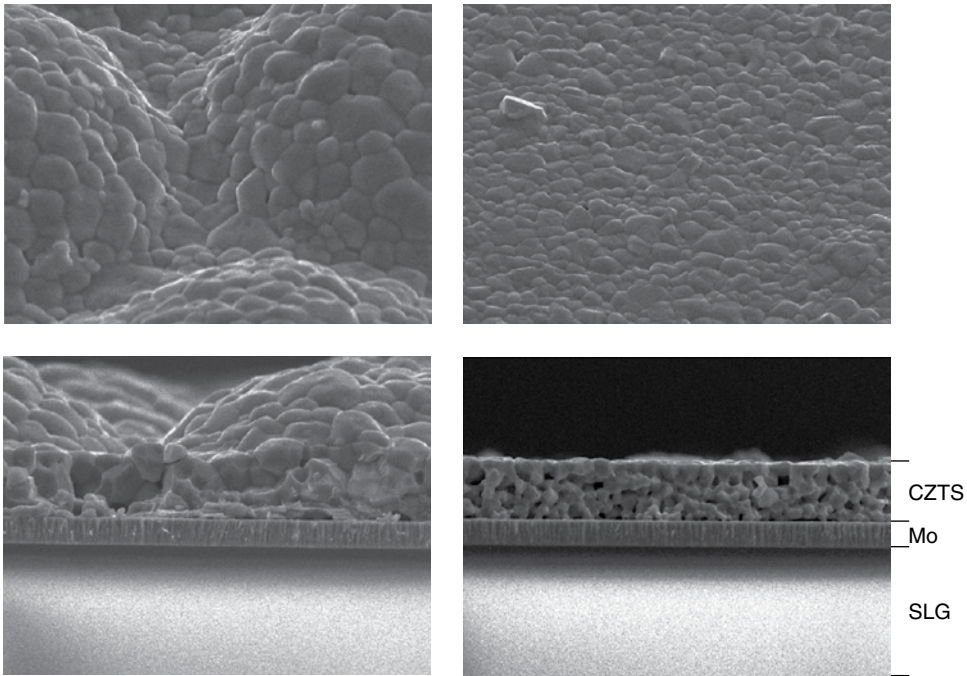


**Figure 8.7** Change in the composition ratio through both heat treatments



**Figure 8.8** Optical properties of CZTS thin films

We can see that the band-gap energy of around 1.2 eV of the precursor increases to 1.5 eV after both heat treatments. In this figure, two lines obtained after both heat treatments were almost overlapping. Furthermore, the gradient of the curve became steeper after the heat treatments. In many studies of CZTS films, an optical band-gap energy of around 1.5 eV has been quoted. As mentioned before, on Figure 8.6 of XRD the sharp (112) peak was observed with a near-stoichiometric target. At first we thought a polycrystalline film of high quality was successfully formed by simple sputtering. However, considering these

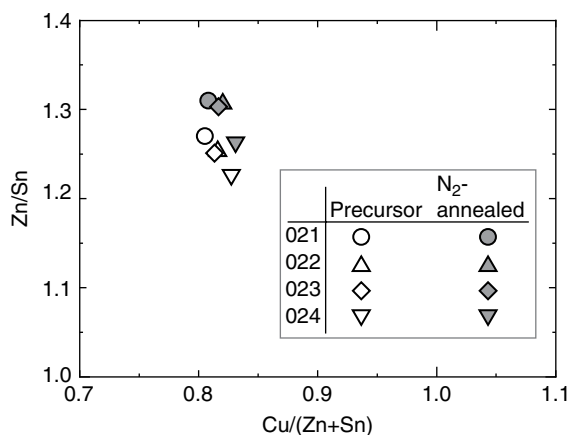


**Figure 8.9** Comparison of the SEM images of both  $N_2$ -annealed and sulfurized films

changes in the optical properties, the film quality of as-sputtered film was not so desirable for an absorber.

Figure 8.9 shows the comparison of the SEM images of both  $N_2$ -annealed and sulfurized films. On the left side, CZTS004 of  $N_2$ -annealed film has a surface with large bumps. On the other hand, CZTS005 of sulfurized film shows a relatively flat surface. Note the difference of the magnification of the SEM images. There were quite large bumps in the  $N_2$ -annealed film. If a high-quality CZTS absorber with good morphology could be produced with single sputtering followed by  $N_2$ -annealing, this would be a very important cost saving for the PV industry. To investigate the influence of temperature on the film morphology, the annealing temperature was varied. As a result, the bumps were formed at temperatures higher than  $460^\circ\text{C}$ . Considering the weak adhesion between the film and Mo back contact, the fabrication of the cell structure using films containing these bumps were relinquished. On the other hand,  $N_2$ -annealed film with  $440^\circ\text{C}$  showed a flat surface and strong adhesion. We tried to fabricate solar cells using this film as an absorber. As a result, the conversion efficiency could not be observed at all because this film was slightly Cu-rich.

To obtain the photovoltaic effect, absorbers with active composition had to be fabricated. A co-sputtering system with two CZTS compound targets were used to control the film composition. One target was near-stoichiometric and another had a Cu-poor and Zn-rich composition. CZTS thin films were therefore co-sputtered with two CZTS compound targets followed by  $N_2$ -annealing. We prepared four samples with nearly active composition. Figure 8.10 depicts the composition change through the  $N_2$ -annealing. Because the slight



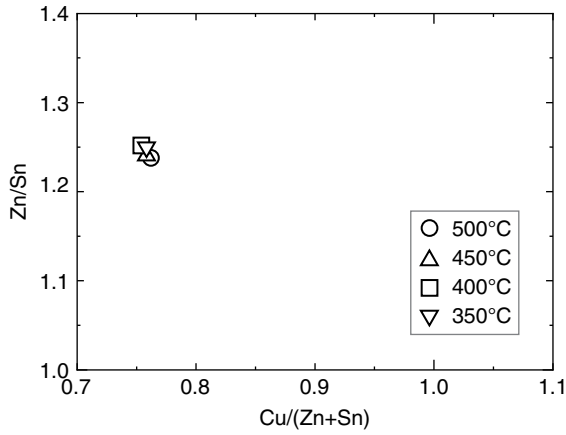
**Figure 8.10** Change in the composition ratio during the  $N_2$ -annealing process

increase in the Zn/Sn ratio could be seen, it was inferred that Sn or  $SnS_x$  was evaporated during the  $N_2$ -annealing; the average change of these compositions was only 4%, however. On the other hand, the change confirmed in Figure 8.7 was 18%. From these results, the amount of the evaporated Sn or  $SnS_x$  was dependent on the composition of as-sputtered films as well as the annealing atmosphere. Solar cells were fabricated using  $N_2$ -annealed CZTS film as an absorber, with nearly active composition. However, all of these solar cells showed quite low conversion efficiencies of  $< 0.5\%$ , caused by the fact that the temperature was kept as low as  $460^\circ\text{C}$ . To suppress the bump formation in the  $N_2$ -annealing, we were not able to elevate the temperature above  $460^\circ\text{C}$ .

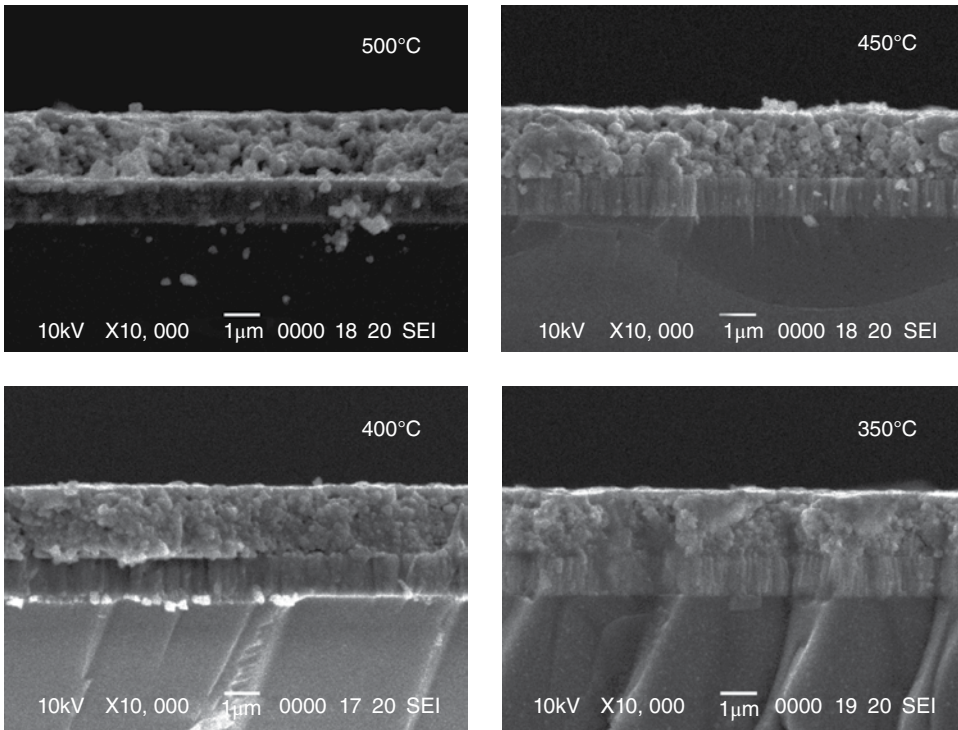
Sulfurization of co-sputtered films was performed at a high temperature. Using the co-sputtering system with two CZTS compound targets, we prepared precursors of active composition. They were heat-treated in the  $H_2S$  atmosphere. In this experiment, the temperature was varied from  $350$  to  $500^\circ\text{C}$ . All samples including the as-sputtered film have almost the same composition as shown in Figure 8.11.

Figure 8.12 shows the comparison of cross-sectional SEM images of sulfurized CZTS films in an  $H_2S$  atmosphere. Despite the high temperature of  $500^\circ\text{C}$ , surface bumps were not observed. From these images, an increase in grain size could be seen by elevating the temperature. Grain growth in the lateral direction was observed, especially near the surface region. Solar cells were fabricated by using these CZTS films as absorbers. Figure 8.13 shows the comparison of  $J$ - $V$  characteristics of those cells. All of the photovoltaic properties ( $V_{oc}$ ,  $J_{sc}$ , FF, and conversion efficiency) were increased by elevating the sulfurization temperature. We achieved the very best parameter values of  $V_{oc} = 657$  mV,  $J_{sc} = 14.5$  mA  $\text{cm}^{-2}$ , FF = 0.549, and conversion efficiency of 5.24 %. The series resistance of the cell was drastically decreased from  $32.8$  to  $8.07$   $\Omega$   $\text{cm}^2$  by elevating the temperature.

Using the same sulfurization condition, namely the temperature of  $500^\circ\text{C}$  and the retention time of 3 hours, the influence of the composition ratio upon the photovoltaic properties were closely examined. Figure 8.14 shows the relation between  $V_{oc}$  and the Cu/(Zn+Sn) ratio achieved in this series of experiments. Despite the small deviation of the composition ratio from 0.79 to 0.84, a varying  $V_{oc}$  from 660 to 580 mV could be seen. The samples of



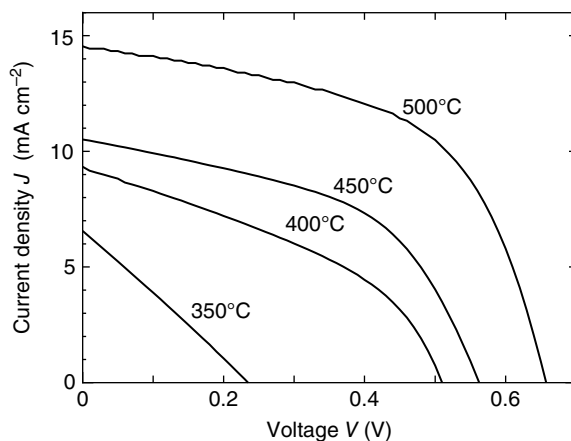
**Figure 8.11** Composition ratio of CZTS films with various sulfurization temperatures



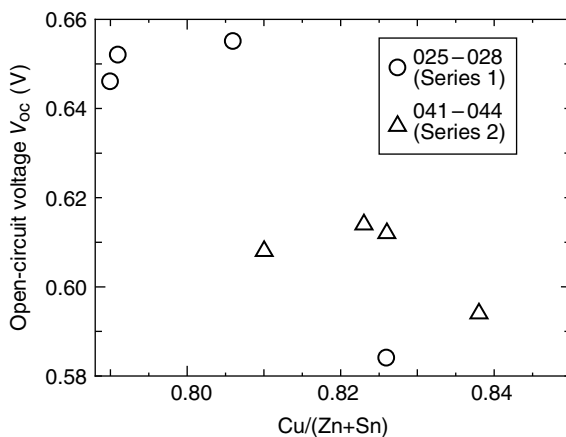
**Figure 8.12** Comparison of cross-sectional SEM images of SLG/Mo/CZTS stacked layers with various sulfurization temperatures

each series were fabricated by the same batch process except the RF power applied to the targets at the stage of precursor fabrication. The photovoltaic characteristics, especially  $V_{oc}$ , were much affected by the Cu/(Zn+Sn) ratio.





**Figure 8.13** Comparison of  $J$ - $V$  characteristics of CZTS thin-film solar cells. The sulfurization temperature was set as a parameter

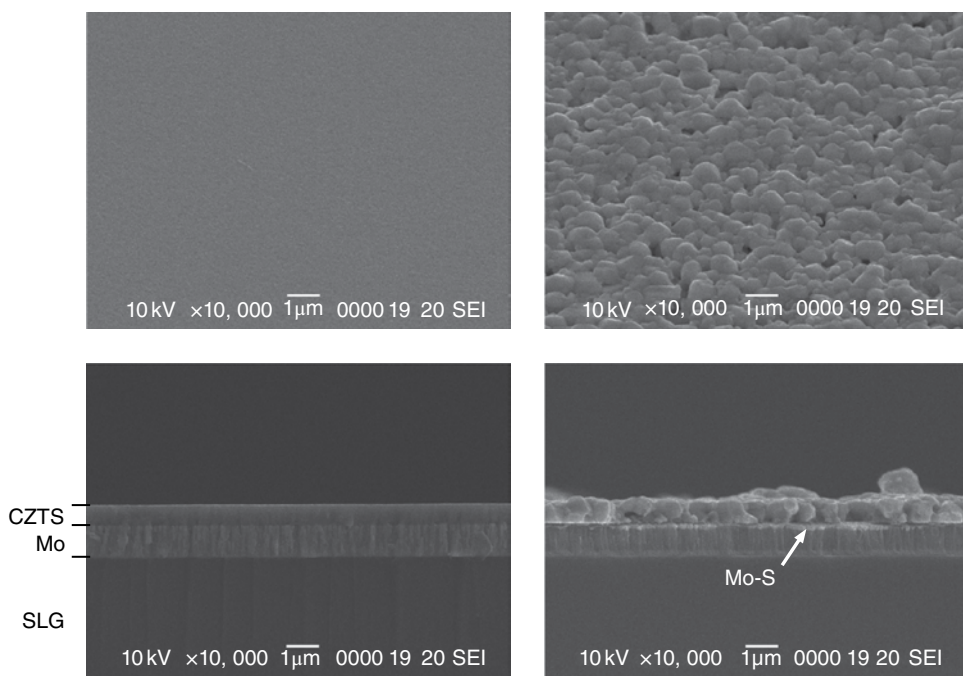


**Figure 8.14** Relation between  $V_{oc}$  and  $Cu/(Zn+Sn)$  ratio

In general, the compositional deviation of the film from the compound target depends on the sputtering condition including the density of the target. Because the CZTS film of active composition was needed after the sulfurization, the composition of the target had to be controlled. Considering the results mentioned above, a new CZTS compound target which could provide the active composition was prepared. The CZTS absorber prepared using a simple single sputter target was then sulfurized.

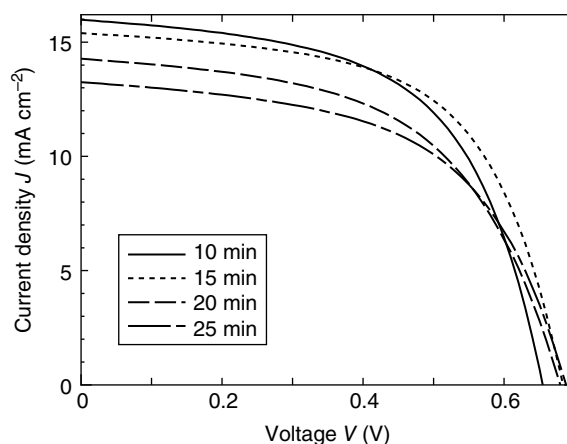
CZTS precursors were prepared by using a magnetron RF sputtering system of a side deposition type. RF power of 120 W was applied to a CZTS compound target of 76.2 mm in diameter. The distance between a target and a substrate was 100 mm, and the offset distance of those centers was set at 65 mm. The substrate was rotated with the velocity of 6 rpm in this experiment. A precursor of 600 nm in thickness was obtained after sputtering for 1 hour. This precursor was then sulfurized for 1 hour at 520°C in the atmosphere of



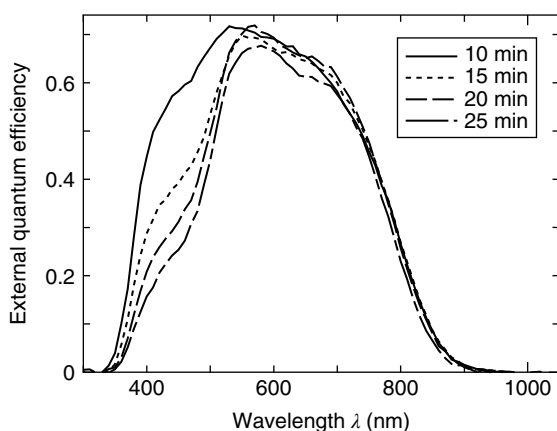


**Figure 8.15** Comparison of SEM images of CZTS films. The left-hand side shows the as-sputtered film and the right-hand side corresponds to the sulfurized film

$\text{N}_2 + \text{H}_2\text{S}$  (5 vol%). Figure 8.15 shows the comparison of SEM images of CZTS films. The left side shows the as-sputtered film and the other side corresponds to the sulfurized film. From the cross-sectional images, it was found that the as-sputtered film had a so-called columnar structure and the sulfurized film consisted of grains as large as film thickness. Considering the thickness of Mo of 1000 nm, we found that the thickness of CZTS increased from 600 nm to almost 700 nm by sulfurization. The surface morphology of the sulfurized CZTS film seemed to be degraded due to the grain growth. The XRF measurements revealed that the sulfurized CZTS film had the active composition, namely  $\text{Cu}/(\text{Zn}+\text{Sn})=0.79$ ,  $\text{Zn}/\text{Sn}=1.27$ , and  $\text{S}/\text{Metal}=1.17$ . At the stage of chemical bath deposition (CBD) of the CdS buffer layer, the dipping time was set as a parameter. Figures 8.16 and 8.17 show  $J$ - $V$  properties and external quantum efficiency (EQE) in this experiment, respectively. From Figure 8.17, the EQE for the wavelength range  $< 500$  nm increased with the decrease in dipping time. Because the thickness of the CdS buffer layer depends on the dipping time, this improvement in the EQE was due to the reduction in light absorption of CdS. This improvement also affected  $J_{\text{sc}}$  as shown in Figure 8.16. It could be seen that  $J_{\text{sc}}$  was decreased by the increase of the dipping time. On the other hand, the dependence of  $V_{\text{oc}}$  upon the thickness of the CdS buffer layer could not be clarified. The thinnest sample (dipping time 10 min) showed a  $V_{\text{oc}}$  of 650 mV, while other samples showed nearly the same value of 680 mV. The highest conversion efficiency was obtained among the samples whose buffer layer was deposited with a dipping time of 15 min. The photovoltaic properties were  $V_{\text{oc}} = 683$  mV,  $J_{\text{sc}} = 15.4 \text{ mA cm}^{-2}$ ,  $\text{FF} = 0.590$ , and conversion efficiency of 6.23%.



**Figure 8.16** Comparison of  $J$ - $V$  characteristics of CZTS thin-film solar cells. The dipping time at the CBD process was set as a parameter



**Figure 8.17** EQE spectra of CZTS thin-film solar cells. These cells are the same as those depicted in Figure 8.16

To evaluate the effect of the series resistance on these cells, we focused on  $J$ - $V$  curves in the vicinity of  $V_{oc}$ . In our experiment, about 20 cells of  $4 \times 4 \text{ mm}^2$  area were fabricated on the substrate of  $25 \times 25 \text{ mm}^2$ . After measuring the  $J$ - $V$  characteristics of all cells, three cells having the highest conversion efficiency in one substrate were selected. The average series resistance of these three cells in each sample was  $6.36 \Omega \text{ cm}^2$  for 10 min,  $7.35 \Omega \text{ cm}^2$  for 15 min,  $10.5 \Omega \text{ cm}^2$  for 20 min, and  $9.49 \Omega \text{ cm}^2$  for 25 min. In this experiment, all processes were performed on the same batch while the dipping time for CBD was varied as above. Series resistances should therefore only depend on the thickness of CdS. In fact, the series resistance increased by increasing the dipping time, and then tended to be saturated. Furthermore, when the dipping time was longer we were able to see that the

incremental decrease of EQE in the shorter-wavelength region was suppressed as shown in Figure 8.17. We interpret this as further evidence of the saturation of CdS thickness with the dipping time.

## 8.10 Conclusions

In this chapter we have described the sulfurization of physical vapor-deposited precursor layers. Precursors were initially prepared by sequential EB evaporation; a co-sputtering method was then introduced and, finally, simple single-sputtering was performed. In any case, all of these fabrication methods are of a two-stage type including sulfurization. We believe that this two-stage process can be easily applied in large-scale production.

Table 8.1 provides the results of our early work. We modified the fabrication process and changed the means of measurements in several ways according to the research period. Accordingly, there were a few inconsistent results; in particular, the relationship between  $V_{oc}$  and the composition ratio is not easily understood from this table. However, we now recognize that in order to achieve a high-conversion-efficiency cell, Cu-poor and Zn-rich composition is preferable to stoichiometric CZTS.  $V_{oc}$  increased with a decreasing ratio of Cu/(Zn+Sn), changing from 610 mV to 655 mV at the vicinity of 0.81 of Cu/(Zn+Sn) as shown in Figure 8.14. However, taking into account the band-gap energy of about 1.5 eV of CZTS, these  $V_{oc}$  are not sufficient. It is thought that this  $V_{oc}$  deficit is caused by the recombination at the interface between the absorber and the buffer layer. In order to investigate a new type of buffer layer instead of CBD-CdS and to clarify the precise device properties and increase the conversion efficiency, we have to establish a CZTS absorber fabrication process of high reproducibility.

## References

- [1] Marchionna, S., Garattini, P., Le Donne, A., Acciarri, M., Tombolato S. & Binetti, S. (2013)  $\text{Cu}_2\text{ZnSnS}_4$  solar cells grown by sulphurisation of sputtered metal precursors. *Thin Solid Films*, **542**, 114–118.
- [2] Dhakal, T. P., Peng, C.-Y., Tobias, R. R., Dasharathy, R. & Westgate, C. R. (2014) Characterization of a CZTS thin film solar cell grown by sputtering method. *Solar Energy*, **100**, 23–30.
- [3] Shin, B., Gunawan, O., Zhu, Y., Bojarczuk, N. A., Chey, S. J. & Guha, S. (2011) Thin film solar cell with 8.4% power conversion efficiency using an earth-abundant  $\text{Cu}_2\text{ZnSnS}_4$  absorber. *Progress in Photovoltaics: Research and Applications*, doi: 10.1002/pip.1174.
- [4] Repins, I., Beall, C., Vora, N., DeHart, C., Kuciauskas, D., Dippo, P., To, B., Mann, J., Hsu, W.-C., Goodrich, A. & Noufi, R. (2012) Co-evaporated  $\text{Cu}_2\text{ZnSnSe}_4$  films and devices. *Solar Energy Materials and Solar Cells*, **101**, 154–159.
- [5] Jung, S., Gwak, J., Yun, J. H., Ahn, S., Nam, D., Cheong, H., Ahn, S., Cho, A., Shin, K. & Yoon, K. (2013)  $\text{Cu}_2\text{ZnSnS}_4$  thin film solar cells based on a single-step co-evaporation process. *Thin Solid Films*, **535**, 52–56.
- [6] Tampo, H., Makita, K., Komaki, H., Yamada, A., Furue, S., Ishizuka, S., Shibata, H., Matsubara, K. & Niki, S. (2014) Composition control of  $\text{Cu}_2\text{ZnSnSe}_4$ -based solar cells grown by coevaporation. *Thin Solid Films*, **551**, 27–31.
- [7] Moholkar, A. V., Shinde, S. S., Babar, A. R., Sim, K.-U., Kwon, Y.-B., Rajpure, K. Y., Patil, P. S., Bhosale, C. H. & Kim, J. H. (2011) Development of CZTS thin films solar cells by pulsed laser deposition: Influence of pulse repetition rate. *Solar Energy*, **85**, 1354–1363.

- [8] Surgina, G. D., Zenkevich, A. V., Sipaylo, I. P., Nevolin, V. N., Drube, W., Tetelin, P. E. & Minnekaev, M. N. (2013) Reactive pulsed laser deposition of  $\text{Cu}_2\text{ZnSnS}_4$  thin films in  $\text{H}_2\text{S}$ . *Thin Solid Films*, **535**, 44–47.
- [9] Katagiri, H., Sasaguchi, N., Hando, S., Hoshino, S., Ohashi, J. & Yokota, T. (1997) Preparation and evaluation of  $\text{Cu}_2\text{ZnSnS}_4$  thin films by sulfurization of E-B evaporated precursors. *Solar Energy Materials and Solar Cells*, **49**, 407–414.
- [10] Katagiri, H., Ishigaki, N., Ishida, T. & Saitoh, K. (2011) Characterization of  $\text{Cu}_2\text{ZnSnS}_4$  thin films prepared by vapor phase sulfurization. *Japanese Journal of Applied Physics*, **40**(1), 500–504.
- [11] Katagiri, H., Saitoh, K., Washio, T., Shinohara, H., Kurumadani, T. & Miyajima, S. (2001) Development of thin film solar cell based on  $\text{Cu}_2\text{ZnSnS}_4$  thin films. *Solar Energy Materials and Solar Cells*, **65**, 141–148.
- [12] Katagiri, H., Jimbo, K., Moriya, K. & Tsuchida, K. (2003) Solar cell without environmental pollution by using CZTS thin film. In *Proceedings of WCPEC-3*, 2874–2879, Osaka.
- [13] Katagiri, H. (2005)  $\text{Cu}_2\text{ZnSnS}_4$  thin film solar cells. *Thin Solid Films*, **480–481**, 426–432.
- [14] Jimbo, K., Kimura, R., Kamimura, T., Yamada, S., Maw, W. S., Araki, H., Oishi, K. & Katagiri, H. (2007)  $\text{Cu}_2\text{ZnSnS}_4$ -type thin film solar cells using abundant materials. *Thin Solid Films*, **515**, 5997–5999.
- [15] Katagiri, H., Jimbo, K., Yamada, S., Kamimura, T., Maw, W. S., Fukano, T., Ito, T. & Motohiro, T. (2008) Enhanced conversion efficiencies of  $\text{Cu}_2\text{ZnSnS}_4$ -based thin film solar cells by using preferential etching technique. *Applied Physics Express*, **1**, 041201.
- [16] Katagiri, H., Jimbo, K., Tahara, M., Araki, H. & Oishi, K. (2009) The influence of the composition ratio on CZTS-based thin film solar cells. *Materials Research Society Symposium Proceedings*, **1165**, M04-01.

# 9

## Reactive Sputtering of CZTS

*Charlotte Platzer-Björkman, Tove Ericson, Jonathan Scragg and Tomas Kubart*

*Ångström Solar Centre, Solid State Electronics, Department for Engineering Sciences, Uppsala University, SE-751 21 Uppsala, Sweden*

### 9.1 Introduction

This chapter describes the use of reactive sputtering to make  $\text{Cu}_2\text{ZnSnS}_4$  (CZTS) films, either directly or in a two-stage process with annealing of sputtered precursor films. We first describe the reactive sputtering process, and some of the particular issues related to CZTS deposition in  $\text{H}_2\text{S}$ . We then describe properties of sputtered films as a function of process parameters. Due to the relatively poor stability of CZTS at high temperature in vacuum, annealing of sputtered films at high pressure is commonly used to make device-quality films. This annealing process, and its influence on device performance, is also discussed in this chapter. Investigations of reactive sputtering of CZTS are relatively recent, and several aspects remain to be studied. This chapter summarizes some of the present knowledge.

Reactive sputtering refers to sputtering with the addition of a reactive gas to the plasma. Typically, metal targets are used and common examples are deposition of nitrides or oxides from metal targets in nitrogen or oxygen plasma. The advantages of this process in comparison to sputtering from compound targets can be a higher deposition rate and the possibility to vary the composition by simply changing the flow of reactive gas. In addition, metal targets are cheaper to manufacture and have better mechanical properties. In some cases, stoichiometric composition is difficult to achieve in compound sputtering, while addition of reactive gas can compensate for losses during sputtering.

Sputtering in general is a well-established process which is widely used in industry, and up-scaling for large-area PV production is highly feasible. The motivation for using reactive sputtering for CZTS, in addition to the high deposition rate and scalability, is mainly the possibility to obtain sufficient chalcogen incorporation in the films. For research purposes, the process also offers excellent flexibility in tuning of the composition. Most of the studies described in this chapter concern sputtering of sulfides using  $\text{H}_2\text{S}$ . However, the corresponding process for selenides using  $\text{H}_2\text{Se}$  can also be used. The toxicity of  $\text{H}_2\text{S}$  and  $\text{H}_2\text{Se}$  requires careful safety consideration, but is no barrier for industrial production.

Reactive sputtering of CZTS has only been studied by Liu *et al.* [1], Chawla & Clemens [2] and Ericson *et al.* [3, 4]. Reference [2] includes the variation of metal composition for  $\text{H}_2\text{S}/\text{Ar}$  ratio of 14%: 86% and varied substrate temperature from 100°C to 530°C. In this study, grain size was reported to increase with substrate temperature while morphology was not strongly affected by composition. In reference [1], growth in 100%  $\text{H}_2\text{S}$  with a substrate temperature of 500°C was reported to give strongly oriented CZTS films with dense structure. Ericson *et al.* reported variation of  $\text{H}_2\text{S}/\text{Ar}$  ratio for substrate temperatures between room temperature and 300°C [3] and variation in metal composition for 100%  $\text{H}_2\text{S}$  [5]. Annealing of reactively sputtered precursors was mentioned in reference [4] and described in more detail in reference [6].

In this chapter we distinguish between one-stage and two-stage processes, both of which have drawbacks and advantages. The advantages of a one-stage approach, where a kesterite CZTS film is deposited at elevated substrate temperature, are the simplified deposition process and use of a single deposition chamber. In addition, diffusion and reaction processes occurring in post annealing can be avoided. However, the drawback of a one-stage process in the case of CZTS is the difficulty of avoiding decomposition and preferential losses of tin and sulfur at high temperature in vacuum. Even if sufficient deposition rates of these elements can be used during deposition, the risk of losses is large during cool-down (i.e. the loss rate increases when the sputter flux is switched off). Moreover, energetic negative ions of electronegative elements, such as sulfur, form in the sputtering process. Because their energies reach up to hundreds of electron-volts, they may have a detrimental effect on the as-deposited film. So far, there are no reports of successful use of single-stage reactive sputtering for high-efficiency CZTS. In the device section of this chapter, we include the available single-stage results; for the rest of the chapter however, we focus on two-stage processing for which most of the promising results have been obtained.

In a two-stage process, precursor films can be deposited at any temperature in the first stage; in the second stage, annealing at an elevated temperature is performed in an atmosphere of sulfur and sometimes tin sulfide. These two processes are covered in some detail in this chapter. Since annealing is performed in the second stage, the requirements for the quality of the precursor film are relaxed, even if annealing conditions might need to be adjusted to specific precursor properties. To date, it has not been shown that CZTS with a crystallized kesterite phase would be preferable in a precursor film to more disordered structures. In this chapter we describe the latter approach for which very rapid recrystallization of a disordered reactively sputtered precursor film was shown.

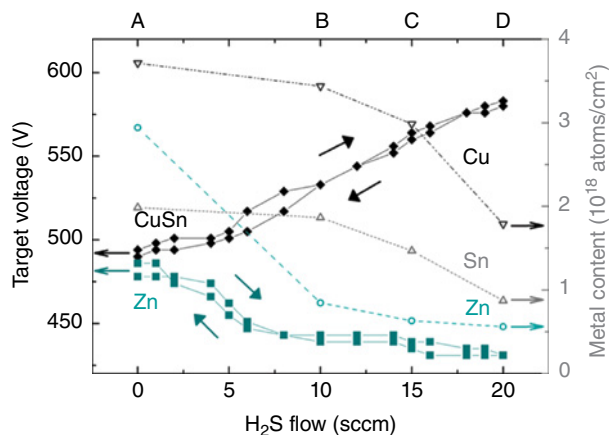
## 9.2 The Reactive Sputtering Process

Two distinct modes of operation exist in reactive magnetron sputtering, depending on the state of the sputtering target [7]. Starting with operation in pure Ar, the target surface is metallic. With increasing mass flow of the reactive gas, a compound starts to form at the target surface; when the surface is fully covered by this layer the target is referred to as being in compound mode. Depending on the material system, the difference in sputtering yield between metal and compound, and the configuration of the sputtering system, the transition between these two modes can be abrupt or gradual. In the case of an abrupt transition, a hysteresis effect is often seen. The change in the surface composition has a pronounced effect on the ion-induced secondary electron yield, which in turn is the main determinant of the discharge voltage. The discharge voltage can therefore serve as a measure of the surface status of the target [8]. Formation of a compound at the surface is also accompanied by a change in the sputtering yield and hence the deposition rate, which can also be used as a measure of the transition between modes. In order to characterize a sputtering process, a process curve is typically used. It is represented by either deposition rate or discharge voltage as a function of the reactive gas flow.

A process curve for Zn and CuSn sputtered in varying Ar:H<sub>2</sub>S plasma is shown in Figure 9.1. The sputter system is a Von Ardenne CS600 with two magnetrons and a front side heater, all facing the substrate with an angle of 45° at 160 mm distance. The targets are 102 mm in diameter and 6 mm thick. Due to the limited number of magnetrons, a CuSn-alloy target (Cu: 67 at% and Sn: 33 at%; purity 99.99 %) together with a Zn target (purity 99.994–99.995%) were used. Pulsed DC with a frequency of 20 kHz was supplied by two Huttinger PFG 3000 DC power supplies equipped with Advanced Energy Sparc-le 20 pulsing units. Both targets were operated in constant power mode, 600 W for the CuSn target and 330 W for the Zn target. The base pressure was below 10<sup>-4</sup> Pa. H<sub>2</sub>S with a purity of 99.5% and Ar were used at mass flow rates between 0 and 20 sccm (standard cubic centimeters per minute), giving a total constant flow of 20 sccm and a constant total pressure of 0.67 Pa.

Increasing the H<sub>2</sub>S flow from 0 sccm to 5 sccm does not significantly influence the voltage on the CuSn target. However, the voltage on the Zn target drops considerably, indicating that this target is sulfurized first and that the majority of the supplied H<sub>2</sub>S is consumed by it. This agrees with ZnS having a more negative free energy of formation than Cu-S and Sn-S compounds. The abrupt transition indicates high reactivity and a large difference in sputtering yield between Zn and ZnS. The voltage decrease indicates an increase in secondary electron yield for ZnS, and this agrees well with earlier reports [9]. Increasing the H<sub>2</sub>S flow also leads to formation of a compound on the CuSn target. This transition from metal to compound mode is more gradual and the voltage continuously increases from around 500 V at 5 sccm to 580 V at the end point of 20 sccm H<sub>2</sub>S. This agrees with earlier work which reported an increase in voltage for reactive sputtering of pure Cu in H<sub>2</sub>S [10]. Also seen in Figure 9.1 is that this sputtering process does not show any hysteresis.

Long equilibration times were observed in the above-described sputtering process. About five hours of sputtering was required to achieve stable process after introduction of H<sub>2</sub>S with respect to both the film composition and deposition rate. Similar behavior was reported earlier by Thornton *et al.* in reactive sputtering of Cu<sub>2</sub>S where the final stable voltage in a constant H<sub>2</sub>S flow rate was not seen until after sputtering for about 30 min [11].



**Figure 9.1** Process curve for reactive sputtering from Zn and CuSn targets (left axis) and metal content as measured by X-ray fluorescence (XRF) on samples A to D (right axis). Reprinted from [3]. With permission from Elsevier

Since energy dispersive spectroscopy (EDS) analysis revealed very low concentration of tin at the surface of the CuSn target, the equilibration time has been attributed to the formation of very thick sulfide layer at the surface. Whereas typical ion ranges in sputtering are a few nanometres as is well known, it was revealed by EDS that the sulfide layer is thicker than 1  $\mu\text{m}$ . Pronounced diffusion in the target is therefore expected. This effect can explain both the long response time as well as variations in the film composition. The equilibration time is important for a stable operation and should be accounted for in a suitable deposition routine.

### 9.3 Properties of Sputtered Precursors

Reactive sputtering provides the possibility of tuning several film properties. In the following sections we cover variation in temperature, H<sub>2</sub>S/Ar ratio, pressure and some variation in metal composition. Low stress and high density is usually preferable for thin films, which points towards the use of slightly elevated deposition temperatures. Another parameter, not covered here, is additional ion bombardment of the growing film which is commonly used in other sputtering deposition processes. This could possibly be used to further adjust the precursor properties.

#### 9.3.1 Film Properties as a Function of H<sub>2</sub>S/Ar Ratio

When varying the amount of H<sub>2</sub>S in the process, films with varying sulfur content can be obtained. For example, as shown in Table 9.1, samples deposited with four different H<sub>2</sub>S/Ar ratios as indicated in Figure 9.1 show the expected transition from metal to compound mode. The other process parameters were kept constant with 600 W on the CuSn target, 330 W on the Zn target, 800 s sputtering time, and a 0.67 Pa process pressure. The Zn rate drops quickly as a result of lower sputtering yield of ZnS while the CuSn rate decreases

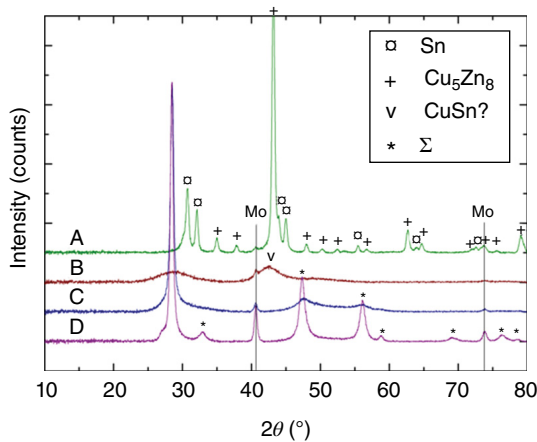


slowly, agreeing well with the metal-to-compound transition types observed with the voltage measurement. Due to the difference in transition behavior the deposited samples vary in Zn content, as can be seen in Table 9.1. The purely metallic sample A is very Zn-rich, since the deposition rate from the metallic Zn target is high. When  $\text{H}_2\text{S}$  is added, the Zn rate drops rapidly and samples B and C are Zn-poor. At the highest  $\text{H}_2\text{S}$  flow rate used for sample D, the CuSn rate has decreased enough to result in a higher relative Zn content. The sulfur content of the film increases fairly linearly with increasing  $\text{H}_2\text{S}$  flow, and the films sputtered in 20 sccm pure  $\text{H}_2\text{S}$  have, according to EDS, a close to stoichiometric sulfur content of 51 at%.

Figure 9.2 shows the grazing incidence X-ray diffraction (GIXRD) for the samples in Table 9.1. Sample A, sputtered without  $\text{H}_2\text{S}$ , shows reflections from elemental Sn [12] and  $\text{Cu}_5\text{Zn}_8$  [13]. Comparing this with the phase diagram in [14] (shown for 180–250°C) it would have been expected to find Sn, CuZn and  $\text{Cu}_6\text{Sn}_5$  for this composition. However, the region in the phase diagram in which Sn and  $\text{Cu}_5\text{Zn}_8$  are expected is fairly close so, considering the non-equilibrium conditions present during sputtering, this is not an unreasonable result. Also stated in [14] is that the reason for forming a CuZn compound rather than any

**Table 9.1** Process parameters, composition and thickness for samples indicated in Figure 9.1. The  $\text{H}_2\text{S}/\text{Ar}$  ratio was varied while power, process pressure, and time were kept constant at 600 W for the CuSn target, 330 W for the Zn target, 0.67 Pa and 800 s respectively. Reprinted from [3]. With permission from Elsevier

Sample	$\text{H}_2\text{S}$ flow (sccm)	Ar flow (sccm)	Cu/Sn	Zn/(Cu+Sn)	S/Metals	Thickness (nm)
A	0	20	1.90	0.49	0.03	960
B	10	10	1.86	0.16	0.44	1050
C	15	5	2.04	0.14	0.73	1170
D	20	0	1.99	0.21	1.03	830



**Figure 9.2** Grazing incidence diffractogram from samples in Table 9.1. Reprinted from [3]. With permission from Elsevier

other combination of the three metals is the high reactivity of Zn and that Cu diffuses easily. For sample B, where the process gas consists of 50%  $\text{H}_2\text{S}$ , the film sputtered is mostly amorphous with only two very broad peaks seen at around  $28.6^\circ$  and  $42.5^\circ$ . The first matches the most intense peaks from sphalerite ZnS [15] and the second agrees with the most intense peak of several CuSn phases, for example  $\text{Cu}_{40}\text{Sn}_{11}$  [16]. This also agrees with the process curve (Fig. 9.1) which indicates that the Zn target should be sulfurized at this point but the CuSn target is in the transition between metal and compound mode. The two samples sputtered at higher  $\text{H}_2\text{S}$  flow both show reflections from a zinc-blende structure. These peaks are common for CZTS [17],  $\text{Cu}_2\text{SnS}_3$  (CTS) [18–20], and sphalerite ZnS with small shifts. None of the weak reflections specific to CZTS or CTS were observed. We refer to this pattern as  $\Sigma$ , following the notation introduced by Weber *et al.* [21]. The  $\Sigma$  peaks are more intense for the fully sulfurized sample, and in this diffractogram an unidentified shoulder just below the main peak is also seen. In all samples the two strongest reflections from the back contact Mo [22] can be observed.

From Raman scattering, no clear peaks can be seen for the metallic (A) and the low-sulfur film (B). For samples C and D a clear but broad peak at  $336$  and  $332\text{ cm}^{-1}$  respectively is seen.

Peak fitting with Lorentzian curves for sample D gave good agreement for four peaks between  $200$  and  $500\text{ cm}^{-1}$ . The resulting peak positions for the weaker contributions are at  $256$ ,  $290$ , and  $354\text{ cm}^{-1}$ . According to Himmrich and Haeuseler [23], Raman scattering from CZTS should show three peaks at  $285$ ,  $336$ , and  $362\text{ cm}^{-1}$  where the middle peak is most intense. These peak positions are close to three of the fitted Raman frequencies and have similar intensity distribution. Several IR peaks are reported [23] and the peak at  $255\text{ cm}^{-1}$  agrees well with our peak fitted at  $256\text{ cm}^{-1}$ . CZTS is therefore a plausible match for the sample. As described however [24], several other compounds have intensities in the same range such as ZnS,  $\text{Cu}_2\text{SnS}_3$ , and  $\text{Cu}_3\text{SnS}_4$ , and cannot be ruled out.

SEM images confirm the crystallinity information from the XRD measurement. Sample B appears mostly amorphous and samples A, C, and D crystalline. However, samples C and D have a clear columnar structure while sample A appears more disordered. This is possibly due to the structural difference between Sn and  $\text{Cu}_5\text{Zn}_8$  compared to the similarities between CZTS, ZnS, and CTS, or due to the lower melting point of  $\text{Cu}_5\text{Zn}_8$  and Sn compared to the sulfides.

### 9.3.2 Film Properties as a Function of Pressure

The effect of two different pressures ( $0.67$  and  $1.33\text{ Pa}$ ) and three different  $\text{H}_2\text{S}/\text{Ar}$  ratios have been studied in the Von Ardenne CS600 system [3]. The other process parameters were kept constant with  $600\text{ W}$  on the CuSn target,  $330\text{ W}$  on the Zn target, and a deposition time of  $800\text{ s}$ . The total gas flow was  $30\text{ sccm}$ .

The films are generally very similar at the two different pressures. The only difference seen is at  $10\text{ sccm H}_2\text{S}$  and  $20\text{ sccm Ar}$  where the XRD for  $1.33\text{ Pa}$  setting shows two very broad peaks at around  $28.6^\circ$  and  $42.5^\circ$ . When decreasing the process pressure to  $0.67\text{ Pa}$ , an additional peak at  $36.3^\circ$  appears in the XRD pattern. The peak matches the close-packed plane for elemental Zn [25] and could indicate that this setting does not supply high enough partial pressure of sulfur to completely react the Zn at the

substrate. The two broad peaks matches the most intense peaks from sphalerite ZnS [15] and the most intense peak of several CuSn phases, for example  $\text{Cu}_{40}\text{Sn}_{11}$  [16]. This agrees with the process curve from this system, which shows that the Zn target at this point should be fully sulfurized while the CuSn target is still in transition between metallic and compound mode. It is also very similar to the diffractogram from 10 sccm  $\text{H}_2\text{S}$  and 10 sccm Ar at 0.67 Pa, probably because the partial pressure of  $\text{H}_2\text{S}$  is similar for these settings.

### 9.3.3 Film Properties as a Function of Temperature and Composition

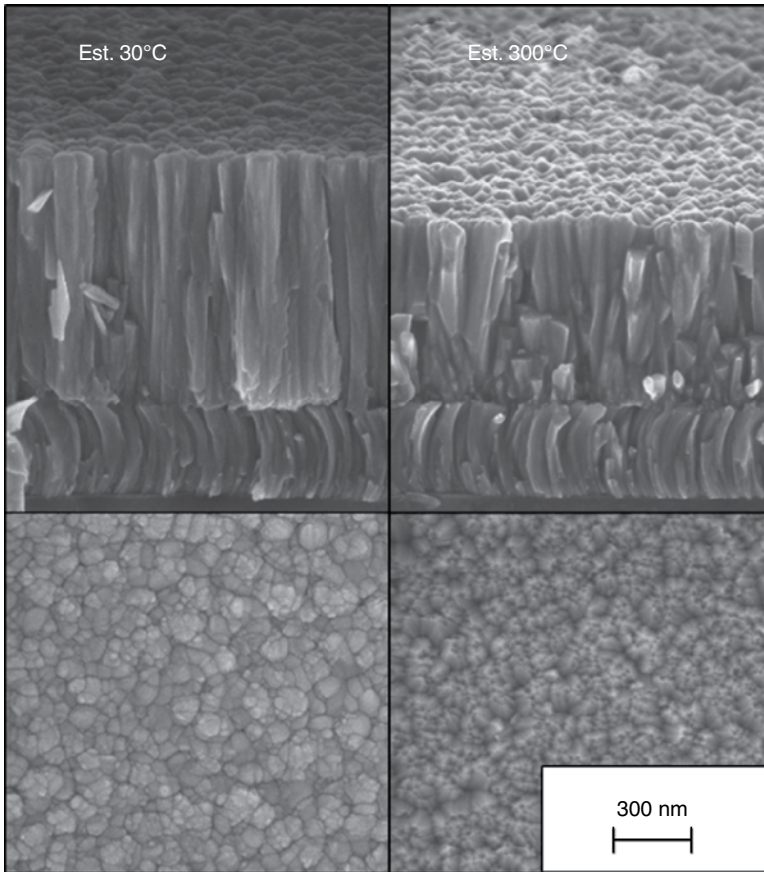
The substrate temperature during deposition is predicted to affect the morphology and stress in the film due to increased surface mobility of the arriving atoms [26, 27]. The CuSn target used in this series had a composition of Cu: 65 at% and Sn: 35 at%. All process parameters besides the substrate temperature were kept constant. The substrate temperature was varied between room temperature and about 300°C and several parameters were affected. The composition changed both in the Cu/Sn ratio, Zn content, and sulfur content. Comparing the raw XRF signals from the metals, the difference is mainly due to a decrease of Zn and Sn content with increasing temperature. This is probably due to the high vapor pressure of Zn and SnS. The lower sulfur content at higher temperatures can also be assigned to the high vapor pressure of  $\text{S}_2$ . This agrees with similar processes for CIS where it was observed that, at higher substrate temperatures, a higher  $\text{H}_2\text{S}$  flow was needed to achieve the same sulfur content in the films [28]. Since different compositions also could affect several other properties of the film, another series was sputtered where three compositions were chosen and kept constant over three temperatures using different CuSn alloy targets (Cu: 62.5 at%, Sn: 37.5 at% and Cu: 65 at%, Sn: 35 at%), and varying the powers to the magnetrons (yielding in total nine samples; Table 9.2). The sulfur loss was however not compensated for, resulting in a lower sulfur content in the high-temperature samples.

The decreasing deposition rates with temperature would naturally yield thinner films if the density is constant. This is also what is observed. However, using the areal density of the metals from the XRF measurement together with the sulfur content from EDS and the thickness, the density was calculated (Table 9.2). It was observed that the decrease cannot only be attributed to fewer atoms in the film but that the high-temperature films are also truly denser. The generally low density of the precursors, compared to the calculated value for CZTS ( $4.58 \text{ g cm}^{-3}$  [30]), is not surprising for films that are sputtered at this rather low temperature [27].

SEM images of the precursors deposited at room temperature and the highest temperature are shown in Figure 9.3. The structure of these films can be compared to previous studies of vacuum-deposited coatings within the general structure zone model (SZM) for sputtering [26]. This model relates the film structure to process parameters, in particular the substrate temperature  $T$  and the melting point of the coating material (here CZTS)  $T_m$ . Three main zones were distinguished in the SZM: zone 1 at low  $T/T_m$  where the films consist of crystallites with rounded surfaces; zone 2 at intermediate  $T/T_m$  showing columnar grains with faceted surface; and zone 3 at high  $T/T_m$  with large grains and flat grain tops. For the CZTS precursor films in Figure 9.3, the low-temperature depositions exhibit features of zone 1 with a columnar structure and rounded surface. The high-temperature

**Table 9.2** Properties of precursor and corresponding annealed films. Samples A1–C1 had a Cu/Sn ratio of 1.69–1.85, A2–C2 of 1.95–1.99, and A3–C3 of 2.04–2.16. After annealing the 2 $\theta$  XRD value for the (112) peak was generally just below 28.5°, close to the CZTS powder reference value 28.4502° [29]

Sample	S/Metals	Thickness (nm)	Precursor			Annealed			Anneal/Etch behavior
			Thickness (nm)	Calculated density (g cm <sup>-2</sup> )	Avg. stress (MPa)	(111)/(112) 2 $\theta$ from XRD (°)	Thickness(nm)	Calculated density (g cm <sup>-2</sup> )	
A1	1.15	2080		3.82	-143	28.306	1990	3.89	Cracked/ peeled off
A2	1.03	2020		3.99	-4	28.319	1940	4.04	Cracked/ OK
A3	1.05	1890		3.95	-18	28.313	1880	3.97	Cracked/ OK
B1	1.03	1950		4.08	-183	28.294	1900	4.19	OK/OK
B2	0.97	2040		4.10	-75	28.342	2040	4.19	OK/OK
B3	0.96	2020		4.16	-43	28.356	2080	N/A	OK/OK
C1	0.99	1970		3.98	-161	28.298	1920	4.22	OK/OK
C2	1.00	1860		4.06	-120	28.323	1850	4.20	OK/OK
C3	0.94	2080		3.54	34	28.412	2020	3.64	Porous/ partly peeled off



**Figure 9.3** SEM images of precursors sputtered at RT and 300°C. Reprinted from [3]. With permission from Elsevier

deposition appearance is closer to zone 2 morphology with faceted surface and angled grain boundaries within the film. When calculating the approximate  $T/T_m$  for these depositions it agrees well with what is expected from the SZM.

Stress measurement from deflection of thin glass substrates show compressive stress for all samples except for C3, which has a different morphology. For the series with constant process parameters there is possibly a trend giving lower stress values for higher temperature. These are also the samples with the highest copper content. For the constant composition series there is a slight correlation between high copper content and lower stress, but no trend with temperature. A further possible explanation for the stress variations in the constant composition series is that the copper-rich samples were made with a different sputtering target and at a higher deposition rate, which theoretically should increase compressive stress [27], the opposite to what is seen here. Additionally, direct comparisons of stress levels in films deposited from different targets is not straightforward, since the angular distribution of the energetic species changes with the evolution of the racetrack, resulting in different growth conditions.

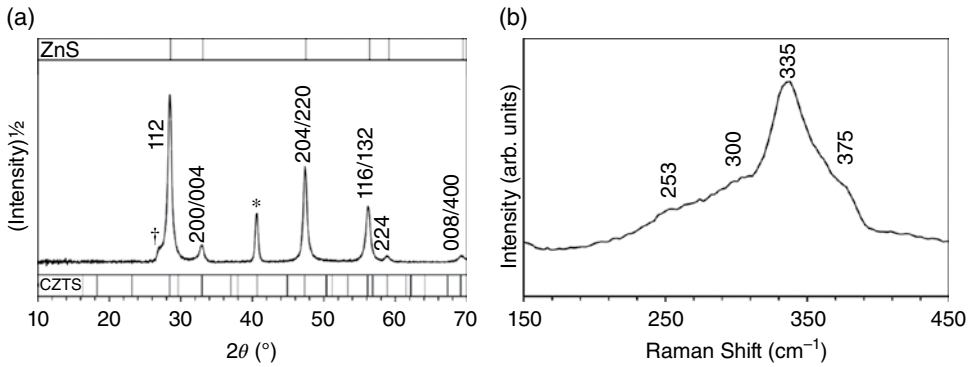
Using XRD for residual stress measurements on a sample which had high stress and weak preferred orientation showed good agreement with the corresponding curvature measurement. When trying this method on samples with more texture however, it was apparent that this made the XRD measurement uncertain.

Differences in stress values can also give rise to peak shifts in  $\theta$ - $2\theta$  XRD although several other factors, such as composition and phase mixture, could also have an influence. For these samples, all the visible  $\Sigma$  peaks are slightly shifted to lower angles while the peaks from the Mo-back contact are well aligned. The shifts are about  $0.1$ – $0.3^\circ$  compared to ZnS or CZTS ( $28.531^\circ$  and  $28.4502^\circ$  respectively [15, 29]). Combining the results from the two series we conclude that at least some of the peak shift comes from the Cu/Sn ratio; the samples with the most stoichiometric Cu/Sn ratio have peaks close to the powder reference. However, the sample which exhibits a significantly small peak shift is C3, that is, the only sample for which a positive stress value was recorded.

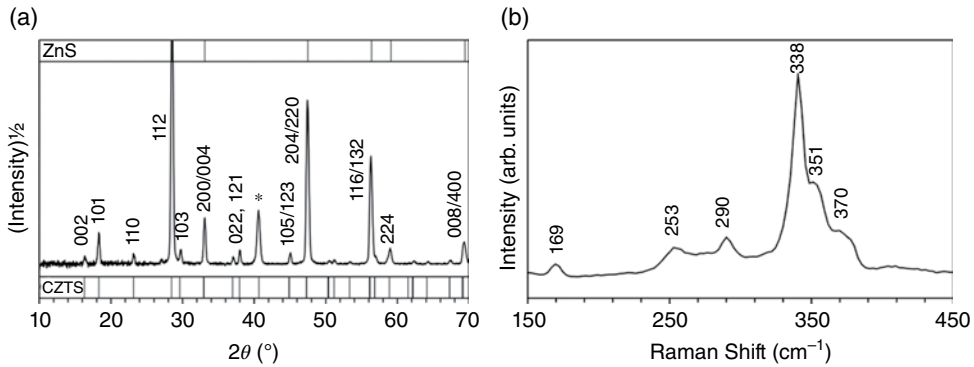
Otherwise  $\theta$ - $2\theta$  XRD shows the  $\Sigma$  pattern and the unidentified shoulder just below the main peak at  $28^\circ$  for all the depositions. The intensities of the peaks change within the series. The intensity of the main peak increases with increasing deposition temperature while those of the peaks at  $33^\circ$ ,  $47^\circ$ , and  $56^\circ$  decrease. The peak at  $28^\circ$  corresponds to the (111) plane in sphalerite ZnS and (112) in the kesterite structure. The peak with the same orientation ((222)/(224)) at  $59^\circ$  overlaps with Mo but the intensity at this position also increases with temperature. The Mo peak at  $74^\circ$ , which is free from overlap, shows that the signal from the Mo is fairly constant with temperature. This indicates that the intensity increase at  $59^\circ$  originates from the  $\Sigma$  signal and that the film becomes more oriented towards the (111) or (112) plane with higher temperature. This kind of texture, with the closest packed plane horizontal to the substrate, is common for sputtered films [26]. A (200) pole figure was recorded, and this confirms that the film has a (111)/(112) preferred orientation and also that no in-plane orientation exists.

### 9.3.4 Disordered Phase in Precursor Films

Reactive sputtering at intermediate temperatures can be considered a non-equilibrium deposition process. This is because the kinetic energy, and therefore temperature, of the sputtered atoms or ions is far greater than the temperature of the growing film. This commonly results in deposits that exhibit different crystal structures than the ground-state structure. A pertinent example is the observation of non-equilibrium Cu-Au-type cation ordering in reactively sputtered  $\text{CuInS}_2$  prepared below  $420^\circ\text{C}$  [31]. Accordingly, the fully sulfurized CZTS precursor films sputtered at temperatures of about  $300^\circ\text{C}$  are crystalline, but do not possess the structure expected for kesterite. Instead, a combined X-ray diffraction (XRD) and Raman analysis lead us to propose that the crystal structure of the sputtered precursors is similar to the reported high-temperature cubic form of CZTS that normally occurs above  $866^\circ\text{C}$  [32]. In this form, the anion substructure remains in the face-centered-cubic arrangement shared by, among others, ZnS and CZTS, but the cations adopt a statistical (rather than systematic) arrangement among the available tetrahedral sites [6]. This extensive cation disorder results in a cubic symmetry, giving an X-ray diffraction pattern that resembles that of ZnS with none of the tetragonal peaks that would be expected for the ground-state kesterite CZTS phase (Fig. 9.4a). At the same time, the Raman spectrum of the sputtered films (recorded in both surface mode and on cross-sections) reveals a spectrum morphologically similar to that of kesterite, but with peaks that are extensively broadened and



**Figure 9.4** (a) XRD pattern (\*molybdenum; †unidentified peak) and (b) Raman spectrum from CZTS precursor film deposited at 300°C



**Figure 9.5** (a) XRD pattern (\*molybdenum) and (b) Raman spectrum after annealing of the precursor film in Figure 5.4

slightly shifted (Fig. 9.4b). Spectra recorded using a UV excitation wavelength ruled out the presence of large amounts of ZnS, which means the cubic XRD pattern is best explained by the proposed extensive cation disorder in the CZTS phase.

Whereas peaks in XRD result from interaction of X-rays with long-range order in the crystal structure, the Raman shift is primarily determined by the nearest-neighbor interactions of the vibrating atoms.[33] The main effect of the cation disorder on the Raman spectrum is a peak broadening, while the peak positions are not strongly affected. This can be understood by taking the example of the A1 peak occurring at 338 cm<sup>-1</sup> in the kesterite spectrum. This peak is identified with a “breathing” mode of the S atoms [23], and its position is determined by the nearest-neighbor interactions of the S atoms. In the kesterite structure, every S atom has two Cu, one Zn, and one Sn atom as its nearest neighbors. In the disordered model of the sputtered precursor, a statistical distribution of cations among the tetrahedral sites occurs. This distribution still results (on average) in the same combination of nearest neighbors, however. The A1 peak in the precursor spectrum is observed at 331–335 cm<sup>-1</sup> as shown in Figure 9.4b, while that of the true kesterite phase is at 338 cm<sup>-1</sup> (see Fig. 9.5b). In fact, the occurrence of a peak at 331 cm<sup>-1</sup> has since been separately attributed to the presence of Cu-Zn disorder in CZTS samples [34].

In contrast to the case of films sputtered at a substrate temperature of 300°C described above, initial experiments have shown that the kesterite phase can be obtained when sputtering at higher temperature (475°C, in our case). The exact transition temperature for obtaining the kesterite phase as well as film properties for a larger range of substrate temperatures remains to be studied.

## 9.4 Annealing of Sputtered Precursors

### 9.4.1 The Annealing Process

The reactive sputtering process results in films that have the desired metal composition and sulfur content, as well as excellent uniformity. In the case of low-temperature deposition however, the films are also disordered and have a very small grain size. The purpose of the annealing step is to maintain this uniformity while promoting recrystallization into the kesterite phase, along with grain growth and the annihilation of crystal defects, ultimately yielding a film that is capable of performing the job of a solar cell absorber layer.

The annealing equipment used in our laboratory consists of a modified tube furnace with a base pressure of around  $10^{-4}$  mbar, capable of operating up to atmospheric pressure. A static or flowing atmosphere of argon can be provided. Samples are placed inside a closed graphite container, which fits onto a substrate holder in the furnace. The substrate holder can be transferred between the hot zone of the furnace and an adjoining cold zone by means of a transfer rod. This allows heating and cooling rates of up to  $\pm 5^\circ\text{C s}^{-1}$ .

Even very short annealing treatments of the order of minutes are sufficient to convert the reactively sputtered precursor from the disordered state described in Section 9.3.4 and shown in Figure 9.4 into crystalline kesterite films. This transformation is accompanied by the emergence of the kesterite diffraction pattern in XRD (Fig. 9.5a), a narrowing of the Raman peaks from the bulk phase (Fig. 9.5b), and rapid grain growth [6]. We associate these changes with a reordering of the cation substructure, from a fully disordered to an ordered state. In energetic terms, the disordered precursor structure that results from reactive sputtering has, by definition, a higher energy than the ground-state kesterite structure. The thermal energy provided by annealing appears to facilitate rapid relaxation into the equilibrium structure. The rapid increase in grain size may be partly driven by the potential energy released in this transformation [6].

### 9.4.2 Preventing Decomposition of the CZTS Phase During Annealing

The considerations that ought to be applied when annealing CZTS have been widely discussed in the literature; here, we provide only a short summary. As a direct consequence of the low stability of Sn in its +IV oxidation state (the state that occurs in CZTS), two detrimental reactions, neither of which happen in  $\text{Cu(In,Ga)Se}_2$  synthesis, can occur during CZTS annealing. Both reactions involve extraction of S atoms from Sn-S bonds, causing the CZTS phase to decompose into the binary compounds  $\text{Cu}_2\text{S}$ ,  $\text{ZnS}$ , and  $\text{SnS}$ , where Sn is reduced to its +II oxidation state to compensate the loss of S [35]. The first



reaction occurs at the CZTS surface, driven by the very high vapor pressure of sulfur at typical annealing temperatures, and leads to evaporation of S and then SnS [21]. The second reaction occurs at the Mo back contact where, when thermal energy is provided, formation of  $\text{MoS}_2$  is sufficiently favorable to allow extraction of S atoms from the CZTS phase or  $\text{SnS}_2$  secondary phases, with the resulting decomposition of CZTS into the binaries.

It should be noted that exactly the same considerations apply to the selenide, CZTSe. The occurrence of the two S-loss reactions described can be counteracted by supplying a high S pressure during annealing. This acts to suppress both the surface decomposition and the back contact reaction (the former more successfully than the latter [36]). If the anneal volume is large, SnS vapor will also be required to prevent the surface decomposition [37]. At higher temperatures, the required pressures of S and SnS are increased [38]. These considerations can and should be applied to all CZTS deposition and annealing processes, and ours is no exception. Even though the reactively sputtered precursors already contain a stoichiometric quantity of S, the two S-loss reactions described require us to supply excess S during annealing. This was done simply by adding pellets of elemental S to the graphite sample container.

In the following section, we discuss the influence of annealing without S on device performance.

## 9.5 Device Performance

Available device results from reactively sputtered films, with and without post-annealing, are shown in Table 9.3. The two one-stage devices both show low efficiency, 0.3% and 1.3%, correlated to reduced values in all device parameters. Details of the deposition parameters for the latter cell were not given but, in the case of the former film, deposition temperature was around 300°C. This is too low to form the kesterite structure as discussed in Section 9.3.4. Even for devices sputtered at higher temperature, high efficiency from a one-stage process is expected to be difficult to achieve due to the poor stability of CZTS at high temperature in vacuum.

Three examples of devices from annealed precursors are shown in Table 9.3. Early results (2 and 5 in Table 9.3) show modest efficiencies while our optimized anneal (3) gives an efficiency of 7.9%. These are all pure sulfide films and can be compared to the best selenium-free CZTS device by Kato *et al.* [39]. The higher current density in this record sub-module can be partly ascribed to the use of antireflective coating. Kato *et al.* [39] also discuss the occurrence of a ZnS layer at the back interface, dependent on metal stacking order and anneal process. Devices without ZnS back layer, or with ZnS segregating toward the front surface, show reduced efficiency, mainly due to significant reduction in current. The reason for reduced efficiency from ZnS at the front interface could be blocking of the photo current by the insulating ZnS, similar to the effect of ZnSe in CZTSe [40]. The reason for improvement with ZnS at the back interface is not clear.

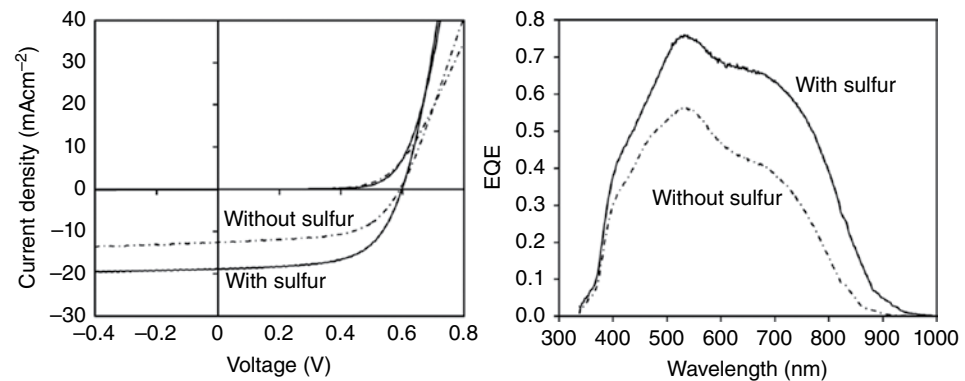
In Section 9.4.1, the necessity of supplying S during annealing was described. In Figure 9.6 (and Table 9.4) we highlight the effects of annealing with and without S on the performance of CZTS solar cells made from otherwise identical precursors. In both cases, samples were annealed with a static atmosphere of Ar (350 mbar) for 10 min at 560–570°C.

**Table 9.3** Device parameters from one-stage and two-stage processes. Device 6 is from a sub-module where  $V_{oc}$  is given per cell. Sample 2 was annealed without any added sulfur, with a glass cover on the film surface to minimize losses due to decomposition. Sample 3 was annealed in a graphite box with additional sulfur, at 560–570°C for 10 min

Sample	$V_{oc}$ (mV)	$J_{sc}$ (mA cm <sup>-2</sup> )	FF (%)	Efficiency (%)	Ref.
1. Precursor ( $T_{sub}$ 300°C)	183	6.22	27.9	0.31	[6]
2. Annealed (3 min at 550°C)	513	14.6	60.8	4.6	[6]
3. Annealed (graphite box with S)	667	19.6	60.0	7.9	[41]
4. One-stage reactively sputtered	343	9.52	41.3	1.3	[2]
5. Sputtered and annealed in H <sub>2</sub> S	428	12.4	63.5	3.4	[4]
6. Best-published CZTS device	708	21.6	60	9.2	[39]

**Table 9.4** Performance metrics for the devices shown in Figure 9.6

Anneal condition	Efficiency (%)	$V_{oc}$ (mV)	$J_{sc}$ (mA cm <sup>-2</sup> )	FF (%)
Without S	3.75	601	10.5	59.5
With S	6.47	594	17.3	62.9



**Figure 9.6** Current-voltage (left) and quantum efficiency (right) curves for devices processed from identical CZTS layers, showing the detrimental effect of annealing without S excess

For the case with sulfur, samples were placed in a closed graphite box. For annealing without sulfur, samples were placed in a heat-cleaned graphite box with a glass cover placed directly onto the sample surfaces. In this configuration, annealing without sulfur can be performed without severe decomposition at the CZTS top surface. The detrimental effect of annealing without added S is still clear, resulting in a much lower short-circuit current density ( $J_{sc}$ ) as well as a more sloping spectral response. Scragg *et al.* [41] correlate this

behavior to the detrimental decomposition reaction at the Mo/CZTS contact when annealing without sulfur, by comparing samples with standard molybdenum back contact to samples with thin TiN barrier layers between Mo and CZTS. To date however, a detailed understanding of this device behavior is lacking.

Ericson *et al.* [5] compare the annealing behavior and device performance for reactively sputtered films of varying composition and substrate temperature during sputtering from room temperature to 300°C. The annealing was performed in a static Ar pressure of 350 mbar at 560°C for 3 min without an additional supply of sulfur. Films deposited at room temperature showed cracks after annealing and poor adhesion during CBD processing, so were not suitable for device processing. For elevated substrate temperatures, no correlation between device performance and sputter process parameters was seen.

## 9.6 Summary

We have shown how reactive sputtering can be used to make fully sulfurized precursor films that can be processed into device-quality CZTS in a rapid anneal. The reactive sputtering process can be used to tune precursor properties, but to date there are no reports of a high-efficiency one-stage reactive sputter process. A disordered, non-equilibrium phase is obtained when sputtering at lower substrate temperatures, while the kesterite phase can be obtained at higher temperatures. The need for high-pressure post-annealing could be due to the known instability of CZTS at high temperature in vacuum. A one-stage process would require a very rapid cool-down or other measures in order to protect the surface from decomposition.

## References

- [1] Liu, F., Li, Y., Zhang, K., Wang, B., Yan, C., Lai, Y., Zhang, Z., Li, J. & Liu, Y. (2010) In situ growth of  $\text{Cu}_2\text{ZnSnS}_4$  thin films by reactive magnetron co-sputtering. *Solar Energy Materials and Solar Cells*, **94**, 2431–2434.
- [2] Chawla, V. & Clemens, B. (2010) Inexpensive, abundant, non-toxic thin films for solar cell applications grown by reactive sputtering. In *Proceedings of 35th IEEE PV Specialists Conference*. Honolulu, US.
- [3] Ericson, T., Kubart, T., Scragg, J. & Platzer-Björkman, C. (2012) Reactive sputtering of precursors for  $\text{Cu}_2\text{ZnSnS}_4$  thin film solar cells. *Thin Solid Films*, **520**, 7093–7099.
- [4] Li, J., Chawla, V. & Clemens, B. (2012) Investigating the role of grain boundaries in CZTS and CZTSSe thin film solar cells with scanning probe microscopy. *Advanced Materials*, **24**(6), 720.
- [5] Ericson, T., Scragg, J.J., Kubart, T., Törndahl, T. & Platzer-Björkman, C. (2013) Annealing behavior of reactively sputtered precursor films for  $\text{Cu}_2\text{ZnSnS}_4$  solar cells. *Thin Solid Films*, **535**, 22–26.
- [6] Scragg, J., Ericson, T., Fontané, X., Izquierdo-Roca, V., Perez Rodriguez, A., Kubart, T., Edoff, M. & Platzer-Björkman, C. (2014) Rapid annealing of reactively sputtered precursors for  $\text{Cu}_2\text{ZnSnS}_4$  solar cells. *Progress in Photovoltaics: Research and Applications*, **22**(1), 10–17.
- [7] Berg, S. & Nyberg, T. (2005) Fundamental understanding and modeling of reactive sputtering processes. *Thin Solid Films*, **476**(2), 215–230.
- [8] Depla, D., Heirwegh, S., Mahieu, S., Haemers, J. & De Gryse, R. (2007) Understanding the discharge voltage behavior during reactive sputtering of oxides. *Journal of Applied Physics*, **101**(1) 013301.
- [9] Ashraf, M., Ullah, S., Hussain, S., Dogar, A.H. & Qayyum, A. (2011) Ion-induced secondary electron emission from ZnS thin films deposited by closed-spaced sublimation. *Applied Surface Science*, **258**(1), 176–181.

- [10] Seeger, S., Harbauer, K. & Ellmer, K. (2009) Ion-energy distributions at a substrate in reactive magnetron sputtering discharges in Ar/H<sub>2</sub>S from copper, indium, and tungsten targets. *Journal of Applied Physics*, **105**(5), 053305.
- [11] Thornton, J.A., Cornog, D.G., Hall, R.B. & Dinetta, L.C. (1982) Apparatus surface conditioning effects in copper sulfide reactive sputtering for photovoltaic applications. *Journal of Vacuum Science and Technology*, **20**(3), 296–299.
- [12] Swanson, H.E. & Tatge, E. (1953) JCPDS 00-004-0673 Sn. *National Bureau of Standards, US*, **539**(1), 24.
- [13] Brandon, J.K., Brizard, R.Y., Chieh, P.C., Mcmillan, R.K. & Pearson, W.B. (1974) New refinements of gamma-brass type structures Cu<sub>5</sub>Zn<sub>8</sub>, Cu<sub>5</sub>Cd<sub>8</sub> and Fe<sub>3</sub>Zn<sub>10</sub>. *Acta Crystallographica Section B: Structural Science*, **B30** (Jun15) 1412–1417.
- [14] Chou, C.Y. & Chen, S.W. (2006) Phase equilibria of the Sn-Zn-Cu ternary system. *Acta Materialia*, **54**(9), 2393–2400.
- [15] Jumpertz, E.A. (1955) Über die Elektronendichteverteilung in der Zinkblende. *Zeitschrift für Elektrochemie*, **59**(5), 419–425.
- [16] Booth, M.H., Brandon, J.K., Brizard, R.Y., Chieh, C. & Pearson, W.B. (1977) Gamma-brasses with F cells. *Acta Crystallographica Section B: Structural Science*, **33**(Jan15), 30–36.
- [17] Schäfer, W.N. (1974) Tetrahedral quaternary chalcogenides of the type Cu<sub>2</sub>-II-IV-S<sub>4</sub>(Se<sub>4</sub>). *Materials Research Bulletin*, **9**, 645–654.
- [18] Palatnik, L.S., Komnik, I.F., Belova, E.K. & Koshkin, V.M. (1961) A certain group of ternary semiconducting compounds. *Doklady Akademii Nauk Sssr*, **137**(1), 68.
- [19] Chen, X.A., Wada, H., Sato, A. & Mieno, M. (1998) Synthesis, electrical conductivity, and crystal structure of Cu<sub>4</sub>Sn<sub>7</sub>S<sub>16</sub> and structure refinement of Cu<sub>2</sub>SnS<sub>3</sub>. *Journal of Solid State Chemistry*, **139**(1), 144–151.
- [20] Onoda, M., Chen, X.A., Sato, A. & Wada, H. (2000) Crystal structure and twinning of monoclinic Cu<sub>2</sub>SnS<sub>3</sub>. *Materials Research Bulletin*, **35**(9), 1563–1570.
- [21] Weber, A., Mainz, R. & Schock, H.W. (2010) On the Sn loss from thin films of the material system Cu-Zn-Sn-S in high vacuum. *Journal of Applied Physics*, **107**(1), 013516.
- [22] Swanson, H.E. & Tatge, E. (1953) JPCDS 00-042-1120 Mo. *National Bureau Standards, US*, **539**(1) 20.
- [23] Himmrich, M. & Haeuseler, H. (1991) Far infrared studies on stannite and wurtzstannite type compounds. *Spectrochimica Acta, Part A*, **47**, 933–942.
- [24] Fontané, X., Calvo-Barrio, L., Izquierdo-Roca, V., Saucedo, E., Perez-Rodriguez, A., Morante, J.R., Berg, D.M., Dale, P.J. & Siebentritt, S. (2011) In-depth resolved Raman scattering analysis for the identification of secondary phases: Characterization of Cu<sub>2</sub>ZnSnS<sub>4</sub> layers for solar cell applications. *Applied Physics Letters*, **98**(18), 181905.
- [25] Swanson, H.E. & Tatge, E. (1953) JCPDS 04-0831 Zn. *National Bureau of Standards, US*, **539**(I), 16.
- [26] Thornton, J.A. (1974) Influence of apparatus geometry and deposition conditions on structure and topography of thick sputtered coatings. *Journal of Vacuum Science and Technology*, **11**(4), 666–670.
- [27] Thornton, J.A. & Hoffman, D.W. (1989) Stress-related effects in thin-films. *Thin Solid Films*, **171**(1), 5–31.
- [28] He, Y.B., Kramer, T., Polity, A., Hardt, M. & Meyer, B.K. (2003) Influence of the preparation conditions on the properties of CuInS<sub>2</sub> films deposited by one-stage RF reactive sputtering. *Thin Solid Films*, **431**, 126–130.
- [29] Schorr, S., Hoebler, H.J. & Tovar, M. (2007) A neutron diffraction study of the stannite-kesterite solid solution series. *European Journal of Mineralogy*, **19**(1), 65–73.
- [30] Siebentritt, S. & Schorr, S. (2012) Kesterites: a challenging material for solar cells. *Progress in Photovoltaics: Research and Applications*, **20**(5), 512–519.
- [31] Unold, T., Sieber, I. & Ellmer, K. (2006) Efficient CuInS<sub>2</sub> solar cells by reactive magnetron sputtering. *Applied Physics Letters*, **88**(21), doi: 10.1063/1.2205756.
- [32] Schorr, S. & Gonzalez-Aviles, G. In-situ investigation of the structural phase transition in kesterite. *Physica Status Solidi (A)*, **206**, 1054.

- [33] Gouadec, G. & Colombari, P. (2007) Raman spectroscopy of nanomaterials: How spectra relate to disorder, particle size and mechanical properties. *Progress in Crystal Growth and Characterization of Materials*, **53**(1), 1–56.
- [34] Fontané, X., Izquierdo-Roca, V., Saucedo, E., Schorr, S., Yuhymchuk, V.O., Valakh, M.Y., Pérez-Rodríguez, A. & Morante, J.R. (2012) Vibrational properties of stannite and kesterite type compounds: Raman scattering analysis of  $\text{Cu}_2(\text{Fe,Zn})\text{SnS}_4$ . *Journal of Alloys and Compounds*, **539**(0), 190–194.
- [35] Scragg, J.J., Dale, P.J., Colombari, D. & Peter, L.M. (2012) Thermodynamic aspects of the synthesis of thin-film materials for solar cells. *ChemPhysChem*, **13**(12), 3035–3046.
- [36] Scragg, J.J., Wätjen, J.T., Edoff, M., Ericson, T., Kubart, T. & Platzer-Björkman, C. (2012) A detrimental reaction at the molybdenum back contact in  $\text{Cu}_2\text{ZnSn}(\text{S,Se})_4$  thin-film solar cells. *Journal of American Chemical Society*, **134**(47), 19330–19333.
- [37] Redinger, A., Berg, D., Dale, P.J. & Siebentritt, S. (2011) The consequences of kesterite equilibria for efficient solar cells. *Journal of American Chemical Society*, **133**(10), 3320–3323.
- [38] Scragg, J., Ericson, T., Kubart, T., Edoff, M. & Platzer-Björkman, C. (2011) Chemical insights into the instability of  $\text{Cu}_2\text{ZnSnS}_4$  films during annealing. *Chemistry of Materials*, **23**(20), 4625.
- [39] Kato, T., Hiro, H., Sakai, N., Muraoka, S. & Sugimoto, H. (2012) Characterization of front and back interfaces on  $\text{Cu}_2\text{ZnSnS}_4$  thin-film solar cells. In *Proceedings of 27th European Photovoltaic Solar Energy Conference*, Frankfurt.
- [40] Wätjen, J.T., Engman, J., Edoff, M. & Platzer-Björkman, C. (2012) Direct evidence of current blocking by ZnSe in  $\text{Cu}_2\text{ZnSnSe}_4$  solar cells. *Applied Physics Letters*, **100**(17), 173510.
- [41] Scragg, J., Kubart, T., Wätjen, J.T., Ericson, T., Linnarsson, M. & Platzer-Björkman, C. (2013) Effects of back contact instability on  $\text{Cu}_2\text{ZnSnS}_4$  devices and processes. *Chemistry of Materials*, **25**, 3162–3171.



# 10

## Coevaporation of CZTS Films and Solar Cells

*Thomas Unold, Justus Just and Hans-Werner Schock*

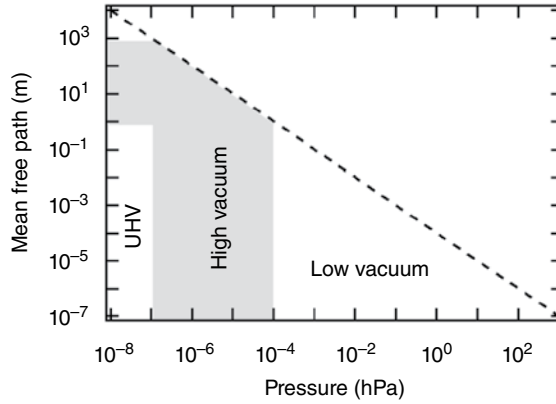
*Helmholtz Centre Berlin for Materials and Energy, Dept. Complex Compound  
Semiconductors for PV, Hahn-Meitner Platz 1, 14109 Berlin Germany*

### 10.1 Introduction

Physical vapor deposition is a well-established method of depositing polycrystalline compound semiconductor materials. For thin-film chalcopyrite absorber materials this method has so far yielded the best electronic quality, leading to thin-film solar cells with solar conversion efficiencies of more than 20% [1]. In principle, coevaporation provides very good control over the elemental flux, substrate temperature, and purity of source materials. While epitaxial layers can be achieved using very slow growth rates and lattice-matched substrates at high temperatures under ultra-high vacuum (UHV) conditions (e.g. molecular beam epitaxy), polycrystalline absorber materials used in photovoltaics are typically grown under high vacuum conditions at high deposition rates ( $\sim 100 \text{ nm min}^{-1}$ ) using glass substrates held at moderate temperatures ( $350^\circ\text{C}$ – $600^\circ\text{C}$ ).

### 10.2 Basic Principles

Deposition by evaporation involves three processes: evaporation of the source material; transport of the atoms or molecules to the substrate; and condensation of the vapor atoms or molecules on the substrate. The evaporation process takes place in vacuum to minimize



**Figure 10.1** Mean free path of vapor phase species as a function of the total pressure

the effect of residual gases in the evaporation system, and to enable a sufficiently large mean free path of the evaporated elements. The mean free path of atoms or molecules can be approximated [2]:

$$\lambda = \frac{k_B T}{\sqrt{2} P \pi d^2} \quad (10.1)$$

where  $k_B$  is the Boltzmann constant,  $T$  is the temperature,  $d$  is the diameter of the gas species, and  $P$  is pressure. The resulting mean free paths are shown in Figure 10.1 for an atomic diameter of 0.3 nm and a temperature of 300 K, for pressures ranging from atmospheric conditions to UHV. The ratio of the mean free path  $\lambda$  and the typical process equipment length scale  $L$  defines the Knudsen number ( $K_n = \lambda/L$ ) and determines whether the evaporation takes place in the molecular flow ( $K_n > 1$ ) or in the viscous flow regime ( $K_n < 0.01$ ). Evaporation processes for polycrystalline thin films are typically performed in the molecular flow regime, that is, for mean free paths  $> 10$  cm, corresponding to pressures smaller than  $10^{-3}$  hPa. However, at high vapor pressures of the source materials (as required for deposition rates in high-throughput fabrication of solar cells), the mean free path can be in the centimetre-range which can lead to significant reactions in the gas phase. The intermediate species formed in these reactions may also influence the properties of the growing film in the evaporation process.

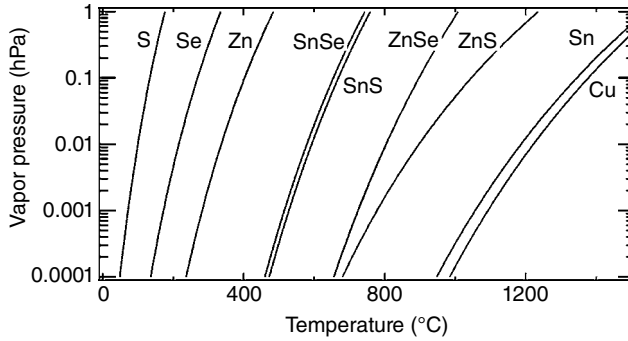
The evaporation rate of the source materials is directly related to the equilibrium vapor pressure of the source material, which depends on the temperature  $T$  and the latent heat  $\Delta H_L$  and can be described by the Clausius–Clapeyron equation:

$$\ln(P) = -\frac{\Delta H_L}{R} \frac{1}{T} + C \quad (10.2)$$

where  $R$  is the gas constant and  $C$  is an element-specific constant [2]. Because of the temperature dependence of the latent heat, Equation (10.2) is only strictly valid over a limited temperature range. Vapor pressures as a function of temperature are shown for the different elements and compounds involved in the evaporation of CZTSSe in Figure 10.2.

Even at relatively low temperatures the vapor pressures of sulfur, selenium, and zinc are considerably high ( $> 10$  hPa), with the vapor pressure of sulfur exceeding that of selenium





**Figure 10.2** Equilibrium vapor pressures of elements and binary compounds involved in the coevaporation of CZTSSe [3–8]

by more than four orders of magnitude. It can also be seen that the vapor pressures of SnS and SnSe are relatively high at temperatures around 500°C ( $P_{\text{eq}} \approx 10^{-3}$  hPa), which indicates that a loss of tin by re-evaporation of SnS or SnSe from the substrate can be a serious issue in deposition of kesterites under vacuum conditions.

In order to achieve sufficiently high evaporation rates, the temperatures of the source materials have to be high enough to provide the required vapor pressure for a desired evaporation rate, as described below. On the other hand, the substrate temperature has to be low enough to prevent re-evaporation and decomposition of the deposited material.

Different types of sources are commonly used in thermal evaporation systems. A principal distinction can be made between directly heated sources, for example resistively heated metal boats made from Mo, Ta, or W, and indirectly heated sources consisting of a crucible surrounded by a heater. Accordingly, the evaporation of the source material occurs directly from the surface of the melt in a metal boat, while it is more spatially confined by the design of a crucible.

The principle behind the evaporation process is the generation of a sufficiently high vapor pressure directly above the source material by rising its temperature. Using kinetic gas theory the evaporation flux  $\phi_e$  (in units of atoms per second and  $\text{cm}^2$ ) associated with a vapor pressure  $P_{\text{eq}}(T)$  above an open surface can be calculated from the Hertz–Knudsen equation [2]:

$$\phi_e = \gamma_e \alpha_e \frac{P_{\text{eq}}(T) - P_0}{\sqrt{MT}} \quad \text{where} \quad \gamma_e = \sqrt{\frac{N_A}{2\pi k_B}} \approx 2.6 \times 10^{22} \frac{\sqrt{\text{g} \cdot \text{K} \cdot \text{mol}^{-1}}}{\text{hPa} \cdot \text{s} \cdot \text{cm}^2} \quad (10.3)$$

where  $M$  is the molar mass in g/mol,  $P_0$  is the background partial pressure of the evaporant in hPa,  $T$  is the source temperature and  $N_A$  is the Avogadro constant. The evaporation coefficient  $\alpha_e$  ranges between 0 and 1 and depends on the surface energy of the evaporating species and the source geometry. The mass evaporation rate  $\Gamma_e$  (in units of  $\text{g cm}^{-2} \text{s}^{-1}$ ) is obtained by multiplying the atomic flux by the mass of an individual atom or molecule, yielding:

$$\Gamma_e = \frac{\alpha_e \cdot \gamma_e}{N_A} \sqrt{\frac{M}{T}} (P_{\text{eq}}(T) - P_0). \quad (10.4)$$

For  $\alpha_e = 1$ ,  $P_0 = 0$ , and  $P_{\text{eq}} = 10^{-2}$  hPa (e.g. copper at  $T = 1220^\circ\text{C}$ ), a mass evaporation rate of  $10^{-4}$  grams per second per  $\text{cm}^2$  of evaporant area is found for many elements.

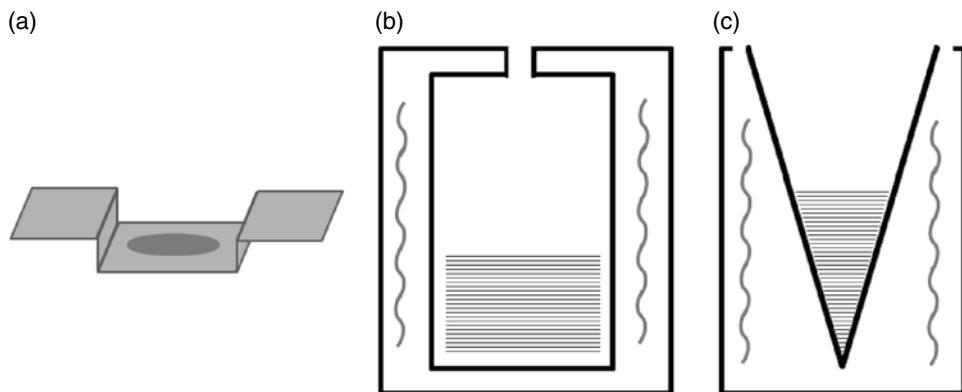
Evaporation from a free surface, for example an evaporation boat, has the advantage of low cost and the possibility of fast rate changes due to its low thermal mass. The disadvantages are the low stability of the system due to the open design and small quantity of evaporating material, and therefore a resulting difficulty in maintaining constant evaporation rates.

In so-called Knudsen cells or effusion cells, the evaporation occurs through the orifice of a crucible holding the source material (Fig. 10.3b). Here the crucible is indirectly heated by a heater filament and the orifice acts as the evaporating surface [9]. The evaporation cell can be held at a uniform and constant temperature such that the equilibrium vapor pressure of the source material is well defined. In a Knudsen cell the equilibrium vapor pressure within the crucible should be maintained at a small enough value such that the mean free path of the evaporating species is much larger than the orifice dimensions and the molecular beam emanating through the aperture does not significantly affect the internal pressure, leading to an evaporation coefficient  $\alpha$  equal to 1 for this type of cell design. The effusion profile from the crucible orifice of a Knudsen cell follows a cosine distribution, in analogy to a Lambertian radiator in geometrical optics. The mass deposition rate per substrate area  $dA_s$  at an angle  $\theta$  and a distance  $r$  from the source with area  $A_e$  is given by:

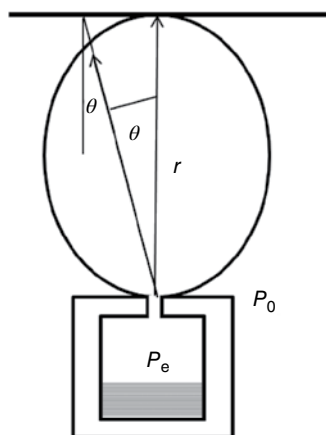
$$\frac{d\Gamma_s}{dA_s} = \int_{A_e} \frac{1}{\pi r^2} \cos^2(\theta) \Gamma_{\text{evap}} dA_e \quad (10.5)$$

where the square of the cosine comes from assuming that the substrate is parallel to the surface of the evaporation cell, as illustrated in Figure 10.4. For a substrate–source distance of  $r=20\text{ cm}$  and a mass evaporation rate of  $\Gamma_e = 10^{-4}\text{ g cm}^{-2}\text{ s}^{-1}$  as estimated above, the mass deposition rate is  $\Gamma_s \approx 1.6 \times 10^{-6}\text{ g cm}^{-2}\text{ s}^{-1}$ , which corresponds to a deposition rate of approximately  $100\text{ nm min}^{-1}$  for copper.

If high deposition rates and a greater ease of handling are required, evaporation cells can be used. These are similar to the Knudsen cell design, but consist of crucibles with large orifices (larger source area  $A_e$ ) and are therefore less mechanically complex and easier to fill (Fig. 10.3c). These sources have many applications including low temperature and high temperature evaporation as well as molecular beam epitaxy. Because of the large orifice the spatial distribution is not of true cosine form. The exact shape depends on the geometry of the source and can be empirically approximated with a  $\cos^n(\theta)$  distribution, where  $n$  is an



**Figure 10.3** Evaporation sources used in coevaporation: (a) directly heated metal boat; (b) Knudsen cell; and (c) evaporation cell



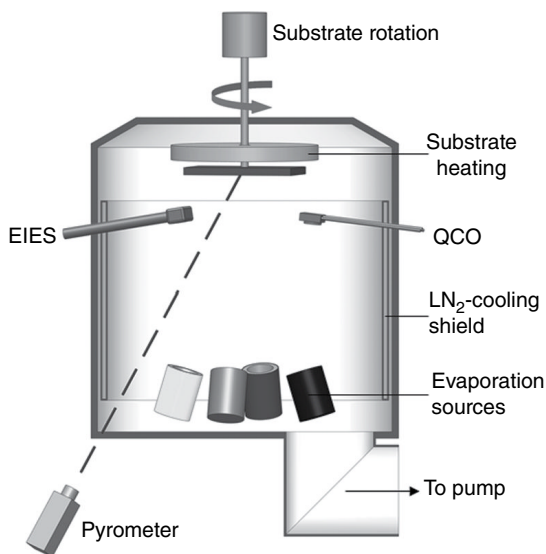
**Figure 10.4** Vapor distribution from a Knudsen cell

integer number (typically of value 2–6). For large  $n$  the vapor flux is highly directed which is the case for deep narrow crucibles [10]. Note that the particle energy in evaporation processes is related to the thermal energy of the evaporants within the source which, for an assumed source temperature of 1000°C, corresponds to about 0.2 eV.

In contrast to some II–VI compounds, kesterite compounds do not evaporate congruently, that is, the composition of the vapor differs from the composition of the source material making a separate evaporation of the constituent components and a precise control essential. This can be achieved by individual evaporation of the pure metals in addition to sulfur or selenium, or by using binary compounds such as ZnS or ZnSe for evaporation. Because of the high vapor pressure of sulfur and selenium, closed (Knudsen-type) evaporation sources are advisable for these elements. ZnS and ZnSe sublimate, which makes it difficult to achieve constant rates in open crucible evaporation sources. This problem can be solved by using either closed sources or baffles realized by high-temperature stable material such as quartz frits. For large deposition systems, an inline arrangement of linear sources has been shown to yield good results, for example in the production of Cu(In,Ga)Se<sub>2</sub> modules.

A typical laboratory physical-vapor-deposition- (PVD-) growth chamber is depicted in Figure 10.5. The chamber is enclosed by a cooling shroud to improve the background pressure and to carry away radiant heat from the sources and the substrate heater. The evaporation sources at the bottom are directed towards the substrate and include shutters to allow the flux of the individual sources to be quickly turned on and off. The substrates are mounted on a radiatively heated manipulator.

In laboratory systems substrate rotation is often used to ensure a homogeneous composition over a large area. However, non-rotating substrate holders may also be used with the advantage of creating intentional lateral gradients in composition within single growth runs, which could even be used for combinatorial approaches. Appropriate pumping systems have to be used which include measures to protect the pump from condensation of chalcogens, other evaporation material and dust. In general, turbomolecular pumps equipped with a cold trap serve this purpose. Shutters at the sources are used for conditioning of the sources or intentional interruption of the vapor flux during growth.

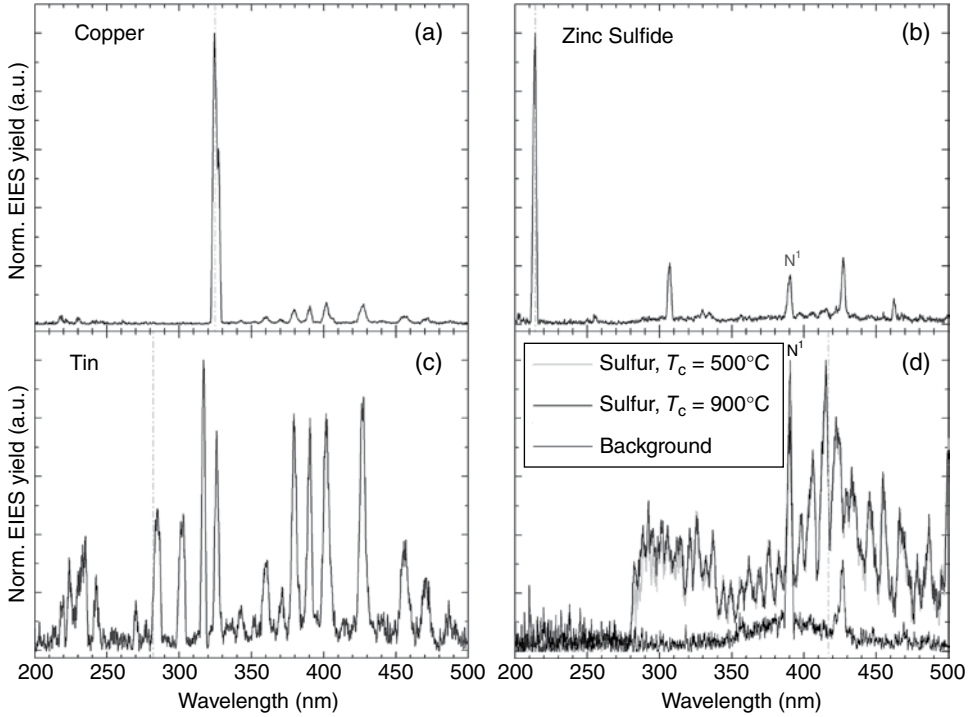


**Figure 10.5** Typical growth chamber for coevaporation of thin-film semiconductors

Excellent control over the evaporation fluxes is essential for controlling film thickness and composition of the growing film. This can be achieved by several different methods: the most prominent techniques are quartz crystal monitors (QCM), atomic absorption spectroscopy (AAS), and electron impact emission spectroscopy (EIES). Quartz crystal monitors are standard tools to monitor evaporation flux and film thickness by measuring the detuning of the resonance frequency of a crystal oscillator coated by the elemental flux of the evaporation source. With QCMs the flux of single elemental sources can be measured very accurately; the deposition rate on the substrate can therefore be determined if the temperature of the substrate and the QCM do not deviate too strongly from each other. However, for full control of all rates crystal monitors for each source are required and the crystal oscillators have to be renewed in relatively short intervals.

Alternative methods to monitor source flux utilize atomic absorption spectroscopy (AAS) or electron impact emission spectroscopy (EIES). In AAS specific atomic emission, lines of the source elements (e.g. Cu or Zn) provided by hollow cathode lamps are transmitted through the evaporation cone of the source while the absorption of the transmitted light through the vapor is monitored. In EIES the atoms in the evaporation cone are excited by electrons accelerated from a cathode placed in the evaporation chamber. The excited atoms and molecules show element-specific characteristic emission lines or bands, which can be detected and calibrated to the source flux. The advantage of EIES over AAS is that no element-specific light sources are required, and that in principle all elements in the vapor can be characterized simultaneously.

Typical EIES spectra for the elements contained in CZTS growth are shown in Figure 10.6. In Figure 10.6a an EIES spectrum recorded during the evaporation of copper is shown. The main emission here is a strong doublet emission peak at 325 nm. In Figure 10.6b only the ZnS evaporation source was in operation. It can be seen that several characteristic Zn emission lines are observed, with the strongest line located at 213 nm. The



**Figure 10.6** Electron impact emission spectra (EIES) measured during the evaporation of: (a) copper; (b) zinc sulfide; (c) tin; and (d) sulfur

line observed at 390 nm corresponds to nitrogen from the remaining residual gas in the chamber. For the EIES spectrum recorded during the evaporation of tin shown in Figure 10.6c, a large number of emission lines are observed. In order to avoid overlap with atomic emission from the other elements, a band pass filter at 282 nm should give the best results for this element during CZTS coevaporation.

For the sulfur emission shown in Figure 10.6d a rather broad emission band extending from 280 nm to 500 nm is observed, which can be attributed to the sulfur molecules. Interestingly, the shape of the emission does not change when the cracker-tube of the sulfur source is heated up to 900°C instead of the standard 500°C. Comparing the spectra for the different elements needed in CZTS coevaporation, it is clear that all four elements can be monitored with a single EIES set-up if appropriate band pass filters are used.

### 10.3 Process Variations

#### 10.3.1 Single-Step Process

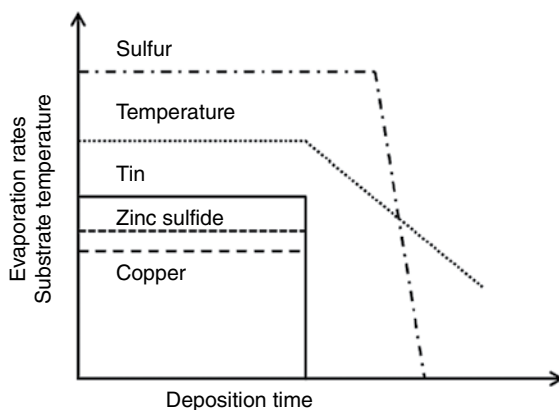
The simplest coevaporation process envisioned consists of a simultaneous evaporation of the different source elements while the substrate is held at high temperature. Such single-step coevaporation processes have also been used for the growth of  $\text{Cu(In,Ga)Se}_2$ , although multi-stage coevaporation processes have been found to yield higher conversion efficiencies

for chalcopyrite solar cells [11, 12]. There are a number of reports in the literature for deposition of CZTS by single-step coevaporation, although there are only a few reports on electrical characteristics of solar cells resulting from such processes [13–18].

Redinger and Siebentritt investigated single-step coevaporation of CZTSe in a molecular beam epitaxy (MBE) system by using effusion cells for copper, tin, zinc, and selenium [19]. In the deposition process the metal rates were held at  $1\text{--}2\text{ \AA s}^{-1}$  and the partial pressure of selenium was varied between  $6 \times 10^{-7}\text{ hPa}$  and  $5 \times 10^{-6}\text{ hPa}$ . It was observed that for substrate temperatures higher than  $350^\circ\text{C}$  Sn was not sufficiently incorporated into the growing film, and that at temperatures higher than  $430^\circ\text{C}$  Zn desorption occurred. It was concluded that single-step coevaporation of CZTSe can only be performed at substrate temperatures lower than  $380^\circ\text{C}$  and at selenium partial pressures higher than  $5 \times 10^{-6}\text{ hPa}$ . It was also found that the limited incorporation of Sn in the beginning of the growth process leads to a significant presence of ZnSe as a secondary phase at the back of the thin films.

Some of the problems encountered by Redinger and Siebentritt for growth conditions with low chalcogen partial pressure and low deposition rates can be resolved if higher deposition rates are used in the process. In the following, the  $\text{Cu}_2\text{ZnSnS}_4$  (CZTS) single-step coevaporation process demonstrated by Schubert *et al.* is described [18]. In this process CZTS is deposited from evaporation cells containing Cu, Sn, and ZnS, whereas sulfur is evaporated from a valved cracker source. The temperature profile and source rate profiles are indicated in Figure 10.7. The sulfur partial pressure was maintained at  $2\text{--}3 \times 10^{-5}\text{ hPa}$  during the entire deposition process. The substrate was heated up to a nominal temperature  $550^\circ\text{C}$  and held at that temperature during the growth process. Growth rates larger than  $60\text{ nm min}^{-1}$  were used in order to minimize the loss of tin at the elevated substrate temperature used. After the completion of the growth process, the shutters of the metal sources were closed and the substrate was cooled down under continued evaporation of sulfur to a temperature of  $200^\circ\text{C}$ . When this temperature was reached, the sulfur source was closed and the substrate was cooled down to room temperature radiatively. SEM images of two absorber layers with different compositions obtained by this technique are shown in Figure 10.8.

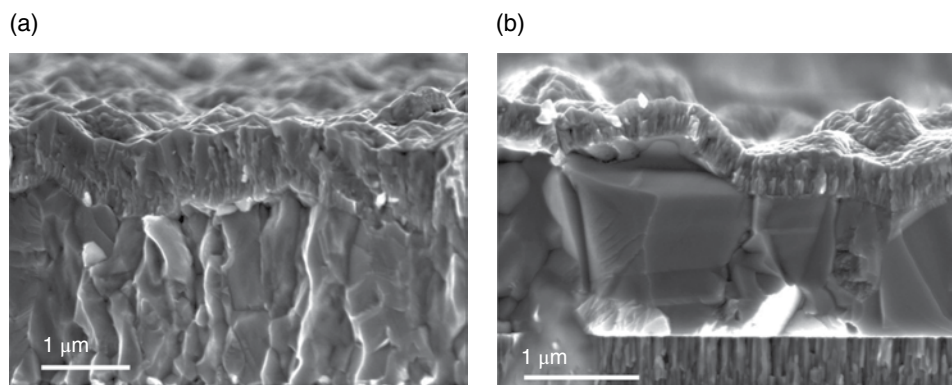
The absorber layers were grown with different source flux ratios, yielding an overall copper-poor ( $[\text{Cu}]/[\text{Zn}] + [\text{Sn}] \approx 0.92$ ) and an overall copper-rich ( $[\text{Cu}]/[\text{Zn}] + [\text{Sn}] \approx 1.16$ )



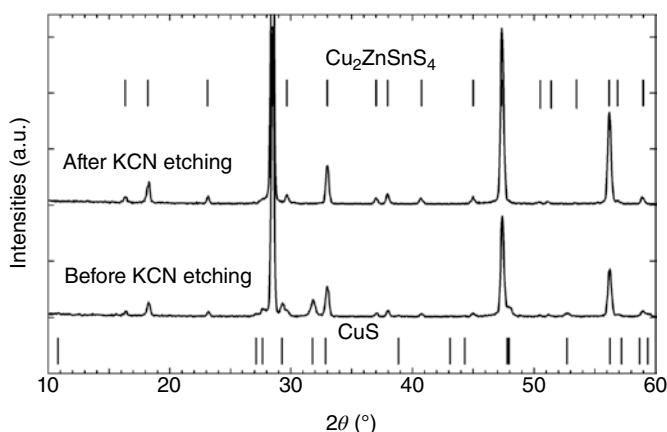
**Figure 10.7** Rate and temperature profiles for single-step coevaporation process

composition. It can be seen that the grain size significantly increases for Cu-rich growth compared to Cu-poor growth. This has been a general observation for the coevaporation of chalcopyrite thin films [20], and has also been observed for the coevaporation of  $\text{Cu}_2\text{ZnSnS}_4$  [21].

As has also been found for the copper-chalcopyrite system, excess Cu during growth leads to the segregation of Cu-S secondary phases which can be removed after growth by etching in diluted KCN [22]. X-ray diffraction (XRD) diffractograms of a coevaporated  $\text{Cu}_2\text{ZnSnS}_4$  absorber with copper-rich composition are shown in Figure 10.9 before and after etching with KCN. In addition to the expected kesterite reflexes CuS diffraction signals are also observed before KCN etching, which disappear after the etching process. Energy-dispersive X-ray spectroscopy (EDX) measurements after KCN etching showed a composition of  $\text{Cu}/(\text{Zn} + \text{Sn}) \approx 1$ , indicating that removing Cu-S secondary phases left behind a stoichiometric film with respect to the  $\text{Cu}/(\text{Zn} + \text{Sn})$  ratio.



**Figure 10.8** CZTS solar cells with single-step coevaporated absorber layers of different composition: (a)  $\text{Cu}/(\text{Zn} + \text{Sn}) = 0.92$ ; and (b)  $\text{Cu}/(\text{Zn} + \text{Sn}) = 1.16$



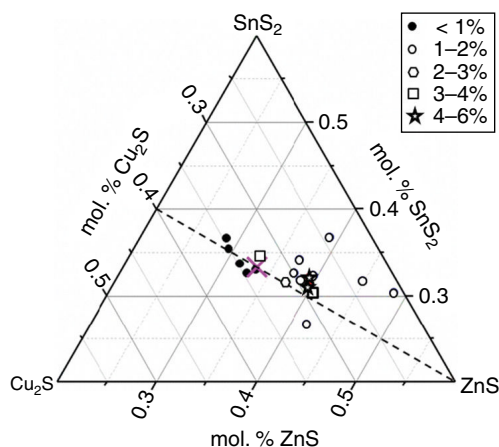
**Figure 10.9** X-ray diffractograms of Cu-rich grown  $\text{Cu}_2\text{ZnSnS}_4$  before and after KCN etching. Reproduced with permission from [18]. Copyright © 2011, John Wiley and Sons Ltd.

Solar cells have been fabricated from these CZTS absorber layers by depositing a 50 nm thick CdS buffer layer in a chemical bath followed by a window layer consisting of an intrinsic ZnO and aluminum-doped ZnO layer deposited by magnetron sputtering.

Although the large grains obtained from Cu-rich growth might be expected to be beneficial for kesterite thin-film solar cells it has been found, in analogy with the experience from chalcopyrite-type solar cells, that the highest conversion efficiencies are obtained not for Cu-rich but for Cu-poor growth. In Figure 10.10 a ternary diagram is shown containing the compositions of different coevaporated CZTS solar cell absorbers. Note that these compositions are integral compositions determined by XRF measurements, and do not take into account depth inhomogeneities or secondary phases.

It can be seen that the best efficiencies were obtained for slightly Cu-poor ( $[\text{Cu}]/[\text{Zn}] + [\text{Sn}] \approx 0.9$ ) and Zn-rich ( $[\text{Zn}]/[\text{Sn}] \approx 1.1$ ) samples, as observed by many other groups [23].

A room-temperature dark and illuminated *IV*-measurement of a 5% efficiency CZTS solar cell onto which a  $\text{MgF}_2$  antireflection coating was applied is shown in Figure 10.11a. It can be seen that the illuminated *J-V* curve shows strong bias-dependent current collection, indicative of a very short diffusion length. This is consistent with the EQE measured on the same sample shown in Figure 10.11b. The decay in the EQE for wavelengths larger than 500 nm can be explained with a relatively short diffusion length of <200 nm, whereas the decay for wavelengths smaller than 500 nm is due to parasitic absorption in the CdS buffer and ZnO window layer. A one-diode fit of the dark *J-V* curve yields a series resistance of  $3 \Omega \text{ cm}^2$  and a parallel shunt resistance of  $1.7 \text{ k}\Omega \text{ cm}^2$ . The relatively large series resistance has been observed for kesterite-type solar cells by many groups and is partly responsible for the relatively low fill factor of this solar cell [24]. The dark *J-V* fit also yields a diode factor close to 2 and a dark saturation current density of  $1.5 \times 10^{-4} \text{ mA cm}^{-2}$ , indicating strong recombination in the space charge region and/or at the heterojunction interface. From the EQE a band-gap value of  $E_g = 1.51 \text{ eV}$  can be determined, either by fitting to an analytical expression or by taking the inflection point in the decay between



**Figure 10.10** Ternary phase diagram showing the relation of efficiencies to composition of different coevaporated CZTS solar cells. The large x in the center of the phase diagram indicates the point of stoichiometry

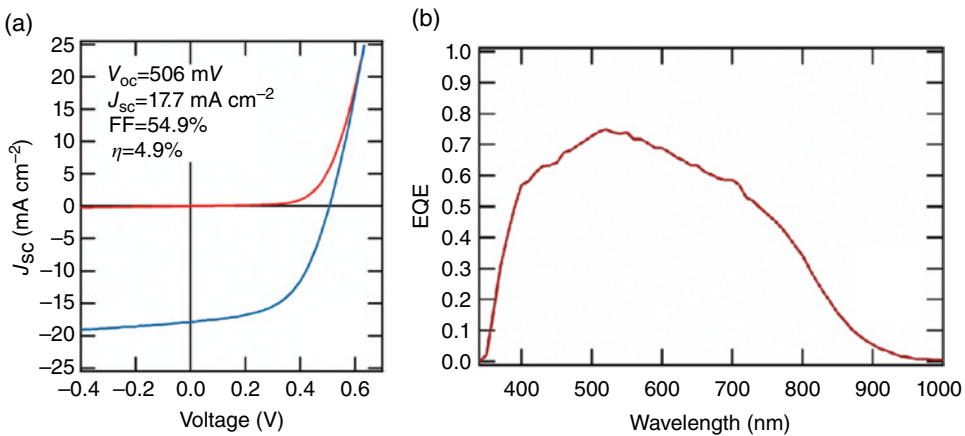


700 and 1000 nm. The observed open-circuit voltage loss  $(E_g/q) - V_{oc} \approx 1 \text{ V}$  is very large compared to typical values of 0.5 V observed in chalcopyrite solar cells [25]. The solar cell delivers only about 60% of the current expected for a 1.5 eV band gap ( $28.5 \text{ mA cm}^{-2}$ ), which is mainly a result of the high bulk and interface recombination.

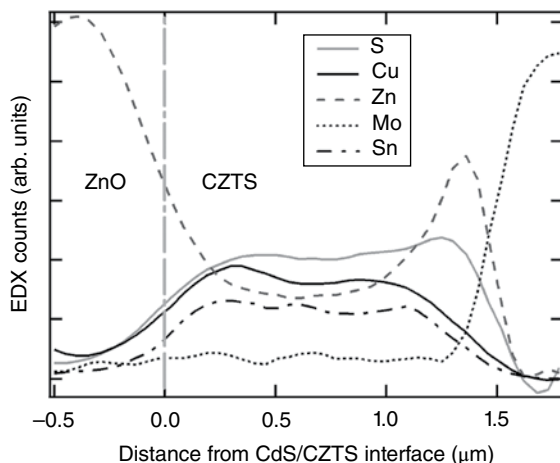
Another explanation for the high series resistance as well as the poor short-circuit current can be found in the presence of secondary phases in the absorber layer. Although secondary phases such as ZnS or  $\text{Cu}_2\text{SnS}_3$  were not detected by XRD measurements, the presence of such phases cannot be excluded due to similarity of their lattice constants with that of the kesterite phase. On the other hand, Just *et al.* have investigated the presence of secondary phases in coevaporated CZTS by means of X-ray absorption spectroscopy [26]. In these experiments the X-ray absorption near edge structure (XANES) at the sulfur K-edge of ZnS, CuS, CZTS, and  $\text{Cu}_2\text{SnS}_3$  were analyzed separately. This allowed an absolute determination of the ZnS volume content in coevaporated CZTS absorber layers by linear combination analysis. For all of the investigated samples, ZnS was found to be present in concentrations up to 20 vol%. For the investigated samples a general correlation was found between the Zn/Sn ratio and the ZnS content [26].

EDX-mapping measurements of absorber cross-sections also showed regions with excessively high Zn content, in particular close to the back contact which can be attributed to segregations of the ZnS secondary phase. This is shown in Figure 10.12 where elemental depth profiles for a typical coevaporated solar cell are shown. It can be seen that the Zn content increases strongly towards the back contact, whereas the Cu and Sn content decreases accordingly. The fact that the gradient of the elemental profiles are very broad close to the heterointerface is an averaging artifact caused by the inhomogeneity in the absorber thickness. The elemental line profiles indicate the presence of ZnS close to the back contact, which may be partly resulting from the  $\text{MoS}_2$  reaction leading to a decomposition of CZTS into secondary phases close to the molybdenum back contact, as described by Scragg *et al.* [27].

Finally, correlation of the ZnS secondary phase content determined by XANES analysis with the electrical parameters of corresponding solar cells clearly showed the detrimental



**Figure 10.11** (a) Dark and illuminated J-V curve for a coevaporated CZTS solar cell; and (b) external quantum efficiency for the same solar cell



**Figure 10.12** Elemental depth profiles determined by EDX mapping analysis of a cross-section of a coevaporated CZTS solar cell. For the EDX measurement an acceleration voltage of 7 kV was used.

effect of this phase on the solar cell performance, indicating that the content of ZnS secondary phases should be minimized in CZTS solar cells [26].

Most of the coevaporated CZTS solar cells grown at the Helmholtz Zentrum Berlin (HZB) were KCN-treated after growth, no matter whether the absorber layer was grown intentionally Cu-rich or Cu-poor, as this treatment was observed to generally improve the solar cell performance. This effect can be partly explained by XPS/UPS (X-ray/ultraviolet photoemission spectroscopy) investigations of the absorber surface before and after KCN etching, which showed a significant widening of the surface band gap after the KCN treatment [28].

Investigations of the band alignment between coevaporated CZTS absorbers and chemical-bath-deposited CdS by photoemission spectroscopy and inverse photoemission spectroscopy (IPES) by Bär *et al.* showed a cliff-type heterojunction offset. This favors interface recombination, in line with our observation of very low open-circuit voltages considering the large band gap of the sulfur-based material [29].

So far it has not been possible to grow sulfur-based CZTS absorber layers for solar cells with efficiencies close to 10% by single-step coevaporation without additional annealing in a high-pressure sulfur atmosphere. We believe that this is due to the limitations caused by the high vapor pressure of sulfur and tin sulfide, leading to significant tin loss during the evaporation processes in high vacuum [30, 31]. Coevaporation of sulfur-based kesterites might be more successful if multi-stage processes or annealing steps involving high sulfur partial pressures are employed [32].

### 10.3.2 Multi-stage Processes

Multi-stage coevaporation processes, consisting of different evaporation stages with varying rates and possibly varying substrate temperatures, have a number of advantages over single-stage coevaporation where all constituting elements condense simultaneously on the growing film. Different evaporation sequences allow the implementation of compositional

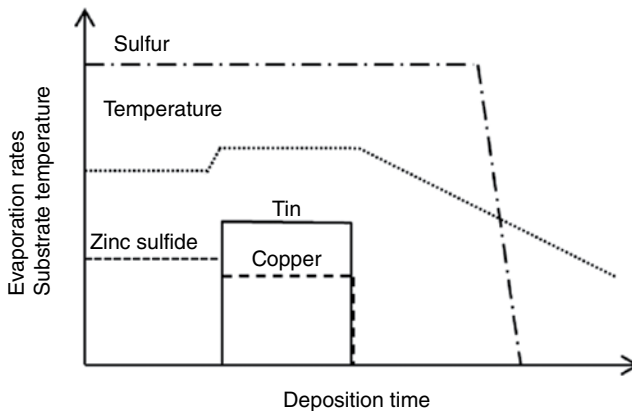
gradients in the film or the evolution of material phases to be influenced during growth, which can be used for band-gap or defect engineering. Multi-stage evaporation may also allow the application of process control by endpoint detection or by the detection of specific points of distinguished composition during film growth, for example when stoichiometry is reached. This may be achieved by monitoring the substrate temperature or heater power, reflectometry or laser light scattering [33]. The latter technique uses the fact that film morphology may change at particular points during multi-stage growth, for example when a secondary phase segregates on the surface [34].

Considering these advantages multi-stage coevaporation has also been explored for CZTS. Different layer sequences can be envisioned for a CZTS multi-stage process. Because the crystal lattices of  $\text{Cu}_2\text{SnS}_3$ , ZnS, and CZTS are all based on sphalerite structure [35] with similar lattice constants, topotactical growth may be expected to occur for evaporation sequences of  $\text{Cu}_2\text{SnS}_3$  followed by ZnS, or of ZnS followed by  $\text{Cu}_2\text{SnS}_3$ .

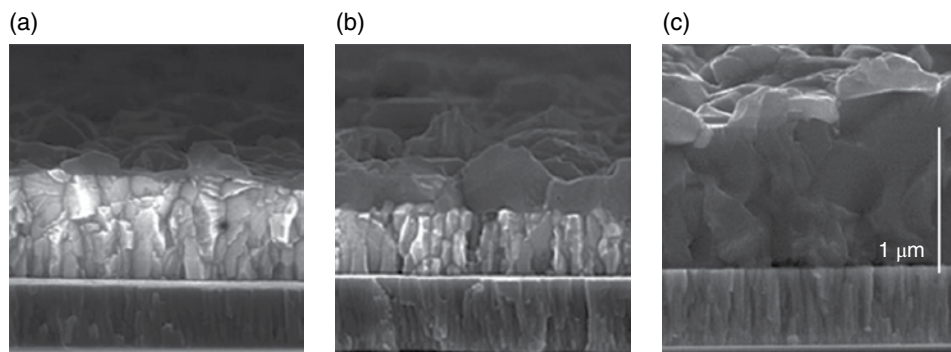
Regarding the interdiffusion and kesterite formation within coevaporated multilayer stacks of SnS/CuS/ZnS an annealing study was performed by Weber *et al.* [36], where the composition and phase formation was monitored by *in-situ* energy-dispersive X-ray diffraction and fluorescence. In this study it was concluded that although the formation of kesterite was limited by the interdiffusion of the different cations, kesterite CZTS can be formed from binary layer stacks within several minutes at a temperature of 500°C [36].

#### 10.3.2.1 $\text{Cu}_2\text{SnS}_3$ Growth on ZnS

Multi-stage coevaporation growth of CZTS using a ZnS precursor followed by the growth of  $\text{Cu}_2\text{SnS}_3$  (CTS) at higher temperature was explored by Weber *et al.* [37, 38]. ZnS was deposited on Mo-coated soda-lime glass substrates in a coevaporation system using a nominal substrate temperature of 50°C. After deposition of the ZnS film, the substrates were heated to 380°C where Cu, Sn, and S were coevaporated onto the ZnS precursor layer. In order to counteract weak Sn adsorption and Sn re-evaporation from the film, a high Sn/Cu ratio was used for the evaporation rates. After defined deposition intervals, the substrates were cooled down (Fig. 10.13).



**Figure 10.13** Rate and temperature profiles for two-stage coevaporation ZnS/Cu-Sn-S



**Figure 10.14** SEM cross-section of samples from a two-stage process in which Cu-Sn-S was evaporated at a substrate temperature of 380°C onto a ZnS precursor layer for three different time periods: (a) 2.5 min; (b) 5.5 min; and (c) 20.5 min [39]

In Figure 10.14 SEM cross-sections of CTS deposited on ZnS precursors for time periods of 2.5 min, 5.5 min, and 20.5 min are shown. Because ZnS shows a strong contrast with regard to CZTS in SEM images, it can be inferred from the images that after 2.5 min the layer mainly consists of ZnS, after 5.5 min half of the ZnS layer has been converted to CZTS, and after 20 min the whole ZnS precursor layer has been transformed into CZTS. The formation of CZTS was confirmed by XRD measurements, where after 20 min the typical kesterite diffraction patterns could be detected. Texture measurements using pole figures showed that the ZnS precursor as well as the CZTS layer on top showed a  $\langle 111 \rangle$  fiber texture. For the CZTS layer an additional  $\langle 100 \rangle$  texture was detected. This fact, together with the observation of incoherent lattice orientations between ZnS and CZTS observed by high-resolution transmission electron microscopy (TEM), was taken as an indication that the growth mechanism is not generally topotactical for this type of process sequence.

Despite the fact that this two-stage process was able to produce relatively large-grained kesterite absorber layers, the conversion efficiencies of corresponding solar cell devices did not exceed an efficiency of 1.1%, mainly limited by a very low short-circuit current density of  $6 \text{ mA cm}^{-2}$  [37]. This indicates that these devices are severely affected by surviving secondary phases from the ZnS-precursor and by those deposited during the second stage.

### 10.3.2.2 NREL Two-stage Process for CZTSe

In the development of chalcopyrite thin-film solar cells, the introduction of a two-stage coevaporation process consisting of a Cu-rich stage followed by a Cu-poor stage (later called “Boeing process”) led to a conversion efficiency of 9.4%, which was recognized as a major step forward for thin-film solar cells [40]. As it had been observed that, for chalcopyrite thin films, considerably larger grains could be obtained under Cu-rich growth conditions, this process allowed the growth of large grains while still ending up with an overall Cu-poor composition, which was found to be necessary to obtain good device efficiencies.

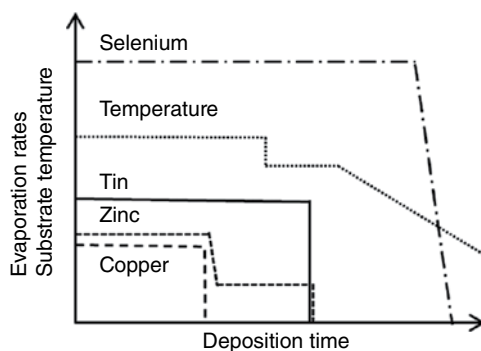
Since similar boundary conditions have been observed to apply to kesterite solar cells, the Boeing process was adapted by Repins *et al.* for the coevaporation growth of  $\text{Cu}_2\text{ZnSnSe}_4$

[41]. In contrast to the MBE growth demonstrated by Redinger *et al.*, higher Se-partial pressures (up to  $10^{-4}$  hPa) and higher growth rates (up to  $60 \text{ nm min}^{-1}$ ) were used for these studies.

Mo-coated soda-lime glass was used as a substrate and a NaF precursor layer was deposited onto the molybdenum to increase the Na supply to the absorber layer during growth. Cu, Sn, Zn, and Se were used in separate open-boat evaporation sources with the rates controlled by EIES as described in Section 10.2. Note that this type of equipment allows for rapid changes in the deposition rates, which cannot be easily achieved using larger effusion cells.

The evaporation profile used is depicted in Figure 10.15. In the first stage, Cu, Zn, Sn, and Se are evaporated, leading to a slightly copper-rich composition of the film, to enable the growth of large grains. In the second stage the copper source is completely turned off, while the Sn rate is kept constant and the Zn rate is lowered. The substrate temperature was found to increase markedly when the Cu-Se phases present during the first stage are consumed in this second stage, thus indicating the time when the material becomes stoichiometric. As suggested by the authors this pronounced increase in substrate temperature may be used as an end-point detection [41], as utilized by many groups in the coevaporation of chalcopyrites. In the NREL process the substrate temperature was held below  $500^\circ\text{C}$  in order to avoid Sn loss, which is known to occur at higher temperatures. When the desired copper deficiency was reached, the sample was cooled down to about  $450^\circ\text{C}$  under continued evaporation of Sn and Zn and held at this temperature with the intention of removing possible Sn vacancies. Further cool down was performed with finite Se, Sn, and Zn rates, which were adjusted to compensate possible loss of Se and Sn without depositing further material. At a temperature of  $300^\circ\text{C}$  the selenium vapor flux was turned off and the sample was cooled down to room temperature [41].

The composition of typical absorber films obtained from this process was  $[\text{Cu}]/[\text{Zn}] + [\text{Sn}] = 0.86$  and  $[\text{Zn}]/[\text{Sn}] = 1.15$  as measured by XRF. Best small area devices fabricated using these coevaporated absorbers in the standard device configuration Mo/CZTSe/CdS/ZnO/MgF<sub>2</sub> have yielded an efficiency of 9.15% with an open-circuit voltage  $V_{\text{oc}} = 0.377 \text{ V}$ , a short-circuit density of  $J_{\text{sc}} = 37.4 \text{ mA cm}^{-2}$ , and a fill factor of  $\text{FF} = 64.9\%$ . Further analysis of *IV* characteristics gave a diode quality factor of  $A = 1.8$ , and a low series resistance of  $R_s = 0.2 \text{ } \Omega \text{ cm}^2$ . Interestingly, no cross-over and no obvious bias-dependent



**Figure 10.15** Rate and temperature profiles for Cu-rich/Cu-poor two-stage coevaporation of CZTSe

current collection were observed for these devices. The fact that the series resistance in these devices is very low, indicates that the back contact resulting from this type of coevaporation process is much more ideal than back contacts obtained from most of the two-step processes based on annealing and selenization of precursor layers. Assuming a band gap of 1 eV, more than 80% of the total possible current is collected, whereas the open-circuit voltage reaches only half of the theoretically attainable value. Time-resolved photoluminescence measurements on this material yielded minority carrier lifetimes of about 2 ns [41], which is very small compared to lifetimes of the order 250 ns observed for high-quality chalcopyrite materials [42]. This is consistent with the low value for the open-circuit voltage and shows that minority carrier recombination is still a major issue for this material.

The NREL group also investigated a Zn-rich growth path in the coevaporation of  $\text{Cu}_2\text{ZnSnSe}_4$  [43]. For this type of process, Cu, Sn, and Zn was deposited in the first stage at a substrate temperature of 500°C with a strong excess of Zn. In the second stage only copper and tin were evaporated to convert the film into a Cu-poor composition with  $\text{Cu}/(\text{Zn} + \text{Sn}) = 0.85$  and  $\text{Zn}/\text{Sn} = 1.25$ . Large-grained growth could also be obtained using this deposition process based on a Zn-rich first stage, instead of a Cu-rich first stage as described above. The device efficiencies obtained for this growth path were nearly identical to the devices obtained from Cu-rich growth, with about 9.1% efficiency obtained for both pathways. The authors explain this phenomenon with the presence of  $\text{Cu}_x\text{Se}_y$  phases from the beginning of growth, regardless of whether the growth conditions are copper-rich or zinc-rich, because of the high volatility of  $\text{SnSe}_x$  expected for the growth rates (on average  $10 \text{ Å s}^{-1}$ ) and high selenium partial pressure (up to  $10^{-4} \text{ hPa}$ ) used in their experiment.

## Acknowledgements

The authors gratefully acknowledge financial support from the EU FP-7 KESTCELLS Project (Nr. 316488), as well as from the Helmholtz-Association Initiative and Networking Fund (HNSEI Project).

## References

- [1] Jackson, P., Hariskos, D., Lotter, E., Paetel, S., Wuerz, R., Menner, R., Wischmann, W. & Powalla, M. (2011) New world record efficiency for  $\text{Cu}(\text{In,Ga})\text{Se}_2$  thin-film solar cells beyond 20%. *Progress in Photovoltaics: Research and Applications*, **19**, 894–897.
- [2] Ohring, M. (2002) *Material Science of Thin Films*. Academic Press.
- [3] Klimova, A.M., Ananichev, V.A., Arif, M. & Blinov, L.N. (2005) Investigation of the saturated vapor pressure of zinc, selenium, and zinc selenide. *Glass Physics and Chemistry*, **31**, 760.
- [4] Tukhlibaev O. & Alimov, U. Zh. (2000) Laser photoionization spectroscopy of the zinc atom and the study of zinc sulfide evaporation. *Optics and Spectroscopy*, **88**, 506–509.
- [5] Piacente, V., Foglia, S. & Scardala, P. (1991) Sublimation Study of  $\text{SnS}_2$ ,  $\text{Sn}_2\text{S}_3$ ,  $\text{SnS}$ . *Journal of Alloys and Compounds*, **177**, 17–30.
- [6] Peng, D.-Y. & Zhao, J. (2001) Representation of the vapour pressure of sulfur. *Journal of Chemical Thermodynamics*, **33**, 1121–1131.
- [7] Hirayama, C., Ichikawa, Y. & DeRoo, A. M. (1963) Vapor pressures of tin selenide and tin telluride. *Journal of Physical Chemistry*, **67**, 1039–1042.

- [8] Geiger, F., Busse, C.A. & Loehrke, R.I. (1987) The vapor pressure of indium, silver, gallium, copper, tin, and gold between 0.1 and 3.0 bar. *International Journal of Thermophysics*, **8**, 425–436.
- [9] Knudsen, M. (1909) Die Gesetze der Molekularströmung und der inneren Reibungsströmung der Gase durch Röhren. *Annalen der Physik*, **333**, 75–130; see also Die Molekularströmung der Gase durch Öffnungen und die Effusion. *Annalen der Physik*, **333**, 999–1016.
- [10] Pulker, H.K. (1984) *Coatings on Glass*. Elsevier, Amsterdam.
- [11] Shafarman, W. & Zhu, J. (2000) Effect of substrate temperature and deposition profile on evaporated Cu(In,Ga)Se<sub>2</sub> films and devices. *Thin Solid Films*, **361–362**, 473–477.
- [12] Hanna, G., Jasenek, A., Rau, U. & Schock, H.W. (2001) Influence of the Ga-content on the bulk defect densities of Cu(In,Ga)Se<sub>2</sub>. *Thin Solid Films*, **71–73**, 387.
- [13] Friedlmeier, T.M., Wieser, N., Walter, T., Ditttrich, H. & Schock, H.W. (1997) Heterojunctions based on Cu<sub>2</sub>ZnSnS<sub>4</sub> and Cu<sub>2</sub>ZnSnSe<sub>4</sub> thin films. *Proceedings of the 14th European Photovoltaic Specialists Conference*, Barcelona, 1242–1245.
- [14] Tanaka, T., Nakamura, N., Asahi, T., Tsumori, T., Agui, A., Mizumaki, M. and Osaka, T. (2006) Fabrication of Cu<sub>2</sub>ZnSnS<sub>4</sub> thin films by co-evaporation. *Physica Status Solidi (C)*, **3**, 2844–2847.
- [15] Park, D., Nam, D., Jung, S., An, S., Gwak, J., Yoon, K., Yun, J.H. & Cheong, H. (2011) Optical characterization of CZTSe grown by thermal coevaporation. *Thin Solid Films*, **519**, 7386–7389.
- [16] Oishi, K., Saito, G., Ebina, K., Nagahashi, M., Jimbo, K., Maw, W.S., Katagiri, H., Yamzaki, M., Araki, H. & Takeuchi, A. (2008) Growth of CZTS thin films on Si(100) substrates by multi-source evaporation. *Thin Solid Films*, **517**, 1449–1452.
- [17] Redinger, A., Berg, D.M., Dale, P.J., Djemour, R., Gutay, L., Eisenbarth, T., Valle, N. and Siebentritt, S. (2011) Route toward high-efficiency single-phase CZTSSe thin film solar cells: model experiments and literature review. *IEEE Journal of Photovoltaics*, **1**, 200.
- [18] Schubert, B.A., Marsen, B., Cinque, S., Unold, T., Klenk, R., Schorr, S. & Schock, H.W. (2011) CZTS thin film solar cells by fast coevaporation. *Progress in Photovoltaics: Research and Applications*, **19**, 93.
- [19] Redinger, A. & Siebentritt, S. (2010) Coevaporation of Cu<sub>2</sub>ZnSnSe<sub>4</sub> thin films. *Applied Physics Letters*, **97**, 092111.
- [20] Caballero, R., Kaufmann, C.A., Efimova, V., Rissom, T., Hoffmann, V. & Schock, H.W. (2013) Investigation of Cu(In,Ga)Se<sub>2</sub> thin-film formation during the multi-stage co-evaporation process. *Progress in Photovoltaics: Research & Application*, **21**, 30–46.
- [21] Repins, I., Vora, N., Beall, C., Wei, S.-H., Yan, Y., Romero, M., Teeter, G., Du, H., To, B., Young, M. & Noufi, R. (2011) Kesterites and chalcopyrites: a comparison of close cousins. *Materials Research Society Symposium Proceedings*, **1324**, doi: 10.1557/opl.2011.844.
- [22] Scheer, R. & Lewerenz, H.J. (1994) Photoemission study of evaporated CuInS<sub>2</sub> thin film. *Journal of Vacuum Science and Technology*, **A12**, 56.
- [23] Katagiri, H., Jimbo, K., Tahara, M., Araki, H. & Oishi, K. (2009) The influence of the composition ratio on CZTS-based thin film solar cells. *Materials Research Society Symposium Proceedings*, **1165**, doi: 10.1557/PROC-1165-M04-01.
- [24] Wang, K., Gunawan, O., Todorov, T., Shin, B., Chey, S. J., Bojarczuk, N. A., Mitzi, D. & Guha, S. (2010) Thermally evaporated Cu<sub>2</sub>ZnSnS<sub>4</sub> solar cells. *Applied Physics Letters*, **97**, 143508.
- [25] Unold, T. & Schock, H.W. (2011) Nonconventional (non-silicon-based) photovoltaic materials. *Annual Review of Material Science*, **41**, 297–321.
- [26] Just, J., Lützenkirchen-Hecht, D., Frahm, R., Schorr, S. & Unold, T. (2011) Determination of secondary phases in kesterite Cu<sub>2</sub>ZnSnS<sub>4</sub> thin films by x-ray absorption near edge structure analysis. *Applied Physics Letters*, **99**, 262105.
- [27] Scragg, J.J., Wätjen, J.T., Edoff, M., Ericson, T., Kubart, T. & Platzter-Björkman, C. (2012) A detrimental reaction at the molybdenum back contact in Cu<sub>2</sub>ZnSn(S,Se)<sub>4</sub> thin-film solar cells. *Journal of American Chemical Society*, **134**(47), 19330–19333.
- [28] Bär, M., Schubert, B.-A., Marsen, B., Krause, S., Pookpanratana, S., Unold, T., Weinhardt, L., Heske, C. & Schock, H.W. (2011) Impact of KCN etching on the chemical and electronic surface structure of Cu<sub>2</sub>ZnSnS<sub>4</sub> thin-film solar cell absorbers. *Applied Physics Letters*, **99**, 152111.

- [29] Bär, M., Schubert, B.-A., Marsen, B., Wilks, R.G., Pookpanratana, S., Blum, M., Krause, S., Unold, T., Yang, W., Weinhardt, L., Heske, C. & Schock, H.-W. (2011) Cliff-like conduction band offset and KCN-induced recombination barrier enhancement at the CdS/Cu<sub>2</sub>ZnSnS<sub>4</sub> thin-film solar cell heterojunction. *Applied Physics Letters*, **99**, 222105.
- [30] Scragg, J.J., Ericson, T., Kubart, T., Edoff, M. & Platzer-Björkmann, C. (2011) Chemical insights into the instability of Cu<sub>2</sub>ZnSnS<sub>4</sub> films during annealing. *Chemistry of Materials*, **23**, 4625–4633.
- [31] Weber, A., Mainz, R. & Schock, H.W. (2010) On the Sn loss from thin films of the material system Cu-Zn-Sn-S in high vacuum. *Journal of Applied Physics*, **107**, 013516.
- [32] Wang, K., Gunawan, O., Todorov, T., Shin, B., Chey, S.J., Bojarczuk, N.A., Mitzi, D. & Guha, S. (2010) Thermally evaporated Cu<sub>2</sub>ZnSnS<sub>4</sub> solar cells. *Applied Physics Letters*, **97**, 143508.
- [33] Sakurai, K., Hunger, R., Scheer, R., Kaufmann, C.A., Yamada, A., Baba, T., Kimura, Y., Matsubara, K., Fons, P., Nakanishi, H. & Niki, S. (2004) In situ diagnostic methods for thin-film fabrication: utilization of heat radiation and light scattering. *Progress in Photovoltaics: Research and Applications*, **12**, 219–234.
- [34] Scheer R., Neisser, A., Sakurai, K., Fons, P. & Niki, S. (2003) CuIn<sub>1-x</sub>Ga<sub>x</sub>Se<sub>2</sub> growth studies by in situ spectroscopic light scattering. *Applied Physics Letters*, **82**, 2091.
- [35] Hergert, F. & Hock, R. (2007) Predicted formation reactions for the solid-state syntheses of the semiconductor materials Cu<sub>2</sub>SnX<sub>3</sub> and Cu<sub>2</sub>ZnSnX<sub>4</sub> (X=S, Se) starting from binary chalcogenides. *Thin Solid Films*, **515**, 5953–5956.
- [36] Weber, A., Mainz, R., Unold, T., Schorr, S. & Schock H.W. (2009) In-situ XRD on formation reactions of Cu<sub>2</sub>ZnSnS<sub>4</sub> thin films. *Physica Status Solidi (C)*, **6**, 1245–1248.
- [37] Weber, A., Krauth, H., Perl, S., Schubert, B., Kötschau, I., Schorr, S. & Schock, H.W. (2009) Multi-stage evaporation of Cu<sub>2</sub>ZnSnS<sub>4</sub> thin films. *Thin Solid Films*, **517**, 2524–2526.
- [38] Weber, A., Schmidt, S., Abou-Ras, D., Schubert-Bischoff, P., Denks, I., Mainz, R. & Schock, H.W. (2009) Texture inheritance in thin-film growth of Cu<sub>2</sub>ZnSnS<sub>4</sub>. *Applied Physics Letters*, **95**, 041904.
- [39] A. Weber (2009) Wachstum von Dünnschichten des Materialsystems Cu-Zn-Sn-S. PhD thesis, University of Erlangen.
- [40] Mickelsen, R.A. & Chen, W.S. (1981) Development of a 9.4% efficient thin-film CuInSe<sub>2</sub>/CdS solar cell. *Proceedings of the 15th IEEE Photovoltaic Specialists Conference*, New York, 800–804.
- [41] Repins, I., Beall, C., Vora, N., DeHart, C., Kuciauskas, D., Dipppo, P., To, B., Mann, J., Hsu, W.C., Goodrich, A. & Noufi, R. (2012) Co-evaporated Cu<sub>2</sub>ZnSnSe<sub>4</sub> films and devices. *Solar Energy Materials and Solar Cells*, **101**, 154–159.
- [42] Metzger, W.K., Repins, I. L. & Contreras, M.A. (2008) Long lifetimes in high-efficiency Cu(In,Ga)Se<sub>2</sub> solar cells. *Applied Physics Letters*, **93**, 022110.
- [43] Hsu, W.-C., Repins, I., Beall, C., DeHart, C., To, B., Yang, W., Yang, Y. & Noufi, R. (2014) Growth mechanisms of coevaporated kesterite: a comparison of Cu-rich and Zn-rich composition paths. *Progress in Photovoltaics: Research and Applications*, **22**, 35–43.



# 11

## Synthesis of CZTSSe Thin Films from Nanocrystal Inks

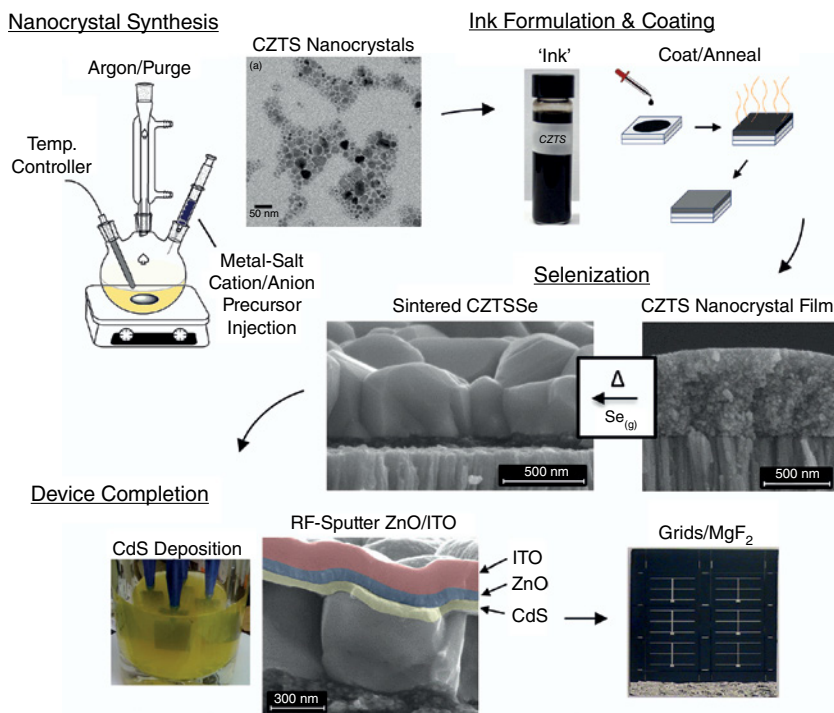
*Charles J. Hages and Rakesh Agrawal*

*Purdue University, School of Chemical Engineering, Forney Hall of Chemical Engineering,  
480 Stadium Mall Dr., West Lafayette, IN 47907-2100, USA*

### 11.1 Introduction

Progress in the field of solution-processed  $\text{Cu}_2\text{ZnSn}(\text{S}_x\text{Se}_{1-x})_4$  (CZTSSe) solar cells has shown the potential of this technique as a scalable method for the inexpensive and high-throughput manufacturing of efficient solar cells composed of Earth-abundant elements. In fact, solution-processed techniques have shown the highest power-conversion efficiencies (pce) to date for this material system, with record efficiencies reaching 12.6% compared to 9.7% for vacuum-based processes [1, 2]. The benefits of these solution-processed solar cells can potentially be realized through many aspects including relatively low-energy, non-vacuum processing for the CZTSSe absorber layer, as well as low-cost high-throughput solution deposition of this layer via roll-to-roll manufacturing. Additionally, the challenges associated with absorber stability and elemental volatility during high-temperature processing have made solution-based methods particularly attractive for CZTSSe fabrication.

Solution-based processing for CZTSSe solar cells has been demonstrated using various techniques including spray pyrolysis [3–5], sol-gel sulfurization [6, 7], electrodeposition [8–10], soluble molecular/metal salt precursors [11, 12], hydrazine-based slurry coating [13, 14], as well as nanocrystal-ink-based approaches [15–21]; the fabrication of solar cells based on coated films of nanocrystal inks is the focus of this chapter. To date, among the non-hydrazine solution-based methods, the most successful fabrication of CZTSSe solar



**Figure 11.1** Process flow diagram illustrating the nanocrystal-ink-based approach for the formation of CZTSSe solar cells: nanocrystal synthesis and ink formation; nanocrystal film coating and annealing; selenization of nanocrystals for dense absorber formation; and CdS/ZnO/ITO/Grid/MgF<sub>2</sub> deposition. ITO/ZnO/CdS layers are digitally enhanced for clarification. TEM image reproduced with permission from [22]. Copyright © 2014, John Wiley and Sons Ltd

cells has been through the selenization of films derived from nanocrystal inks, with current progress achieving greater than 9% total-area power-conversion efficiencies (greater than 9.8% active-area) for CZTSSe-based solar cells [22, 23].

This nanocrystal-ink-based approach, illustrated in Figure 11.1, begins with the synthesis of  $\text{Cu}_2\text{ZnSnS}_4$  (CZTS) nanocrystals and the formulation of printable nanocrystal inks. These inks are deposited onto a desired substrate to form nanocrystal films which are subsequently sintered into dense CZTSSe absorbers through reactive sintering at an elevated temperature under selenium vapor. This approach has attractive benefits over other solution-based techniques, including the ability for absorber material synthesis with relatively non-toxic chemicals as well as nanoscale homogeneity and control of absorber film composition.

The initial motivation for the selenization of nanocrystal-ink-based CZTS films followed the success of similar techniques in the fabrication of  $\text{Cu}(\text{In}_y\text{Ga}_{1-y})(\text{S}_x\text{Se}_{1-x})_2$  (CIGSSe) solar cells from selenized films of  $\text{Cu}(\text{In}_y\text{Ga}_{1-y})\text{S}_2$  (CIGS) nanocrystal inks [24, 25]. Along with the initial success and promise, the application of this nanocrystal ink and selenization approach to the CZTSSe material system has brought attention to some unique challenges due to the nature of this quaternary material structure. The key challenges for progress

with this technology involve understanding and controlling the stability of CZTSSe formation in competition with the formation of secondary phases in both the nanocrystals and sintered films, as well as understanding and controlling compositional and structural homogeneity when transitioning from nanocrystals to sintered films. Despite these challenges, significant progress has been made towards controlling the quality of CZTSSe kesterite absorber layers due to increasing research in material and optoelectrical characterization of this system.

This chapter focuses on current progress and challenges in CZTS nanocrystal synthesis as well as the selenization of the nanocrystal films to fabricate CZTSSe solar cells. The first section will involve an overview of the solution-based nanocrystal synthesis technique, with reference to applications and challenges associated with CZTS growth. This will be followed by a brief overview of characterization techniques specific to CZTS nanocrystals. Finally, an overview of the selenization process will be given with analysis of the key factors found to impact sintered film formation.

## 11.2 Nanocrystal Synthesis

The synthesis of CZTS nanocrystals was first demonstrated independently by three research groups in 2009 [15, 19, 20]. This followed previous work in the colloidal synthesis of inorganic nanocrystals such as Cd(S,Se,Te), Pb(S,Se), In(P,As), Ga(P,As), GaInP<sub>2</sub>, Zn(S,Se), MgS, Cu<sub>2</sub>S, and Cu(In,Ga)(S,Se)<sub>2</sub> [24, 26–37]. These well-established and widely adopted colloidal synthesis techniques have since been applied numerous times in the field of CZTSSe research, and the application for these nanocrystals has been studied for both quantum dot solar cells as well as the more conventional thin-film solar cells. While the fabrication of thin-film CZTSSe solar cells from CZTS nanocrystal inks relies on sintering of the nanocrystal films through techniques such as selenization, it has also been found that solution-processed thin-film CZTSSe absorbers can be fabricated through the selenization of other nanocrystal systems such as binary/ternary nanocrystal precursors [18]. Additionally, chalcogenide nanocrystals have been used in the fabrication of CZTSSe absorbers from other techniques such as annealed nanocrystal-molecular metal chalcogenide (NC-MCC) films [38] as well as annealed hydrazine-based mixed molecular precursor-nanocrystal films [13]. Applications of CZTS nanocrystals, as well as the binary and ternary nanocrystal derivatives of this quaternary system, stress the importance in understanding the synthesis techniques for chalcogenide nanocrystals.

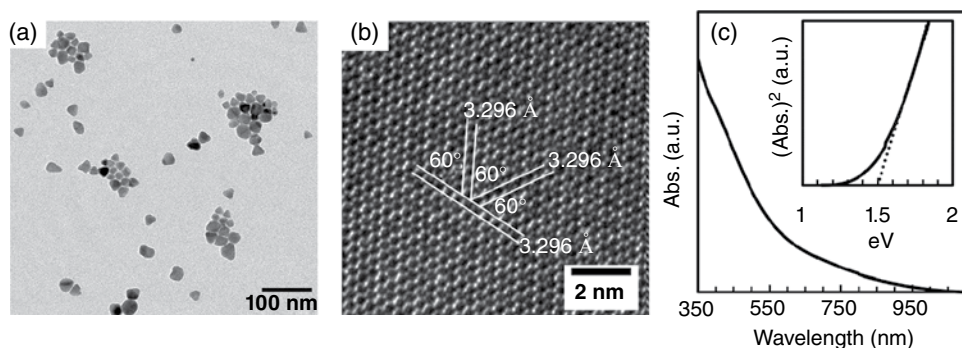
Techniques developed for the synthesis of a wide variety of colloidal nanocrystals include aqueous and non-aqueous coprecipitation, hydrothermal/solvothermal processing, sol-gel processing, and microemulsions/micelle template directed growth [39–41]. However, one of the most successful routes for the synthesis of CZTS solar cells has been achieved using nanocrystals synthesized in a method of non-aqueous coprecipitation. This synthesis technique is based off the hot-injection synthesis method used for binary nanocrystal syntheses and utilizes surfactant controlled growth of colloidal nanocrystals in a hot organic solvent [39, 42]. Work in this field has followed the success of the synthesis of nanocrystals of CuInS<sub>2</sub> (CIS) and CIGS, in which the nanocrystal synthesis reaction is very similar [24, 37].

The hot-injection synthesis technique follows upon the work of La Mer and Dinegar who have shown the importance of discrete nucleation followed by growth for the synthesis of monodisperse nanocrystals [43]. This method was pioneered by Bawendi *et al.* for the synthesis of monodisperse Cd(S,Se,Te) nanocrystals, and by Alivisatos *et al.* for the synthesis of monodisperse CdSe and InAs nanocrystals [30, 31, 44]. Three variations of this technique were initially demonstrated for quaternary CZTS synthesis [15, 19, 20], which involve variations in the precursor injection procedure, reaction temperature, and choice of solvent as described in the following sections.

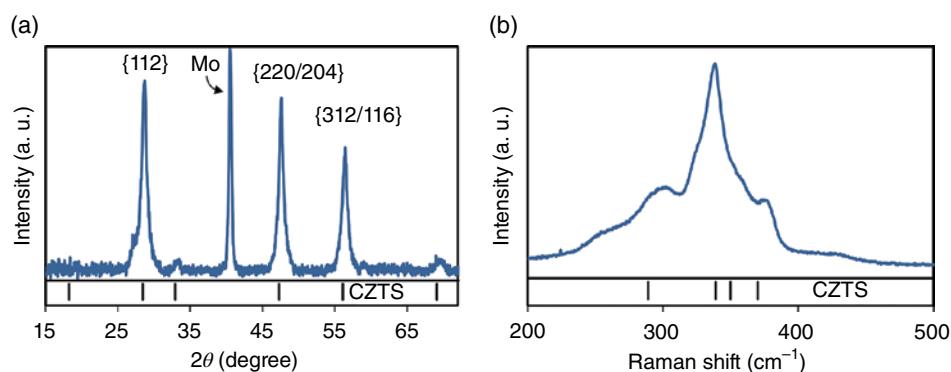
### 11.2.1 Kesterite/Stannite CZTS Nanocrystals

A typical reaction for the synthesis of CZTS nanocrystals as described by Guo *et al.* [15] initially consists of anion/cation precursors and organic surfactants/solvents. In this synthesis, oleylamine (OLA) performs the dual function of both the surfactant and solvent, and organometallic precursor salts as acetylacetonates supply the needed cations of Cu, Zn, and Sn. Typically, weighed quantities of the cation precursors are first preheated in OLA to the desired reaction temperature of 225°C. The reaction is initiated through the injection of the dissolved sulfur anion precursor in OLA into the flask of the heated solvent and cation precursors. Following injection, nucleation immediately occurs as anion and cation precursors react to form monomers that supersaturate the solution. The elevated reaction temperature of 225°C is maintained following the nucleation step to allow for subsequent growth to occur as additional monomers in solution incorporate into the nucleated nanocrystals. After the desired growth has occurred (0.5 hour), the reaction is cooled and the OLA capped nanocrystals are washed in solvent/antisolvent solutions such as hexane/isopropyl alcohol to remove any un-reacted precursors and excess organic solvent. The washed nanocrystals from the reaction are then dispersed in the desired solvent for coating which forms the nanocrystal ink. The described synthesis technique can be used for the synthesis of a wide range of crystal stoichiometries in CZTS, as verified through energy-dispersive X-ray spectroscopy (EDX), achieved through manipulation of the initial cation precursor ratios.

The described reaction procedure yields CZTS nanocrystals in the range 15–25 nm as shown in Figure 11.2a. Observation of high-resolution transmission electron microscopy (HR-TEM), Figure 11.2b, illustrates crystals with interplanar spacings which correspond to the {112} and {220} planes in the zinc-blende-derived kesterite/stannite structure of CZTS. Additionally, UV-vis absorption (Fig. 11.2c) reveals an estimated band gap of 1.5 eV for the CZTS nanocrystals, which is in good agreement with the reported literature values for this system [45]. Typical X-ray diffraction (XRD) for synthesized kesterite/stannite CZTS nanocrystals along with simulated tetragonal (I 4) CZTS (JCPDF #26-575) can be seen in Figure 11.3a. In addition to the identified tetragonal peaks associated with CZTS, a shoulder on the left side of the {112} reflection suggests the presence of a stacking fault caused by Cu/Sn intermixing [22]. Typical Raman spectra for the synthesized CZTS nanocrystals (Fig. 11.3b) reveal a main peak at 338 cm<sup>-1</sup> which corresponds to the main A/A<sub>1</sub> mode for CZTS [46]. While these characterization techniques support the formation of CZTS nanocrystals, a definitive structural and phase purity identification of CZTS nanoparticles using TEM, XRD, and Raman spectroscopy can be challenging, as discussed in the nanoparticle characterization section (Section 11.3).



**Figure 11.2** (a) TEM image; (b) high-resolution TEM image (aligned to the  $\langle 221 \rangle$  zone axis); and (c) UV-vis absorption spectrum for the as-synthesized CZTS nanocrystals. (a) Reprinted and (c) Adapted with permission from [15]. Copyright © 2009, American Chemical Society



**Figure 11.3** Typical (a) XRD and (b) Raman spectra for as-synthesized CZTS nanocrystals

A similar technique was also demonstrated by Riha *et al.* [20] for the synthesis of CZTS nanocrystals. In this variation, cation precursors are first dissolved in OLA at 125–150°C. Similarly, elemental sulfur is dissolved separately in OLA. This synthesis differs from Guo *et al.* in that both the anion and cation precursors are simultaneously injected into a heated solution (300°C) of trioctylphosphine oxide (TOPO). This variation of the injection procedure eliminates the preheating of the cation precursors in OLA to the reaction temperature prior to the reaction; the cation precursors are maintained below 150°C prior to injection into the 300°C TOPO. This step minimizes the formation of reduced metal nanoparticles, particularly Cu [47], that can occur in OLA at temperatures above 160°C. Furthermore, TOPO has been introduced as an additional organic surfactant. This synthesis technique has been shown to deliver fairly monodisperse CZTS nanocrystals with an average particle size of  $12.8 \pm 1.8$  nm following fractionation, verified through TEM analysis. When the presence of TOPO is undesirable, this co-injection procedure for the anion and cation precursors can similarly be carried out in preheated OLA without the need for TOPO [22].

A third variation of this synthesis technique for CZTS nanocrystals was reported by Steinhagen *et al.* [19] utilizing high-temperature arrested precipitation instead of hot-injection.

In this method, cation precursors are initially charged with the elemental sulfur in OLA at room temperature. In contrast to the previously described synthesis mechanisms, the cation and anion precursors are heated together in OLA up to the reaction temperature (280°C). In this technique none of the precursors are hot-injected; the reaction flask is kept at 280°C for 1 hour and then cooled to room temperature. The reported size of the nanocrystals is in the range  $10.6 \pm 2.9$  nm for the fraction collected, verified through TEM.

Following the initial work in CZTS nanocrystal synthesis described above, these techniques were subsequently applied to the synthesis of  $\text{Cu}_2\text{ZnSnSe}_4$  (CZTSe) and CZTSSe tunable-band-gap nanocrystals through variations in the preparation of the chalcogenide anion precursor and the solvent/surfactant choice. A comparison of selected reaction schemes for kesterite/stannite CZTS, CZTSe, and CZTSSe nanocrystal syntheses is provided in Table 11.1.

**Table 11.1** Comparison of reaction conditions for select CZTS, CZTSe, CZTGeS, and CZTSSe nanocrystal synthesis

Nanocrystal	Cation precursors	Anion precursor	Solvent/surfactant	Injection/reaction temperature (°C)	Injection procedure	Ref.
CZTS	(Cu, Zn, Sn) acac*	S	OLA	225	Sulfur-OLA injection into cation-OLA	[15]
CZTS	Copper (II) acac*, zinc acetate, tin (IV) acetate	S	OLA, TOPO	300	Sulfur-OLA and cation-OLA injection into TOPO	[20]
CZTS	Copper (II) acac*, zinc acetate, tin (II) dichloride dihydrate	S	OLA	280	-	[19]
CZTSe	$\text{CuCl}_2$ , $\text{ZnCl}_2$ , $\text{SnCl}_4$	TOPSe*	OLA, TOPO, HDA*, octadecene	295	TOPSe* injection into Cation-HDA*-octadecene	[48]
CZTSSe	Copper (II) acac*, zinc acetate, tin (IV) acetate	S, Se	OLA, TOPO	325/285	S/Se-OLA- $\text{NaBH}_4$ and cation-OLA injection into TOPO	[49]
CZTSSe	(Cu, Zn, Sn) sterates	Thiourea, Se	OLA	270	Cation-OLA injection into thiourea/Se	[50]
CZTS	$\text{Cu}(\text{dedc}^*)_2$ , $\text{Zn}(\text{dedc}^*)_2$ , $\text{Zn}(\text{dedc}^*)_2$	-	OLA, octadecene, oleic acid	150–175	OLA into cation-octadecene-oleic acid	[51]
CZTGeS	(Cu, Zn, Sn) acac*, $\text{GeCl}_4$ /Gel <sub>4</sub>	S	OLA	225	Sulfur-OLA injection into cation-OLA	[23, 52]

\*acac = acetylacetonate; TOPSe = trioctylphosphine selenide; HDA = hexadecylamine; dedc = diethyldithiocarbamate

### 11.2.2 Wurtzite CZTS Nanocrystals

The synthesis of metastable wurtzite-derived CZTS nanocrystals has also recently been demonstrated for application in CZTSSe solar cells [53–55]. The wurtzite-derived kesterite/stannite structures are higher-energy phases than the zinc-blende-derived kesterite/stannite structures, with modification of the crystallographic stacking from ABCABC for zinc-blende to ABABAB for wurtzite [56]. To achieve wurtzite CZTS synthesis, modification of the organic solvent is performed to provide the necessary kinetic control for metastable nanocrystal growth to occur; this has been demonstrated with the use of dodecanethiol (DDT) and hexadecanethiol (HDT) as the organic solvent/anion precursor [53–55]. Similarly, wurtzite CZTSe and CZTSSe nanocrystals can be synthesized with the addition of diphenyl diselenide as the selenium source [57]. Modification of the organic solvent and anion source in the reaction is suggested to promote the formation of the metastable phase through modification of the stable intermediate products formed during the reaction [55], similarly reported for controlling the structure in  $\text{CuInSe}_2$  (CISe) nanocrystals [58].

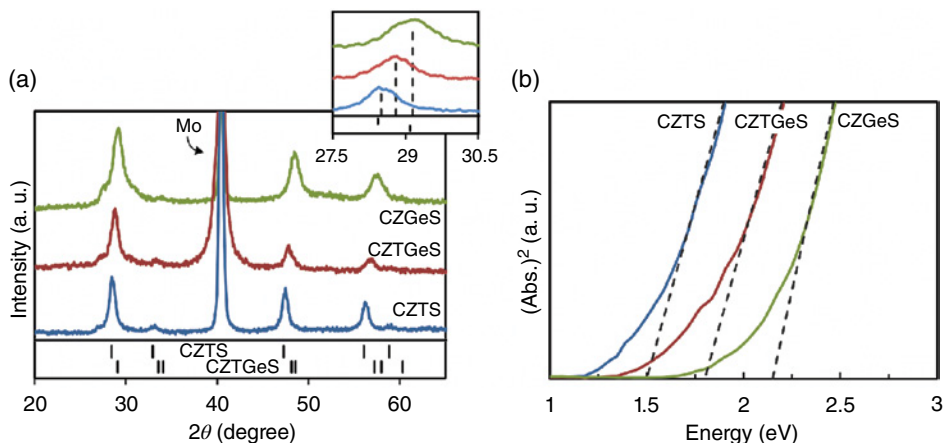
### 11.2.3 Binary/Ternary Nanocrystals

The synthesis of binary and ternary metal chalcogenide nanocrystals is also of interest in the formation of CZTSSe solar-cell absorbers. The application for these nanocrystals arises from their use in nanocrystal-molecular metal chalcogenide (NC-MCC) films [38] as well as annealed hydrazine-based mixed molecular precursor-nanocrystal films [13]. Additionally, the direct selenization of binary/ternary metal chalcogenide nanocrystals has demonstrated success in the formation of sintered CZTSSe absorbers [18].

The synthesis of  $\text{Cu}_x\text{S}$ ,  $\text{Cu}_2\text{SnS}_3$ ,  $\text{ZnS}$ , and  $\text{SnS}_x$  binary and ternary nanocrystals follows similar reaction techniques to those previously described for CZTS nanocrystal syntheses [27]. In fact, many issues associated with phase stability and phase purity in quaternary nanocrystal synthesis are alleviated in the synthesis of binary/ternary nanocrystals as these materials are often intermediate phases involved in quaternary nanocrystal growth. Additionally, understanding the reaction kinetics in binary and ternary nanocrystal synthesis is important when controlling the phase purity and growth of quaternary nanocrystals where multiple competing binary, ternary, and quaternary synthesis reactions are taking place.

### 11.2.4 $\text{Cu}_2\text{Zn}(\text{Sn}_y\text{Ge}_{1-y})\text{S}_4$ (CZTGeS)

Research in tunable-band-gap solar cells has recently shown the potential for the Ge-alloyed  $\text{Cu}_2\text{Zn}(\text{Sn}_y\text{Ge}_{1-y})(\text{S}_x\text{Se}_{1-x})_4$  (CZTGeSSe) material system as an alternative to CZTSSe thin-film Earth-abundant solar cells [17, 23, 52, 59]. Similar to In/Ga substitution in high-efficiency CIGSSe solar cells, Ge/Sn substitution in CZTGeSSe can also achieve tunable-band-gap absorbers without the need for control of the anion [S]/[Se] ratio; theoretical band gaps for this material range from 1.0 eV to 1.5 eV for the S-free  $\text{Cu}_2\text{Zn}(\text{Sn}_y\text{Ge}_{1-y})\text{Se}_4$  (CZTGeSe) absorber, similar to the band-gap range achievable for CZTSSe through [S]/[Se] control [23, 60]. Progress in this research field has demonstrated improved performance of Ge-alloyed CZTGeSSe solar cells over similarly processed CZTSSe solar cells through enhanced electrical properties of the device, with total-area power-conversion efficiencies reported as 9.4% [23].



**Figure 11.4** (a) XRD and (b) UV-vis spectra for various CZTGeS nanocrystals synthesized with varying degrees of Ge-incorporation. For CZTGeS curves,  $[Ge]/([Ge] + [Sn])$  is 0.50 [52]. Adapted with permission from [52]. Copyright © 2011, American Chemical Society

The fabrication of CZTGeS solar cells was first demonstrated by Ford *et al.* using the nanocrystal-ink-based approach of selenizing CZTGeS nanocrystal films [52]. The synthesis of CZTGeS nanocrystals follows similar procedures to those described by Guo *et al.* for the synthesis of CZTS with  $GeI_4$  or  $GeCl_4$  used as the Ge-precursor; the relative quantity of the Ge- and Sn-precursors in the nanocrystal reaction is used to control the ratio of  $[Ge]/([Ge] + [Sn])$  in the resulting nanocrystals. In addition to EDX, XRD can be used to characterize the incorporation of Ge into the CZTGeS crystal lattice, seen as a shift in the diffraction peaks upon Ge incorporation as the lattice constants in the crystal decrease [52], shown in Figure 11.4a. Additionally, the shift in absorption edge with increasing Ge content in the nanocrystals illustrates the increasing band gap of CZTGeS with increasing Ge-content in the nanocrystal [52] (Fig. 11.4b).

### 11.2.5 Choice of Reaction Conditions

The appropriate choice of reaction conditions is essential in the growth of CZTS nanocrystals due to their effect on phase purity, defect formation, and homogeneity in the growing crystals. The control of these factors is important due to the unique challenges that they can impose on the material and electrical properties of the resulting CZTS solar absorber films. However, while many techniques involving the choice of reaction conditions have been developed for control of uniform nanocrystal syntheses, this necessity becomes less of an issue when nanocrystal films are subsequently exposed to selenization conditions. Generally, variations that arise in homogeneity and uniformity during nanocrystal synthesis are resolved during the subsequent selenization process where diffusion and rearrangement of atoms in the growing crystals takes place; in fact, the presence of particle size or compositional heterogeneities in the synthesized nanocrystals may be desirable to enhance sintering when compared to monodisperse (uniform in size/shape/composition) nanocrystals [61, 62]. Nonetheless, an understanding of the effect of synthesis reaction conditions can allow for control of the synthesized nanocrystals with favorable sintering properties.



While the exact mechanism of particle growth in CZTS is not yet fully understood, it is likely that CZTS nanocrystals are formed from the reaction of intermediate phases of binary and ternary monomers such as CuS, Cu<sub>2</sub>S, SnS, SnS<sub>2</sub>, ZnS, and Cu<sub>2</sub>SnS<sub>3</sub>, as similarly proposed for the formation of CIS nanocrystals from binary phases [58, 63, 64]. The competing nucleation and reaction of these various secondary phases all with different nucleation thresholds and reaction rates makes the nature of quaternary nanocrystal synthesis more challenging than the initial work in this field for binary nanocrystals. In light of this, control of the nanocrystal growth rate during synthesis through temperature, solvent/surfactant, and precursor choice can be used to tune the selectivity and size distribution of the resulting nanocrystals.

#### 11.2.5.1 Solvent

One of the most important parameters that controls crystal growth rate in the described hot-injection synthesis reactions is the solvent/surfactant choice during synthesis. This is because controlled growth relies on the dynamic solvation of the nanocrystals as the surfactant molecules bind/unbind with the nanocrystal surface [30, 39]. This dynamic solvation allows for slow growth rates on the nanoscale despite the long reaction times as the nanocrystal surface is only transiently available for growth. A decreased growth rate can be achieved by a reduction in the reaction temperature as the surfactant become less likely to leave the nanocrystal surface or, equivalently, dynamic solvation can be achieved at much lower temperatures by using a more weakly adherent surfactant [39]. Additionally, the surfactant molecule acts as a capping ligand which provides a steric barrier to particle agglomeration/flocculation [30, 42].

#### 11.2.5.2 Temperature

In addition to surfactant choice, the crystal growth rate during synthesis can also be tuned through control of the reaction temperature. The thermodynamic competition between the formation of various other stable phases of Cu, Zn, Sn, and S reaction products makes the reaction temperature an important parameter that can be used to minimize the formation energy of CZTS in relation to other stable secondary phases. However, this parameter can also have an influence on the crystallographic disorder in the growing crystal as well as growth mechanism during the reaction.

Generally, a relatively higher reaction temperature is desired in the described nanocrystal reaction procedures above, as elevated temperatures allow for annealing and rearrangement to occur within the growing crystals [39]. The increased mobility of atoms during nanocrystal growth at elevated temperatures can lead to crystals with minimal defects and lattice disorder; this can be especially important in CZTS synthesis as various binary and ternary monomers join together to form an ordered CZTS crystal structure. This effect was demonstrated in the synthesis of wurtzite CZTS nanocrystals as rearrangement/annealing in the growing crystal at the reaction temperature led to incorporation of initially heterogeneous segregated Cu<sub>x</sub>S phases on the CZTS crystal surface [55], also similarly reported for the synthesis of CIS nanocrystals [63, 64].

Additionally, increased crystal growth rates are generally desirable to achieve a relatively monodisperse nanocrystal synthesis; typically, an increased reaction temperature will lead to an increase in crystal growth rate [65]. While the focus of many binary

nanocrystal synthesis mechanisms is to synthesize particles with monodisperse size distributions, monodisperse nanocrystal growth for *quaternary* CZTS synthesis is important due to issues of inter-particle compositional heterogeneity, which is not a concern for binary nanocrystal growth. It has been found that CZTS growth conditions that result in a large particle size distribution can also lead to variations in particle composition between the different particle sizes [61, 66]. When this occurs, traditional methods to achieve monodisperse nanocrystals *a posteriori*, such as “size-selective precipitation” [30, 42], are no longer effective due to compositional variations between the separated particle size classes. Furthermore, these heterogeneities in particle size and composition have been found to directly affect the sintering mechanism of the nanocrystal films [61]. While the diffusion of cations during selenization of CZTS nanocrystal films at temperatures near 500°C has the tendency to modify the initial cation concentration fluctuations that may arise due to inter-particle compositional differences within the nanocrystal film, the desire to synthesize monodisperse and uniform nanocrystals stems from the need for nanoscale homogeneity to deliver precise, consistent, and eventually predictable results from the sintered films. Furthermore, achieving relatively uniform nanocrystal synthesis can allow for control of the heterogeneities present in the pre-sintered nanocrystal film, which can be beneficial to the sintering mechanism during selenization.

In general, particle size distributions can arise during nanoparticle synthesis due to inhomogeneous nucleation and low crystal growth rates [39, 44]. To narrow the resulting particle size distribution during synthesis – and subsequently reduce interparticle compositional heterogeneity – the growth mechanism can be tuned to “focus” the particle size distribution as described by Peng *et al.* [44]. This is generally achieved by increasing the crystal growth rate, demonstrated for the synthesis of monodisperse binary nanocrystals through control of the reaction temperature [30] and monomer concentration [44]. For the synthesis of CZTS nanocrystals, narrowing of the particle size distribution through an increase in reaction temperature (as well as modification of the monomer nucleation step) resulted in a narrower particle size distribution as predicted, leading to more compositionally uniform nanocrystals with controllable stoichiometries [22].

Although an elevated reaction temperature can be beneficial to nanocrystal growth in terms of *intraparticle* uniformity (within the particle) from thermal annealing and *interparticle* uniformity (between particles) from favorable crystal growth rates, elevated reaction temperatures can also pose a unique challenge in quaternary nanocrystal synthesis in terms of their thermodynamic stability when compared to other binary/ternary material systems. Under equilibrium growth conditions, where energetically favorable spherical nanocrystals are formed [39], the thermodynamic competition between the formation of various other stable secondary phases can lead to issues of phase purity following the reaction. To control this, the formation energy of CZTS should be minimized in relation to other stable secondary phases through manipulation of the reaction conditions. While CZTS has a relatively favorable formation enthalpy compared to other stable binary/ternary phases (i.e. CuS, Cu<sub>2</sub>S, SnS, SnS<sub>2</sub>, ZnS, and Cu<sub>2</sub>SnS<sub>3</sub>) [67], the formation entropy becomes increasingly important in determining the relative formation energy of CZTS at temperatures greater than 0 K, as described by the free energy of reaction:  $\Delta G = \Delta H - T\Delta S$  [68]. Due to this, the synthesis of pure-phase CZTS can be increasingly more difficult at the high temperatures desired for uniform particle growth if favorable reaction conditions are not maintained through precursor and solvent choice.

While achieving the appropriate growth rate for CZTS synthesis through solvent and temperature choice has been described in terms of phase purity and uniformity for this system, it is additionally important in the synthesis of tunable-shape nanostructures, such as for the synthesis of CZTS and CZTS<sub>Se</sub> nanorods and nanowires [69, 70]. These high-surface-energy anisotropic particles can be grown under high crystal growth rates, where the growth mechanism shifts from thermodynamically controlled to kinetically controlled [29, 39]. Alternatively, growth mechanisms such as “oriented attachment” or selective adhesion can also be exploited which similarly rely on the surface properties of the growing crystals [39, 71]. In light of these effects, the appropriate temperature and surfactant choice for nanocrystal growth must be made to achieve the desired balance in particle size, shape, and selectivity.

#### 11.2.5.3 Relative Precursor Concentrations

In addition to thermodynamic considerations of CZTS stability associated with temperature, altering the cation chemical potentials can also be used to modify the thermodynamic stability of CZTS growth. However, issues can arise when stable crystal growth conditions conflict with the stoichiometries necessary for the desired electrical performance of the material, such as for the widely adopted Cu-poor/Zn-rich conditions utilized in high-efficiency CZTS<sub>Se</sub> devices [1, 13, 16, 23, 72]. First-principle calculations by Chen *et al.* predict that the stable growth region for CZTS is enhanced under Cu-rich conditions [67]; similarly, experimental work has shown enhanced grain growth of CZTS films under Cu-rich conditions [73–76] as well as in the synthesis of Cu-rich CZTS nanocrystals. Therefore, synthesis of CZTS nanocrystals under the relatively unstable Cu-poor/Zn-rich growth conditions becomes increasingly more prone to compositional heterogeneity issues.

Due to these challenges, phase purity and compositional homogeneity can be expected to present a continuous challenge in the formation of pure-phase homogeneous quaternary materials. However, the most important aspect of the nanocrystal morphology and composition is that it should allow sintering and large grain growth during selenization of the nanocrystal films, resulting in an absorber film with optimal optoelectronic properties for solar cells.

### 11.3 Nanocrystal Characterization

Proper characterization techniques are essential to determine the structure, phase purity, uniformity, and optoelectronic properties of the synthesized nanocrystals. However, the nanoscale size of these crystals imposes difficult challenges to their characterization, often necessitating the use of a combination of methods to ensure accuracy when performing structural, optical, or compositional measurements. Here we present a brief overview of various techniques and issues associated with nanocrystal characterization.

X-ray diffraction (XRD) is a commonly used tool to determine the crystal structure of the synthesized nanocrystals. However, while quite useful, difficulties can arise with this technique due to the nanoscale domain sizes associated with these crystals. These small domain sizes lead to peak broadening in the XRD pattern of CZTS nanocrystals, and often make identification of subtle peak shifts from differences due to atomic stacking

(i.e. kesterite v. stannite) and cation substitutions increasingly difficult [22]. Additionally, identification of the presence of secondary tetragonal phases in addition to CZTS, such as  $\text{Cu}_2\text{SnS}_3$  and  $\text{ZnS}$ , is challenging from X-ray diffraction as these materials share virtually identical peak locations with CZTS (CTS: JCPDS #33-0501;  $\text{ZnS}$ : JCPDS #65-5476); this issue is further mystified by the peak broadening due to the nanoscale of the material. Furthermore, the diffraction signal is weighted by the degree of crystallinity in the sample; this can lead to issues when the synthesized nanocrystals have a heterogeneous particle size distribution, as small particles (<3 nm) can be significant in quantity yet contribute little to the signal from XRD due to their size. These issues make XRD alone inadequate for phase purity investigation.

Raman spectroscopy can also be used for the structural identification of nanocrystals. One benefit of this method is that there is no need for long-range order, so small and amorphous nanoparticles not seen in XRD can be identified through Raman spectroscopy. Additionally, the sensitivity of Raman over short ranges in the crystal lattice makes identification of defects in the lattice possible [77, 78]. Furthermore, identification of similar tetragonal structures to CZTS becomes easier with Raman spectroscopy due to distinguishable peak locations between CZTS,  $\text{Cu}_2\text{SnS}_3$ , and  $\text{ZnS}$  [79]. However, phonon confinement effects in nanoscale crystals can lead to modification of the Raman signal through peak broadening and shifting [77], leading to similar issues regarding phase purity identification as mentioned with XRD. Additionally, differences in absorption properties for secondary phases make quantitative analysis by Raman spectroscopy difficult [80]. Careful consideration of the laser energy used for the measurement should also be taken when measuring Raman, as certain materials such as  $\text{ZnS}$  can be challenging to identify without the use of *resonant* Raman spectroscopy [77, 81]. Lastly, the laser intensity should be carefully monitored when measuring the Raman signal, as nanocrystals can easily heat up during measurement causing signal distortion over time as well as destructive local annealing/sintering of the sample. While XRD and Raman are useful techniques that can be applied for non-destructive, fairly straightforward characterization of CZTS nanocrystals, more detailed structural analysis of nanocrystals can also be achieved using extended X-ray absorption fine structure (EXAFS), X-ray absorption near edge structure (XANES), and small-angle X-ray scattering (SAXS) [42, 80].

Additionally, structural characterization of nanocrystals can be explored using (high-resolution) transmission electron microscopy (TEM/HRTEM), as illustrated in Figure 11.2a and b. In addition to information regarding particle size and shape, determination of the lattice spacings and diffraction planes of the nanocrystals is possible; however, sensitivity due to defects in the crystal can occur in the electron diffraction signal. In addition to structural analysis, TEM can be used for energy-dispersive X-ray spectroscopy (STEM-EDX) and electron energy loss spectroscopy (EELS) to measure particle composition and compositional uniformity [54, 66, 82]. However, due to the time involved in each measurement these techniques can only be used to sample a small number of particles. Additionally, overlapping signals (Cu and Zn in EELS) as well as damage from the use of a high-energy electron beam (STEM-EDX) can present challenges.

In contrast to the small sample size in TEM, scanning electron microscopy energy-dispersive X-ray spectroscopy (SEM-EDX) can be used to sample bulk compositions of a large number of nanocrystals. However, care must be taken when calculating quantitative compositional values from this technique, and calibration measurements should be

conducted on appropriate samples. Further verification or calibration of bulk compositions can be accomplished using techniques such as atomic absorption spectroscopy (AAS) [73], inductively coupled plasma mass spectroscopy (ICP-MS) [83], or X-ray fluorescence (XRF) [74, 80]. Additionally, phase purity analysis of samples through thermal treatments can be carried out using differential thermal analysis (DTA), differential scanning calorimeter (DSC), and/or thermogravimetric analysis (TGA) [20].

As shown in Figure 11.2c, optical characterization of nanocrystals is often conducted using ultraviolet-visible spectroscopy (UV-vis). This technique can be used to estimate the band gap of the synthesized nanocrystals, although it is important to note that shifts in the absorption edge due to quantum confinement effects can occur in nanocrystals below a certain size [51]. When such small particles with quantum confinement are present in a given particle size distribution, a clear absorption edge is therefore often not observable making determination of the optical band gap difficult with this technique. Due to these effects however, UV-vis can be used as a relative measure of monodispersity in samples from the observed sharpness of the absorption edge [30].

Lastly, analysis of the nanocrystal surface chemistry can be conducted using techniques such as X-ray photoelectron spectroscopy (XPS), nuclear magnetic resonance spectroscopy (NMR), and Fourier transform infrared spectroscopy (FTIR) [31, 51]. These techniques are powerful tools which can be used for analysis such as nanocrystal surface bonding geometry, nanocrystal oxidation, analysis of the nanocrystal surface composition, and identification of capping ligands on the nanocrystal surface. Identification of surface ligands is an important aspect of characterization when nanocrystal films are subsequently selenized, as the presence of organic material in the final films may be detrimental to device performance; tailoring of the surface ligands present in the nanocrystal film to achieve optimal sintering is an active area of research for CZTS [38].

## 11.4 Sintering

Though the fabrication of semiconducting nanocrystals can be a facile, scalable, and relatively low-energy process, direct application of nanomaterials to photovoltaic systems has historically delivered poor device performance. Despite benefits of tunable optical properties from quantum confinement effects [84, 85] as well as the elimination of any further thermal absorber processing [86], nanocrystal solar cells typically suffer from poor carrier transport and significant internal losses. The origin of these losses lie in the large number of interfaces associated with nanocrystalline systems, which directly contribute to surface trapping of charge carriers, as well as the presence of electrically insulating organic ligands commonly found on the nanocrystal surfaces [26, 86–88]. While unique device architectures have been exploited to fabricate nanocrystalline colloidal quantum dot PbS/TiO<sub>2</sub> solar cells with c. 5% efficiency [89], nanocrystalline chalcogenide photovoltaic absorbers have so far only shown efficiencies as high as 4.0% for CIS [90] and less than 1% for CZTS [19].

The detrimental electrical properties of the inorganic nanocrystal absorber layers can be significantly decreased through annealing of the nanocrystal film at elevated temperatures (350–600 °C) [21, 26, 37]. In fact, the formation of dense, micron-sized large-grain absorber layers similar to those fabricated from coevaporation techniques can be achieved through specific sintering techniques of nanocrystal precursors [16, 22, 24]. The ability to achieve

high-quality large-grain absorbers is a key step in solar cell fabrication from nanocrystal precursors, as this morphological feature is common to high-efficiency thin-film devices [16, 72]. Understanding and controlling the sintering step is therefore essential to device fabrication as carrier transport, defect formation, and other important electrical properties are a direct result of the quality of the sintered absorber layer.

The sintering of nanocrystal films offers unique benefits over other approaches. In addition to the high-throughput low-energy scalable coating techniques available for the formation of the pre-sintered nanocrystal films, the use of inks with nanocrystals of varying compositions can also allow for nanoscale control of compositional gradients during film formation. A film can be formed through nanocrystal coatings which has the desired composition gradient prior to sintering [91]. To exploit these properties however, a detailed understanding of the sintering/grain growth mechanism as well as the elemental diffusion properties within the film during the sintering step are necessary.

In order to fully exploit the benefits of using nanocrystal precursors, an appropriate sintering technique must be chosen to compliment the properties of the precursor material. The most successful route towards developing solar cells from nanocrystal precursors involves “reactive” sintering, where the film sintering is enhanced through the choice of the annealing atmosphere as well as specifics of the chosen precursors. This reactive sintering technique can allow for design of a mechanism that favors densification of the film, while avoiding phase segregation and elemental losses in the process [62]. Additionally, reactive sintering can allow for relatively low-temperature processing compared to other sintering techniques which is beneficial for scale-up costs, substrate choice, and in reducing elemental losses. A low-temperature sintering mechanism is further feasible with the use of nanocrystal precursor films, as these materials can exhibit significant reductions in melting temperature due to their unique nanoscale properties [62, 85, 92].

Notably, a reactive sintering technique known as selenization has proven success in the formation of device-quality absorber layers from nanocrystal films [24, 62, 91, 93]. This technique utilizes the vapor pressure of selenium during the annealing process to drive the formation of the large-grain chalcogenide absorber layer. In particular, the technique originally proposed by Guo *et al.* [24] whereby sulfide nanocrystal films are selenized leads to the successful formation of high-quality CIGSSe, CZTSSe, and CZTGeSSe absorbers [16, 17, 22, 23, 25].

#### 11.4.1 Selenization

To achieve successful sintering, an energetically favorable driving force must be established between the starting precursor material and final sintered film. Early work in the selenization of stacked metallic Cu and In layers into sintered CIGSSe was successful due to the favorable reactivity of Cu and In in the presence of reactive selenium in the temperature range of 300–750°C:  $\text{Cu} + \text{In} + 2 \text{H}_2\text{Se} \leftrightarrow \text{CuInSe}_2$  [94]. Additionally, densification of the film is driven by the volume expansion of the precursors upon conversion into CIGSSe [62, 95]. However, the sintering of nanocrystals to form large-grain absorbers presents a unique challenge as these materials lose their driving force for densification if they are in their final material form prior to selenization [62, 93]. For this reason, initial work in the selenization of CIGSSe nanocrystal films into sintered CIGSSe absorbers under selenium vapor at 450–550°C demonstrated limited success, with minimal densification and grain growth achieved using the selenide nanocrystal precursors [37, 93].

Key progress in the selenization of nanocrystals arose when this process was applied to sulfide nanocrystal precursors rather than the selenide nanocrystals [24]. The switch to sulfide nanocrystals allowed for enhanced grain growth during selenization (and subsequently enhanced device performance) by establishing a reactive driving force for film formation that was missing while using the selenide nanocrystal precursors; namely, the driving force from the sulfide-to-selenide transition:  $\text{Cu}(\text{In}_{1-y}\text{Ga}_y)_2\text{S}_{2(s)} + \text{Se}_{x(g)} \leftrightarrow \text{Cu}(\text{In}_{1-y}\text{Ga}_y)_2\text{Se}_{2(s)} + \text{S}_{x(g)}$  [24].

Following the success of selenization from CIS nanocrystal films, these selenization techniques have been applied to CZTS research in the formation of CZTS<sub>Se</sub> solar cells from CZTS nanocrystal inks [16], based on the reaction  $\text{Cu}_2\text{ZnSnS}_{4(s)} + \text{Se}_{x(g)} \leftrightarrow \text{Cu}_2\text{ZnSnSe}_{4(s)} + \text{S}_{x(g)}$ . While extension of the selenization method from CIGS to CZTS was fairly straightforward, CZTS is found to impose its own unique challenges in the formation of high-quality absorber layers due to crystal instabilities of this quaternary system. Although selenization is beneficial due to its relatively low-temperature (c. 500°C) sintering mechanism as well as its reactive sintering properties which assists in crystal stability, the identification and mitigation of elemental losses and secondary phases present in the film following this step are active areas of research.

Although the selenization of quaternary CZTS or CZTGeS nanocrystals have shown the greatest device performance to date for nanocrystal-ink-based thin-film solar cells of this material, a suitable driving force for sintering can also be achieved in the selenization of a mixture of binary and ternary sulfide nanocrystals. This technique has been demonstrated with notable device performance of 8.5% pce by Cao *et al.* [18], following the reaction  $\text{Cu}_2\text{SnS}_{3(s)} + \text{ZnS}_{(s)} + \text{SnS}_{x(s)} + \text{Se}_{x(g)} \leftrightarrow \text{Cu}_2\text{ZnSnSe}_{4(s)} + \text{S}_{x(g)}$ . The successful selenization of binary and ternary nanocrystals with a reasonably uniform film composition following selenization illustrates the high cation mobility during selenization. Additionally, the success of this approach demonstrates the robustness of the selenization technique in absorber formation from heterogeneous precursor materials. In fact, recent *in situ* EDXRD studies during the selenization of CZTS nanocrystals suggests that CZTS transitions through various binary and ternary phases prior to sintered CZTS<sub>Se</sub> formation [96]. However, the use of CZTS nanocrystals is expected to assist in the homogeneous distribution of elements on the nanoscale prior to sintering, regardless of their breakdown into binary and ternary phases, when compared to a mixture of binary and ternary sulfide nanocrystals.

While the extreme case of the selenization of binary/ternary sulfide nanocrystals has proven successful in absorber layer formation through selenization, the use of heterogeneous precursor materials has also been explored in CZTS<sub>Se</sub> film formation from quaternary CZTS nanocrystals. In fact, sintering from CZTS nanocrystals is found to be enhanced (along with device performance) when a mixture of nanocrystals with some variation in size and composition is used [61]. The use of heterogeneous precursor materials can demonstrate beneficial sintering effects by including nanocrystals with desirable size/composition properties to assist in the reactive sintering mechanism (i.e. Cu-rich phases [61, 97]), or by delaying the formation of the desired single-phase absorber material. When the formation of the final single-phase homogeneous material is delayed, mass transport and interdiffusion can assist in densification of the film [62], as these parameters play an important role in many sintering mechanisms [98]. This effect was observed in the selenization of CuSe and InSe to form CISE absorbers when the reaction to form CISE occurred faster than the sintering mechanism [93]; once the CISE had formed, sintering became much

more difficult. Therefore, in addition to the sulfide-to-selenide transition, a suitable driving force for reactive sintering through mass transport can also be achieved through heterogeneities in the pre-sintered material, as demonstrated by the selenization of heterogeneous CZTS nanocrystals as well as for the extreme case of the selenization of binary/ternary nanocrystals to form CZTSSe. These effects aid in the formation of CZTSSe absorbers specifically from quaternary nanocrystal inks, as intra- and interparticle composition heterogeneities that can arise during quaternary nanoparticle synthesis can be beneficial to some extent during sintered film formation.

Even though many techniques and variations are possible to achieve a sintered CZTSSe absorber from nanocrystal precursors, the following section will outline an example selenization process used for the fabrication of CZTSSe absorbers from quaternary CZTS nanocrystal inks.

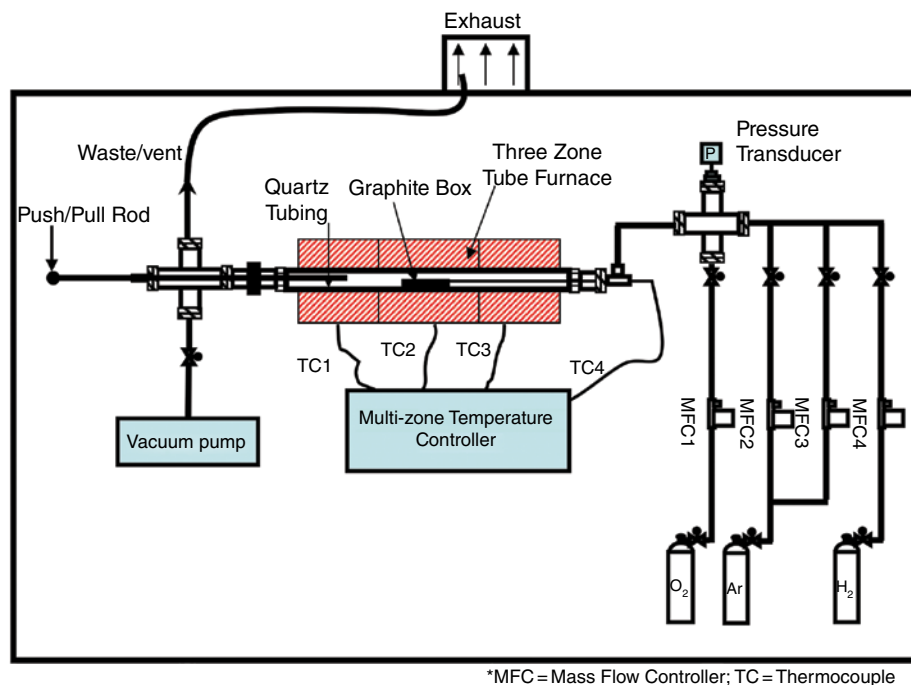
#### 11.4.2 Example Selenization

A typical procedure for the selenization of CZTS nanocrystals begins with preparation of the nanocrystal film. Following CZTS nanocrystal synthesis, the washed nanocrystals are dispersed in the desired solvent for coating, which forms the nanocrystal ink. The appropriate choice of solvent in the nanocrystal ink relies on the desired coating technique to be used, choice of substrate, as well as the nature of the organic capping ligand on the nanocrystal surface. Briefly, the organic capping ligand and ink-solvent must be miscible to allow for proper nanocrystal dispersion, the solvent must have desirable wetting properties with the substrate to avoid film reticulation, and the volatility of the solvent must deliver the desired ink-drying rate once coated. Additionally, the dielectric constant of the solvent must be considered when applying spray techniques controlled by an electric field, such as electrospray deposition or certain ink-jet printing techniques [99]. In general, reproducible nanocrystal films of controlled thickness can be achieved through doctor blading, drop casting, dip coating, spin coating, (electro)spray coating, or printing of the nanocrystal ink.

For typical film formation, oleylamine-capped CZTS nanocrystals dispersed in hexanethiol are doctor bladed onto molybdenum (Mo)-coated soda-lime glass substrates [16]. In addition to desirable wetting properties with Mo and miscibility with oleylamine, hexanethiol is also advantageous in delivering reproducible coatings due to its favorable volatility point. Once the film is coated and dried on the substrate, an annealing step in air at a relatively low temperature (c. 200°C) is applied to remove any excess solvent from the film. Additionally, this annealing step directs the formation of the final sintered film into the desired morphology, as discussed below.

A selenization apparatus used in the Agrawal lab at Purdue University is depicted in Figure 11.5. In this apparatus, the nanocrystal films are annealed in a tube furnace in an evaporated selenium gas atmosphere. To achieve this, the coated nanocrystal films and elemental selenium pellets are initially loaded into a graphite enclosure; this graphite enclosure provides uniform heating of the samples as well as helps maintain the evaporating selenium gas at or near its vapor pressure during the selenization reaction. A typical procedure for selenization begins with loading the graphite box containing the nanocrystal-coated substrates and elemental selenium pellets into the quartz tube reactor. Initially, the graphite box is placed outside of the tube furnace heating zones which allows for





**Figure 11.5** Thermal treatment apparatus used for selenization [100]

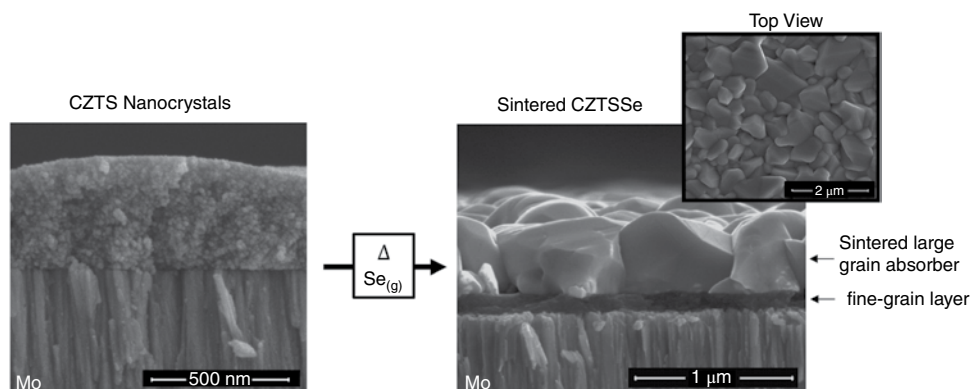
preheating of the furnace. Following evacuation/purging of the system, the furnace is preheated to the desired selenization reaction temperature, typically ranging from 500°C to 600°C. Once heated, a push/pull rod is used to insert the graphite box assembly into the center of the heated furnace which initiates the selenization reaction. Once the reaction is completed, typically between 10 and 45 minutes, the sample is quickly cooled down to room temperature.

During the selenization reaction, evaporated selenium gas initially diffuses throughout the porous nanocrystal film. Following this, sintered absorber formation occurs via a reaction front initiated at the surface of the film. While the details of the reaction mechanism depend on the specifics of the selenization conditions (i.e. chalcogenide atmosphere and reaction time/temperature profiles), sintered film formation typically occurs via the formation of large-grain binary and/or ternary selenides [96]; additional cations from the nanocrystal precursors diffuse to the reaction front and are incorporated into the growing grains to form the final CZTSSe absorber. The formation of the quaternary phase during reactive sintering follows the initial formation of large-grain  $\text{Cu}_x\text{Se}$  [96], as similarly reported in the formation of ternary and quaternary sulfide nanocrystals following  $\text{Cu}_x\text{S}$  formation [55, 58]. It should be noted that despite the nominal Cu-poor composition of the initial CZTS nanocrystals typically used, grain growth of CZTSSe during reactive sintering initially occurs under Cu-rich growth conditions (via  $\text{Cu}_x\text{Se}$ ); the formation of the final Cu-poor composition of the CZTSSe absorber is a self-regulating process as the remaining cations from the nanocrystal precursors are incorporated into the final sintered film [96]. CZTSSe growth under Cu-rich conditions has been linked with enhanced stability of the

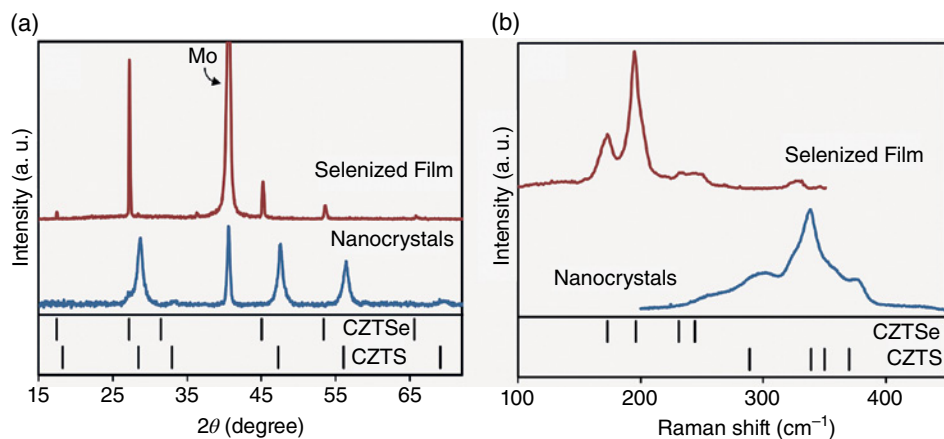
quaternary material as well as enhanced grain growth during quaternary phase formation [67, 74–76], as similarly discussed concerning the synthesis of CZTS nanocrystals (Section 11.2.5.3). Following the reactive sintering mechanism, the large-grain CZTSSe absorber sits on top of a fine-grain layer which can contain residual Se that initially diffused throughout the nanocrystal film, residual carbon from the nanocrystal precursors, and any unreacted cations during selenization.

A comparison of cross-sectional SEM images of a CZTS nanocrystal film before and after the selenization process is shown in Figure 11.6. During selenization, the nanocrystal clusters have sintered to form dense micron-sized grains that span the thickness of the sintered absorber layer. Additionally, minimal void spaces (notably near the bottom of the film) are achieved; these characteristics are in contrast to the properties of high-efficiency CZTS absorbers fabricated using other processing techniques [2, 14]. The bi-layer morphology of the selenized CZTSSe film can be observed, comprising the large-grain CZTSSe absorber on top of a fine-grain layer, a common feature of this nanocrystal/selenization process [16–18, 24, 101, 102], discussed below. Typical large-grain absorber layer thicknesses are  $611 \pm 108$  nm, with variations arising due to surface roughness of the film. In contrast, the thickness of the fine-grain layer can vary depending on the specifics of the selenization conditions as well as nanocrystal precursors. It should be noted that excellent carrier collection is achieved in nanocrystal-ink-based CZTSSe solar cells, despite the ultra-thin absorber layers typically utilized.

In addition to cross-sectional SEM imaging, the reactive sintering of the nanocrystals into large grains can also be observed through comparison of XRD data before and after selenization (Fig. 11.7a) where the peaks become sharper and the decrease in full-width-half-max indicates an increase in grain size [15]. In addition to grain growth, the transition from S to Se can also be observed from the XRD spectra due to a shift in the peak locations as the lattice parameters increase upon selenization [15]. Similarly, the sulfur-to-selenide transition can be more clearly observed through comparison of Raman spectra before and after selenization (Fig. 11.7b) as the  $A_1/A_2$  breathing mode at  $338.5\text{ cm}^{-1}$  and  $196\text{ cm}^{-1}$  is distinct for CZTS and CZTSe phases, respectively [46]. Following the



**Figure 11.6** SEM image of a CZTS nanocrystal film (left: cross-section) and a sintered CZTSSe absorber following selenization (right: cross-section and plan view)



**Figure 11.7** Typical (a) XRD and (b) Raman spectra comparing the as-synthesized CZTS nanocrystals to the selenized CZTSSe film

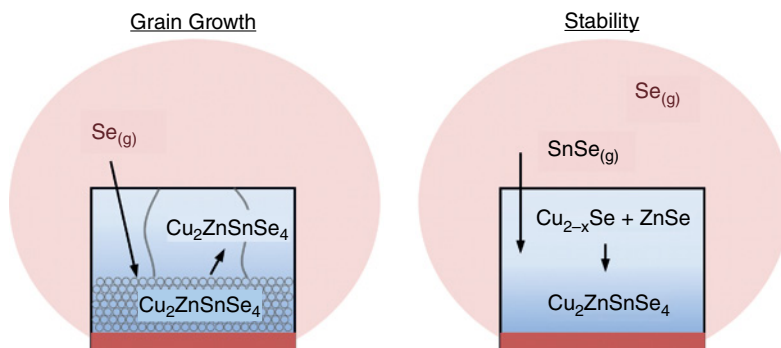
selenization process, it is estimated that less than 10% of the original sulfur remains in the film [15]; the residual sulfur in the lattice is indicated by the minor peaks that appear near  $320\text{ cm}^{-1}$  in the Raman spectra of the selenized film as well as in a shift of the peak locations in XRD (due to the decreased lattice parameters) for the selenized CZTSSe film when compared to the standard peak locations for CZTSe. Additionally, EDX mapping, grazing incident XRD, and surface-sensitive Raman measurements [23] indicate a slightly increasing  $[\text{S}]/[\text{Se}]$  ratio toward the back of the sintered CZTSSe absorber, which can be beneficial for charge carrier collection through a slight band-gap grading toward the back of the absorber [103].

### 11.4.3 Selenization Process Challenges

While the selenization of sulfide nanocrystals has been a particularly successful approach to achieve grain growth and sintering for absorber formation, this process is not without its own challenges. Here we discuss some major challenges that deserve careful attention in order to control the optoelectronic properties of the selenized absorber layer.

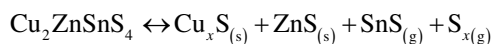
#### 11.4.3.1 Phase Purity, Elemental Losses and Grain Growth

While the importance of the chalcogenide atmosphere has been discussed in terms of achieving a driving force for grain growth and densification of the nanocrystal precursors, the reactive selenium atmosphere is also important in terms of stability of the quaternary absorber and phase purity of the film relative to impurities such as  $\text{Cu}_{2-x}\text{Se}$ ,  $\text{ZnSe}$ ,  $\text{SnSe}$ , and/or  $\text{Cu}_2\text{SnSe}_3$ . Specifically, the stability of the CZTSSe molecular structure at elevated processing temperatures should be considered. Figure 11.8 illustrates the role that the  $\text{Se}_{(\text{g})}$  atmosphere has in both grain growth (the  $\text{Se}_{(\text{g})}$  atmosphere drives the conversion of CZTS nanocrystals into large-grain sintered CZTSe) and stability (the  $\text{Se}_{(\text{g})}$  atmosphere drives the formation of the quaternary CZTSe phase from binary  $\text{SnSe}$ ,  $\text{Cu}_{2-x}\text{Se}$ , and  $\text{ZnSe}$ ) of CZTSSe, discussed below.

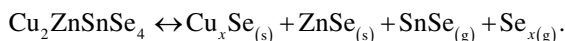


**Figure 11.8** Graphical illustration of the role that the reactive chalcogenide atmosphere plays in both grain growth and stability of CZTSSe films during selenization

Analysis of the decomposition of quaternary CZTSSe into its constituent secondary phases at annealing temperatures  $\geq 500^\circ\text{C}$  yields the reversible reaction [104, 105]:



or



Phase purity concerns with respect to secondary phases therefore arise during the fabrication of CZTSSe absorbers requiring processing at elevated temperatures. Additionally, CZTSSe can also suffer from significant elemental losses due to the described decomposition, specifically with regards to Sn [104–106], as both SnS and SnSe have significant vapor pressures at temperatures  $\geq 400^\circ\text{C}$  [104].

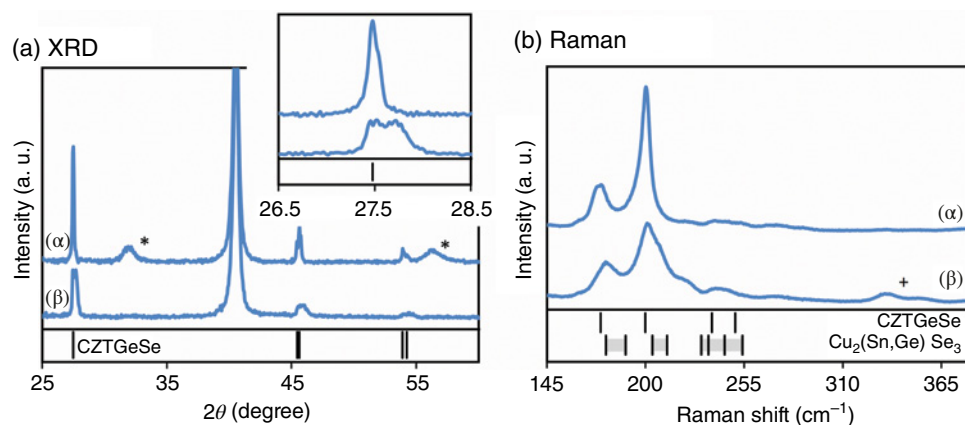
To mitigate issues of phase purity and elemental losses that can occur during absorber processing, the equilibrium reaction above can be exploited according to La Chatelier's principle by controlling the reaction atmosphere. Accordingly, annealing in an atmosphere containing a high partial pressure of  $\text{S}_{x(g)}$ ,  $\text{Se}_{x(g)}$ , or  $\text{Sn}(\text{S},\text{Se})_{(g)}$  can be used to shift the reaction towards the quaternary phase, minimizing CZTSSe decomposition. To limit the degree of elemental losses and secondary phase formation from the nanocrystal-ink-based CZTSSe films processed in the Agrawal lab, selenization temperatures are typically kept below  $550^\circ\text{C}$  and the  $\text{Se}_{(g)}$  partial pressure is kept high by limiting the diffusion rate of  $\text{Se}_{(g)}$  out of the graphite box. Bulk EDX analysis of the resulting CZTSSe absorbers following selenization shows minimal losses of Cu, Zn, and Sn using this technique [23]. Alternatively, the use of  $\text{SnS}_{(g)}$  in the annealing atmosphere as well as variations in the selenization pressure have also been explored to assist in stabilizing the described CZTSSe instabilities [104, 106].

The presence of a critical partial pressure of  $\text{Se}_{(g)}$  throughout the reactive sintering process is essential not only for stability of the CZTSSe film, but also for growth of the quaternary phase from binary and/or ternary selenides, as characterized during the selenization of CZTS nanocrystal films [96]. Both of these processes can be described by the equilibrium reactions above. Therefore, if after selenization binary or ternary phases are observed in the film, they could be the result of two factors: (1) following quaternary phase formation, sufficient  $\text{Se}_{(g)}$

is not supplied at the elevated reaction temperature resulting in decomposition of the film; or (2) sufficient  $\text{Se}_{(\text{g})}$  is not supplied during the reactive sintering process, resulting in incomplete formation (i.e. incomplete selenization) of the quaternary phase. Additionally, as the  $\text{Se}_{(\text{g})}$  atmosphere drives the reactive sintering of CZTSSe, variations in the reactive chalcogenide atmosphere can also lead to variations in grain growth during selenization.

The effect of the  $\text{Se}_{(\text{g})}$  atmosphere on secondary phase formation and grain growth during selenization is illustrated in Figure 11.9 for selenized CZTGeSSe films prepared via: ( $\alpha$ ) complete selenization under a sufficient  $\text{Se}_{(\text{g})}$  atmosphere and ( $\beta$ ) incomplete selenization where the critical partial pressure of  $\text{Se}_{(\text{g})}$  is not maintained throughout the reactive sintering process. Both films are selenized at 500°C for 40 minutes; however, the diffusion rate of  $\text{Se}_{(\text{g})}$  away from the samples during reactive sintering is varied for the two films. CZTGeSSe films with 50% alloying of  $[\text{Ge}]/([\text{Ge}] + [\text{Sn}])$  are used to illustrate secondary phase formation, as both pure-phase CZTSSe and CZGeSSe XRD peaks can overlap with those of secondary tetragonal/cubic phases of interest (see Section 11.3), while the 50/50 CZTGeSSe alloy has distinct peak locations according to Vegard's law [107]. XRD analysis of both samples demonstrates diffraction peaks corresponding to the desired CZTGeSSe (50 at% Ge) absorber, while only sample ( $\beta$ ) contains an additional signal due to the presence of a secondary phase in the film (Fig. 11.9a insert). Similarly, Raman spectroscopy shows the presence of shoulders on the CZTGeSSe (50 at% Ge) peaks in sample ( $\beta$ ), at c. 180  $\text{cm}^{-1}$  and 210  $\text{cm}^{-1}$ . From the Raman spectra, the identified peaks for sample ( $\beta$ ) are attributed here to a  $\text{Cu}_x(\text{Sn},\text{Ge})\text{Se}_y$  impurity phase [108–110]. In addition to a reduction in secondary phase formation, sample ( $\alpha$ ) also exhibits an increase in grain size as indicated by the sharper diffraction peaks and corresponding decrease in full-width-half-max for this film [15]. Furthermore, sample ( $\alpha$ ) also exhibits an increase in the  $[\text{Se}]/[\text{S}]$  ratio of the selenized absorber, indicated by the reduction in minor Raman peaks near c. 320  $\text{cm}^{-1}$  from residual sulfur in the crystal lattice in sample ( $\beta$ ) [46].

While the importance of a sufficient  $\text{Se}_{(\text{g})}$  atmosphere is demonstrated here in terms of grain growth, phase purity, and composition (i.e.  $[\text{Se}]/[\text{S}]$ ) of the selenized CZTSSe absorber, excess  $\text{Se}_{(\text{g})}$  partial pressures can also lead to the undesirable formation of excessive  $\text{MoSe}_2$  in the film



**Figure 11.9** (a) XRD and (b) Raman spectroscopy of CZTGeSSe (50 at% Ge) films selenized under various chalcogenide atmospheres (indicated as  $\alpha$  and  $\beta$ ; see text); (\*) indicates diffraction peaks from  $\text{MoSe}_2$ ; (+) indicates Raman signal from residual S in the CZTGeSSe crystal lattice

(discussed in Section 11.4.3.3), observed in the diffraction signal of sample ( $\alpha$ ). It should be noted that sample ( $\alpha$ ) is presented here to illustrate the potential of  $\text{MoSe}_2$  formation during selenization; however, typical high-efficiency nanocrystal-ink-based devices are selenized under conditions which limit  $\text{MoSe}_2$  formation (see Fig. 11.12a). Therefore, careful control of the reactive chalcogenide atmosphere is necessary to ensure complete selenization, to maximize phase purity and grain growth of the absorber, and to minimize the formation of  $\text{MoSe}_2$ .

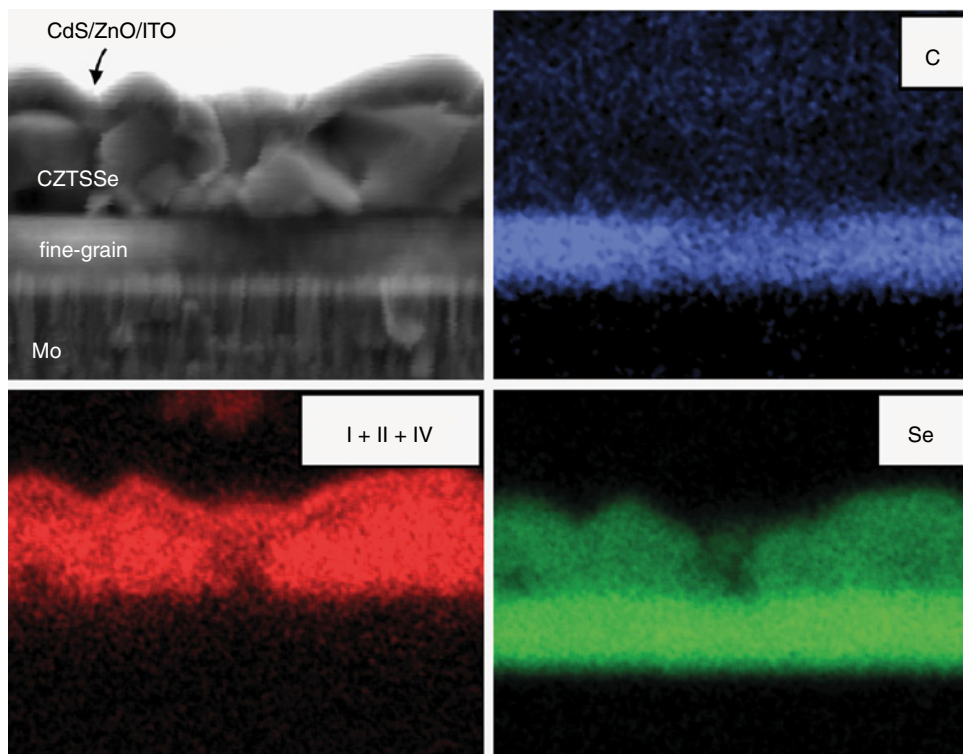
#### 11.4.3.2 *Fine-Grain Layer*

One particular outcome of the nanocrystal film/selenization approach to device fabrication involves the formation of a selenium-rich fine-grain layer located between the sintered CZTSSe layer and Mo back contact of the film, illustrated in Figure 11.6. This bi-layer structure is a common feature of selenized nanocrystal films; however, the origin and composition of this layer can vary depending on the particular selenization approach and processing conditions utilized. A challenge for researchers is how to minimize or preferably eliminate this fine-grain layer through control of the selenization reaction conditions as well as purity of the pre-sintered films (i.e. the presence of carbonaceous material).

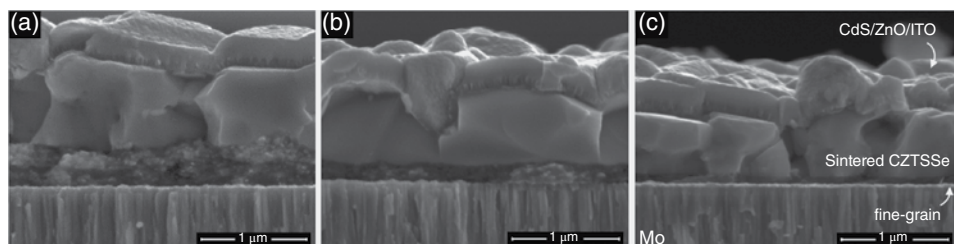
EDX mapping of “champion” selenized quaternary nanocrystal-ink-based devices (Fig. 11.10) has demonstrated the composition of the fine-grain layer to be composed primarily of selenium and carbon as opposed to unreacted nanocrystal precursors [23]; this is in contrast to similar fine-grain structures reported from the selenization of binary and ternary nanocrystals, where the fine-grain layer is found to contain both unsintered CZTSSe and binary/ternary nanocrystals embedded in a carbonaceous matrix [18]. Additionally, selenized CZTS nanocrystals have also been reported with unreacted cations present in the fine-grain layer, namely Zn, as this element is last to be incorporated into the growing CZTSSe grains [96]. While the composition of this layer can vary depending on the specific selenization conditions used and the composition distribution of the nanocrystal precursors, the presence of carbon and selenium is a common feature. The origin of carbon in the device is most likely attributed to capping ligands on the nanocrystal surface (originally used to stabilize the nanocrystal inks) as well as residual solvent from the ink coating. The exact role of the fine-grain layer on the electrical performance of the device is an active area of research.

In efforts to minimize/eliminate the formation of the fine-grain layer, research has indicated the fine-grain layer thickness is heavily dependent upon the selenization reaction conditions, illustrated in Figure 11.11. Here we find that an increase in selenization time or an increase in selenization temperature can lead to reductions in the fine-grain layer thickness: (a) represents standard selenization conditions (500°C, 20 min); (b) represents selenization at increased temperatures (550°C, 15 min); and (c) represents selenization for increased time (500°C, 40 min). As this layer is primarily composed of Se that initially diffused throughout the nanocrystal film, increased selenization time/temperature can lead to reduced fine-grain thickness as residual Se is allowed to evaporate from the film following the reactive sintering process. However, complete removal of this fine-grain layer will most likely involve elimination of carbon from the pre-sintered nanocrystal films, which is an active research area in nanocrystal-ink-based devices. The described selenization optimization has recently pushed selenized nanocrystal-ink-based CZTSSe devices to 9.0% total-area efficiency (9.8% active-area) when combined with optimized nanocrystal synthesis conditions [22].



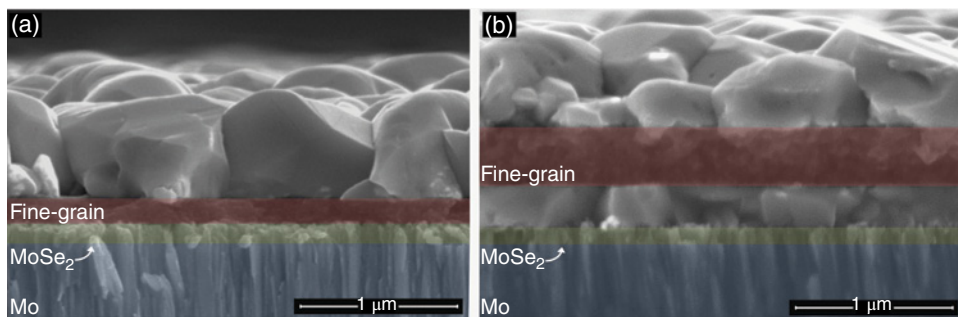


**Figure 11.10** Cross-sectional SEM-EDX mapping demonstrating that the composition of the fine-grain layer resulting from the selenization of a quaternary nanocrystal film mostly comprises Se and C with minimal signal from Cu, Zn, and Sn. The original un-sintered CZTS nanocrystals are therefore absent from the fine-grain layer [23]. For color details, please see color plate section



**Figure 11.11** Cross-sectional SEM imaging of CZTSSe films selenized under various reaction conditions, as described in the text. The fine-grain layer thickness is shown to vary according to the selenization time and temperature profiles during the reaction (see text)

In addition to the role selenization reaction conditions play in the formation of the fine-grain layer, pre-selenization annealing treatments of the nanocrystal film can also be used to direct the morphology of the final sintered absorber. Typically, nanocrystal films are annealed in air prior to selenization as described above, resulting in a bi-layer morphology (Fig. 11.12a).



**Figure 11.12** Cross-sectional SEM images illustrating: (a) standard bi-layer morphology typical of high-efficiency devices (annealed in air prior to selenization); and (b) undesirable tri-layer morphology of CZTSSe films following selenization (not annealed prior to selenization). For color details, please see color plate section

Since the reactive sintering process initiates from the surface of the film, residual Se, C, and/or cations remain at the bottom of the film following selenization. However, it was found that the use of un-annealed nanocrystal films, or samples annealed in a nitrogen environment, can lead to an undesirable tri-layer structure following selenization as illustrated in Figure 11.12b. In the tri-layer structure, the reactive sintering mechanism was initiated at both the surface and bottom of nanocrystal film, resulting in the fine-grain layer of residual Se, C, and/or cations being sandwiched between two sintered large-grain layers located at the top and bottom of the film. This tri-layer structure has resulted in unfavorable electrical performance of the device. Similar results concerning the effect of pre-sintering annealing treatments have also been reported [101]. It has also been demonstrated that an inverted device architecture, with the fine-grain layer located on top of the large-grain absorber, is possible; however, reproducibility of this morphology is difficult to achieve [101].

#### 11.4.3.3 $\text{MoSe}_2$

An additional concern during the selenization of CZTS nanocrystals is the formation of  $\text{MoSe}_2$ . Due to the aggressive conditions used for selenization (high partial pressures of reactive selenium at temperature in excess of  $450^\circ\text{C}$ ), extensive  $\text{MoSe}_2$  formation may be an issue during selenization if proper reaction conditions are not controlled. While some  $\text{MoSe}_2$  formation can be beneficial for enhanced film adhesion as well in the formation of a quasi-ohmic back contact, reported for CIGSSe devices [111], extensive conversion of Mo into  $\text{MoSe}_2$  can lead to film delamination issues in addition to increased series resistance of the stack [112]. To control  $\text{MoSe}_2$  formation during selenization, specific Mo morphologies can be utilized which suppress the reaction rate of  $\text{MoSe}_2$  formation [112]; however, this relies on control of the Mo sputtering condition. Alternatively, barrier layers such as TiN can be used to limit  $\text{MoSe}_2$  formation, notably for selenization temperatures greater than  $550^\circ\text{C}$  [113]. Typical high-efficiency devices selenized from nanocrystal precursors exhibit only 50–100 nm of  $\text{MoSe}_2$  formation, illustrated in Figure 11.12a. These devices are fabricated on Mo deposited in the Agrawal lab, as careful control of soda-lime glass cleaning and Mo deposition conditions allows for the fabrication of Mo with superior adhesion that is notably resistant to selenization.



#### 11.4.3.4 Summary

In addition to phase purity, grain growth, absorber morphology, fine-grain layer thickness, and  $\text{MoSe}_2$  formation, the choice of absorber processing conditions are also associated with issues such as defect formation, surface roughness, grain morphology (i.e. faceting), and alloy (compositional) uniformity. It is therefore necessary to have rigid control over the absorber formation parameters to ensure the successful formation of a sintered absorber layer with desirable optoelectronic properties. Only when the influence of various reactive sintering parameters can be understood and effectively controlled will investigation and optimization of the properties of the nanocrystal precursors be effective. Ideally, the combination of tunable nanocrystal precursor properties as well as selenization parameters will allow for the fabrication of films with tunable defect properties, phase purity, and compositional uniformity, all which ultimately contribute to the optoelectronic performance of the device.

#### 11.4.4 $\text{Cu}_2\text{Zn}(\text{Sn}_y\text{Ge}_{1-y})(\text{S}_x\text{Se}_{4-x})$ (CZTGeSSe)

One limitation to the formation of high-efficiency kesterite absorber layers utilizing the selenization process lies in the inability to tune the band gap of the absorber. This issue arises from the fact that a typical selenization process leads to >90% substitution of S for Se into the crystal lattice, delivering a CZTSSe absorber layer with a lower than optimal band gap of 1.05–1.10 eV. While high-efficiency CZTSSe solar cells have typically utilized control of the [S]/[Se] ratio for band-gap tuning [114], fine control of the [S]/[Se] ratio from sulfurization/selenization processes can be challenging. However, the use of Ge-substituted CZTGeS nanocrystals (Section 11.2.4) has had proven success in the formation of dense, sintered, tunable-band-gap CZTGeSSe absorber layers through selenization.

The formation of CZTGeSSe absorber films from CZTGeS nanocrystal inks follows similar processing to that of CZTSSe from CZTS nanocrystals. Bulk band-gap tuning is achieved in the selenized absorber film through control of the  $[\text{Ge}]/([\text{Ge}] + [\text{Sn}])$  ratio in the nanocrystal precursors [17, 23, 52]. In addition to bulk band gap tuning, Ge-substitution can be used to achieve a band gap grading throughout the film through modification of the conduction band level [17], as similarly demonstrated with Ga-grading in high-efficiency CIGSSe devices [115]. Furthermore, substitution of Ge for Sn has been suggested to enhance the electrical properties of the CZTGeSSe absorber through a reduction in the concentration of the multi-valent Sn atom, which can contribute to undesirable recombination in the device [116].

While promising results have been achieved, the Ge-alloyed CZTGeSSe material system is not without its own challenges. Current research indicates that Ge-loss is a concern for the CZTGeSSe absorber, which is associated with the relatively higher vapor pressure of  $\text{Ge}(\text{S},\text{Se})$  compared to that of  $\text{Sn}(\text{S},\text{Se})$  [17, 23, 59]. Ge-loss from selenized CZTGeSSe films has been linked to absorber processing conditions (specifically the partial pressure of the reactive chalcogenide and selenization temperature); however, optimized nanocrystal properties and selenization conditions have led to control of elemental losses and enhanced device performance [23]. Despite this, alloy compositional uniformity as well as surface (<3 nm) elemental losses are identified as present limitations to improved device performance [23].

Ultimately, Ge-alloyed CZTGeSSe is a promising material for nanocrystal-ink-based solar cells; device performance is improved compared to similarly processed CZTSSe solar cells as a result of enhanced electrical properties (e.g. minority carrier lifetime) [23, 59] of the Ge-alloyed absorber as well as the opportunity for optimal band-gap tuning in the selenized nanocrystal film.

## 11.5 Conclusion

Device fabrication from the selenization of nanocrystal inks has proven to be a relatively facile process to achieve the successful formation of high-efficiency CZTSSe solar cells. While many challenges and complexities have been addressed concerning CZTS nanocrystal synthesis, characterization, and selenization, this approach has proven to be forgiving in terms of device fabrication from various processing conditions, absorber compositions, and purity requirements. The key to successful device fabrication from this technique lies in the synthesis of CZTS nanocrystals which have optimal properties to favor dense film formation upon sintering, as well as having control over the reactive sintering parameters to deliver films with minimal phase segregation, compositional heterogeneities, and defect formation. The reactive sintering process originally developed by Guo *et al.* at Purdue University [15, 24], where selenization is paired with nanocrystal sulfide inks, has proven to be a robust technique which utilizes the beneficial properties of reactive sintering to fabricate high-quality absorber layers. For this CZTSSe route, total-area pce of greater than 9% have been demonstrated by the Agrawal research group [22, 23]. These pce values are among the highest efficiencies reported to date by any method and provide us with confidence in the potential of the robust low-cost nanocrystal-ink-based route for solar cell fabrication.

## References

- [1] Wang, W., Winkler, M. T., Gunawan, O., Gokmen, T., Todorov, T. K., Zhu, Y. & Mitzi, D. B. (2013) Device characteristics of CZTSSe thin-film solar cells with 12.6% efficiency. *Advanced Energy Materials*, **4**(7), doi: 10.1002/aenm.201301465.
- [2] Brammertz, G., Buffière, M., Oueslati, S., ElAnzeery, H., Ben Messaoud, H., Sahayaraj, S., Köble, C., Meuris, M. & Poortmans, J. (2013) Characterization of defects in 9.7% efficient  $\text{Cu}_2\text{ZnSnSe}_4$ -CdS-ZnO solar cells. *Applied Physics Letters*, **103**(16), 163904.
- [3] Nakayama, N. & Ito, K. (1996) Sprayed films of stannite  $\text{Cu}_2\text{ZnSnS}_4$ . *Applied Surface Science*, **92**, 171–175.
- [4] Kamoun, N., Bouzouita, H. & Rezig, B. (2007) Fabrication and characterization of  $\text{Cu}_2\text{ZnSnS}_4$  thin films deposited by spray pyrolysis technique. *Thin Solid Films*, **515**(15), 5949–5952.
- [5] Kishore Kumar, Y. B., Suresh Babu, G., Uday Bhaskar, P. & Sundara Raja, V. (2009) Preparation and characterization of spray-deposited  $\text{Cu}_2\text{ZnSnS}_4$  thin films. *Solar Energy Materials and Solar Cells*, **93**(8), 1230–1237.
- [6] Tanaka, K., Moritake, N. & Uchiki, H. (2007) “Preparation of  $\text{Cu}_2\text{ZnSnS}_4$  thin films by sulfurizing sol-gel deposited precursors. *Solar Energy Materials and Solar Cells*, **91**(13), 1199–1201.
- [7] Tanaka, K., Fukui, Y., Moritake, N. & Uchiki, H. (2011) Chemical composition dependence of morphological and optical properties of  $\text{Cu}_2\text{ZnSnS}_4$  thin films deposited by sol-gel sulfurization and  $\text{Cu}_2\text{ZnSnS}_4$  thin film solar cell efficiency. *Solar Energy Materials and Solar Cells*, **95**(3), 838–842.

- [8] Araki, H., Kubo, Y., Mikaduki, A., Jimbo, K., Maw, W. S., Katagiri, H., Yamazaki, M., Oishi, K. & Takeuchi, A. (2009) Preparation of  $\text{Cu}_2\text{ZnSnS}_4$  thin films by sulfurizing electroplated precursors. *Solar Energy Materials and Solar Cells*, **93**(6–7), 996–999.
- [9] Schurr, R., Hölzing, A., Jost, S., Hock, R., Voß, T., Schulze, J., Kirbs, A., Ennaoui, A., Lux-Steiner, M., Weber, A., Kötschau, I. & Schock, H.-W. (2009)  $\text{Cu}_2\text{ZnSnS}_4$  thin film solar cells from electroplated precursors: Novel low-cost perspective. *Thin Solid Films*, **517**(7), 2511–2514.
- [10] Scragg, J. J., Dale, P. J. & Peter, L. M. (2009) Synthesis and characterization of  $\text{Cu}_2\text{ZnSnS}_4$  absorber layers by an electrodeposition-annealing route. *Thin Solid Films*, **517**(7), 2481–2484.
- [11] Fischereider, A., Rath, T., Haas, W., Amenitsch, H., Albering, J., Meischler, D., Larissegger, S., Edler, M., Saf, R., Hofer, F. & Trimmel, G. (2010) Investigation of  $\text{Cu}_2\text{ZnSnS}_4$  formation from metal salts and thioacetamide. *Chemistry of Materials*, **22**(11), 3399–3406.
- [12] Ki, W. & Hillhouse, H. W. (2011) Earth-abundant element photovoltaics directly from soluble precursors with high yield using a non-toxic solvent. *Advanced Energy Materials*, **1**(5), 732–735.
- [13] Todorov, T. K., Reuter, K. B. & Mitzi, D. B. (2010) High-efficiency solar cell with Earth-abundant liquid-processed absorber. *Advanced Materials*, **22**(20), E156–E159.
- [14] Todorov, T. K., Tang, J. T., Bag, S., Gunawan, O., Gokmen, T., Zhu, Y. & Mitzi, D. B. (2013) Beyond 11% efficiency: characteristics of state-of-the-art  $\text{Cu}_2\text{ZnSn}(\text{S},\text{Se})_4$  solar cells. *Advanced Energy Materials*, **3**(1), 34–38.
- [15] Guo, Q., Hillhouse, H. W. & Agrawal, R. (2009) Synthesis of  $\text{Cu}_2\text{ZnSnS}_4$  nanocrystal ink and its use for solar cells. *Journal of American Chemical Society*, **131**, 11672–11673, 2009.
- [16] Guo, Q., Ford, G. M., Yang, W.-C., Walker, B. C., Stach, E. A., Hillhouse, H. W. & Agrawal, R. (2010) Fabrication of 7.2% efficient CZTSSe solar cells using CZTS nanocrystals. *Journal of American Chemical Society*, **132**(49), 17384–17386.
- [17] Guo, Q., Ford, G. M., Yang, W.-C., Hages, C. J., Hillhouse, H. W. & Agrawal, R. (2012) Enhancing the performance of CZTSSe solar cells with Ge alloying. *Solar Energy Materials and Solar Cells*, **105**, 132–136.
- [18] Cao, Y., Denny Jr., M. S., Caspar, J. V., Farneth, W. E., Guo, Q., Ionkin, A. S., Johnson, L. K., Lu, M., Malajovich, I., Radu, D., Rosenfeld, H. D., Choudhury, K. R. & Wu, W. (2012) High-efficiency solution-processed  $\text{Cu}_2\text{ZnSn}(\text{S},\text{Se})_4$  thin-film solar cells prepared from binary and ternary nanoparticles. *Journal of American Chemical Society*, **134**(38), 15644–15647.
- [19] Steinhagen, C., Panthani, M. G., Akhavan, V., Goodfellow, B., Koo, B. & Korgel, B. A. (2009) Synthesis of  $\text{Cu}_2\text{ZnSnS}_4$  nanocrystals for use in low-cost photovoltaics. *Journal of American Chemical Society*, **131**(35), 12554–12555.
- [20] Riha, S. C., Parkinson, B. A. & Prieto, A. L. (2009) Solution-based synthesis and characterization of  $\text{Cu}_2\text{ZnSnS}_4$  nanocrystals. *Journal of American Chemical Society*, **131**(34), 12054–12055.
- [21] Riha, S. C., Fredrick, S. J., Sambur, J. B., Liu, Y., Prieto, A. L. & Parkinson, B. A. (2011) Photoelectrochemical characterization of nanocrystalline thin-film  $\text{Cu}_2\text{ZnSnS}_4$  photocathodes. *ACS Applied Materials and Interfaces*, **3**(1), 58–66.
- [22] Miskin, C. K., Yang, W.-C., Hages, C. J., Carter, N. J., Joglekar, C. S., Stach, E. A. & Agrawal, R. (2014) 9.0% efficient  $\text{Cu}_2\text{ZnSn}(\text{S},\text{Se})_4$  solar cells from selenized nanoparticle inks. *Progress in Photovoltaics: Research and Applications*, doi: 10.1002/pip.2472.
- [23] Hages, C. J., Levenco, S., Miskin, C. K., Alsmeier, J. H., Abou-Ras, D., Wilks, R. G., Bar, M., Unold, T. & Agrawal, R. (2013) Improved performance of Ge-alloyed CZTGeSSe thin-film solar cells through control of elemental losses. *Progress in Photovoltaics: Research and Applications*, doi: 10.1002/pip.2442.
- [24] Guo, Q., Ford, G. M., Hillhouse, H. W. & Agrawal, R. (2009) Sulfide nanocrystal inks for dense  $\text{Cu}(\text{In}_{1-x}\text{Ga}_x)(\text{S}_{1-y}\text{Se}_y)_2$  absorber films and their photovoltaic performance. *Nano Letters*, **9**(8), 3060–3065.
- [25] Guo, Q., Ford, G. M., Agrawal, R. & Hillhouse, H. W. (2013) Ink formulation and low-temperature incorporation of sodium to yield 12% efficient  $\text{Cu}(\text{In},\text{Ga})(\text{S},\text{Se})_2$  solar cells from sulfide nanocrystal inks. *Progress in Photovoltaics: Research and Applications*, **21**(1), 64–71.
- [26] Gur, I., Fromer, N. A., Geier, M. L. & Alivisatos, A. P. (2005) Air-stable all-inorganic nanocrystal solar cells processed from solution. *Science* (80-.), **310**, 462–465.

- [27] Joo, J., Bin Na, H., Yu, T., Yu, J. H., Kim, Y. W., Wu, F., Zhang, J. Z. & Hyeon, T. (2003) Generalized and facile synthesis of semiconducting metal sulfide nanocrystals. *Journal of American Chemical Society*, **125**(36), 11100–11105.
- [28] Vossmeier, T., Katsikas, L., Giersig, M., Popovic, I. G., Diesner, K., Chemseddine, A., Eychemuller, A. & Weller, H. (1994) CdS nanoclusters: synthesis, characterization, size dependent oscillator strength, temperature shift of the excitonic transition energy, and reversible absorbance shift. *Journal of Physical Chemistry*, **98**, 7665–7673.
- [29] Peng, Z. A. & Peng, X. (2002) Nearly monodisperse and shape-controlled CdSe nanocrystals via alternative routes: nucleation and growth. *Journal of American Chemical Society*, **124**(13), 3343–3353.
- [30] Murray, C. B., Norris, D. J. & Bawendi, M. G. (1993) Synthesis and characterization of nearly monodisperse CdE (E = S, Se, Te) semiconductor nanocrystallites. *Journal of American Chemical Society*, **115**(4), 8706–8715.
- [31] Katari, J. E. B., Colvin, V. L. & Alivisatos, A. P. (1994) X-ray photoelectron spectroscopy of CdSe nanocrystals with applications to studies of the nanocrystal surface. *Journal of Physical Chemistry*, **98**(15), 4109–4117.
- [32] Guzelian, A. A., Banin, U., Kadavanich, A. V., Peng, X. & Alivisatos, A. P. (1996) Colloidal chemical synthesis and characterization of InAs nanocrystal quantum dots. *Applied Physics Letters*, **69**(10), 1432.
- [33] Guzelian, A. A., Katari, J. E. B., Kadavanich, A. V., Banin, U., Hamad, K., Juban, E., Alivisatos, A. P., Wolters, R. H., Arnold, C. C. & Heath, J. R. (1996) Synthesis of size-selected, surface-passivated InP nanocrystals. *Journal of Physical Chemistry*, **100**(17), 7212–7219.
- [34] Murray, C. B., Sun, S., Gaschler, W., Doyle, H., Betley, T. A. & Kagan, C. R. (2001) Colloidal synthesis of nanocrystals and nanocrystal superlattices. *IBM Journal of Research and Development*, **45**(1), 47–56.
- [35] Kigel, A., Brumer, M., Sashchiuk, A., Amirav, L. & Lifshitz, E. (2005) PbSe/PbSe<sub>x</sub>S<sub>1-x</sub> core-alloyed shell nanocrystals. *Materials Science and Engineering C*, **25**(5–8), 604–608.
- [36] Panthani, M. G., Akhavan, V., Goodfellow, B., Schmidtke, J. P., Dunn, L., Dodabalapur, A., Barbara, P. F. & Korgel, B. A. (2008) Synthesis of CuInS<sub>2</sub>, CuInSe<sub>2</sub>, and Cu(In<sub>x</sub>Ga<sub>1-x</sub>)Se<sub>2</sub> (CIGS) nanocrystal ‘inks’ for printable photovoltaics. *Journal of American Chemical Society*, **130**, 16770–16777.
- [37] Guo, Q., Kim, S. J., Kar, M., Shafarman, W. N., Birkmire, R. W., Stach, E. A., Agrawal, R. & Hillhouse, H. W. (2008) Development of CuInSe<sub>2</sub> nanocrystal and nanoring inks for low-cost solar cells. *Nano Letters*, **8**(9), 2982–2987.
- [38] Jiang, C., Lee, J. & Talapin, D. V. (2012) Soluble precursors for CuInSe<sub>2</sub>, CuIn<sub>1-x</sub>Ga<sub>x</sub>Se<sub>2</sub>, and Cu<sub>2</sub>ZnSn(S,Se)<sub>4</sub> based on colloidal nanocrystals and molecular metal chalcogenide surface ligands. *Journal of American Chemical Society*, **134**, 5010–5013.
- [39] Yin, Y. & Alivisatos, A. P. (2005) Colloidal nanocrystal synthesis and the organic-inorganic interface. *Nature*, **437**(7059), 664–670.
- [40] Cushing, B. L., Kolesnichenko, V. L. & O’Connor, C. J. (2004) Recent advances in the liquid-phase syntheses of inorganic nanoparticles. *Chemical Reviews*, **104**(9), 3893–3946.
- [41] Pileni, M.-P. (2003) The role of soft colloidal templates in controlling the size and shape of inorganic nanocrystals. *Nature Materials*, **2**(3), 145–150.
- [42] Murray, C. B., Kagan, C. R. & Bawendi, M. G. (2000) Synthesis and characterization of monodisperse nanocrystals and close-packed nanocrystal assemblies. *Annual Reviews of Materials Science*, **30**, 545–610.
- [43] LaMer, V. K. & Dinegar, R. H. (1950) Theory, production and mechanism of formation of monodispersed hydrosols. *Journal of American Chemical Society*, **72**(11), 4847–4854.
- [44] Peng, X., Wickham, J. & Alivisatos, A. P. (1998) Kinetics of II-VI and III-V colloidal semiconductor nanocrystal growth: ‘focusing’ of size distributions. *Journal of American Chemical Society*, **120**, 5343–5344.
- [45] Chen, S., Walsh, A., Yang, J.-H., Gong, X. G., Sun, L., Yang, P.-X., Chu, J.-H. & Wei, S.-H. (2011) Compositional dependence of structural and electronic properties of Cu<sub>2</sub>ZnSn(S,Se)<sub>4</sub> alloys for thin film solar cells. *Physical Review B*, **83**(12), 125201.

- [46] Grossberg, M., Krustok, J., Raudoja, J., Timmo, K., Altosaar, M. & Raadik, T. (2011) Photoluminescence and Raman study of  $\text{Cu}_2\text{ZnSn}(\text{Se}_x\text{S}_{1-x})_4$  monograins for photovoltaic applications. *Thin Solid Films*, **519**(21), 7403–7406.
- [47] Mott, D., Galkowski, J., Wang, L., Luo, J. & Zhong, C.-J. (2007) Synthesis of size-controlled and shaped copper nanoparticles. *Langmuir*, **23**(10), 5740–5745.
- [48] Shavel, A., Arbiol, J. & Cabot, A. (2010) Synthesis of quaternary chalcogenide nanocrystals: stannite  $\text{Cu}_2\text{Zn}_x\text{Sn}_{1-x}\text{Se}_{1+x+2y}$ . *Journal of American Chemical Society*, **132**, 4514–4515.
- [49] Riha, S. C., Parkinson, B. A. & Prieto, A. L. (2011) Compositionally tunable  $\text{Cu}_2\text{ZnSn}(\text{S}_{1-x}\text{Se}_x)_4$  nanocrystals: probing the effect of Se-inclusion in mixed chalcogenide thin films. *Journal of American Chemical Society*, **133**, 15272–15275.
- [50] Ou, K.-L., Fan, J.-C., Chen, J.-K., Huang, C.-C., Chen, L.-Y., Ho, J.-H. & Chang, J.-Y. (2012) Hot-injection synthesis of monodispersed  $\text{Cu}_2\text{ZnSn}(\text{S}_{1-x}\text{Se}_x)_4$  nanocrystals: tunable composition and optical properties. *Journal of Materials Chemistry*, **22**(29), 14667.
- [51] Khare, A., Wills, A. W., Ammerman, L. M., Norris, D. J. & Aydil, E. S. (2011) Size control and quantum confinement in  $\text{Cu}_2\text{ZnSnS}_4$  nanocrystals. *Chemical Communications*, **47**(42), 11721–11723.
- [52] Ford, G. M., Guo, Q., Agrawal, R. & Hillhouse, H. W. (2011) Earth-abundant element  $\text{Cu}_2\text{Zn}(\text{Sn}_{1-x}\text{Ge}_x)\text{S}_4$  nanocrystals for tunable band gap solar cells: 6.8% efficient device fabrication. *Chemistry of Materials*, **23**, 2626–2629.
- [53] Yang, W.-C., Miskin, C. K., Hages, C. J., Hanley, E. C., Handwerker, C., Stach, E. A. & Agrawal, R. (2014) Kesterite  $\text{Cu}_2\text{ZnSn}(\text{S},\text{Se})_4$  absorbers converted from metastable, wurtzite-derived  $\text{Cu}_2\text{ZnSnS}_4$  nanoparticles. *Chemistry of Materials*, **26**(11), 3530–3534.
- [54] Lu, X., Zhuang, Z., Peng, Q. & Li, Y. (2011) Wurtzite  $\text{Cu}_2\text{ZnSnS}_4$  nanocrystals: a novel quaternary semiconductor. *Chemical Communications*, **47**(11), 3141–3143.
- [55] Regulacio, M. D., Ye, C., Lim, S. H., Bosman, M., Ye, E., Chen, S., Xu, Q.-H. & Han, M.-Y. (2012) Colloidal nanocrystals of wurtzite-type  $\text{Cu}_2\text{ZnSnS}_4$ : facile noninjection synthesis and formation mechanism. *Chemistry: A European Journal*, **18**(11), 3127–3131.
- [56] Chen, S., Walsh, A., Luo, Y., Yang, J.-H., Gong, X. G. & Wei, S.-H. (2010) Wurtzite-derived polytypes of kesterite and stannite quaternary chalcogenide semiconductors. *Physical Review B*, **82**(19), 195203.
- [57] Lin, X., Kavalakkatt, J., Kornhuber, K., Abou-Ras, D., Schorr, S., Lux-Steiner, M. C. & Ennaoui, A. (2012) Synthesis of  $\text{Cu}_2\text{Zn}_x\text{Sn}_y\text{Se}_{1+x+2y}$  nanocrystals with wurtzite-derived structure. *RSC Advances*, **2**(26), 9894–9898.
- [58] Kar, M., Agrawal, R. & Hillhouse, H. W. (2011) Formation pathway of  $\text{CuInSe}_2$  nanocrystals for solar cells. *Journal of American Chemical Society*, **133**(43), 17239–17247.
- [59] Bag, S., Gunawan, O., Gokmen, T., Zhu, Y. & Mitzi, D. B. (2012) Hydrazine-processed Ge-substituted CZTSe solar cells. *Chemistry of Materials*, **24**(23), 4588–4593.
- [60] Chen, S., Gong, X., Walsh, A. & Wei, S.-H. (2009) Electronic structure and stability of quaternary chalcogenide semiconductors derived from cation cross-substitution of II-VI and I-III-VI<sub>2</sub> compounds. *Physical Review B*, **79**(16), 165211.
- [61] Carter, N. J., Yang, W.-C., Miskin, C. K., Hages, C. J., Stach, E. A. & Agrawal, R. (2014)  $\text{Cu}_2\text{ZnSn}(\text{S},\text{Se})_4$  solar cells from inks of heterogeneous Cu-Zn-Sn-S nanocrystals. *Solar Energy Materials and Solar Cells*, doi: 10.1016/j.solmat.2014.01.016.
- [62] Eberspacher, C., Fredric, C., Pauls, K. & Serra, J. (2001) Thin-film CIS alloy PV materials fabricated using non-vacuum, particles-based techniques. *Thin Solid Films*, **387**(1–2), 18–22.
- [63] Connor, S. T., Hsu, C.-M., Weil, B. D., Aloni, S. & Cui, Y. (2009) Phase transformation of biphasic  $\text{Cu}_2\text{S-CuInS}_2$  to monophasic  $\text{CuInS}_2$  nanorods. *Journal of American Chemical Society*, **131**(13), 4962–4966.
- [64] Kruszynska, M., Borchert, H., Parisi, J. & Kolny-Olesiak, J. (2010) Synthesis and shape control of  $\text{CuInS}_2$  nanoparticles. *Journal of American Chemical Society*, **132**(45), 15976–15986.
- [65] Sugimoto, T. (1987) Preparation of monodispersed colloidal particles. *Advances in Colloid and Interface Science*, **28**, 65–108.
- [66] Haas, W., Rath, T., Pein, A., Rattenberger, J., Trimmel, G. & Hofer, F. (2011) The stoichiometry of single nanoparticles of copper zinc tin selenide. *Chemical Communications*, **47**(7), 2050–2052.

- [67] Chen, S., Yang, J.-H., Gong, X. G., Walsh, A. & Wei, S.-H. (2010) Intrinsic point defects and complexes in the quaternary kesterite semiconductor  $\text{Cu}_2\text{ZnSnS}_4$ . *Physical Review B*, **81**(24), 35–37.
- [68] Tester, J. W. & Modell, M. (1996) *Thermodynamics and its Applications*, 3rd edition. Prentice-Hall, Inc., Upper Saddle River, NJ.
- [69] Shi, L., Pei, C., Xu, Y. & Li, Q. (2011) Template-directed synthesis of ordered single-crystalline nanowires arrays of  $\text{Cu}_2\text{ZnSnS}_4$  and  $\text{Cu}_2\text{ZnSnSe}_4$ . *Journal of American Chemical Society*, **133**(27), 10328–10331.
- [70] Singh, A., Geaney, H., Laffir, F. & Ryan, K. M. (2012) Colloidal synthesis of wurtzite  $\text{Cu}_2\text{ZnSnS}_4$  nanorods and their perpendicular assembly. *Journal of American Chemical Society*, **134**(6), 2910–2913.
- [71] Alivisatos, A. (2000) Naturally aligned nanocrystals. *Science* (80-), **289**(5480), 736–737.
- [72] Repins, I., Beall, C., Vora, N., DeHart, C., Kuciauskas, D., Dippo, P., To, B., Mann, J., Hsu, W.-C., Goodrich, A. & Noufi, R. (2012) Co-evaporated  $\text{Cu}_2\text{ZnSnSe}_4$  films and devices. *Solar Energy Materials and Solar Cells*, **101**, 154–159.
- [73] Scragg, J. J. (2010) Studies of  $\text{Cu}_2\text{ZnSnS}_4$  films prepared by sulfurisation of electrodeposited precursors. PhD Thesis, University of Bath.
- [74] Repins, I., Vora, N., Beall, C., Wei, S.-H., Yan, Y., Romero, M., Teeter, G., Du, H., To, B., Young, M. & Noufi, R. (2011) Kesterites and chalcopyrites: a comparison of close cousins. *Materials Research Symposium Spring Meeting*, doi:10.1557/opl.2011.844.
- [75] Tanaka, T., Yoshida, A., Saiki, D., Saito, K., Guo, Q., Nishio, M. & Yamaguchi, T. (2010) Influence of composition ratio on properties of  $\text{Cu}_2\text{ZnSnS}_4$  thin films fabricated by co-evaporation. *Thin Solid Films*, **518**(21), S29–S33.
- [76] Suresh Babu, G., Kishore Kumar, Y. B., Uday Bhaskar, P. & Raja Vanjari, S. (2010) Effect of Cu/(Zn+Sn) ratio on the properties of co-evaporated  $\text{Cu}_2\text{ZnSnSe}_4$  thin films. *Solar Energy Materials and Solar Cells*, **94**(2), 221–226.
- [77] Alvaraz-Garcia, J., Izquierdo-Roca, V. & Perez-Rodriguez, A. (2011) Raman Spectroscopy on thin films for solar cells. In *Advanced Characterization Techniques for Thin Film Solar Cells* (eds D. Abou-Ras, T. Kirchartz, and U. Rau). Wiley VCH Verlag GmbH & Co. KGaA, Weinheim, Germany, pp. 365–384.
- [78] Scragg, J. J. S., Choubrac, L., Lafond, A., Ericson, T. & Platzer-Björkman, C. (2014) A low-temperature order-disorder transition in  $\text{Cu}_2\text{ZnSnS}_4$  thin films. *Applied Physics Letters*, **104**(4), 041911.
- [79] Fernandes, P. A., Salome, P. M. P. & da Cunha, A. F. (2011) Study of polycrystalline  $\text{Cu}_2\text{ZnSnS}_4$  films by Raman scattering. *Journal of Alloys and Compounds*, **509**, 7600–7606.
- [80] Just, J., Lützenkirchen-Hecht, D., Frahm, R., Schorr, S. & Unold, T. (2011) Determination of secondary phases in kesterite  $\text{Cu}_2\text{ZnSnS}_4$  thin films by x-ray absorption near edge structure analysis. *Applied Physics Letters*, **99**(26), 262105.
- [81] Fontané, X., Calvo-Barrio, L., Izquierdo-Roca, V., Saucedo, E., Pérez-Rodríguez, A., Morante, J. R., Berg, D. M., Dale, P. J. & Siebentritt, S. (2011) In-depth resolved Raman scattering analysis for the identification of secondary phases: Characterization of  $\text{Cu}_2\text{ZnSnS}_4$  layers for solar cell applications. *Applied Physics Letters*, **98**(18), 181905.
- [82] Zou, C., Zhang, L., Lin, D., Yang, Y., Li, Q., Xu, X., Chen, X. & Huang, S. (2011) Facile synthesis of  $\text{Cu}_2\text{ZnSnS}_4$  nanocrystals. *CrystEngComm*, **13**(10), 3310.
- [83] Hlaing OO, W. M., Johnson, J. L., Bhatia, A., Lund, E. A., Nowell, M. M. & Scarpulla, M. A. (2011) Grain size and texture of  $\text{Cu}_2\text{ZnSnS}_4$  thin films synthesized by cosputtering binary sulfides and annealing: effects of processing conditions and sodium. *Journal of Electronic Materials*, **40**(11), 2214–2221.
- [84] Trindade, T., O'Brien, P. & Pickett, N. L. (2001) Nanocrystalline semiconductors: synthesis, properties, and perspectives. *Chemistry of Materials*, **13**, 3843–3858.
- [85] Alivisatos, A. P. (1996) Semiconductor clusters, nanocrystals, and quantum dots. *Science* (80-), **271**(5251), 933–937.
- [86] Akhavan, V. A., Goodfellow, B. W., Panthani, M. G., Steinhagen, C., Harvey, T. B., Stolle, C. J. & Korgel, B. A. (2012) Colloidal CIGS and CZTS nanocrystals: A precursor route to printed photovoltaics. *Journal of Solid State Chemistry*, **189**, 2–12.

- [87] Luther, J. M., Law, M., Beard, M. C., Song, Q., Reese, M. O., Ellingson, R. J. & Nozik, A. J. (2008) Schottky solar cells based on colloidal nanocrystal films. *Nano Letters*, **8**(10), 3488–3492.
- [88] Ma, W., Luther, J. M., Zheng, H., Wu, Y. & Alivisatos, A. P. (2009) Photovoltaic devices employing ternary  $\text{PbS}_{1-x}\text{Se}_x$  nanocrystals. *Nano Letters*, **9**(4), 1699–1703.
- [89] Pattantyus-Abraham, Á. G., Kramer, I. J., Barkhouse, A. R., Wang, X., Konstantatos, G., Debnath, R., Levina, L., Raabe, I., Nazeeruddin, M. K., Grätzel, M. & Sargent, E. H. (2010) Depleted-heterojunction colloidal quantum dot solar cells. *ACS Nano*, **4**(6), 3374–3380.
- [90] Li, L., Coates, N. & Moses, D. (2009) Solution-processed inorganic solar cell based on in situ synthesis and film deposition of  $\text{CuInS}_2$  nanocrystals. *Journal of American Chemical Society*, **132**, 22–23.
- [91] Kapur, V. K., Fisher, M. & Roe, R. (2001) Nanoparticle oxides precursor inks for thin film copper indium gallium selenide (CIGS) solar cells. *Materials Research Society Symposium Proceedings*, **668**, p. H2.6.
- [92] Goldstein, A. N., Echer, C. M. & Alivisatos, A. P. (1992) Melting in semiconductor nanocrystals. *Science* (80-. ), **256**(5062), 1425–1427.
- [93] Ginley, D. S., Curtis, C. J., Ribelin, R., Alleman, J. L., Mason, A., Jones, K. M., Matson, R. J., Khaselev, O. & Schulz, D. L. (1999) Nanoparticle precursors for electronic materials. *Materials Research Society Symposium Proceedings*, **536**, 237–244.
- [94] Chu, T. L., Chu, S. S., Lin, S. C. & Yue, J. (1984) Large grain copper indium diselenide films. *ECS Journal: Solid-State Science and Technology*, **131**(9), 2182.
- [95] Adurodija, F. O., Song, J., Kim, S. D., Kim, S. K. & Yoon, K. H. (1998) Characterization of  $\text{CuInS}_2$  thin films grown by close-spaced vapor sulfurization of co-sputtered Cu-In alloy precursors. *Japanese Journal of Applied Physics*, **37**, 4248–4253.
- [96] Mainz, R., Walker, B., Schmidt, S. S., Zander, O., Weber, A., Rodríguez-Alvarez, H., Just, J., Klaus, M., Agrawal, R. & Unold, T. (2013) Real-time observation of  $\text{Cu}_2\text{ZnSn}(\text{S},\text{Se})_4$  solar cell absorber layer formation from nanoparticle precursors. *Physical Chemistry, Chemical Physics*, **15**, 18281–18289.
- [97] Walker, B. & Agrawal, R. (2012) Grain growth enhancement of selenide CIGSe nanoparticles to densified films using copper selenides. *Proceedings of 38th IEEE Photovoltaic Specialists Conference*, 002654–002657.
- [98] Blendell, J. E. & Handwerker, C. A. (1986) Effect of chemical composition on sintering of ceramics. *Journal of Crystal Growth*, **75**, 138–160.
- [99] Jaworek, A. (2007) Electrospray droplet sources for thin film deposition. *Journal of Materials Science*, **42**, 266–297.
- [100] Guo, Q. (2009) Development of multinary chalcogenide nanocrystal inks for low cost solar cells. PhD thesis, Purdue University.
- [101] Leidholm, C., Hotz, C., Breeze, A., Sunderland, C., Ki, W. & Zehnder, D. (2012) Final report: Sintered CZTS nanoparticle solar cells on metal foil. *Contract*, **303**, 275–3000.
- [102] Kaelin, M., Rudmann, D., Kurdesau, F., Meyer, T., Zogg, H. & Tiwari, A. N. (2003) CIS and CIGS layers from selenized nanoparticle precursors. *Thin Solid Films*, **431–432**, 58–62.
- [103] Scheer, R. & Schock, H.-W. (2011) *Chalcogenide Photovoltaics*. Wiley VCH Verlag GmbH & Co. KGaA, Weinheim, Germany.
- [104] Redinger, A., Berg, D. M., Dale, P. J. & Siebentritt, S. (2011) The consequences of kesterite equilibria for efficient solar cells. *Journal of American Chemical Society*, **133**(10), 3320–3323.
- [105] Weber, A., Mainz, R. & Schock, H. W. (2010) On the Sn loss from thin films of the material system Cu–Zn–Sn–S in high vacuum. *Journal of Applied Physics*, **107**, 013516.
- [106] Salomé, P. M. P., Fernandes, P. A., da Cunha, A. F., Leitão, J., Malaquias, J., Weber, A., González, J. & da Silva, M. I. N. (2010) Growth pressure dependence of  $\text{Cu}_2\text{ZnSnSe}_4$  properties. *Solar Energy Materials and Solar Cells*, **94**(12), 2176–2180.
- [107] Vegard, L. (1921) Die Konstitution der Mischkristalle und die Raumfüllung der Atome. *Zeitschrift für Physik*, **5**(1), 17–2.
- [108] Marcano, G., Rincón, C., López, S. A., Sánchez Pérez, G., Herrera-Pérez, J. L., Mendoza-Alvarez, J. G. & Rodríguez, P. (2011) Raman spectrum of monoclinic semiconductor  $\text{Cu}_2\text{SnSe}_3$ . *Solid State Communications*, **151**(1), 84–86.

- [109] Marcano, G., Rincón, C., Marín, G., Delgado, G. E., Mora, A. J., Herrera-Pérez, J. L., Mendoza-Alvarez, J. G. & Rodríguez, P. (2008) Raman scattering and X-ray diffraction study in  $\text{Cu}_2\text{GeSe}_3$ , *Solid State Communications*, **146**(1–2), 65–68.
- [110] Choi, S. G., Donohue, A. L., Marcano, G., Rincón, C., Gedvilas, L. M., Li, J. & Delgado, G. E. (2013) Optical properties of cubic-phase  $\text{Cu}_2\text{GeSe}_4$  single crystal. *Journal of Applied Physics*, **114**(3), 033531.
- [111] Wada, T., Kohara, N., Nishiwaki, S. & Negami, T. (2001) Characterization of the  $\text{Cu(In,Ga)Se}_2/\text{Mo}$  interface in CIGS solar cells. *Thin Solid Films*, **387**, 118–122.
- [112] Yoon, J.-H., Kim, J.-H., Kim, W. M., Park, J.-K., Baik, Y.-J., Seong, T.-Y. & Jeong, J. (2014) Electrical properties of CIGS/Mo junctions as a function of  $\text{MoSe}_2$  orientation and Na doping. *Progress in Photovoltaics: Research and Applications*, **22**(1), 90–96.
- [113] Shin, B., Zhu, Y., Bojarczuk, N. A., Jay Chey, S. & Guha, S. (2012) Control of an interfacial  $\text{MoSe}_2$  layer in  $\text{Cu}_2\text{ZnSnSe}_4$  thin film solar cells: 8.9% power conversion efficiency with a TiN diffusion barrier. *Applied Physics Letters*, **101**(5), 053903.
- [114] Barkhouse, D. A. R., Gunawan, O., Gokmen, T., Todorov, T. K. & Mitzi, D. B. (2011) Device characteristics of a 10.1% hydrazine-processed  $\text{Cu}_2\text{ZnSn(Se,S)}_4$  solar cell. *Progress in Photovoltaics: Research and Applications*, **20**(1), 6–11.
- [115] Jackson, P., Hariskos, D., Lotter, E., Paetel, S., Wuerz, R., Menner, R., Wischmann, W. & Powalla, M. (2011) New world record efficiency for  $\text{Cu(In,Ga)Se}_2$  thin-film solar cells beyond 20%. *Progress in Photovoltaics: Research and Applications*, **19**(7), 894–897.
- [116] Biswas, K., Lany, S. & Zunger, A. (2010) The electronic consequences of multivalent elements in inorganic solar absorbers: Multivalency of Sn in  $\text{Cu}_2\text{ZnSnS}_4$ . *Applied Physics Letters*, **96**(20), 201902.



# 12

## CZTS Thin Films Prepared by a Non-Vacuum Process

*Kunihiko Tanaka*

*Nagaoka University of Technology, Department of Electrical Engineering,  
1603-1 Kamitomioka, Nagaoka, Niigata, 940-2188, Japan*

### 12.1 Introduction

Quaternary chalcogenide  $\text{Cu}_2\text{ZnSnS}_4$  (CZTS) is one of the most interesting materials for the absorber layer of thin-film solar cells because: (1) constituent elements are non-toxic, abundant in the crust of the Earth, and inexpensive; and (2) this compound semiconductor has optimal optical properties for solar cells, namely a direct band gap of c. 1.5 eV which is equal to an optimum band gap for single-junction photovoltaic devices, and a large absorption coefficient of the order  $10^4 \text{ cm}^{-1}$ .

In 1988, Ito and Nakazawa reported on the fabrication of CZTS thin films and CZTS thin-film solar cells [1]. They fabricated CZTS thin films using the atomic beam sputtering technique and investigated their properties. They found that CZTS has an optical band gap of 1.45 eV and observed a photovoltaic effect of 165 mV in the CZTS solar cells.

Katagiri and coworkers have reported many works on the preparation of CZTS thin-film solar cells [2–5]. Their CZTS solar cell demonstrated an efficiency of almost 7% [4], initiating much research on CZTS solar cells by others. Their high-efficiency solar cell consisted of an Al/ZnO:Al/CdS/CZTS/Mo/soda-lime glass (SLG) substrate structure, where the CZTS thin film was prepared by a two-step process: (1) RF co-sputtering of a precursor layer on the Mo-coated SLG; and (2) sulfurization of the precursor layer by annealing. The highest-reported efficiency of a CZTS solar cell in 2014 was 9.2%, where the CZTS absorber layer was deposited by use of the sputtering method [6].

The preparation methods mentioned above involve vacuum process, which usually requires expensive and complicated evacuation systems. Non-vacuum methods have the advantage of low cost and easy operation, however. Several research groups have already reported the synthesis of CZTS under non-vacuum conditions. To the best of our knowledge, Nakayama and Ito were the first to fabricate CZTS thin films under non-vacuum conditions. They deposited a precursor layer by spray pyrolysis and then annealed it in  $\text{H}_2\text{S}$  atmosphere to obtain CZTS thin films [7]. However, they did not report the application of these films to solar cells.

We started our own research on how to deposit CZTS thin films under non-vacuum conditions and in 2007 we reported for the first time that CZTS thin films can be prepared by a two-stage process which we refer to as sol-gel sulfurization [8]. During the first stage a Cu-, Zn-, and Sn-containing solution is coated as a precursor onto a substrate. At the second stage the precursor is sulfurized by annealing in a  $\text{H}_2\text{S}$ -containing atmosphere. We reported in 2009 that CZTS thin-film solar cells can be obtained by non-vacuum process [9]. Using the sol-gel sulfurization method we deposited not only the CZTS thin film as an absorber layer but also CdS buffer and  $\text{ZnO:Al}$  window layers. Efficiency of the first CZTS solar cell thus obtained was 1.01%; this was later improved to 4.13%.

In this chapter, preparation of CZTS thin films by the sol-gel sulfurization method and their application to CZTS thin-film solar cells is described in detail.

## 12.2 Sol-Gel Sulfurization Method

### 12.2.1 Concept of Sol-Gel Sulfurization Method

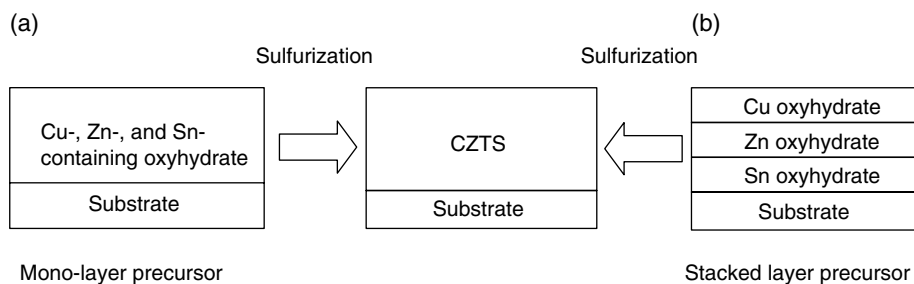
The sol-gel method is usually based on hydrolysis and polycondensation reactions of a molecular precursor in a liquid to form an oxide network [10]. To deposit an oxyhydrate precursor by the sol-gel method, we first coat a sol-gel solution on a substrate and then dry the coated substrate. We then obtain an oxide layer by annealing the oxyhydrate in air. This very simple and low-cost process is one of the non-vacuum processes. However, sulfides cannot be deposited directly by the sol-gel method because the coating solution does not contain S atoms. To obtain sulfides, the deposited oxides must absorb S atoms. Kavanagh reported that zinc sulfide thin films were produced from films of zinc oxide obtained by the sol-gel method from a solution of metal alkoxide in ethanol. The zinc oxide films were converted into zinc sulfide films by annealing in an atmosphere containing hydrogen sulfide [11].

Since sulfide films cannot be directly obtained by the sol-gel method, we prepared the CZTS thin films by a two-step process: (1) oxyhydrate precursor layers were first deposited by the sol-gel method; and (2) they are then sulfurized.

### 12.2.2 Coating Solution

Selecting an appropriate solution for coating is highly important for the sol-gel method. The following points must be carefully adhered to.

1. The solution must contain Cu, Zn, and Sn. To obtain CZTS thin films by the sol-gel sulfurization process there are two options (see Fig. 12.1): (a) sulfurizing a mono-layer prepared by a coating solution which contains all metal elements; or (b) sulfurizing



**Figure 12.1** Precursors for CZTS

stacked layers prepared by coating solutions which contain only one metal element. In case (a), the chemical composition of films may be easy to control because it reflects the chemical composition of metals in the solution. In case (b) however, the chemical composition may be difficult to control because it depends on the film thickness of each layer. It is therefore preferable to use a solution containing Cu, Zn, and Sn.

2. All starting materials must be dissolved completely and the dissolved state maintained for a long time. If there are any precipitations in the solution, the deposition of smooth precursors becomes very difficult and could result in the formation of impurity phases rather than CZTS.
3. The solution must have an optimal viscous property. If the viscosity of the solution is too high, spreading the solution uniformly becomes very difficult.
4. The solution must not react with a Mo-coated substrate. If the solution erodes Mo coating, which is usually used as a bottom electrode for the CZTS solar cell, cell efficiency is deteriorated.
5. Metal sources should be inexpensive in order to reduce material costs for solar cell fabrication.
6. A high concentration solution must be prepared; otherwise, we need to deposit the precursor many times until the required thickness is obtained.

#### 12.2.2.1 Metal Sources and a Solvent

A coating solution was prepared consistent with the required conditions. There are many reports on how to prepare a Cu-, Zn-, or Sn- containing oxide, such as Y-Ba-Cu-O superconductor, zinc oxide, and indium tin oxide using the sol-gel method [12–14]. In many cases, Cu acetate, Zn acetate, or Sn chloride was used as a metal source and 2-methoxyethanol (2-ME) was used as a solvent. Copper (II) acetate monohydrate (Cu-Acet), zinc (II) acetate dihydrate (Zn-Acet), and tin (II) chloride dihydrate ( $\text{SnCl}_2$ ) were therefore selected as metal sources. These sources are not expensive, the material costs of Cu-Acet, Zn-Acet, and  $\text{SnCl}_2$  are US\$ 0.12  $\text{g}^{-1}$ , US\$ 0.06  $\text{g}^{-1}$ , and US\$ 0.15  $\text{g}^{-1}$ , respectively. A 2-ME solvent is also inexpensive, costing only US\$ 16  $\text{L}^{-1}$ .

#### 12.2.2.2 Stabilizer

To obtain thick films after a few coating cycles, a solution with a high concentration of metal elements (1.75 M) was targeted. The metal sources are not dissolved at the same time in the solvent of 2-ME without stabilizer(s). To dissolve the metal sources of Cu-Acet,

Zn-Acet, and  $\text{SnCl}_2$  completely at a time, it was necessary to add to the solvent a stabilizer of monoethanolamine (MEA) or ammonium acetate with  $\text{H}_2\text{O}$ . Ammonium acetate with  $\text{H}_2\text{O}$  could dissolve metal sources. However, metal sources must be added to the solvent little by little in order to obtain a high-concentration (1.75 M) solution. On the other hand, a stabilizer of MEA could be helpful to easily dissolve high-concentration metal sources into the 2-ME. To obtain thick films in a few coating cycles we need to use a high-concentration solution; however, this erodes the Mo-coating. A low-concentration solution is therefore also necessary and ammonium acetate with  $\text{H}_2\text{O}$  was suitable for the stabilizer of the low-concentration solution. Details of Mo erosion and the low-concentration solution are described in Section 12.3.3.

Here we describe the preparation of solutions in detail. Cu-Acet, Zn-Acet, and  $\text{SnCl}_2$  were dissolved in 30 mL of 2-ME. The chemical composition of metal sources was Cu/(Zn+Sn) = 1.0 for a stoichiometric sample or <1.0 for a Cu-poor sample, Zn/Sn = 1.0 for a stoichiometric sample or >1.0 for a Zn-rich sample. The concentration of metal sources was 1.75 M or 0.35 M. For the 1.75 M solution, 3.5 mL of MEA was added as the stabilizer; for the 0.35 M solution, 0.55 M of ammonium acetate and 1 mL of  $\text{H}_2\text{O}$  were added as the stabilizers. Those solutions were stirred at 45°C for 1 hour to dissolve the metal sources.

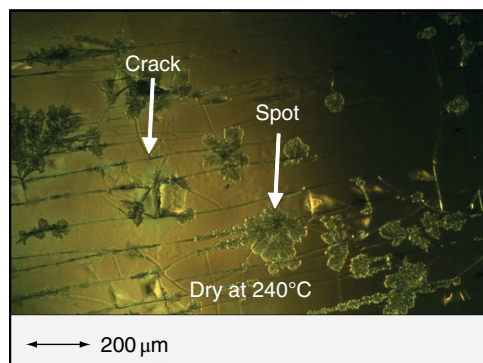
## 12.3 Preparation of CZTS Thin Films by Sol-Gel Sulfurization Method

### 12.3.1 Preparation of Precursors on Soda-Lime Glass

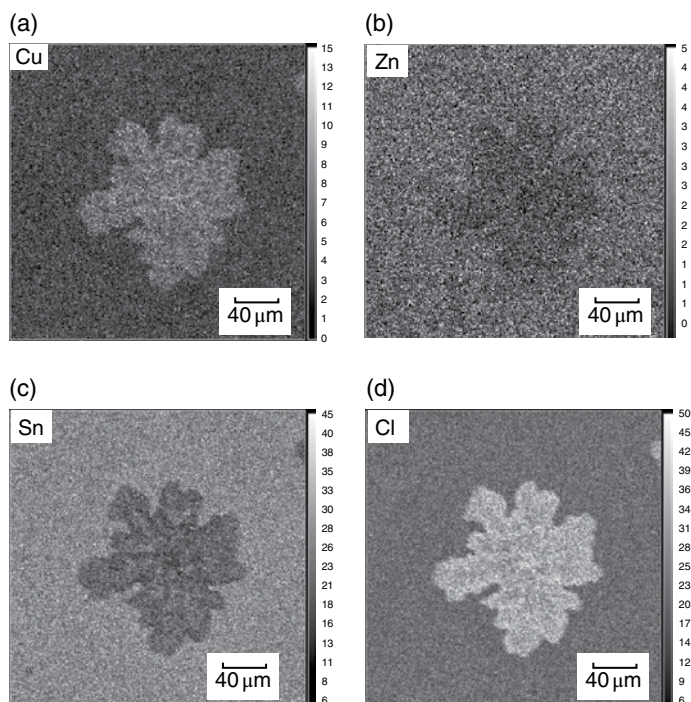
CZTS thin films were prepared by: (1) coating the solution on a substrate by spin coating; (2) drying the coated substrate in the air by a hot-plate; (3) repeating the coating/drying cycle several times to obtain a rather thick film on a substrate, which we may call a precursor; and (4) sulfurizing the precursor, that is, annealing the precursor in the  $\text{H}_2\text{S}+\text{N}_2$  atmosphere.

To obtain high-quality CZTS thin films it is important to deposit smooth and hole-free precursors. We investigated whether the precursor surface morphology depends on the drying temperature. Chemical composition of the coating solution was stoichiometric, Cu/(Zn+Sn) = 1.0, and Zn/Sn = 1.0, and the concentration of the metallic elements was 1.75 M. The coating solution was dropped onto the SLG substrate rotating at 3000 rpm for 30 s. After deposition by spin coating, the coated film was dried in air at 160–300°C for 5 min. The coating/drying cycle was repeated 5 times.

The precursors dried at 240–280°C had many spots and cracks as shown in Figure 12.2 [15]. It is clearly shown in Figure 12.3 that the spots consisted of compounds formed between copper and chlorine. Since the precursors were dried at a temperature lower than 280°C, the chlorine remained in the precursors without evaporation. The precursors dried at 180–280°C had many cracks while the precursors dried at 160°C or higher than 300°C had no cracks. The boiling points of 2-ME and MEA are 124.5°C and 171°C, respectively. While only 2-ME was evaporated at 160°C, at a higher drying temperature both 2-ME and MEA were evaporated immediately. At a lower drying temperature, 2-ME was evaporated fast while MEA evaporated slowly. The origin of the crack may be related to the time delay in the evaporation process of MEA. To verify the origin of the cracks, further study is necessary.



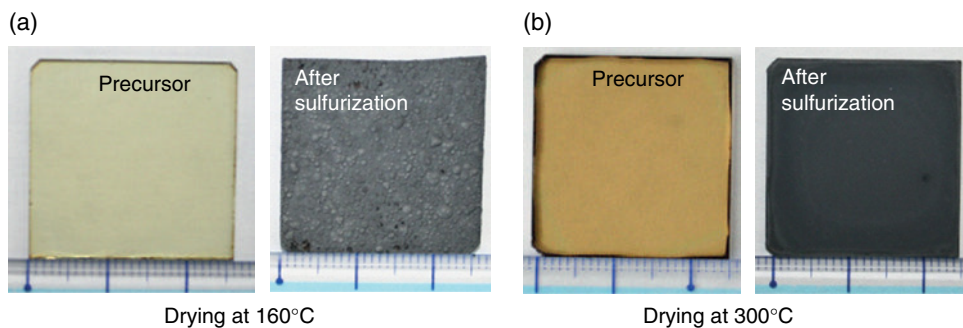
**Figure 12.2** Precursor dried at 240°C. There are many cracks and spots on the surface. Reproduced with permission from [15]. Copyright (2008), The Japan Society of Applied Physics



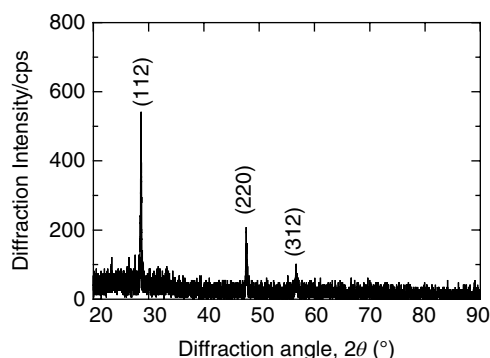
**Figure 12.3** EDX images of the spot. For each image, white and black contrasts represent higher and lower concentration, respectively

### 12.3.2 Sulfurization of the Precursors

The precursors dried at 160°C and 300°C had a very smooth surface. These precursors were then annealed at 500°C in  $\text{H}_2\text{S}$  (5%)+ $\text{N}_2$  atmosphere for 1 hour. Before and after annealing, they were heated and cooled at a rate of  $2^\circ\text{C min}^{-1}$ .



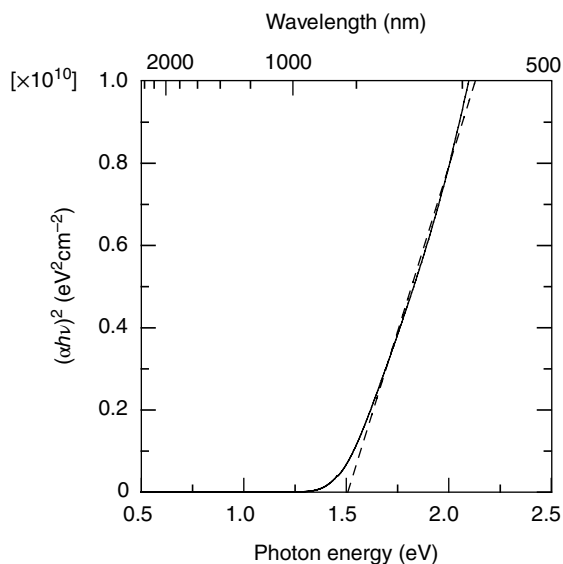
**Figure 12.4** Surface images of precursors before and after sulfurization, with drying temperatures of (a) 160°C and (b) 300°C



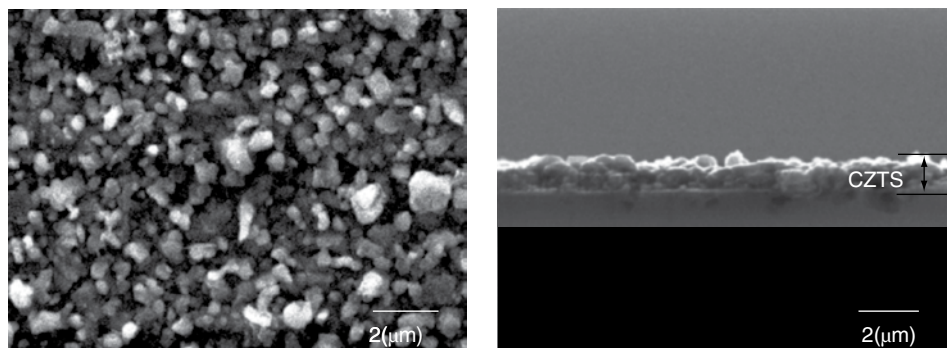
**Figure 12.5** XRD of the sulfurized precursor dried at 300°C

Figure 12.4 depicts surface images of precursors before and after sulfurization. The drying temperatures for Figure 12.4a and b are 160°C and 300°C, respectively. As shown in Figure 12.4a, for the precursor dried at 160°C the sulfurized film has a very rough surface and flakes off easily from the substrate. There is no evaporation of MEA from the precursor at 160°C because its boiling point is 171°C. However, for the short drying period of 5 min 2-ME may not be evaporated completely at 160°C. The remaining organic materials therefore evaporate during sulfurization and the sulfurized film then flakes off easily.

Figure 12.5 shows the X-ray diffraction (XRD) pattern of the sulfurized precursor dried at 300°C. This shows the three XRD peaks which can be attributed to (112), (220), and (312) reflections of CZTS crystal. Chemical composition of the sulfurized precursor was Cu:Zn:Sn:S = 24:12:14:50. The chemical composition of the sulfurized precursor was almost stoichiometric, and the chemical composition of the sulfurized precursor reflects that of the coating solution. Figure 12.6 shows the plot of  $(\alpha h\nu)^2$  v.  $h\nu$  plot, where  $\alpha$  ( $\text{cm}^{-1}$ ) and  $h\nu$  (eV) represent the absorption coefficient and photon energy, respectively [8]. As shown in Figure 12.6 the sulfurized precursor shows a feature of direct band-gap semiconductors; the band-gap energy was 1.50 eV and the absorption coefficient in the visible region is  $>10^4$   $\text{cm}^{-1}$ . Figure 12.7 depicts the surface image and cross-section of a sulfurized precursor.



**Figure 12.6**  $(\alpha h\nu)^2$  v.  $h\nu$  plot of the sulfurized precursor dried at 300°C

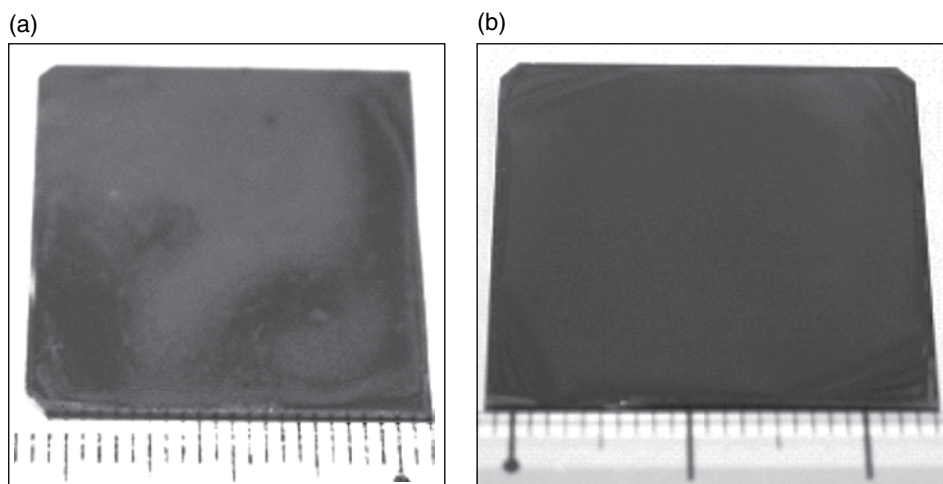


**Figure 12.7** Surface and cross-section images of sulfurized precursor dried at 300°C

As shown, the film is constructed with sub-micron particles and the film thickness is c. 1.1  $\mu\text{m}$ . Consequently, the precursor dried at 300°C becomes a CZTS thin film by sulfurization process, which can be applied to the absorber layer of thin-film solar cells.

### 12.3.3 Preparation of CZTS Thin Films on Mo by Sol-gel Sulfurization Method

The Mo thin film was deposited at a thickness of c. 1  $\mu\text{m}$  on a SLG substrate by electron beam evaporation. Chemical composition ratios of the solution were  $\text{Cu}/(\text{Zn}+\text{Sn}) = 1.0$  and  $\text{Zn}/\text{Sn} = 1.0$  and concentration of the metal sources was 1.75 M.



**Figure 12.8** Macroscopic image of the precursor which is deposited from the 1.75 M solution onto the (a) Mo/SLG and (b) 0.35 M solution with ammonium acetate having  $H_2O$ -coated Mo/SLG. For color details, please see color plate section

**Table 12.1** Coating solutions on the Mo/SLG

Sample name	Solvent, stabilizer	Metal source
Cu-coat	2-metho 30 mL, MEA 0.7 mL	Cu-Acet, 0.35 M
Zn-coat	2-metho 30 mL, MEA 0.7 mL	Zn-Acet, 0.35 M
Sn-coat	2-metho 30 mL, MEA 0.7 mL	Sn-Acet, 0.35 M
MEA coat	2-metho 30 mL, MEA 0.7 mL	None
2-ME coat	2-metho 30 mL	None

The coating/drying process was as described in Section 12.3.1. Figure 12.8a depicts the surface image of the precursor deposited from the 1.75 M solution onto the Mo/SLG. As seen in Figure 12.8a there are spots on the Mo surface, indicating that the coating solution erodes Mo.

To investigate the cause of the erosion, solutions listed in Table 12.1 were coated on the Mo/SLG and annealed in air at  $500^{\circ}\text{C}$  for 5 min. After annealing, only the Cu-coat and Sn-coat samples had holes. Since the Cu-coat film had larger holes, it was determined to be the main cause of the Mo erosion. The Cu-coat film after annealing exhibits XRD peaks attributed to  $\text{CuMoO}_4$ , indicating that the Cu in the solution reacts with Mo.

To prevent erosion, a solution which contains no or little Cu and Sn was coated between the 1.75 M solution and the Mo/SLG. The Zn-coat solution shown in Table 12.1 seems to prevent the erosion. If the Zn-coat solution is however used, control of the chemical composition of the precursor would be difficult because the precursor should be a stacked layer of Cu-Zn-Sn/Zn/Mo/SLG as mentioned before.

A low-concentration (0.35 M) solution is another candidate for an anti-erosion solution. As described in Section 12.2.2, MEA or ammonium acetate with  $H_2O$  could be a stabilizer for the 0.35 M solution. Both the 0.35 M Cu-coat and Sn-coat solutions were examined.



The Mo/SLG substrates were soaked in the 0.35 M solution with MEA for 24 h, resulting in many holes in the precursor. On the other hand, no holes were observed when Mo/SLG was soaked in the solution with ammonium acetate and  $H_2O$ . Figure 12.8b depicts the surface image of the precursor which was prepared by coating the 1.75 M solution after coating with the anti-erosion solution. Compared to Figure 12.8a, Figure 12.8b exhibits a very smooth surface without spots. The macroscopic image shown in Figure 12.8a appears to be grayish because the solution reacts with Mo, while that of Figure 12.8b is greenish.

## 12.4 Chemical Composition Dependence

### 12.4.1 Why is Chemical Composition Important?

It is well known that chemical composition of the CZTS thin film is very important for high-efficiency CZTS solar cells. Many workers reported that higher efficiencies were obtained using Cu-poor and Zn-rich CZTS absorber layers [16, 17]. Chen *et al.* attributed these findings to the fact that Cu-poor conditions enhance the formation of Cu vacancies which give rise to shallow acceptors in CZTS, while Zn-rich conditions suppress the substitution of Cu at Zn sites which gives rise to relatively deep acceptors [18]. We investigated whether the chemical composition of the CZTS thin films deposited by the sol-gel sulfurization method could be controlled by varying the chemical composition of the coating solution. We also determined the influence of the chemical composition of the coating solution on the properties of CZTS thin films.

### 12.4.2 Sample Preparation

Preparation conditions for CZTS thin films were as follows. Mo/SLG and SLG were used as substrates. The SLG substrate was used for characterizing the optical properties of the thin films. The coating solutions were Cu-poor and Zn-rich with chemical compositions of  $Cu/(Zn+Sn) = 0.73$ – $1.00$  and  $Zn/Sn = 1.15$ . In addition, a stoichiometric coating solution of  $Cu/(Zn+Sn) = 1.00$  and  $Zn/Sn = 1.00$  was used for comparison. Table 12.2 lists the chemical compositions of the coating solutions used [19]. Concentrations of metal sources in the coating solutions were 1.75 M and 0.35 M. The solutions were spin-coated on the substrate at 3000 rpm for 30 s and then dried at  $300^\circ C$  for 5 min. The 0.35 M solution was coated three times to prevent erosion of Mo and the 1.75 M solution was coated five times.

**Table 12.2** Chemical composition of sol-gel solutions and CZTS thin films [19]

Sample name	Sol-gel solution		CZTS thin film					
	Cu/(Zn+Sn)	Zn/Sn	Cu/(Zn+Sn)	Zn/Sn	Cu (at%)	Zn (at%)	Sn (at%)	S (at%)
CZTS073	0.73	1.15	0.91	1.23	22.9	13.8	11.2	52.2
CZTS080	0.80	1.15	0.92	1.17	22.5	13.2	11.3	52.9
CZTS084	0.84	1.15	0.95	1.18	22.7	12.9	11.1	53.4
CZTS087	0.87	1.15	0.97	1.10	23.5	12.7	11.5	52.3
CZTS100	1.00	1.15	0.99	1.13	23.3	12.4	11.1	53.3
CZTS-St	1.00	1.00	1.03	1.03	22.7	11.1	10.8	55.3

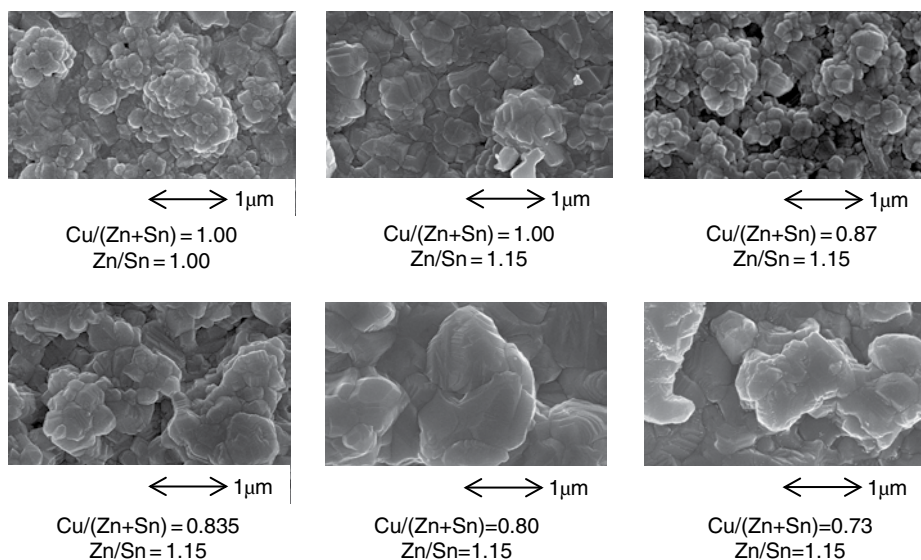
Since SLG is not eroded by the 1.75 M solution, the same coating procedure was applied to SLG substrates which were used to characterize the optical properties of the thin films. The precursors were sulfurized in a  $\text{H}_2\text{S}$  (5%) +  $\text{N}_2$  atmosphere at  $500^\circ\text{C}$  for 1 h.

### 12.4.3 Compositional Dependence of the Properties of CZTS Thin Films

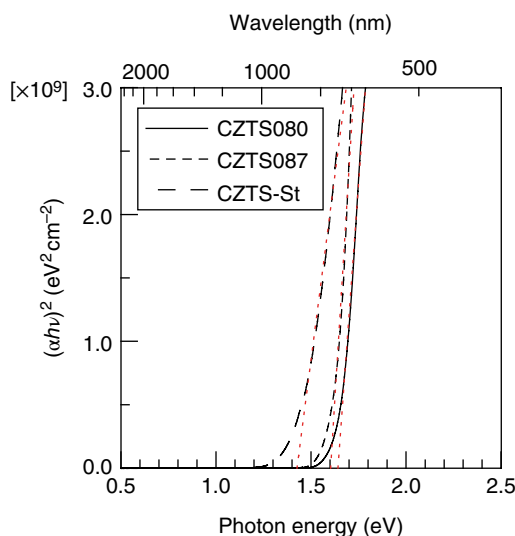
Table 12.2 lists the chemical compositions of the CZTS thin films [19], which was different from that of the coating solutions. However, the composition ratio  $\text{Cu}/(\text{Zn}+\text{Sn})$  of CZTS thin film was approximately proportional to that of the coating solution. The  $\text{Zn}/\text{Sn}$  ratio of both coating solutions and CZTS thin films was larger than 1.0. In addition, chemical composition of the CZTS thin films deposited by this method can be roughly controlled by varying the chemical composition of the coating solution, although  $\text{Cu}/(\text{Zn}+\text{Sn})$  of the CZTS thin films decreased more gradually than that of the coating solutions. This indicates that the amount of Zn and/or Sn in the CZTS thin films decreases with increasing Cu ratio in the coating solution. The reduction in the amounts of Zn and Sn is considered to be due to evaporation.

Although chemical composition of the films can be changed by using different coating solutions, there is no observable difference in the XRD patterns obtained from the CZTS thin films.

Figure 12.9 depicts the surface images of the CZTS thin films with various chemical compositions [19]. Here, samples CZTS-st, CZTS100, and CZTS087 consist of small grains of c.  $0.1\ \mu\text{m}$  in size. The grain size of the CZTS films increased as the  $\text{Cu}/(\text{Zn}+\text{Sn})$  ratio of coating solution decreased. The grain size of samples CZTS080 and CZTS073 was larger than  $1\ \mu\text{m}$ .



**Figure 12.9** SEM images of CZTS thin films. The chemical composition ratio of sol-gel solutions was varied. Reproduced from [19]. With permission from Elsevier



**Figure 12.10**  $(\alpha h\nu)^2$  v.  $h\nu$  of CZTS thin films of varying chemical composition. Reproduced from [19]. With permission from Elsevier

Since CuSe (whose melting point is low) works as a flux in the synthesis of CIGS and CIS thin films, their grain sizes tend to be enlarged when Cu-rich conditions are met [20, 21]. CIGS and CIS films are therefore first deposited under a Cu-rich condition and then excess CuSe is removed by KCN etching. In contrast, a Cu-poor condition is rather favorable to increase grain sizes of CZTS films prepared by the sol-gel sulfurization method. As mentioned above, Zn and Sn compositions decreased during the sulfurization process. In the precursor, Zn or Sn could exist as hydroxide, oxide, or other complexes. These Zn or Sn complexes could melt during the sulfurization process and would therefore work as fluxes, resulting in the CZTS film with large grain sizes. The melted Zn or Sn complexes evaporate at a later stage of sulfurization process.

As depicted in Figure 12.9 and listed in Table 12.2, the CZTS thin films are categorized into three groups: Cu-poor with large grain sizes; slightly Cu-poor with small grain sizes; and stoichiometric. Figure 12.10 depicts the plots of  $(\alpha h\nu)^2$  v.  $h\nu$  for Cu-poor CZTS080, slightly Cu-poor CZTS087, and stoichiometric CZTS-st [19]. Band-gap energy becomes larger as the Cu content of the film decreases. The band-gap energy of CZTS080, CZTS087, and CZTS-st were 1.64, 1.60, and 1.43 eV, respectively. Suresh Babu *et al.* investigated  $\text{Cu}_2\text{ZnSnSe}_4$  (CZTSe), analogous to CZTS, in terms of the chemical composition ratio of  $\text{Cu}/(\text{Zn}+\text{Sn})$  and reported that band-gap energy of CZTSe shifts toward a lower energy side as  $\text{Cu}/(\text{Zn}+\text{Sn})$  increases [22]. They attributed the origin of the shift to changes in the extent of  $p$ - $d$  hybridization between Cu  $d$ -levels and Se  $p$ -levels. An antibonding of Cu 3 $d$  and Se 4 $p$  orbitals are responsible for constructing the valence band maximum (VBM) of CZTSe [23]. The VBM of CZTS is an antibonding state of the Cu 3 $d$  and S 3 $p$  orbital [24]. The shift in band-gap energy mentioned above might therefore also be attributed to changes in  $p$ - $d$  hybridization between Cu  $d$ -level and S  $p$ -levels.

## 12.5 H<sub>2</sub>S Concentration Dependence

### 12.5.1 Why is H<sub>2</sub>S Concentration Important?

The precursor, which does not contain any S constituent, is annealed in a H<sub>2</sub>S+N<sub>2</sub> atmosphere. The H<sub>2</sub>S gas is expensive, toxic, and causes offensive odors, so the use of low-concentration H<sub>2</sub>S gas is more beneficial than that of high-concentration. However, this may cause an S deficiency in the CZTS thin film. The S vacancies in the CZTS thin film are expected to affect its optical and electrical properties and eventually the performance of solar cells. Here we investigate how film growth depends on the H<sub>2</sub>S concentration during the sulfurization process.

### 12.5.2 Sample Preparation

Preparation conditions for CZTS thin films include the following: Mo/SLG and SLG were used as substrates; SLG substrate was used for evaluating the optical properties of the thin films; coating solution was Cu-poor and Zn-rich, that is, with a chemical composition of Cu/(Zn+Sn) = 0.87 and Zn/Sn = 1.15; the precursors were sulfurized at 500°C for 1 hour in the H<sub>2</sub>S + N<sub>2</sub> atmosphere; and the H<sub>2</sub>S concentration was varied from 0.5% to 20%.

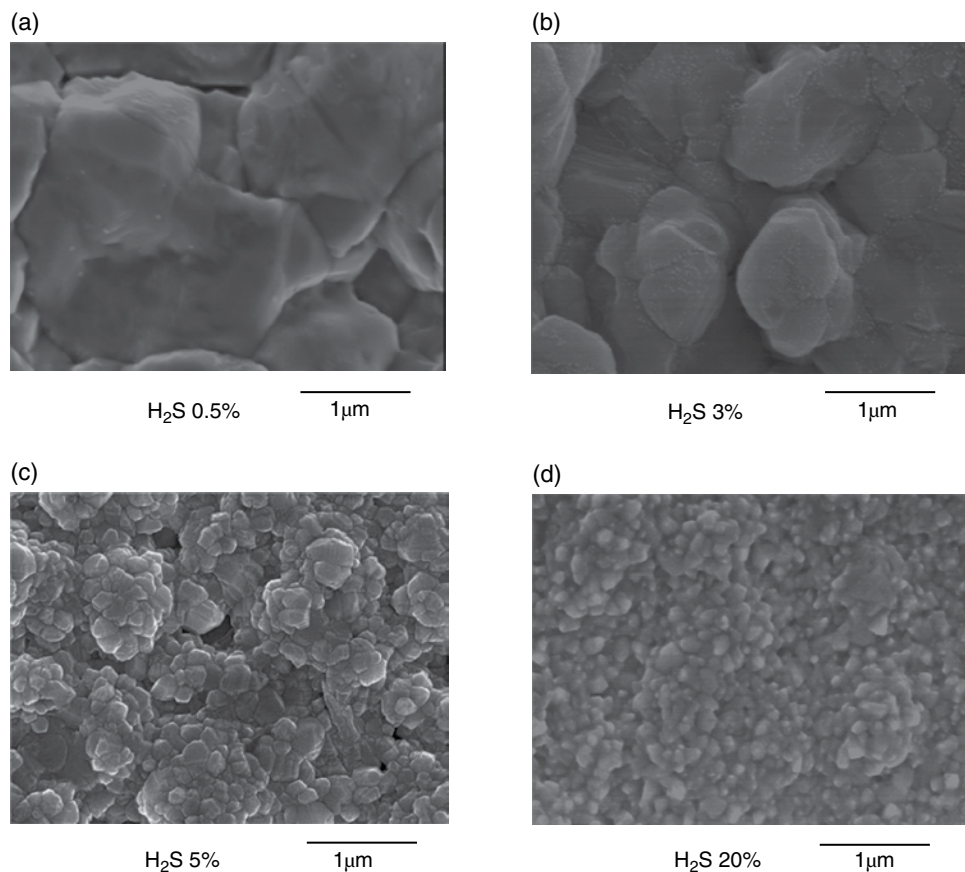
### 12.5.3 H<sub>2</sub>S Dependence of CZTS Properties

Table 12.3 lists the chemical composition of the CZTS thin films as a function of H<sub>2</sub>S concentration. Although this composition differed from that of the coating solution, that is, Cu/(Zn+Sn) = 0.87 and Zn/Sn = 1.15, all of the films tended to be Cu-poor and Zn-rich. Contrary to our expectation that low H<sub>2</sub>S concentration causes S-deficient CZTS thin films, the chemical composition of S was 44.8–48.8% independent of the H<sub>2</sub>S concentration.

Figure 12.11 shows the SEM images of CZTS thin films which were sulfurized under different H<sub>2</sub>S concentrations [25, 26]. The CZTS thin films sulfurized under a H<sub>2</sub>S concentration higher than 5% were composed of grains of c. 100 nm in size. On the other hand, the CZTS thin films sulfurized under a H<sub>2</sub>S concentration lower than 3% were composed of packed grains larger than 1 μm in size.

**Table 12.3** Chemical composition of the CZTS thin films as a function of H<sub>2</sub>S concentration [25, 26]

H <sub>2</sub> S (%)	Atomic percent				Ratio		
	Cu	Zn	Sn	S	Cu/(Zn+Sn)	Zn/Sn	S/metal
0.5	27.6	13.8	12.8	45.7	1.04	1.09	0.84
1	25.6	13.6	12.0	48.8	1.00	1.13	0.95
3	25.2	16.0	12.0	46.8	0.90	1.32	0.88
5	27.2	15.1	13.0	44.8	0.97	1.16	0.81
10	26.2	15.3	12.6	46.0	0.94	1.22	0.85
20	25.0	15.5	11.8	47.6	0.92	1.31	0.91



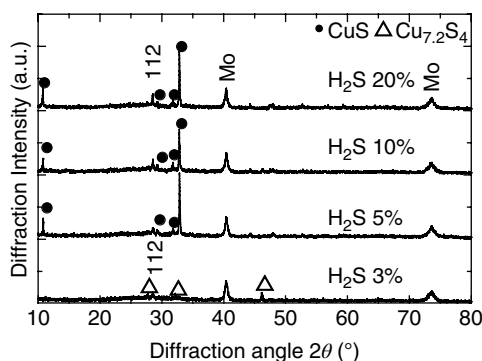
**Figure 12.11** Surface SEM images with varying  $H_2S$  concentration. Reproduced with permission from [25], Copyright (2008), The Japan Society of Applied Physics, and from [26], with permission from Elsevier

To investigate the effect of gas concentration of  $H_2S$ , sulfurization at  $250^\circ\text{C}$  and  $400^\circ\text{C}$  for 1 min under several  $H_2S$  concentrations was performed as shown in Table 12.4 [26]. For sulfurization at  $250^\circ\text{C}$ , the chemical composition of S increased with  $H_2S$  concentration. When  $H_2S$  concentration increases from 3% to 5%, the increasing rate of S composition in the annealed film was larger than at higher  $H_2S$  concentrations. The amount of S incorporated into the film was therefore nearly saturated at  $H_2S$  concentrations higher than 5%. Although the ratio of S/metal in the film was less than 1 when sulfurized at  $250^\circ\text{C}$ , it was almost unity and independent of the  $H_2S$  concentration when sulfurized at  $400^\circ\text{C}$ .

Figure 12.12 shows XRD patterns of thin films sulfurized at  $250^\circ\text{C}$  for 1 min under several  $H_2S$  concentrations [26]; solid circles and triangles indicate XRD peaks due to CuS and  $Cu_{7.2}S_4$ , respectively. The XRD patterns of thin films sulfurized under  $H_2S$  concentration higher than 5% clearly show the peaks which can be attributed to CuS. On the other hand, the XRD pattern of the thin film sulfurized under 3%  $H_2S$  shows peaks attributed to  $Cu_{7.2}S_4$ . In other words, the low concentration of  $H_2S$  gives rise to a low sulfide of copper,

**Table 12.4** Composition of CZTS thin films as a function of  $H_2S$  concentration at 250°C and 400°C for 1 min [26]

Temperature (°C)	$H_2S$ (%)	Atomic percent				Ratio		
		Cu	Zn	Sn	S	Cu/(Zn+Sn)	Zn/Sn	S/metal
250	3	35.5	21.7	14.1	28.7	1.10	1.53	0.40
	5	37.6	14.6	11.9	35.9	1.42	1.23	0.56
	10	42.3	11.9	9.2	36.7	2.06	1.28	0.58
	20	36.4	15.7	8.1	39.8	1.55	1.94	0.66
400	3	26.9	12.1	11.8	49.1	1.13	1.03	0.97
	5	24.2	14.1	11.7	50.0	0.94	1.24	1.00
	10	26.3	13.2	12.2	48.3	1.04	1.09	0.93
	20	26.3	13.5	12.1	48.1	1.03	1.12	0.93

**Figure 12.12** XRD patterns of thin films sulfurized at 250°C for 1 min under several  $H_2S$  concentrations. Reproduced with permission from [26]. With permission from Elsevier

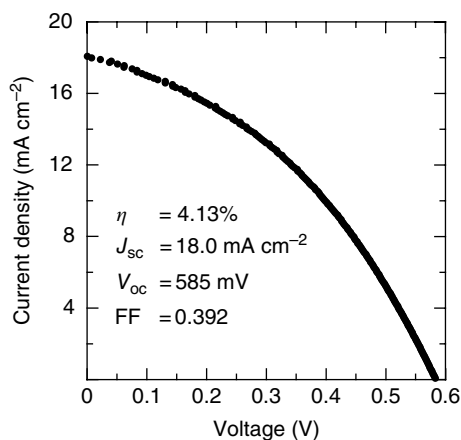
while the high concentration of  $H_2S$  yields a persulfide of copper. The XRD patterns of thin films sulfurized at 500°C for 1 hour did not exhibit either CuS or  $Cu_{7.2}S_4$  peaks independent of the  $H_2S$  concentration.

As shown in Figure 12.11 the grain size of CZTS thin films sulfurized under 3%  $H_2S$  concentration was almost 10 times larger than that under  $H_2S$  concentration equal to or higher than 5%. The larger grain size is considered to be due to the presence of a  $Cu_{7.2}S_4$  phase, which might be expected to lead to a higher short-circuit current density of solar cells.

## 12.6 CZTS Solar Cell Prepared by Non-vacuum Processes

In our laboratory, all semiconductor layers of the CZTS thin-film solar cells were prepared under a non-vacuum condition and consisted of an Al/ZnO:Al/CdS/CZTS/Mo/SLG structure.

The precursor layer was first deposited by sol-gel process. Chemical composition ratios of the coating solution were controlled as  $Cu/(Zn+Sn) = 0.87$  and  $Zn/Sn = 1.15$ . The



**Figure 12.13** J–V characteristic of the best-performing solar cell of our laboratory

precursor was then sulfurized in  $\text{H}_2\text{S}$  (3%) +  $\text{N}_2$  atmosphere at  $500^\circ\text{C}$  for 1 hour. Film thickness of the CZTS absorber layer was c.  $1.2 \mu\text{m}$ . Before depositing a CdS buffer layer, the CZTS absorber layer was etched in 35% HCl for 5 min. The buffer layer was deposited by chemical bath deposition (CBD) from an aqueous solution of  $\text{CdI}_2$  ( $3.51 \times 10^{-3} \text{ M}$ ) and ammonia (2.90 M) at  $65^\circ\text{C}$  for 120 min. The ZnO:Al window layer was eventually deposited by the sol-gel method. Zn-Acet and 2 mol% of aluminum chloride hexahydrate were dissolved in 2-ME and MEA was added as a stabilizer. The concentration of the ZnO:Al solution was 0.35 M. This solution was spin-coated on the CdS/CZTS/Mo/SLG and dried at  $300^\circ$ . The coating/drying cycle was repeated 15 times. The resistivity of the ZnO:Al window layer was c.  $10 \Omega \text{ cm}$ . After the ZnO:Al window layer was deposited, the Al top electrode was deposited by evaporation. A typical active area of prepared CZTS cells was  $0.14 \text{ cm}^2$ .

Figure 12.13 shows the J–V characteristics of a CZTS thin-film solar cell which exhibits the highest performance in our laboratory. The solar cell demonstrated an open-circuit voltage of  $V_{oc} = 585 \text{ mV}$ , short-circuit current density of  $J_{sc} = 18.0 \text{ mA cm}^{-2}$ , fill factor  $FF = 0.392$ , and conversion efficiency of  $\eta = 4.13\%$ . In particular, the fill factor of our cell is smaller than 0.658, that is, the fill factor of the CZTS thin-film solar cell prepared by coevaporation [27]. One of the reasons for our low fill factor is thought to be due to the high resistivity of our window layer. When the drying temperature for ZnO:Al deposition process is higher than c.  $500^\circ\text{C}$ , the resistivity of ZnO:Al can be made lower than  $10^{-2} \Omega \text{ cm}$ . However, these high drying temperatures cause excess CdS diffusion into CZTS absorber layers, which in turn reduces FF. Low values of FF might also be caused by the presence of the impurity Cl in the absorber as a tin chloride solution is used.

## References

- [1] Ito, K. & Nakazawa, T. (1988) Electrical and optical properties of stannite-type quaternary semiconductor thin films. *Japanese Journal of Applied Physics*, **27**, 2094–2097.
- [2] Katagiri, H., Sasaguchi, N., Hando, S., Hoshino, S., Ohashi, J. & Yokota, T. (1997) Preparation and evaluation of  $\text{Cu}_2\text{ZnSnS}_4$  thin films by sulfurization of EB evaporated precursors. *Solar Energy Materials and Solar Cells*, **49**, 407–414.

- [3] Katagiri, H. (2005)  $\text{Cu}_2\text{ZnSnS}_4$  thin film solar cells. *Thin Solid Films*, **480–481**, 426–432.
- [4] Katagiri, H., Jimbo, K., Yamada, S., Kamiura, T., Maw, W. S., Fukano, T. & Motohiro, T. (2008) Enhanced conversion efficiencies of  $\text{Cu}_2\text{ZnSnS}_4$ -based thin film solar cells by using preferential etching technique. *Applied Physics Express*, **1**, 041201.
- [5] Katagiri, H., Jimbo, K., Maw, W. S., Oishi, K., Yamazaki, M., Araki, H. & Takeuchi, A. (2009) Development of CZTS-based thin film solar cells. *Thin Solid Films*, **517**, 2455–2460.
- [6] Kato, T., Hiroi, H., Sakai, N., Muraoka, S. & Sugimoto, H. (2012) Characterization of front and back interfaces on  $\text{Cu}_2\text{ZnSnS}_4$  thin-film solar cells. In *Proceedings of the 27th European Photovoltaic Solar Energy Conference and Exhibition (EU-PVSEC)*, pp. 2236–2239.
- [7] Nakayama, N. & Ito, K. (1996) Sprayed films of stannite  $\text{Cu}_2\text{ZnSnS}_4$ . *Applied Surface Science*, **92**, 171–175.
- [8] Tanaka, K., Moritake, N. & Uchiki, H. (2007) Preparation of  $\text{Cu}_2\text{ZnSnS}_4$  thin films by sulfurizing sol-gel deposited precursors. *Solar Energy Materials and Solar Cells*, **91**, 1199–1201.
- [9] Tanaka, K., Oonuki, M., Moritake, N. & Uchiki, H. (2009)  $\text{Cu}_2\text{ZnSnS}_4$  thin film solar cells prepared by non-vacuum processing. *Solar Energy Materials and Solar Cells*, **93**, 583–587.
- [10] Sakka, S. (1985) Sol-gel synthesis of glasses: present and future. *American Ceramic Society Bulletin*, **64**, 1463–1466.
- [11] Kavanagh, Y. & Cameron, D.C. (2001) Zinc sulfide thin films produced by sulfidation of sol-gel deposited zinc oxide. *Thin Solid Films*, **398–399**, 24.
- [12] Kaur, J., Kumar, R. & Bhatnagar, M.C. (2007) Effect of indium-doped  $\text{SnO}_2$  nanoparticles on  $\text{NO}_2$  gas sensing properties. *Sensors and Actuators B*, **126**, 478–484.
- [13] Yang, J., Weng, W. & Ding, Z. (1995) The drawing behavior of Y-Ba-Cu-O sol from non-aqueous solution by a complexing process. *Journal of Sol-Gel Science and Technology*, **4**, 187–193.
- [14] Lee, J.-H. & Park, B.-O. (2003) Transparent conducting  $\text{ZnO:Al}$ , In and Sn thin films deposited by the sol-gel method. *Thin Solid Films*, **426**, 94–99.
- [15] Tanaka, K., Moritake, N., Oonuki, M. & Uchiki, H. (2008) Pre-annealing of precursors of  $\text{Cu}_2\text{ZnSnS}_4$  thin films prepared by sol-gel sulfurizing method. *Japanese Journal of Applied Physics*, **47**, 598–601.
- [16] Katagiri, H., Jimbo, K., Maw, W. S., Oishi, K., Yamazaki, M., Araki, H. & Takeuchi, A. (2009) Development of CZTS-based thin film solar cells. *Thin Solid Films*, **517**, 2455–2460.
- [17] Ennaoui, A., Lux-Steiner, M., Weber, A., Abou-Ras, D., Kötschau, I., Schock, H.-W., Schurr, R., Hölzing, A., Jost, S., Hock, R., Voß, T., Schulze, J. & Kirbs, A. (2009)  $\text{Cu}_2\text{ZnSnS}_4$  thin film solar cells from electroplated precursors: Novel low-cost perspective. *Thin Solid Films*, **517**, 2511–2514.
- [18] Chen, S., Gong, X.G., Walsh, A. & Wei, S. (2010) Defect physics of the kesterite thin-film solar cell absorber  $\text{Cu}_2\text{ZnSnS}_4$ . *Applied Physics Letters*, **96**, 021902.
- [19] Tanaka, K., Fukui, Y., Moritake, N. & Uchiki, H. (2011) Chemical composition dependence of morphological and optical properties of  $\text{Cu}_2\text{ZnSnS}_4$  thin films deposited by sol-gel sulfurization and  $\text{Cu}_2\text{ZnSnS}_4$  thin film solar cell efficiency. *Solar Energy Materials and Solar Cells*, **95**, 838–842.
- [20] Gabor, A. M., Tuttle, J. R., Albin, S. S., Contrears, M. A. & Noufi, R. (1994) High-efficiency  $\text{CuInGa}_{1-x}\text{Se}_2$  solar cells made from  $(\text{In}_x\text{Ga}_{1-x})_2\text{Se}_3$  precursor film. *Applied Physics Letters*, **65**, 198–200.
- [21] Michkeksen, R. A., Chen, W. S., Hsiao, Y. R. & Lowe, V. E. (1984) Polycrystalline thin-film  $\text{CuInSe}_2/\text{CdZnS}$  solar cells. *IEEE Transactions on Electron Devices*, **31**, 542–546.
- [22] Suresh Babu, G., Kishore Kumar, Y.B., Uday Bhaskar, P. & Raja Vanjari, S. (2010) Effect of Cu/(Zn+Sn) ratio on the properties of co-evaporated  $\text{Cu}_2\text{ZnSnSe}_4$  thin films. *Solar Energy Materials and Solar Cells*, **94**, 221–226.
- [23] Nakamura, S., Maeda, T. & Wada, T. (2009) Electronic structure of stannite-type  $\text{Cu}_2\text{ZnSnSe}_4$  by first principles calculations. *Physica Status Solidi C*, **6**, 1261–1265.
- [24] Paier, J., Asahi, R., Nagoya, A. & Kresse, G. (2009)  $\text{Cu}_2\text{ZnSnS}_4$  as a potential photovoltaic material: A hybrid Hartree-Fock density functional theory study. *Physical Review B*, **79**, 115126.



- [25] Maeda, K., Tanaka, K., Nakano, Y., Fukui, Y. & Uchiki, H. (2011)  $\text{H}_2\text{S}$  concentration dependence of properties of  $\text{Cu}_2\text{ZnSnS}_4$  thin film prepared under non vacuum condition. *Japanese Journal of Applied Physics*, **50**, 05FB09.
- [26] Maeda, K., Tanaka, K., Fukui, Y. & Uchiki, H. (2011) Influence of  $\text{H}_2\text{S}$  concentration on the properties of  $\text{Cu}_2\text{ZnSnS}_4$  thin films and solar cells prepared by sol-gel sulfurization. *Solar Energy Materials and Solar Cells*, **95**, 2855–2860.
- [27] Shin, B., Gunawan, O., Zhu, Y., Bojarczuk, N. A., Chey, S. J. & Guha, S. (2011) Thin film solar cell with 8.4% power conversion efficiency using an earth-abundant  $\text{Cu}_2\text{ZnSnS}_4$  absorber. *Progress in Photovoltaics: Research and Applications*, **21**(1), 72–76.



# 13

## Growth of CZTS-Based Monograins and Their Application to Membrane Solar Cells

*Enn Mellikov, Mare Altosaar, Marit Kauk-Kuusik, Kristi Timmo, Dieter Meissner,  
Maarja Grossberg, Jüri Krustok and Olga Volobujeva*

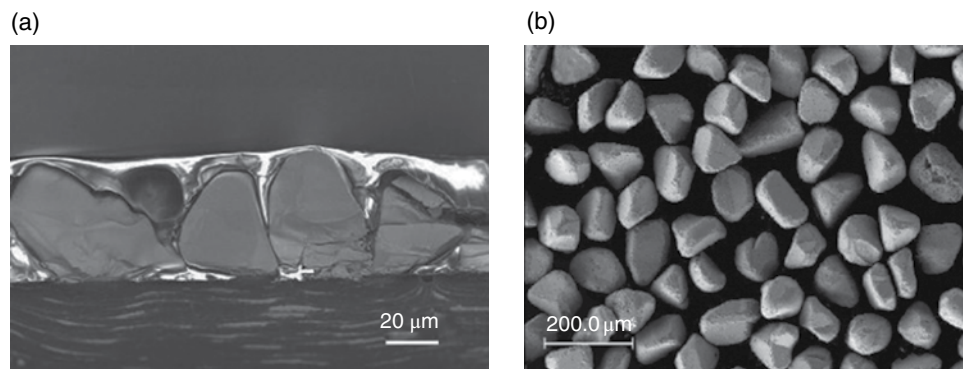
*Department of Materials Science, Tallinn University of Technology, Ehitajate tee 5,  
19086 Tallinn, Estonia*

### 13.1 Introduction

The idea of producing solar cells from powder materials is nearly as old as the history of modern silicon-based solar cells. Just three years after AT&T Bell Lab's Chapin, Fuller, and Pearson released their first commercially attractive silicon solar cell [1], Hoffman's Electronics patented a method to produce solar modules from silicon powders [2]. Based on Hoffman's Electronics' patents, Ties Siebold te Velde from Philips Company in Eindhoven filed the first patent on monograin membrane devices for radiation detection, use in a solar battery, a LED, etc. [3]. Eighteen further patents had been filed by 1973, specifying methods of membrane production as well as new applications such as the production of printed circuits. Philips Company continued to produce monograin membrane-based photoconductive elements containing 35–45  $\mu\text{m}$  Cu-doped CdS particles in Hamburg until the mid-1990s. Meanwhile, in the mid-1970s the technology to produce silicon spheres and insert these into an aluminum foil with appropriately placed holes had been developed at Texas Instruments in order to electrolyze a solution to store light energy as chemical energy in electrolysis products [4].

Following this first patent, several more were filed at the beginning of the 1990s. In 1985, Texas Instruments in cooperation with the Southern California Edison Company (SCE) started to develop a Spheral Solar Cell using metallurgical silicon of low purity. This device, represented by more than 40 worldwide patents, comprises tiny silicon spheres bonded between thin flexible aluminum foil substrates to form solar cells, which are then assembled into durable, lightweight modules that can be applied to virtually any surface. Kyosemi Corporation, Japan has developed Sphelar, a spherical solar-cell technology that captures sunlight in three dimensions. The technology is based on an array of single-crystalline silicon spheres, each with dimension 1–2 mm across, embedded in a transparent medium. Each sphere functions as an individual, miniature solar cell [5]. Further historical background of powder-based solar cell applications can be found in [6].

Research and development of monograin-layer (MGL) solar cells at Tallinn University of Technology (TUT) began in 1996 after a two-year period of research in the field of  $\text{CuInSe}_2$  monograin powder growth. Monograin is a single-crystalline powder particle consisting of one single crystal or several single-crystalline blocks grown into a compact grain. The cross-section of the MGL solar cell is depicted in Figure 13.1a. The MGL solar cells have a superstrate structure of graphite/MGL/CdS/ZnO/glass, where the monograin layer is a monolayer of powder grains of one size embedded into an organic resin so that the upper part of the grains remains uncovered. CdS is deposited on top of the MGL (or onto the surface of the monograins before MGL formation) by chemical bath deposition, followed by RF-sputtering of i-ZnO and conductive ZnO:Al layers. Finally, highly conductive grid contacts are evaporated on top of the ZnO window layer, and the structure is glued onto a glass or some other durable transparent substrate. For back conducting, the bottom side of the MGL is polished to remove polymer from powder crystals and to expose monograins before applying graphite contacts. Our group of authors began conducting research to create and commercialize modules of powder-based  $\text{Cu}_2\text{ZnSn}(\text{S}_x\text{Se}_{1-x})_4$  (CZTSSe) MGL solar cells in 2008 and has continued in collaboration with the TUT spin-off company *crystalsol OÜ*. A pilot production line is set up in the research and development facility of *crystalsol GmbH* in Austria.



**Figure 13.1** (a) Cross-section of monograin layer solar cell structure; and (b) SEM micrograph of a  $\text{Cu}_2\text{ZnSn}(\text{S},\text{Se})_4$  monograin powder synthesized in KI flux (size fraction 90–100  $\mu\text{m}$ )

The MGLs combine the high photoelectrical parameters of single crystals and the advantages of polycrystalline materials and technologies, that is, low cost and simple technology of materials and devices, and the possibility of making flexible devices and using the materials up to 100%. MGL technology allows the separation of materials formation from module fabrication. Large-area modules are fabricated at room temperature in a continuous roll-to-roll process. Homogeneous composition of powders gives an additional advantage, leading to homogeneous modules without any up-scaling problem.

### 13.2 Monograin Powder Growths, Basics of the Process

Molten salts have proven to be useful as alternative reaction media for various organic and inorganic reactions [7, 8]. Single crystals or single-crystalline powders can be obtained at temperatures above the melting point of the used salt at temperatures lower than the melting point of the semiconductor itself. Synthesis in molten salts enhances the rate of solid-state reactions due to the much higher diffusion rates between reaction components in the molten media [9], lowering the reaction temperature, increasing the homogeneity of the solid product, and controlling the particle size and shape as well as their agglomeration state.

In the material formation-nucleation stage, the precursors: (1) can dissolve completely in the molten salt, with the nuclei of the product formed in the liquid phase (growth of single crystals); or (2) initial solid particles of low-solubility precursors react with each other in the molten salt media, and the formed solid particles of the product compound start to recrystallize and grow by the mechanism of Ostwald ripening [10] (monograin powder growth). In the growth of monograin powders, the crystals are formed in the presence of the liquid phase of the used flux salt. The characteristics of monograin powder crystals are controlled by selection of the synthesis temperature, as well as the nature and amount of the salt. The volume of the used molten salt has to exceed the volume of voids between precursor particles. In this case the formed liquid phase is sufficient to repel both the solid precursor particles and the formed powder particles from each other and to avoid sintering caused by the contracting capillary forces arising in the solid-liquid phase boundaries. The amounts of precursors for CZTSSe and flux salt are therefore usually taken so that the ratio of the forming volumes of solid phase  $V_s$  and liquid phase  $V_L$  is within the range 0.6–1.0 [11]. After the synthesis, the used salt is removed by washing with a suitable solvent and the released monograin powder is dried and sieved (Fig. 13.1b).

Research on monograin powder growth of II–VI compounds monograin powder growth in  $\text{Na}_2\text{S}_x$  and  $\text{CdCl}_2$  was initiated at Tallinn University of Technology in the 1970s and the research into  $\text{CuInSe}_2$  monograin powders in the 1990s [11]. During the first investigations, Se, CuSe, and mixtures of Se–CuSe were used as flux materials for  $\text{CuInSe}_2$  [12–14] and Te or  $\text{CdCl}_2$  for  $\text{CdTe}$  monograin production [15, 16]. Although monograins with nearly stoichiometric  $\text{CuInSe}_2$  composition were obtained using CuSe–Se as a flux, the removal of the flux material after the synthesis was difficult; CuSe–Se was therefore soon replaced by water-soluble potassium iodide (KI) [17]. KI has low hygroscopicity and also low solubility in  $\text{CuInSe}_2$ . Since 2006, research and development of monograin powder technology has mainly been directed to  $\text{Cu}_2\text{ZnSnSe}_4$ ,  $\text{Cu}_2\text{ZnSnS}_4$ , and their solid solutions [18, 19]. KI, NaI, and  $\text{CdI}_2$ , with their low melting point, low vapor pressure, and high solubility in water, were used as flux materials [20–22].

### 13.2.1 Chemical Pathway of $\text{Cu}_2\text{ZnSnSe}_4$ Formation in the Presence of Flux Salts

The pathway of  $\text{Cu}_2\text{ZnSnSe}_4$  formation from binary chalcogenides (ZnSe, CuSe, and SnSe) in KI, NaI, and  $\text{CdI}_2$  was studied by DTA, micro-Raman, XRD, SEM, and EDX methods combined with the determination of enthalpy values and thermodynamic calculations [20–22]. DTA, XRD and Raman analyses confirm that the formation of a liquid phase is the initiator of chemical reactions; CZTSe can be recognized at  $380^\circ\text{C}$  after the melting of Se that results from the transformation of CuSe to  $\text{Cu}_{2-x}\text{Se}$  and Se. In the presence of solid salt, the CZTSe formation process is then impeded to a great extent until the flux salt melts. The melting is immediately followed by the extensive exothermic process of CZTSe formation. The chemical pathway begins after the release of Se from CuSe at the peritectic phase transformation temperature ( $380^\circ\text{C}$  [20–22]) of CuSe to  $\text{Cu}_{2-x}\text{Se} + \text{Se}$  in all the precursor-flux mixtures studied. Se then reacts with SnSe resulting in  $\text{SnSe}_2$ , and  $\text{Cu}_{2-x}\text{Se}$  reacting with  $\text{SnSe}_2$  then forms  $\text{Cu}_2\text{SnSe}_3$ . The reaction of  $\text{Cu}_2\text{SnSe}_3$  with ZnSe ends the chemical route of CZTSe formation. Before the formation of the liquid phase of flux, the resultant amounts of formed CZTSe and  $\text{Cu}_2\text{SnSe}_3$  are low and the reflections of unreacted phases of  $\text{Cu}_{1.8}\text{Se}$ , CuSe, ZnSe, SnSe, and  $\text{SnSe}_2$  are present in the XRD patterns of samples heated at temperatures below the melting temperature of the used salt. The CZTSe synthesis reactions before the formation of liquid phase of flux are probably inhibited due to a number of different factors. First, the formed Se overpressure in the closed vacuum ampoules suppresses the further decomposition of CuSe and therefore also the supply of Se. Second, the large amount of solid NaI between solid particles of precursors inhibits the diffusion rate of reaction components and, due to this, the rate of CZTSe formation is also suppressed. After the melting of KI (NaI) the formation of CZTSe is readily completed.

The use of  $\text{CdI}_2$  as flux results in the formation of  $\text{Zn}_{1-x}\text{Cd}_x\text{Se}$  solid solution as an intermediate product and  $\text{Cu}_2(\text{Zn}_{1-x}\text{Cd}_x)\text{SnSe}_4$  as a final product, in which the amount of incorporated Cd changes from 1.3 to 3 at% depending on the synthesis temperature used. In the studies of CZTSe formation in NaI, the specific enthalpy of exothermic  $\text{Cu}_2\text{ZnSnSe}_4$  formation  $-36 \pm 3$  kJ/mol was determined experimentally. The formation of ternary compound  $\text{Na}_2\text{SnSe}_3$  was detected during the synthesis process in NaI. If present in NaI,  $\text{NaI} \cdot 2\text{H}_2\text{O}$  was found to be a critical issue in the synthesis process of CZTSe monograin powders in molten NaI, as it gave rise to the formation of oxygen-containing by-products  $\text{Na}_2\text{SeO}_4$  and  $\text{Na}_2\text{Cu}(\text{OH})_4$ . It was found that the formation of oxygen containing compounds can be avoided by using completely dehydrated NaI.

As the CZTSe monograin powder crystals grow in molten KI (NaI), they saturate with K (Na) and I. The solubility of K in CZTSe is determined by ICP-MS as  $5.5 \times 10^{17}$  at.  $\text{cm}^{-3}$ .

### 13.2.2 Elemental and Phase Compositions of CZTS-Based Monograins

It has been found that the crystal growth of single-phase CZTS with Cu-poor and Zn-rich composition is a prerequisite for improving the efficiency of kesterite thin-film solar cells. Cu-poor conditions enhance the formation of Cu vacancies, which gives rise to shallow acceptors in CZTS, while Zn-rich conditions suppress the substitution of Cu at Zn sites, which gives rise to relatively deep acceptors [23]. It is therefore very important to determine the composition and compositional limits of formation of single-phase kesterite powders and to control these parameters in the powder growth process. One of the main tools for controlling parameters and phase structure of CZTS and CZTSe monograin powders is

to change the initial precursor composition [24, 25]. Compositional variations of precursors and product material are ordinarily expressed by two parameters:  $[\text{Cu}]/([\text{Zn}]+[\text{Sn}])$  and  $[\text{Zn}]/[\text{Sn}]$ , where  $[\text{Cu}]$ ,  $[\text{Zn}]$ , and  $[\text{Sn}]$  are atomic concentrations (at%) of elements in the bulk of powder crystals.

### 13.2.2.1 $\text{Cu}_2\text{ZnSnS}_4$

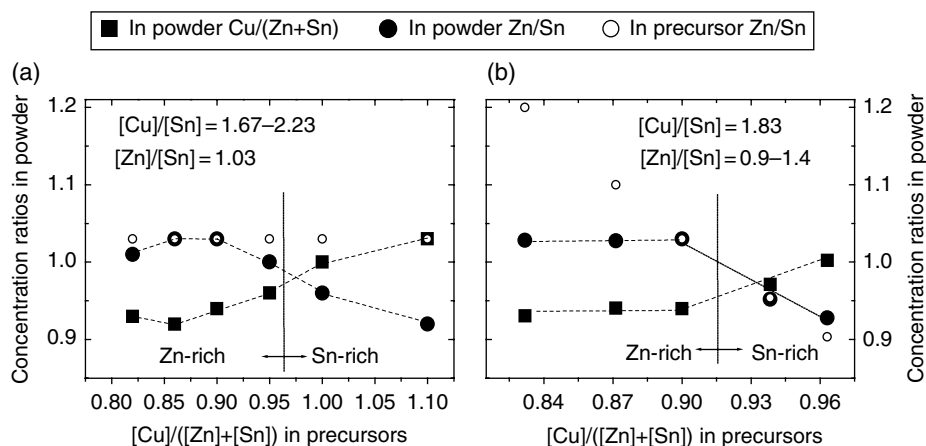
Figure 13.2 gives the values of compositional ratios  $\text{Cu}/(\text{Zn}+\text{Sn})$  and  $\text{Zn}/\text{Sn}$  of the synthesized CZTS monograins depending on the composition of precursors.

In slightly Zn-rich conditions ( $\text{Zn}/\text{Sn}=1.03$ ), the increase in the ratio of  $[\text{Cu}]/([\text{Zn}]+[\text{Sn}])$  in the precursor mixture decreased the ratio of  $[\text{Zn}]/[\text{Sn}]$  from 1.03 to 0.92 in the final product (see Fig. 13.2a). When the ratio of  $[\text{Cu}]/([\text{Zn}]+[\text{Sn}])$  in precursors was increased to over 0.95, the powder composition became Sn-rich in addition to Cu-rich. It was found that, in these growth conditions, secondary phases such as Cu- and Sn-binaries and  $\text{Cu}_2\text{SnS}_3$  were formed together with quaternary compound.

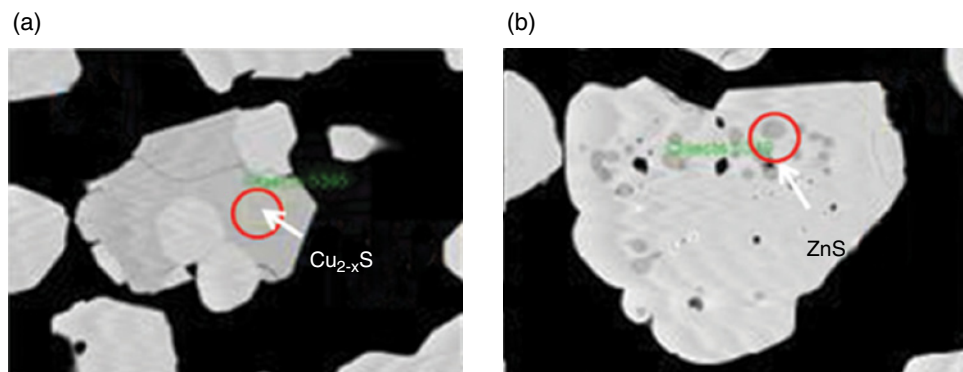
In Zn-rich growth conditions ( $1.03 < \text{Zn}/\text{Sn} \leq 1.2$ ) with constant Cu content in precursors (Fig. 13.2b), the composition of formed CZTS powder crystals was invariable. Only an amount of ZnS secondary phase was increased by the addition of Zn in the precursors' mixture.

In Zn-poor growth conditions ( $\text{Zn}/\text{Sn} < 1.0$ ) with constant Cu content in precursors, the composition of CZTS powder crystals became Cu-rich and Sn-rich. In the case of the highest Cu content in the precursors ( $\text{Cu}/(\text{Zn}+\text{Sn})=1.1$ ), additional phases of SnS,  $\text{SnS}_2$ , and  $\text{Sn}_2\text{S}_3$  were detected by Raman and EDX analysis.

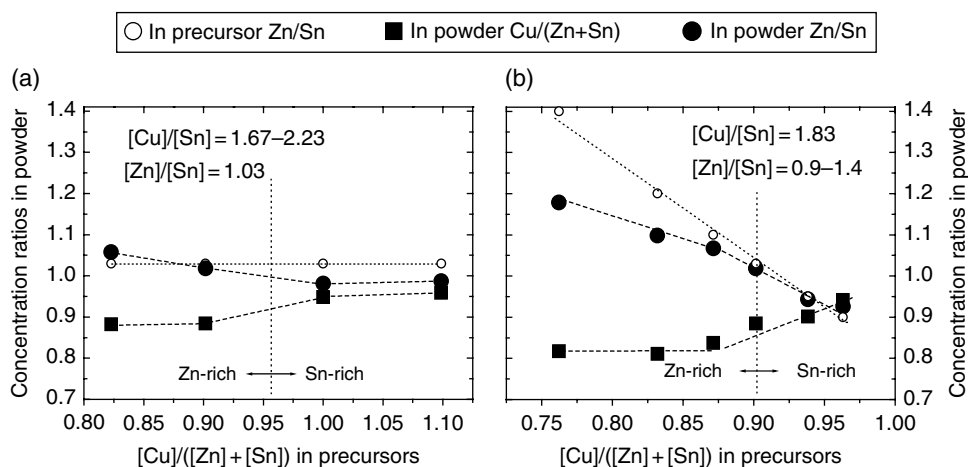
SEM images of polished CZTS crystals are shown in Figure 13.3a and b. The formation of a separate phase of  $\text{Cu}_{2-x}\text{S}$  in powders with an excess of Cu is in agreement with the phase diagram assembled by Olekseyuk *et al.* [26]. The SEM, EDX and Raman



**Figure 13.2**  $[\text{Cu}]/([\text{Zn}]+[\text{Sn}])$  (filled squares) and  $[\text{Zn}]/[\text{Sn}]$  (filled dots) ratios of  $\text{Cu}_2\text{ZnSnS}_4$  monograin powders determined by EDX as a function of the  $[\text{Cu}]/([\text{Zn}]+[\text{Sn}])$  ratio in precursors when (a)  $[\text{Zn}]/[\text{Sn}]$  was kept constant and (b)  $[\text{Cu}]/[\text{Sn}]$  was kept constant. Hollow dots represent the Zn to Sn concentration ratio in precursors. Reproduced from [24]. With permission from Elsevier



**Figure 13.3** SEM images of mechanically polished (a) Cu-rich and (b) Zn-rich CZTS crystals, indicating the existence of different separate binary phases in monograins. Reproduced from [24]. With permission from Elsevier



**Figure 13.4**  $[Cu]/([Zn]+[Sn])$  (filled squares) and  $[Zn]/[Sn]$  (filled dots) ratios of  $Cu_2ZnSnSe_4$  monograin powders depending on the  $[Cu]/([Zn]+[Sn])$  ratio in precursors if (a)  $[Zn]/[Sn]=1.03$  and (b)  $[Cu]/[Sn]=1.83$ . Hollow dots represent the Zn/Sn concentration ratio in precursors. Reproduced from [25]. With permission from Elsevier

investigations showed that powders with initial compositional ratio of  $Cu/(Zn+Sn)$  below 0.95 and  $Zn/Sn > 1.03$  contain a separate phase of ZnS.

### 13.2.2.2 $Cu_2ZnSnSe_4$

Similar investigations to those presented in the previous section were made with a  $Cu_2ZnSnSe_4$  system. Several powders with different Cu and Zn content in precursors were grown to study the influence of precursor composition on the Cu and Zn content in CZTSe monograin powders [25]. The metal composition ratios of the initial (hollow dots) and synthesized (filled squares and dots) monograins are shown in Figure 13.4a and b.



In slightly Zn-rich growth conditions ( $\text{Zn}/\text{Sn}=1.03$ ), the increase in the ratio of  $[\text{Cu}]/([\text{Zn}]+[\text{Sn}])$  in the precursor mixture decreased the ratio of  $\text{Zn}/\text{Sn}$  in the final product from 1.03 to 0.98 (see Fig. 13.4a). The deviation from precursor composition is much smaller than in the sulfide system. When the compositional ratio of  $\text{Cu}/(\text{Zn}+\text{Sn})$  in precursors was increased to  $>1.0$ , the powder composition also became slightly Sn-rich in addition to being Cu-rich. In the latter growth conditions,  $\text{Cu}_x\text{Se}$  and  $\text{SnSe}_2$  secondary phases were detected by Raman analysis.

In highly Zn-rich conditions ( $\text{Zn}/\text{Sn} = 1.1\text{--}1.4$ ) with constant  $\text{Cu}/\text{Sn}$  ratio in precursors, the CZTSe powder crystals had a stable  $\text{Cu}/(\text{Zn}+\text{Sn})$  compositional ratio of about 0.81. Only the presence of ZnSe secondary phase was always detected in these powder crystals by Raman spectroscopy. In the sulfide system, the compositional ratio of  $\text{Cu}/(\text{Zn}+\text{Sn})$  in monograin powders was much higher (0.94).

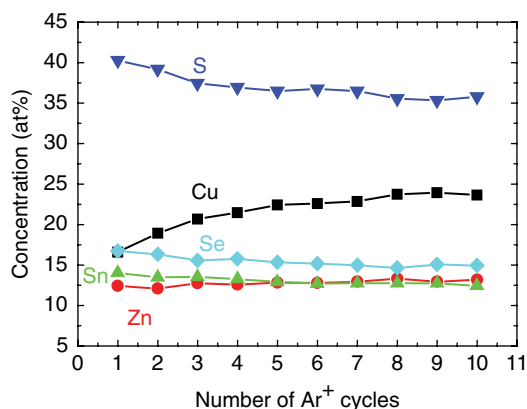
When we compare a  $\text{Cu}_2\text{ZnSnS}_4$  system with a  $\text{Cu}_2\text{ZnSnSe}_4$  system, the existence of a composition region for the synthesis of single-phase quaternary monograins extends toward the pure selenide and is mainly regulated by Cu and Zn content in precursors. Cu and Zn content in the synthesized material are interchangeable to some extent: higher copper content in the initial precursors is always accompanied by lower Zn content in the product material and vice versa.

### 13.3 Influence of Chemical Etching on the Surface Composition of Monograins

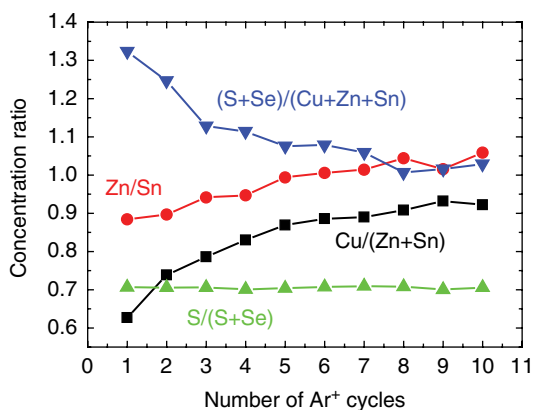
The solubility of CZTSe in KI is 0.6 mole% for CZTSe, while those of CuSe, ZnSe, and SnSe are 3.6, 0.09, and 0.3 mole%, respectively, at  $740^\circ\text{C}$  [21]. This means that at high temperatures, a part of the precursors and the synthesized kesterite dissolves in the flux. During cooling from a growth temperature, some part of the dissolved precursors and CZTSe precipitate on the surface of the monograins; the surface composition of crystals therefore depends on their precipitations. The EDS analysis revealed that the surface composition of as-grown crystals was Sn-rich while the bulk of monograins was Zn-rich. In addition, it was confirmed by XPS analysis that the surface of monograins exhibits Cu deficiency and an excess of Sn and chalcogens (Fig. 13.5). The  $[\text{Zn}]/[\text{Sn}]$  (Fig. 13.6) changes from 0.88 at the surface to 1.06 in the bulk and the  $[\text{Cu}]/([\text{Zn}]+[\text{Sn}])$  increases from 0.63 at the surface to 0.92 in the bulk.

Chemical treatments with several etchants ( $\text{HCl}$ , KCN, Bromine in methanol ( $\text{Br}_2\text{-MeOH}$ ) and  $\text{NH}_4\text{OH}$ ) were performed in order to improve the active interface of solar cells [27]. Polarographic analysis of the leaching solutions indicated that preferably Sn and chalcogen were removed from the surface by  $\text{HCl}$  etching, probably due to the complexation of Sn in  $\text{HCl}$  solution and formation of  $[\text{SnCl}_4]^{2-}$  [28]. The KCN etching is well known as a process to remove Cu-Se binary phases [29], but we also detected Sn in the leaching solutions. The ammonia solution selectively removed Cu and chalcogen from the surface.

Figure 13.7 represents XPS spectra of the as-grown and  $\text{Br}_2\text{-MeOH}$ -etched  $\text{Cu}_2\text{ZnSn}(\text{S,Se})_4$  monograin surfaces. The intensity of Cu2p, CuLMM peaks decreases and the intensity of the Sn and O1s peaks increases after etching materials with  $\text{Br}_2\text{-MeOH}$ . Zn2p and ZnLMM peaks are almost undetectable for materials etched with  $\text{Br}_2\text{-MeOH}$ .



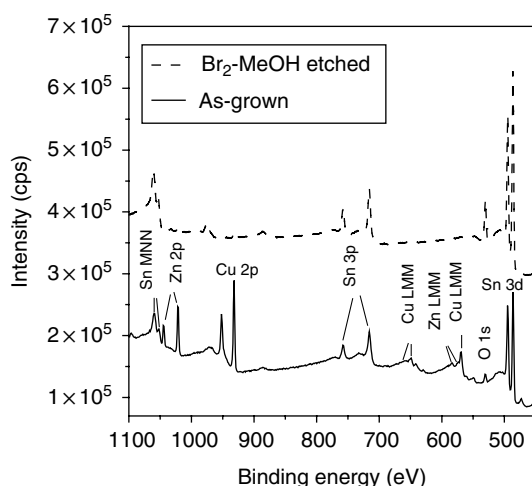
**Figure 13.5** XPS depth profiling of element concentrations of CZTSSe monograin powder crystal surface



**Figure 13.6** Concentration ratios of elements of CZTSSe monograin powder crystal surface

The relative atomic concentrations of Zn, Cu, Sn, and Se were determined from integrated peak areas of high-resolution XPS core level spectra. The S2p peak area was determined by core level curve-fitting procedures since this peak overlaps with the Se3p core level. The composition of the  $\text{Cu}_2\text{ZnSn}(\text{S},\text{Se})_4$  monograin surface etched in the  $\text{Br}_2$ -MeOH solution was determined by XPS with the following result: Cu : Zn : Sn : S+Se : O = 1.2 : 1.2 : 37.0 : 12.8 : 47.7 at%. Comparison of the XPS spectra of the as-grown and the  $\text{Br}_2$ -MeOH-etched samples allows us to conclude that  $\text{Br}_2$ -MeOH-etching mainly removes Cu and Zn. This fits well with the results of the polarographic analysis of the leaching solutions (Table 13.1).

Solar cell parameters made from chemically treated  $\text{Cu}_2\text{ZnSn}(\text{S}_{0.45}\text{Se}_{0.55})_4$  monograin powders are given in Table 13.2. All the etched powders were post-annealed in the isothermal conditions in closed ampoules at 740°C before fabricating MGL solar cells.



**Figure 13.7** XPS spectra of surfaces of the as-grown and  $\text{Br}_2$ -MeOH etched CZTSSe monograins

**Table 13.1** Molar ratios of elements in leaching solutions determined polarographically [28]

Etchant/element	Cu: Zn: Sn: Se
KCN	1.0 : 0 : 0.4 : 1.5
HCl	1.0 : 0.1 : 5.8 : 6.5
$\text{NH}_4\text{OH}$	1.0 : 0.2 : 0 : 2.2
$\text{Br}_2$ -MeOH	1.0 : 0.8 : 0.7 : 0.3

**Table 13.2** Performance parameters (open-circuit voltage  $V_{oc}$ , short-circuit current density  $J_{sc}$ , fill factor  $FF$ , solar cell efficiency  $\eta$ ) of  $\text{Cu}_2\text{ZnSn}(\text{S}_{0.45}\text{Se}_{0.55})_4$  monograin layer solar cells made from non-etched and etched absorber crystals [27]

Etchant	$V_{oc}$ (mV)	$J_{sc}$ ( $\text{mA cm}^{-2}$ )	$FF$ (%)	$\eta$ (%)
None	300	10.0	40	1.2
Conc. HCl	342	11.5	48	1.9
2M $\text{NH}_4\text{OH}$	422	10.5	44	1.9
1% $\text{Br}_2$ -MeOH	563	8.5	54	2.6
10% KCN	490	13.5	49	3.2
1% $\text{Br}_2$ -MeOH + 10% KCN	575	13.7	55	4.3

It can be seen that etching of the powder crystals improves the parameters of monograin layer solar cells. The combined chemical etching (1%  $\text{Br}_2$ -MeOH followed by etching with 10% KCN) of absorber material resulted in the highest values of solar cell parameters with efficiencies of approximately 4%. Higher efficiencies were obtained after further optimized surface thermal treatments.

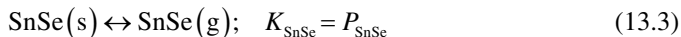
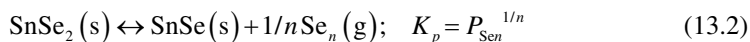
### 13.4 Thermal Treatment of CZTS-Based Monograins

In general, monograin growth does not ensure an optimal absorber surface for solar cell formation. In addition to surface treatments by chemical etching, the composition of monograin surface could be adjusted by additional thermal treatments. The thermal process is more easily controlled by the temperature and atmosphere of treatment than the chemical etching.

High temperatures of up to 740°C are ordinarily used for thermal treatments of kesterites but, as reported earlier by different authors [30–32], kesterites start to decompose at temperatures of about 400°C. In order to prevent decomposition of the material, we needed to apply external vapor pressure in closed ampoules. In our experiments all post-treatments were carried out using two temperature zone arrangements. The temperatures of both zones were regulated and controlled independently. This allows more precise control of the vapor pressure during annealing.

#### 13.4.1 $\text{Cu}_2\text{ZnSnSe}_4$

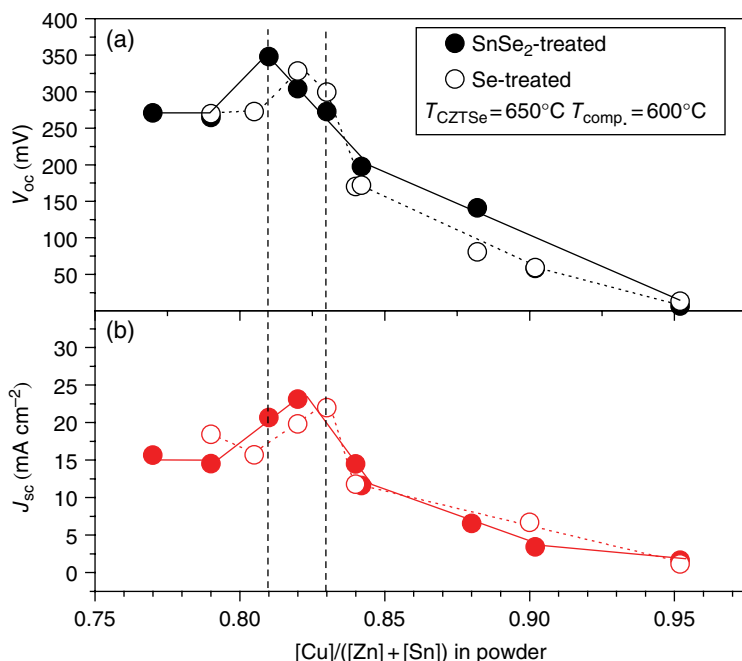
$\text{SnSe}_2$  or Se sources were used to regulate composition of the gas phase over  $\text{Cu}_2\text{ZnSnSe}_4$  monograin powders. The following reactions describe the decomposition of  $\text{Cu}_2\text{ZnSnSe}_4$  (Equation (13.1)) [31] and the formation of the gas phase (Equations (13.2)–(13.4)) at higher temperatures [33].



where  $K$  is the equilibrium constant and  $P$  is the partial pressure of the component.

Mass-spectrometric analysis [34] revealed that the vapor phase over solid  $\text{SnSe}$  consists mainly of  $\text{SnSe}$  vapor molecules as described by Equation (13.3), and that the equilibrium vapor pressure of pure  $\text{SnSe}$  is more than 4 orders of magnitude lower than the vapor pressure of pure  $\text{SnSe}_2$  or Se. It is estimated from Equation 13.4 in chemical equilibrium that the reaction is shifted to the left side if  $\log P_{\text{Sen}} > 1/n (\log K_{\text{CZTSe}} - \log P_{\text{SnSe}})$  and the incorporation of Sn from the gas phase of  $\text{SnSe}_2$  into the  $\text{Cu}_2\text{ZnSnSe}_4$  takes place. When the applied vapor pressure of Se is lower than the equilibrium vapor pressure, the decomposition of  $\text{Cu}_2\text{ZnSnSe}_4$  is to an extent determined by the applied Se pressure.

Monograin powders with a large deviation of compositional ratios ( $0.79 < \text{Cu}/(\text{Zn} + \text{Sn}) < 0.95$  and  $0.93 < \text{Zn}/\text{Sn} < 1.2$ ) were used to study the influence of CZTSe thermal treatments on the performance of MGL solar cells [35]. During the annealing, the



**Figure 13.8** Values of (a) short-circuit current density  $J_{sc}$  and (b) open-circuit voltage  $V_{oc}$  of CZTSe MGL solar cells as a function of  $[Cu]/([Zn]+[Sn])$  ratio in the powder

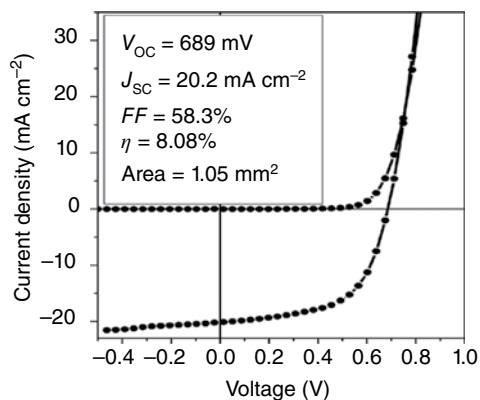
temperature in the material zone was 650°C and the temperature of the component zone (SnSe<sub>2</sub> or Se) was 600°C. The results (Fig. 13.8) showed that the values of  $V_{oc}$  depend on the Cu/(Zn+Sn) and Zn/Sn concentration ratios in the powder. The highest value  $V_{oc} = 350$  mV was attained with the use of Cu-poor (Cu/(Zn+Sn) = 0.81–0.83) and Zn-rich (Zn/Sn = 1.1) powders. The measured value of  $J_{sc} = 23.8$  mA cm<sup>-2</sup> was also the highest in a limited range of Cu/(Zn+Sn) ratios. The solar cell characteristics were very low when the Cu-rich powders with the composition of Cu/(Zn+Sn) > 0.85 were used. An increase in the Cu content in powders resulted in a decrease in the Zn/Sn concentration ratio and Cu<sub>2</sub>ZnSnSe<sub>4</sub> powders were of Sn-rich (Zn/Sn < 1) composition.

The highest CZTSe-based solar cell efficiency (4.4%) was achieved with SnSe<sub>2</sub>-annealed monograin powders with the composition Cu/(Zn+Sn) = 0.81 and Zn/Sn = 1.12 [35].

### 13.4.2 Cu<sub>2</sub>ZnSnS<sub>4</sub>

For sulfurization studies, the powders had Cu-poor (Cu/(Zn+Sn) = 0.89) and Zn-rich (Zn/Sn = 1.1) composition. EDX analysis confirmed that there was no change in the bulk composition of materials during the annealing in S or SnS<sub>2</sub> vapor [36]. By changing the parameters of sulfurization, optimal conditions for an effective absorber material were found. Detailed description of annealing parameters is provided in the literature [36].

Parameters of MGL solar cells consisting of S- or SnS<sub>2</sub>-annealed absorbers were significantly affected by annealing temperatures. Efficiencies of Cu<sub>2</sub>ZnSnS<sub>4</sub> MGL solar cells increased continuously with increasing material zone temperature from 550 to 740°C

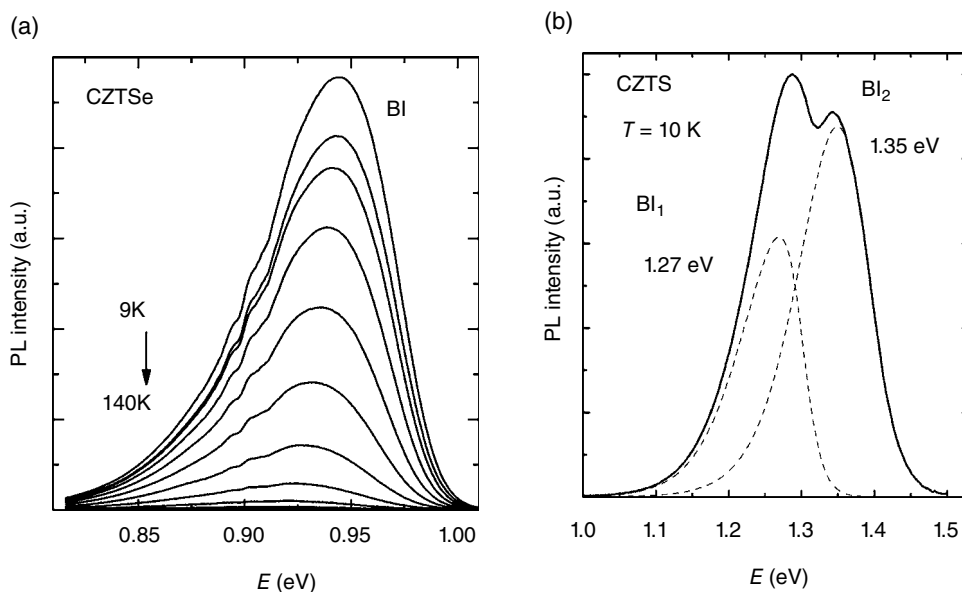


**Figure 13.9** I-V characteristics of CZTS single-grain solar cell

(at sulfur pressure >100 Torr). These MGL solar cells show values of  $V_{oc}$  up to 690 mV and FF of up to 62%. Further increase in the sulfur vapor pressure did not lead to improvements of the solar cell parameters. When the vapor pressure of sulfur was <100 Torr, the precipitation of  $\text{SnS}_2$  on the walls of the ampoules was visible. This means that relatively low S vapor pressure ( $P_s < 100$  Torr) did not prevent Sn loss from  $\text{Cu}_2\text{ZnSnS}_4$  and hence the decomposition of the surface region. A decomposed surface is not favorable for the formation of a working pn-junction, and our results confirm the statement of Wang *et al.* [37]. The highest values of  $J_{sc} = 18.4 \text{ mA cm}^{-2}$  and  $V_{oc} = 768 \text{ mV}$  were obtained using the  $\text{Cu}_2\text{ZnSnS}_4$  powder that was annealed at  $740^\circ\text{C}$  in  $\text{SnS}_2$  vapor. This value of  $V_{oc}$  was close to the highest value ever reported for  $\text{Cu}_2\text{ZnSnS}_4$  [38]. Due to the use of epoxy, the active area and total area in MGL solar cells do not match. To evaluate the performance of separate monograins, a single-grain solar cell was constructed. The active area ( $1.05 \text{ mm}^2$ ) of the measured single monograin was determined by using the light-beam-induced current (LBIC) experiment. The open area of grain on the optical image and active area on the LBIC image are equal. Therefore, the performance of CZTS monograin powder material is 8.08% with the values of  $V_{oc} = 689 \text{ mV}$ ,  $J_{sc} = 20.2 \text{ mA cm}^{-2}$ , and FF = 58.2% (Fig. 13.9).

### 13.5 Optoelectronic Properties of CZTS-Based Monograins and Polycrystals

The optoelectronic properties of semiconductor materials are mainly determined by native and foreign defects. One prerequisite for obtaining high-efficiency solar cells is therefore to control the defect structure of the absorber material. Theoretical first-principles calculations [39, 40] predict low defect formation energies of the order a few hundred milli-electron volts for many isolated point defects as well as defect complexes in CZTS and CZTSe, meaning that control over the defect structure of these compounds is rather complicated. We studied defects in CZTS and CZTSe monograins and polycrystals using mainly photoluminescence (PL) spectroscopy. Admittance spectroscopy (AS) was used for the determination of deep levels in the corresponding MGL solar cells.



**Figure 13.10** (a) Temperature dependence of the PL spectra of CZTSe monograins; and (b) low-temperature PL spectrum of CZTS polycrystals together with the fitting result. Reproduced from [44] and [45], respectively. With permission from Elsevier

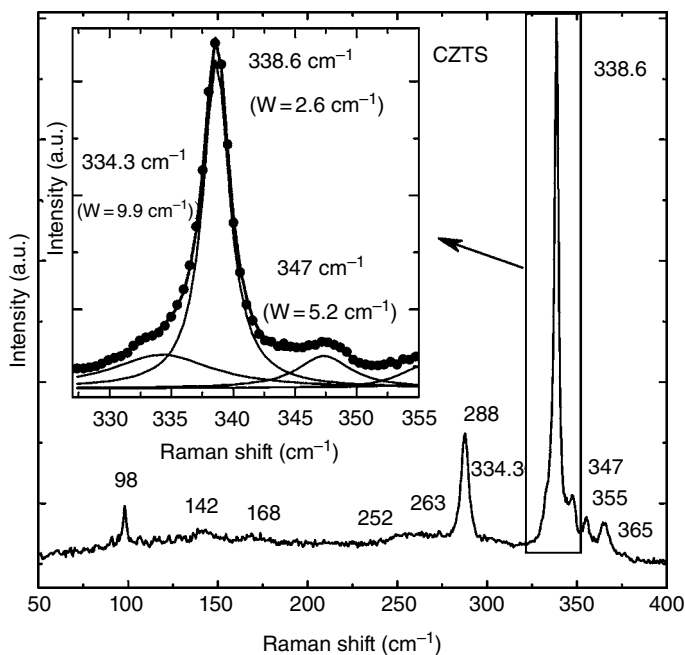
In good-quality CZTS crystals and CZTSe thin films, excitonic emission together with a PL emission involving shallow defect levels have been detected [41, 42]. However, the PL spectra of both CZTS and CZTSe monograins at  $T = 10$  K consist of broad (full-width at half-maximum or FWHM being more than 100 meV) asymmetric PL bands (Fig. 13.10) [43–45]. An asymmetric shape of the PL bands and a large blue-shift of the order more than 10 meV/decade with increasing laser power are commonly seen in heavily doped and compensated semiconductors where spatial potential fluctuations are present [46–49]. The conditions of heavy doping in the present case originate from the high concentration of native defects that is often observed in multinary semiconductor compounds. The spatial potential fluctuations lead to a local perturbation of the band structure, giving rise to broadened defect energy levels and also band tails. In a p-type material and in the case of small effective mass of electrons, radiative recombination can therefore mainly arise from four different channels [46]: band-to-tail recombination (BT) that is associated with a free electron and a hole which is localized in the valence band tail; band-to-band recombination (BB) that involves a free electron and a free hole; band-to-impurity (BI) recombination that involves an acceptor state that is deep enough not to overlap with the valence band tail; and donor–acceptor pair (DAP) recombination that involves an acceptor and a donor state that are deep enough not to overlap with the corresponding band tails.

For comparison, PL and Raman scattering of CZTS polycrystalline powders and monograins were studied. It was found that, in some cases, much narrower PL bands and Raman peaks measured from the polycrystalline powders enabled a better description of the recombination processes and vibrational properties of CZTS.

PL analysis of the CZTSe monograins indicates that the dominant recombination mechanism at low temperatures is BI recombination [44]. The BI-type PL band in CZTSe was found at 0.95 eV at  $T = 10$  K (see Fig. 13.10a) and could be attributed to acceptor defects with ionization energy of  $E_t = 69 \pm 4$  meV [44].

In polycrystalline CZTS, two PL bands were observed at 1.27 eV and 1.35 eV at  $T = 10$  K, as shown in Figure 13.10b. Both PL bands showed similar dependence on temperature and excitation power corresponding to BI recombination [45]. Interestingly, similar thermal activation energies around 280 meV were determined from the temperature dependence of these PL bands in CZTS. Considering the Raman scattering results of the polycrystalline powder, we proposed that the observed PL bands arise from the BI recombination process involving the same deep acceptor defect with ionization energy of around 280 meV, but different CZTS phase (kesterite and disordered kesterite) with different band-gap energy [45].

Very narrow Raman peaks of CZTS polycrystals (FWHM of the  $A_1$  peak was  $2.6\text{ cm}^{-1}$ ; see Fig. 13.11) enabled us to detect the co-existence of two polytypes in CZTS: the kesterite and the disordered kesterite phase [45]. The general consensus is that the kesterite structure is the ground-state structure but, according to the theoretical calculations [50], the formation energy difference between the different polytypes is only of the order of a few milli-electron volts per atom, indicating that the disorder in the cation sublattice may occur under standard growth conditions. The disorder is predicted to cause a band-gap energy difference of around 0.1 eV for the kesterite and the disordered kesterite or stannite phase

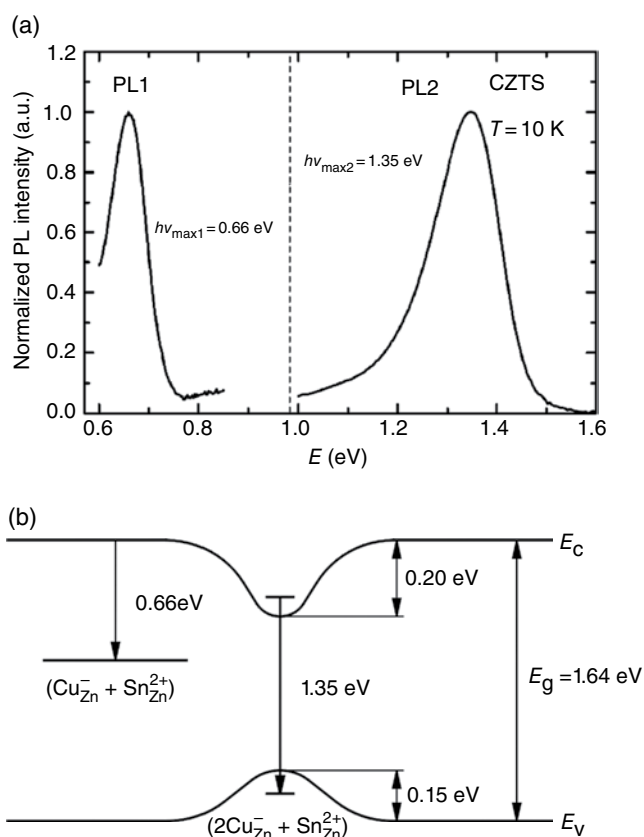


**Figure 13.11** Raman spectrum of CZTS polycrystals. The fitting result for the  $A_1$  peak is shown on the inset graph, where the original spectrum is represented by symbols. A shoulder peak corresponding to  $A_1$  mode of disordered kesterite phase is observed at  $334.3\text{ cm}^{-1}$  [45]



in CZTS, the kesterite having the largest band-gap energy [50]. Neutron diffraction measurements [51, 52] also showed that a partially disordered kesterite structure exists. Although the vibrational spectra of these phases are also similar, according to theoretical calculations [53, 54] there is a difference at least in  $A_1$  phonon modes of kesterite, disordered kesterite, and stannite CZTS. Since such narrow Raman peaks are usually not seen, they are not resolved; however, the coexistence of the different polytypes should always be considered.

In addition to the BI recombination involving deep acceptor defect, there is another recombination mechanism possible in CZTS resulting in the PL emission at the same energy of around 1.3 eV, but lower thermal quenching activation energy of about 100 meV. Our low-temperature PL measurements of near-stoichiometric CZTS monograins and polycrystals revealed a very deep PL band at 0.66 eV (PL1) together with the 1.35 eV emission (PL2) (see Fig. 13.12a) [55]. The dominant radiative recombination mechanism in this case is the recombination between electrons and holes in the quantum well caused by the  $(2\text{Cu}_{\text{Zn}}^- + \text{Sn}_{\text{Zn}}^{2+})$  defect clusters that induce a significant band-gap decrease of 0.35 eV, as

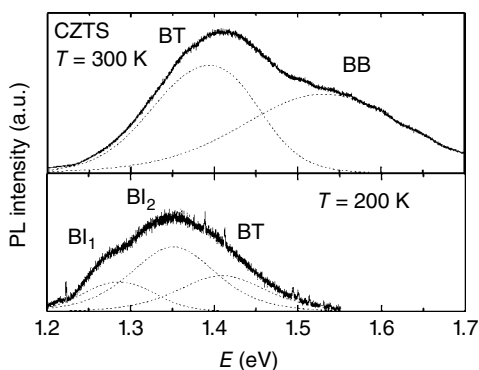


**Figure 13.12** (a) Low-temperature ( $T=10$  K) PL spectrum of near-stoichiometric CZTS; and (b) the corresponding radiative recombination model. Reproduced from [55]. With permission from Elsevier

shown in [40]. As a result, the PL2 band at 1.35 eV arises. At low temperatures BI recombination involving deep donor level is also present, giving the PL1 band with the peak position of 0.66 eV. We propose that it originates from the partially compensated ( $\text{Cu}_{\text{Zn}}^- + \text{Sn}_{\text{Zn}}^{2+}$ ) defect cluster. According to the theoretical calculations [40], the donor level is situated at 0.63 eV below the conduction band minimum (the recombination model is presented in Fig. 13.12b). Theoretical calculations [40] predict a high concentration of ( $2\text{Cu}_{\text{Zn}}^- + \text{Sn}_{\text{Zn}}^{2+}$ ) and ( $\text{Cu}_{\text{Zn}}^- + \text{Sn}_{\text{Zn}}^{2+}$ ) defect clusters in nearly stoichiometric CZTS. Other types of defect clusters were also predicted in CZTS [56]. These defect clusters will either produce deep recombination centers for electron–hole pairs or cause trapping of charge carriers. Both mechanisms are detrimental to solar cell parameters and should be avoided. Interestingly, it is predicted [40] that the detrimental effect of both defect clusters is weaker in CZTSe since the donor levels induced by  $\text{Sn}_{\text{Zn}}$  are shallower in CZTSe than in CZTS. To date, there is no experimental evidence of the presence of these defect clusters in CZTSe.

At lower temperatures, BI or quantum well types of recombination always dominate in CZTS monograins and polycrystalline powders. BT emission, which is very common for other heavily doped multinary compounds, has very low intensity in CZTS and can be detected at 1.39 eV (and the BB band at 1.53 eV) at high temperatures only, when the BI or quantum well type of recombinations are quenched, and at a high excitation level (see Fig. 13.13) [57]. The results of our RT micro-PL experiments at high excitation level confirm that the model of heavily doped semiconductors [46] also applies to CZTS.

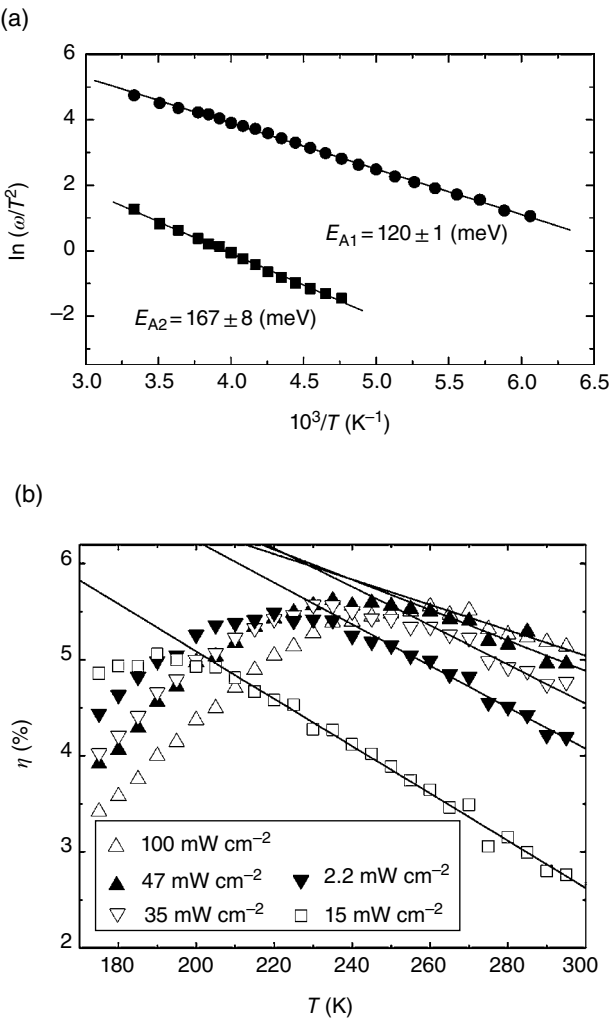
Deep defect levels in CZTS and CZTSe MGL solar cells have also been studied by admittance spectroscopy (AS) [58, 59]. We found two deep defect states in both materials from temperature-dependent AS measurements (Table 13.3; Fig. 13.14a). The first state ( $E_{A1}$ ) was present in different CZTS and CZTSe cells, while the second state ( $E_{A2}$ ) had somewhat different properties in different cells. The activation energy of the latter defect state varied in different cells and was dependent on the applied bias voltage (0 V, –1 V), which is uncommon for bulk defect states. The first state is therefore attributed to an acceptor level and the second to the interface states. The corresponding activation energies are presented in Table 13.3. The activation energies of the acceptor defects are in agreement with the values obtained from the PL analysis of the corresponding CZTS and CZTSe monograins.



**Figure 13.13** Micro-PL spectra of CZTS. Reproduced with permission from [57]. SPIE

**Table 13.3** Activation energies found by AS of the measured heterojunctions. Results for an aged device are in brackets.  $E_{A2}$  is attributed to the interface states and  $E_{A1}$  to acceptor defects [52, 53]

Material	$E_{A1}$ (meV)	$E_{A2}$ (meV)
$\text{Cu}_2\text{ZnSnSe}_4$	$75 \pm 2$ ( $74 \pm 2$ )	$87 \pm 3$ ( $100 \pm 3$ )
$\text{Cu}_2\text{ZnSn}(\text{Se}_{0.75}\text{S}_{0.25})_4$	$25 \pm 5$	$154 \pm 7$
$\text{Cu}_2\text{ZnSnS}_4$	$120 \pm 1$	$167 \pm 8$



**Figure 13.14** (a) Arrhenius plot showing the calculated activation energies of the defect levels in CZTS. The measurements are performed at bias 0 V. (b) Temperature dependence of the relative efficiency  $\eta$  of a CZTS<sub>Se</sub> MGL solar cell under different light intensities. Reproduced from [58] and [60], respectively. With permission from Elsevier

We have also studied the temperature dependence of the output parameters of the  $\text{Cu}_2\text{ZnSn}(\text{Se}_{0.3}\text{S}_{0.7})_4$  monograin layer solar cells [60]. We found that for a light intensity of  $100 \text{ mW cm}^{-2}$ ,  $dV_{\text{oc}}/dT = -1.91 \text{ mV K}^{-1}$ . Especially important is the temperature dependence of the relative efficiency  $\eta$  of solar cells (Fig. 13.14b). Calculated efficiencies are not calibrated because a halogen light source was used and therefore AM1.5 spectral conditions were not followed. It can be seen that the efficiencies have a maximum value below room temperature. The corresponding maximum efficiency temperature increases with light intensity and at  $100 \text{ mW cm}^{-2}$  is at about 250 K. At low temperatures, efficiency starts to diminish with decreasing temperature. The same behavior can also be observed at temperatures above 250 K. In the higher temperature region, the decrease of efficiency is nearly linear with temperature. For a standard light intensity, the relative efficiency of the solar cell decreases with the temperature at a slope of  $0.013\% \text{ K}^{-1}$ .

Measured temperature coefficients of CZTSSe MGL solar cells indicate that in many cases they are lower than for other types of solar cells. For example,  $\text{Cu}(\text{In,Ga})\text{Se}_2$  cells usually show  $dV_{\text{oc}}/dT$  values from  $-2.01$  to  $-3.3 \text{ mV K}^{-1}$  and  $d\eta/dT$  values from  $-0.017$  to  $-0.064\% \text{ K}^{-1}$  [61]. Si cells show  $dV_{\text{oc}}/dT$  values from  $-2.07$  to  $-2.17 \text{ mV K}^{-1}$  and a  $d\eta/dT$  value of about  $-0.042\% \text{ K}^{-1}$  [62]. The same applies to the situation in CdTe cells, where  $dV_{\text{oc}}/dT$  is typically in the range of  $-2.1$  to  $-2.2 \text{ mV K}^{-1}$  [63]. These low values of measured temperature coefficients of CZTSSe solar cells show a great potential for this compound.

### 13.6 Conclusion

In conclusion, we have shown that monograin powder technology is one of the methods for the growth of high-quality CZTSSe absorber materials for solar cells. In the growth of kesterite-type monograin powders, the crystals are formed in the presence of the liquid phase of water-soluble flux salts ( $\text{KI}$ ,  $\text{NaI}$ ,  $\text{CdI}_2$ ) that increases the homogeneity of the product absorber material and control the particle size and shape as well as their agglomeration state. The method enables the growth of different solid solutions  $\text{Cu}_2\text{ZnSn}(\text{S}_{1-x}\text{Se}_x)_4$ ,  $\text{Cu}_2(\text{Zn}_x\text{Cd}_{1-x})\text{SnS}_4$ ,  $\text{Cu}_2\text{Zn}(\text{Sn}_x\text{Ge}_{1-x})\text{Se}_4$ . The highest solar energy conversion efficiency of CZTS based monograin layer solar cell is 8.1 %. The optical and physical investigations have shown that the kesterite-type absorber materials include a high concentration of native defects that give rise to a strong recombination in the bulk of the absorber. The observed radiative recombination involves deep acceptor defects acting as carrier traps, or defect clusters which decrease the band-gap energy of the material. Strong recombination in the bulk of the absorber and the interface recombination in the solar cells are responsible for current and voltage losses in the kesterite-based solar cells.

### References

- [1] Chapin, D.M., Fuller, C.S. & Pearson, G.L. (1954) A new silicon *p-n* junction photocell for converting solar radiation into electrical power. *Journal of Applied Physics*, **25**, 676–677.
- [2] Paradise, M.E. (1957) Large area solar energy converter and method for making the same. US Patent 2,904,613, August 26.

- [3] Ties Siebolt Te Velde (1965) Electrical monograin layers having a radiation permeable electrode. US3480818 A, August 4.
- [4] Kilby, J.S., Lathrop, J.W. & Porter, W.A. (1977) Solar energy conversion. US4021323A, May 3.
- [5] Taira, K. & Nakata, J. (2010) Silicon cells: catching rays. *Nature Photonics*, **4**, 602–603.
- [6] Meissner, D. (2013) Photovoltaics based on semiconductor powders. In: *Materials and Processes for Energy: Communicating Current Research and Technological Developments* (ed. A. Méndez-Vilas), Formatex Research Center Badajoz, Spain.
- [7] Sundermeyer, W. (1963) Fused salts and their use as reaction media. *Angewandte Chemie, International Edition*, **4**, 222–238.
- [8] Kerridge, D.H. (1975) Recent advances in molten salts as reaction media. *Pure and Applied Chemistry*, **41**, 355–371.
- [9] Arendt, R.H. (1973) The molten salt synthesis of single magnetic domain  $\text{BaFe}_{12}\text{O}_{19}$  and  $\text{SrFe}_{12}\text{O}_{19}$  crystals. *Journal of Solid State Chemistry*, **8**, 339–347.
- [10] Boistelle, R. & Astier, J.P. (1988) Crystallization mechanisms in solution. *Journal of Crystal Growth*, **90**, 14–30.
- [11] Mellikov, E., Hiie, J. & Altosaar, M. (2007) Powder materials and technologies for solar cells. *International Journal of Materials and Product Technology*, **28**, 291.
- [12] Altosaar, M., Hiie, J., Mellikov, E. & Mädasson, J. (1996) Recrystallization of CIS powders in molten fluxes. *Crystal Research and Technology*, **31**, 505–508.
- [13] Hiie, J., Altosaar, M. & Mellikov, E. (1999) Comparative study of isothermal grain growth of CdS and CdTe in the presence of halide fluxes. *Solid State Phenomena*, **67–68**, 303–308.
- [14] Altosaar, M. & Mellikov, E. (1999)  $\text{CuInSe}_2$  monograin growth in  $\text{CuSe-Se}$  liquid phase. *Japanese Journal of Applied Physics*, **39**, 65–66.
- [15] Hiie, J., Altosaar, M., Mellikov, E., Kuk, P., Sapogova, J. & Meissner, D. (1999) growth of CdTe monograin powders. *Physica Scripta*, **T69**, 155–158.
- [16] Hiie, J., Altosaar, M., Mellikov, E., Mikli, V., Mädasson, J. & Sapogova, J. (1997) Isothermal grain growth of CdTe in  $\text{CdCl}_2$  and Te fluxes. In: *Conference Records of the 26th IEEE Photovoltaic Specialists Conference. IEEE Operations Center*, 455–458.
- [17] Timmo, K., Altosaar, M., Kauk, M., Raudoja, J. & Mellikov, E. (2007)  $\text{CuInSe}_2$  monograin growth in the liquid phase of potassium iodide. *Thin Solid Films*, **515**, 5884–5886.
- [18] Altosaar, M., Raudoja, J., Timmo, K., Danilson, M., Krunks, M. & Mellikov, E. (2006)  $\text{Cu}_2\text{ZnSnSe}_4$  monograin powders for solar cell application. In: *Conference Record of the 2006 IEEE 4th World Conference on Photovoltaic Energy Conversion*. Waikoloa, HI, May 07–12. IEEE Electron Devices Society, 468–470.
- [19] Altosaar, M., Raudoja, J., Timmo, K., Danilson, M., Grossberg, M., Krustok, J. & Mellikov, E. (2008)  $\text{Cu}_2\text{Zn}_{1-x}\text{Cd}_x\text{Sn}_{1-y}\text{S}_y$  solid solutions as absorber materials for solar cells. *Physica Status Solidi A*, **205**, 167–170.
- [20] Leinemann, I., Raudoja, J., Grossberg, M., Traksmaa, R., Kaljuvee, T., Altosaar, M. Meissner, D. (2010) Comparison of copper zinc tin selenide formation in molten potassium iodide and sodium iodide as flux materials. In: *Proceedings of the Conference of Young Scientists on Energy Issues*, Kaunas, Lithuania 2010, 1–8.
- [21] Klavina, I., Kaljuvee, T., Timmo, K., Raudoja, J., Traksmaa, R., Altosaar, M. & Meissner, D. (2011) Study of  $\text{Cu}_2\text{ZnSnSe}_4$  monograin formation in molten KI starting from binary chalcogenides. *Thin Solid Films*, **519**, 7399–7407.
- [22] Nkwusi, G., Leinemann, I., Grossberg, M., Kaljuvee, T., Traksmaa, R., Altosaar, M. & Meissner, D. (2012) Formation of copper zinc tin sulfide in cadmium iodide for monograin membrane solar cells. In: *Proceedings of the 9th International Conference of Young Scientists on Energy Issues*, Kaunas, May 24–25 2012, 38–46.
- [23] Chen, S., Gong, X.G., Walsh, A. & Wei, S.H. (2010) Defect physics of the kesterite thin-film solar cell absorber  $\text{Cu}_2\text{ZnSnS}_4$ . *Applied Physics Letters*, **96**, 021902.
- [24] Muska, K., Kauk, M., Altosaar, M., Pilvet, M., Grossberg, M. & Volobujeva, O. (2011) Synthesis of  $\text{Cu}_2\text{ZnSnS}_4$  monograin powders with different compositions. *Energy Procedia*, **10**, 203–207.
- [25] Muska, K., Kauk, M., Grossberg, M., Raudoja, J. & Volobujeva, O. (2011) Influence of compositional deviations on the properties of  $\text{Cu}_2\text{ZnSnSe}_4$  monograin powders. *Energy Procedia*, **10**, 323–327.

- [26] Oleksyuk, I.D., Dudchak, I.V. & Piskach, L.V. (2004) Phase equilibria in the  $\text{Cu}_2\text{S}$ – $\text{ZnS}$ – $\text{SnS}_2$  system. *Journal of Alloys and Compounds*, **368**, 135–143.
- [27] Timmo, K., Altosaar, M., Raudoja, J., Grossberg, M., Danilson, M., Volobujeva, O. & Mellikov, E. (2010) Chemical etching of  $\text{Cu}_2\text{ZnSn}(\text{S},\text{Se})_4$  monograin powder. In: *Proceedings of 35th IEEE Photovoltaic Specialists Conference*, Honolulu, HI, June 20–25 2010, 1982–1985.
- [28] Pourbaix, M. (1974) *Atlas of Electrochemical Equilibria in Aqueous Solutions II*. National Association of Corrosion Engineers, Houston, US.
- [29] Scheer, R., Walter, T., Schock, H.W., Fearheiley, M.L. & Lewerenz, H.J. (1993)  $\text{CuInS}_2$  based thin film solar cell with 10.2% efficiency. *Applied Physics Letters*, **63**, 3294–3296.
- [30] Weber, A., Mainz, R. & Schock, H.W. (2010) On the Sn loss from thin films of the material system  $\text{Cu}$ – $\text{Zn}$ – $\text{Sn}$ – $\text{S}$  in high vacuum. *Journal of Applied Physics*, **107**, 013516.
- [31] Scragg, J., Ericson, T., Kubart, T., Edoff, M. & Platzer-Björkman, C. (2011) Chemical insights into the instability of  $\text{Cu}_2\text{ZnSnS}_4$  films during annealing. *Chemistry of Materials*, **23**, 4625–4633.
- [32] Redinger, A., Berg, D.M., Dale, P.J., Djemour, R., Gütay, L., Eisenbarth, T., Valle, N. & Siebentritt, S. (2011) Route toward high-efficiency single-phase  $\text{Cu}_2\text{ZnSn}(\text{S},\text{Se})_4$  thin-film solar cells: model experiments and literature review. *IEEE Journal of Photovoltaics*, **1**, 200–206.
- [33] Gerasimov, J.I., Krestovnikov, A. & Gorbov, V. (1974) *Chimitscheskaja termodinamika v cvetnoi metallurgii*. Metallurgia, Moscow (in Russian).
- [34] Brebrick, R.F. & Strauss, A.J. (1964) Partial pressures in equilibrium with group IV tellurides I, Optical absorption method and results for  $\text{PbTe}$ . *Journal of Chemical Physics*, **40**, 3230–3241.
- [35] Kauk-Kuusik, M., Altosaar, M., Muska, K., Pilvet, M., Raudoja, J., Timmo, K., Varema, T., Grossberg, M., Mellikov, E. & Volobujeva, O. (2013) Post-growth annealing effect on the performance of  $\text{Cu}_2\text{ZnSnSe}_4$  monograin layer solar cells. *Thin Solid Films*, **535**, 18–21.
- [36] Kauk, M., Muska, K., Altosaar, M., Raudoja, J., Pilvet, M., Varema, T., Timmo, K. & Volobujeva, O. (2011) Effects of sulphur and tin disulphide vapour treatments of  $\text{Cu}_2\text{ZnSn}(\text{S},\text{Se})_4$  absorber materials for monograin solar cells. *Energy Procedia*, **10**, 197–202.
- [37] Wang, K., Shin, B., Reuter, K.B., Todorov, T., Mitzi, D.B. & Guha, S. (2011) Structural and elemental characterization of high efficiency  $\text{Cu}_2\text{ZnSnS}_4$  solar cells. *Applied Physics Letters*, **98**, 051912.
- [38] Katagiri, H., Ishigaki, N., Ishida, T. & Saito, K. (2001) Characterization of  $\text{Cu}_2\text{ZnSnS}_4$  thin films prepared by vapor phase sulfurization. *Japanese Journal of Applied Physics*, **40**, 500–504.
- [39] Chen, S., Yang, J.H., Gong, X.G., Walsh, A. & Wei, S.H. (2010) Intrinsic point defects and complexes in the quaternary kesterite semiconductor  $\text{Cu}_2\text{ZnSnS}_4$ . *Physical Review B*, **81**, 245204.
- [40] Chen, S., Wang, L.W., Walsh, A., Gong, X.G. & Wei, S.H. (2012) Abundance of  $\text{Cu}_{\text{Zn}}$ + $\text{Sn}_{\text{Zn}}$  and  $2\text{Cu}_{\text{Zn}}$ + $\text{Sn}_{\text{Zn}}$  defect clusters in kesterite solar cells. *Applied Physics Letters*, **101**, 223901.
- [41] Hönes, K., Zscherpel, E., Scragg, J. & Siebentritt, S. (2009) Shallow defects in  $\text{Cu}_2\text{ZnSnS}_4$ . *Physica B: Condensed Matter*, **404**, 4949–4952.
- [42] Luckert, F., Hamilton, D.I., Yakushev, M.V., Beattie, N.S., Zoppi, G., Moynihan, M., Forbes, I., Karotki, A.V., Mudryi, A.V., Grossberg, M., Krustok, J. & Martin, R.W. (2011) Optical properties of high quality  $\text{Cu}_2\text{ZnSnSe}_4$  thin films. *Applied Physics Letters*, **99**, 062104.
- [43] Grossberg, M., Krustok, J., Raudoja, J., Timmo, K., Altosaar, M. & Raadik, T. (2011) Photoluminescence and Raman study of  $\text{Cu}_2\text{ZnSn}(\text{Se}_x\text{S}_{1-x})_4$  monograins for photovoltaic applications. *Thin Solid Films*, **519**, 7403–7406.
- [44] Grossberg, M., Krustok, J., Timmo, K. & Altosaar, M. (2009) Radiative recombination in  $\text{Cu}_2\text{ZnSnSe}_4$  monograins studied by photoluminescence spectroscopy. *Thin Solid Films*, **517**, 2489–2492.
- [45] Grossberg, M., Krustok, J., Raudoja, J. & Raadik, T. (2012) The role of structural properties on deep defect states in  $\text{Cu}_2\text{ZnSnS}_4$  studied by photoluminescence spectroscopy. *Applied Physics Letters*, **101**, 102102.
- [46] Levanyuk, A.P. & Osipov, V.V. (1981) Edge luminescence of direct-gap semiconductors. *Soviet Physik Uspekhi*, **24**, 187–215.

- [47] Krustok, J., Jagomägi, A., Grossberg, M., Raudoja, J. & Danilson, M. (2006) Photoluminescence properties of polycrystalline  $\text{AgGaTe}_2$ , *Solar Energy Materials and Solar Cells*, **90**, 1973–1982.
- [48] Krustok, J., Collan, H., Yakushev, M. & Hjelt, K. (1999) The role of spatial potential fluctuations in the shape of the PL bands of multinary semiconductor compounds. *Physica Scripta*, **T79**, 179–182.
- [49] Krustok, J., Raudoja, J., Yakushev, M., Pilkington, R.D. & Collan, H. (1999) On the shape of the close-to-band-edge photoluminescent emission spectrum in compensated  $\text{CuGaSe}_2$ . *Physica Status Solidi (A)*, **173**, 483–490.
- [50] Chen, S., Gong, X.G., Walsh, A. & Wei, S.H. (2009) Crystal and electronic band structure of  $\text{Cu}_2\text{ZnSnX}_4$  (X=S and Se) photovoltaic absorbers: First-principles insights. *Applied Physics Letters*, **94**, 041903.
- [51] Schorr, S., Hoebler, H.J. & Tovar, M. (2007) A neutron diffraction study of the stannite-kesterite solid solution series. *European Journal of Mineralogy*, **19**, 65–73.
- [52] Schorr, S. (2011) The crystal structure of kesterite type compounds: A neutron and X-ray diffraction study. *Solar Energy Materials and Solar Cells*, **95**, 1482–1488.
- [53] Gürel, T., Sevik, C. & Cagin, T. (2011) Characterization of vibrational and mechanical properties of quaternary compounds  $\text{Cu}_2\text{ZnSnS}_4$  and  $\text{Cu}_2\text{ZnSnSe}_4$  in kesterite and stannite structures. *Physics Reviews B*, **84**, 205201.
- [54] Khare, A., Himmetoglu, B., Johnson, M., Norris, D.J., Cococcioni, M. & Aydil, E.S. (2012) Calculation of the lattice dynamics and Raman spectra of copper zinc tin chalcogenides and comparison to experiments. *Journal of Applied Physics*, **111**, 083707.
- [55] Grossberg, M., Raadik, T., Raudoja, J. & Krustok, J. (2014) Photoluminescence study of defect clusters in  $\text{Cu}_2\text{ZnSnS}_4$  polycrystals. *Current Applied Physics*, **14**, 447–450.
- [56] Huang, D. & Persson, C. (2013) Band gap change induced by defect complexes in  $\text{Cu}_2\text{ZnSnS}_4$ . *Thin Solid Films*, **535**, 265–269.
- [57] Grossberg, M., Salu, P., Raudoja, J. & Krustok, J. (2013) Microphotoluminescence study of  $\text{Cu}_2\text{ZnSnS}_4$  polycrystals. *Journal of Photonics for Energy*, **3**, 030599.
- [58] Kask, E., Raadik, T., Grossberg, M., Josepson, R. & Krustok, J. (2011) Deep defects in  $\text{Cu}_2\text{ZnSnS}_4$  monograin solar cells. *Energy Procedia*, **10**, 261–265.
- [59] Kask, E., Grossberg, M., Josepson, R., Salu, P., Timmo, K. & Krustok, J. (2013) Defect studies in  $\text{Cu}_2\text{ZnSnSe}_4$  and  $\text{Cu}_2\text{ZnSn}(\text{Se}_{0.75}\text{S}_{0.25})_4$  by admittance and photoluminescence spectroscopy. *Materials Science in Semiconductor Processing*, **16**, 992–996.
- [60] Krustok, J., Josepson, R., Danilson, M. & Meissner, D. (2010) Temperature dependence of  $\text{Cu}_2\text{ZnSn}(\text{Se}_{1-x}\text{S}_x)_4$  monograin solar cells. *Solar Energy*, **84**, 379–383.
- [61] Kniese, R., Hariskos, D., Voorwinden, G., Rau, U. & Powalla, M. (2003) High band gap  $\text{Cu}(\text{In,Ga})\text{Se}_2$  solar cells and modules prepared with in-line co-evaporation. *Thin Solid Films*, **431–432**, 543–547.
- [62] Singh, P., Singh, S.N., Lal, M. & Husain, M. (2008) Temperature dependence of I-V characteristics and performance parameters of silicon solar cell. *Solar Energy Materials and Solar Cells*, **92**, 1611–1616.
- [63] Phillips, J.E., Shafarman, W.N. & Shan, E. (1994) Evidence for amorphous like behavior in small grain thin film polycrystalline solar cells. In: *Proceedings of IEEE First WCPEC (24th IEEE PVSC)*, 303–306.





# **Part IV**

## **Device Physics of Thin-Film Solar Cells**



# 14

## The Role of Grain Boundaries in CZTS-Based Thin-Film Solar Cells

Joel B. Li<sup>1</sup> and Bruce M. Clemens<sup>2</sup>

<sup>1</sup>*Department of Electrical Engineering, Stanford University,  
Stanford, CA 94305, USA*

<sup>2</sup>*Department of Materials Science & Engineering, Stanford University,  
Stanford, CA 94305, USA*

### 14.1 Introduction

Silicon is one of the most-studied semiconductor materials, with techniques to control and manipulate its properties well established by the integrated-circuit (IC) industry. While silicon wafer-based technology constitutes about 85% of the photovoltaics (PV) market [1], there are compelling reasons to develop thin-film solar cells. These include potential material cost and energy savings achievable with thin absorber layers of direct band-gap thin-film materials, and the potential for incorporation of thin-film PV onto inexpensive, flexible, or building material substrates [2, 3], which opens up the possibility of new applications.

Among the various thin-film technologies, CdTe and Cu(In,Ga)(S,Se)<sub>2</sub> (CIGSSe), dominate the thin-film PV market [4]. In recent years however, the photovoltaic community has seen growing interest in CZTS-based thin-film solar cells which include Cu<sub>2</sub>ZnSnS<sub>4</sub> (CZTS), Cu<sub>2</sub>ZnSnSe<sub>4</sub> (CZTSe), and Cu<sub>2</sub>ZnSn(S,Se)<sub>4</sub> (CZTSSe) solar cells. This interest is driven by their potential to replace Cu(In,Ga)Se<sub>2</sub> (CIGSe) and CdTe solar cells which face material scarcity, toxicity, and market acceptance issues. Indium is expected to limit CIGSe production to between 20 and 100 GW a<sup>-1</sup> [5]. The low annual production of tellurium (250–300 t a<sup>-1</sup>) will limit CdTe production to 4–5 GW<sub>p</sub> a<sup>-1</sup> [6]. The use of Cd is also restricted in selected countries such as Japan, partly because of previous environmental and health incidents

related to the handling of toxic Cd [4]. As such, CZTS is an attractive alternative to CIGSe and CdTe solar cells due to its Earth-abundant and non-toxic elemental composition.

Apart from material benefits, CZTS has optical properties that make it highly suitable as a single-junction solar cell material. CZTS is reported to have a direct band gap of 1.32–1.85 eV and a band edge absorption coefficient of above  $10^4 \text{ cm}^{-1}$  [7–9].

In recent years, CZTS and CZTSSe solar cells have achieved efficiencies of up to 8.5% [10] and 12.6% [11], respectively. In comparison, polycrystalline CIGSe and CdTe solar cells have achieved 20.8% [12] and 21.0% [13] efficiencies, respectively. It is surprising that CuInSe<sub>2</sub> (CISE) and CdTe's single-crystal counterparts have only achieved 12% and 13.5%, respectively [14, 15]. In optoelectronic or transistor applications, semiconductor materials such as silicon, germanium, and gallium arsenide typically perform better in single-crystal form. This is attributed to the higher concentration of dangling bonds and defects found at grain boundaries (GBs), which results in electronic states in the gap and strong carrier recombination. However, for polycrystalline CIGSe-based (CIGSe, CISE, CuGaSe<sub>2</sub>(CGSe)) and CdTe solar cells, GBs do not seem to affect solar cell efficiency as much. In fact, some studies have identified GBs as the source of high efficiency in polycrystalline CIGSe-based and CdTe solar cells [16–20].

One prevailing theory is that GBs in CIGSe-based and CdTe films possess crystal defects or impurities that trap majority carriers, resulting in the formation of a space charge region (SCR) and GB potential. The presence of this GB potential sets up an electric field within the SCR [21], which increases charge separation by assisting electron flow towards the GB and repelling holes from it [16, 17]. Overall, this leads to enhanced minority carrier collection in CIGSe-based and CdTe solar cells.

## 14.2 CIGSe and CdTe Solar Cells

CIGSe-based and CZTS-based films are similar in terms of growth methods, optoelectronic, and crystallographic properties. Because of these similarities and the benign nature of GBs in CIGSe-based and CdTe films, it is useful to examine the properties of GBs in these materials.

### 14.2.1 Simulation Results

First-principle calculations conducted by Yan *et al.* showed that GBs in CISE are benign and do not possess strong recombination sites [22]. Other first-principle calculations showed that a larger hole barrier that repels holes and reduces recombination at the GBs is formed in CISE through Cu vacancy surface reconstruction [23] or in cation-terminated CISE and CGSe [24].

### 14.2.2 Experimental Results

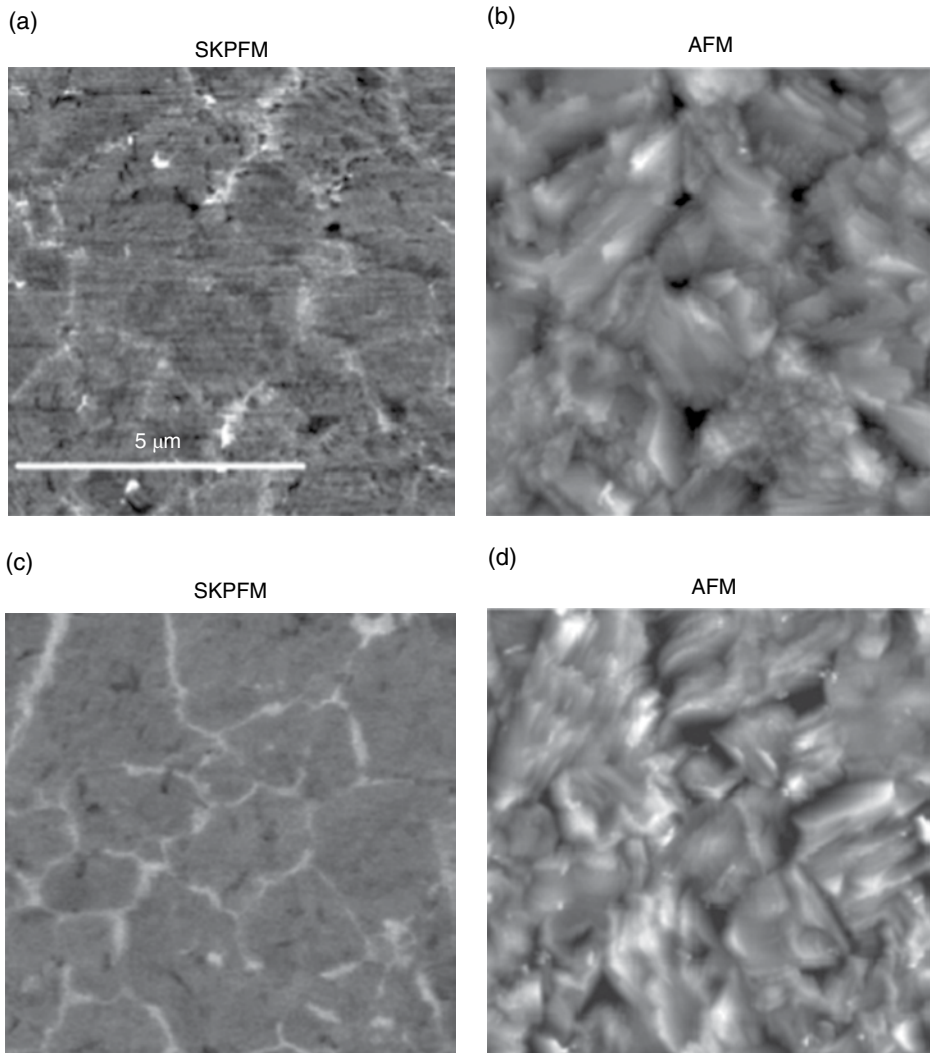
#### 14.2.2.1 Grain Boundary Potential

GB potential is the potential formed due to trapping of majority carriers by crystal defects or impurities at the GB. It arises because uncompensated dopant atoms near the GB set up an electric field in the depletion region, forming the GB potential. This GB potential appears as a dip in the energy band diagram of p-type CIGSe and CdTe. It is an important parameter to measure because it can greatly influence solar cell performance through its influence on carrier collection, mobility, and lifetime. As such, there are efforts to measure GB potential on CIGSe [17, 25–35] and CdTe [16, 36–40] using scanning Kelvin probe

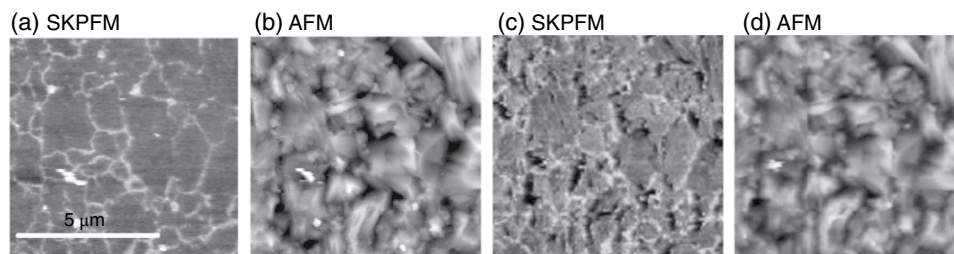
microscopy (SKPM). However, the reported polarity type and potential barrier heights have not always been consistent.

Baier *et al.* performed SKPM measurements on CIGSe at the cantilever's second resonance frequency and found GB potential barriers to vary from  $-118$  mV to  $+114$  mV with some GBs not exhibiting any potential barriers [32]. He also found no dependence of GB potential on Ga-content in CIGSe, contrary to what was reported by Jiang *et al.* [17].

Jiang *et al.* proposed that measurement inconsistency could be due to differences in material quality or SKPM set-up [31, 35]. In order to obtain a high-quality potential image with uniform grain surface potential and clear GB potential contrast as in Figure 14.1, it



**Figure 14.1** Two-dimensional (a) SKPM and (b) AFM maps on low-performance CIGSe films. Two-dimensional (c) SKPM and (d) AFM maps on high-performance CIGSe films. Grey scales are 400 mV in the potential images and 200 nm in the AFM images. © 2012 IEEE. Reprinted, with permission, from [35]



**Figure 14.2** All measurements were performed on the same area of a high-performance CIGSe film. Two-dimensional (a) SKPM and (b) AFM maps conducted with low-frequency mode. Two-dimensional (c) SKPM and (d) AFM maps conducted with second harmonic frequency mode. Grey scales are 400 mV in the potential images and 200 nm in the AFM images. © 2012 IEEE. Reprinted, with permission, from [35]

was shown that it is essential to have high-quality film surface with minimal surface defects/charges and inverted/depleted GBs.

Jiang *et al.* also found that using the low-frequency (c. 20 kHz) instead of second-harmonic-frequency (250–400 kHz) mode during SKPM reduces the topographical effect, as shown in Figure 14.2. Scanning capacitance microscopy (SCM) was also performed on these CIGSe films and supported the SKPM measurements.

SKPM measurements performed by Li *et al.* at low-frequency mode on identically grown CIGSe samples to those of Jiang *et al.* yielded similar GB potential values [33, 34].

Other methods such as conductivity and Hall measurements have also been used to measure GB potentials of CIGSe-based films. The reported values measured with these techniques ranged from below 20 meV to 350 meV [41–50]. The large variations in measured potential barrier heights of GB can be attributed to a compositional difference between samples [41–50], whether or not Na was incorporated [49, 50], and also whether air-annealing was performed [41].

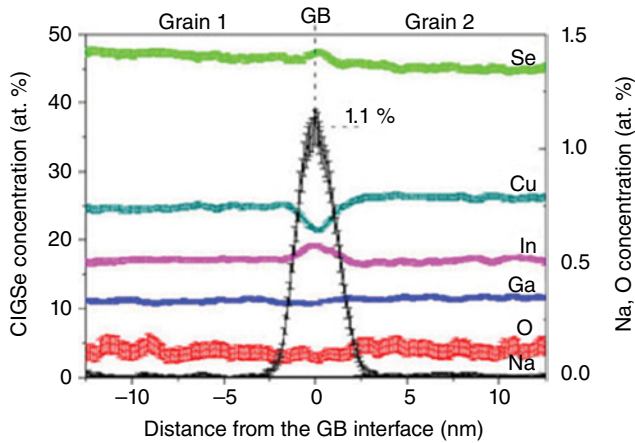
#### 14.2.2.2 Composition, Recombination Centers, and GB Passivation

To investigate if composition differences exist between the GBs and grain interior of CIGSe, Hetzer *et al.* performed micro-Auger electron spectroscopy. His results showed that, relative to the grain interior, the GB had a Cu composition decrease of as large as a factor of 2 [51].

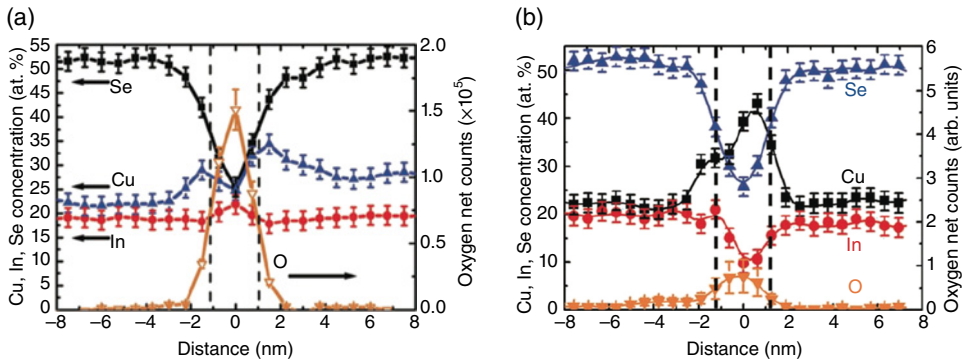
However, energy-dispersive X-ray spectroscopy (EDS) performed on CIGSe by another group showed that there is little composition differences (less than 0.5 at%) between grain interior and GBs [52]. O and Na were also not detected at the GBs.

Atom probe tomography (APT) measurements performed on CIGSe found significant Cu depletion associated with In and Se composition increase at the GB, as shown in Figure 14.3 [53]. This suggests that surface reconstruction has taken place and a Cu-poor structure is formed at the GB interface.

Recently, electron energy loss spectroscopy (EELS) measurements on CIGSe revealed that composition changes at the GBs are confined to regions of only about 1 nm in width, and are not due to secondary phases but rather atomic or ionic redistribution within the atomic planes close to the GBs [54]. The measurements showed that compositional changes at GBs are not consistent and there are GBs with Cu depletion (Fig. 14.4a) and GBs with



**Figure 14.3** Se, Cu, In, Ga, O, and Na elemental distribution profiles of CIGSe by APT. © 2011 IEEE. Reprinted, with permission, from [53]



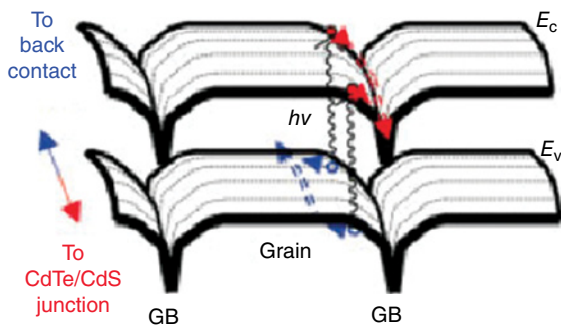
**Figure 14.4** Elemental distribution profiles of CIGSe by EELS at two different spots (a, b). Reproduced with permission from [54]. Copyright © 2012 WILEY-VCH Verlag GmbH & Co. KGaA, Weinheim

Cu enrichment (Fig. 14.4b). It was however observed that if the Cu signal increases, the In signal reduces and *vice versa*. This is suggestive of atomic redistribution at the GBs.

Further investigation by the same group found that at Se-Se terminated  $\Sigma 3\{112\}$  twin boundaries, there is Cu depletion and In enrichment [55]. On the other hand, at a cation-Se terminated twin boundary, Cu depletion and In enrichment was detected. In the case of non-twin GBs, there is always a strong anticorrelation of Cu and In signals which suggests that  $\text{In}_{\text{Cu}}$  or  $\text{Cu}_{\text{In}}$  antisites have formed.

Other studies have found O and Na to be passivating the GBs of CIGSe [54, 56, 57] and CIGSe [58].

To study defect densities at GBs of CIGSe, Abou-Ras *et al.* performed electron-beam scattering diffraction (EBSD) and cathodoluminescence (CL) measurements to show that there is a considerably lower defect density at  $\Sigma 3$  twin boundaries compared to random grain boundaries [59].



**Figure 14.5** Illustration of band diagram versus spatial coordinate of CdTe grains in the solar cell. Blue and red circles represent hole and electrons, respectively. Blue and red arrows show their direction of movement respectively. Electron-hole pairs are photogenerated near the GB and undergo charge separation due to the GB potential. This is followed by holes travelling within the grain towards the back contact and electrons channeling along the GB core towards the CdTe/CdS junction. Reproduced with permission from [16]. © 2004 WILEY-VCH Verlag GmbH & Co. KGaA, Weinheim. For color details, please see color plate section

#### 14.2.2.3 Conduction Channels Along GBs

The result of enhanced charge separation and negligible recombination in the GBs means that photogenerated electrons can be attracted into the GBs and travel along them towards the CdS and ZnO layers to be collected as shown in Figure 14.5 [16, 17]. Several groups have reported experimental results that are consistent with the theory that GBs in CdTe [16] and CIGSe [19, 26, 33, 60] are inverted and act as conducting channels for minority carriers. However, this property is not always detected at all GBs. The proposed explanations include variations in crystallographic orientation [19, 61], GB band bending differences [26], presence of contaminants, tip-GB contact quality, and electrical connection quality with the Mo back contact [19].

### 14.3 CZTS-Based Thin-Film Solar Cells

CIGSe and CdTe solar cells are able to achieve high efficiencies as their GBs possess certain beneficial properties. Determining whether polycrystalline CZTS and CZTSSe films have the same GB properties as CIGSe and CdTe can indicate if CZTS and CZTSSe solar cells have the potential to achieve similar high efficiencies. As such, understanding the properties of grain boundaries in CZTS-based materials has become an active area of research pursued by theorists and experimentalists [33–35, 62–67].

In this section, we discuss the various growth techniques and simulation and experimental results of CZTS-based solar cells.

#### 14.3.1 Growth Techniques

CZTS-based films have been grown using the hydrazine solution-based process [68, 69], variation of the hydrazine process [70], simultaneous deposition and reaction under high



vacuum [71], using inks of nanoparticles [72–75] and performing low-temperature co-evaporation at 150 °C followed by atmospheric annealing [76]. Other techniques include: reactive sputtering of Cu, Zn, and Sn targets in 50% H<sub>2</sub>S/Ar mixture [33]; co-sputtering of compound targets Cu<sub>x</sub>(S,Se)<sub>y</sub>, Zn<sub>x</sub>(S,Se)<sub>y</sub>, and Sn<sub>x</sub>(S,Se)<sub>y</sub> [77, 78]; co-sputtering of Cu, SnS, and ZnS targets [79, 80]; vapor phase selenization of vacuum deposited metallic and/or sulfides precursors [81]; reactive sputtering of a Cu-Zn-Sn-S precursor followed by rapid annealing [82]; sol-gel process with [83] and without sulfurization [84]; sputtering of Cu-Zn-Sn target followed by selenization or sulfo-selenization [85]; sputtering of Cu<sub>2</sub>ZnSnS<sub>4</sub> compound target [86]; and electrochemical methods [87].

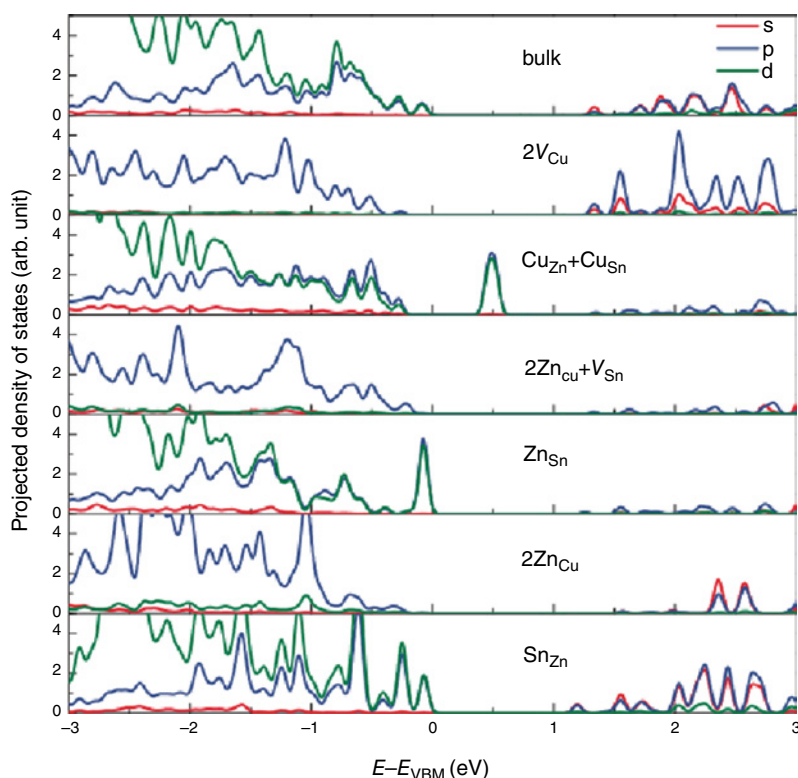
### 14.3.2 Simulation Results

Density functional theory (DFT) simulations together with conventional phase-contrast imaging technique or Z-contrast imaging showed that defect levels in Si and CdTe are deep within their band gaps but shallower in the band gaps of CISE and CZTSe [62]. It was also observed that if a material has a stronger covalent bonding nature, the GBs create deeper gap levels; if however a material has a stronger ionic bonding nature, the GBs create shallower gap levels. As such, grain boundary passivation is needed for Si and CdTe but is not so critical for CIGSe, CZTSe, and CZTS.

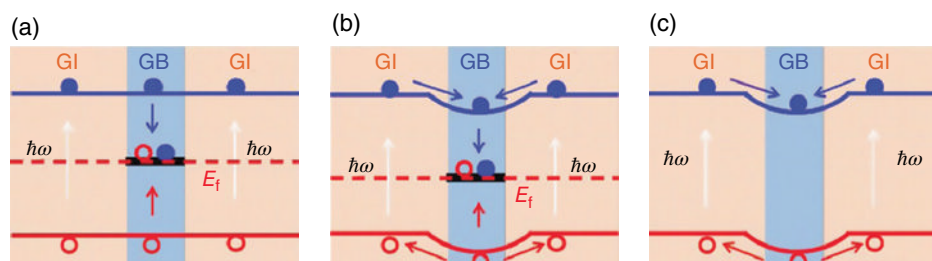
Another group performed DFT simulation and found that constituent atoms at the GB in CZTSe create localized defect states that promote the recombination of photon-excited electrons and holes [63]. It was found that in CZTSe, Cu, and Zn atoms in position 3 of GB-II as described in [63] relaxed from sp<sup>3</sup>-bonded to sp<sup>2</sup>-bonded. Cu<sub>3</sub> atoms in GB-IV also have a bonding change from sp<sup>3</sup> to sp<sup>2</sup> while Sn<sub>3</sub> atoms move toward its counterpart Sn<sub>3</sub>' atoms to form dimers of distance 2.86 Å. For CISE, In<sub>3</sub> and In<sub>3</sub>' in GB-VI form a dimer of distance 2.73 Å while Cu<sub>3</sub> atoms changed from sp<sup>3</sup> to sp<sup>2</sup> configuration. The large relaxation experienced by atoms at the GB of CISE decreases defect states in the band gap but the structural change does not have a similar effect in CZTSe. Their investigations suggest that it is crucial to remove these defect states in order to improve the efficiency of CZTSe solar cells.

The simulation of Xu *et al.* showed that cation-terminated (112) surfaces in stoichiometric CZTS preferentially form Cu-enriched defects (Cu<sub>Zn</sub> and Cu<sub>Sn</sub>) while anion-terminated ( $\bar{1}\bar{1}\bar{2}$ ) surfaces favor Cu-depleted defects (2V<sub>Cu</sub>, 2Zn<sub>Cu</sub>, 2Zn<sub>Cu</sub> + V<sub>Sn</sub>) [88]. Growing a sample under Cu-poor and Zn-rich condition also favors the formation of non-stoichiometric samples, which preferentially form Cu-depleted defects on both surfaces. Through electronic structure analysis, it was found that Cu-enriched surfaces result in detrimental states in the band gap while Cu-depleted surfaces do not form deep band-gap states as shown in the projected density of states (PDOS) in Figure 14.6. This is consistent with the observation that Cu-poor and Zn-rich CZTS devices tend to have higher efficiencies.

Yin *et al.* reported that intrinsic kesterite-CZTSe Σ3(114) GBs are detrimental and the Fermi level is pinned at defect states created by the wrong bonds [64]. These deep defect states at GBs lead to strong carrier recombination as shown in Figure 14.7a. In the case when interstitial Na ions (Na<sub>i</sub><sup>+</sup>) gather at the GBs, a negative potential for electrons is created leading to a dip in the conduction and valence band edges around the GBs. This band bending would repel holes and attract electrons to the GB of CZTSe, enhancing charge separation. However, the deep defect states created by the Cu-Sn and Se-Se wrong bonds are still present and act as recombination centers. Around the GB, defect



**Figure 14.6** Partial density of states (PDOS) with different surface defects. Reprinted with permission from [88]. Copyright © 2013 by the American Physical Society. For color details, please see color plate section



**Figure 14.7** Band diagram of (a) an intrinsic CZTSe GB; (b) an intrinsic CZTSe GB with only  $\text{Na}_i^+$ ; and (c) CZTSe GB passivated by  $(\text{Zn}_{\text{Sn}}, \text{O}_{\text{Se}})$  or  $(\text{Zn}_{\text{Sn}}, \text{O}_{\text{Se}}, \text{Na}_i^+)$ . Reproduced with permission from [64]. © 2013 WILEY-VCH Verlag GmbH & Co. KGaA, Weinheim

states and band edge are pulled down together but the defect level is still deep and the Fermi level remains pinned at the GB. This indicates that  $\text{Na}_i^+$  doping induces band bending around CZTSe GB, but cannot remove the deep defect states that result in poor solar cell performance as shown in Figure 14.7b. GB passivation can be achieved by

having ( $\text{Zn}_{\text{Sn}}, \text{O}_{\text{Se}}$ ) or ( $\text{Zn}_{\text{Sn}}, \text{O}_{\text{Se}}$ , and  $\text{Na}_i^+$ ) segregate at the GBs. This reduces deep defect states within the band gap and simultaneously forms a hole barrier and electron attractor as shown in Figure 14.7c.

### 14.3.3 Experimental Results

#### 14.3.3.1 Grain Boundary Potential and Conduction Channels

Experimentally, SKPM measurements reveal higher positive surface potential at the GBs compared to the grain, as shown in Figure 14.8. In addition, C-AFM measurements show higher current flow in the vicinity of the GBs as shown in Figure 14.9 [33, 34]. Together they demonstrate the enhanced minority carrier collection taking place at the GBs of CZTS and CZTSSe.

Similarly, Repins reported a SKPM image of a National Renewable Energy Laboratory (NREL) CZTSe absorber, as shown in Figure 14.10 [5]. They found GB potential to vary between 100 and 500 mV, with an average value of around 400 mV over the  $10\text{ }\mu\text{m} \times 10\text{ }\mu\text{m}$  area. It was also observed that GB potential decreases in magnitude with prolonged exposure to humid air [42], similar to NREL's CIGSe samples. This degradation was suggested to be caused by movement of Na, which has been observed in increased amounts on exposed CIGSe samples.

SKPM and C-AFM measurements on CZTSSe films performed by another group also showed higher positive surface potential for the majority of the GBs [89].

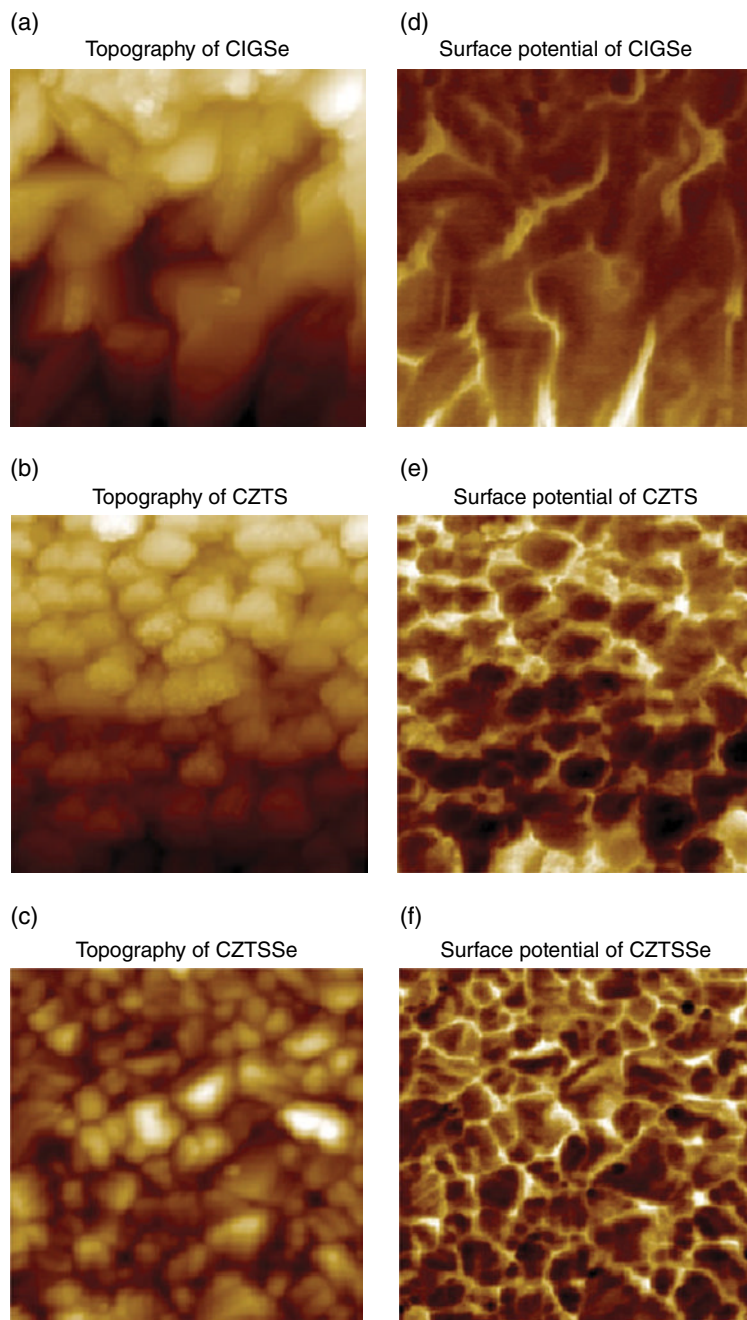
Another method to measure GB potential is through temperature-dependent conductivity measurements. This method reveals that GB barrier height in Cu-poor CZTS films increases monotonically with annealing time [90]. The barrier heights measured ranged from 50 to 150 meV. It was also discovered that the barrier height is sensitive to the  $[\text{Cu}]/([\text{Zn}] + [\text{Sn}])$  ratio but not to the  $[\text{Zn}]/[\text{Sn}]$  ratio.

#### 14.3.3.2 Composition, Recombination Centers, and GB passivation

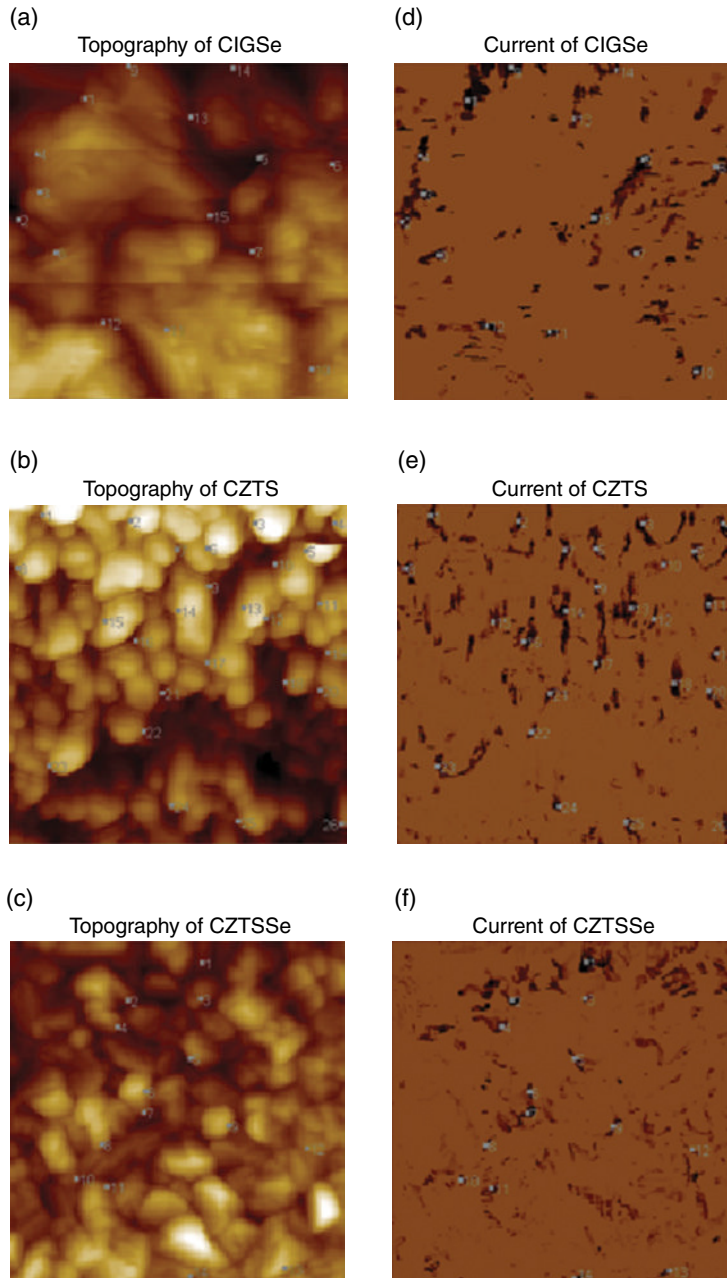
In the study of composition variations within the CZTS film, EDS analysis performed by Wang *et al.* found that GBs in the CZTS films appear to have either the same composition as the bulk or are Cu rich [65]. There are no cases of Cu deficiency observed at the GBs, as observed in CIGSe films. This result can be seen from Figure 14.11.

From the same research group, Bag *et al.* also found that GBs within CZTSe absorber layer appear to be Cu rich relative to the overall Cu-poor bulk film stoichiometry [66], as shown in Figure 14.12.

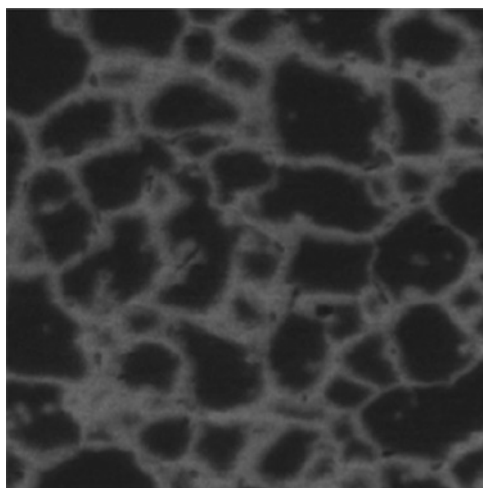
In order to investigate carrier recombination at GBs of CZTS, Mendis *et al.* performed cathodoluminescence (CL) measurements to measure the recombination velocity of heterointerfaces between CZTS and  $\text{Cu}_x\text{Sn}_y\text{S}_z$  [67]. It was found that the CZTS/ $\text{Cu}_x\text{Sn}_y\text{S}_z$  and CZTS/ZnS heterointerfaces have smaller recombination velocities than the bulk carrier diffusion velocity while CZTS/SnS had higher recombination velocity. Secondary phases such as ZnS and  $\text{CuSnS}_3$  have almost the same bond length as that of CZTS and are likely to form heterointerfaces with small misfit strain and thus possess low interfacial recombination. On the other hand, SnS is orthorhombic and has different lattice parameters to tetragonal CZTS, which can result in large interfacial misfit strain and high recombination velocity. In all, it is suggested that ZnS and  $\text{CuSnS}_3$  can provide GB passivation but not SnS.



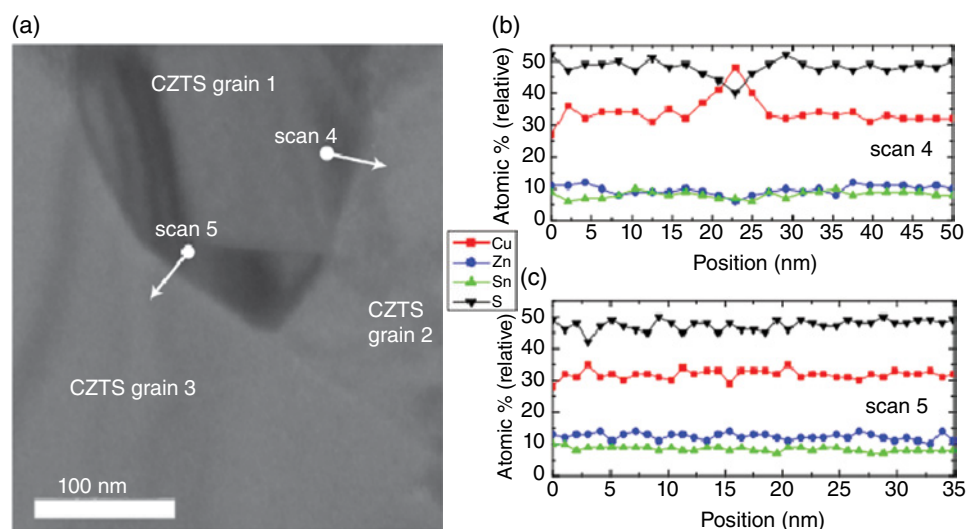
**Figure 14.8** Two-dimensional topography spatial maps of (a) CIGSe; (b) CZTS; and (c) CZTSSe. Two-dimensional surface potential spatial maps of (d) CIGSe; (e) CZTS; and (f) CZTSSe. Reproduced with permission from [33]. Copyright © 2012 WILEY-VCH Verlag GmbH & Co. KGaA, Weinheim



**Figure 14.9** Two-dimensional topography spatial maps of (a) CIGSe; (b) CZTS; and (c) CZTSSe. Two-dimensional current spatial maps of (d) CIGSe; (e) CZTS; and (f) CZTSSe at a sample bias of 0 V. Reproduced with permission from [33]. Copyright © 2012 WILEY-VCH Verlag GmbH & Co. KGaA, Weinheim



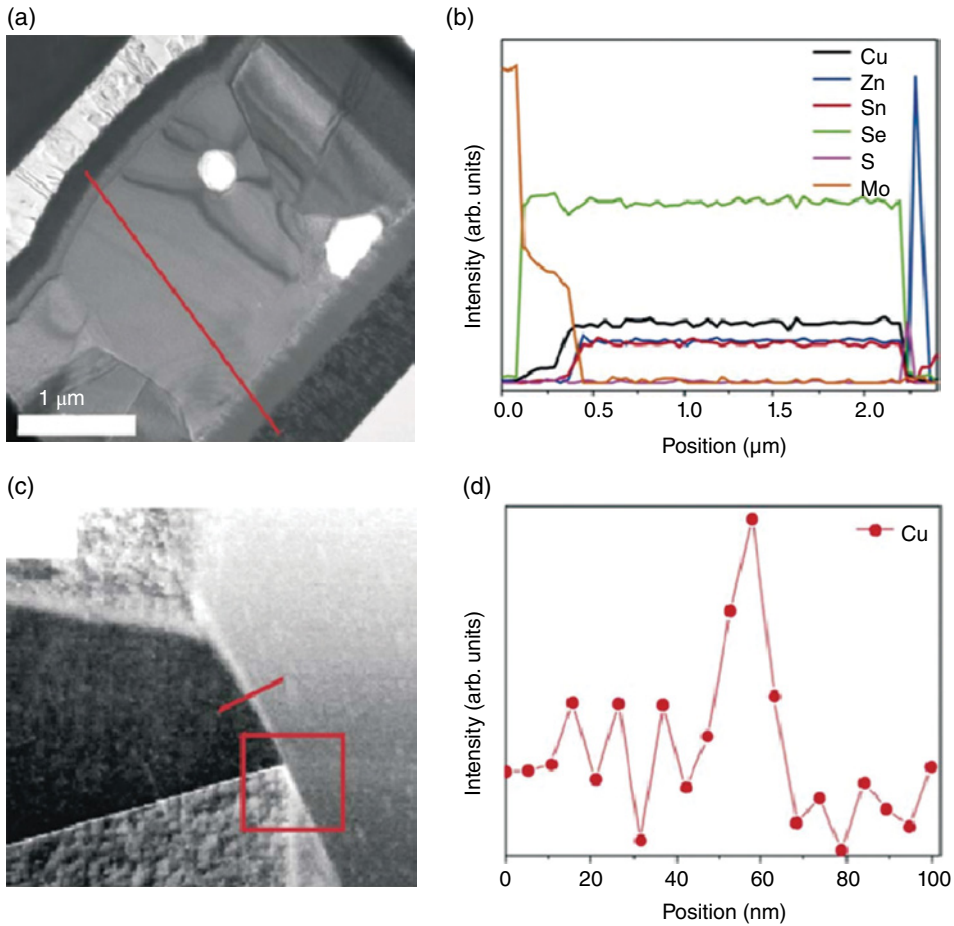
**Figure 14.10** SKPM spatial map of CZTSe [5]. GB potential barrier varied between 100 and 500 mV, with an average value of around 400 mV over  $10\ \mu\text{m} \times 10\ \mu\text{m}$  area



**Figure 14.11** EDS analysis of CZTS grain boundaries. Reprinted with permission from [65]. Copyright 2011, AIP Publishing LLC

However, Mendis *et al.* also pointed out that passivating GBs with secondary phases might not lead directly to higher-efficiency solar cells as there are other factors to be considered, such as the presence of secondary phase with a band gap that is not in the ideal 1.4–1.5 eV range, and the nature of the heterointerface with CZTS (i.e. type-I v. type-II). For a type-I heterostructure, minority carriers (electrons) will be trapped within the smaller band-gap semiconductor. Carrier separation and collection efficiency would therefore be reduced if this semiconductor is the secondary phase. For type-II heterostructure however, they can behave as resistive

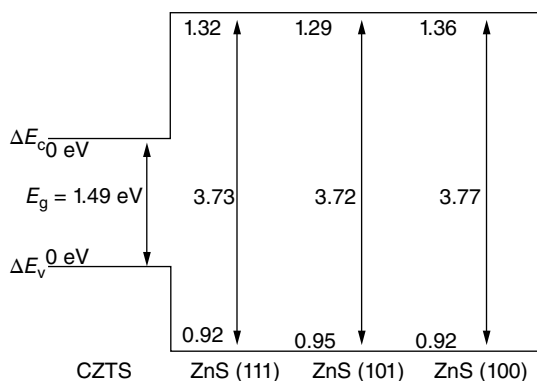




**Figure 14.12** (a) Cross-sectional TEM image and (b) EDS line scan of the low-band-gap champion CZTSe cell. (c) TEM image and (d) EDS line scan of the same cell showing Cu-rich grain boundary. The lines in (a) and (c) indicate the path examined in the EDS line scans of (b) and (d). Reproduced from [66] with permission of The Royal Society of Chemistry. For color details, please see color plate section

barriers for electrons but as potential wells for holes. The location of the secondary phase will be important if the interface is a resistive barrier to the minority carrier electrons in p-type CZTS. If the secondary phase is precipitated within the space charge region, it should ideally be a high resistive barrier in order to increase shunt resistance. On the other hand, if secondary phases formed within the quasi-neutral region, they should be low-resistive barriers so that series resistance is small and the negative impact on carrier separation is reduced.

Nagoya *et al.* found that ZnS phase which precipitates within CZTS under the Cu-poor, Zn-rich growth conditions forms a high barrier for both electrons and holes as shown in Figure 14.13 [91]. As such, it acts neither as a recombination center nor a carrier trap, but as a non-active high-resistivity domain.



**Figure 14.13** Heterojunction between CZTS and ZnS. Band gaps of ZnS are slightly smaller than the bulk value of 3.84 eV due to the strain induced by the lattice misfit with CZTS of about 0.5% [91]. © IOP Publishing. Reproduced by permission of IOP Publishing. All rights reserved

CZTSSe/ZnS was also found to form a high barrier to electrons [92]. Ultraviolet spectroscopy (UPS) on CZTSSe showed a valence band offset of 1.3 eV. Since ZnS has a band gap of approximately 3.6 eV, the conduction band offset should be a “spike” of 1.1 eV, which will be a substantial barrier to electrons and result in high series resistance.

NREL recently performed cross-sectional electron-beam-induced current (EBIC) measurements on their CZTSe absorber layer and found a greater signal attenuation when the electron beam moved from the top to the bottom of the cell rather than grain to GB [93]. This suggests that the dominant mechanism for current loss in this measurement is recombination centers within the absorber layer rather than GBs.

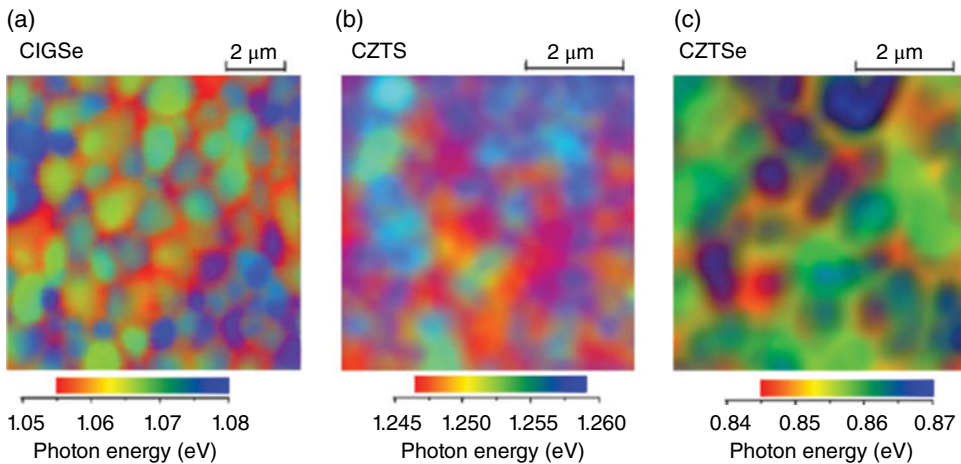
Using three independent measurement techniques – EBIC, quantum efficiency, and time-resolved photoluminescence – NREL found that their CZTSe absorber layer had a minority-carrier lifetime of a few nanoseconds, which is low compared to the 250 ns minority-carrier lifetime measured in high-performance CIGS devices [94]. By performing current–voltage measurements and device modeling, they found that this low minority-carrier lifetime imposes a significant limitation on the device voltage.

#### 14.3.3.3 Luminescence Spectroscopy of GBs

Romero performed luminescence spectroscopy on CIGSe, CZTS, and CZTSe and found that Cu-poor kesterites (CZTS and CZTSe) and Cu-poor CIGSe have electrostatic and chemical potential fluctuations [95]. At the GBs, there is a large red shift of about 10–15 meV in the luminescence of GBs in CIGSe as shown in Figure 14.14a. For CZTS, the red shift at the GBs is not clearly seen and the spatial variation in the emission spectrum is largely dominated by grain-to-grain inhomogeneity, as shown in Figure 14.14b. Red shift at GBs of CZTS is much less pronounced with only 2–4 meV. On the other hand, for CZTSe a red shift at the GBs can be seen from Figure 14.13c and the magnitude of the red shift is of the same order as the GBs of CIGSe (10–15 meV).

This result suggests that the CZTSe might have similar GB electronic structure as those found in chalcopyrites. This can be attributed to similar atomistic configuration and point defect structure. Unfortunately, not all GBs in CZTSe show this effect as compared to





**Figure 14.14** Spectrum imaging of the luminescence from (a) CIGSe; (b) CZTS; and (c) CZTSe. © 2012 IEEE. Reprinted, with permission, from [95]. For color details, please see color plate section

CIGSe, where this red shift is widespread. This luminescence observation for GB in kesterite is similar to that of chalcopyrites and is in agreement with the neutral barrier model, which is thought to be responsible for the benign behavior of GBs and critical to achieving high conversion efficiencies.

## 14.4 Conclusion

GBs have been found to be less deleterious to CIGSe and CdTe solar cell performance compared to conventional Si solar cells. This has enabled CIGSe and CdTe solar cells to achieve high efficiencies despite their polycrystalline nature. Determining the roles which GBs play in CZTS-based solar cells is of great importance, and will assist research on achieving high-efficiency solar cells.

Record efficiencies of CZTS-based solar cells are currently considerably lower than that of CIGSe and CdTe solar cells. This has been largely attributed to the low open-circuit voltage  $V_{oc}$  of these devices [68]. Low  $V_{oc}$  can result from high carrier recombination at intra-grain defects, interfacial recombination, or GBs. In order to develop a high-efficiency CZTS-based solar cell, we must determine which of these parameters is limiting  $V_{oc}$ .

Theoretical and experimental work has been undertaken to investigate the recombination nature and property of GBs in CZTS-based solar cells. Due to the wide variety of preparation methods, alloy compositions, sample quality, experimental set-up, and simulations used in investigating GBs in CIGS, CdTe, and CZTS-based films, the results have not been consistent. However, there are currently more simulation and experimental results that support the benign nature of GBs in CZTS-based films. These initial results are encouraging, but there is still a need for more research in this area to gain a better understanding of GBs and their role in solar cell performance. One possible way would be to fabricate devices out

of epitaxial CZTS-based [96] and polycrystalline CZTS-based films. Comparing their device performance can reveal the roles that GBs play and narrow down the factors limiting CZTS-based solar cell efficiency.

## References

- [1] Wolden, C. A., Kurtin, J., Baxter, J. B., Repins, I., Shaheen, S. E., Torvik, J. T., Rockett, A. A., Fthenakis, V. M. & Aydil, E. S. (2011) Photovoltaic manufacturing: Present status, future prospects, and research needs. *Journal of Vacuum Science and Technology: A*, **29**, 030801.
- [2] Wiedeman, S., Albright, S., Britt, J. S., Schoop, U., Schuler, S., Stoss, W. & Verebelyi, D. (2010) Manufacturing ramp-up of flexible CIGS PV. In *Proceedings of 35th IEEE Photovoltaic Specialists Conference (PVSC)*, Honolulu, pp. 003485–003490.
- [3] Chirilă, A., Buecheler, S., Pianezzi, F., Bloesch, P., Gretener, C., Uhl, A. R., Fella, C., Kranz, L., Perrenoud, J., Seyrling, S., Verma, R., Nishiwaki, S., Romanyuk, Y. E., Bilger, G. & Tiwari, A. N. (2011) Highly efficient Cu(In,Ga)Se<sub>2</sub> solar cells grown on flexible polymer films. *Nature Materials*, **10**, 857–861.
- [4] Mitzi, D. B., Gunawan, O., Todorov, T. K. & Barkhouse, D. A. R. (2013) Prospects and performance limitations for Cu–Zn–Sn–S–Se photovoltaic technology. *Philosophical Transactions of the Royal Society A: Mathematical, Physical and Engineering Sciences*, **371**, 20110432–20110432.
- [5] Repins, I. L., Romero, M. J., Li, J. V., Wei, S.-H., Kuciauskas, D., Jiang, C.-S., Beall, C., DeHart, C., Mann, J., Hsu, W.-C., Teeter, G., Goodrich, A. & Noufi, R. (2013) Kesterite successes, ongoing work, and challenges: a perspective from vacuum deposition. *IEEE Journal of Photovoltaics*, **3**, 439–445.
- [6] Chawla, V. (2011) A study of CZTS thin films for solar cell applications. PhD thesis, Stanford University.
- [7] Scragg, J. J., Dale, P. J. & Peter, L. M. (2009) Synthesis and characterization of Cu<sub>2</sub>ZnSnS<sub>4</sub> absorber layers by an electrodeposition-annealing route. *Thin Solid Films*, **517**, 2481–2484.
- [8] Katagiri, H., Jimbo, K., Yamada, S., Kamimura, T., Maw, W. S., Fukano, T., Ito, T. & Motohiro, T. (2008) Enhanced conversion efficiencies of Cu<sub>2</sub>ZnSnS<sub>4</sub>-based thin film solar cells by using preferential etching technique. *Applied Physics Express*, **1**, 041201.
- [9] Ito, K. & Nakazawa, T. (1988) Electrical and optical properties of stannite-type quaternary semiconductor thin films. *Japanese Journal of Applied Physics*, **27**, 2094–2097.
- [10] Green, M. A., Emery, K., Hishikawa, Y., Warta, W. & Dunlop, E. D. (2013) Solar cell efficiency tables (version 42). *Progress in Photovoltaics: Research and Applications*, **21**, 827–837.
- [11] Winkler, M. T., Wang, W., Gunawan, O., Hovel, H. J., Todorov, T. K. & Mitzi, D. B. (2013) Optical designs that improve the efficiency of Cu<sub>2</sub>ZnSn(S,Se)<sub>4</sub> solar cells. *Energy and Environmental Science*, doi: 10.1039/c3ee42541j.
- [12] Jackson, P., Hariskos, D., Wuerz, R., Wischmann, W. & Powalla, M. (2014) Compositional investigation of potassium doped Cu(In,Ga)Se<sub>2</sub> solar cells with efficiencies up to 20.8%. *Physica Status Solidi (RRL)*, **8**(3), 219–222.
- [13] Roselund, C. (2014) First Solar Sets New World Record for Thin Film Solar PV at 21%. Available at <http://www.pv-magazine.com>. (accessed 16 September 2014).
- [14] Du, H., Champness, C. H. & Shih, I. (2005) Results on monocrystalline CuInSe<sub>2</sub> solar cells. *Thin Solid Films*, **480–481**, 37–41.
- [15] Nakazawa, T., Takamizawa, K. & Ito, K. (1987) High efficiency indium oxide/cadmium telluride solar cells. *Applied Physics Letters*, **50**, 279.
- [16] Visoly-Fisher, I., Cohen, S. R., Ruzin, A. & Cahen, D. (2004) How polycrystalline devices can outperform single-crystal ones: Thin film CdTe/CdS solar cells. *Advanced Materials*, **16**, 879–883.
- [17] Jiang, C. S., Noufi, R., Ramanathan, K., AbuShama, J. A., Moutinho, H. R. & Al-Jassim, M. M. (2004) Does the local built-in potential on grain boundaries of Cu(In,Ga)Se<sub>2</sub> thin films benefit photovoltaic performance of the device? *Applied Physics Letters*, **85**, 2625.

- [18] Rau, U. & Taretto, K. (2009) Grain boundaries in  $\text{Cu(In,Ga)(Se,S)}_2$  thin-film solar cells. *Applied Physics A: Materials*, **96**, 221–234.
- [19] Azulay, D., Millo, O., Balberg, I., Schock, H.-W., Visoly-Fisher, I. & Cahen, D. (2007) Current routes in polycrystalline  $\text{CuInSe}_2$  and  $\text{Cu(In,Ga)Se}_2$  films. *Solar Energy Materials and Solar Cells*, **91**, 85–90.
- [20] Metzger, W. K. & Gloeckler, M. (2005) The impact of charged grain boundaries on thin-film solar cells and characterization. *Journal of Applied Physics*, **98**, 063701.
- [21] Seto, J. Y. W. (1975) The electrical properties of polycrystalline silicon films. *Journal of Applied Physics*, **46**, 5247–5254.
- [22] Yan, Y., Jiang, C. S., Noufi, R., Wei, S.-H., Moutinho, H. & Al-Jassim, M. (2007) Electrically benign behavior of grain boundaries in polycrystalline  $\text{CuInSe}_2$  films. *Physics Reviews Letters*, **99**, 235504 (2007).
- [23] Persson, C. & Zunger, A. (2003) Anomalous grain boundary physics in polycrystalline  $\text{CuInSe}_2$ : the existence of a hole barrier. *Physics Reviews Letters*, **91**, 266401.
- [24] Persson, C. & Zunger, A. (2005) Compositionally induced valence-band offset at the grain boundary of polycrystalline chalcopyrites creates a hole barrier. *Applied Physics Letters*, **87**, 211904.
- [25] Jiang, C. S., Noufi, R., AbuShama, J. A., Ramanathan, K., Moutinho, H. R., Pankow, J. & Al-Jassim, M. M. (2004) Local built-in potential on grain boundary of  $\text{Cu(In,Ga)Se}_2$  thin films. *Applied Physics Letters*, **84**, 3477.
- [26] Sadewasser, S., Abou-Ras, D., Azulay, D., Baier, R., Balberg, I., Cahen, S., Cohen, S., Gartsman, K., Ganesan, K., Kavalakkatt, J., Li, W., Millo, O., Rissom, T., Rosenwaks, Y., Schock, H. W., Schwarzman, A. & Unold, T. (2011) Nanometer-scale electronic and microstructural properties of grain boundaries in  $\text{Cu(In,Ga)Se}_2$ . *Thin Solid Films*, **519**, 7341–7346.
- [27] Sadewasser, S. & Visoly-Fisher, I. (2011) Scanning probe microscopy on inorganic thin films for solar cells. In: *Advanced Characterization Techniques for Thin Film Solar Cells* (eds Abou-Ras, D., Kirchartz, T. & Rau, U.). Wiley-VCH Verlag GmbH & Co. KGaA, Weinheim, Germany.
- [28] Sadewasser, S. (2006) Surface potential of chalcopyrite films measured by KPFM. *Physica Status Solidi (A)*, **203**, 2571–2580.
- [29] Takihara, M., Minemoto, T., Wakisaka, Y. & Takahashi, T. (2010) Band profile around grain boundary of  $\text{Cu(In,Ga)Se}_2$  solar cell material characterized by scanning probe microscopy. In *Proceedings of 35th IEEE Photovoltaic Specialists Conference (PVSC)*, Austin, pp. 002512–002515.
- [30] Takihara, M., Minemoto, T., Wakisaka, Y. & Takahashi, T. (2011) An investigation of band profile around the grain boundary of  $\text{Cu(In,Ga)Se}_2$  solar cell material by scanning probe microscopy. *Progress in Photovoltaics: Research and Applications*, **21**(4), 595–599.
- [31] Jiang, C. S., Contreras, M. A., Repins, I., Moutinho, H. R., Yan, Y., Romero, M. J., Mansfield, L. M., Noufi, R. & Al-Jassim, M. M. (2012) How grain boundaries in  $\text{Cu(In,Ga)Se}_2$  thin films are charged: Revisit. *Applied Physics Letters*, **101**, 033903–033904.
- [32] Baier, R., Lehmann, J., Lehmann, S., Rissom, T., Alexander Kaufmann, C., Schwarzmann, A., Rosenwaks, Y., Lux-Steiner, M. C. & Sadewasser, S. (2012) Electronic properties of grain boundaries in  $\text{Cu(In,Ga)Se}_2$  thin films with various Ga-contents. *Solar Energy Materials and Solar Cells*, **103**, 86–92.
- [33] Li, J. B., Chawla, V. & Clemens, B. M. (2012) Investigating the role of grain boundaries in CZTS and CZTSSe thin film solar cells with scanning probe microscopy. *Advanced Materials*, **24**, 720–723.
- [34] Li, J. B., Chawla, V. & Clemens, B. M. (2012) Understanding the role of grain boundaries in sulfide thin film solar cells with scanning probe microscopy. In *Proceedings of 38th IEEE Photovoltaic Specialists Conference (PVSC)*, IEEE, Austin, pp. 000668–000670.
- [35] Jiang, C. S., Contreras, M. A., Repins, I., Moutinho, H. R., Noufi, R. & Al-Jassim, M. M. (2012) Determination of grain boundary charging in  $\text{Cu(In,Ga)Se}_2$  thin films. In *Proceedings of 38th IEEE Photovoltaic Specialists Conference (PVSC)*, IEEE, Austin, pp. 001486–001491.
- [36] Visoly-Fisher, I., Cohen, S. & Cahen, D. (2003) Direct evidence for grain-boundary depletion in polycrystalline  $\text{CdTe}$  from nanoscale-resolved measurements. *Applied Physics Letters*, **82**, 556–558.

- [37] Fisher, I. V. & Cohen, S. (2006) Understanding the beneficial role of grain boundaries in polycrystalline solar cells from single-grain-boundary scanning probe microscopy. *Advanced Functional Materials*, **16**, 649–660 (2006).
- [38] Moutinho, H. R., Dhere, R. G., Jiang, C. S., Albin, D. S. & Al-Jassim, M. M. (2010) Electrical properties of CdTe/CdS and CdTe/SnO<sub>2</sub> solar cells studied with scanning Kelvin probe microscopy. In *Proceedings of 35th IEEE Photovoltaic Specialists Conference (PVSC)*, IEEE, Honolulu, pp. 001955–001959.
- [39] Moutinho, H. R., Dhere, R. G., Jiang, C. S., Yan, Y., Albin, D. S. & Al-Jassim, M. M. (2010) Investigation of potential and electric field profiles in cross sections of CdTe/CdS solar cells using scanning Kelvin probe microscopy. *Journal of Applied Physics*, **108**, 074503.
- [40] Nowell, M. M., Wright, S. I., Scarpulla, M. A., Compaan, A. D., Liuc, X., Paudel, N. R. & Wieland, K. A. (2012) The correlation of performance in CdTe photovoltaics with grain boundaries. In *Proceedings of 19th IEEE International Symposium on the Physical and Failure Analysis of Integrated Circuits (IPFA 2012)*, IEEE, pp. 1–7.
- [41] Datta, T., Noufi, R. & Deb, S. K. (1985) Electrical conductivity of p-type CuInSe<sub>2</sub> thin films. *Applied Physics Letters*, **47**, 1102.
- [42] Chakrabarti, R., Matiti, B., Chaudhuri, S. & Pal, A. (2002) Photoconductivity of Cu(In, Ga)Se<sub>2</sub> films. *Solar Energy Materials and Solar Cells*, **43**, 237–247.
- [43] Kazmerski, L. L., Ayyagari, M. S. & Sanborn, G. A. (1975) CuInS<sub>2</sub> thin films: Preparation and properties. *Journal of Applied Physics*, **46**, 4865.
- [44] Schuler, S., Nishiwaki, S., Beckmann, J., Rega, N., Brehme, S., Siebentritt, S. & Lux-Steiner, M. C. (2004) Charge carrier transport in polycrystalline CuGaSe<sub>2</sub> thin films. In *Proceedings of 29th IEEE Photovoltaic Specialists Conference*, New Orleans, pp. 504–507.
- [45] Siebentritt, S. & Schuler, S. (2003) Defects and transport in the wide gap chalcopyrite CuGaSe<sub>2</sub>. *Journal of Physics and Chemistry of Solids*, **64**, 1621–1626.
- [46] Rissom, B. (2007) Elektrische Transporteigenschaften von epitaktischen und polykristallinen Chalkopyrit-Schichten. PhD thesis, Freie Universität.
- [47] Siebentritt, S. S., Sadewasser, S. S., Wimmer, M. M., Leendertz, C. C., Eisenbarth, T. T. & Lux-Steiner, M. C. M. (2006) Evidence for a neutral grain-boundary barrier in chalcopyrites. *Physical Reviews Letters*, **97**, 146601–146601.
- [48] Meyer, T. (1999) Reversible Relaxationsphänomene im elektrischen Transport von Cu(In,Ga)Se<sub>2</sub>. PhD thesis, Universität Oldenburg.
- [49] Holz, J., Karg, F. & von Philipsborn, H. (1994) The effect of substrate impurities on the electronic conductivity in CIS thin films. In *Proceedings of 12th European Photovoltaic Solar Energy Conference*, Amsterdam, p. 1592.
- [50] Virtuani, A., Lotter, E., Powalla, M., Rau, U., Werner, J. H. & Acciarri, M. (2006) Influence of Cu content on electronic transport and shunting behavior of Cu(In,Ga)Se<sub>2</sub> solar cells. *Journal of Applied Physics*, **99**, 014906.
- [51] Hetzer, M. J., Strzhemechny, Y. M., Gao, M., Contreras, M. A., Zunger, A. & Brillson, L. J. (2005) Direct observation of copper depletion and potential changes at copper indium gallium diselenide grain boundaries. *Applied Physics Letters*, **86**, 162105.
- [52] Lei, C., Li, C. M., Rockett, A. & Robertson, I. M. (2007) Grain boundary compositions in Cu(In,Ga)Se<sub>2</sub>. *Journal of Applied Physics*, **101**, 024909.
- [53] Couzinie-Devy, F., Cadel, E., Barreau, N., Pareige, P. & Kessler, J. (2011) Atom probe contribution to the characterisation of CIGSe grain boundaries. In *Proceedings of 37th IEEE Photovoltaic Specialists Conference (PVSC)*, IEEE, pp. 001966–001971.
- [54] Abou-Ras, D., Schmidt, S. S., Caballero, R., Unold, T., Schock, H.-W., Koch, C. T., Schaffer, B., Schaffer, M., Choi, P.-P. & Cojocaru-Mirédin, O. (2012) Confined and chemically flexible grain boundaries in polycrystalline compound semiconductors. *Advanced Energy Materials*, **2**, 992–998.
- [55] Abou-Ras, D., Schaffer, B., Schaffer, M., Schmidt, S. S., Caballero, R. & Unold, T. (2012) Direct insight into grain boundary reconstruction in polycrystalline Cu(In,Ga)Se<sub>2</sub> with atomic resolution. *Physical Review Letters*, **108**(7), 075502.
- [56] Kronik, L., Rau, U., Guillemoles, J. F., Braunger, D., Schock, H. W. & Cahen, D. (2000) Interface redox engineering of Cu(In,Ga)Se<sub>2</sub>-based solar cells: oxygen, sodium, and chemical bath effects. *Thin Solid Films*, **361–362**, 353–359.

- [57] Kronik, L. & Cahen, D. (1998) Effects of sodium on polycrystalline Cu(In,Ga)Se<sub>2</sub> and its solar cell performance. *Advanced Materials*, **10**, 31–36.
- [58] Cahen, D. & Noufi, R. (1989) Defect chemical explanation for the effect of air anneal on CdS/CuInSe<sub>2</sub> solar cell performance. *Applied Physics Letters*, **54**, 558–560.
- [59] Abou-Ras, D., Koch, C. T., Küstner, V., van Aken, P. A., Jahn, U., Contreras, M. A., Caballero, R., Kaufmann, C. A., Scheer, R., Unold, T. & Schock, H. W. (2009) Grain-boundary types in chalcopyrite-type thin films and their correlations with film texture and electrical properties. *Thin Solid Films*, **517**, 2545–2549.
- [60] Jiang, C. S., Repins, I. L., Mansfield, L. M., Contreras, M. A., Moutinho, H. R., Ramanathan, K., Noufi, R. & Al-Jassim, M. M. (2013) Electrical conduction channel along the grain boundaries of Cu(In,Ga)Se<sub>2</sub> thin films. *Applied Physics Letters*, **102**, 253905.
- [61] Shin, R. H., Jo, W., Kim, D. W., Yun, J. H. & Ahn, S. (2011) Local current–voltage behaviors of preferentially and randomly textured Cu(In,Ga)Se<sub>2</sub> thin films investigated by conductive atomic force microscopy. *Applied Physics A*, **104**, 1189–1194.
- [62] Yan, Y. (2011) Understanding of defect physics in polycrystalline photovoltaic materials: Preprint. In *Proceedings of 37th IEEE Photovoltaic Specialists Conference (PVSC)*, pp. 001218–001222.
- [63] Li, J., Mitzi, D. B. & Shenoy, V. B. (2011) Structure and electronic properties of grain boundaries in earth-abundant photovoltaic absorber Cu<sub>2</sub>ZnSnSe<sub>4</sub>. *ACS Nano*, **5**, 8613–8619.
- [64] Yin, W.-J., Wu, Y., Wei, S.-H., Noufi, R., Al-Jassim, M. M. & Yan, Y. (2013) Engineering grain boundaries in Cu<sub>2</sub>ZnSnSe<sub>4</sub> for better cell performance: a first-principle study. *Advanced Energy Materials*, doi: 10.1002/aenm.201300712.
- [65] Wang, K., Shin, B., Reuter, K. B., Todorov, T., Mitzi, D. B. & Guha, S. (2011) Structural and elemental characterization of high efficiency Cu<sub>2</sub>ZnSnS<sub>4</sub> solar cells. *Applied Physics Letters*, **98**, 051912.
- [66] Bag, S., Gunawan, O., Gokmen, T., Zhu, Y., Todorov, T. K. & Mitzi, D. B. (2012) Low band gap liquid-processed CZTSe solar cell with 10.1% efficiency. *Energy and Environmental Science*, **5**, 7060–7065.
- [67] Mendis, B. G., Goodman, M. C. J., Major, J. D., Taylor, A. A., Durose, K. & Halliday, D. P. (2012) The role of secondary phase precipitation on grain boundary electrical activity in Cu<sub>2</sub>ZnSnS<sub>4</sub> (CZTS) photovoltaic absorber layer material. *Progress in Photovoltaics: Research and Applications*, **112**, 124508.
- [68] Barkhouse, D. A. R., Gunawan, O., Gokmen, T., Todorov, T. K. & Mitzi, D. B. (2012) Device characteristics of a 10.1% hydrazine-processed Cu<sub>2</sub>ZnSn(S<sub>2</sub>Se)<sub>4</sub> solar cell. *Progress in Photovoltaics: Research and Applications*, doi: 10.1002/pip.1160.
- [69] Todorov, T., Sugimoto, H., Gunawan, O., Gokmen, T. and Mitzi, D. B. (2014) High-efficiency devices with pure solution-processed Cu<sub>2</sub>ZnSn(S,Se)<sub>4</sub> absorbers. *IEEE Journal of Photovoltaics*, **4**(1), 483–485.
- [70] Todorov, T., Gunawan, O., Chey, S. J., de Monsabert, T. G., Prabhakar, A. & Mitzi, D. B. (2011) Progress towards marketable earth-abundant chalcogenide solar cells. *Thin Solid Films*, **519**, 7378–7381.
- [71] Repins, I., Beall, C., Vora, N., DeHart, C., Kuciauskas, D., Dippo, P., To, B., Mann, J., Hsu, W.-C., Goodrich, A. & Noufi, R. (2012) Co-evaporated Cu<sub>2</sub>ZnSnSe<sub>4</sub> films and devices. *Solar Energy Materials and Solar Cells*, **101**, 154–159.
- [72] Guo, Q., Cao, Y., Caspar, J. V., Farneth, W. E., Ionkin, A. S., Johnson, L. K., Lu, M., Malajovich, I., Radu, D. & Choudhury, K. R. (2012) A simple solution-based route to high-efficiency CZTSSe thin-film solar cells. In *Proceedings of 38th IEEE Photovoltaic Specialists Conference (PVSC)*, 002993–002996.
- [73] Woo, K., Kim, Y. & Moon, J. (2012) A non-toxic, solution-processed, earth abundant absorbing layer for thin-film solar cells. *Energy and Environmental Science*, **5**(1), 5340–5345.
- [74] Cao, Y., Denny Jr., M. S., Caspar, J. V., Farneth, W. E., Guo, Q., Ionkin, A. S., Johnson, L. K., Lu, M., Malajovich, I., Radu, D., Rosenfeld, H. D., Choudhury, K. R. & Wu, W. (2012) High-efficiency solution-processed Cu<sub>2</sub>ZnSn(S,Se)<sub>4</sub> thin-film solar cells prepared from binary and ternary nanoparticles. *Journal of American Chemical Society*, **134**(38), 15644–15647.

- [75] Miskin, C. K., Yang, W.-C., Hages, C. J., Carter, N. J., Joglekar, C. S., Stach, E. A. & Agrawal, R. (2014) 9.0% efficient  $\text{Cu}_2\text{ZnSn}(\text{S},\text{Se})_4$  solar cells from selenized nanoparticle inks. *Progress in Photovoltaics: Research and Applications*, doi: 10.1002/pip.2472.
- [76] Shin, B., Gunawan, O. & Zhu, Y. (2011) Thin film solar cell with 8.4% power conversion efficiency using an earth-abundant  $\text{Cu}_2\text{ZnSnS}_4$  absorber. *Progress in Photovoltaics: Research and Applications*, doi: 10.1002/pip.1174.
- [77] Li, J. B., Chawla, V. & Clemens, B. M. (2012) Investigating the role of grain boundaries in CZTS and CZTSSe thin film solar cells with scanning probe microscopy. *Advanced Materials*, **24**, 720–723.
- [78] Chawla, V. & Clemens, B. (2012) Effect of composition on high efficiency CZTSSe devices fabricated using co-sputtering of compound targets. In *Proceedings of 38th IEEE Photovoltaic Specialists Conference (PVSC)*, Austin, pp. 002990–002992.
- [79] Dhakal, T. P., Ramesh, D. N., Tobias, R. R., Peng, C.-Y. & Westgate, C. R. (2013) Enhancement of efficiency in  $\text{Cu}_2\text{ZnSnS}_4$  (CZTS) solar cells grown by sputtering. In *Proceedings of 39th IEEE Photovoltaic Specialists Conference (PVSC)*, IEEE, pp. 1949–1952.
- [80] Khalkar, A., Lim, K. S., Yu, S. M., Patole, S. P. & Yoo, J. B. (2014) Deposition of  $\text{Cu}_2\text{ZnSnS}_4$  thin films by magnetron sputtering and subsequent sulphurization. *Electronic Materials Letters*, **10**(1), 43–49.
- [81] Grenet, L., Bernardi, S., Kohen, D., Lepoittevin, C., Noël, S., Karst, N., Brioude, A., Perraud, S. & Mariette, H. (2012)  $\text{Cu}_2\text{ZnSn}(\text{S}_{1-x}\text{Se}_x)_4$  based solar cell produced by selenization of vacuum deposited precursors. *Solar Energy Materials and Solar Cells*, **101**, 11–14.
- [82] Scragg, J. J., Ericson, T., Fontané, X., Izquierdo Roca, V., Pérez Rodríguez, A., Kubart, T., Edoff, M. & Platzer Björkman, C. (2012) Rapid annealing of reactively sputtered precursors for  $\text{Cu}_2\text{ZnSnS}_4$  solar cells. *Progress in Photovoltaics: Research and Applications*, doi: 10.1002/pip.2265.
- [83] Maeda, K., Tanaka, K., Fukui, Y. & Uchiki, H. (2011) Influence of  $\text{H}_2\text{S}$  concentration on the properties of  $\text{Cu}_2\text{ZnSnS}_4$  thin films and solar cells prepared by sol-gel sulfurization. *Solar Energy Materials and Solar Cells*, **95**, 2855–2860.
- [84] Park, H., Hwang, Y. H. & Bae, B.-S. (2012) Sol-gel processed  $\text{Cu}_2\text{ZnSnS}_4$  thin films for a photovoltaic absorber layer without sulfurization. *Journal of Sol-Gel Science and Technology*, **65**, 23–27.
- [85] Kuo, D.-H. & Hsu, J.-P. (2013) Property characterizations of  $\text{Cu}_2\text{ZnSnSe}_4$  and  $\text{Cu}_2\text{ZnSn}(\text{S},\text{Se})_4$  films prepared by sputtering with single Cu–Zn–Sn target and a subsequent selenization or sulfo-selenization procedure. *Surface and Coatings Technology*, **236**, 166–171.
- [86] Nakamura, R., Tanaka, K., Uchiki, H., Jimbo, K., Washio, T. & Katagiri, H. (2014)  $\text{Cu}_2\text{ZnSnS}_4$  thin film deposited by sputtering with  $\text{Cu}_2\text{ZnSnS}_4$  compound target. *Japanese Journal of Applied Physics*, **53**(2), 02BC10.
- [87] Ikeda, S., Septina, W., Lin, Y., Kyoraiseiki, A., Harada, T. & Matsumura, M. (2013) Electrochemical synthesis of  $\text{Cu}_2\text{ZnSnS}_4$  and  $\text{Cu}_2\text{ZnSnSe}_4$  thin films for solar cells. In *Proceedings of International Renewable and Sustainable Energy Conference (IRSEC)*, pp. 1–4.
- [88] Xu, P., Chen, S., Huang, B., Xiang, H. J., Gong, X.-G. & Wei, S.-H. (2013) Stability and electronic structure of  $\text{Cu}_2\text{ZnSnS}_4$  surfaces: First-principles study. *Physical Review B*, **88**, 045427.
- [89] Kim, G. Y., Kim, J. R., Jo, W., Son, D.-H., Kim, D.-H. & Kang, J.-K. (2014) Nanoscale observation of surface potential and carrier transport in  $\text{Cu}_2\text{ZnSn}(\text{S},\text{Se})_4$  thin films grown by sputtering-based two-step process. *Nanoscale Research Letters*, **9**(1), 10.
- [90] Kosyak, V., Karmarkar, M. A. & Scarpulla, M. A. (2012) Temperature dependent conductivity of polycrystalline  $\text{Cu}_2\text{ZnSnS}_4$  thin films. *Applied Physics Letters*, **100**, 263903.
- [91] Nagoya, A., Asahi, R. & Kresse, G. (2011) First-principles study of  $\text{Cu}_2\text{ZnSnS}_4$  and the related band offsets for photovoltaic applications. *Journal of Physics: Condensed Matter*, **23**, 404203.
- [92] Barkhouse, D. A. R., Haight, R., Sakai, N., Hiroi, H., Sugimoto, H. & Mitzi, D. B. (2012) Cd-free buffer layer materials on  $\text{Cu}_2\text{ZnSn}(\text{S}_x\text{Se}_{1-x})_4$ : Band alignments with ZnO, ZnS, and  $\text{In}_2\text{S}_3$ . *Applied Physics Letters*, **100**, 193904.
- [93] Repins, I. L., Moutinho, H., Choi, S. G., Kanevce, A., Kuciauskas, D., Dippo, P., Beall, C. L., Carapella, J., DeHart, C., Huang, B. & Wei, S. H. (2013) Indications of short minority-carrier lifetime in kesterite solar cells. *Journal of Applied Physics*, **114**, 084507.

- [94] Metzger, W. K., Repins, I. L. & Contreras, M. A. (2008) Long lifetimes in high-efficiency Cu(In,Ga)Se<sub>2</sub> solar cells. *Applied Physics Letters*, **93**, 022110.
- [95] Romero, M. J., Repins, I., Teeter, G., Contreras, M. A., Al-Jassim, M. & Noufi, R. (2012) A comparative study of the defect point physics and luminescence of the kesterites Cu<sub>2</sub>ZnSnS<sub>4</sub> and Cu<sub>2</sub>ZnSnSe<sub>4</sub> and chalcopyrite Cu(In,Ga)Se<sub>2</sub>. In *Proceedings of 38th IEEE Photovoltaic Specialists Conference (PVSC)*, Austin, pp. 003349–003353.
- [96] Shin, B., Zhu, Y., Gershon, T., Bojarczuk, N. A. & Guha, S. (2014) Epitaxial growth of kesterite Cu<sub>2</sub>ZnSnS<sub>4</sub> on a Si(001) substrate by thermal co-evaporation. *Thin Solid Films*, **556**(C), 9–12.





# 15

## CZTS-Based Thin-Film Solar Cells Prepared via Coevaporation

Byungha Shin,<sup>1,2</sup> Talia Gershon<sup>1</sup> and Supratik Guha<sup>1</sup>

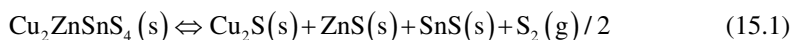
<sup>1</sup>IBM Thomas J. Watson Research Center, New York, USA

<sup>2</sup>Department of Materials Science and Engineering, Korea Advanced  
Institute of Science and Technology, Daejeon, Republic of Korea

### 15.1 Introduction

A photovoltaic effect involving the kesterite compound  $\text{Cu}_2\text{ZnSnS}_4$  (CZTS) was first observed by Ito and Nakazawa in the late 1980s [1]. Around this time, promising optical properties of CZTS were demonstrated and an open-circuit voltage  $V_{\text{oc}}$  of 165 mV was reported from a CZTS solar cell with cadmium tin oxide transparent conductive layer. Beginning in the late 1990s, Katagiri *et al.* [2] conducted pioneering work in improving the efficiencies of CZTS-based solar cells; in 2008 they published a record efficiency of 6.77% [3]. Two years later, Todorov *et al.* [4] at IBM published a new record efficiency of 9.66%, which was accomplished by using a solution-based method with Se added to the absorber. This work spurred a wave of interest in CZTS due to the potential of achieving high efficiencies with this material as well as the Earth-abundance and non-toxicity of its constituent elements. The current record efficiency is now 12.6% [5]. Many different methods exist for preparing CZTS films, including thermal coevaporation [6–17], sputtering [18, 19], electroplating [20, 21], pulsed laser deposition [22], atomic layer deposition [23], sintering of CZTS nanocrystals [24–26], and solution-based approaches [27–31]. This chapter summarizes the key aspects of coevaporated CZTS photovoltaic technology.

The properties of CZTS films and the performance of CZTS-based solar cells are often compared against its “cousin”, the Cu(In,Ga)Se<sub>2</sub> (CIGS) system, which is a more mature technology and currently holds the record efficiency among polycrystalline thin-film solar cells. In fact, the device architecture of the current record CZTS device (with Se) [5] is very similar to that of the record CIGS device, with direct substitution of a CZTS absorber for a CIGS absorber. The device stack includes a ZnO/Sn-doped In<sub>2</sub>O<sub>3</sub> (ITO) transparent conducting oxide bi-layer, a CdS buffer layer, and a Mo bottom contact. Absorber layers in the highest-efficiency CIGS solar cells are produced by thermal coevaporation using a three-stage growth, during which the fluxes of Cu, Ga, and In are modulated and the substrate temperature is varied from 400°C to 600°C. This is done to enhance grain growth and to create band-gap grading, that is, larger-band-gap material is grown at both the bottom and top interfaces of CIGS [32]. The success of thermal coevaporation in CIGS technology led to an interest in thermal coevaporation for CZTS materials. However, conventional thermal coevaporation (where the as-grown film possesses more-or-less the desired crystalline structure without the need for further thermal treatment) is complicated with CZTS. Above c. 500°C, that is, the temperature required for a high-quality film, the CZTS phase is unstable and decomposes in the absence of sufficiently high-pressure S vapor. Scragg *et al.* [33] undertook a thorough thermodynamic and kinetic analysis of CZTS decomposition. They found that the decomposition of CZTS is a two-step process:



These results indicate that CZTS phase decomposition can be avoided if two conditions are met: (1) the S partial pressure ( $p_{\text{S}_2}$ ) must be greater than a critical value, which is temperature-dependent, and (2) the *product* of  $p_{\text{S}_2}$  and the SnS partial pressure  $p_{\text{SnS}}$  must also be greater than a threshold value. Satisfying these conditions at 550°C, for example, requires a minimum of  $p_{\text{S}_2} \approx 1.7 \times 10^{-4}$  Torr when  $p_{\text{SnS}} \geq 1.9 \times 10^{-3}$  Torr or a minimum of  $p_{\text{SnS}} \approx 1.5 \times 10^{-6}$  Torr when  $p_{\text{S}_2} \geq 225$  Torr. These conditions are not easily sustainable in a typical vacuum thermal evaporating system. There have therefore been relatively few literature reports on thermal deposition of CZTS films at elevated substrate temperature. In the work by Tanaka *et al.* [16], CZTS films were grown at 400–600°C with four elemental effusion cells (Cu, Zn, Sn, and S) in a chamber where the pressure during deposition was kept at  $< 7.5 \times 10^{-7}$  Torr. A single-phase kesterite structure was claimed in the paper based on X-ray diffraction (XRD) measurements. However, as discussed in Section 15.2, due to the overlap between the XRD peaks of CZTS, Cu<sub>2</sub>SnS<sub>3</sub>, and ZnS, the claim of a single-phase CZTS structure from XRD is always questionable. Moreover, this work contained several additional unidentified peaks and none of the known CZTS peaks when the film was grown at 600°C, suggesting that the film was grown in the regime of CZTS instability [16].

Oishi *et al.* [15] employed high-temperature coevaporation of CZTS to grow a film epitaxially onto a Si(001) substrate. In this work, elemental Cu, Sn, and S sources and a binary ZnS source were simultaneously evaporated onto a substrate held at 430–500°C at a slow growth rate of c. 1.7 nm min<sup>-1</sup> with the chamber pressure maintained  $< 4.5 \times 10^{-5}$  Torr. As identified by reflection high-energy electron diffraction (RHEED) and XRD, polycrystalline films were grown with grains preferentially orientated in the same direction as the

substrate. It should be noted that complete and functional solar cells were not reported by Oishi *et al.* [15] or by Tanaka *et al.* [16]. Fully operational CZTS devices prepared using thermal coevaporation at a high temperature were first reported by Schubert *et al.* [17]. In this work, CZTS was coevaporated onto a substrate held at 550°C using ZnS, Sn, Cu, and S sources with S partial pressure of  $1.5\text{--}2.3 \times 10^{-5}$  Torr and demonstrated devices with 4.1% efficiency after KCN etching to eliminate the CuS phase present in the as-deposited CZTS.

Similar to the case of full-sulfide CZTS, strict growth conditions must be employed to coevaporate the full-selenide compound  $\text{Cu}_2\text{ZnSnSe}_4$  (CZTSe) at a high substrate temperature. For example, Redinger and Siebentritt [12] found that with Se partial pressure kept at  $4 \times 10^{-6}$  Torr, no Sn was incorporated (substrate temperature  $\geq 450^\circ\text{C}$ ). However, the conditions for the selenide appear to be more forgiving than for the sulfide, perhaps due to the fact that selenium is less volatile than sulfur. The equilibrium vapor pressure of Se at 450°C, for instance, is c. 15 Torr while that of S is c. 760 Torr, making it more difficult for the first step of the CZTSe decomposition reaction to occur (i.e. the selenide equivalent of Reaction (15.1) above). The ability to prepare high-quality device-grade CZTSe films by thermal coevaporation at elevated substrate temperatures was first demonstrated by researchers at NREL, where a three-stage growth scheme produced CZTSe solar cells with an efficiency as high as 9.15% [10].

Another approach to thermal coevaporation of CZTS is to employ a growth temperature low enough that the Sn is not volatile and the CZTS film is stable. It is then necessary to anneal the as-deposited film at a high temperature to enhance the crystallinity and grain structure. This is the route that IBM uses to prepare coevaporated CZTS (or CZTSe) absorbers [6–9]. Using this approach we have demonstrated CZTS solar cells with efficiencies as high as 8.4% [8] and CZTSe solar cells with efficiencies of 8.9% [9].

In the remainder of this chapter, we review our processes for producing high-quality CZTS and CZTSe absorbers and high-efficiency solar cells. We discuss our findings from in-depth analysis of these absorbers and devices. In Section 15.2, we provide experimental details on how our CZTS and CZTSe films are prepared. In Section 15.3, we describe the fundamental properties of coevaporated CZTS and CZTSe absorbers. We discuss device characteristics of CZTS solar cells in Section 15.4. In Section 15.5 we discuss device characteristics of CZTSe solar cells, paying close attention to the effect of a bottom interfacial  $\text{MoSe}_2$  layer thickness on performance. Finally, a chapter summary is provided in Section 15.6.

## 15.2 Preparation of CZTS and CZTSe Absorbers

The evaporation chambers for the deposition of CZTS and CZTSe host three effusion cells for elemental Cu, Zn, and Sn as well as commercial valved crackers for S and Se (Veeco Process Equipment, Inc.). The purity of sources is all of six nines (i.e. 6N, 99.9999) except for Sn, which is 5N. Typical cell temperatures during growth are c. 1080–1115°C, c. 190–290°C, and c. 1010–1050°C for Cu, Zn, and Sn, respectively. The resulting atomic beam fluxes are  $2\text{--}3 \times 10^{-8}$ ,  $1\text{--}2 \times 10^{-7}$ , and  $5\text{--}6 \times 10^{-8}$  Torr for Cu, Zn, and Sn, respectively, as measured by an ion gauge or mass spectrometer held near the growth position. Fluxes in this range yield CZTS films whose compositions are  $\text{Cu}/\text{Sn} \approx 1.7\text{--}1.8$  and  $\text{Zn}/\text{Sn} \approx 1.2\text{--}1.3$  as measured by calibrated X-ray fluorescence (XRF) (150°C growth temperature).

**Table 15.1** Distribution of a sulfur beam flux from the S cracker, the cracking zone temperature of which is kept at 350°C.

Species	S	S <sub>2</sub>	S <sub>3</sub>	S <sub>4</sub>	S <sub>5</sub>	S <sub>6</sub>	S <sub>7</sub>	S <sub>8</sub>
Relative %	16.1	77.1	2.0	2.2	0.8	1.5	0.1	0.3

These composition ranges are known to give the best device performance [34]. The bulk and cracking zones of the S (Se) sources are kept at 170°C (270°C) and 350–500°C (520°C), respectively. As listed in Table 15.1, more than 90% of the S beam flux escaping the cracking zone at 350–500°C consists of atomic and di-atomic S. As for the thermal cracking of Se, only atomic Se is detected at the cracking zone temperature of 520°C. The fluxes of both S and Se are  $3\text{--}4 \times 10^{-6}$  Torr. The deposition rate is approximately  $10 \text{ nm min}^{-1}$ . Unless otherwise stated, the thicknesses of CZTS and CZTSe films used in completed solar cells are c. 600–700 nm and c. 1500 nm, respectively. The growth temperature is 150°C and the substrate is continuously rotated with a speed of 10–20 rpm for thickness uniformity.

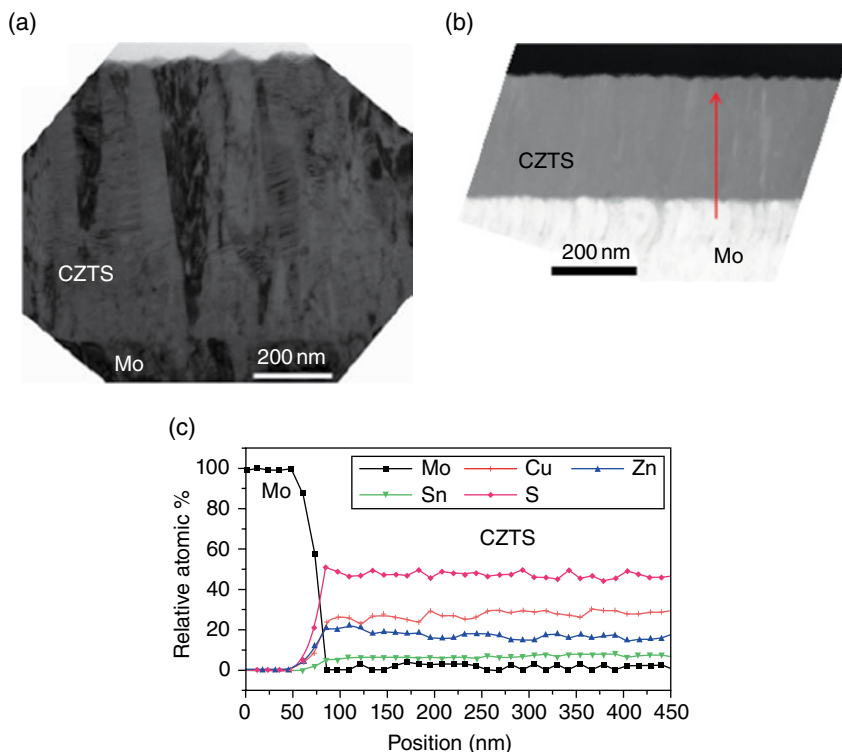
After the deposition, CZTS films are subjected to a brief thermal treatment under a S (or Se) ambient [34]. Typical annealing temperatures and durations are 570–600°C and 5–10 min, respectively. For sulfide materials, the partial pressure of sulfur during the annealing is kept at c. 50 Torr. Note that our anneal times are significantly shorter than those commonly used in an  $\text{H}_2\text{S}$  ambient for the sulfurization of sputtered CZTS [3]. As discussed in the next section, 5–10 min is sufficient to achieve a grain structure where the average size of CZTS grains is comparable to the CZTS thickness (c. 600–700 nm). It should be noted that short anneals have recently been adapted to sputtered CZTS films where the rapid growth of CZTS grains is also observed [18]. For CZTSe films, as discussed in Section 15.3, various annealing temperatures and Se partial pressures ( $p_{\text{Se}}$ ) have been tested.

The structure of a completed CZTS (CZTSe) solar cell is: soda-lime glass (SLG) substrate/700 nm Mo/CZTS (CZTSe) absorber/c. 60–100 nm CdS buffer layer/c. 80 nm i-ZnO/c. 450 nm ZnO:Al (AZO) or c. 130 nm  $\text{In}_2\text{O}_3$ :Sn (ITO) transparent conducting oxide (TCO)/Ni-Al metal fingers/c. 105 nm  $\text{MgF}_2$  anti-reflection coating. The CdS layer is prepared by chemical bath deposition (CBD) and i-ZnO, AZO, and ITO are prepared by RF sputtering. CZTS (CZTSe) films were treated with 1 M NaCN solution for 3 min before CdS deposition. This step is to remove  $\text{Cu}_x\text{S}$  ( $\text{Cu}_x\text{Se}$ ) if present in the CZTS (CZTSe) layer [11]. The device area is defined by mechanical scribing and is c.  $0.45 \text{ cm}^2$  (exact area may vary slightly from one device to another).

## 15.3 Fundamental Properties of Coevaporated CZTS and CZTSe Absorbers

### 15.3.1 Structural Properties of CZTS Absorbers

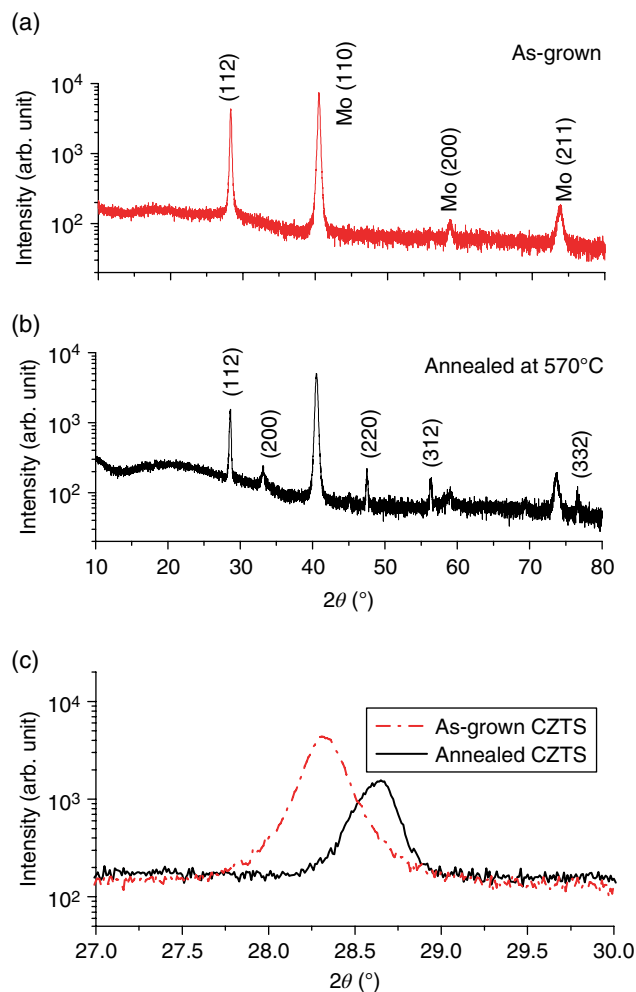
Figure 15.1a presents a transmission electron microscopy image of a typical as-deposited CZTS film (on Mo-coated SLG), which consists of columnar grains. These grains are approximately 100 nm wide and they extend across the entire thickness of the CZTS film. An XRD measurement from the as-deposited CZTS is shown in Figure 15.2a. The XRD



**Figure 15.1** (a) Bright-field TEM image of the typical as-deposited CZTS film on Mo showing columnar grain structure. (b) Dark-field STEM image of the as-deposited CZTS film from which an EDX line scan was taken. The vertical arrow represents the direction of the EDX scan. (c) Elemental profiles determined by the EDX scan which illustrates uniform composition across the film thickness

pattern exhibits a peak whose position is close to that of the (112) reflection from CZTS; the remaining peaks are from the Mo layer underneath the CZTS. The columnar grains seen in the scanning electron microscopy (SEM) image are therefore mostly aligned along the [112] direction. The (112) planes in the kesterite structure correspond to alternating close-packed planes populated exclusively by either metal cations (Cu, Zn, Sn) or anions (S). The horizontal lines observed in some of the grains are most likely stacking faults. Compositional variation within the CZTS is minimal, as revealed by energy-dispersive X-ray spectroscopy (EDX) measurements in scanning transmission electron microscopy (STEM) mode. Figure 15.1c depicts an example of elemental analysis from an EDX line scan collected from a dark-field STEM image (Fig. 15.1b).

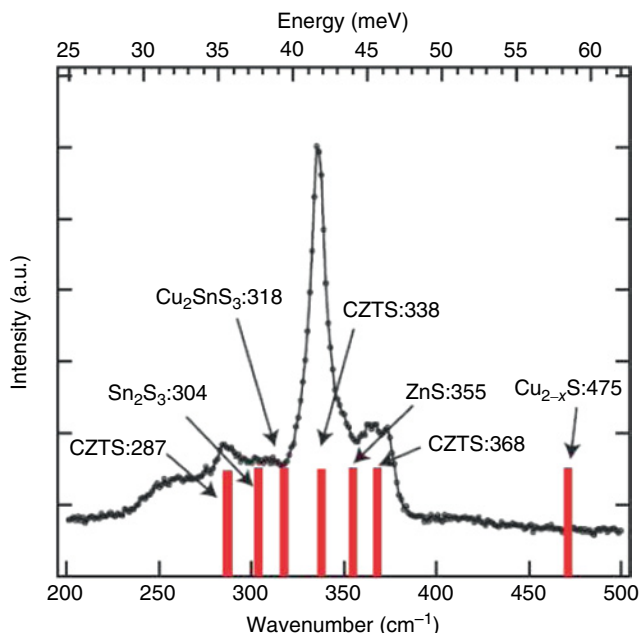
Figure 15.2b presents XRD patterns after annealing on a hot plate for 5 min at 570°C. Characteristic peaks of the kesterite CZTS structure are apparent while the intensity of the (112) reflection becomes weaker compared to that in Figure 15.2a, revealing a grain structure with less preferential orientation. Figure 15.2c compares XRD from the as-deposited and annealed CZTS, expanded around the (112) peak. From Figure 15.2c, it is clear that the (112) XRD peak position of the as-deposited CZTS is at a lower  $2\theta$  than that of the annealed



**Figure 15.2**  $\theta$ - $2\theta$  XRD measurements from (a) the as-deposited CZTS and (b) the annealed CZTS. (c) XRD measurements expanded around (112) peak before and after the annealing illustrating shift of the (112) peak

CZTS, which is very close to the value published in the literature [35, 36]. The (112) interplanar spacing of the as-deposited CZTS is larger than the equilibrium spacing, suggesting substantial cation disordering. Cation disorder has also been reported from CZTS films prepared by reactive co-sputtering at a substrate temperature of 120°C [18].

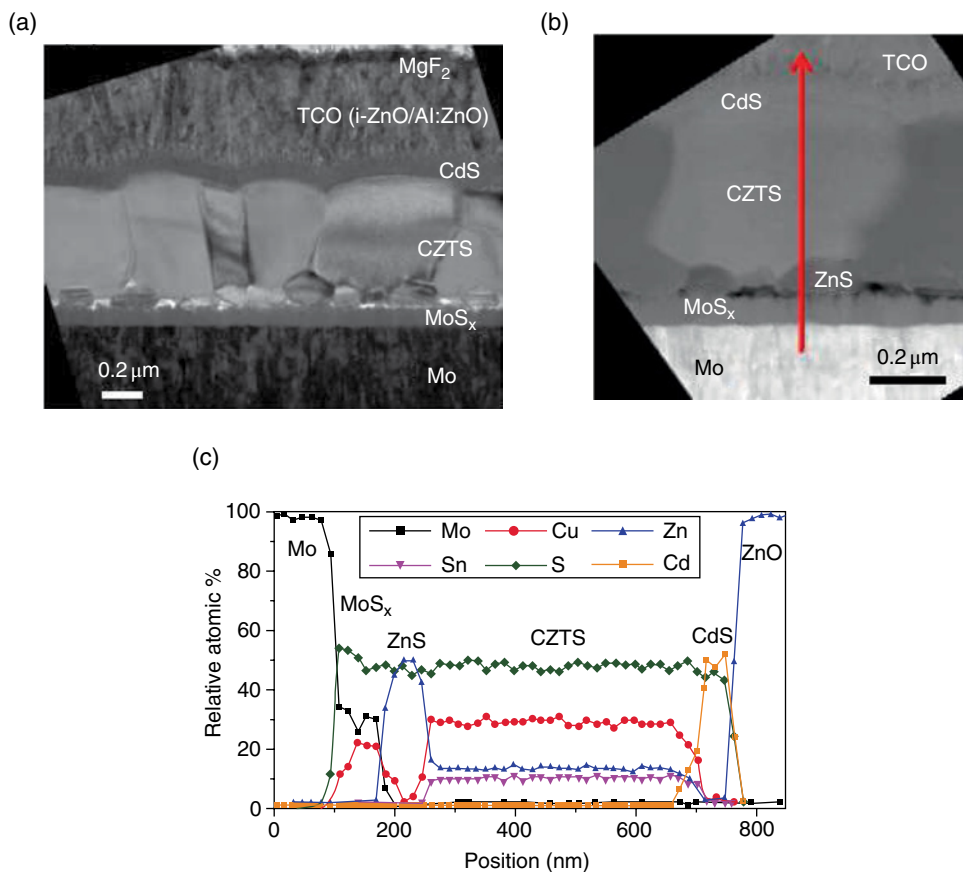
Although all the peaks in XRD can in principle be assigned to CZTS, the presence of secondary phases such as ZnS or  $\text{Cu}_2\text{SnS}_3$  in the annealed CZTS cannot be excluded because many of the ZnS or  $\text{Cu}_2\text{SnS}_3$  peaks overlap with those of CZTS [37]. We also use Raman spectroscopy to further characterize the CZTS absorber layer (Fig. 15.3). The laser wavelength is 632 nm and illuminates the top surface. All of the peaks in the Raman spectrum fall on Raman shifts known for CZTS such as 287, 338, and 368  $\text{cm}^{-1}$  [37, 38] with no



**Figure 15.3** Raman spectroscopy of the annealed CZTS. Reproduced with permission from [7]. Copyright © 2011, AIP Publishing LLC

clear indication of secondary phases such as  $\text{Cu}_{2-x}\text{S}$ ,  $\text{ZnS}$ ,  $\text{Cu}_2\text{SnS}_3$ , or  $\text{Sn}_2\text{S}_3$ , whose main Raman peaks show up at  $475\text{ cm}^{-1}$  [39],  $355\text{ cm}^{-1}$  [38],  $318\text{ cm}^{-1}$  [39], and  $304\text{ cm}^{-1}$  [38]. However, it should be noted that the probing laser ( $632\text{ nm}$ ) used for the Raman measurements would be strongly absorbed by the top  $100\text{--}200\text{ nm}$  of CZTS and therefore the sampling depth by the Raman will be limited to this region of the film. Both XRD and Raman results are therefore not conclusive in determining which phases are present in the annealed CZTS films. Other structural analysis methods, such as TEM and EDX, must be used for conclusive phase determination.

Figure 15.4a depicts a cross-sectional bright-field TEM image of our best CZTS solar cell ( $8.4\%$  efficiency, CZTS thickness *c.*  $600\text{ nm}$ ) whose current-voltage ( $I$ - $V$ ) characteristics and photovoltaic parameters are described in Section 15.4. The grain structure of the film annealed for  $5\text{ min}$  at  $570^\circ\text{C}$  is significantly improved compared to the as-deposited CZTS (Figs 15.1a and 15.4a). Most of the grains span the entire film thickness. Despite the disordering of the cations found in the as-deposited films, planes of cations and anions alternate with the (112)-like sequence of equilibrium CZTS. This may explain why only  $5\text{ min}$  of annealing at  $570^\circ\text{C}$  is sufficient to achieve large grains; no long-range diffusion is necessary as atoms are well-intermixed as-grown. This interpretation was proposed by Scragg *et al.* [18] where a fast-grain growth of co-sputtered CZTS was observed, and a similar phenomenon is observed in our coevaporated samples. In addition to the large grains that almost extend from the bottom to the top of the CZTS, we observe smaller grains ( $100\text{--}200\text{ nm}$  in size) which can be identified as  $\text{ZnS}$ , localized near the bottom interface. Additionally, a continuous interfacial layer approximately  $110\text{ nm}$  thick has formed between the CZTS and the Mo; this can be identified as  $\text{MoS}_2$  as discussed in the following.



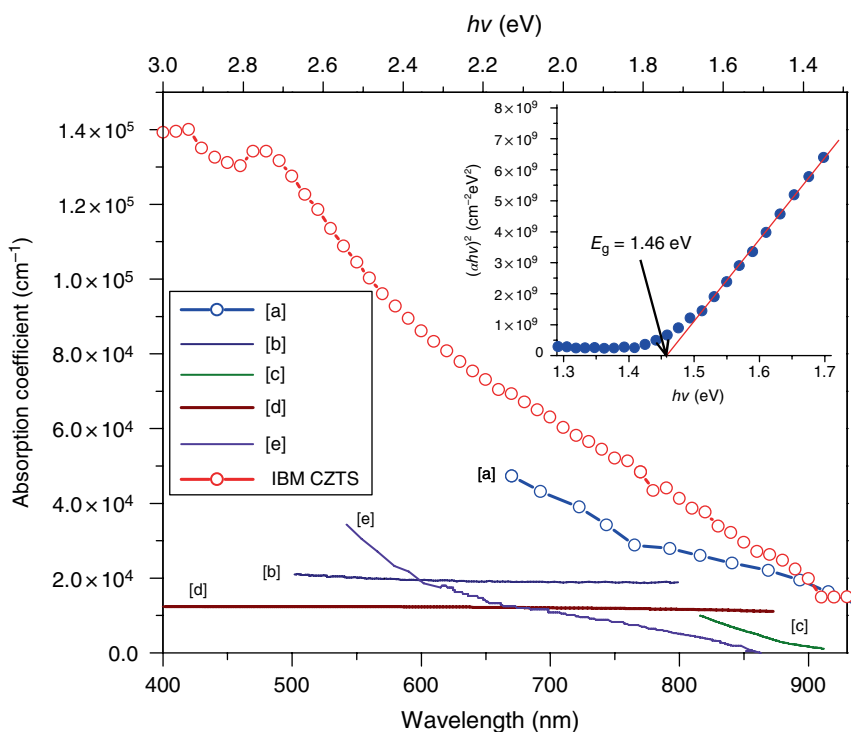
**Figure 15.4** (a) Bright-field TEM image of 8.4% CZTS solar cell, illustrating bimodal distribution of grain structure of CZTS. (b) Dark-field STEM image of 8.4% CZTS solar cell. The vertical arrow, which extends from Mo to ZnO, marks the direction of EDX line scan. (c) Elemental profiles determined by EDX scan (vertical arrow in (b)), which demonstrates the presence of ZnS near the CZTS/ $\text{MoS}_2$  interface. Reproduced with permission from [8]. Copyright © John Wiley & Sons, Ltd

Figure 15.4b shows a dark-field STEM image from the 8.4% CZTS solar cell. The vertical arrow, which extends from Mo to ZnO, marks the direction of an EDX line scan. Elemental profiles determined from the EDX scan are shown in Figure 15.4c which reveals that the large grain is CZTS, the small grain is ZnS, and the interfacial layer on top of the Mo is  $\text{MoS}_2$ . In addition to ZnS, we sometimes observe plate-like grains that are mainly  $\text{Cu}_x\text{Sn}_y$ . It is not surprising that these secondary phases form, given the non-stoichiometric initial compositions of as-deposited CZTS ( $\text{Cu}/\text{Sn} \approx 1.8$  and  $\text{Zn}/\text{Sn} \approx 1.2$ ), which are known to be the optimal elemental ratios for higher-performance solar cells [40]. There is still some disagreement as to why these off-stoichiometric compositions yield the best-performing CZTS devices. Our speculation is that these are the conditions – Cu-deficient and Zn-rich – where the densities of detrimental point defects and defect clusters, or aggregates, reach their minimum values. This is discussed further in Section 15.4.

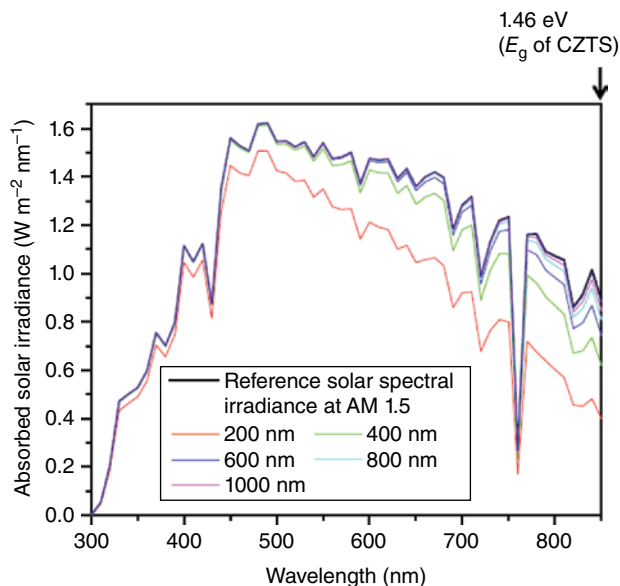


### 15.3.2 Absorption Characteristics of CZTS

Figure 15.5 provides absorption coefficient ( $\alpha$ ) data obtained via transmittance measurements performed on a CZTS film grown on a glass substrate. Shown in the inset of Figure 15.5 is a plot of  $(\alpha h\nu)^2$  v.  $h\nu$ , where  $h\nu$  is the energy of incident photons. From this plot, the band gap  $E_g$  of the CZTS is estimated as 1.46 eV. Along with  $\alpha$  of our CZTS films, values for CZTS films published in the literature [1, 41–44] are also shown. Immediately noticeable is the larger absorption coefficients of our material compared to those published in the literature over the range of wavelengths relevant to solar cell operation. From the absorption characteristics shown in Figure 15.5, we have constructed a plot of absorbed solar irradiance for different thicknesses of CZTS (Fig. 15.6) by multiplying the tabulated Air Mass 1.5G solar spectrum (see <http://redc.nrel.gov/solar/spectra/am1.5>) with the quantity  $1 - \exp(-\alpha d)$ , where  $d$  is the film thickness. As a consequence of the relatively large absorption coefficients of our CZTS film, a thick absorber is not necessary to fully capture solar radiation; 600 nm is thick enough to absorb >97% of the total sunlight that



**Figure 15.5** Absorption coefficients of our CZTS (prepared by thermal coevaporation and brief post-deposition annealing under *S* ambient) as well as those from the literature: (a) CZTS prepared by sputtering of a CZTS target [1]; (b) CZTS prepared by spray pyrolysis [41]; (c) CZTS prepared by sulfurization of stacked metal layers deposited by e-beam evaporator [42]; (d) CZTS prepared by reactive magnetron co-sputtering [43]; and (e) CZTS prepared by sulfurization of stacked metal layers deposited [44]. Inset is a plot of  $(\alpha h\nu)^2$  v.  $h\nu$ , from which the band gap of CZTS is determined



**Figure 15.6** Calculated solar irradiance absorbed by a CZTS of various thicknesses using the measured absorption coefficients shown in Figure 15.5. For color details, please see color plate section

can be absorbed by a material with  $E_g$  of 1.46 eV. This allows us to achieve a short-circuit current  $J_{sc}$  close to  $20 \text{ mA cm}^{-2}$  (c. 87% of the maximum possible  $J_{sc}$ ) with only 600 nm of CZTS, as described in Section 15.4.

### 15.3.3 Electrical Properties of CZTS Absorbers

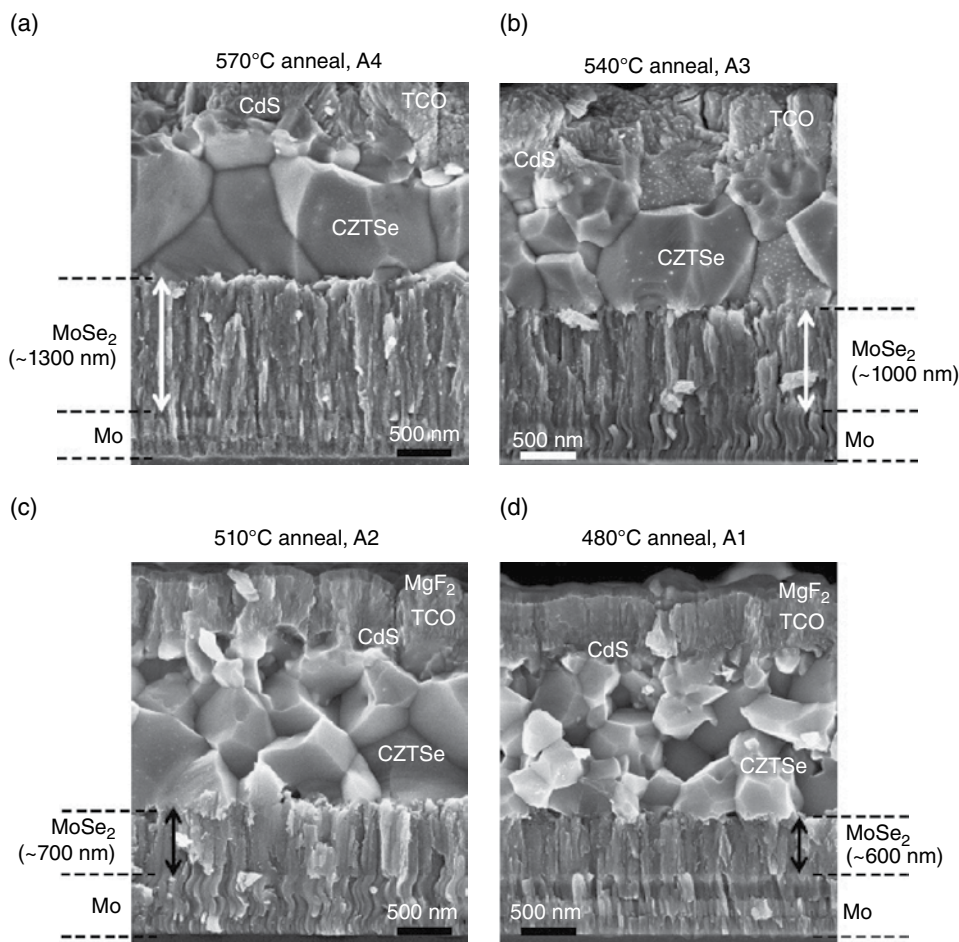
From Hall measurements (O. Gunawan *et al.*, personal communication, 2013) the hole concentration and the hole mobility in our CZTS films after annealing (5 min at  $570^\circ\text{C}$  in the presence of S vapor) are found to be c.  $1 \times 10^{14} \text{ cm}^{-3}$  and c.  $1 \text{ cm}^2 \text{ V}^{-1} \text{ s}^{-1}$ . Values of CZTS resistivity published in the literature range from 0.1–1  $\Omega \text{ cm}$  and hole mobilities as high as  $12.6 \text{ cm}^2 \text{ V}^{-1} \text{ s}^{-1}$  have been reported. Mitzi *et al.* [34] summarize literature resistivity and the hole mobility measurements in their table 2. However, publications reporting high carrier mobility do not contain device results, and those that do often demonstrate poor efficiency (e.g. 0.49% [45], CZTS hole mobility reported as  $12.6 \text{ cm}^2 \text{ V}^{-1} \text{ s}^{-1}$ ). It is plausible that conductive secondary phases such as  $\text{Cu}_x\text{S}$  or  $\text{Cu}_x\text{SnS}_y$  may have been present in the above CZTS films, which would influence the measurements. A recent study by Tanaka *et al.* [11] has in fact demonstrated that the apparent hole concentration is found to increase by almost three orders of magnitude when  $\text{Cu}_2\text{Se}$  coexists with CZTSe. After subjecting the sample to a KCN etch (which removes the  $\text{Cu}_2\text{Se}$ ) the hole concentration decreases, illustrating that electrical measurements of CZTS and CZTSe are sensitive to the phase purity of the compound.

One of the most important quantities in solar cell operation is the minority carrier mobility which for p-type CZTS is the electron mobility,  $\mu_n$ . Persson [46] studied the electronic band structure of CZTS using first-principle calculations and found that the electron

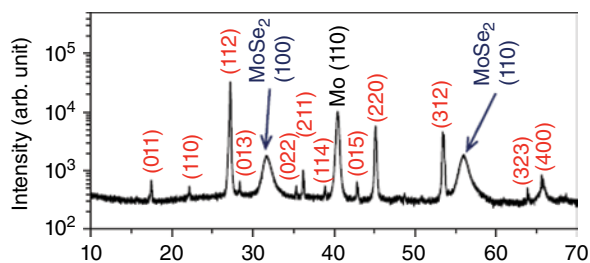
effective mass is smaller than hole effective mass by a factor of 1.1–3.9, depending on crystallographic directions (1.1 along [001] and 3.9 along [110] or [010]). This means that  $\mu_e$  of CZTS will be 1.1–3.9 times higher than  $\mu_h$ . With  $\mu_h$  of c.  $1 \text{ cm}^2 \text{ V}^{-1} \text{ s}^{-1}$  determined above, our estimation of  $\mu_e$  is therefore  $1\text{--}4 \text{ cm}^2 \text{ V}^{-1} \text{ s}^{-1}$ .

### 15.3.4 CZTSe Absorbers

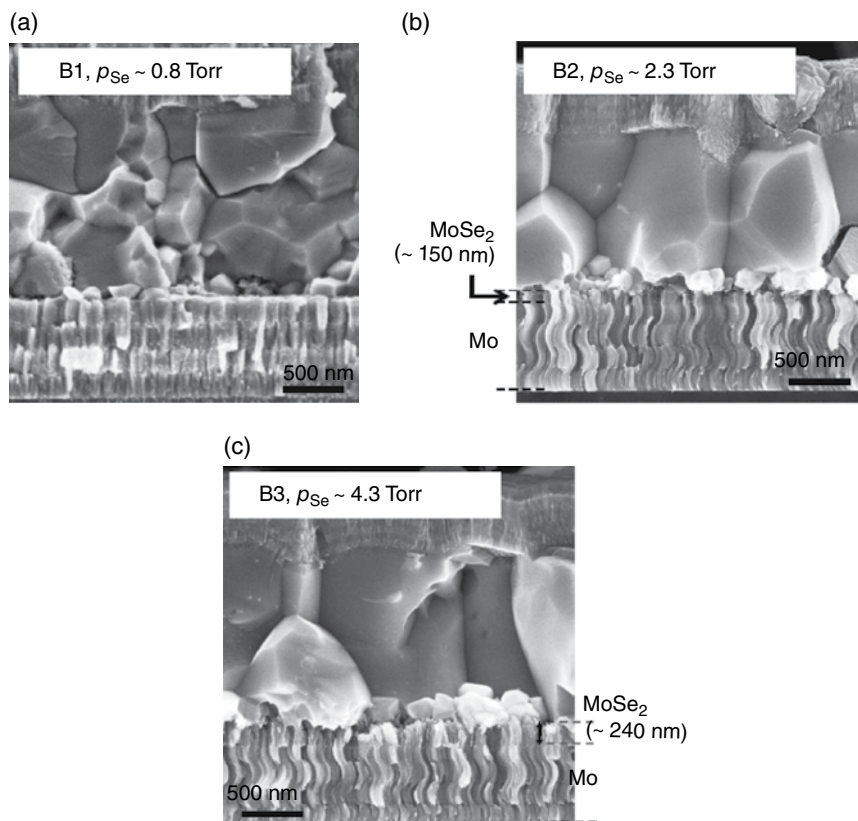
Now we switch the topic to the full selenide CZTSe absorbers. Figure 15.7a shows an SEM image of a CZTSe device that is processed similarly to CZTS absorbers that led to our 8.4% champion CZTS solar cell (deposition temperature c.  $150^\circ\text{C}$ ; deposition rate c.



**Figure 15.7** Cross-sectional SEM images of CZTSe solar cells. After CZTSe deposition, the samples were annealed at (a)  $570^\circ\text{C}$  (A4); (b)  $540^\circ\text{C}$  (A3); (c)  $510^\circ\text{C}$  (A2); and (d)  $480^\circ\text{C}$  (A1) under an Se atmosphere of partial pressure larger than equilibrium Se vapor pressure at each annealing temperature. Reproduced with permission from [9]. Copyright © 2012, AIP Publishing LLC



**Figure 15.8**  $\theta$ - $2\theta$  XRD measurement from CZTSe films annealed at 570°C for 5 min under  $p_{\text{Se}} \approx 165$  Torr

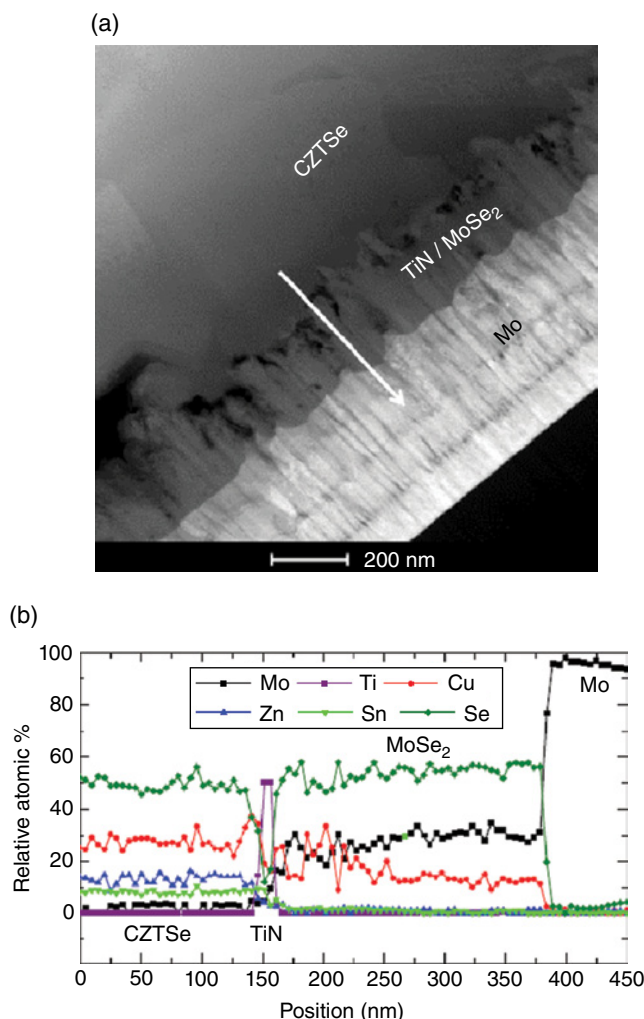


**Figure 15.9** Cross-sectional SEM images of CZTSe solar cells annealed under different  $p_{\text{Se}}$ : (a) 0.8 Torr; (b) 2.3 Torr; and (c) 4.3 Torr. The annealing temperature is 540°C for all cases

10 nm min<sup>-1</sup>; annealing duration/temperature of 5 min/570°C; and a partial pressure of chalcogen vapor during annealing of c. 160 Torr). Note the very thick bottom interfacial layer. XRD measurements performed on a sample prepared similarly to that shown in Figure 15.7a are provided in Figure 15.8. There are two peaks at  $2\theta$  at c. 32° and 56° that cannot be

accounted for either by CZTSe or Mo, but do correspond to  $\text{MoSe}_2$  (100) and (110) reflections. The absence of  $\text{MoSe}_2$  (00n) peaks indicates that the  $c$ -axis of the  $\text{MoSe}_2$  layer is parallel to the Mo surface, which is a configuration that has been shown to promote a good adhesion of the Se-containing absorber to the Mo layer [47]. In the following, we describe three different approaches that we have employed in order to suppress the formation of this thick  $\text{MoSe}_2$  layer.

We first lowered the post-deposition annealing temperature below  $570^\circ\text{C}$  while selenium vapor partial pressure  $p_{\text{Se}}$  was kept higher than the equilibrium vapor pressure of



**Figure 15.10** (a) Dark-field cross-sectional TEM image focusing on the bottom interface of CZTSe solar cell of 8.9% efficiency (sample C1 TiN). (b) Elemental profiles determined by EDX line scans. The scan direction is indicated by the arrow in (a). Reproduced with permission from [9]. Copyright © 2012, AIP Publishing LLC

Se at each annealing temperature to prevent possible decomposition of the CZTSe. The annealing duration was 5 min. As can be seen in SEM images of Figure 15.9, the lower annealing temperature reduced the  $\text{MoSe}_2$  layer thickness. However, the average grain size also decreased.

In the second approach, we kept the annealing temperature high ( $540^\circ\text{C}$ ) while varying  $p_{\text{Se}}$  from 0.8 Torr to 4.3 Torr. This parameter was adjusted by varying the amount of Se included in the annealing chamber along with the CZTSe sample. As anticipated, the  $\text{MoSe}_2$  thickness scaled with the quantity of Se added; in fact, the  $\text{MoSe}_2$  layer was nearly absent when  $p_{\text{Se}}$  was below 1 Torr (Fig. 15.9a). The CZTSe grain structure was almost unaffected by the quantity of Se present. However, annealing under low  $p_{\text{Se}}$  resulted in the formation of defect states in the gap as discussed in Section 15.5.

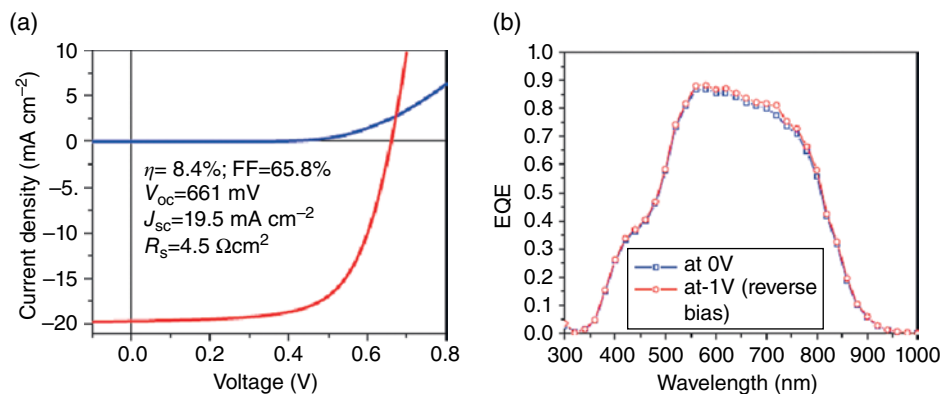
The final approach used a high substrate temperature and a high  $p_{\text{Se}}$  but introduced a diffusion barrier (c. 20 nm TiN) between CZTSe and Mo. Figure 15.10a shows a dark-field cross-sectional TEM image of a solar cell (sample TiN2) with a nominally c. 20 nm thick TiN layer deposited on the Mo layer prior to CZTSe deposition. This device achieved 8.9% power conversion efficiency. The sample was annealed at  $570^\circ\text{C}$  under c. 165 Torr of Se vapor. Elemental profiling from the EDX line scan shown in Figure 15.10b shows that at  $570^\circ\text{C}$  some Se atoms still manage to diffuse through the TiN forming  $\text{MoSe}_2$  underneath, along with some incorporation of Cu from the absorber. However, the  $\text{MoSe}_2$  layer thickness (c. 220 nm) is much smaller than an otherwise identical sample without a TiN layer (sample A4 in Fig. 15.7a;  $\text{MoSe}_2$  thickness c. 1300 nm). Another sample (sample TiN1) with a 20 nm TiN layer that was annealed at  $480^\circ\text{C}$  exhibited no apparent interfacial layer within the detection limit of SEM. Therefore, at lower annealing temperatures c. 20 nm TiN is thick enough to completely suppress the formation of  $\text{MoSe}_2$ .

All three approaches described above successfully reduce  $\text{MoSe}_2$  thickness. The effect of different annealing conditions (temperature and  $p_{\text{Se}}$ ) on the device performance is the focus of Section 15.5.

## 15.4 Device Characteristics of Full-Sulfide CZTS Thin-Film Solar Cells

### 15.4.1 Analysis of $J_{\text{sc}}$

Figure 15.11a shows the current density v. voltage ( $J$ - $V$ ) characteristics of our 8.4% solar cell with a 600 nm thick CZTS absorber in the dark and under 1-sun illumination, which was measured by the external certification laboratory at Newport, Inc. The photovoltaic parameters of this device are also listed in the figure. We first discuss the meaning of the measured  $J_{\text{sc}}$ , more specifically how effectively our CZTS absorber collects photo-generated carriers. As discussed in Section 15.3.2, a 600 nm thick CZTS layer is capable of absorbing almost 97% of the sunlight with photon energies of 1.46 eV and above. A device with this thickness of CZTS has a theoretical  $J_{\text{sc}}$  limit of  $30.0 \text{ mA cm}^{-2}$  if 100% collection efficiency is assumed. In reality, the losses from the TCO layer and the CdS buffer layer must be considered. External quantum efficiency (EQE) in Figure 15.11b shows nearly no response below c. 350 nm due to the complete absorption by the TCO layers (80 nm i-ZnO plus 450 nm ZnO:Al). There is also a significantly reduced response below c. 520 nm due to the partial absorption by the CdS whose  $E_{\text{g}}$  is c. 2.4 eV (i.e. c. 520 nm absorption onset). The theoretical limit to the  $J_{\text{sc}}$  after



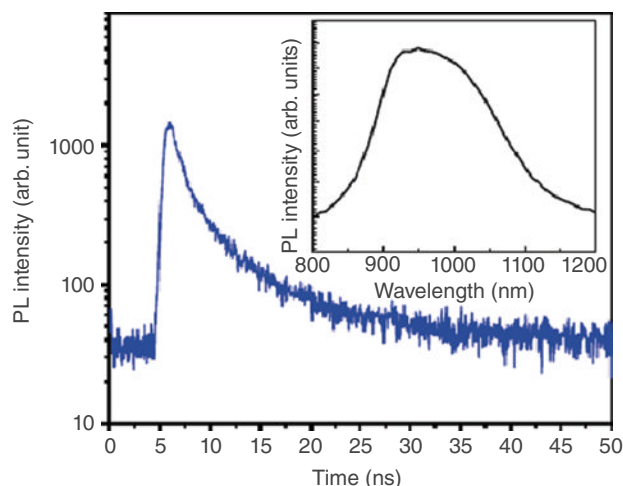
**Figure 15.11** (a) I–V characteristics under dark and 1 sun illumination. Light I–V was measured by an external accredited laboratory (Newport Technology and Applications Center’s Photovoltaic Lab) and it is very similar to our own measurement (not shown here). (b) EQEs measured at zero and at a reverse bias (–1 V). Reproduced with permission from [8]. Copyright © John Wiley & Sons, Ltd

accounting for the losses from the ZnO and CdS layers is  $23.8 \text{ mA cm}^{-2}$ . The measured  $J_{sc}$  of  $19.5 \text{ mA cm}^{-2}$  amounts to nearly 82% of this maximum suggesting a reasonable, but not perfect, collection efficiency. The imperfect collection of photo-generated carriers is also evident from the comparison of EQEs at zero bias (curve with open squares in Fig. 15.11b) and at a reverse bias of –1 V (curve with open circles in Fig. 15.11b). As shown in Figure 15.11b, the EQE spectra under reserve bias conditions are larger than under zero bias and the degree of the improvement increases with increasing wavelength. This indicates a reduced collection efficiency of photo-carriers created deep in the absorber (i.e. those generated by incident photons of longer wavelengths). The application of a reverse bias extends the depletion layer into the absorber layer so that a larger fraction of the minority photo-carriers are swept by the field. Another point to note from the EQE in Figure 15.12b is that the maximum EQE at c. 550 nm still does not reach 100% (reflection loss off the surface at this wavelength is minimal, c. 2–3% at the most). This wavelength corresponds to photons generated in the immediate vicinity of CdS/CZTS interface; however, not all of them contribute to  $J_{sc}$ . We speculate that this is related to the “spike”-type band offset between CdS and CZTS (c. 0.41 eV), which is larger than the optimal range (0.1–0.3 eV) [48] as revealed by an ultraviolet photoelectron spectroscopy (UPS) study carried out by Haight *et al.* [49].

#### 15.4.2 Lifetime of Photo-Generated Carriers

Figure 15.12 depicts a room-temperature time-resolved photoluminescence (TRPL) spectrum captured for an emission wavelength of 960 nm. This wavelength corresponds to the peak position of a broad PL spectrum collected as a function of wavelength at room temperature (see the inset of Fig. 15.12). The photon energy (c. 1.3 eV) is smaller than the estimated band-gap energy of 1.45 eV, as determined by the EQE measurement. However, the TRPL spectrum measured at 860 nm (c. 1.45 eV) is almost identical to the TRPL at 960 nm except for a higher level of noise due to the weaker luminescence signal at 860 nm. Due to the pulsed nature of the excitation source (15 kHz), the initial excess carrier





**Figure 15.12** TRPL spectrum at the emission wavelength of 960 nm. Carrier lifetime of c. 8 ns was determined by a single exponent fit to the spectrum (15–25 ns). Plot of PL v. wavelength is shown in the inset. Reproduced with permission from [8]. Copyright © John Wiley & Sons, Ltd

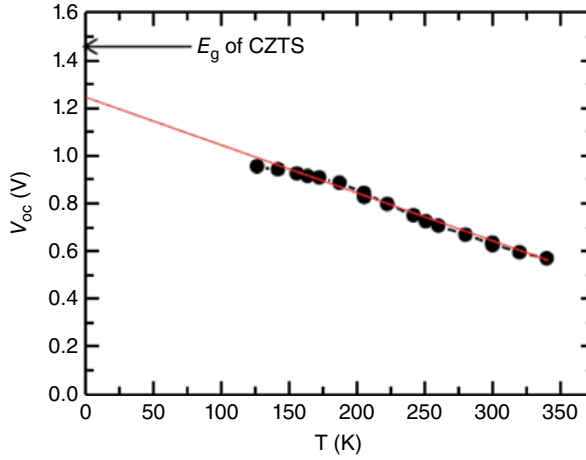
concentration created by each pulse of the laser is approximately 5000 times larger than the steady-state excess carrier concentration during continuous illumination at the same power density, that is, a high injection regime. TRPL therefore decays fast initially. We use a later portion of the spectrum (15–25 ns) to avoid the initial fast decay to fit with a single exponent, extracting a carrier recombination lifetime  $\tau$  of c. 8 ns.

### 15.4.3 Examining the $V_{oc}$ Deficit

Consistent with the literature reports [18, 50], our CZTS devices suffer from a pronounced  $V_{oc}$  deficit wherein the value  $(E_g/q) - V_{oc}$  exceeds 0.5 V, which is a value typical for efficient thin-film solar cells [51]. Temperature-dependent  $V_{oc}$  measurements (Fig. 15.13) reveal that the  $V_{oc}$  extrapolated to 0 K falls short of  $E_g/q$  by almost 210 mV. Two prevailing explanations for the cause of this deficit are: (1) non-ideal interfaces in the device, either at the Mo back electrode or at the interface with CdS [50]; and (2) high concentrations of point defects in CZTS, which cause adverse band tailing effects and limit carrier mobilities and lifetimes [52]. In this section, we discuss results that directly measure the relationship between the  $V_{oc}$  deficit and the defect density in vacuum-deposited CZTS materials. These results indicate that quasi donor-acceptor pair (QDAP) defects are at least partly related to  $V_{oc}$  losses in CZTS devices. Here, the word “quasi” is used to indicate likely deviations from the classical model, for example due to defect clustering.

Low-temperature (4 K) intensity-dependent PL measurements were performed on CZTS films with varying compositions and device efficiencies (532 nm pulsed laser, frequency 15 kHz). Figure 15.14a shows the 4 K intensity-dependent PL spectra of the CZTS device in a 8.3% solar cell [53]. As seen in Figure 15.14a, at low excitation intensity the spectrum consists of one peak centered at c. 1.14 eV. As the excitation intensity increases, the peak position blue-shifts until it reaches a value of c. 1.21 eV. At yet higher excitation, a high-energy shoulder appears and the low-energy peak saturates in height and slightly red-shifts. These measurements are discussed in detail by Gershon *et al.* [53].





**Figure 15.13**  $V_{oc}$  as a function of cell temperature. Extrapolated  $V_{oc}$  at 0 K is c. 1.25 V, which is c. 0.21 V short of 1.46 V expected from CZTS absorber ( $E_g \approx 1.46$  eV) if bulk recombination is dominant

From a careful analysis of the relationships between peak height, peak position, and excitation intensity, as well as the appearance of a high-energy shoulder at high excitation intensity, it can be determined that the low-energy blue-shifting peak corresponds to emission through localized QDAP defect states at 4 K [53]. This is further supported by the difference in PL lifetime at 1.16 eV and 1.43 eV; while the low-energy peak has a decay lifetime of c. 12  $\mu$ s, the shoulder at 1.43 eV has a lifetime of the order 2 ns, based on fits to a rate equation of the form

$$n(t) = \frac{n_0 \exp(-t/\tau)}{1 + (C/A)n_0 [1 - \exp(-t/\tau)]}, \quad (15.3)$$

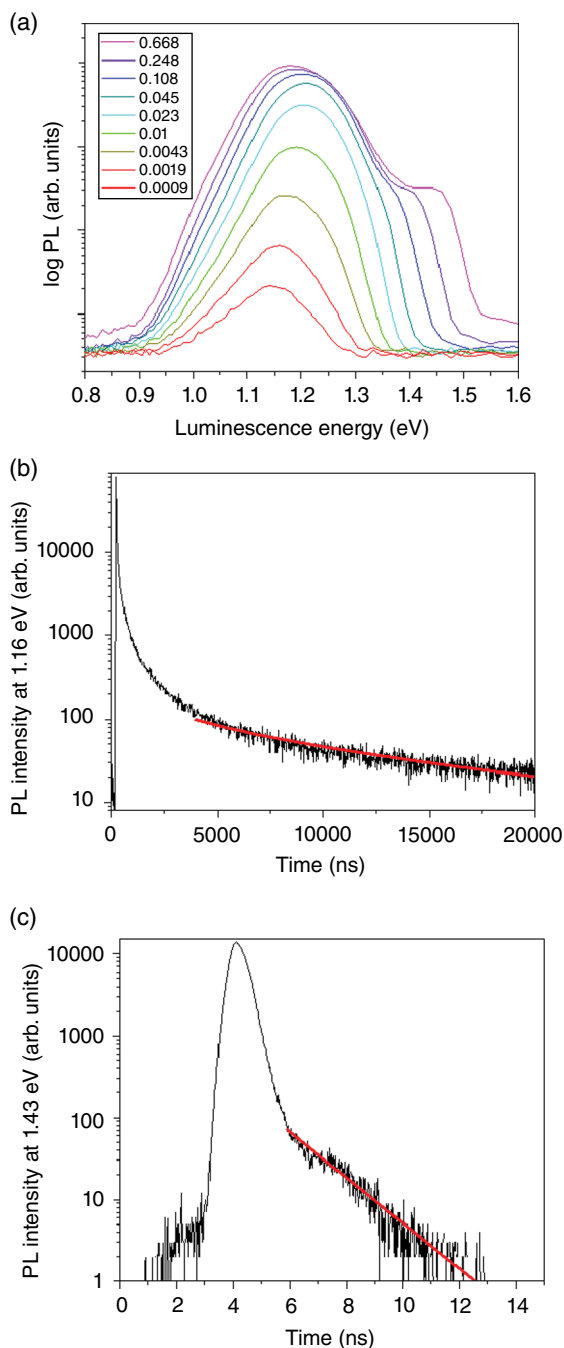
displayed directly in Figure 15.14b and c [54]. The large difference in PL lifetime at the two different energies stems from the fact that the low-energy transition involves tunneling between localized states which is inefficient, while the high-energy transition involves *delocalized* states, or states in which charge carriers are more mobile.

The luminescence energy resulting from recombination through QDAP states is expected to roughly follow Equation (15.4) below [55], where  $E_A$  is the acceptor ionization energy,  $E_D$  is the donor ionization energy,  $\epsilon$  is the dielectric constant of CZTS, and  $r$  is the spacing between QDAP defects:

$$E = E_g - E_D - E_A + \frac{q^2}{4\pi\epsilon r}. \quad (15.4)$$

When  $r$  is known, the defect density may be estimated from the relationship [56]:

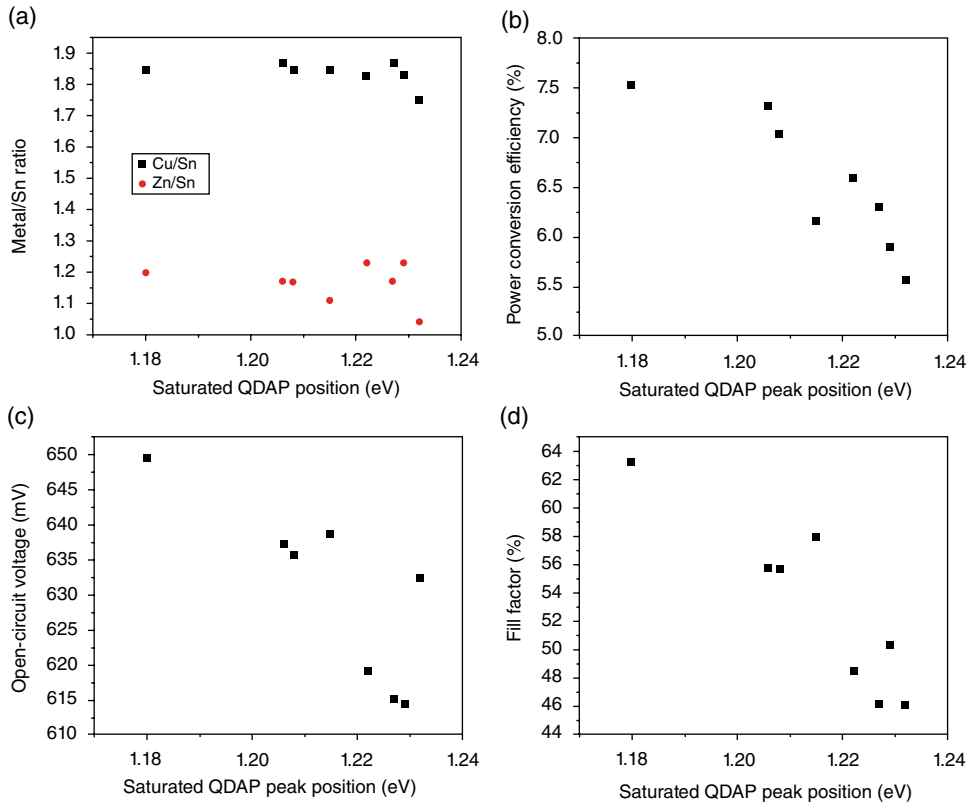
$$r = \left( \frac{4\pi N_D}{3} \right)^{-1/3}. \quad (15.5)$$



**Figure 15.14** (a) Low-temperature (4K) intensity-dependent PL of a CZTS layer giving an 8.3% efficient device; the numbers in the legend correspond to average  $W\text{ cm}^{-2}$ . PL lifetimes associated with emission at (b) 1.16 eV and (c) 1.43 eV. Measurements were made using an average laser intensity of  $0.668\text{ W cm}^{-2}$ . Reproduced with permission from [53]. Copyright © 2013, AIP Publishing LLC. For color details, please see color plate section

The Coulombic term in Equation (15.4) represents the interaction energy between *neutral* quasi donors and acceptors, where the donor is populated by an electron and the acceptor is populated by a hole. The proximity of neutral QDAP defects is proportional to the excitation intensity, thereby causing the blue-shift. At low excitation, the average QDAP defects are spaced far enough apart that the Coulombic interaction between them is small. Thus,  $r$  can be estimated by equating the energy of the blue-shift with the Coulombic term in Equation (15.4). Through this analysis, a total radiative defect density of  $c. 1 \times 10^{19} \text{ cm}^{-3}$  was found for the CZTS layer in an 8.3% efficient device.

This method was applied to examine the relationship between total radiative defect density in a CZTS thin film and the performance of the resulting device [57]. Figure 15.15 displays the performance characteristics of eight different CZTS devices, seven of which contain a similar starting composition ( $\text{Cu}/\text{Sn}=1.75\text{--}1.87$ ;  $\text{Zn}/\text{Sn}=1.11\text{--}1.23$ ), and one of which is considered slightly Zn-poor ( $\text{Cu}/\text{Sn}=1.75$ ,  $\text{Zn}/\text{Sn}=1.04$ ). From Figure 15.15a, it can be seen that samples containing the same starting metals ratio may also contain varying saturated QDAP peak positions (which correlate directly with the defect density



**Figure 15.15** Relationship between the saturated QDAP PL peak position and (a) sample composition; (b) power conversion efficiency; (c) open-circuit voltage; and (d) fill factor values for eight different devices, one of which is considered Zn-poor. All samples were grown, annealed, and processed in the same way using the same tools. Reproduced with permission from [57]. Copyright © 2013, AIP Publishing LLC

in the absorber, as all of these samples displayed the same starting peak position at the lowest excitation of  $c. 1.14 \pm 0.01$  eV; data not shown). The wide variation in device performance is however well-correlated with the concentration of QDAP defects in the absorber. For the same metals composition, samples displaying higher defect densities also display lower  $V_{oc}$  and fill factor FF values. The sample displaying the highest defect density and lowest performance characteristics is the Zn-poor sample. In addition to other statistical data not shown [57], this indicates that QDAP defects may be related to the empirical observation that Zn-rich and Cu-poor materials give on average better device performance.

## 15.5 Device Characteristics of Full-Selenide CZTSe Thin-Film Solar Cells

We described three different approaches to control  $\text{MoSe}_2$  thickness in Section 15.3. In sample set A, the annealing temperature is varied while enough  $p_{\text{Se}}$  is introduced so that  $p_{\text{Se}}$  is much larger than the equilibrium vapor pressure of Se at the annealing temperature to suppress phase decomposition. In sample set B, the annealing temperature was set at  $540^\circ\text{C}$  while  $p_{\text{Se}}$  was varied. In sample set TiN, a 20 nm thick TiN layer was deposited before the CZTSe growth while both the temperature and  $p_{\text{Se}}$  were kept high. The annealing conditions and photovoltaic parameters of all of these samples are listed in Table 15.2. From sample set A, we see that all photovoltaic parameters degrade with the increasing temperature (and hence with increasing  $\text{MoSe}_2$  thickness) despite the increase in grain size, which suggest a reverse correlation between device performance and the  $\text{MoSe}_2$  thickness. This is consistent with literature reports where adverse effects of a thick  $\text{MoSe}_2$  interfacial layer on device performance of CIGS solar cells have been observed [58]. From sample set B, we again notice an overall degradation of performance with thickening of the  $\text{MoSe}_2$  layer with the exception of B2, which suffers from degraded  $J_{sc}$  and FF values for reasons that are unclear. It is worth pointing out that the  $\text{MoSe}_2$  is nearly absent in B1, yet a decent efficiency (6.3%) with a very good series resistance  $R_s$  is demonstrated. This is contrary to the claim that  $\text{MoSe}_2$  is required for CIGS to form an Ohmic contact to Mo [47].

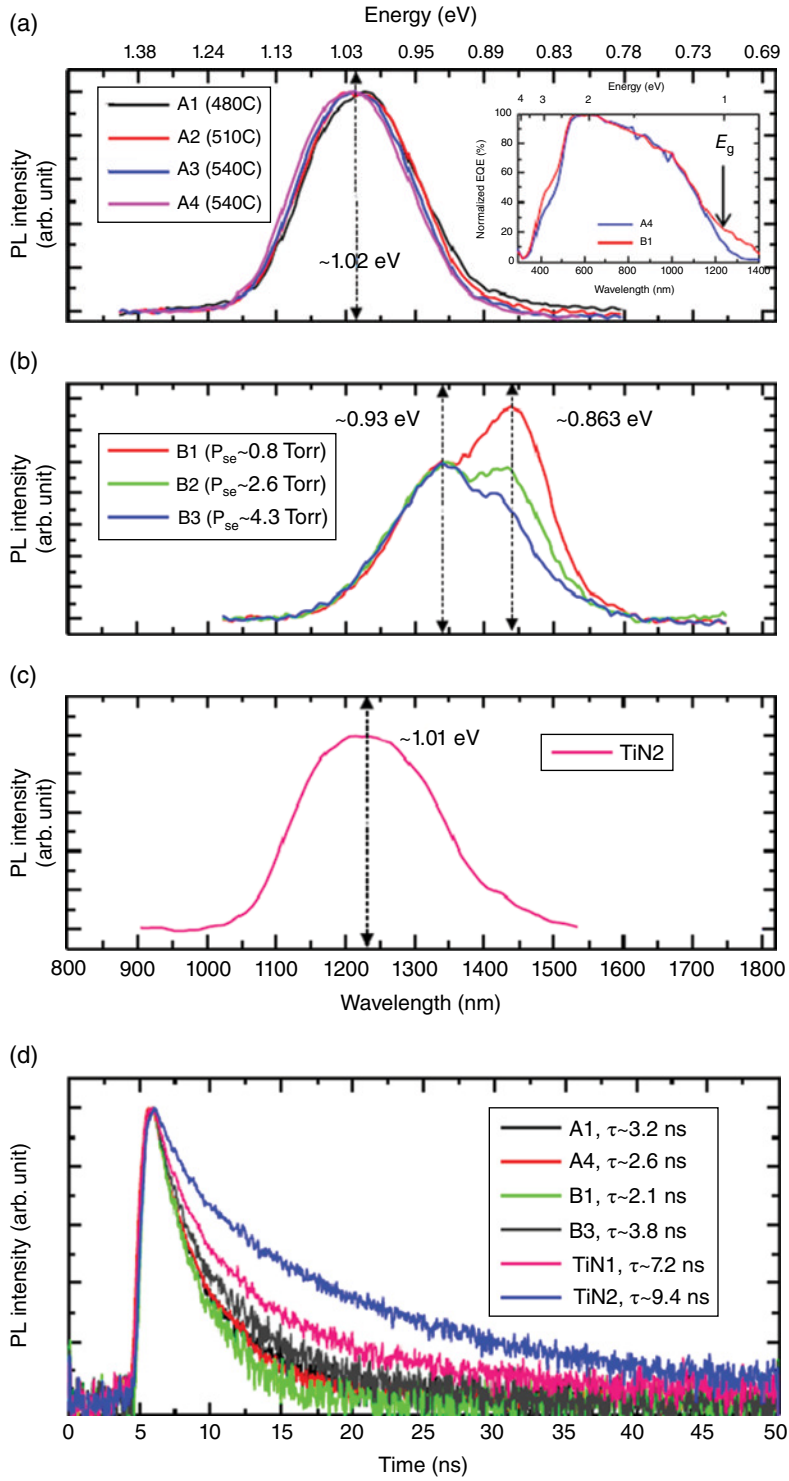
Figure 15.16 provides a room-temperature PL study of the CZTSe samples. In the samples annealed under higher  $p_{\text{Se}}$  than the equilibrium Se vapor pressure (A1–A4), the PL peak has a maximum at  $c. 1.0$  eV near the estimated band gap of CZTSe of 1.0 eV, as determined by external quantum efficiency (EQE) shown in the inset of Figure 15.16a. In contrast, those annealed under low  $p_{\text{Se}}$  (B1–B3) contain PL emission peaks at lower values ( $c. 0.93$  eV and  $c. 0.86$  eV). This sub-band-gap PL emission indicates transitions either directly involving mid-gap defect states or resulting from severe band tailing caused by the presence of defects, which suggests that reducing  $p_{\text{Se}}$  increases the defect density in the CZTSe. Furthermore, the sample with the lowest  $p_{\text{Se}}$  displayed the highest relative PL intensity for the sub-band-gap transition, suggesting that defects originating from Se deficiency act as radiative centers. The presence of states in the gap is independently confirmed by EQE. The inset of Figure 15.16a shows a comparison of the EQE spectra of sample A4 (annealed at  $570^\circ\text{C}$  with enough  $p_{\text{Se}}$ , that is,  $p_{\text{Se}}$  larger than the equilibrium Se vapor pressure at  $570^\circ\text{C}$ ) and sample B1 (annealed at  $540^\circ\text{C}$  with  $p_{\text{Se}} \approx 0.8$  Torr). In sample B1, sub-band-gap absorption is

**Table 15.2** List of CZTSe samples with their annealing conditions, photovoltaic parameters, and MoSe<sub>2</sub> interfacial thickness. In sample set A, post-deposition annealing temperature is varied while Se partial pressure during the annealing is kept similar. In sample set B, Se partial pressure is varied at a fixed annealing temperature of 540°C. In sample set TiN, a c. 20 nm thick TiN diffusion barrier is inserted between CZTSe and Mo back contact. Reproduced with permission from [9]. Copyright © 2012, AIP Publishing LLC.

Sample ID	Anneal temp. (°C)	Approx. Se partial pressure during annealing (Torr)	Approx. equilibrium Se vapor pressure (Torr) <sup>a</sup>	Efficiency (%)	V <sub>oc</sub> (mV)	J <sub>sc</sub> (mAcm <sup>-2</sup> )	FF (%)	R <sub>s</sub> (Ωcm <sup>2</sup> )	Approx. MoSe <sub>2</sub> thickness (nm)
A1	480	35	28	5.95 <sup>a</sup>	333	31.5	56.8	2.0	600
A2	510	60	52	5.26 <sup>a</sup>	327	30.1	53.5	2.4	700
A3	540	100	90	4.08	293	27.4	51	2.6	1000
A4	570	160	150	2.95	264	25.4	44	3.4	1300
B1	540	0.8	90	6.36 <sup>a</sup>	308	34.9	59.2	1.4	<10 <sup>b</sup>
B2	540	2.3	90	3.4	291	27.6	42.4	3.1	150
B3	540	4.3	90	5.56 <sup>a</sup>	289	33.6	57.3	1.6	240
A3	540	100	90	4.08	293	27.4	51	2.6	1000
TiN1	480	35	28	6.3	369	39.3	43.5	2.5	<10 <sup>b</sup>
TiN2	570	160	150	8.9 <sup>a</sup>	385	42.6	54.2	1.8	220

<sup>a</sup>With c. 110 nm thick MgF<sub>2</sub> anti-reflection coating, which typically results in an increase in efficiency of 0.3–0.5%;

<sup>b</sup> Less than the detection limit of SEM

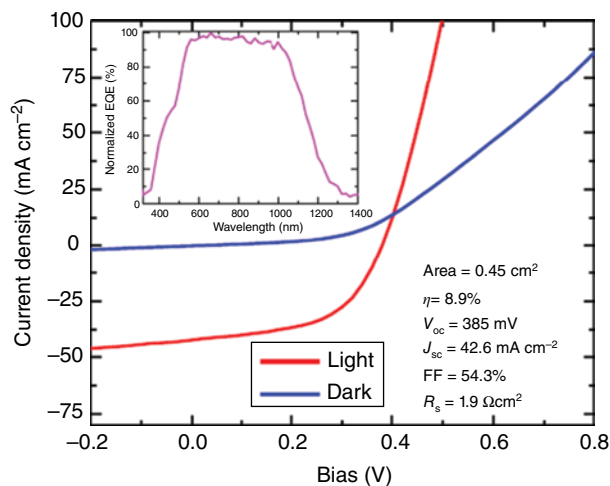


**Figure 15.16** Room-temperature PL spectra of CZTSe samples: (a) samples A1–A4; (b) samples B1–B3; and (c) sample TiN2. EQE of A4 and B1 are shown in the inset of (a). (d) TRPL spectra of some representative samples. Reproduced with permission from [9]. Copyright © 2012, AIP Publishing LLC. For color details, please see color plate section

evident from the EQE response at wavelengths longer than those anticipated based on the band gap of CZTSe. Defects in the gap can act as recombination centers, which would adversely impact  $V_{oc}$ .

The room-temperature carrier recombination lifetimes  $\tau$  of some representative samples are shown in Figure 15.16d. The lifetimes of samples A1–A4 are similar, while those of samples B1–B3 increase monotonically with  $p_{sc}$ . Despite the increasing lifetime with  $p_{sc}$  in samples B1–B3, the  $V_{oc}$  slightly decreases unexpectedly. It therefore appears that the  $V_{oc}$  in these devices may be more significantly affected by other factors such as the  $\text{MoSe}_2$  layer thickness, which may alter band alignment between CZTSe and  $\text{MoSe}_2/\text{Mo}$ . This is not completely understood at the present time, however.

The lifetimes of the samples containing a TiN diffusion barrier (annealed under high  $p_{sc}$  of c. 160 Torr) are significantly improved:  $>7$  ns for TiN1, which is annealed at  $480^\circ\text{C}$  and has nearly no  $\text{MoSe}_2$  interfacial layer, and  $>9$  ns for TiN2, which is annealed at  $570^\circ\text{C}$  and has a c. 220 nm thick  $\text{MoSe}_2$  layer. The lifetime of TiN2 ( $>9$  ns) is comparable to the record carrier lifetime reported in this material system [31]. Furthermore, the peak in the PL emission from TiN2 is near the band gap of CZTSe as shown in Figure 15.16c. Based on these TRPL results, an improved device performance is expected from the samples with a TiN layer. TiN1 exhibits an efficiency of 6.3% and the efficiency of TiN2 was 8.9%. The  $J$ – $V$  characteristics of TiN2 in the dark and under 1-sun illumination are shown in Figure 15.17. As anticipated from the long lifetime, the EQE remains high over the range of wavelengths corresponding to photons absorbed in the CZTSe (see the inset of Fig. 15.17). This is in contrast with EQE spectra obtained from other samples (inset of Fig. 15.16a), which show reduced collection efficiency with increasing wavelength. Consistent with the EQE, the measured  $J_{sc}$  is very high at  $42.6\text{ mA cm}^{-2}$ , c. 88% of the maximum theoretically estimated for an absorber with 1.0 eV band gap. As is the case for CZTS devices, the  $V_{oc}$  deficit ( $(E_g/q) - V_{oc}$ )  $\approx 0.63$  V is again the



**Figure 15.17**  $I$ – $V$  curves of 8.9% efficiency CZTSe solar cell with a TiN layer (sample C1, TiN) under dark and 1 sun illumination. Normalized EQE is shown in the inset. Reproduced with permission from [9]. Copyright © 2012, AIP Publishing LLC.

most serious challenge that must be overcome in order to achieve higher efficiencies. Additionally, from comparing the device performance of TiN1 and TiN2 we learn that a higher annealing temperature is beneficial.

## 15.6 Summary

In this chapter, we discussed the preparation of CZTS and CZTSe absorbers using thermal coevaporation. We employed thermal coevaporation at the low temperature of 150°C in order to avoid complications arising from the instability of CZTS at high temperatures. Using this approach, we have successfully demonstrated an 8.4% thin-film solar cell based on full-sulfide CZTS absorbers with excellent absorption characteristics. This 8.4% CZTS device currently holds the record efficiency among full-sulfide CZTS prepared by any method. Through extensive analysis of the 8.4% CZTS device, we find a reduced collection efficiency of photo-carriers generated away from the CdS/CZTS interface. Additionally, we speculate that the conduction band offset between CdS and CZTS that is slightly larger than the optimal range is responsible for limiting  $J_{sc}$ . The measured  $J_{sc}$  is reasonably good however, amounting to c. 82% of the maximum  $J_{sc}$  attainable from a solar cell consisting of ZnO/CdS/600 nm CZTS. The  $V_{oc}$  deficit is one of the most serious challenges in achieving higher efficiency. It has been shown that this  $V_{oc}$  deficit is at least partly related to a high density of compensating donor and acceptor defects, which cause spatial potential fluctuations of the bands. Additionally, other factors such as recombination at the CdS/CZTS interface could contribute to further  $V_{oc}$  losses. We have also presented device results from full-selenide CZTSe solar cells. Compared to the full-sulfide system, a much thicker (>1  $\mu\text{m}$ )  $\text{MoSe}_2$  layer forms during annealing under similar conditions. This layer is a serious issue for performance. We have demonstrated a CZTSe power conversion efficiency of 8.9% by controlling the  $\text{MoSe}_2$  thickness via a thin TiN diffusion barrier just below the CZTSe. This TiN layer allows us to maintain high annealing temperatures and  $p_{se}$ , which are necessary for preparing high-performance devices.

## References

- [1] Ito, K. & Nakazawa, T. (1988) Electrical and optical properties of stannite-type Quaternary semiconductor thin films. *Japanese Journal of Applied Physics*, **27**, 2094.
- [2] Katagiri, H., Sasaguchi, N., Hando, S., Hoshino, S., Ohashi, J. & Yokota, T. (1997) Preparation and evaluation of  $\text{Cu}_2\text{ZnSnS}_4$  thin films by sulfurization of E-B evaporated precursors. *Solar Energy Materials and Solar Cells*, **49**, 407.
- [3] Katagiri, H., Jimbo, K., Yamada, S., Kamimura, T., Maw, W.S., Fukano, T., Ito, T. & Motohiro, T. (2008) Enhanced conversion efficiencies of  $\text{Cu}_2\text{ZnSnS}_4$ -based thin film solar cells by using preferential etching technique. *Applied Physics Express*, **1**, 041201, doi: 10.1143/APEX.1.041201.
- [4] Todorov, T.K., Reuter, K.B. & Mitzi, D.B. High-efficiency solar cell with earth-abundant liquid-processed absorber. *Advanced Materials*, **22**, E156, doi: 10.1002/adma.200904155.
- [5] Wang, W., Winkler, M.T., Gunawan, O., Gokmen, T., Todorov, T.K., Zhu, Y. & Mitzi, D.B. (2013) Device characteristics of CZTSSe thin-film solar cells with 12.6% efficiency. *Advanced Energy Materials*, doi: 10.1002/aenm.201301465.



- [6] Wang, K., Gunawan, O., Todorov, T., Shin, B., Chey, S.J., Bojarczuk, N.A., Mitzi, D. & Guha, S. (2010) Thermally evaporated  $\text{Cu}_2\text{ZnSnS}_4$  solar cells. *Applied Physics Letters*, **97**, 143508, doi: 10.1063/1.3499284.
- [7] Wang, K., Shin, B., Reuter, K.B., Todorov, T., Mitzi, D.B. & Guha, S. (2011) Structural and elemental characterization of high efficiency  $\text{Cu}_2\text{ZnSnS}_4$  solar cells. *Applied Physics Letters* **98**, 051912, doi: 10.1063/1.3543621.
- [8] Shin, B., Gunawan, O., Zhu, Y., Bojarczuk, N.A., Chey, S.J. & Guha, S. (2011) Thin film solar cell with 8.4% power conversion efficiency using an earth-abundant  $\text{Cu}_2\text{ZnSnS}_4$  absorber. *Progress in Photovoltaics: Research and Applications*, **21**, 72–76, doi: 10.1002/pip.1174.
- [9] Shin, B., Zhu, Y., Bojarczuk, N.A., Chey, S.J. & Guha, S. (2012) Control of an interfacial  $\text{MoSe}_2$  layer in  $\text{Cu}_2\text{ZnSnSe}_4$  thin film solar cells: 8.9% power conversion efficiency with a TiN diffusion barrier. *Applied Physics Letters* **101**, 053903, doi: 10.1063/1.4740276.
- [10] Repins, I., Beall, C., Vora, N., DeHart, C., Kuciauskas, D., Dippo, P., To, B., Mann, J., Hsu, W.-C., Goodrich, A. & Noufi, R. (2012) Co-evaporated  $\text{Cu}_2\text{ZnSnSe}_4$  films and devices. *Solar Energy Materials and Solar Cells*, doi: 10.1016/j.solmat.2012.01.008.
- [11] Tanaka, T., Sueishi, T., Saito, K., Guo, Q., Nishio, M., Yu, K.M. & Walukiewicz, W. (2012) Existence and removal of  $\text{Cu}_2\text{Se}$  second phase in coevaporated  $\text{Cu}_2\text{ZnSnSe}_4$  thin films. *Journal of Applied Physics*, **111**, 053522.
- [12] Redinger, A. & Siebentritt, S. (2010) Coevaporation of  $\text{Cu}_2\text{ZnSnS}_4$  thin films. *Applied Physics Letters*, **97**, 092111, doi: 10.1063/1.3483760.
- [13] Redinger, A., Berg, D.M., Dale, P.J. & Siebentritt, S. (2011) The consequence of kesterite equilibria for efficient solar cells. *Journal of American Chemical Society*, doi: dx.doi.org/10.1021/ja111713g.
- [14] Babu, B., Kumar, K., Bhaskar, U. & Vanjari, S.R. (2010) Effect of  $\text{Cu}/(\text{Zn}+\text{Sn})$  ratio on the properties of co-evaporated  $\text{Cu}_2\text{ZnSnSe}_4$ . *Solar Energy Materials and Solar Cells*, **94**, 221, doi: 10.1016/j.solmat.2009.09.005.
- [15] Oishi, K., Saito, G., Ebina, K., Nagahashi, M., Jimbo, K., Maw, W.S., Katagiri, H., Yamazaki, M., Araki, H. & Takeuchi, A. (2008) Growth of  $\text{Cu}_2\text{ZnSnS}_4$  thin films on Si (100) substrates by multisource evaporation. *Thin Solid Films* **517**, 1449, doi: 10.1016/j.tsf.2008.09.056.
- [16] Tanaka, T., Kawasaki, D., Nishio, M., Guo, Q. & Ogawa, H. (2006) Fabrication of  $\text{Cu}_2\text{ZnSnS}_4$  thin films by co-evaporation. *Physica Status Solidi (C)*, **3**, 2844, doi: 10.1002/pssc.200669631.
- [17] Schubert, B.-A., Marsen, B., Cinque, S., Unold, T., Klenk, R., Schorr, S. & Schock, H.-W. (2011)  $\text{Cu}_2\text{ZnSnS}_4$  thin film solar cells by fast coevaporation. *Progress in Photovoltaics: Research and Applications*, **19**, 93, doi: 10.1002/pip.976.
- [18] Scragg, J.J., Ericson, T., Fontané, X., Izquierdo-Roca, V., Perez-Rodriguez, A., Kubart, T., Edoff, M. & Platzer-Björkman, C. (2012) Rapid annealing of reactively sputtered precursors for  $\text{Cu}_2\text{ZnSnS}_4$  solar cells. *Progress in Photovoltaics: Research and Applications*, doi: 10.1002/pip.2265.
- [19] Salome, P.M.P., Malaquias, J., Fernandes, P.A., Ferreira, M.S., da Cunha, A.F., Leitao, J.P., Gonzalez, J.C. & Matinaga, F.M. (2012) Growth and characterization of  $\text{Cu}_2\text{ZnSn}(\text{S},\text{Se})_4$  thin films for solar cells. *Solar Energy Materials and Solar Cells*, **101**, 147, doi: 10.1016/j.solmat.2012.02.031.
- [20] Schurr, R., Hoelzing, A., Jost, S., Hock, R., Voss, T., Schulze, J., Kirbs, A., Ennaoui, A., Lux-Steiner, M., Weber, A., Koetschau, I. & Schock, H.-W. (2009) The crystallization of  $\text{Cu}_2\text{ZnSnS}_4$  thin film solar cell absorbers from co-electroplated Cu-Zn-Sn precursors. *Thin Solid Films*, **517**, 2465, doi: 10.1016/j.tsf.2008.11.019.
- [21] Ahmed, S., Reuter, K.B., Gunawan, O., Guo, L., Romankiw, L.T. & Deligianni, H. (2011) A high efficiency electroplated  $\text{Cu}_2\text{ZnSnS}_4$  solar cell. *Advanced Energy Materials* **2**, 253, doi: 10.1002/aenm.201100526.
- [22] Moriya, K., Tanaka, H. & Uchiki, H. (2008)  $\text{Cu}_2\text{ZnSnS}_4$  thin films annealed in  $\text{H}_2\text{S}$  atmosphere for solar cell absorber prepared by pulsed laser deposition. *Japanese Journal of Applied Physics*, **47**, 602, doi: 10.1143/JJAP.47.602.

- [23] Thimsen, E., Riha, S.C., Baryshev, S.V., Martinson, A.B.F., Elam, J.W. & Pellin, M.J. (2012) Atomic layer deposition of the quaternary chalcogenide  $\text{Cu}_2\text{ZnSnS}_4$ . *Chemistry of Materials*, doi: 10.1021/cm3015463.
- [24] Cao, Y., Denny, M.S., Caspar, J.V., Farneth, W.E., Guo, Q., Ionkin, A.S., Johnson, L.K., Lu, M., Malajovich, I., Radu, D., Rosenfeld, H.D., Choudhury, K.R. & Wu, W. (2012) High-efficiency solution-processed  $\text{Cu}_2\text{ZnSn}(\text{S},\text{Se})_4$  thin-film solar cells prepared from binary and ternary nanoparticles. *Journal of the American Ceramic Society*, doi: 10.1021/ja3057985.
- [25] Ford, G.M., Guo, Q., Agrawal, R. & Hillhouse, H.W. (2011) Earth abundant element  $\text{Cu}_2\text{Zn}(\text{Sn}_{1-x}\text{Ge}_x)\text{S}_4$  nanocrystals for tunable band gap solar cells: 6.8% efficient device fabrication. *Chemistry of Materials*, doi: 10.1021/cm2002836.
- [26] Steinhagen, C., Panthani, M.G., Akhavan, V., Goodfellow, B., Koo, B. & Korgel, B.A. (2009) Synthesis of  $\text{Cu}_2\text{ZnSnS}_4$  nanocrystals for use in low-cost photovoltaics. *Journal of the American Ceramic Society*, **131**, 12554, doi: 10.1021/ja905922.
- [27] Todorov, T.K., Tang, J., Bag, S., Gunawan, O., Gokmen, T., Zhu, Y. & Mitzi, D.B. (2012) Beyond 11% efficiency: characteristics of state-of-the-art  $\text{Cu}_2\text{ZnSn}(\text{S},\text{Se})_4$  solar cells. *Advanced Energy Materials*, doi: 10.1002/aenm.201200348.
- [28] Barkhouse, D.A.R., Gunawan, O., Gokmen, T., Todorov, T.K. & Mitzi, D.B. (2011) Device characteristics of a 10.1% hydrazine-processed  $\text{Cu}_2\text{ZnSn}(\text{Se},\text{S})_4$  solar cell. *Progress in Photovoltaics: Research and Applications*, doi: 10.1002/pip.1160.
- [29] Yang, W., Duan, H.-S., Bob, B., Zhou, H., Lei, B., Chung, C.-H., Li, S.-H., Hou, W.W. & Yang, Y. (2012) Novel solution processing of high-efficiency earth-abundant  $\text{Cu}_2\text{ZnSn}(\text{S},\text{Se})_4$  solar cells. *Advanced Materials*, doi: 10.1002/adma.201201785.
- [30] Fella, C.M., Uhl, A.R., Romanyuk, Y.E. & Tiwari, A.N. (2012)  $\text{Cu}_2\text{ZnSnSe}_4$  absorbers processed from solution deposited metal salt precursors under different selenization conditions. *Physica Status Solidi A*, doi: 10.1002/pssa.201228003.
- [31] Bag, S., Gunawan, O., Gokmen, T., Zhu, Y., Todorov, T.K. & Mitzi, D.B. (2012) Low band gap liquid-processed CZTSe solar cell with 10.1% efficiency. *Environmental Science and Technology*, **5**, 7060–7065, doi: 10.1039/c2ee00056c.
- [32] Repins, I., Contreras, M.A., Egaas, B., DeHart, C., Scharf, J., Perkins, C.L., To, B. & Noufi, R. (2008) 19.9%-efficient  $\text{ZnO}/\text{CdS}/\text{CuInGaSe}_2$  solar cell with 81.2% fill factor. *Progress in Photovoltaics: Research and Applications*, **16**, 235, doi: 10.1002/pip.822.
- [33] Scragg, J.J., Ericson, T., Kubart, T., Edoff, M. & Platzer-Bjoerkman, C. (2011) Chemical insights into the instability of  $\text{Cu}_2\text{ZnSnS}_4$  films during annealing. *Chemistry of Materials*, doi: dx.doi.org/10.1021/cm202379s.
- [34] Mitzi, D.B., Gunawan, O., Todorov, T.K., Wang, K. & Guha, S. (2011) The path towards a high-performance solution-processed kesterite solar cell. *Solar Energy Materials and Solar Cells*, **95**, 1421, doi: 10.1016/j.solmat.2010.11.028.
- [35] Nagaoka, A., Yoshino, K., Taniguchi, H., Taniyama, T. & Miyake, H. (2012) Preparation of  $\text{Cu}_2\text{ZnSnS}_4$  single crystals from Sn solution. *Journal of Crystal Growth*, **341**, 38, doi: 10.1016/j.crysgro.2011.12.046.
- [36] Momose, N., Htay, M.T., Yudasaka, T., Igarashi, S., Seki, T., Iwano, S., Hashimoto, Y. & Ito, K. (2011)  $\text{Cu}_2\text{ZnSnS}_4$  thin film solar cells utilizing sulfurization of metallic precursor prepared by simultaneous sputtering of metal targets. *Japanese Journal of Applied Physics*, **50**, doi: 10.1143/JJAP.50.01BG09.
- [37] Cheng, A.-J., Manno, M., Khare, A., Leighton, C., Campbell, S.A. & Aydil, E.S. (2011) Imaging and phase identification of  $\text{Cu}_2\text{ZnSnS}_4$  thin films using confocal Raman spectroscopy. *Journal of Vacuum Science and Technology A*, **29**, 051203.
- [38] Fernandes, P.A., Salome, P.M.P. & da Cunha, A.F. (2009) Growth and Raman scattering characterization of  $\text{Cu}_2\text{ZnSnS}_4$  thin films. *Thin Solid Films*, **517**, 2519, doi: 10.1016/j.tsf.2008.11.031.
- [39] Fernandes, P.A., Salome, P.M.P. & da Cunha, A.F. (2010) A study of ternary  $\text{Cu}_3\text{SnS}_3$  and  $\text{Cu}_3\text{SnS}_4$  thin films prepared by sulfurizing stacked metal precursors. *Journal of Physics D: Applied Physics*, **43**, 215403.
- [40] Katagiri, H., Jimbo, K., Tahara, M., Araki, H. & Oishi, K. (2009) The influence of the composition ratio on CZTS-based thin film solar cells. *Materials Research Society Symposium Proceedings*, **1165**, M04.

- [41] Kamoun, N., Bouzouita, H. & Rezig, B. (2007) Fabrication and characterization of  $\text{Cu}_2\text{ZnSnS}_4$  thin films deposited by spray pyrolysis technique. *Thin Solid Films*, **515**, 5969, doi: 10.1016/j.tsf.2006.12.144.
- [42] Kobayashi, T., Jimbo, K., Tsuchida, K., Shinoda, S., Oyanagi, T. & Katagiri, H. (2005) Investigation of  $\text{Cu}_2\text{ZnSnS}_4$ -based thin film solar cells using abundant materials. *Japanese Journal of Applied Physics*, **44**, 783.
- [43] Liu, F., Li, Y., Zhang, K., Wang, B., Yan, C., Lai, Y., Zhang, Z., Li, J. & Liu, Y. (2010) *In situ* growth of  $\text{Cu}_2\text{ZnSnS}_4$  thin films by reactive magnetron co-sputtering. *Solar Energy Materials and Solar Cells*, **94**, 2431, doi: 10.1016/j.solmat.2010.08.003.
- [44] Tanaka, T., Nagatomo, T., Kawasaki, D., Nishio, M., Guo, Q., Wakahara, A., Yoshida, A. & Ogawa, H. (2005) Preparation of  $\text{Cu}_2\text{ZnSnS}_4$  thin films by hybrid sputtering. *Journal of Physics and Chemistry of Solids*, **66**, 1978, doi: 10.1016/j.jpcs.2005.09.037.
- [45] Zhou, Z., Wang, Y.C., Xu, D. & Zhang, Y. (2010) Fabrication of  $\text{Cu}_2\text{ZnSnS}_4$  screen printed layers for solar cells. *Solar Energy Materials and Solar Cells*, **94**, 2042, doi: 10.1016/j.solmat.2010.06.010.
- [46] Persson, C. (2010) Electronic and optical properties of  $\text{Cu}_2\text{ZnSnS}_4$  and  $\text{Cu}_2\text{ZnSnSe}_4$ . *Journal of Applied Physics*, **107**, 053710, doi: 10.1063/1.3318468.
- [47] Nishiwaki, S., Kohara, N., Negami, T. & Wada, T. (1998)  $\text{MoSe}_2$  layer formation at  $\text{Cu}(\text{In,Ga})\text{Se}_2/\text{Mo}$  interfaces in high efficiency  $\text{Cu}(\text{In}_{1-x}\text{Ga}_x)\text{Se}_2$  solar cells. *Japanese Journal of Applied Physics*, **37**, L71.
- [48] Gloeckler, M. & Sites, J.R. (2005) Efficiency limitations for wide-band-gap chalcopyrite solar cells. *Thin Solid Films*, **480–481**, 241.
- [49] Haight, R., Barkhouse, A., Gunawan, O., Shin, B., Copel, M., Hopstaken, M. & Mitzi, D.B. (2011) Band alignment at the  $\text{Cu}_2\text{ZnSn}(\text{S}_x\text{Se}_{1-x})/\text{CdS}$  interface. *Applied Physics Letters*, **98**, 253502.
- [50] Gunawan, O., Todorov, T.K. & Mitzi, D.B. (2010) Loss mechanisms in hydrazine-processed  $\text{Cu}_2\text{ZnSn}(\text{Se,S})_4$  solar cells. *Applied Physics Letters*, **97**, 233506, doi: 10.1063/1.3522884.
- [51] Mitzi, D.B., Gunawan, O., Todorov, T.K. & Barkhouse, A.R. (2013) Prospects and performance limitations for Cu-Zn-Sn-S-Se photovoltaic technology. *Philosophical Transactions of Royal Society of London, Series A*, **371**, 20110432.
- [52] Gokmen, T., Gunawan, O., Todorov, T.K. & Mitzi, D.B. (2013) Band tailing and efficiency limitation in kesterite solar cells. *Applied Physics Letters*, **103**, 103506.
- [53] Gershon, T., Shin, B., Bojarczuk, N.A., Gokmen, T., Lu, S. & Guha, S. (2013) Photoluminescence characterization of a high-efficiency  $\text{Cu}_2\text{ZnSnS}_4$  device. *Journal of Applied Physics*, **114**, 154905.
- [54] Ohnesorge, B., Weigand, R., Bacher, G., Forchel, A., Riedl, W. & Karg, F.H. (1998) Minority-carrier lifetime and efficiency of  $\text{Cu}(\text{In,Ga})\text{Se}_2$  solar cells. *Applied Physics Letters*, **73**, 1224.
- [55] Pankove, J.I. (1971) *Optical Processes in Semiconductors*. Dover Publications, Inc, New York.
- [56] Shklovskii, B.I. & Efros, A.L. (1984) *Electronic Properties of Doped Semiconductors*. Springer-Verlag, Berlin Heidelberg.
- [57] Gershon, T., Shin, B., Bojarczuk, N.A., Gokmen, T., Lu, S. & Guha, S. (2013) Relationship between  $\text{Cu}_2\text{ZnSnS}_4$  quasi donor-acceptor pair density and solar cell efficiency. *Applied Physics Letters*, **103**, 193903.
- [58] Zhu, X., Zhou, Z., Wang, Y., Zhang, L., Li, A. & Huang, F. (2012) Determining factor of  $\text{MoSe}_2$  formation in  $\text{Cu}(\text{In,Ga})\text{Se}_2$  solar cells. *Solar Energy Materials and Solar Cells*, **101**, 57, doi: 10.1016/j.solmat.2012.02.015.



# 16

## Loss Mechanisms in Kesterite Solar Cells

*Alex Redinger and Susanne Siebentritt*

*University of Luxembourg, Laboratory for Photovoltaics, L-4422 Belvaux, Luxembourg*

### 16.1 Introduction

In this chapter we discuss the main loss mechanisms in current kesterite solar cells. Kesterite solar cells have achieved 12.6% power conversion efficiency [1], which is still low compared to the related chalcopyrites which reach more than 20% efficiency [2]. We use the available data in the literature and our own measurements to study the loss mechanisms that lead to this lower efficiency. Our own cells are prepared by a precursor annealing process, where the precursor is deposited by coevaporation [3]. The precursors are annealed in an atmosphere of the chalcogen and tin chalcogenide to avoid the well-known decomposition reaction [4, 5]. Further details of the annealing process are discussed in Chapter 5 of this book. To further improve the solar cells, we have developed two new specialized processes: a capping process and the CAPRI (cyanide absorber etching prior to annealing) process. The capping process [6] involves a standard Cu-poor, Zn-rich precursor made by coevaporation. At the end of the coevaporation process an  $\text{SnSe}_2$  layer is deposited on top of the precursor by coevaporation. The precursor is annealed in a Se-containing atmosphere. After the heat treatment the majority of the  $\text{SnSe}_2$  has been transformed to  $\text{SnSe}$ . The remaining  $\text{SnSe}$  on top of the  $\text{CZTSe}$  is etched off by  $\text{HCl}$ . The  $\text{SnSe}_2$  capping layer allows for a simplified annealing without the need to add Sn chalcogenides. The CAPRI process [7] involves a Cu-rich precursor, which is etched in  $\text{KCN}$  before annealing. This etching prevents the formation of a detrimental Cu-Sn phase during the

annealing in Se and SnSe. The use of a Cu-rich precursor leads to absorbers with better transport properties. Solar cells with efficiencies of 7.5% have been achieved.

In the following we discuss solar cells based on sulfide absorbers  $\text{Cu}_2\text{ZnSnS}_4$  (CZTS), as well as selenide absorbers  $\text{Cu}_2\text{ZnSnSe}_4$  (CZTSe) and mixed sulfo-selenide absorbers  $\text{Cu}_2\text{ZnSn}(\text{S,Se})_4$  (CZTSSe).

## 16.2 Current State-of-the-Art CZTS-Based Thin-Film Solar Cells

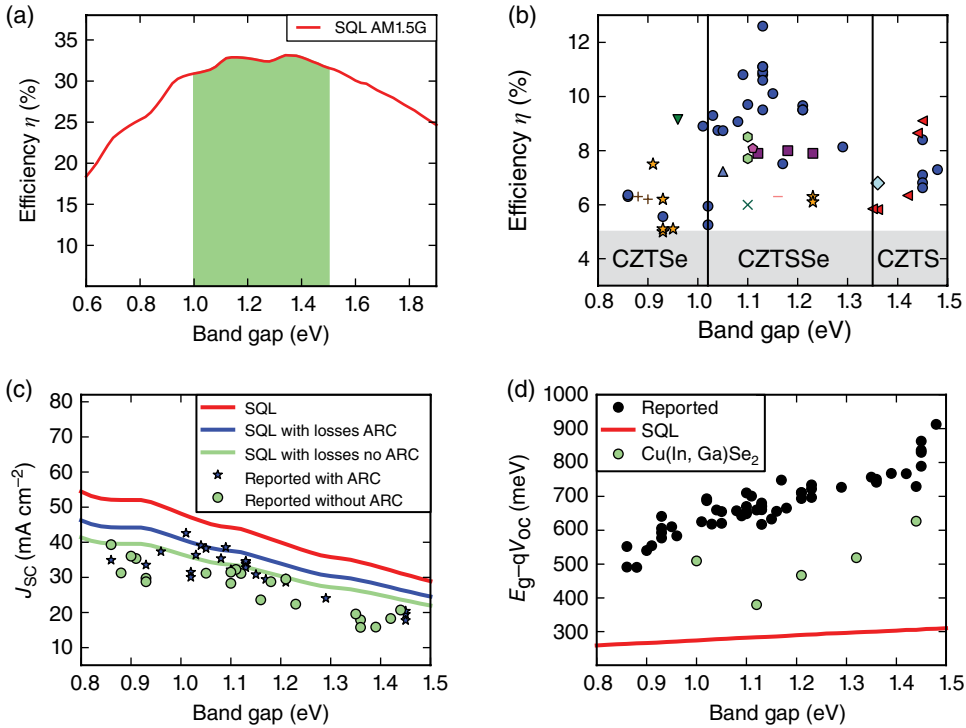
In order to lay the foundation for a discussion of the loss mechanisms of the current CZTS thin-film solar cells, a literature survey has been performed and is presented in Figure 16.1. The solar cell device parameters (with efficiencies exceeding 5%) are compared with an ideal solar cell without losses, that is, the Shockley Queisser limit [8], in order to identify the dominant losses.

The theoretical limit of a single-junction solar cell can be determined by assuming a quantum efficiency  $\text{QE}=1$  for photon energies above the band gap and a diode quality factor  $A=1$ . The generated photocurrent of this ideal solar cell is determined by the illumination spectrum (AM1.5G without concentration) and the band gap of the absorber  $E_g$ . The band gap of CZTSSe can be tuned by varying the sulfur to selenium ratio. The Se devices exhibit a band gap of roughly 1 eV whereas S devices have a band gap of roughly 1.5 eV (see Siebentritt and Schorr [9] for a discussion of the different band gaps). The theoretical efficiencies are presented in Figure 16.1a as a function of the absorber band gap. The vertical lines have been chosen according to Siebentritt and Schorr [9]. From Figure 16.1a, it follows that the band gap of kesterites can be varied in the ideal energy range.

The reported efficiencies [1, 6, 7, 10–43] are however much lower as shown in Figure 16.1b where the reported solar cell efficiencies are plotted against the absorber band gap  $E_g$  (this plot is based on literature reports up to December 2012, with the exception of the current CZTSSe record device [1]). In the case where the band gap is not given explicitly in the reference, the quantum efficiency data has been used to extract  $E_g$  via linear extrapolation or from the photoluminescence spectra recorded at room temperature. The vertical lines in Figure 16.1b indicate the transition from pure-Se to mixed-SSe up to pure-S devices. The best-performing devices [1] are currently produced at IBM with a solution-based (hydrazine) method. Other efficient methods include coevaporation [11], or sputter- or solution-based precursor deposition followed by a high-temperature treatment [12, 13, 44].

The current densities of these solar cells are compared with the theoretical limitations in Figure 16.1c. In addition to the (unrealistic) Shockley–Queisser limit (SQL) limit we introduced the SQ limit with optical losses [45] where the current is reduced by 15% in order to account for the losses due to grid shadowing, absorption in the ZnO and in the CdS buffer layer, and due to incomplete collection and absorption. This number is based on high-efficiency CIGS devices. Reflection at the ZnO can be reduced drastically by using an anti-reflective coating (ARC). The presented data are therefore categorized in the devices with ARC (15%) and without ARC where 24% losses can be assumed.

Finally, the voltage deficits of the devices are plotted against the absorber band gap (Fig. 16.1d). The voltage deficit can be deduced by comparing the band gap and the open-circuit voltage  $V_{oc}$  multiplied with the elementary charge  $q$  and evaluating  $E_g - qV_{oc}$ . Again,



**Figure 16.1** (a) Solar cell efficiency as a function of the absorber band gap  $E_g$  deduced from the Shockley–Queisser limit (SQL) model with an AM1.5G solar spectrum. The band gap range of kesterites is marked. (b) Efficiency as a function of absorber band gap for various CZTSSe solar cell devices reported in the literature. The vertical lines depict the transition from pure Se to SSe and from SSe to S devices. The vertical lines are omitted in (c), (d), and Figures 16.2 and 16.9. The efficiencies are reported by the following groups: • IBM, ▼ NREL, ◀ Solar Frontier, ■ Stanford University, ◆ Nagaoka National College, ▲ Purdue University, ◆ University of California, Los Angeles, ● E.I. du Pont de Nemours and Company, – Avancis GmbH, + IMEC, × CEA, ★ University of Luxembourg. The two devices at the Se/SSe transition are pure-Se devices. (c) Reported short-circuit current density  $J_{sc}$  as a function of  $E_g$  for various CZTSSe devices compared to the SQL with and without optical losses. Stars depict devices with an anti-reflective coating (ARC), dots represent devices without ARC. (d) Open-circuit voltage losses as a function of band gap. CZTSSe devices are depicted in black, the SQL is shown as a solid grey line and the grey dots represent some high-efficiency CIGS devices

we compare the current best-performing devices with the theoretical limit ( $E_g - qV_{oc,SQL}$ ). In order to compare the results with Cu(In,Ga)Se<sub>2</sub> (CIGS) a number of high-performance devices with different band gaps are shown for comparison [46–48].

From Figure 16.1c, it follows that some of the CZTSSe devices already reach the  $J_{sc}$  level of the best CIGS devices; the optical losses are therefore comparable. For other devices the current densities in CZTSSe devices can still be optimized to a certain degree. It is however clear that the current density losses in CZTSSe are not limiting state-of-the-art solar cell efficiencies.

The main problem in the current CZTSSe devices is clearly visible in Figure 16.1d: the reported open-circuit voltages are too low compared to the record CIGS thin-film solar cells and obviously also compared to the SQ-limit. Throughout this chapter, the possible sources of the voltage losses are discussed.

Before analyzing the devices in more detail, a brief comment on the reported band gaps for the different devices has to be made. It is known from the literature that the band gap of CZTSe can be increased if sulfur is introduced in the absorber (e.g. [15, 49, 50]). The band gap differences reported for both pure-Se and pure-S devices presented in Figure 16.1 are somewhat unexpected. There is meanwhile a general consensus in the literature that the band gap of the Se devices is around 1 eV and the S devices exhibit a band gap of around 1.5 eV. However, there is a significant scatter around these two values for the pure-S and -Se devices. Some of this scatter can be attributed to different methods of extracting the band gap from the QE data, and some due to more fundamental reasons as discussed in the following section.

### 16.3 Dominant Recombination Path

Open-circuit voltage losses are recombination losses. The dominant recombination path can be studied via temperature-dependent current–voltage analysis. This technique enables us to study (a) the temperature dependence of the open-circuit voltage, and (b) the temperature dependence of the diode quality factor. Assuming that the solar cell can be described with a one-diode model, and neglecting the parasitic resistances, the open-circuit voltage is given by [51]:

$$V_{oc} \approx \frac{AkT}{q} \ln \left( \frac{J_L}{J_0} \right) \quad (16.1)$$

where  $A$  describes the diode quality factor,  $k$  the Boltzmann constant,  $q$  the elemental charge,  $T$  the temperature,  $J_0$  the saturation current density, and  $J_L$  the photocurrent density. The saturation current density, which is a generation current density, is defined:

$$J_0 = J_{00} \exp \left( -\frac{\Phi_B}{AkT} \right) \quad (16.2)$$

where  $J_{00}$  denotes the prefactor of the saturation current density and  $\Phi_B$  the energy difference of the generation/recombination process (referred to as barrier height in the following). Inserting Equation (16.2) into Equation (16.1) yields an expression for the temperature dependence of the open-circuit voltage [52]:

$$V_{oc} = \frac{\Phi_B}{q} - \frac{AkT}{q} \ln \left( \frac{J_{00}}{J_L} \right). \quad (16.3)$$

From Equation (16.3) it follows that an extrapolation of the open-circuit voltage to 0 K immediately leads to the barrier height  $\Phi_B$ . Recombination can occur in the bulk of the absorber in the quasi-neutral zone as band-to-band recombination, via defects, or in the space charge region. In all these cases, the barrier height corresponds to the band gap of the absorber. The dominant recombination path can also be located at the interface

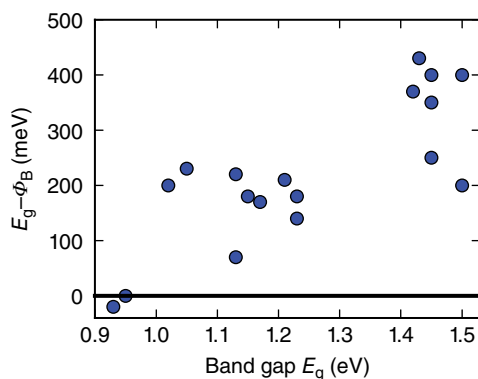


between the buffer and the absorber or at the buffer–window interface. Here, the barrier height can also be smaller than the band gap. A reduced barrier height can have two causes: Fermi level pinning at the interface, or a cliff in the conduction band alignment, that is, the conduction band edge of the buffer (or the window layer) is lower than the conduction band edge in the absorber. In the case of Fermi level pinning, the barrier height corresponds to the barrier for holes which are the minority carriers at the interface, that is, the energy difference between the Fermi level and the valence band edge at the interface [53]. In the case of a cliff, the barrier is determined by the energy distance between the conduction band edge of the buffer or the window layer and the valence band edge of the absorber [54, 55]. From temperature-dependent current–voltage analysis, it cannot be determined whether Fermi level pinning or reduced interface band gap is responsible for the reduction of the barrier height  $\Phi_b$ . However, the determination of the barrier height and comparison with the band gap allows the determination of the location of the dominant recombination mechanism: at the interface or in the bulk.

The band alignment between kesterite absorbers and the usual CdS buffer can be investigated by photoemission spectroscopy, which has been studied by Haight *et al.* [49] and Bär *et al.* [56]. The results are contradictory since Haight *et al.* found a spike-like conduction band offset for all CZTSSe devices independent of the S/Se content, that is, the conduction band edge of the CdS buffer is assumed to always be higher than the conduction band edge of the kesterite. Only the magnitude of the spike changed to some degree with the variation of the S/Se content. On the other hand, Bär *et al.* found a cliff-like conduction band offset for pure-S devices. Haight *et al.* measured the valence band offset under illumination using the assumption that the illumination suffices to ensure flat band conditions. They base their conclusions on the additional assumption that the conduction band offset can be determined from the valence band offset using the bulk band gaps. In contrast, Bär *et al.* performed a direct measurement of the actual surface band gaps using photoemission and inverse photoemission spectroscopy and taking the band bending into account by measuring core levels in the photoemission spectra. We therefore conclude that the data of Bär *et al.* are more reliable. Theoretical studies of the conduction band alignment do not agree either: one reports a spike-like configuration for the sulfide [57], two other studies determine a cliff at the sulfide interface [58, 59], while another study reports a spike for selenides [60].

Several groups have studied the temperature dependence of  $V_{oc}$  for CZTSSe solar cells with different S/Se ratios [10, 15, 19, 20, 23, 30, 31, 38, 61–63]. In order to obtain a measure for the degree of interface recombination, the difference between  $\Phi_b$  and  $E_g$  is plotted versus the absorber band gap (Fig. 16.2). The main result of the graph can be summarized as follows. As soon as the absorber contains a significant amount of sulfur, the activation energy is always smaller than the band gap. The difference is largest for the pure-S-based solar cells with differences up to 450 meV, whereas the sulfur-free CZTSe solar cells exhibit the same activation energy as the absorber band gap. The experimental results are in agreement with the band alignment study by Bär *et al.* for the sulfur devices, but contradict the measurements by Haight *et al.*

In order to gain deeper insights into the differences between Se-based and SSe-based devices we compare CZTSe and a CZTSSe thin-film solar cells [19] which have been prepared via coevaporation and annealing. Both devices have efficiencies slightly higher than 6%. The current–voltage characteristics, the quantum efficiency measurements, and the extrapolation of the open-circuit voltage with temperature are shown in Figure 16.3.



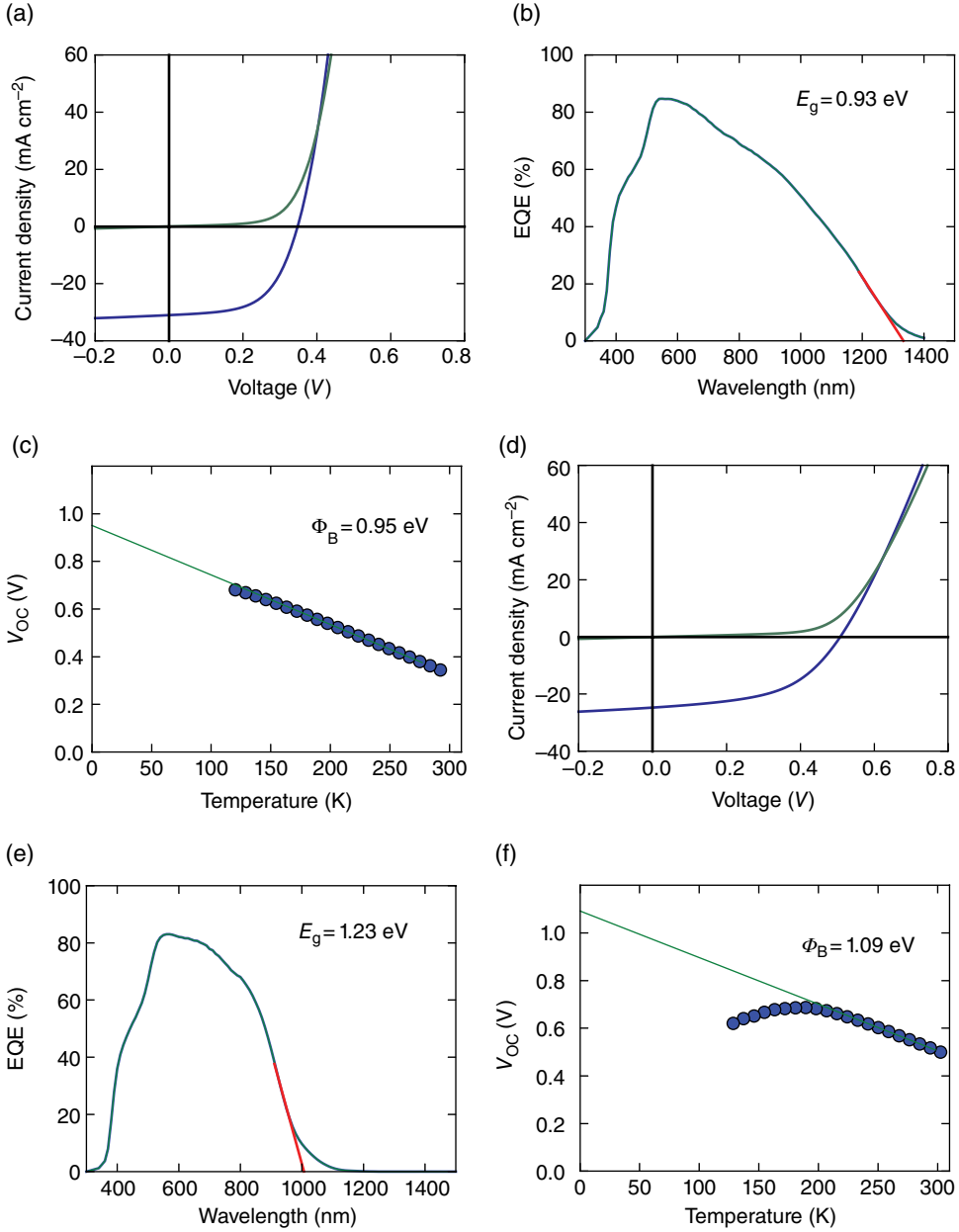
**Figure 16.2** Difference between absorber band gap and reported barrier height as a function of absorber band gap for various devices reported in literature

The temperature dependence of the diode quality factor and of the saturation current density is presented in Figure 16.4 and the solar cell parameters are summarized in Table 16.1.

The  $J$ - $V$  curves presented in Figure 16.3a, d exhibit several important differences. The short-circuit current density for the Se device is much higher than that for the SSe device. Moreover,  $V_{oc}$  is larger for the SSe device. These properties are a direct consequence of the different band gaps of the devices. The SSe device has a band gap of 1.23 eV, whereas the Se device has a band gap of 0.93 eV. The band gaps have been deduced from a linear extrapolation of the low-energy part of the EQE curves presented in Figure 16.3b and e. Additionally, the room-temperature series resistance  $R_s$  of both devices are different ( $0.6 \Omega \text{ cm}^2$  for the Se device compared to  $2.7 \Omega \text{ cm}^2$  for the SSe device).

In Table 16.1, the CZTSe solar cell presented in Figure 16.3a can be compared to the current record CZTSe made at IMEC [44]. The open-circuit voltage of the device presented in Figure 16.3a (column I) is 55 meV smaller than that of the current record device (column II). The short-circuit currents are similar taking into account that the IMEC device was prepared with an anti-reflective coating. The biggest difference between the devices is the FF; apparently the FF can be improved significantly if the surface of the CZTSe is oxidized prior to the CdS deposition [11]. For the devices presented in Figure 16.3a, d, no oxidation was performed. However, it is currently not clear why this treatment improves the FF significantly. If we compare the current record CZTSe to the best CuInSe<sub>2</sub> [48] (column III) device, the biggest deficit of the kesterite device is clearly the open-circuit voltage which is more than 80 mV lower than the chalcopyrite device with a very similar band gap. The comparison between our CZTSSe device (column IV) and a previous record device made at IBM [15] with a comparable band gap (column V) is similar where we observe the biggest losses in the FF. However, the comparison with the closely related CIGS with a similar band gap [47] (column VI) shows again that the largest deficits can be found in the open-circuit voltage. The record CZTSSe [1] (column VII) with a band gap of 1.1 eV is also produced at IBM, and this device also shows a significant deficit in  $V_{oc}$  compared to the current record CIGS device [2].

All CZTSSe devices exhibit too low open-circuit voltages independent of the sulfur content. However, the difference between band gap and  $V_{oc}$  is smaller for the low-band-gap



**Figure 16.3** (a) J–V curve of a 6.2% CZTSe device with (b) the corresponding EQE and (c) the evolution of the open-circuit voltage  $V_{oc}$  with temperature  $T$ . (d) J–V curve, (e) EQE and (f)  $V_{oc}$  v.  $T$  for the case of a 6.3% CZTSe device. The solar cell parameters of the two devices are listed in Table 16.1

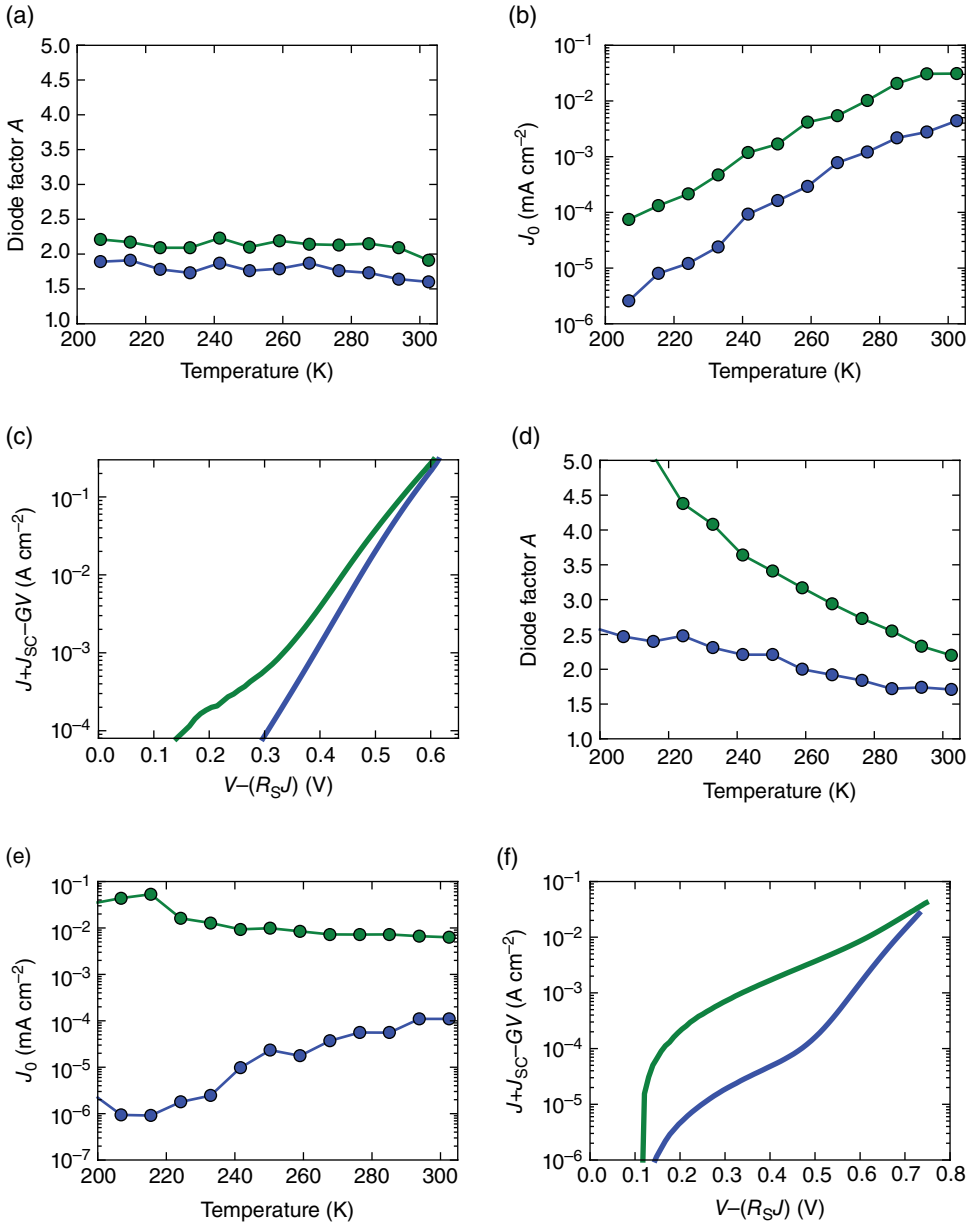
**Table 16.1** Solar cell efficiency, open-circuit voltage  $V_{oc}$ , short-circuit current density  $J_{sc}$ , fill factor  $FF$  and reported band gap  $E_g$  for various CZTSSe and CIGS devices. (I) CZTSe device presented in Figure 16.3a–c; (II) record CZTSe device; (III)  $CuInSe_2$  record device; (IV) CZTSSe device presented in Figure 16.3d–f; (V) best CZTSSe device with a band gap of 1.2 eV (In brackets: band gap deduced via linear extrapolation); (VI) current  $Cu(In,Ga)Se_2$  device with a band gap of 1.2 eV (the band gap value is a rough indication since the devices have been grown using a three-stage process which leads to a significant gradient in the In/Ga ratio and thus the band gap); (VII) record CZTSSe device; and (VIII) record  $Cu(In,Ga)Se_2$  device

	I. CZTSe Figure 16.3 (a)–(c)	II. CZTSe Record [44]	III. $CuInSe_2$ [48]	IV. CZTSSe Figure 16.3 (d)–(f) ( $\approx 1.2$ eV)	V. CZTSSe ( $\approx 1.2$ eV) [15]	VI. CIGS ( $\approx 1.2$ eV) [47]	VII. CZTSSe Record [1]	VIII. CIGS Record [2]
$\eta$ (%)	6.2	9.7	15.0	6.3	9.66	18.7	12.6	20.8
$V_{oc}$ (mV)	353	408	491	508	516	743	513	757
$J_{sc}$ (mA cm <sup>-2</sup> )	34	38.9	40.58	24	28.6	31.9	35.2	34.8
$FF$ (%)	52	61.4	75.15	51	65.4	78.75	69.8	79.2
$E_g$ (eV)	0.93	1.0	1.0	1.23	1.21 (1.14)	1.21	1.13	

devices (see Fig. 16.1). The question arises of whether this is due to an un-optimized CZTS/CdS heterojunction interface. Temperature-dependent current–voltage analysis has therefore been performed in order to extract the extrapolation of  $V_{oc}$  with temperature as described above; the results are shown in Figure 16.3c, f. The CZTSe exhibits a band gap  $E_g = 0.93 \pm 0.2$  eV and a barrier height  $\Phi_b = 0.95 \pm 0.3$  eV. The evolution of the open-circuit voltage with temperature shows that the activation energy of the dominant recombination/generation process is equal to the band gap of the absorber. The finding is in contrast to the results of the CZTSSe device presented in Figure 16.3e, f where the deduced activation energy is significantly smaller than the band gap.

The investigation shows that the Se devices are not dominated by interface recombination, which is a very important insight since it points towards a favorable spike-like band alignment at the CZTSe/CdS heterointerface. The CZTSSe device exhibits dominant interface recombination, which can be induced by a cliff-like conduction band offset or Fermi-level pinning at a position far from the conduction band edge.

In order to obtain more information about the recombination we investigated the temperature dependence of the diode quality factor  $A$  and the saturation current density in a temperature range 200–300 K. It should be kept in mind that the extraction of  $J_0$  and  $A$  values from  $J$ – $V$  curves under illumination can be considerably flawed by a voltage-dependent photocurrent. The results are presented in Figure 16.4 for the two devices introduced in Figure 16.3. In the dark, the diode factors for the Se device are  $<2$  and we observe only a small temperature dependence (Fig. 16.4a). Under illumination with white light, the diode factor increases to values which are slightly higher than 2 but we are still observing little variation with temperature. The saturation current densities are, compared to state-of-the-art CIGS, too high but decrease exponentially with decreasing temperature (Fig. 16.4b). The situation changes significantly if sulfur is introduced into the absorber layer. The diode factors depicted in Figure 16.4d show a larger temperature dependence in the dark, starting below two



**Figure 16.4** Evaluation of the diode quality factor and of the saturation current density for the two devices presented in Figure 16.3: (a, b) CZTSe device; (d, e) CZTSSe device; (c, f)  $J$ - $V$  curve at 224 K plotted on a logarithmic scale after correction of  $R_s$  (series resistance) and  $G_{sh}$  (shunt conductance) for the (c) Se device and (f) SSe device. Black curves show values in the dark and grey curves values under illumination

and ending at roughly 2.5. In the illuminated case, the situation changes significantly and we observe a large temperature dependence with values  $>2$  for all temperatures. The difference between the dark and the illuminated case can also be found in the temperature dependence of the saturation current density. The value for the illuminated case stays roughly constant for the complete investigated temperature regime in contrast to the dark case and to the Se-case.

The physical reason for the observed differences can be explained with the help of Figure 16.4c, f where  $J$ - $V$  curves at 224 K are presented. The  $J$ - $V$  curves have been corrected for series resistance and shunt conductance and the current densities are plotted on a logarithmic scale. For the Se case, we observe that the illuminated and dark curves are only somewhat shifted but the general behavior stays the same. Moreover, we observe more or less the same characteristic slope in these plots. In the SSe-case we observe: (1) completely different behavior of dark and light  $J$ - $V$  characteristics; and (2) a change in the slope of the dark  $J$ - $V$  curve. At low bias voltages, the slopes of dark and illuminated  $J$ - $V$  characteristics are quite similar. At larger forward voltages (in the  $V_{oc}$  region) however, the slope in the dark changes significantly. From this observation we can immediately conclude that the superposition principle is no longer fulfilled and that we cannot use the values of the dark  $J$ - $V$  curves to investigate the temperature dependence of the diode factor in more detail. Alternatively, the parameters could be extracted from  $J_{sc}/V_{oc}$  plots [64]. However, as we will see in the following sections, there is a significant barrier for the forward current in the SSe devices which depends to some extent on the illumination intensity and renders the  $J_{sc}/V_{oc}$  method not applicable.

The overall observation is that the Se device does not exhibit a strong temperature dependence of  $A$  with a value around 2 which points towards dominant Shockley–Read–Hall recombination in the depletion region. The temperature dependence and the large value of the diode factor  $A$  in the SSe devices point towards tunneling-induced recombination, which is unfavorable for solar cells. Moreover, the different slopes in the  $J$ - $V$  curves show that the dominant recombination path changes with applied bias and with illumination. Interestingly, a similar behavior has been observed in  $\text{CuInS}_2$  solar cells [54, 65]. These solar cells also show a different recombination behavior in the dark and under illumination, and exhibit a cliff-like band alignment at the interface.

This section can be summarized as follows. The comparison of the Se and SSe devices shows that the two types of solar cells exhibit significant differences. The extrapolation of  $V_{oc}$  with temperature suggests that we have dominant bulk recombination in the Se devices and dominant interface recombination in the SSe devices. There is a chance that the interface recombination in CZTSSe devices can be avoided by using another buffer and window layer with a lower electron affinity. However, the recombination in the SSe devices is tunneling-assisted which is another undesirable feature of the incorporation of sulfur in the absorber which most likely cannot be circumvented by using another buffer. The Se devices therefore show more beneficial properties for future high-efficiency thin-film solar cells.

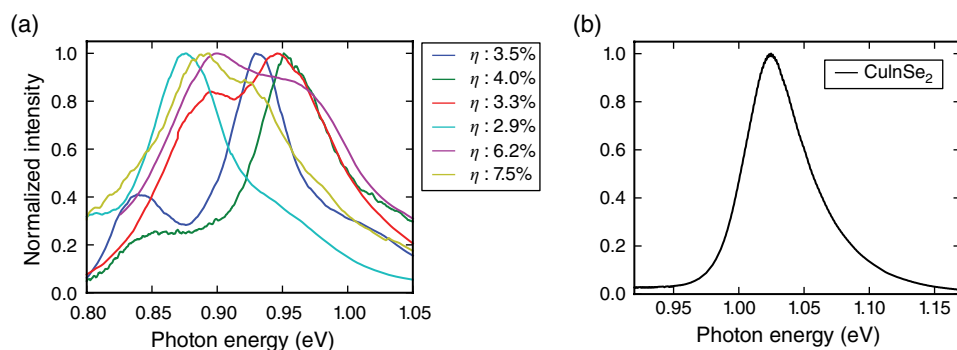
## 16.4 Band-Gap Variations

Although the Se devices exhibit dominant bulk recombination, the measured open-circuit voltages are low and too much recombination occurs in the absorbers. A possible origin of the voltage losses can be seen in Figure 16.5a where room-temperature photoluminescence

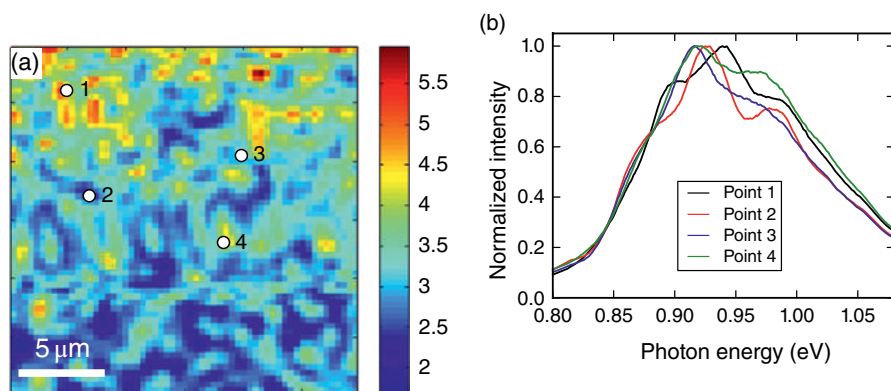
(PL) measurements of different CZTSe absorbers are shown [67]. Solar cells made from these absorbers show efficiencies in the range 2.9–7.5%. In all cases the PL spectrum consists of several peaks with energies between 0.85 eV and 1.02 eV. Since the photoluminescence spectra have been recorded at room temperature, the observed transitions either arise from a number of defects present in high densities (comparable to the effective density of states in the band), or from band-to-band transitions in materials with different band gaps. A comparison with the corresponding QE spectra suggests that at least three of these transitions are related to band-to-band transitions, while one could also represent a defect-related transition. Preliminarily, the band-to-band transitions are assigned to the co-existence of kesterite, disordered kesterite, and stannite phases. Solar cells with a strong emission at 0.85 eV show generally lower values of  $V_{oc}$ .

Figure 16.5b shows a room-temperature PL measurement of a  $\text{CuInSe}_2$  absorber layer. This emission spectrum can be nicely fitted by Planck's generalized law with one band gap [68]. The comparison between the two graphs immediately leads to the conclusion that massive improvements have to be made in order to remove the multiple peak structure in CZTSe. Recently Shin *et al.* [16] showed that the occurrence of various PL transitions is influenced by the annealing temperature and by the Se vapor pressure during the high-temperature treatment. From their experiments, they conclude that Se vapor pressures which are not high enough lead to deep defects in the band gap of the CZTSe, which consequently yields different PL transitions. However, the Se pressure and the temperature might also influence the occurrence of secondary phases with different band gaps.

The occurrence of the transitions presented in Figure 16.5a does not follow a specific pattern and cannot be correlated directly to different integral absorber compositions. Moreover, we do not only observe differences between different absorbers but also within one absorber. The only systematic variation we observe is that the total PL yield is higher for high-quality absorbers.



**Figure 16.5** (a) Normalized room-temperature photoluminescence spectra of different CZTSe absorber layers which resulted in solar cell devices with efficiencies in the range 2.9–7.5%. (b) For comparison, a typical room-temperature PL spectrum of a polycrystalline  $\text{CuInSe}_2$  absorber with an efficiency of 12.5% and  $V_{oc} = 471$  mV is shown [66]. For color details, please see color plate section



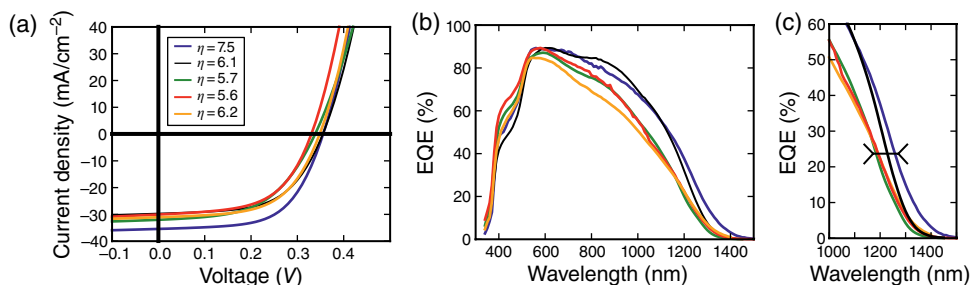
**Figure 16.6** Micrometer-resolved photoluminescence intensity recorded on a 7.5% CZTSe device. Four normalized point spectra located in (a) are shown in (b)

Spatially resolved Figure 16.6a depicts the photoluminescence intensity recorded on an absorber layer which resulted in a 7.5% device. A 514.5 nm laser is scanned over the surface with a lateral resolution of roughly 800 nm. The luminescence light is collected confocally. In Figure 16.6a the total photoluminescence intensity (integrated from 0.8 eV to 1.1 eV) is plotted versus the position. We observe that the intensity varies as a function of position.

Figure 16.6b depicts individual PL-spectra on specific positions on the sample indicated in Figure 16.6a. We observe different shapes of the PL spectra on the different positions. This indicates that the broad PL-spectrum presented in Figure 16.5 is most likely the result of the superposition of the different PL transitions which arise from different locations of the sample. However, even with sub-micrometer resolution we detect different transitions, indicating that the different materials leading to the various transitions are closely intertwined on a sub-micrometer scale. We attribute the various shapes we observe in different absorbers (Fig. 16.5) or in different spots of the same absorber (Fig. 16.6) to changing quantities of the different materials with varying band gaps within the CZTSe layer. There is no correlation between the occurrence of individual transitions and the efficiency of the solar cells. Moreover, there is no systematic variation of the PL yield as a function of the transition observed. The only systematic variation we observe is that the total PL yield is higher for high-quality absorbers, which is also expected. The analysis presented here indicates that even in solar cell absorbers up to an efficiency of 7.5%, different band gaps on small length scales are present. This increases the recombination and is an extremely undesirable situation since the band-gap fluctuations will significantly reduce the performance of these absorbers, in particular the open-circuit voltage [69]. It should be noted that the currently best-performing devices reported in literature exhibit one dominating PL transition. Nevertheless, even in these absorbers the PL spectra show small shoulders, which is an indication of multiple transitions [10, 11].

It is important to note that we not only observe different transitions in PL but also different band gaps in the quantum efficiency measurements. Figure 16.7 summarizes  $J$ - $V$  and QE characteristics of some CZTSe solar cells made by coevaporation and annealing produced in our laboratory. The solar cell devices exhibit comparable open-circuit voltages of roughly 350 meV and currents which vary between  $30 \text{ mA cm}^{-2}$  and  $35 \text{ mA cm}^{-2}$ . All of the





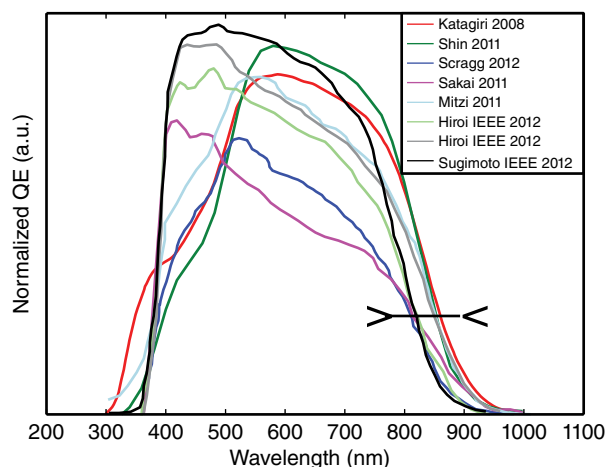
**Figure 16.7** (a) J–V characteristics of CZTSe solar cell devices and (b, c) the corresponding QE spectra. For color details, please see color plate section

QE spectra of the devices show the characteristic features of state-of-the-art CZTSe devices: a decrease for wavelengths shorter than about 500 nm, which can be attributed to absorption in the CdS buffer layer; a maximum of 85–90% at 600–800 nm; and a significant drop with a rather gradual slope in the QE at high wavelengths. Figure 16.7c shows a magnification of Figure 16.7b to the high wavelength region. A linear extrapolation of the low-energy slope of the QE spectrum can be used to obtain a rough value for the band gap of the device. It can be seen immediately that the extrapolation does not yield a single value, but we observe a significant scatter of around 50 meV in the band-gap energy. The band gap deduced from QE reflects the average bulk band gap of the CZTSe absorber layers, favoring the lower band gaps. We will not observe the same scatter of the band gaps as in the PL data shown in Figures 16.5 and 16.6. The information depth of the PL is a few hundred nanometers and small amounts of different materials can be detected with a high lateral resolution. In QE spectra, we tend to see the lowest band gap averaged over the whole device.

The sulfur-based CZTS cells show a similar behavior as the Se devices presented in Figure 16.7. Figure 16.8 summarizes QE measurements of S-based solar cells published in the literature [15, 28, 29, 31, 33–35]. In order to compare the different measurements, all spectra have been normalized in a first step. In a second step the different plots are scaled with the short-circuit current density of the devices. In this way the different measurements can be compared. Similar to the Se-based devices, we observe a significant scatter of the band-gap energy in the devices. The variations are roughly 60 meV and we observe mainly two different band-gap energies at 1.35 eV and 1.41 eV.

The most plausible explanation for the occurrence of two band gaps is a mixture of the kesterite and stannite polymorph which have been calculated to have only a small difference in the formation energy (3 meV per atom difference in the binding energy of the crystal [70–73]). Moreover, the different crystal structures exhibit different calculated band-gap energies. The difference for the Se-based absorbers and S-based devices are roughly 150 meV and 190 meV, respectively (the values presented here are average values of different density functional theory calculations presented in the literature [70–73]).

The thermodynamically favored structure for CZTS and CZTSe is kesterite, and neutron measurements on powder samples confirm the results of density functional theory calculations [74]. However, these samples have been synthesized at much higher temperatures than the thin-film samples discussed here. Nozaki *et al.* [75] studied the crystal structure of



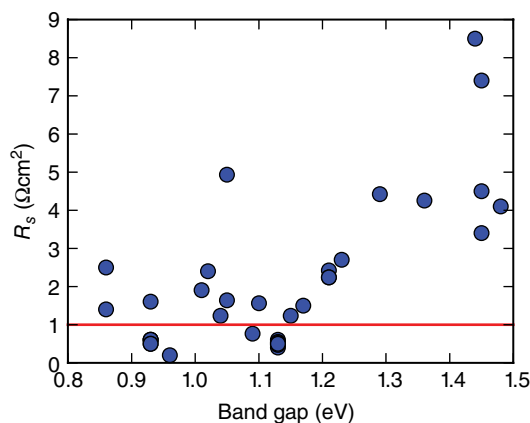
**Figure 16.8** Reported quantum efficiency data for Se-free devices. The QE data have been normalized and then scaled with the reported  $J_{sc}$  values. A linear extrapolation of the low-energy slopes yield at least 60 meV difference in band gap. For color details, please see color plate section

CZTS absorber layers via anomalous X-ray diffraction. They identified the kesterite structure as the dominant phase in the absorber materials. However, these methods cannot exclude a minority stannite phase. The data presented in Figure 16.1 show an even more severe scatter of the band gaps of pure CZTS and pure CZTSe. The data shown here indicate that part of this scatter is due to different band gaps occurring because of different phases of the semiconductor. However, different methods to determine the band gap from the QE data also lead to different values even for the same band gap, that is, the band gap estimated from the inflection point is always higher than the band gap estimated from a linear extrapolation. This exaggerates the differences in band gaps.

In this section we showed that the occurrence of different band gaps in CZTS and CZTSe is likely the cause of some of the voltage losses observed in the current devices. PL spectra show several peaks even when measured on a sub-micrometer scale, indicating closely intertwined materials with different band gaps. Quantum efficiency data presented in this section also show that there is some scatter in the reported band-gap energies. One of the most important steps toward high-efficiency CZTS thin-film solar cells is to understand the origin of the different transitions and to control them to such an extent that they no longer limit the solar cell efficiencies.

## 16.5 Series Resistance and its Relation to $V_{oc}$ Losses

The high series resistance  $R_s$  in CZTSSe devices has often been identified as one of the main limitations of the current CZTSSe thin-film solar cells (e.g. [15]). Only very recently, some of the record devices exhibit room-temperature series resistances well below  $1 \Omega \text{ cm}^2$  [1, 6, 7, 10, 11, 19, 61]. The reported room-temperature series resistances [10–12,

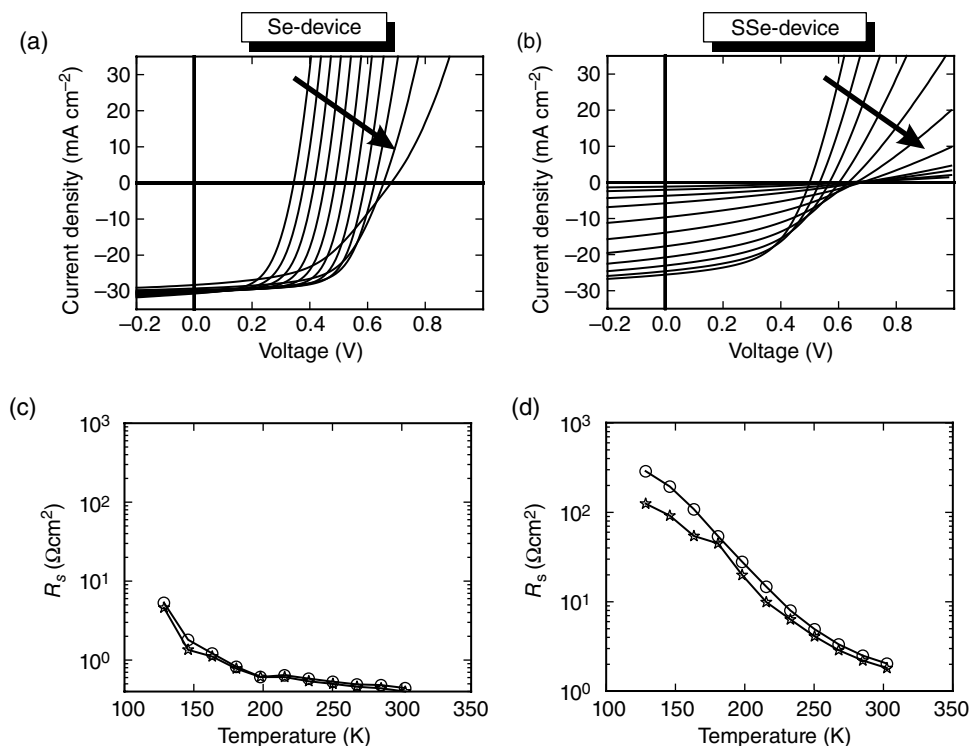


**Figure 16.9** Reported room-temperature series resistances  $R_s$  as a function of band gap for various devices reported in literature

15–17, 19, 21–24, 28–30, 36, 37] are summarized in Figure 16.9. The line indicates an  $R_s = 1 \, \Omega \, \text{cm}^2$ . The first observation is that all the devices with low series resistance are Se-rich. The problem of high series resistance is apparently much more severe in the S-based devices. In the literature, the high series resistance has been assigned to a blocking back contact barrier which arises due to a Schottky-type contact at the MoS(e)/CZTS(e) interface [15, 20, 22, 30]. More recently, another study however relates the high series resistance to carrier freeze-out, induced by a relatively deep acceptor state that quenches the solar cell efficiency [76]. Both models cannot explain the observed difference between selenide and sulfide devices. The question arises if the high series resistance is an intrinsic property of the CZTSSe devices. We show in this section that this is not the case, and that the series resistance in the CZTS is probably caused by a secondary phase in the absorber layer.

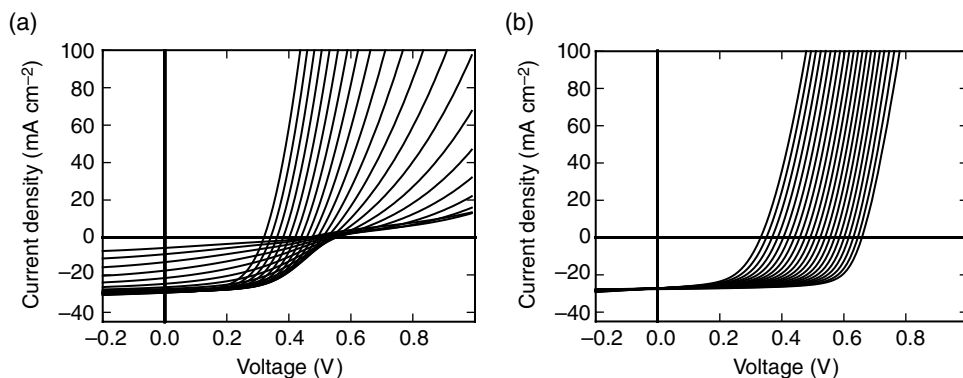
In order to analyze the differences in the series resistance in more detail, the devices presented in Figure 16.3 have been analyzed via temperature-dependent current–voltage analysis [19] shown in Figure 16.10. The Se device (Fig. 16.10a) exhibits the usual temperature-dependent behavior of a pn-diode under illumination. The open-circuit voltage increases with decreasing temperature and the other solar cell parameters do not change significantly. A loss in FF is only observed at the lowest temperature. The series resistance (deduced with the method proposed by Sites and Mauk [77]) is low in the complete temperature range as shown in Figure 16.10c. The SSe device shown in Figure 16.10b, d exhibits a very different behavior. As soon as the temperature is decreased, the short-circuit current decreases considerably and the series resistance increases. At temperatures below 150 K the series resistance is higher than  $100 \, \Omega \, \text{cm}^2$ . This high series resistance completely blocks the photocurrent and consequently the efficiency decreases strongly. This observation is in line with the reports in the literature for devices where a significant amount of sulfur is present in the absorbers (e.g. [15]).

From these observations one might speculate that the high series resistance is only a problem in the SSe and S devices. Our observations suggest that the high series resistance



**Figure 16.10**  $J$ - $V$ - $T$  analyses of the devices presented in Figure 16.3. (a, b)  $J$ - $V$  curves for temperatures in the range 120–300 K. The arrow points towards lower temperatures. (c, d) Extracted series resistances  $R_s$  as a function of temperature

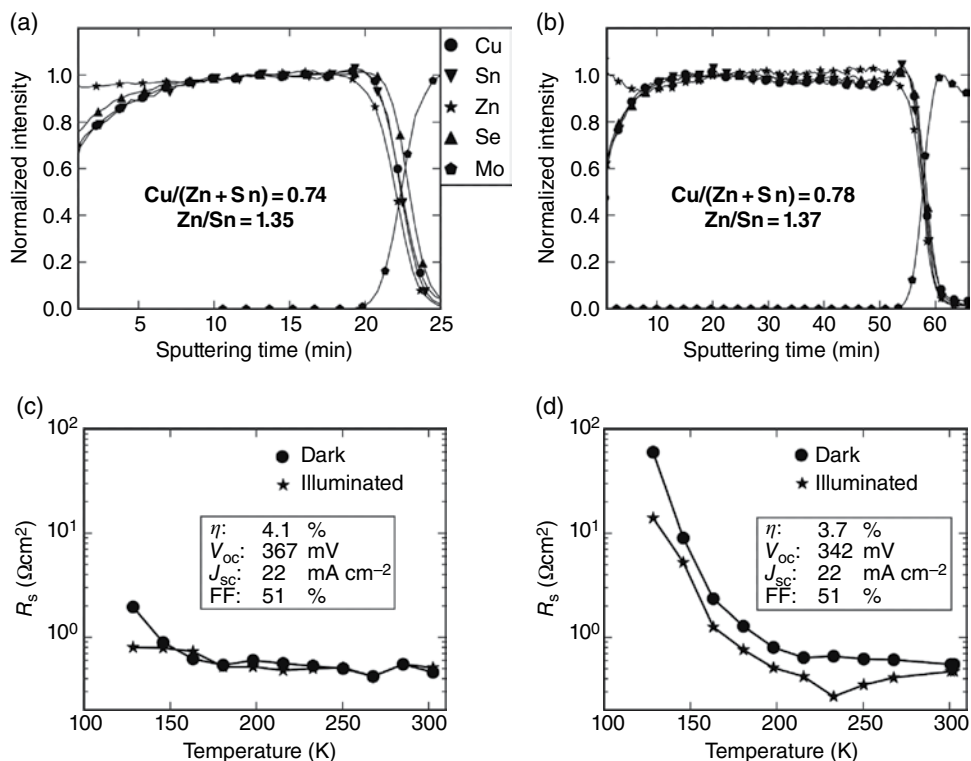
is also strongly influenced by the composition of the sample. The temperature-dependent current–voltage analysis of two Se devices is presented in Figure 16.11. Both devices have an efficiency slightly exceeding 5%. As shown in Figure 16.11a, we can observe a very similar behavior as for the SSe devices also in pure selenide devices: the current drops sharply with decreasing temperature and we observe a high series resistance. Figure 16.11b shows a device which is very similar to that shown in Figure 16.10a where practically no increase in series resistance is observed [6]. The devices presented in Figure 16.11 are extreme cases with a very high and very low series resistance. The  $J$ - $V$ - $T$  characteristics of most other CZTSe devices falls in between those two examples. This clearly shows that the high series resistance is not an intrinsic material property but is strongly influenced by the preparation route and the sample composition. It is not however possible to relate the occurrence of a high resistance to integral compositions of the absorber layers: absorbers with very similar integral compositions can demonstrate very different behavior concerning the series resistance of the devices. The barrier for the current has to be present somewhere in the space charge region. This can be concluded from the differences between the series resistance in the dark and under illumination, where  $R_s$  is larger in the dark. It is hard to imagine that a barrier at the back is considerably changed by illumination, since light hardly reaches the back side.



**Figure 16.11**  $J$ - $V$ - $T$  curves for two different CZTSe devices with an efficiency which slightly exceeds 5%

As a consequence, a depth profiling method has to be used in order to relate the occurrence of a high series resistance to a composition. We analyzed absorber layers which showed a different behavior in the  $J$ - $V$ - $T$  analysis [19]. Two of those absorber layers are presented in Figure 16.12, where one shows a moderate series resistance at low temperature (Fig. 16.12a, c) and the other a high series resistance at low temperature (Fig. 16.12b, d). The efficiencies of the resulting solar cells are presented in the inset of Figure 16.12c, d. Figure 16.12a, b depicts secondary ion mass spectrometry measurements performed with  $\text{Cs}^+$  ions. The count rates are normalized at the middle of the absorber. The integral Zn/Sn ratio of the two samples, deduced via energy-dispersive X-ray analysis at 20 keV, only changes slightly but the amount of Zn in the near-surface region is significantly different. In both cases, more Zn is present at the heterojunction compared to the bulk. However, in the sample presented in Figure 16.12b we observe an increase in the Zn content towards the surface, whereas the sample in Figure 16.12a still shows a slight decrease of the Zn content towards the surface. The series resistance is depicted in Figure 16.12c, d. The solar cell in Figure 16.12a does not exhibit a large series resistance at low temperature (Fig. 16.12c), whereas a large series resistance (Fig. 16.12d) is observed in the device with an increasing amount of Zn at the heterojunction. As a consequence, the occurrence of a high series resistance can be related to an increasing Zn concentration near the heterojunction of the devices.

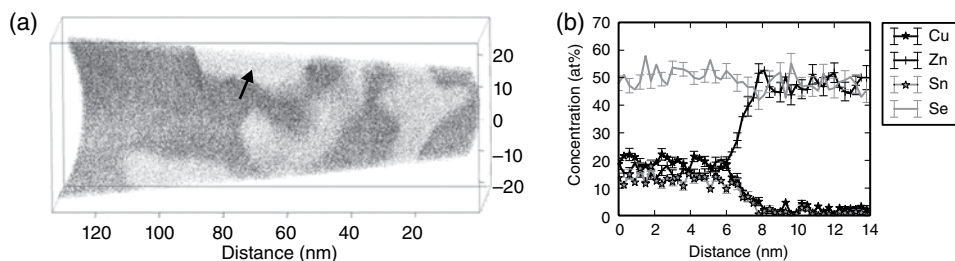
The CZTSe devices are produced Zn-rich which very likely leads to the formation of a ZnSe secondary phase. Although the devices are dominated by bulk recombination, a ZnSe phase near the interface is detrimental. If too much ZnSe is present, the devices suffer from current losses and exhibit a high series resistance. In accordance with the results presented above, Wätjen *et al.* [78] showed that at those areas of the solar cell devices which have a large amount of ZnSe present at the heterojunction the current is completely blocked. Moreover, they showed that the regions with less ZnSe present at the heterojunction exhibit much better solar cell parameters, such as a smaller series resistance and (even more important) a much lower saturation current density. The results show that the ZnSe present in the CZTSe not only reduces the current but has other deteriorating effects on the overall device performance. ZnSe present in the CZTSe is therefore another reason for the open-circuit voltage losses observed in the current devices, since it acts as a possible recombination center.



**Figure 16.12** (a, b) Secondary-ion mass spectrometry measurements of two absorber layers which showed a different behavior in terms of temperature dependence of the series resistance presented in (c, d). The insets in (c, d) are the resulting solar cell efficiencies of the absorber layers

The question arises of where the ZnSe secondary phase can be found in the CZTSe. The occurrence of the secondary phases of course depends to some extent on the fabrication method. One of the methods which yields a high amount of intermixing is coevaporation; in this case, all elements are brought together at the same time on a hot substrate. Depending on the growth conditions, ZnSe can be found at the back contact or at the front contact [79, 80]. From this observation, it might be speculated that the ZnSe secondary phase segregates to one of the interfaces depending on the growth conditions. This situation would be highly desirable, since then the growth conditions could be tuned such that the secondary phase is present at the absorber surface from where it could then be subsequently removed via a chemical treatment.

However, first experiments performed on CZTSe absorbers produced by coevaporation and annealing do not corroborate this assumption. Figure 16.13 shows an atom probe tomography study performed on a CZTSe absorber, which resulted in a 6.2% efficient solar cell [7]. A small volume was analyzed which was situated roughly 200 nm away from the CdS buffer layer, that is, still in the space charge region but not directly at the interface. It can be clearly seen in the 3D representation and in the atom probe composition profile that the absorber consists of CZTSe with an interconnected network of ZnSe. These ZnSe inclusions are highly doped with roughly 1 at% of Cu and 1 at% of Sn; they are most likely



**Figure 16.13** (a) Atom probe tomography map of a 6.2% CZTSe absorber layer (the slice is taken near the top of the absorber and is 6 nm thick perpendicular to the plane of the image); and (b) compositional line profile indicated with the arrow in (a). The light grey areas in (a) comprise only Zn and Se; the dark grey areas comprise Cu, Zn, Sn and Se

the reason for the high series resistance and, even more important, the high recombination rates in the current CZTSe devices. The ZnSe inclusions are of some tens of nanometers in diameter and will not be distinguishable in scanning electron microscopy, conventional Raman spectroscopy, or X-ray diffraction. Currently it is not clear if this CZTSe/ZnSe network is also present in other high-efficiency devices grown under Cu-poor and Zn-rich conditions. However, we showed in the previous section that a diverging series resistance at low temperatures is an indication of a ZnSe secondary phase. Since many devices described in the literature show a high series resistance, it is very likely that a similar network is also present in those devices. The nanometer-sized ZnSe inclusions act as a barrier for the current. It is likely that the barrier is higher if the inclusions consist of higher-band-gap Zn(S,Se) or ZnS compared to pure ZnSe. At room temperature a significant amount of the carriers can still pass this barrier due to thermionic emission. A decrease in temperature leads to a decrease of the amount of thermionic emission and consequently to a loss in current and an increase in the series resistance, as observed in many temperature-dependent current–voltage analyses. Since all the best-performing devices described in the literature are Cu-poor and Zn-rich, the formation of ZnS(e) is likely. Moreover, these secondary phase inclusions may also play a major role in the strong recombination currents observed in all CZTSSe solar cells. It is interesting to note that the record efficiency devices [10, 44] are not only high in Se, but also almost stoichiometric concerning their Zn content, thus reducing the formation of Zn(S,Se) inclusions. It is likely that all good solar cells are formed in the compositional region where ZnS(e) is the expected secondary phase, since the existence region of kesterite is small and other compositions provoke even more detrimental secondary phases such as SnS(e), SnS(e)<sub>2</sub>, Cu<sub>x</sub>S(e), or Cu<sub>2</sub>SnSe<sub>3</sub> [81]. However, the previous discussion also shows that the formation of the ZnS(e) secondary phase has to be avoided.

## 16.6 Conclusion

We have shown that the limiting factor in all current CZTS(e) devices, independent of the production method and of the S/Se ratio, is the low open-circuit voltage. This shows that too much recombination takes place in the devices. Temperature-dependent current–voltage

analysis reveals that the dominant recombination path is different for selenium-based devices compared to sulfo-selenide devices. This finding suggests that the CdS buffer layer is suitable for CZTSe, but the buffer layer and the n-type window layer has to be exchanged for SSe devices. The observation is most easily explained by the formation of a cliff at the absorber–buffer interface, when the conduction band of the absorber is shifted upwards by the addition of sulfur. The photoluminescence and the quantum efficiency measurements of both Se- and S-based devices show a significant scatter of the band gap. This finding suggests that more than one material is present in the absorber layers. It is very likely that the current absorber layers exhibit a mixture of kesterite/stannite structures plus additional secondary phases. Finally, the high series resistance is attributed to a ZnS(e) secondary phase which limits the current, increases the series resistance, and is most likely the major reason for the high reverse-saturation current density and the low open-circuit voltage. A ZnS(e) secondary phase is precipitated in an absorber layer according to the phase diagram, since all current CZTS(e) thin films are prepared using a Cu-poor and Zn-rich precursor/absorber.

## Acknowledgements

We gratefully acknowledge financial support by the Luxembourgish Fonds National de la Recherche and funding through the European initial training network program Kestcells, project number FP7-PEOPLE-2012-ITN316488. We thank all our colleagues from the Laboratory of Photovoltaics for numerous helpful discussions. In particular, we thank Rabie Djemour for providing the PL measurements prior to publication.

## References

- [1] Wang, W., Winkler, M. T., Gunawan, O., Gokmen, T., Todorov, T., Zhu, Y. & Mitzi, D. B. (2013) Device characteristics of CZTSSe thin-film solar cells with 12.6% efficiency. *Advanced Energy Materials*, doi: 10.1002/aenm.201301465.
- [2] Green, M. A., Emery, K., Hishikawa, Y., Warta, W. & Dunlop, E. D. (2014) Solar cell efficiency tables (version 43). *Progress in Photovoltaics: Research and Applications*, **22**, 1–9.
- [3] Redinger, A. & Siebentritt, S. (2010) Coevaporation of  $\text{Cu}_2\text{ZnSnSe}_4$  thin films. *Applied Physics Letters*, **97**, 092111.
- [4] Redinger, A., Berg, D. M., Dale, P. & Siebentritt, S. (2011) The consequences of kesterite equilibria for efficient solar cells. *Journal of the American Chemical Society*, **133**, 3320–3323.
- [5] Weber, A., Mainz, R. & Schock, H. W. (2010) On the Sn loss from thin films of the material system Cu–Zn–Sn–S in high vacuum. *Journal of Applied Physics*, **107**, 013516.
- [6] Redinger, A., Mousel, M., Djemour, R., Guetay, L., Valle, N. & Siebentritt, S. (2014)  $\text{Cu}_2\text{ZnSnSe}_4$  thin film solar cells produced via co-evaporation and annealing including a  $\text{SnSe}_2$  capping layer. *Progress in Photovoltaics: Research and Applications*, **22**, 51–57.
- [7] Mousel, M., Schwarz, T., Djemour, R., Weiss, T. P., Sendler, J., Malaquias, J. C., Redinger, A., Cojocaru-Mirédin, O., Choi, P. & Siebentritt, S. (2014) Cu-rich precursors improve kesterite solar cells. *Advanced Energy Materials*, **4**, 1300543.
- [8] Shockley, W. & Queisser, H. J. (1961) Detailed balance limit of efficiency of p–n junction solar cells. *Journal of Applied Physics*, **32**, 510–519.
- [9] Siebentritt, S. & Schorr, S. (2012) Kesterites - a challenging material for solar cells. *Progress in Photovoltaics: Research and Applications*, **20**, 512–519.



- [10] Todorov, T. K., Tang, J., Bag, S., Gunawan, O., Gokmen, T., Zhu, Y. & Mitzi, D. B. (2012) Beyond 11% efficiency: characteristics of state-of-the-art  $\text{Cu}_2\text{ZnSn}(\text{S},\text{Se})_4$  solar cells. *Advanced Energy Materials*, **3**, 34–38.
- [11] Repins, I., Beall, C., Vora, N., De Hart, C., Kuciauskas, D., Dippo, P., To, B., Mann, J., Hsu, W.-C., Goodrich, A. & Noufi, R. (2012) Co-evaporated  $\text{Cu}_2\text{ZnSnSe}_4$  films and devices. *Solar Energy Materials and Solar Cells*, **101**, 154–159.
- [12] Guo, Q., Ford, G. M., Yang, W.-C., Walker, B. C., Stach, E. A., Hillhouse, H. W. & Agrawal, R. (2010) Fabrication of 7.2% efficient CZTSSe solar cells using CZTS nanocrystals. *Journal of the American Chemical Society*, **132**(49), 17384–17386.
- [13] Guo, Q., Cao, Y., Caspar, J. V., Farneth, W. E., Ionkin, A. S., Johnson, L. K., Lu, M., Malajovich, I., Radu, D., Choudhury, K. R., Rosenfeld, H. D. & Wu, W. (2012) A simple solution-based route to high-efficiency CZTSSe thin film solar cells. IEEE Photovoltaics Specialist Conference, Austin.
- [14] Barkhouse, D. A. R., Haight, R., Sakai, N., Hiroi, H., Sugimoto, H. & Mitzi, D. B. (2012) Cd-free buffer layer materials on  $\text{Cu}_2\text{ZnSn}(\text{S}_x\text{Se}_{1-x})_4$ : Band alignments with ZnO, ZnS, and  $\text{In}_2\text{S}_3$ . *Applied Physics Letters*, **100**, 193904.
- [15] Mitzi, D. B., Gunawan, O., Todorov, T. K., Wang, K. & Guha, S. (2011) The path towards a high-performance solution-processed kesterite solar cell. *Solar Energy Materials and Solar Cells*, **95**(6), 1421–1436.
- [16] Shin, B., Zhu, Y., Bojarczuk, N. A., Chey, S. J. & Guha, S. (2012) Control of an interfacial  $\text{MoSe}_2$  layer in  $\text{Cu}_2\text{ZnSnSe}_4$  thin film solar cells: 8.9% power conversion efficiency with a TiN diffusion barrier. *Applied Physics Letters*, **101**(5).
- [17] Shin, B., Zhu, Y., Bojarczuk, N. A., Chey, S. J. & Guha, S. (2012) High efficiency  $\text{Cu}_2\text{ZnSnSe}_4$  solar cells with a TiN diffusion barrier on a molybdenum bottom contact. IEEE Photovoltaics Specialist Conference, Austin.
- [18] Hsu, W.-C., Repins, I., Beall, C., Teeter, G., DeHart, C., To, B., Yang, Y. & Noufi, R. (2012) Growth kinetics during kesterite coevaporation. IEEE Photovoltaics Specialist Conference, Austin.
- [19] Redinger, A., Mousel, M., Wolter, M. H., Valle, N. & Siebentritt, S. (2013) Influence of S/Se ratio on series resistance and on dominant recombination pathway in  $\text{Cu}_2\text{ZnSn}(\text{SSe})_4$  thin film solar cells. *Thin Solid Films*, **535**, 291–295.
- [20] Barkhouse, D. A. R., Gunawan, O., Gokmen, T., Todorov, T. K. & Mitzi, D. B. (2012) Device characteristics of a 10.1% hydrazine-processed  $\text{Cu}_2\text{ZnSn}(\text{Se},\text{S})_4$  solar cell. *Progress in Photovoltaics*, **20**(1), 6–11.
- [21] Todorov, T. K., Reuter, K. B. & Mitzi, D. B. (2010) High-efficiency solar cell with earth-abundant liquid-processed absorber. *Advanced Materials*, **22**, E156.
- [22] Gunawan, O., Todorov, T. K. & Mitzi, D. B. (2010) Loss mechanisms in hydrazine-processed  $\text{Cu}_2\text{ZnSn}(\text{Se},\text{S})_4$  solar cells. *Applied Physics Letters*, **97**, 233506.
- [23] Shin, B., Wang, K., Gunawan, O., Reuter, K. B., Jay, C., Bojarczuk, N. A., Todorov, T., Mitzi, D. B. & Guha, S. (2011) High efficiency  $\text{Cu}_2\text{ZnSn}(\text{S}_x\text{Se}_{1-x})_4$  thin film solar cells by thermal co-evaporation. 37th IEEE Photovoltaics Specialist Conference, Seattle.
- [24] Katagiri, H. (2005)  $\text{Cu}_2\text{ZnSnS}_4$  thin film solar cells. *Thin Solid Films*, **480**, 426.
- [25] Choudhury, K. R., Cao, Y., Caspar, J. V., Farneth, W. E., Guo, Q., Ionkin, A. S., Johnson, L. K., Lu, M., Malajovich, I., Radu, D., Rosenfeld, H. D. & Wu, W. (2012) Characterization and understanding of performance losses in a highly efficient solution-processed CZTSSe thin-film solar cell. 38th Photovoltaic Specialists Conference, Austin.
- [26] Li, J. B., Chawla, V. & Clemens, B. M. (2012) Investigating the role of grain boundaries in CZTS and CZTSSe thin film solar cells with scanning probe microscopy. *Advanced Materials*, **24**, 720.
- [27] Yang, W., Duan, H.-S., Bob, B., Lei, B., Li, S.-H. & Yang, Y. (2012) Novel solution processing of high efficiency Earth abundant CZTSSe solar cells. 38th Photovoltaic Specialists Conference, Austin.
- [28] Shin, B., Gunawan, O., Zhu, Y., Bojarczuk, N. A., Chey, S. J. & Supratik, G. (2013) Thin film solar cell with 8.4% power conversion efficiency using an earth-abundant  $\text{Cu}_2\text{ZnSnS}_4$  absorber. *Progress in Photovoltaics: Research and Applications*, **21**, 72–76.

- [29] Katagiri, H., Jimbo, K., Yamada, S., Kamimura, T., Maw, W. S., Fukano, T., Ito, T. & Motohiro, T. (2008) Enhanced conversion efficiencies of  $\text{Cu}_2\text{ZnSnS}_4$ -based thin film solar cells by using preferential etching technique. *Applied Physics Express*, **1**(4).
- [30] Wang, K., Gunawan, O., Todorov, T., Shin, B., Chey, S. J., Bojarczuk, N. A., Mitzi, D. & Guha, S. (2010) Thermally evaporated  $\text{Cu}_2\text{ZnSnS}_4$  solar cells. *Applied Physics Letters*, **97**, 143508.
- [31] Scragg, J. J., Ericson, T., Fontané, X., Izquierdo-Roca, V., Pérez-Rodríguez, A., Kubart, T., Edoff, M. & Platzer-Björkman, C. (2014) Rapid annealing of reactively sputtered precursors for  $\text{Cu}_2\text{ZnSnS}_4$  solar cell. *Progress in Photovoltaics: Research and Applications*, **22**, 10–17.
- [32] Hiroi, H., Sakai, N. & Sugimoto, H. (2011) Cd-free  $5\times 5\text{ cm}^2$ -sized  $\text{Cu}_2\text{ZnSnS}_4$  submodules. 37th Photovoltaic Specialists Conference, Seattle.
- [33] Sakai, N., Hiroi, H. & Sugimoto, H. (2011) Development of Cd-free buffer layer for  $\text{Cu}_2\text{ZnSnS}_4$  thin film solar cells. 37th Photovoltaic Specialists Conference, Seattle.
- [34] Hiro, H., Sakai, N., Katou, T., Muraoka, S. & Sugimoto, H. (2012) Development of high efficiency  $\text{Cu}_2\text{ZnSnS}_4$  submodule with Cd-free buffer layer. 38th Photovoltaic Specialists Conference, Austin.
- [35] Sugimoto, H., Hiroi, H., Sakai, N., Muraoka, S. & Katou, T. (2012) Over 8% efficiency  $\text{Cu}_2\text{ZnSnS}_4$  submodules with ultra-thin absorber. 38th Photovoltaic Specialists Conference, Austin.
- [36] Ahmed, S., Reuter, K. B., Gunawan, O., Guo, L., Romankiw, L. T. & Deligianni, H. (2012) A high efficiency electrodeposited  $\text{Cu}_2\text{ZnSnS}_4$  solar cell. *Advanced Energy Materials*, **2**, 253.
- [37] Mousel, M., Redinger, A., Djemour, R., Arasimowicz, M., Valle, N., Dale, P. & Siebentritt, S. (2013) HCl and  $\text{Br}_2$ -MeOH etching of  $\text{Cu}_2\text{ZnSnSe}_4$  polycrystalline absorbers. *Thin Solid Films*, **535**, 83–87.
- [38] Redinger, A., Berg, D. M., Dale, P. J., Djemour, R., Gütay, L., Eisenbarth, T., Valle, N. & Siebentritt, S. (2011) Route towards high efficiency single phase  $\text{Cu}_2\text{ZnSn}(\text{S},\text{Se})_4$  thin film solar cells: Model experiments and literature review. *IEEE Journal of Photovoltaics*, **1**, 200.
- [39] Grenet, L., Bernardi, S., Kohen, D., Lepoittevin, C., Noel, S., Karst, N., Brioude, A., Perraud, S. & Mariette, H. (2012)  $\text{Cu}_2\text{ZnSn}(\text{S}_{1-x}\text{Se}_x)_4$  based solar cell produced by selenization of vacuum deposited precursors. *Solar Energy Materials and Solar Cells*, **101**, 11–14.
- [40] Lechner, R., Jost, S., Palm, J., Gowtham, M., Sorin, F., Louis, B., Yoo, H., Wibowo, R. A. & Hock, R. (2013)  $\text{Cu}_2\text{ZnSn}(\text{S},\text{Se})_4$  solar cells processed by rapid thermal processing of stacked elemental layer precursors. *Thin Solid Films*, **535**, 5–9.
- [41] Brammertz, G., Ren, Y., Buffière, M., Mertens, S., Hendrickx, J., Marko, H., Zaghi, A. E., Lenaers, N., Köble, C., Meuris, M., Vleugels, J. & Poortmans, J. (2013) Electrical characterization of  $\text{Cu}_2\text{ZnSnSe}_4$  solar cells from selenization of sputtered metal layers. *Thin Solid Films*, **535**, 348–352.
- [42] Bag, S., Gunawan, O., Gokmen, T., Zhu, Y. & Mitzi, D. B. (2012) Hydrazine-processed Ge-substituted CZTSe solar cells. *Chemistry of Materials*, **24**, 4588–4593.
- [43] Kato, T., Hiroi, H., Sakai, N., Muraoka, S. & Sugimoto, H. (2012) Characterization of front and back interfaces of  $\text{Cu}_2\text{ZnSnS}_4$  thin-film solar cells. *Proceedings of 27th European Photovoltaic Solar Energy Conference Frankfurt*, p. 2236.
- [44] Brammertz, G., Buffière, M., Oueslati, S., ElAnzeery, H., Ben Messaoud, K., Sahayaraj, S., Köble, C., Meuris, M. & Poortmans, J. (2013) Characterization of defects in 9.7% efficient  $\text{Cu}_2\text{ZnSnSe}_4$ -CdS-ZnO solar cells. *Applied Physics Letters*, **103**(16), 163904.
- [45] Shafarman, W. N., Siebentritt, S. & Stolt, L. (2011)  $\text{Cu}(\text{In,Ga})\text{Se}_2$  solar cells. In *Handbook of Photovoltaic Science and Engineering* (eds S. Hegedus & A. Luque), John Wiley & Sons, Chichester.
- [46] Jackson, P., Hariskos, D., Lotter, E., Paetel, S., Wuerz, R., Menner, R., Wischmann, W. & Powalla, M. (2011) New world record efficiency for  $\text{Cu}(\text{In,Ga})\text{Se}_2$  thin-film solar cells beyond 20%. *Progress in Photovoltaics*, **19**, 894.
- [47] Contreras, M., Mansfield, L., Egaas, B., Romero, M., Li, J., Noufi, R. & Rudiger-Voigt, E. (2011) Improved energy conversion efficiency in wide-band gap  $\text{Cu}(\text{In,Ga})\text{Se}_2$  solar cells. 37th Photovoltaic Specialists Conference, Seattle.
- [48] AbuShama, J., Noufi, R., Johnston, S., Ward, S. & Wu, X. (2005) Improved performance in  $\text{CuInSe}_2$  and surface-modified  $\text{CuGaSe}_2$  solar cells. 31th Photovoltaic Specialists Conference, New York.

- [49] Haight, R., Barkhouse, A., Gunawan, O., Shin, B., Copel, M., Hopstaken, M. & Mitzi, D. B. (2011) Band alignment at the  $\text{Cu}_2\text{ZnSn}(\text{S}_x\text{Se}_{1-x})_4/\text{CdS}$  interface. *Applied Physics Letters*, **98**, 253502.
- [50] Levencenco, S., Dumcenco, D., Wang, Y. P., Huang, Y. S., Ho, C. H., Arushanov, E., Tezlevan, V. & Tiong, K. K. (2012) Influence of anionic substitution on the electrolyte electroreflectance study of band edge transitions in single crystal  $\text{Cu}_2\text{ZnSn}(\text{S}_x\text{Se}_{1-x})_4$  solid solutions. *Optical Materials*, **34**, 1362–1365.
- [51] Scheer, R. & Schock, H. W. (2011) Chalcogenide Photovoltaics. Wiley-VCH Verlag GmbH & Co, KGaA, Weinheim.
- [52] Hegedus, S. S. & Shafarman, W. N. (2004) Thin-film solar cells: Device measurements and analysis. *Progress in Photovoltaics*, **12**, 155.
- [53] Rau, U., Jasenek, A., Schock, H. W., Engelhardt, F. & Meyer, T. (2000) Electronic loss mechanisms in chalcopyrite based heterojunction solar cells. *Thin Solid Films*, **361**, 298–302.
- [54] Hengel, I., Neisser, A., Klenk, R. & Lux-Steiner, M. C. (2000) Current transport in  $\text{CuInS}_2/\text{Ga}/\text{CdS}/\text{ZnO}$  - solar cells. *Thin Solid Films*, **361**, 458–462.
- [55] Wilhelm, H., Schock, H.-W. & Scheer, R. (2011) Interface recombination in heterojunction solar cells: Influence of buffer layer thickness. *Journal of Applied Physics*, **109**, 084514.
- [56] Bär, M., Schubert, B. A., Marsen, B., Wilks, R. G., Pookpanratana, S., Blum, M., Krause, S., Unold, T., Yang, W., Weinhardt, L., Heske, C. & Schock, H. W. (2011) Cliff-like conduction band offset and KCN-induced recombination barrier enhancement at the  $\text{CdS}/\text{Cu}_2\text{ZnSnS}_4$  thin-film solar cell heterojunction. *Applied Physics Letters*, **99**, 222105.
- [57] Nagoya, A., Asahi, R. & Kresse, G. (2011) First-principles study of  $\text{Cu}_2\text{ZnSnS}_4$  and the related band offsets for photovoltaic applications. *Journal of Physics-Condensed Matter*, **23**, 404203.
- [58] Chen, S. Y., Yang, J. H., Gong, X. G., Walsh, A. & Wei, S. H. (2010) Intrinsic point defects and complexes in the quaternary kesterite semiconductor  $\text{Cu}_2\text{ZnSnS}_4$ . *Physical Review B*, **81**, 245204.
- [59] Bao, W. & Ichimura, M. (2012) Prediction of the band offsets at the  $\text{CdS}/\text{Cu}_2\text{ZnSnS}_4$  interface based on the first-principles calculation. *Japanese Journal of Applied Physics*, **51**, 10NC31.
- [60] Chen, S. Y., Walsh, A., Yang, J. H., Gong, X. G., Sun, L., Yang, P. X., Chu, J. H. & Wei, S. H. (2011) Compositional dependence of structural and electronic properties of  $\text{Cu}_2\text{ZnSn}(\text{S},\text{Se})_4$  alloys for thin film solar cells. *Physical Review B*, **83**, 125201.
- [61] Bag, S., Gunawan, O., Gokmen, T., Zhu, Y., Todorov, T. K. & Mitzi, D. B. (2012) Low band gap liquid-processed CZTSe solar cell with 10.1% efficiency. *Energy & Environmental Science*, **5**, 7060.
- [62] Unold, T., Kretzschmar, S., Just, J., Zander, O., Schubert, B., Marsen, B. & Schock, H.W. (2011) Correlation between composition and photovoltaic properties of  $\text{Cu}_2\text{ZnSnS}_4$ . 37th IEEE Photovoltaics Specialist Conference, Seattle.
- [63] Gunawan, O., Gokmen, T., Shin, B. S. & Guha, S. (2012) Device characteristics of high performance  $\text{Cu}_2\text{ZnSnS}_4$  solar cell. 38th IEEE Photovoltaics Specialist Conference, Austin.
- [64] Panayotatos, P. & Card, H. C. (1980) Use of  $V_{oc}-J_{sc}$  measurements for determination of barrier height under illumination and for fill-factor calculations in schottky-barrier solar cells. *IEE Proceedings-I Communications Speech and Vision*, **127**, 308.
- [65] Reiss, J., Malmström, J., Werner, A., Hengel, I., Klenk, R. & Lux-Steiner, M. C. (2011) Current transport in  $\text{CuInS}_2$  solar cells depending on absorber preparation. *Materials Research Society Symposium Proceedings*, **668**, H9.4.1.
- [66] Regesch, D. (2013) Photoluminescence and solar cell studies of chalcopyrites: comparison of Cu-rich vs. Cu-poor and polycrystalline vs. epitaxial material. PhD thesis, University of Luxembourg.
- [67] Djemour, R. (2014)  $\text{Cu}_2\text{ZnSnSe}_4$  polymorphs and secondary phases: characterization by Raman spectroscopy and photoluminescence. PhD thesis, University of Luxembourg.
- [68] Regesch, D., Güttay, L., Larsen, J. K., Deprédurand, V., Tanaka, D., Aida, Y. & Siebentritt, S. (2012) Degradation and passivation of  $\text{CuInSe}_2$ . *Applied Physics Letters*, **101**, 112108.
- [69] Rau, U. & Werner, J. H. (2004) Radiative efficiency limits of solar cells with lateral band-gap fluctuations. *Applied Physics Letters*, **84**, 3735.

- [70] Chen, S. Y., Gong, X. G., Walsh, A. & Wei, S. H. (2009) Crystal and electronic band structure of  $\text{Cu}_2\text{ZnSnX}_4$  (X=S and Se) photovoltaic absorbers: First-principles insights. *Applied Physics Letters*, **94**, 041903.
- [71] Paier, J., Asahi, R., Nagoya, A. & Kresse, G. (2009)  $\text{Cu}_2\text{ZnSnS}_4$  as a potential photovoltaic material: A hybrid Hartree-Fock density functional theory study. *Physical Review B*, **79**, 115126.
- [72] Persson, C. (2010) Electronic and optical properties of  $\text{Cu}_2\text{ZnSnS}_4$  and  $\text{Cu}_2\text{ZnSnSe}_4$ . *Journal of Applied Physics*, **107**, 053710.
- [73] Botti, S., Kammerlander, D. & Marques, M. A. L. (2011) Band structures of  $\text{Cu}_2\text{ZnSnS}_4$  and  $\text{Cu}_2\text{ZnSnSe}_4$  from many-body methods. *Applied Physics Letters*, **98**, 241915.
- [74] Schorr, S. (2011) The crystal structure of kesterite type compounds: A neutron and X-ray diffraction study. *Solar Energy Materials and Solar Cells*, **95**, 1482.
- [75] Nozaki, H., Fukano, T., Seno, Y., Ohta, S., Katagiri, H. & Jimbo, K. (2012) Crystal structure determination of solar cell materials:  $\text{Cu}_2\text{ZnSnS}_4$  thin films using X-ray anomalous dispersion. *Journal of Alloys and Compounds*, **524**, 22–25.
- [76] Gunawan, O., Gokmen, T., Warren, C. W., Cohen, J. D., Todorov, T. K., Barkhouse, D. A. R., Bag, S., Tang, J., Shin, B. & Mitzi, D. B. (2012) Electronic properties of the  $\text{Cu}_2\text{ZnSn}(\text{Se},\text{S})_4$  absorber layer in solar cells as revealed by admittance spectroscopy and related methods. *Applied Physics Letters*, **100**, 253905.
- [77] Sites, J. R. & Mauk, P. H. (1989) Diode quality factor determination for thin film solar cells. *Solar Cells*, **27**, 411.
- [78] Wätjen, J. T., Engman, J., Edoff, M. & Platzer-Björkman, C. (2012) Direct evidence of current blocking by ZnSe in  $\text{Cu}_2\text{ZnSnSe}_4$ . *Applied Physics Letters*, **100**, 173510.
- [79] Hsu, W.-C., Repins, I., Beall, C., DeHart, C., To, B., Yang, W., Yang, Y. & Noufi, R. (2012) Growth mechanisms of co-evaporated kesterite: a comparison of Cu-rich and Zn-rich composition paths. *Progress in Photovoltaics: Research and Applications*, doi: 10.1002/pip.2296.
- [80] Redinger, A., Hönes, K., Fontané, X., Izquierdo-Roca, V., Saucedo, E., Valle, N., Pérez-Rodríguez, N. & Siebentritt, S. (2011) Detection of a ZnSe secondary phase in coevaporated  $\text{Cu}_2\text{ZnSnSe}_4$  thin films. *Applied Physics Letters*, **98**, 101907.
- [81] Siebentritt, S. (2013) Why are kesterite solar cells not 20% efficient? *Thin Solid Films*, **535**, 1–4.

# 17

## Device Characteristics of Hydrazine-Processed CZTSSe

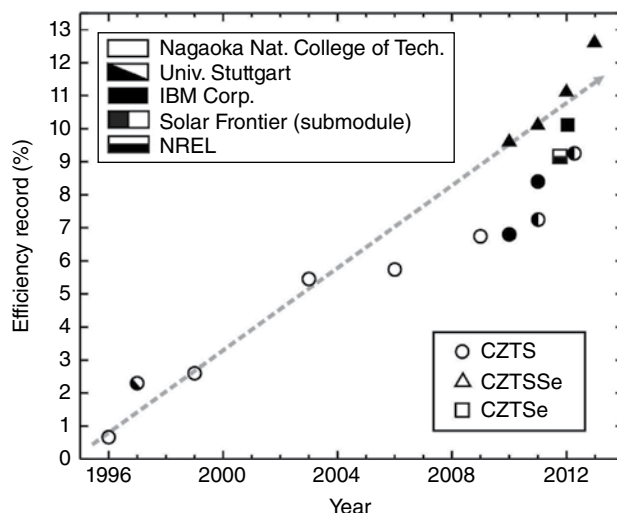
*Okı Gunawan, Tayfun Gokmen and David B. Mitzi*

*IBM Thomas J. Watson Research Center, New York, USA*

### 17.1 Introduction

The kesterite  $\text{Cu}_2\text{ZnSn}(\text{Se}_{1-y}\text{S}_y)_4$  system, generally referred to as CZTSSe, is an emerging thin-film solar cell technology with many properties necessary for high photovoltaic performance, such as direct band gap, high absorption coefficient (c.  $10^5 \text{ cm}^{-1}$ ) and the ability to be deposited by a variety of readily scalable processes [1]. The band gap can be tuned, ranging from  $\sim 1.0 \text{ eV}$  for selenide kesterite (CZTSe,  $y = 0$ ) to  $\sim 1.5 \text{ eV}$  for sulfide kesterite (CZTS,  $y = 1$ ), which covers the optimum single-junction band-gap range of  $1.15\text{--}1.35 \text{ eV}$  using the AM1.5G spectrum according to the Shockley–Quisser limit [2, 3]. Substantial progress has recently been made in improving CZTSSe device performance, as shown in Figure 17.1.

In 1996, Katagiri *et al.* [4, 5] reported a CZTS (no Se incorporated) photovoltaic (PV) device with power conversion efficiency (PCE) of 0.66% and  $V_{\text{oc}}$  of 0.4 V using sequential evaporation of the CZTS film. In the following year, the Stuttgart University group reported improved efficiency of 2.3% for a similarly processed device [6]. In 2007, Katagiri *et al.* reported a major leap in performance for a CZTS device with PCE of 5.7% [7] and 6.8% in 2008 [8]. For analogous selenide CZTSe devices, in 1997 Friedlmeier *et al.* [6] reported a vacuum-fabricated film with a device efficiency of 0.6%; by 2009, the efficiency for CZTSe devices had increased to 3.2% [9]. More recently, vacuum-processed devices have continued to show significant improvement with 8.4% PCE for CZTS [10] and 9.2% for CZTSe [11]. Development of

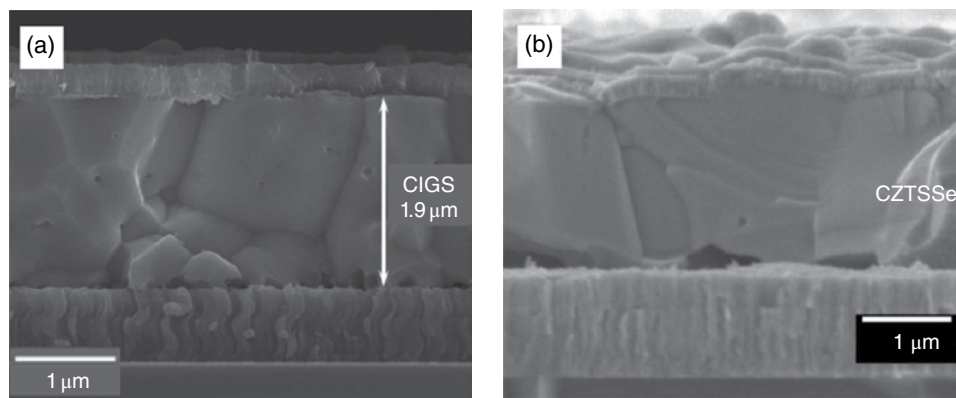


**Figure 17.1** Performance of CZTSSe thin-film solar cells as a function of year, showing consistent progress toward higher efficiency

large-area sub-module-type CZTS devices by Solar Frontier has also been very promising [12, 13] with a record efficiency of 9.2% on a 5×5 cm<sup>2</sup> sub-module device in 2012 [14].

Most of the recent world-record CZTSSe devices have been produced by a hydrazine (N<sub>2</sub>H<sub>4</sub>)-based slurry processing approach [15–17]. Hydrazine can effectively dissolve many metal chalcogenides, including Cu<sub>2</sub>S and SnS, and elemental sulfur and selenium [18–21]. However, ZnS and ZnSe are not readily soluble in hydrazine without an added coordinating agent for the Zn [22]. The hybrid precursor slurry is obtained by dissolving Cu<sub>2</sub>S and SnS(Se) in hydrazine with added elemental Zn powder. The reaction results in ZnS(Se)N<sub>2</sub>H<sub>4</sub> nanoparticles dispersed in the Cu-Sn-S-Se solution. To target high device performance, the metal stoichiometry is tuned to yield Cu-poor and Zn-rich compositions, that is, [Cu]/([Zn]+[Sn]) ≈ 0.8 and [Zn]/[Sn] ≈ 1.1, similar to those described for previous record devices [5]. The CZTSSe film is then deposited by spin-coating or doctor-blading of the precursor material on Mo-coated soda-lime glass, followed by heat treatment and application of the standard top stack of the CdS/ZnO/TCO and Ni/Al grid to obtain the complete device. This approach led to a major advance of PCE to 9.7% reported by the IBM group in 2010 [15] for CZTSSe with mixed sulfur/selenium anions. The method was further refined to yield 10.1% in 2011 [16, 23] and 11.1% in 2012 [17]. Most recently, a hydrazine pure solution approach (employing a soluble coordinated zinc complex) [22] coupled with optimization of the optical stack has led to devices with a PCE of 12.6% [24], which represents the current efficiency record for this absorber material.

In this chapter we focus on the device characteristics of high performance CZTSSe cells, fabricated mostly by hydrazine-based processing. We present the key device characteristics obtained from various measurement techniques and discuss the major loss mechanisms that limit performance. To elucidate the key problems in the present-generation CZTSSe devices, we compare a high-performance 11.1% CZTSSe cell [17] with a 15.2% efficiency CIGSSe cell produced by similar hydrazine-based solution processing [25] and a recent world-record 20.3% CIGSSe cell [26].



**Figure 17.2** Cross section of the (a) 15.2% IBM-CIGSSe [25] and (b) 11.1% IBM-CZTSSe devices. Panel (a) reproduced with permission from [25], John Wiley & Sons

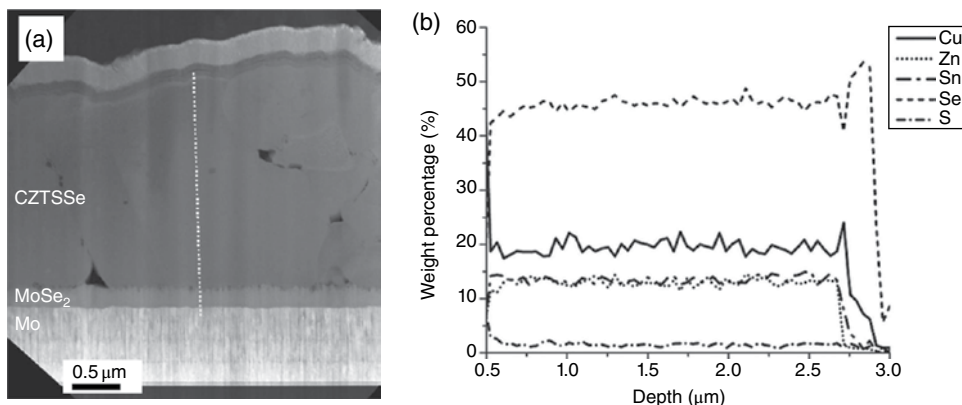
## 17.2 Device Characteristics

### 17.2.1 Film characteristics

Figure 17.2 shows cross-sectional SEM images of the 15.2% IBM-CIGSSe and 11.1% IBM-CZTSSe cells. Both CIGSSe and CZTSSe devices contain a  $\text{MoSe}_2$  layer in between the CIGSSe/CZTSSe and Mo layers, which is more visible in the transmission electron microscopy (TEM) image as shown in Figure 17.3a. The  $\text{Mo}(\text{S},\text{Se})_2$  layer is rather thin ( $\sim 200$  nm) in the current generation champion CZTSSe [17, 24]. Such an interfacial layer has been reported to be important for absorber layer adhesion and for the formation of an ohmic contact between CIGSSe and Mo [27–30], and could be similarly important in CZTSSe devices. The Mo contact has however also been reported to reduce  $\text{Sn}(\text{IV})$  to  $\text{Sn}(\text{II})$  in the CZTSSe and therefore to give rise to phase decomposition at the back contact, in addition to the formation of the  $\text{Mo}(\text{S},\text{Se})_2$  layer [31]. The grain sizes within the CIGS and CZTSSe films are fairly similar ( $>1$   $\mu\text{m}$  dimensions), although issues with void formation may be more pronounced in this generation of CZTSSe devices. Voids at the Mo back contact could elevate series resistance.

CZTSSe has only a small range of chemical potentials for which the formation of the single-phase kesterite is thermodynamically stable [32]; compositional control during CZTSSe thin-film deposition therefore needs to be more stringent than for CIGSSe. Katagiri *et al.* have found that the best CZTSSe cells have a slightly Cu-poor ( $[\text{Cu}]/([\text{Zn}]+[\text{Sn}]) \approx 0.8$ ) and Zn-rich ( $[\text{Zn}]/[\text{Sn}] \approx 1.2$ ) stoichiometry [33] and, similarly, the best CIGSSe devices are also Cu-poor to avoid device shunting. Using first-principles calculation, Chen *et al.* [34] have shown that a high population of detrimental  $\text{Cu}_{\text{Zn}} + \text{Sn}_{\text{Zn}}$  and  $2\text{Cu}_{\text{Zn}} + \text{Sn}_{\text{Zn}}$  clusters can be formed in stoichiometric CZTSSe samples where  $[\text{Cu}]/([\text{Zn}]+[\text{Sn}]) \approx 1$  and  $[\text{Zn}]/[\text{Sn}] \approx 1$ ; Zn-rich and Cu/Sn-poor conditions are therefore proposed to decrease their population, which is consistent with the empirical findings described above.

Despite the high processing temperatures used during fabrication ( $>500^\circ\text{C}$ ) and high vapor pressure of some of the constituent elements, state-of-the-art CZTSSe cells exhibit a nominally uniform composition for all major elements as a function of depth as shown in



**Figure 17.3** (a) TEM image of the 11.1% CZTSSe device. (b) Energy-dispersive spectroscopy (EDX) scan along the dashed line in (a), showing the approximate weight percent of each element as a function of depth in the film. Reproduced with permission from [17], John Wiley & Sons

the energy-dispersive X-ray spectroscopy (EDX) scan in Figure 17.3b. The film also shows low and uniform sulfur content, which suggests a uniform band gap along the depth of the film. S and Se are particularly volatile and ensuring that they are not lost from the bulk of the film requires careful control of the annealing atmosphere. Significant Sn loss has also been observed when annealing at such elevated temperatures [35, 36], due to the high vapor pressure of SnS above 400°C. Incorporating additional Sn and S/Se into the annealing ambient can mitigate this issue. Cu can also be lost at the back of the device due to out-diffusion into the Mo contact [37], leading to the formation of ZnS and Cu-Sn phases at the back contact.

## 17.2.2 Device Performance Characteristics

Table 17.1 presents device performance characteristics of the 11.1% CZTSSe cell, a 20.3% Zentrum für Sonnenenergie- und Wasserstoff-Forschung (ZSW) CIGSSe cell [26], and a 15.2% IBM hydrazine-processed CIGSSe cell [25]. These cells have similar band gap ( $E_g = 1.13$  and 1.17 eV), highlighting a curious similarity between the CZTSSe and CIGSSe optimum band gap [39] (at least at this stage in the development of CZTSSe devices). The absorber band gap is determined from the quantum efficiency (QE) curve using the inflection or derivative technique applied to the data close to the band-gap cut-off wavelength [28]. Since higher band gap leads to higher  $V_{oc}$  and lower  $J_{sc}$ , we can normalize the effect of band gap in comparing the  $V_{oc}$  and  $J_{sc}$  by using  $V_{oc}$  deficit, i.e.  $V_{oc,def} = (E_g/q) - V_{oc}$ , and normalized  $J_{sc}$ , that is,  $J_{sc,N} = J_{sc}/J_{sc,max}$ , as shown in Table 17.1.  $J_{sc,max}$  is the maximum possible short-circuit current for the AM1.5G solar irradiance spectrum ( $S_{AM1.5G}$ ), assuming 100% external quantum efficiency, given as:

$$J_{sc,max} = \int_0^{\lambda_c} S_{AM1.5G}(\lambda) \lambda q / h c d\lambda \quad (17.1)$$



**Table 17.1** Device performance of top performing CIGSSe (from ZSW and IBM) and CZTSSe cells.  $R_{SL}$ ,  $n$ , and  $J_0$  are series resistance under light, diode ideality factor and reverse saturation current determined using Sites' method [38]. The  $n$  values in parentheses are determined from  $J_{sc}-V_{oc}$  measurement (see text).  $J_{sc,N}$  and  $V_{oc,def}$  are normalized- $J_{sc}$  and  $V_{oc}$  deficit, respectively, to normalize the band gap dependence effect (see text)

Device	Efficiency (%)	FF (%)	$J_{sc}$ (mA cm <sup>-2</sup> )	$V_{oc}$ (V)	$E_g$ (eV)	$J_{sc,N}$ (%)	$V_{oc,def}$ (V)	$R_{SL}$ ( $\Omega$ cm <sup>2</sup> )	$n$	$J_0$ (A cm <sup>-2</sup> )	Ref.
ZSW-CIGSSe	20.3	77.7	35.7	0.730	1.14	83.2	0.410	0.23	1.38	$4.2 \times 10^{-11}$	[26]
IBM-CIGSSe	15.2	75.1	32.6	0.623	1.17	78.7	0.547	0.38	1.57 (1.57)	$1.3 \times 10^{-8}$	[25]
IBM-CZTSSe	11.1	69.8	34.5	0.460	1.13	79.5	0.670	0.40	1.48 (1.28)	$1.4 \times 10^{-7}$	[17]

where  $h$ ,  $q$ ,  $c$ ,  $\lambda_c$  are Planck's constant, electron charge, speed of light, and the band-gap cut-off wavelength, respectively.

From Table 17.1 it is apparent that the primary shortcoming in the CZTSSe cell is its low  $V_{oc}$  or correspondingly high  $V_{oc}$  deficit value. We discuss the  $V_{oc}$  deficit issues in the next section in more detail. The second problem is the fill factor FF, which is still lacking compared to the CIGSSe devices. In lower-performance CZTSSe cells, high series resistance contributes to the low FF [40]. However, from Table 17.1 we note that the series resistance under light  $R_{SL}$  of the near-record CZTSSe cell is comparable to the hydrazine-processed CIGSSe analog, indicating that this is not the main problem for the low FF issue. FF is also directly impacted by  $V_{oc}$  from the following phenomenological relationship (ignoring the effect of series and shunt resistances) [41]:

$$FF = \frac{v_{oc} - \ln(v_{oc} + 0.72)}{v_{oc} + 1} \quad (17.2)$$

where  $v_{oc}$  is the "normalized  $V_{oc}$ ", defined as:

$$v_{oc} = \frac{qV_{oc}}{nk_B T}, \quad (17.3)$$

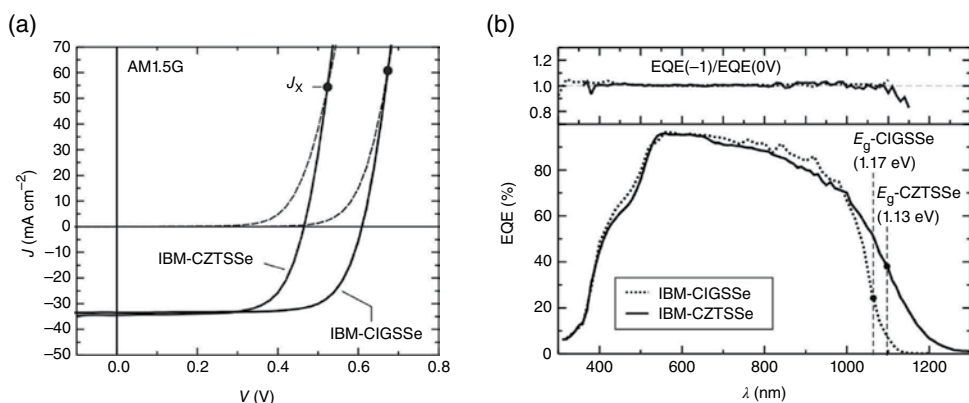
where  $k_B$  is the Boltzmann constant and  $T$  is temperature. Using this relationship we can calculate that the  $\sim 0.16$  V lower  $V_{oc}$  for the IBM-CZTSSe cell accounts for the 7% lower FF. The lower FF in the CZTSSe cell can therefore be mostly attributed to the low  $V_{oc}$  or high  $V_{oc}$  deficit.

The record CZTSSe cell already possesses some favorable characteristics on par with the IBM-CIGSSe device, such as reasonably good diode ideality factor ( $n \approx 1.5$ ), comparable light and dark cross-over point ( $J_x$ ) and low series resistance  $R_s$ . In an ideal solar cell where the light and dark  $J-V$  curves are in linear superposition,  $J_x$  values are very high. However, low  $J_x$  values are common in thin-film solar cells. For earlier generations of lower-performing CZTSSe devices, these cross-over points were lower (worse) [16, 23, 40].

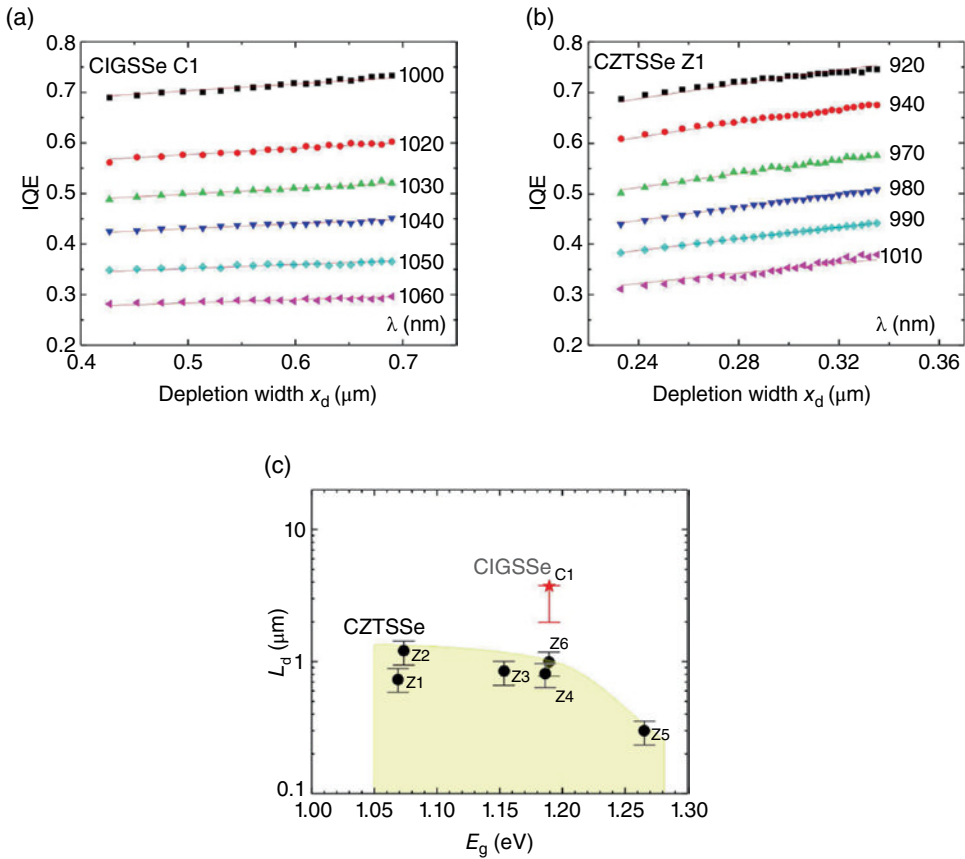
Low dark and light  $J$ - $V$  cross-over behavior in thin-film cells could be attributed to a blocking or non-ohmic back contact, higher active trap densities in the CZTSSe absorber, or a photosensitive or large conduction band offset (CBO) barrier at the buffer-absorber interface [42, 43]. There are two kinds of ideality factor ( $n$ ) values reported in Table 17.1: one extracted from the standard light  $J$ - $V$  curve and the other is from  $J_{sc}$ - $V_{oc}$  measurement (displayed in parentheses in Table 17.1). In an ideal solar cell (clean semiconductor with no defects), both values should be close or the same. The difference between these ideality factors correlates with a  $V_{oc}$  pinning effect due to high bulk resistivity (low carrier density and low mobility), Fermi level pinning states in the surface or the bulk, and possibly also due to non-ohmic back contact (especially in samples with very low carrier density). The IBM-CZTSSe cell shows a large difference between the two  $n$  values indicating a more severe  $V_{oc}$  pinning effect, in contrast to the IBM-CIGSSe devices with similar  $n$  values [44].

The external quantum efficiency (EQE) plots for both IBM CIGSSe and CZTSSe cells are shown in Figure 17.4b. We note that the IBM-CZTSSe cell has a slightly higher  $J_{sc,N}$  compared to the IBM-CIGSSe cell. The short-wavelength EQE responses (300–600 nm) are almost identical for both IBM-CZTSSe and IBM-CIGSSe cells due to similar top layer (buffer and window) stack. However, at long wavelength the QE responses are different. The CIGSSe cell EQE cut-off looks sharper near the band-gap edge, but the CZTSSe cell has more pronounced tailing due to band tail states that give sub-band-gap absorption. This characteristic contributes to higher  $J_{sc}$  in the CZTSSe cell compared to the CIGSSe cell of the same band gap. We discuss the band tail issue in CZTSSe in more detail in Section 17.2.4.

We can probe the collection efficiency of these cells by looking at the EQE bias ratio at different voltage bias, that is, EQE (–1 V)/EQE (0 V) as shown in the upper inset of Figure 17.4b. We observe that the CZTSSe cell shows a practically flat EQE ratio with a value close to unity, indicating good collection efficiency in this cell, which is also the case for CIGSSe. Note that in the lower-performance CZTSSe cells [40] the bias ratio increases with wavelength, indicating limited collection efficiency due to short minority carrier diffusion length (or very short minority carrier lifetime) [42]. In poorer CZTSSe devices,



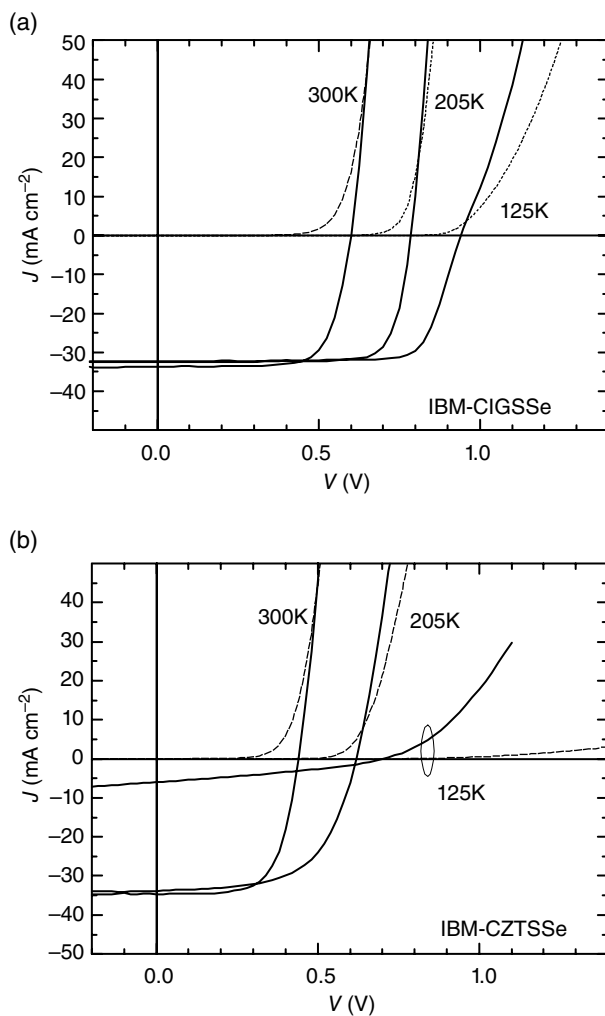
**Figure 17.4** Characteristics of the 11.1% IBM-CZTSSe and 15.2% IBM-CIGSSe cells: (a)  $J$ - $V$  characteristics.  $J_x$  indicates the cross-over point between the dark and light  $J$ - $V$  curves. (b) External quantum efficiency. Upper panel: ratio of the EQE at voltage bias –1 V and 0 V



**Figure 17.5** Minority carrier diffusion length ( $L_d$ ) extraction by probing internal quantum efficiency v. depletion width (or negative voltage bias) in: (a) CIGSSe and (b) CZTSSe. (c)  $L_d$  for CIGSSe and CZTSSe cells as a function of band gap. Reproduced with permission from [45]. Copyright © AIP Publishing, 2013

where the depletion width plus the diffusion length (the region from which the photogenerated carriers can be effectively collected) is less than the absorber thickness, the increase in the reverse bias voltage helps extend the depletion region deeper into the absorber layer, thereby increasing the minority carrier collection.

Furthermore, by studying bias-dependent quantum efficiency (QE) we can extract the minority carrier diffusion length ( $L_d$ ) as shown in Figure 17.5 [45]. In Figure 17.5b we observe that the QE in CZTSSe has stronger dependence with the increase in depletion width (or more negative voltage bias), which indicates a shorter  $L_d$ . The  $L_d$  values can be extracted quantitatively from the data in Figure 17.5a and b and have been studied on a collection of good CZTSSe and CIGSSe cells [45], as summarized in Figure 17.5c. The result shows that CZTSSe cells have lower  $L_d$  ( $<1\mu\text{m}$ ) compared to the reference CIGSSe cell, which highlights another shortcoming in the present generation of CZTSSe cells.

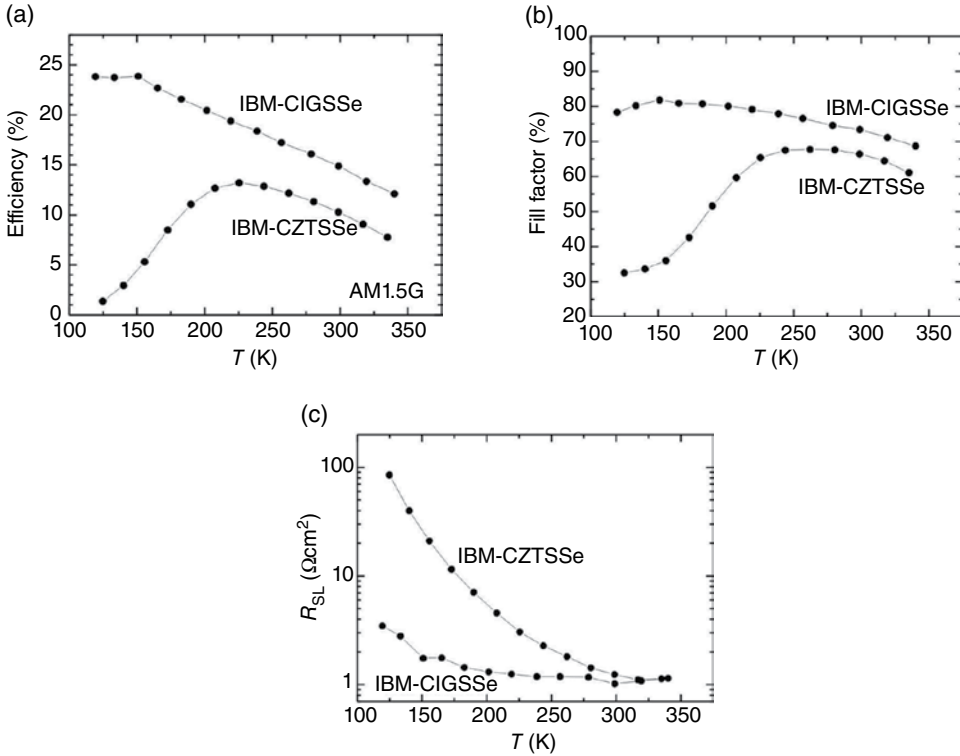


**Figure 17.6** Temperature dependence of the light and dark  $J$ - $V$  curves of the (a) IBM champion CIGSSe and (b) CZTSSe cell. The CZTSSe  $J$ - $V$  curves collapse at low temperature

### 17.2.3 Temperature-Dependent Characteristics

Further insight into the device characteristics of CZTSSe can be obtained by studying temperature dependence (120–340 K) of various device parameters from the light and dark  $J$ - $V$  data. This measurement is done using a liquid nitrogen cryostat integrated within the solar simulator [40]. Some stark contrasts between the CIGSSe and CZTSSe cells are apparent in the  $J$ - $V$  characteristics at low temperature (Figure 17.6); that is, while the  $J$ - $V$  curves for CIGSSe only suffer minor distortion, the CZTSSe  $J$ - $V$  curves collapse at low temperature ( $T \approx 125$  K).

Temperature-dependent behavior of the efficiency, fill factor, and series resistance are shown in Figure 17.7. The efficiency of the CIGSSe solar cell increases monotonically at lower temperature, which is expected for a good solar cell device, reaching values of as high as  $\sim 24\%$  at

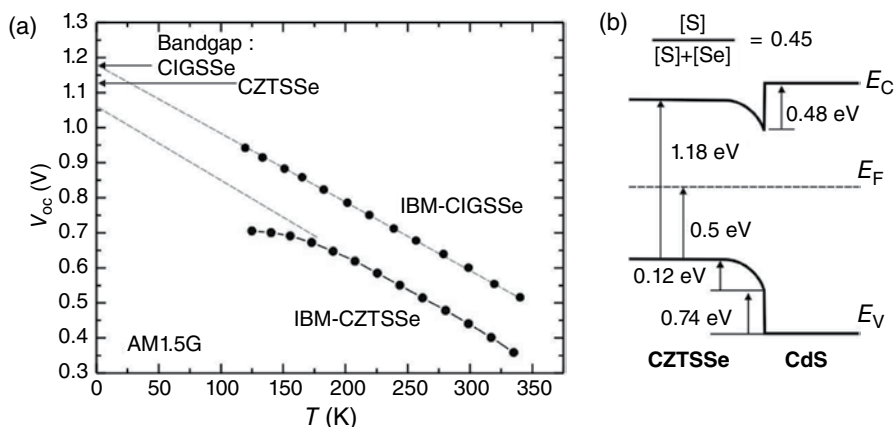


**Figure 17.7** Temperature-dependence characteristics of the IBM-CIGSSe v. IBM-CZTSSe solar cells: (a) efficiency; (b) fill factor; and (c) series resistance under light condition (measured from the difference between the light J–V and pseudo J–V curve [47])

110 K. However, the efficiency of the CZTSSe cell collapses to zero at low temperature. This effect occurs due to the concomitant collapse in the fill factor or large increase ( $\sim 200\times$  over the range 340–125 K) in the CZTSSe series resistance (Fig. 17.7b, c). In contrast, the CIGSSe series resistance is almost constant down to 180 K and increases much less ( $\sim 3\times$ ) at the lowest temperatures (120 K), as expected for an ideal solar cell with good ohmic contact. There are several possible factors that could lead to rising series resistance at low temperature, including: non-ohmic barriers at the back contact between CZTSSe and Mo; potential barriers at the front junction interface between CZTSSe and CdS [46] or between grains in CZTSSe [40]; a carrier freeze-out effect as suggested by an admittance spectroscopy study (Section 17.2.5); or collapse in mobility. The series resistance at room temperature is also strongly influenced by the band gap of the absorber (or S:Se ratio), as is shown in Section 17.2.7.

Important information about the  $V_{oc}$  deficit issue can also be obtained from the temperature dependence of  $V_{oc}$ , as shown in Figure 17.8a. The temperature dependence of  $V_{oc}$  is generally given as [48]:

$$V_{oc} = \frac{E_{A0}}{q} - \frac{nk_B T}{q} \ln \left( \frac{J_{00}}{J_L} \right) \quad (17.4)$$



**Figure 17.8** (a) Temperature dependence of the open circuit voltage  $V_{oc}$  for IBM-CIGSSe and IBM-CZTSSe solar cells. (b) Spike-like CdS/CZTSSe band alignment deduced from femtosecond laser ultraviolet photoelectron spectroscopy. Reproduced with permission from [53]. Copyright © AIP Publishing, 2011

where  $E_{A0}$ ,  $J_{00}$ , and  $J_L$  are the activation energy of the recombination mechanism, reverse saturation current prefactor, and the photocurrent, respectively. Assuming  $n$ ,  $J_{00}$ , and  $J_L$  to be temperature independent, the  $V_{oc}$  v.  $T$  data should yield a straight line and the intercept of the  $V_{oc}$  v.  $T$  plot at 0 K yields the activation energy  $E_{A0}$  of the dominant recombination process [48].

The IBM-CIGSSe cell exhibits the expected behavior of a high-performance solar cell, with activation energy  $E_{A0}$  the same as the band gap of the absorber layer ( $E_g = 1.17$  eV). This indicates that the dominant recombination process occurs in the space charge region or bulk of the absorber. However, we notice that  $E_{A0}$  for the IBM-CZTSSe device is significantly lower than its corresponding band-gap value, which has been the case for all CZTSSe cells studied so far regardless of the band gap [1, 10, 17, 40, 49].

This behavior of  $E_{A0}$  being lower than the band gap points to a fundamental problem with the current generation of CZTSSe devices, and is usually attributed to dominant recombination at the buffer-absorber interface [50, 51]. Another possible contributing factor is the potential of a “cliff”-type band alignment, where the conduction band edge of the absorber is higher than that of the buffer layer [46, 52]. A theoretical study for CIGSe (which has a similar device structure as CZTSSe) by Minemoto *et al.* shows that a favorable conduction band offset (CBO) is spike-like with an offset of 0–0.4 eV [46]. A band alignment study using femtosecond laser ultraviolet photoelectron spectroscopy revealed a favorable spike-like band alignment for CZTSSe [53], albeit a rather large conduction band offset of 0.4–0.5 eV (depending on band gap) as shown in Figure 17.8b. Buffer-absorber band alignment therefore does not appear to be the dominant cause of the  $V_{oc}$  deficit in CZTSSe, although a relatively high offset value could contribute to higher series resistance in CZTSSe in cases where this might be a problem. However, a cliff-like band alignment has been suspected in sulfide kesterite (CZTS) [54, 55], which could negatively impact the  $V_{oc}$ .

There is also another notable characteristic in the CZTSSe  $V_{oc}$  v.  $T$  curve (Fig. 17.8a); that is, the curve bends in the low-temperature regime, departing from a linear trend. This

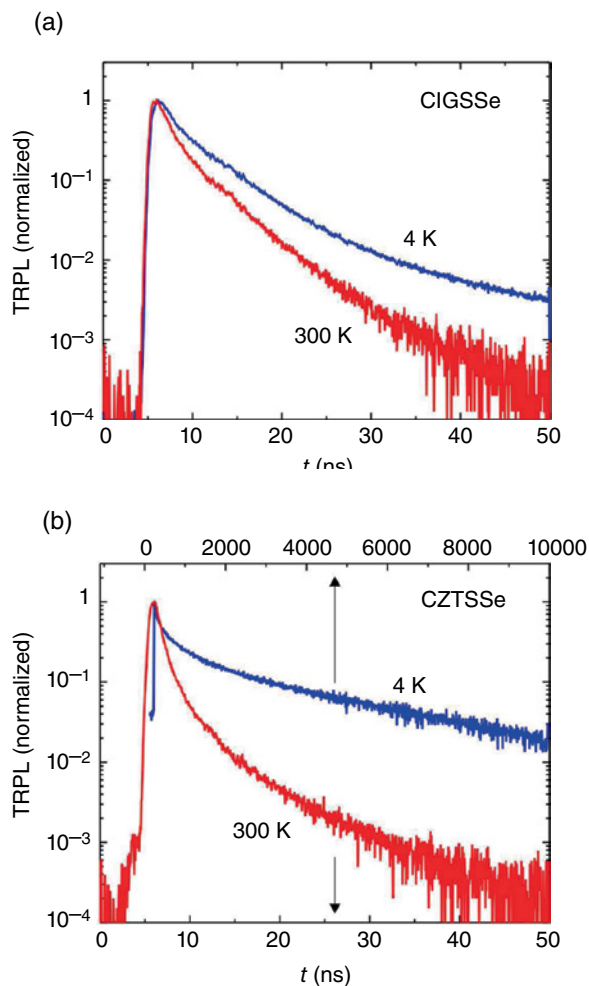
effect is associated with the  $\text{Suns-}V_{\text{oc}}$  (or  $J_{\text{sc}}-V_{\text{oc}}$ ) pinning or bending problem at very low-temperature or very high light intensity [44], suspected to be due to carrier freeze out that reduces the bulk conductivity and possible non-ohmic back contact problem at low temperature.

### 17.2.4 Photoluminescence and Band Tail Characteristics

Other relevant device characteristics of the bulk CZTSSe absorber that are tied to  $V_{\text{oc}}$  include photoluminescence (PL) and time-resolved photoluminescence (TRPL), as shown in Figure 17.9. Minority carrier lifetimes  $\tau$  for the CIGSSe and CZTSSe solar cells are measured using TRPL measurement. The decay curves, which do not follow a simple mono-exponential decay, are typically modeled by the rate equation taking into account both linear and quadratic recombination processes [57]. Considering the 300 K TRPL data and using a quadratic rate equation and a single lifetime model, we extract the minority carrier lifetime at the band edge emission ( $E_{\text{g}} = 1.16$  eV) for the CIGSSe layer, which yields  $\tau \approx 5.4$  ns. This lifetime is approximately constant in the vicinity of the band-gap energy ( $E_{\text{g}} = 1.08\text{--}1.28$  eV). We note that this lifetime is lower compared to other reported lifetime measurements in high-performance CIGS solar cells ( $>10$  ns for cells of efficiency 13–16% [58]), which could contribute to the relatively low  $V_{\text{oc}}$  in our IBM-CIGSSe cell (Table 17.1).

Using similar analysis, minority carrier lifetime for the champion CZTSSe solar cell is also extracted. However, in contrast to the CIGSSe solar cell, even when the quadratic recombination processes are taken into account, the TRPL data cannot be adequately fit with a single lifetime. Lifetimes ranging from 5 to 8 ns for the CZTSSe solar cell are obtained as the timescale increases. The observed bending in the TRPL spectrum for the CZTSSe solar cell may be understood once the prospective spatial inhomogeneity of the sample is taken into account. Under the assumption of an inhomogeneous CZTSSe layer, the measured TRPL signal would have individual contributions from different regions with varying lifetimes. Although the regions with shorter lifetimes will luminesce strongly at shorter timescales, eventually longer-lifetime regions dominate the TRPL signal, giving rise to the bending behavior and larger lifetimes at longer timescales.

Except for the non-linearity observed for the CZTSSe samples, the room-temperature TRPL data presented in Figure 17.9a and b for the CIGSSe and CZTSSe solar cells do not show a significant difference in terms of the minority carrier lifetime and therefore cannot account for the observed difference in  $V_{\text{oc}}$  (or  $V_{\text{oc}}$  deficit). More surprisingly, once the samples are cooled to 4 K, a dramatic contrast develops between CIGSSe and CZTSSe samples; the lifetime at 4 K is only slightly enhanced compared to the 300 K value for CIGSSe, whereas for CZTSSe the lifetime increases by more than three orders of magnitude and reaches values close to 10  $\mu\text{s}$  as shown in Figure 17.9 [56]. Conventionally, long lifetimes are believed to be beneficial for solar cell performance. However, this drastic increase in lifetime for CZTSSe samples upon cooling can readily be understood in the context of electrostatic potential fluctuations, which can potentially be a fundamental performance bottleneck for current-generation CZTSSe devices [56]. In the case of electrostatic potential fluctuations, as illustrated in Figure 17.10d, the electrons and holes are spatially separated and any recombination process requires the tunneling of carriers. Moreover because of insufficient thermal energy at reduced temperatures, these electron and holes cannot jump over the fluctuations and therefore become localized in these wells. The electrons and holes separated by short distances rapidly recombine. However, the majority of the carriers

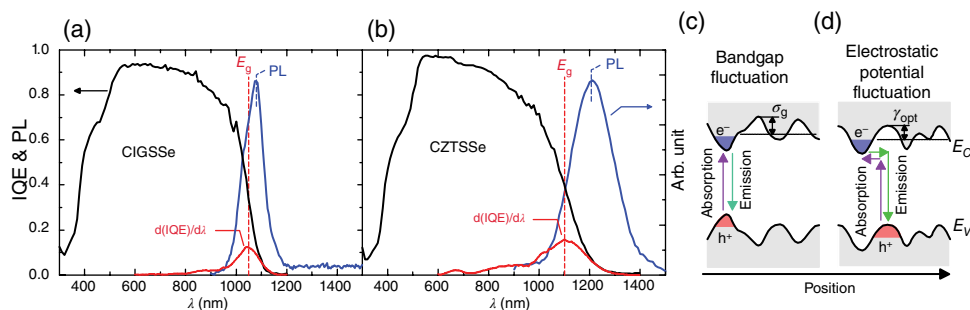


**Figure 17.9** Time-resolved photoluminescence data at temperatures 4 K and 300 K for: (a) CIGSSe; and (b) CZTSSe. The minority carrier lifetime increases dramatically at low temperature for CZTSSe. Reproduced with permission from [56]. Copyright © AIP Publishing, 2013

are separated by high barriers at larger distances and therefore the recombination time becomes large [59]. Note that the previously discussed bending in the room-temperature TRPL spectrum becomes more pronounced at low temperature, consistent with the increasing significance of the electrostatic fluctuations at low temperature.

One obvious consequence of the electrostatic potential fluctuations is the formation of band tail states below the true band-gap energy of the CZTSSe absorber. Important quantitative information regarding the severity of band tails in CZTSSe can be obtained by comparing the internal quantum efficiency (IQE) and the PL spectra of hydrazine-processed CIGSSe (15.0% efficiency) and CZTSSe (10.7% efficiency) devices, as shown in Figure 17.10. These data are obtained using the relation  $\text{IQE} = \text{EQE}/(1-R)$ , where  $R$  is





**Figure 17.10** Band-tailing issue in CZTSSe. The internal quantum efficiency, band gap as determined from the IQE inflection point, and the photoluminescence spectra of high-performance (a) CIGSSe ( $E_g = 1.19$  eV) and (b) CZTSSe ( $E_g = 1.13$  eV) devices. (c) Band-gap fluctuations and (d) electrostatic potential fluctuations. Reproduced with permission from [56]. Copyright © AIP Publishing, 2013

the reflectivity of the sample. The IQE curves for the two samples are similar for a wavelength range higher than  $E_g$ . However, below  $E_g$  there are notable differences, with IQE decreasing precipitously for CIGSSe whereas for CZTSSe the decay is more gradual. Moreover, the PL spectra illustrated in Figure 17.10 show marked differences. Normally, in a clean semiconductor with a low defect concentration, the room-temperature PL spectrum peaks at an energy  $k_B T/2$  higher than  $E_g$  [3]. Although for CIGSSe the PL peak is close to the  $E_g$  value determined from IQE, for CZTSSe the PL peak is shifted to lower energy relative to  $E_g$ . Furthermore, the width of the PL peak is also larger for CZTSSe compared to CIGSSe films. Slow decay in the IQE below  $E_g$ , a red shift of the PL peak relative to  $E_g$ , and broadening of the PL peak can all be attributed to more severe band tailing in CZTSSe samples. It is clear from the IQE data in Figure 17.10 that the tail region is roughly twice as severe for CZTSSe compared to CIGSSe.

It could be argued that the formation of band tails may also result from band-gap fluctuations, as illustrated in Figure 17.10c. As discussed by Gokmen *et al.* [56], although these two models may have different functional forms in terms of predicting the density of states, absorption spectra, and photoluminescence spectra below the band gap, they are equally good at explaining the features observed in IQE and PL. However, the distinction between band gap and electrostatic potential fluctuations can readily be made from the low-temperature TRPL data. In the case of band-gap fluctuations, electrons and holes are not in general spatially separated and therefore enhanced lifetimes at low temperatures are not expected. The low-temperature TRPL data therefore suggest that a dominant contribution to the observed band tailing in CZTSSe samples comes from the electrostatic potential fluctuations [56].

For a non-uniform sample with tailing in the density of states, the maximum achievable  $V_{oc}$  should be reduced compared to the uniform sample, due to recombination mediated by the tail states [3, 60]. Even though a model was presented by Rau and Werner [3] for the case of band-gap fluctuations, this cannot be directly applied to CZTSSe because electrostatic potential fluctuations are likely a dominant factor giving rise to the tail states in CZTSSe, as discussed above. For a disordered material with electrostatic potential fluctuations, depending on the correlation between defect complexes and the type of defects that

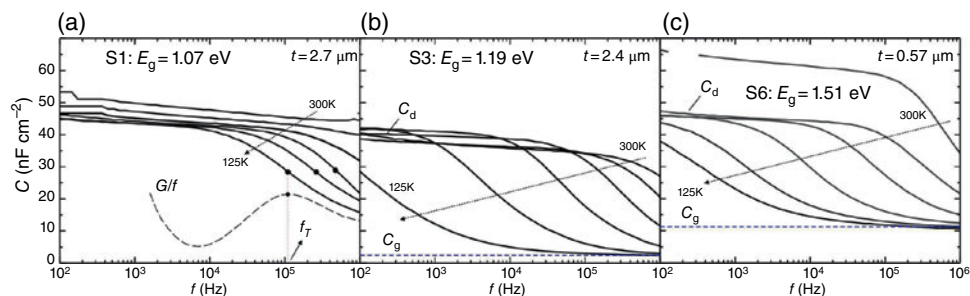
are forming, band tails with different functional forms are predicted [61]. Given the lack of knowledge regarding the density of states in the forbidden gap for CZTSSe, the behavior of  $V_{oc}$  cannot currently be accurately modeled. However, from the above discussion one dominant mechanism of open-circuit voltage reduction and therefore of efficiency limitation in CZTSSe is likely the more severe band tailing as indicated by IQE and PL measurements. Clearly, an important area for future exploration is the more detailed mapping of the density of states in the band gap, so that more meaningful modeling can be conducted.

Low-temperature (4 K) PL study has also been performed on high-performance sulfide kesterite (CZTS) [62, 63]. The PL spectra have been studied with increasing laser excitation intensity and show a blue shift of the low-energy ( $\sim 1.14$  eV) intensity peak, which is related to the “quasi-donor acceptor pair” (QDAP) defect density. This study yields an estimate of QDAP defect density of as much as  $5 \times 10^{19} \text{ cm}^{-3}$ , consistent with the tail states analysis study based on the EQE data in CZTSSe [56]. The PL study of several CZTS samples has shown that this defect density is well correlated with the open-circuit voltage and efficiency [63].

### 17.2.5 Admittance Spectroscopy

In this section we investigate some important electronic properties of the CZTSSe materials using admittance (capacitance) spectroscopy.

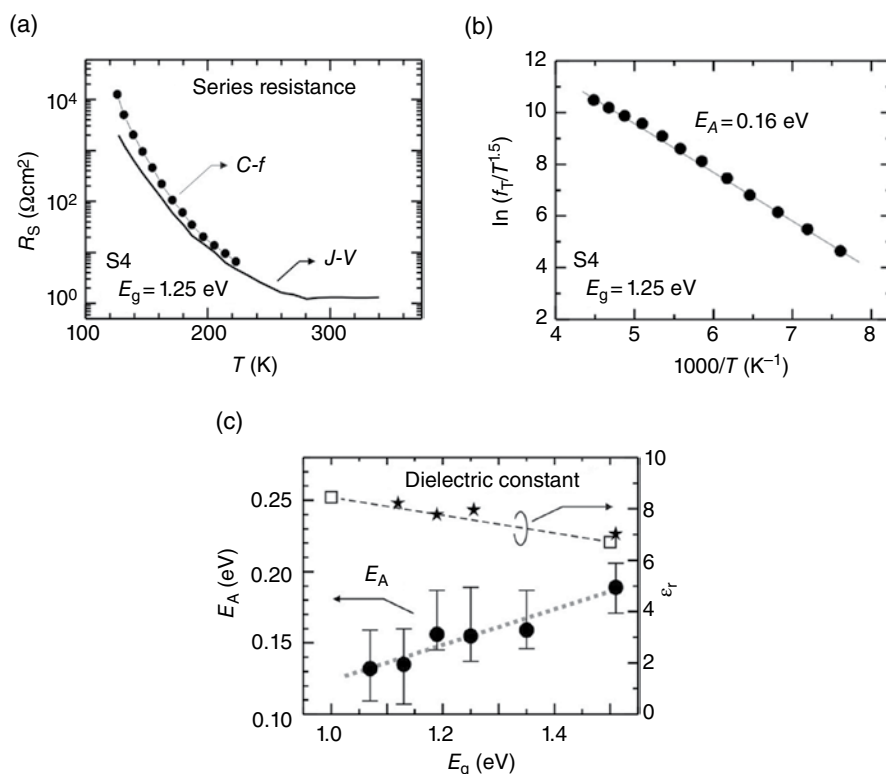
Figure 17.11 shows the capacitance spectra of three high-performance CZTSSe cells (PCE  $\approx 8$ –10%), spanning a band-gap range of 1.1–1.5 eV and taken at temperatures of 125–300 K under dark conditions. There are several distinctive characteristics of the CZTSSe admittance spectra. First, the low-temperature CZTSSe capacitance spectra are rather unique compared to most high-performance CIGSSe cells [65] in that they converge at the highest frequency and medium temperature (120–200 K) to a low capacitance value, namely the geometric capacitance of the cell ( $C_g$ ). This is especially evident for the medium- and high-band-gap samples ( $E_g = 1.19$  and 1.51 eV). The transition frequency to the geometric capacitance is denoted  $f_T$ . In the geometric capacitance regime the dielectric freeze-out effect occurs in the CZTSSe absorber layer because the electrical conductivity



**Figure 17.11** Capacitance spectra of three CZTSSe cells ( $T = 125, 155, 185, 225, 260$ , and  $300$  K) with various band gaps: (a) 1.07 eV; (b) 1.19 eV; and (c) 1.51 eV. The transition frequencies  $f_T$  of the dielectric freeze-out effect are obtained from the peaks of the  $G/f$  curves, where  $G$  is the conductance (black filled circles in panel (a)). The average thickness of the CZTSSe layer  $t$  is indicated in each case. Reproduced with permission from [64]. Copyright © AIP Publishing, 2012

is too low and the system cannot respond fast enough to the high-frequency AC excitation, causing the system to behave like an insulator [66].

The geometric capacitance of the absorber layer is given as  $C_g = \epsilon A_c / t$ , where  $A_c$  is the cell area,  $\epsilon$  is the dielectric constant, and  $t$  is the absorber layer thickness, which can be determined using scanning electron microscopy (SEM). Using these data we can calculate the dielectric constants for the CZTSSe absorbers as shown in Figure 17.12c, which are in reasonable agreement with a theoretical calculation that yields  $\epsilon$  in the range 6.7–8.5 [67] (dashed line in Fig. 17.12c). Note that the dielectric constant decreases with band gap, which has important implication for the tail states issues in CZTSSe as described in the previous section. In CIGSSe, the transition frequency  $f_T$  occurs at much higher frequencies (c. 10 MHz) and is almost independent of temperature ( $125 < T < 300$  K) [66], implying that CIGSSe has a higher conductivity and sustained free hole density, consistent with the fact that CIGSSe is found to have shallow acceptors (thought to be mainly due to copper vacancies,  $V_{Cu}$ ) and reasonably high values for hole mobility ( $2\text{--}20\text{ cm}^2\text{ V}^{-1}\text{ s}^{-1}$ ) [66].



**Figure 17.12** (a) Solar cell series resistance deduced from the dark J–V curves and from capacitance spectra (C–f) (also collected in the dark), demonstrating reasonable agreement. (b) Acceptor level determination from  $\ln(f_T/T^{1.5})$  plot. (c) Summary of the acceptor level and dielectric constants  $\epsilon$  determined from the capacitance spectra. The square points are the theoretical values of  $\epsilon$  [67], the dashed line is the linear interpolation, and the star points are the experimental data. Reproduced with permission from [64]. Copyright © AIP Publishing, 2012

We can relate the transition frequency  $f_T$  values to the electrical characteristics using an admittance circuit model of a depletion region in series with the undepleted quasi-neutral region [66]:

$$\omega_T = \frac{C_g \sigma}{C_d \epsilon} \quad (17.5)$$

where  $\omega_T = 2\pi f_T$ ,  $\sigma$  is the conductivity of the CZTSSe layer, and  $C_d$  is the depletion capacitance, which is the capacitance plateau at lower frequencies. These transition frequencies  $f_T$  can be obtained from the peak values of the  $G/f$  spectra near the transition as shown in Figure 17.11a, where  $G$  is the conductance and  $f$  is the frequency, allowing us to calculate  $\sigma$  as a function of temperature. The transition frequency and thus  $\sigma$  drops rapidly at lower temperature, indicating a large increase in the solar cell series resistance at lower temperature, which in turn quenches the fill factor. Indeed, this quenching of the fill factor has been observed in temperature-dependent measurements for all CZTSSe cells examined to date [1, 40].

To compare with previous measurements of series resistance, we calculate the solar cell dark series resistance (normalized by area)  $R_s$  in the low-temperature regime based on the  $\omega_T$  values from the capacitance spectra using  $R_s = \rho t = C_g t / C_d \omega_T \epsilon$ , where  $\rho$  is the bulk resistivity of the absorber layer. These  $R_s$  values are compared with those extracted directly from the  $J$ - $V$  curves using Sites' method [38] following the relationship:

$$\frac{dV}{dJ} = R_s + \frac{nk_B T}{q(J - G_s V)} \quad (17.6)$$

where  $G_s$  is the shunt conductance, and good consistency is observed between the two as shown in Figure 17.12a. This suggests that indeed the bulk conductivity dominates the series resistance in the CZTSSe device at low temperature.

The conductivity in the bulk CZTSSe is given as  $\sigma = qp\mu_h$  where  $p$  and  $\mu_h$  are the free hole density and mobility, respectively. If the acceptor level  $E_A$  is deep, carrier freeze-out will occur at moderately low temperatures ( $T \approx 100$ – $200$  K) and the free hole density will drop. We assume one dominant acceptor and enough donors to provide a substantial degree of compensation ( $N_D/N_A > 0.1$ ). In the carrier freeze-out regime, the free hole density exhibits a thermally activated behavior [68]:

$$p = \frac{(N_A - N_D)N_V}{4N_D} \exp\left(-\frac{E_A}{k_B T}\right), \quad (17.7)$$

where

$$N_V = 2 \left( \frac{2\pi m_h^* k_B T}{\hbar^2} \right)^{3/2} \quad (17.8)$$

is the effective density of states of the valence band,  $m_h^*$  is the hole effective mass and  $\hbar$  is the reduced Planck's constant. Assuming the mobility is weakly temperature dependent in

this temperature range, we can extract the acceptor energy level  $E_A$  from the plot of  $\ln(\sigma/T^{1.5})$  or  $\ln(f_T/T^{1.5})$  v.  $1/T$  obtaining, for example,  $E_A = 0.16$  eV for the cell with band gap  $E_g = 1.25$  eV, as shown in Figure 17.12b.

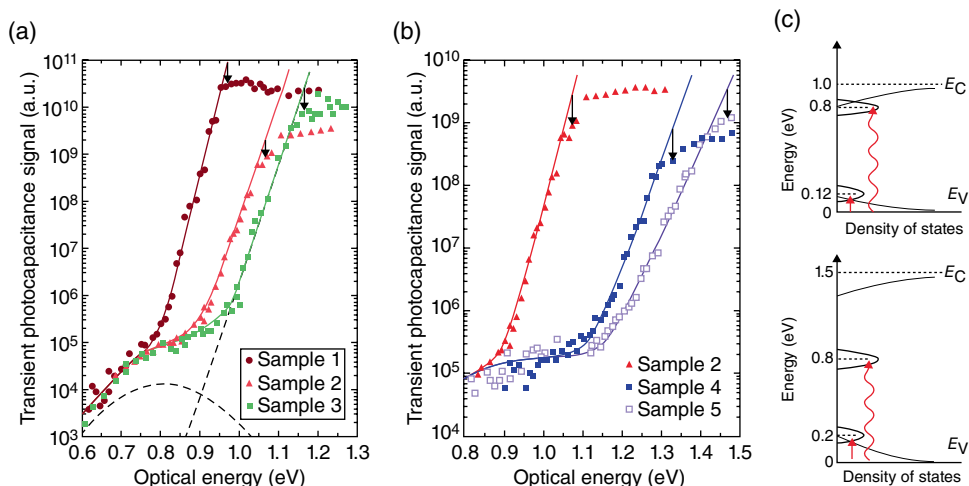
The admittance spectroscopy analysis is repeated on several CZTSSe cells with varying band gaps and the acceptor levels ( $E_A$ ) and dielectric constants are compared in Figure 17.12c. The acceptor level values span the range 0.13–0.20 eV, increasing with band gap. These relatively deep acceptor values appear to be consistent with theoretical studies indicating that the dominant acceptor impurities in CZTSSe are not shallow copper vacancies  $V_{Cu}$  as in CIGSSe, but rather deeper defects such as the  $Cu_{Zn}$  antisite, which becomes dominant because of lower formation energy [32, 69]. This lack of shallow acceptor in CZTSSe could be the main contributing factor to high and diverging series resistance at low temperature, which quenches the fill factor and efficiency as discussed in Section 17.2.3. Two factors contribute to the upward trend of the acceptor level with increasing band gap: (1) the decrease in the dielectric constant with higher band gap; and (2) the shrinking of the lattice constant due to increasing anion substitution from selenium to sulfur. Both effects tend to increase all energy levels within the crystal.

In this analysis, we assume that the freeze-out effect is due to a single deep acceptor level with well-defined activation energy. However, a similar effect could be obtained in a highly doped and highly compensated semiconductor. In this system the defect states start to overlap and broaden in energy and, at high enough concentrations, defect states merge with the valence band and form tail states (see section 17.2.4). This will also lead to a similar freeze-out effect to that discussed above.

### 17.2.6 Transient Photocapacitance

The capacitance spectroscopy described previously can only reveal shallow defect levels not far from the valence band ( $<0.2$  eV). To investigate electrical defects deeper in the CZTSSe band gap, transient photocapacitance (TPC) spectroscopy can be performed. Figure 17.13 shows TPC spectra of five CZTSSe cells spanning a large variation of  $[S]/[Se]$  ratios or band gaps, with PCE in the range 8–9% except for the highest band-gap sample (PCE  $\approx 6.5\%$ ) [70]. TPC measurement produces spectra that appear qualitatively similar to sub-band-gap absorption spectra. However, in this case the signal results from the charge that is optically released from the CZTSSe depletion region due to the device junction rather than the absorbed optical energy. This method directly probes the active power-generating region of the solar cell and is therefore more sensitive than optical absorption measurements. For more details of the TPC method, refer to Gelatos *et al.* [71], Heath *et al.* [72], and Cohen *et al.* [73].

The TPC spectra for the CZTSSe samples reveal a band-tail region with Urbach energies at or below 18 meV for the low band gap ( $E_g < 1.4$  eV) samples, but in the  $\sim 30$  meV range for the higher-band-gap samples [70]. Interestingly, we also observe a deeper defect band centered near 0.8 eV from the valence band in most of the samples (shown as the dashed parabola in Fig. 17.13a). The deeper defect band is remarkably similar to that observed in TPC studies of the CIGS alloys [72]. The location of this 0.8 eV defect center is relatively fixed with respect to the valence band as illustrated in Figure 17.13c. For higher-band-gap CZTSSe, this defect level moves closer to mid-gap and becomes a more efficient carrier recombination center. Although the origin of this 0.8 eV defect in the CZTSSe (similar to

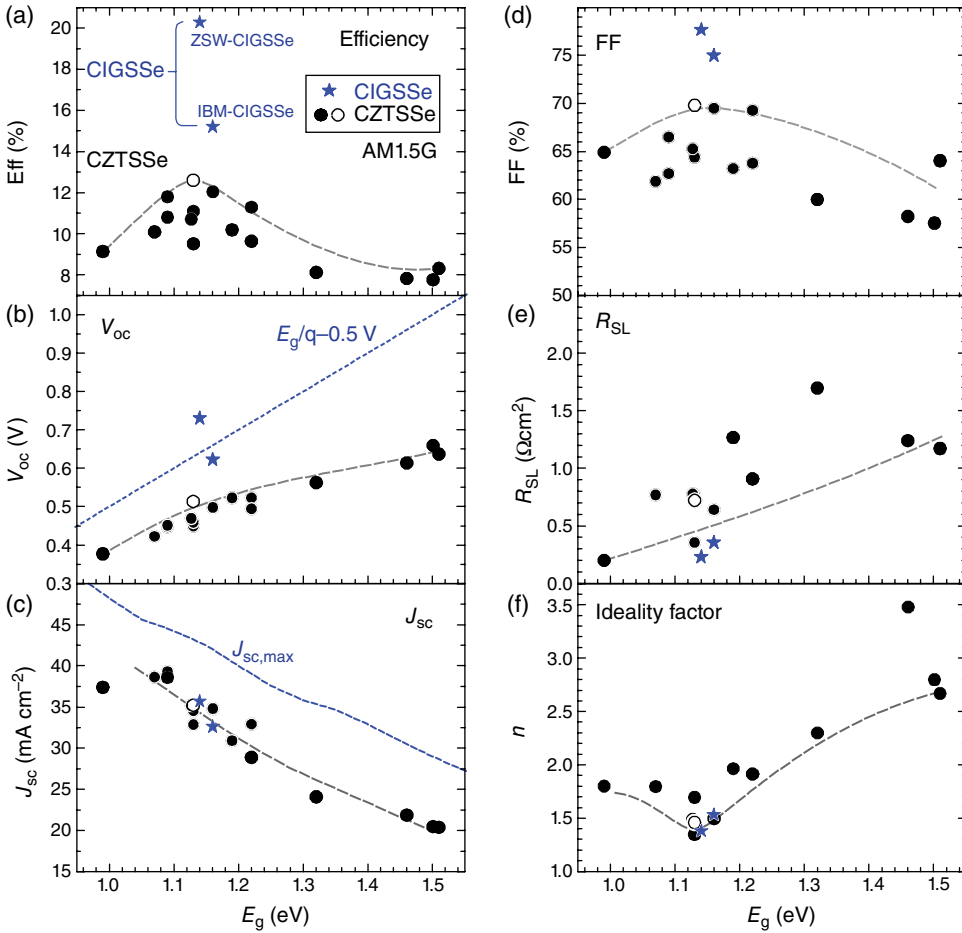


**Figure 17.13** Transient photocapacitance spectra for five CZTSSe samples obtained at 220 K and 5 kHz ( $E_g = 1.07, 1.15, 1.20, 1.47$ , and  $1.51$  eV for samples 1–5, respectively). Sample 5 is pure CZTS. (a) Comparison of the three lower-band-gap samples. All exhibit narrow band tails and also a deeper roughly Gaussian-shaped defect band of transitions centered near 0.8 eV. The dashed line indicates the underlying density of transitions for sample 3. The small arrows at the top indicate estimates of the optical gaps for these samples based on these TPC spectra. (b) Comparison of the TPC spectra for the two higher-band-gap samples along with a replot of the sample 2 TPC spectra for comparison. For these higher-band-gap samples the band tail is much broader. The energy distribution of the deeper band of transitions is less clear. Note that the scales in (a) and (b) are slightly different. (c) Observed defect bands in low- (1.0 eV) and high- (1.5 eV) band-gap CZTSSe showing thermal (straight) and optical transitions (wavy arrow). Reproduced with permission from [70]. Copyright © AIP Publishing, 2012

CIGSSe) samples remains unknown, this feature and the correspondingly higher Urbach energy at a higher band gap likely contributes to declining  $V_{oc}$  and efficiency in cells with a higher band gap [70].

### 17.2.7 Band-Gap-Dependent Characteristics

In this section we review general band-gap-dependent characteristics of top-performing CZTSSe cells that have been reported across the full band gap range (1.0–1.5 eV) and benchmarked against champion-level CIGSSe cells: 20.3% ZSW-CIGSSe [26] and the 15.2% hydrazine-processed IBM-CIGSSe [25] (Fig. 17.14). The band gap is obtained from the inflection of the EQE data near the band edge [28, 76]. First, from Figure 17.14a, the peak efficiency for the CZTSSe cells falls at approximately  $E_g = 1.13$  eV. This is remarkably similar to the “empirical” optimum band gap of CIGSSe at 1.14 eV [39], suggesting some underlying similarities between the two systems [77]. There are competing effects that give rise to the optimal band gap in CZTSSe. In general, in accordance with the Shockley–Queisser analysis, peak efficiency should occur at around 1.15–1.35 eV (using the AM1.5G solar spectrum) [2, 3]. However, in CZTSSe devices, the  $V_{oc}$  deficit, FF, and  $J_{sc}$



**Figure 17.14** Performance characteristics of top-performing CZTSSe devices (solid circles [11, 16, 17, 23, 74, 75] and hollow circle for recent 12.6% champion [24]) as compared with reference CIGSSe cells (star points [25, 26]) across the full spectrum of band gaps under standard conditions (AM1.5G, room temperature): (a) efficiency and (b) open circuit voltage; dotted line represents  $(E_g/q) - 0.5$  [V] line. (c) Short-circuit current; dotted curve indicates the maximum  $J_{sc}$  assuming 100% EQE (Eq. 17.1). (d) Fill factor and (e) series resistance extracted under light [38]. (f) Ideality factor under light; grey dashed curves are guide for the eyes. The highest-band-gap ( $\sim 1.5$  eV) sample is pure CZTS [10, 49] and the lowest-band-gap ( $\sim 1.0$  eV) sample is pure CZTSe [11]

(relative to  $J_{sc,max}$ ; (Equation 17.1)) tend to degrade at a higher band gap, thereby pushing the optimal band gap to lower values in the current generation of devices.

Figure 17.14b shows the  $V_{oc}$  versus band gap data for a full range of CZTSSe (and CIGSSe) devices. An empirical line of  $V_{oc} = (E_g/q) - V_{oc}$  [V] is also shown as a reference to mark the approximate  $V_{oc}$  of the top-performing CIGSSe cells [48]. The best  $V_{oc}$  deficit ( $\sim 0.62$  V) is obtained for the 9.15% selenide kesterite (CZTSe,  $E_g \approx 1.0$  eV) [11] and for the

12.6% champion CZTSSe device ( $E_g = 1.13$  eV) [24]. We observe that the  $V_{oc}$  does not increase proportionately with the band gap, that is, the  $V_{oc}$  deficit increases at higher band gap. Interestingly, this behavior has also been observed in CIGSSe alloys [78, p. 326]. Several factors can account for this effect. First, the deep level defect centered at 0.8 eV from the valence band as revealed by the TPC study (Section 17.2.6) may serve as a more severe recombination center for higher-band-gap devices [70]. Second, the CZTSSe dielectric constant is lower ( $\epsilon_r = 6.7$ ) for higher-band-gap compositions [64, 67], which leads to less-effective screening and more severe potential fluctuations and tail states [56]. Note that in the CIGSSe alloy, there is also another known factor leading to a larger  $V_{oc}$  deficit at a higher band gap; the conduction band offset of the buffer–absorber interface at high band gap becomes cliff-like [78, p. 327], which leads to lower  $V_{oc}$  [46]. However, a UV photoelectron spectroscopy study in CZTSSe yields a favorable spike-like alignment for all CZTSSe samples, including the sulfide kesterite samples (CZTS,  $E_g \approx 1.5$  eV) [53]. This spike-like conduction band offset was confirmed for a pure-Se CZTSe structure in a separate study [79]. Interestingly, one study using inverse and conventional photoemission on different samples did indicate a cliff-like conduction band offset for the sulfide kesterite (CZTS) samples [54]. This discrepancy in our understanding for high-band-gap CZTSSe devices must be resolved in order to have a full appreciation of the mechanisms of  $V_{oc}$  suppression in CZTSSe devices.

Figure 17.14c shows the  $J_{sc}$  versus band gap plot. For comparison, we also plot  $J_{sc,max}$  as a reference. Surprisingly, the  $J_{sc}$  values for the CZTSSe cells are already similar to those of high-performing CIGSSe devices. Presumably, this performance parity can be partially attributed to the tail states that fortuitously increase the sub-band-gap absorption. Note that  $J_{sc}/J_{sc,max}$  tends to drop at higher band gap. This behavior is associated with reduced collection efficiency of the CZTSSe device at higher band gap, which weakens the long-wavelength quantum efficiency response [1]. Similar weaker collection efficiency behavior has also been observed in CIGSSe over a range of band gaps [80].

The FF values do not change dramatically with band gap (there seems to be an optimum of  $\sim 1.13$  eV) as shown in Figure 17.14d. There are two competing factors that control the FF variation with respect to band gap. First, at higher band gaps, higher  $V_{oc}$  tends to increase the FF according to Equation (17.2). Unfortunately, the series resistance increases significantly with higher sulfur content (or band gap) as shown in Figure 17.14e. The lowest series resistance can be obtained from the lowest band gap CZTSSe [11, 23]. Finally, the trend in efficiency seems to be reflected by the trend in ideality factor  $n$  in Figure 17.14f; that is, the lowest ideality factors are found in the optimum band-gap region of  $\sim 1.13$  eV, which is reasonable as more recombination paths will translate to higher ideality factor.

### 17.3 Summary

In this review, key characteristics of high-performance CZTSSe devices produced mostly by hydrazine-based processing have been presented. Surprisingly, the  $J_{sc}$  values (relative to  $J_{sc,max}$ ) of the top-performing CZTSSe cells are already similar to those of the high-performance CIGSSe cells, partly due to the fortuitous band-tailing effect that extends the EQE curve beyond the band-gap cut-off wavelength. Photoluminescence (spectral and time resolved) and quantum efficiency studies give evidence of the existence of this band tailing,



which is attributed to potential fluctuations induced by strong compensation in CZTSSe. Unfortunately, as mentioned above, the same tail states are also at least partly responsible for the severe  $V_{oc}$  deficit in CZTSSe. Indeed, the  $V_{oc}$  deficit ( $V_{oc,def} = (E_g/q) - V_{oc}$ ) has been identified as the main problem in the present generation of CZTSSe technology, with the best value of  $V_{oc,def} \approx 0.62$  V being achieved for the selenide kesterite device (CZTSe,  $E_g \approx 1.0$  eV) and the 12.6% champion CZTSSe device ( $E_g = 1.13$  eV). The elevated  $V_{oc}$  deficit could arise from bulk (defects and tail states, including the deep  $\sim 0.8$  eV defect detected by the transient photocapacitance in Section 17.2.6) and/or interface recombination (as suggested by the temperature-dependence study of  $V_{oc}$ ). A more conclusive characterization effort is still needed to deconvolve the physical origin of various recombination processes. Although enhanced series resistance can contribute to reduced FF, especially for larger-band-gap ( $E_g > 1.2$  eV) samples, the low  $V_{oc}$  still dominates the suppression of FF. We therefore see that reducing the  $V_{oc}$  deficit plays a critical role in increasing efficiency in the CZTSSe family of devices.

Capacitance spectroscopy also reveals distinct characteristics of the CZTSSe films, showing that CZTSSe lacks shallow acceptor impurities. The carrier concentration is dominated by a deeper acceptor, giving rise to diverging series resistance at low temperatures, which quenches the fill factor and efficiency. Concomitantly, at low temperature and high frequency the capacitance collapses to the geometric value, which allows us to extract the dielectric constant in CZTSSe. Low dielectric constant in CZTSSe especially at high band gaps is unfavorable, as it leads to more severe potential fluctuation and tail states. TPC measurement further reveals a deep defect level at 0.8 eV from the valence band and a more substantial band tail (higher Urbach energy) that likely contributes to increased  $V_{oc}$  deficit at high band gaps. Similar findings have been observed in the CIGSSe alloy [72], which suggests a possible explanation for the remarkably similar optimum band gap ( $E_g \approx 1.14$  eV) in the CIGSSe and CZTSSe systems.

The steady march of increasing efficiency (Figure 17.1) so far suggests that CZTSSe technology will be able to ultimately compete with the incumbent thin-film technologies such as CdTe and CIGSSe. In this regards, several recent reports are particularly promising. Monolithically integrated CZTS sub-modules with a record efficiency of 9.2% for a 25 cm<sup>2</sup> aperture area have been demonstrated by Solar Frontier [14]. There have also been serious attempts to move towards a totally Cd-free system by replacing the CdS-based buffer with non-Cd-based buffers in single cells [81] and sub-modules [12]. Furthermore, besides targeting device-efficiency improvements, we need to address the CZTSSe device performance stability. It is yet to be conclusively determined whether CZTSSe devices behave more like Cu<sub>2</sub>S or like CIGSSe in terms of device stability under various operating conditions (e.g. light, heat, electrical load). All these concerted efforts will help to realize CZTSSe as a high-performance, Earth-abundant and commercially viable PV technology.

## Acknowledgements

The IBM CIGSSe research was conducted as part of a joint development project between Tokyo Ohka Kogyo Co., Ltd. and IBM Corporation. The analogous CZTSSe work was performed as part of a joint development project between Tokyo Ohka Kogyo Co., Ltd., DelSolar Co., Ltd., Solar Frontier K. K. and IBM Corporation. This material is based upon work supported by the US Department of Energy under Award Number DE-EE0006334.

## References

- [1] Mitzi, D. B., Gunawan, O., Todorov, T. K., Wang, K. & Guha, S. (2011) The path towards a high-performance solution-processed kesterite solar cell. *Solar Energy Materials and Solar Cells*, **95**, 1421–1436.
- [2] Shockley, W. & Queisser, H. J. (1961) Detailed balance limit of efficiency of *p-n* junction solar cells. *Journal of Applied Physics*, **32**, 510–519.
- [3] Rau, U. & Werner, J. H. (2004) Radiative efficiency limits of solar cells with lateral band-gap fluctuations. *Applied Physics Letters*, **84**, 3735.
- [4] Katagiri, H., Sasaguchi, N., Hando, S., Hoshino, S., Ohashi, J. & Yokota, T. (1997) Preparation and evaluation of  $\text{Cu}_2\text{ZnSnS}_4$  thin films by sulfurization of E-B evaporated precursors. *Solar Energy Materials and Solar Cells*, **49**, 407–414.
- [5] Katagiri, H., Jimbo, K., Maw, W. S., Oishi, K., Yamazaki, M., Araki, H. & Takeuchi, A. (2009) Development of CZTS-based thin film solar cells. *Thin Solid Films*, **517**, 2455–2460.
- [6] Friedlmeier, T. M., Wieser, N., Walter, T., Dittrich, H. & Schock, H. W. (1997) Heterojunctions based on  $\text{Cu}_2\text{ZnSnS}_4$  and  $\text{Cu}_2\text{ZnSnSe}_4$  thin films. In *Proceedings of 14th European Photovoltaic and Solar Energy Conference*, 30 June–4 July, 1242–1245.
- [7] Jimbo, K., Kimura, R., Kamimura, T., Yamada, S., Maw, W. S., Araki, H., Oishi, K. & Katagiri, H. (2007)  $\text{Cu}_2\text{ZnSnS}_4$ -type thin film solar cells using abundant materials. *Thin Solid Films*, **515**, 5997–5999.
- [8] Katagiri, H., Jimbo, K., Yamada, S., Kamimura, T., Maw, W. S., Fukano, T., Ito, T. & Motohiro, T. (2008) Enhanced conversion efficiencies of  $\text{Cu}_2\text{ZnSnS}_4$ -based thin film solar cells by using preferential etching technique. *Applied Physics Express*, **1**, 41201.
- [9] Zoppi, G., Forbes, I., Miles, R. W., Dale, P. J., Scragg, J. J. & Peter, L. M. (2009)  $\text{Cu}_2\text{ZnSnSe}_4$  thin film solar cells produced by selenisation of magnetron sputtered precursors. *Progress in Photovoltaics: Research and Applications*, **17**, 315–319.
- [10] Shin, B., Gunawan, O., Zhu, Y., Bojarczuk, N. A., Chey, S. J. & Guha, S. (2013) Thin film solar cell with 8.4% power conversion efficiency using earth abundant  $\text{Cu}_2\text{ZnSnS}_4$  absorber. *Progress in Photovoltaics: Research and Applications*, **21**, 72.
- [11] Repins, I., Beall, C., Vora, N., DeHart, C., Kuciauskas, D., Dippo, P., To, B., Mann, J., Hsu, W. C., Goodrich, A. & Noufi, R. (2012) Co-evaporated  $\text{Cu}_2\text{ZnSnSe}_4$  films and devices. *Solar Energy Materials and Solar Cells*, **101**, 154.
- [12] Hiroi, H., Sakai, N. & Sugimoto, H. (2011) Development of high efficiency  $\text{Cu}_2\text{ZnSnS}_4$  solar cells and modules. In *Proceedings of 26th European Photovoltaic Solar Energy Conference and Exhibition*, 2448–2451.
- [13] Sugimoto, H., Hiroi, H., Sakai, N., Muraoka, S. & Katou, T. (2012) Over 8% efficiency  $\text{Cu}_2\text{ZnSnS}_4$  submodules with ultra-thin absorber. In *Proceedings of 38th IEEE Photovoltaic Specialist Conference*, 3–8 June 2012, 2997–3000.
- [14] Kato, T., Hiroi, H., Sakai, N., Muraoka, S. & Sugimoto, H. (2012) Characterization of front and back interfaces on CZTS thin film solar cells. In *Proceedings of 27th European Photovoltaic Solar Energy Conference and Exhibition*, 2236–2239.
- [15] Todorov, T. K., Reuter, K. B. & Mitzi, D. B. (2010) High-efficiency solar cell with earth-abundant liquid-processed absorber. *Advanced Materials*, **22**, E156–E159.
- [16] Barkhouse, D. A. R., Gunawan, O., Gokmen, T., Todorov, T. K. & Mitzi, D. B. (2012) Device characteristics of a 10.1% hydrazine-processed  $\text{Cu}_2\text{ZnSn}(\text{Se},\text{S})_4$  solar cell. *Progress in Photovoltaics: Research and Applications*, **20**, 6–11.
- [17] Todorov, T. K., Tang, J., Bag, S., Gunawan, O., Gokmen, T., Zhu, Y. & Mitzi, D. B. (2013) Beyond 11% efficiency: Characteristics of state-of-the-art  $\text{Cu}_2\text{ZnSn}(\text{S},\text{Se})_4$  solar cells. *Advanced Energy Materials*, **3**, 34–38.
- [18] Mitzi, D. B. (2005) Synthesis, structure, and thermal properties of soluble hydrazinium germanium (IV) and tin (IV) selenide salts. *Inorganic Chemistry*, **44**, 3755–3761.
- [19] Mitzi, D. B. (2007)  $\text{N}_4\text{H}_9\text{Cu}_7\text{S}_4$ : A hydrazinium-based salt with a layered  $\text{Cu}_7\text{S}_4$ -framework. *Inorganic Chemistry*, **46**, 926–931.
- [20] Mitzi, D. B., Kosbar, L. L., Murray, C. E., Copel, M. & Afzali, A. (2004) High-mobility ultrathin semiconducting films prepared by spin coating. *Nature*, **428**, 299–303.

- [21] Mitzi, D. B., Yuan, M., Liu, W., Kellock, A. J., Chey, S. J., Deline, V. & Schrott, A. G. (2008) A high-efficiency solution-deposited thin-film photovoltaic device. *Advanced Materials*, **20**, 3657–3662.
- [22] Yang, W., Duan, H. S., Bob, B., Zhou, H., Lei, B., Chung, C. H., Li, S. H., Hou, W. W. & Yang, Y. (2012) Novel solution processing of high-efficiency earth-abundant  $\text{Cu}_2\text{ZnSn}(\text{S},\text{Se})_4$  solar cells. *Advanced Materials*, **24**, 6323–6329.
- [23] Bag, S., Gunawan, O., Gokmen, T., Zhu, Y., Todorov, T. K. & Mitzi, D. B. (2012) Low band gap liquid-processed CZTSe solar cell with 10.1% efficiency. *Energy and Environmental Science*, **5**, 7060–7065.
- [24] Wang, W., Winkler, M. T., Gunawan, O., Gokmen, T., Todorov, T. K., Zhu, Y. & Mitzi, D. B. (2014) Device characteristics of CZTSSe thin film solar cell with 12.6% efficiency. *Advanced Energy Materials*, **4**, 1301465.
- [25] Todorov, T. K., Gunawan, O., Gokmen, T. & Mitzi, D. B. (2013) Solution-processed  $\text{Cu}(\text{In},\text{Ga})(\text{S},\text{Se})_2$  absorber yielding 15.2% efficient solar cell. *Progress in Photovoltaics: Research and Applications*, **21**, 82–87.
- [26] Jackson, P., Hariskos, D., Lotter, E., Paetel, S., Wuerz, R., Menner, R., Wischmann, W. & Powalla, M. (2011) New world record efficiency for  $\text{Cu}(\text{In},\text{Ga})\text{Se}_2$  thin film solar cells beyond 20%. *Progress in Photovoltaics: Research and Applications*, **19**, 894–897.
- [27] Assmann, L., Bernède, J. C., Drici, A., Amory, C., Halgand, E. & Morsli, M. (2005) Study of the Mo thin films and Mo/CIGS interface properties. *Applied Surface Science*, **246**, 159–166.
- [28] Wada, T., Kohara, N., Nishiwaki, S. & Negami, T. (2001) Characterization of the  $\text{Cu}(\text{In},\text{Ga})\text{Se}_2/\text{Mo}$  interface in CIGS solar cells. *Thin Solid Films*, **387**, 118–122.
- [29] Kohara, N., Nishiwaki, S., Hashimoto, Y., Negami, T. & Wada, T. (2001) Electrical properties of the  $\text{Cu}(\text{In},\text{Ga})\text{Se}_2/\text{MoSe}_2/\text{Mo}$  structure. *Solar Energy Materials and Solar Cells*, **67**, 209–215.
- [30] Abou-Ras, D., Kistorz, G., Bremaud, D., Kälin, M., Kurdesau, F. V., Tiwari, A. N. & Döbeli, M. (2005) Formation and characterisation of  $\text{MoSe}_2$  for  $\text{Cu}(\text{In},\text{Ga})\text{Se}_2$  based solar cells. *Thin Solid Films*, **480**, 433–438.
- [31] Scragg, J. J., Wätjen, J. T., Edoff, M., Ericson, T., Kubart, T. & Platzer-Björkman, C. (2012) A detrimental reaction at the molybdenum back contact in  $\text{Cu}_2\text{ZnSn}(\text{S},\text{Se})_4$  thin-film solar cells. *Journal of American Chemical Society*, **134**, 19330–19333.
- [32] Nagoya, A., Asahi, R., Wahl, R. & Kresse, G. (2010) Defect formation and phase stability of  $\text{Cu}_2\text{ZnSnS}_4$  photovoltaic material. *Physics Review B*, **81**, 113202.
- [33] Katagiri, H., Jimbo, K., Tahara, M., Araki, H. & Oishi, K. (2009) The influence of the composition ratio on CZTS-based thin film solar cells. *Materials Research Society Symposium Proceedings*, **1165**, M04-01.
- [34] Chen, S., Wang, L. W., Walsh, A., Gong, X. G. & Wei, S. H. (2012) Abundance of  $\text{Cu}_{\text{Zn}} + \text{Sn}_{\text{Zn}}$  and  $2\text{Cu}_{\text{Zn}} + \text{Sn}_{\text{Zn}}$  defect clusters in kesterite solar cells. *Applied Physics Letters*, **101**, 223901–4.
- [35] Scragg, J. J., Ericson, T., Kubart, T., Edoff, M. & Platzer-Björkman, C. (2011) Chemical insights into the instability of  $\text{Cu}_2\text{ZnSnS}_4$  films during annealing. *Chemistry of Materials*, **23**, 4625–4633.
- [36] Weber, A., Mainz, R. & Schock, H. W. (2010) On the Sn loss from thin films of the material system  $\text{Cu}-\text{In}-\text{Sn}-\text{S}$  in high vacuum. *Journal of Applied Physics*, **107**, 013516.
- [37] Wang, K., Shin, B., Reuter, K. B., Todorov, T., Mitzi, D. B. & Guha, S. (2011) Structural and elemental characterization of high efficiency  $\text{Cu}_2\text{ZnSnS}_4$  solar cells. *Applied Physics Letters*, **98**, 051912.
- [38] Sites, J. R. & Mauk, P. H. (1989) Diode quality factor determination for thin-film solar cells. *Solar Cells*, **27**, 411–417.
- [39] Contreras, M. A., Ramanathan, K., AbuShama, J., Hasoon, F., Young, D. L., Egaas, B. & Noufi, R. (2005) Diode characteristics in state-of-the-art  $\text{ZnO}/\text{CdS}/\text{Cu}(\text{In}_{1-x}\text{Ga}_x)\text{Se}_2$  solar cells. *Progress in Photovoltaics: Research and Applications*, **13**, 209–216.
- [40] Gunawan, O., Todorov, T. K. & Mitzi, D. B. (2010) Loss mechanisms in hydrazine-processed  $\text{Cu}_2\text{ZnSn}(\text{Se},\text{S})_4$  solar cells. *Applied Physics Letters*, **97**, 233506.
- [41] Green, M. A. (1981) Solar cell fill factors-general graph and empirical expressions. *Solid State Electronics*, **24**, 788.

- [42] Hegedus, S. S. & Shafarman, W. N. (2004) Thin-film solar cells: device measurements and analysis. *Progress in Photovoltaics: Research and Applications*, **12**, 155–176.
- [43] Burgelman, M., Engelhardt, F., Guillemoles, J. F., Herberholz, R., Igalson, M., Klenk, R., Lampert, M., Meyer, T., Nadenau, V., Niemegeers, A., Parisi, J., Rau, U., Schock, H. W., Schmitt, M., Seifert, O., Walter, T. & Zott, S. (1997) Defects in Cu(In,Ga)Se<sub>2</sub> semiconductors and their role in the device performance of thin-film solar cells. *Progress in Photovoltaics: Research and Applications*, **5**, 121–130.
- [44] Gunawan, O., Gokmen, T. & Mitzi, D. (2014) Suns- $V_{oc}$  characteristics of high performance kesterite solar cells. *Journal of Applied Physics*, **116**, 084504.
- [45] Gokmen, T., Gunawan, O. & Mitzi, D. B. (2013) Minority carrier diffusion length extraction in Cu<sub>2</sub>ZnSn(Se,S)<sub>4</sub> solar cells. *Journal of Applied Physics*, **114**, 114511.
- [46] Minemoto, T., Matsui, T., Takakura, H., Hamakawa, Y., Negami, T., Hashimoto, Y., Uenoyama, T. & Kitagawa, M. (2001) Theoretical analysis of the effect of conduction band offset of window/CIS layers on performance of CIS solar cells using device simulation. *Solar Energy Materials and Solar Cells*, **67**, 83–88.
- [47] Pysch, D., Mette, A. & Glunz, S. W. (2007) A review and comparison of different methods to determine the series resistance of solar cells. *Solar Energy Materials and Solar Cells*, **91**, 1698–1706.
- [48] Nadenau, V., Rau, U., Jasenek, A. & Schock, H. W. (2000) Electronic properties of CuGaSe<sub>2</sub>-based heterojunction solar cells. Part I. Transport analysis. *Journal of Applied Physics*, **87**, 584.
- [49] Wang, K., Gunawan, O., Todorov, T., Shin, B., Chey, S. J., Bojarczuk, N. A., Mitzi, D. & Guha, S. (2010) Thermally evaporated Cu<sub>2</sub>ZnSnS<sub>4</sub> solar cells. *Applied Physics Letters*, **97**, 143508.
- [50] Turcu, M., Pakma, O. & Rau, U. (2002) Interdependence of absorber composition and recombination mechanism in Cu(In,Ga)(Se,S)<sub>2</sub> heterojunction solar cells. *Applied Physics Letters*, **80**, 2598.
- [51] Scheer, R. (2009) Activation energy of heterojunction diode currents in the limit of interface recombination. *Journal of Applied Physics*, **105**, 104505-6.
- [52] Gloeckler, M. & Sites, J. R. (2005) Efficiency limitations for wide-band-gap chalcopyrite solar cells. *Thin Solid Films*, **480–481**, 241–245.
- [53] Haight, R., Barkhouse, A., Gunawan, O., Shin, B., Copel, M., Hopstaken, M. & Mitzi, D. B. (2011) Band alignment at the Cu<sub>2</sub>ZnSn(S<sub>x</sub>Se<sub>1-x</sub>)<sub>4</sub>/CdS interface. *Applied Physics Letters*, **98**, 253502.
- [54] Bär, M., Schubert, B. A., Marsen, B., Wilks, R. G., Pookpanratana, S., Blum, M., Krause, S., Unold, T., Yang, W. & Weinhardt, L. (2011) Cliff-like conduction band offset and KCN-induced recombination barrier enhancement at the CdS/Cu<sub>2</sub>ZnSnS<sub>4</sub> thin-film solar cell heterojunction. *Applied Physics Letters*, **99**, 222105.
- [55] Siebentritt, S. (2013) Why are kesterite solar cells not 20% efficient? *Thin Solid Films*, **535**, 1–4.
- [56] Gokmen, T., Gunawan, O., Todorov, T. K. & Mitzi, D. B. (2013) Efficiency limitation and band tailing in kesterite solar cells. *Applied Physics Letters*, **103**, 103506.
- [57] Ohnesorge, B., Weigand, R., Bacher, G., Forchel, A., Riedl, W. & Karg, F. H. (1998) Minority-carrier lifetime and efficiency of Cu(In,Ga)Se<sub>2</sub> solar cells. *Applied Physics Letters*, **73**, 1224.
- [58] Shirakata, S. & Nakada, T. (2007) Time-resolved photoluminescence in Cu(In,Ga)Se<sub>2</sub> thin films and solar cells. *Thin Solid Films*, **515**, 6151–6154.
- [59] Levanyuk, A. P. & Osipov, V. V. (1981) Edge luminescence of direct-gap semiconductors, *Soviet Physics Uspekhi*, **24**, 187.
- [60] Tiedje, T. (1982) Band tail recombination limit to the output voltage of amorphous silicon solar cells. *Applied Physics Letters*, **40**, 627–629.
- [61] Miegheem, P. V. (1992) Theory of band tails in heavily doped semiconductors. *Review of Modern Physics*, **64**, 755–793.
- [62] Gershon, T., Shin, B., Bojarczuk, N., Gokmen, T., Lu, S. & Guha, S. (2013) Photoluminescence characterization of a high-efficiency Cu<sub>2</sub>ZnSnS<sub>4</sub> device. *Journal of Applied Physics*, **114**, 154905.
- [63] Gershon, T., Shin, B., Gokmen, T., Lu, S., Bojarczuk, N. & Guha, S. (2013) Relationship between Cu<sub>2</sub>ZnSnS<sub>4</sub> quasi donor-acceptor pair density and solar cell efficiency. *Applied Physics Letters*, **103**, 193903.

- [64] Gunawan, O., Gokmen, T., Warren, C. W., Cohen, J. D., Todorov, T. K., Barkhouse, D. A. R., Bag, S., Tang, J., Shin, B. & Mitzi, D. B. (2012) Electronic properties of the  $\text{Cu}_2\text{ZnSn}(\text{Se},\text{S})_4$  absorber layer in solar cells as revealed by admittance spectroscopy and related methods. *Applied Physics Letters*, **100**, 253905.
- [65] Eisenbarth, T., Unold, T., Caballero, R., Kaufmann, C. A. & Schock, H. W. (2010) Interpretation of admittance, capacitance-voltage, and current-voltage signatures in  $\text{Cu}(\text{In},\text{Ga})\text{Se}_2$  thin film solar cells. *Journal of Applied Physics*, **107**, 034509–034512.
- [66] Lee, J. W., Cohen, J. D. & Shafarman, W. N. (2005) The determination of carrier mobilities in CIGS photovoltaic devices using high-frequency admittance measurements. *Thin Solid Films*, **480–481**, 336–340.
- [67] Persson, C. (2010) Electronic and optical properties of  $\text{Cu}_2\text{ZnSnS}_4$  and  $\text{Cu}_2\text{ZnSnSe}_4$ . *Journal of Applied Physics*, **107**, 053710.
- [68] Sze, S. M. (1981) *Physics of Semiconductor Devices*. John Wiley & Sons, New York.
- [69] Chen, S., Yang, J. H., Gong, X. G., Walsh, A. & Wei, S. H. (2010) Intrinsic point defects and complexes in the quaternary kesterite semiconductor  $\text{Cu}_2\text{ZnSnS}_4$ . *Physics Reviews B*, **81**, 245204.
- [70] Miller, D. W., Warren, C. W., Gunawan, O., Gokmen, T., Mitzi, D. B. & Cohen, J. D. (2012) Electronically active defects in the  $\text{Cu}_2\text{ZnSn}(\text{Se},\text{S})_4$  alloys as revealed by transient photocapacitance spectroscopy. *Applied Physics Letters*, **101**, 142106.
- [71] Gelatos, A. V., Mahavadi, K. K., Cohen, J. D. & Harbison, J. P. (1988) Transient photocapacitance and photocurrent studies of undoped hydrogenated amorphous silicon. *Applied Physics Letters*, **53**, 403–405.
- [72] Heath, J. T., Cohen, J. D., Shafarman, W. N., Liao, D. X. & Rockett, A. A. (2002) Effect of Ga content on defect states in  $\text{CuIn}_{1-x}\text{Ga}_x\text{Se}_2$  photovoltaic devices. *Applied Physics Letters*, **80**, 4540.
- [73] Cohen, J. D., Heath, J. T. & Shafarman, W. N. (2006) *Wide Gap Chalcophyrites*. Springer-Verlag, Heidelberg, Germany. Series in Material Science, vol. 86, pp. 6990.
- [74] Todorov, T. & Mitzi, D. B. (2010) Direct liquid coating of chalcopyrite light absorbing layers for photovoltaic devices. *European Journal of Inorganic Chemistry*, **2010**, 17–28.
- [75] Winkler, M. T., Wang, W., Gunawan, O., Hovel, H. J., Todorov, T. K. & Mitzi, D. B. (2014) Optical designs that improve the efficiency of  $\text{Cu}_2\text{ZnSn}(\text{S},\text{Se})_4$  solar cells. *Energy and Environmental Science*, **7**, 1029–1036.
- [76] Merdes, S., Johnson, B., Sáez-Araoz, R., Ennaoui, A., Klaer, J., Lauermann, I., Mainz, R., Meeder, A. & Klenk, R. (2009) Current transport in  $\text{Cu}(\text{In},\text{Ga})\text{S}_2$  based solar cells with high open circuit voltage-bulk vs. interface. *Materials Research Society Symposium Proceedings*, **1165**, M05–15.
- [77] Repins, I., Vora, N., Beall, C., Wei, S. H., Yan, Y., Romero, M., Teeter, G., Du, H., To, B., Young, M. & Noufi, R. (2011) Kesterites and chalcopyrites: A comparison of close cousins. *Materials Research Society Symposium Proceedings*, 1324.
- [78] Archer, M. D. & Hill, R. (2001) *Clean Electricity from Photovoltaics*. Imperial College Press, London, Series on Photoconversion of Solar Energy vol. 1.
- [79] Li, J., Wei, M., Du, Q., Liu, W., Jiang, G. & Zhu, C. (2013) The band alignment at  $\text{CdS}/\text{Cu}_2\text{ZnSnSe}_4$  heterojunction interface. *Surface and Interface Analysis*, **45**, 682–684.
- [80] Shafarman, W. N., Klenk, R. & McCandless, B. E. (1996) Device and material characterization of  $\text{Cu}(\text{InGa})\text{Se}_2$  solar cells with increasing band gap. *Journal of Applied Physics*, **79**, 7324–7328.
- [81] Barkhouse, D. A. R., Haight, R., Sakai, N., Hiroi, H., Sugimoto, H. & Mitzi, D. B. (2012) Cd-free buffer layer materials on  $\text{Cu}_2\text{ZnSn}(\text{S}_x\text{Se}_{1-x})_4$ : Band alignments with  $\text{ZnO}$ ,  $\text{ZnS}$ , and  $\text{In}_2\text{S}_3$ . *Applied Physics Letters*, **100**, 193904–193905.



# Subject Index

*Note: italic page numbers refer to tables and **bold** page numbers refer to figures.*

The following multinary compounds are abbreviated as shown in square brackets.  
 $\text{Cu}_2\text{ZnSnS}_4$  [CZTS];  $\text{Cu}_2\text{ZnSnSe}_4$  [CZTSe];  $\text{Cu}_2\text{ZnSn}(\text{S}_{1-x}\text{Se}_x)_4$  [CZTSSe];  
 $\text{Cu}_2\text{Zn}(\text{Sn}_{1-x}\text{Ge}_x)(\text{S}_{1-x}\text{Se}_x)_4$  [CZTGeSSe];  $\text{Cu}_3\text{SnS}_2$  [CTS];  $\text{Cu}_3\text{SnSe}_2$  [CTSe];  
 $\text{Cu}(\text{In}_{1-x}\text{Ga}_x)\text{S}_2$  [CIGS];  $\text{Cu}(\text{In}_{1-x}\text{Ga}_x)\text{Se}_2$  [CIGSe];  $\text{CuIn}(\text{S}_{1-x}\text{Se}_x)_2$  [CISSe].

- admittance spectroscopy
  - of CZTS, CZTSe and CZTSSe monograin-layer solar cells, 304, 305
  - of CZTSSe thin-film solar cells, 400–3, **400, 401**
- annealing *see* thermal treatment; thin-film growth
- anti-reflective coating (ARC), 215, 230, **240**, 338, **342**, 355, 364, **365**, 368
- atom probe tomography, of CZTSe absorbers, 380–1, **381** *see also* secondary phases
- band alignment, **396** *see also* conduction band offset
- band gap
  - of alloyed compounds CZTGeSSe, 263–4 CZTSSe, 83, 168–9, **169**, 370
  - of semiconductors, CZTS and related compounds
    - direct band gap, **15**, 29, 83, 165
    - indirect band gap, **15**, 165
  - Varshni equation, 166
- band-gap-dependent characteristics of CZTSSe thin-film solar cells, 364–6, **365**, **377**, 404–6, **405**
- band-gap fluctuation, 374, **399**, 399
- band structure of CZTS and CZTSe, theoretical approach to, 83, **84**, **163**
- density functional theory (DFT), historical, 76–7
- GW approximation, 79
- band tailing, 350, 354, 392, 397–400, **399**, **404**, 406–7
- band-to-band recombination, 9, 301, 373
- barrier height, 315–6, 321, 366–7, **368**
- Boeing process, for co-evaporation of CIGSe thin films, 234
- buffer layers
  - chemical-bath-deposited (CBD) CdS thin films, 35, 184, 185, 188–9, 199–200, **200**, 285
  - wurtzite-type CdS, 24–5, 28, 35
  - zinc-blende-type CdS, 24–5, 35
  - spray-deposited ZnO thin films, 35–6
- carrier freeze-out, 144–5, **145**, 377, 395, 402–3
- carrier lifetime
  - CIGSSe thin films, 397, **398**
  - CZTS thin films, 349, **350**
  - CZTSe thin films, 326, 357
  - CZTSSe thin films, 397, **398**

- carrier recombination, 19, 236, 403–4, **404**
- cell efficiency v. composition of CZTS thin films, **192, 230**
- chemical equilibrium
  - of CIGSe, 108–11, **109**
  - of CZTS and CZTSe, 112, **113**, 114–6, 258, 298
- chemical treatment *see also* device
  - characteristics; surface treatment of CZTS thin films
  - of CZTSSe monograins, 295–6, **297, 297**
  - improvement of device performance by
    - CIS and CIGS thin-film solar cells: KCN treatment, 27, 28
    - CZTS thin-film solar cells: KCN treatment, 232
    - CZTSSe monograin-layer solar cells: Br<sub>2</sub>-MeOH etching followed by KCN etching, 296–7, 297
    - CZTSSe thin-film solar cells: cyanide absorber etching prior to annealing (CAPRI) process, 363
- Clausius–Clapeyron equation, 222
- collection efficiency *see also* quantum efficiency
  - of CZTS thin-film solar cells, 324, 348–9, **349**, 357–8, **357**
  - of CZTSSe thin-film solar cells, 392–3, **392**
- composition of CZTS and CZTSe thin films, estimation by X-ray fluorescence (XRF), 191, 199, **206**, 209, 230, 235, 251, 337
- compound thin-film technologies, 45–9
- conduction band alignment *see* conduction band offset
- conduction band, **84, 85**
- conduction band offset *see also* hetero-junction; hetero-structure
  - assessment of, 27–8, 232, 367, 396
  - cliff-like, 19, 27, 232, 367–72, 382, 396, 406
  - spike-like, 19, 35, 326, 349, 367, 370, 396, 406
- constant energy surfaces, 90, **91**
- crystallography of CZTS and related compounds
  - adamantine family, 57–9, 59
  - body-centered tetragonal, 150
  - crystal density, 151, 152, 155
  - kesterite structure, 28, 31–2, 59, 60, 60–5, **62–4, 70, 75, 76**, 80–1, 82, 150–1, 152
  - lattice parameters (constants), 66, 69, 82, 151, 152
  - orthorhombic structure, **151**, 151
  - space group, 60
  - stannite structure, 60, **62, 70, 76**, 80–1, 82, 150–1, 152
  - superstructure, 59–68
  - unit cell, 56, **76**
  - unit-cell volume, 151, **153**
  - Vegard's law, 33, **33**, 151, **153–4**, 259
  - wurtz-stannite and wurtz-kesterite structures, 59, 66–8, **67–8**, 150, **151, 154**
  - Wyckoff positions, 60, **76**, 80–1
- current-voltage characteristics of solar cells *see also* equivalent circuit
  - theoretical, 16–7
- CZTS, CZTSe, CZTSSe and CZTGeSSe thin-film solar cells *see* CZTS-based thin-film solar cells; device characteristics
- CZTS-based thin-film solar cells
  - prospects for, 36–7, 48–50, 406–7
  - relative Earth-abundance and non-toxicity, 3–4, 28, 335
- dark saturation current density, 17–9, 366
  - see also* saturation current density
- defect clusters in CZTS, 69, 303–4
- defect states due to grain boundaries in CZTSe and CIGSe, density functional theory (DFT) simulation, 319
- density functional theory (DFT) *see also* defect states; density-of-states
  - historical, on CZTS and CZTSe, 76–7



- density-of-states (DOS)  
 of CZTS and CZTSe, 95–7, **96**  
 phonon, of CZTSe, **159**
- detailed balance model, 7–14
- device characteristics  
 chalcopyrite thin-film solar cells  
 efficiency; open-circuit voltage;  
 short-circuit current density;  
 fill factor, 27–8, 370, 391,  
**395, 405**  
 quantum efficiency, **392, 399**  
 series resistance, 391, **395, 405**
- CZTGeSSe thin-film solar cells  
 efficiency, 245
- CZTS monograin-layer solar cells  
 efficiency; open-circuit voltage;  
 short-circuit current density; fill  
 factor, 300
- CZTSe monograin-layer solar cells  
 efficiency; open-circuit voltage;  
 short-circuit current, 299
- CZTS thin-film solar cells  
 efficiency; open-circuit voltage;  
 short-circuit current density; fill  
 factor, 30–1, 186, **198, 216, 230,**  
**231, 285, 348–9, 349, 365**  
 quantum efficiency, 31–3, **34, 200,**  
**216, 231, 349, 376**  
 series resistance, 196, 200, 230, **377**  
 shunt resistance, 230
- CZTSe thin-film solar cells  
 efficiency; open-circuit voltage;  
 short-circuit current density; fill  
 factor, 235, 354–8, **365, 370**  
 quantum efficiency, **34, 356–7, 357,**  
**369, 375**  
 series resistance, 235–6, 355,  
 376–81, **377–8, 380**
- CZTSSe monograin-layer solar cells  
 efficiency; open-circuit voltage;  
 short-circuit current density; fill  
 factor, 297
- CZTSSe thin-film solar cells  
 efficiency; open-circuit voltage;  
 short-circuit current density; fill  
 factor, 33, **365, 370, 391, 405**  
 quantum efficiency, **34, 392, 399**  
 series resistance, **377–8, 391, 401,**  
**405**
- efficient thin-film solar cells  
 efficiency; open-circuit voltage;  
 short-circuit current density; fill  
 factor, 26, 370, 391
- mono-crystalline solar cells  
 direct gap semiconductor (CdTe), 25  
 direct gap semiconductor (GaAs),  
 15, 16  
 direct gap semiconductor (InP), 24–5  
 indirect gap semiconductor (Si),  
 15, 16  
 indirect gap semiconductor (ZnP<sub>2</sub>),  
 23–4
- dielectric constant *see* optical properties
- diode factor of CZTSSe and CZTSe  
 thin-film solar cells, 366 *see also*  
 fill factor  
 band gap dependence, **405**  
 temperature dependence, 370–2, **371**
- diode ideality factor *see* diode factor
- diode quality factor *see* diode factor
- dipole-transition selection rule,  
**163–5**
- disordered kesterite 70–2, 302–3, **302**
- dominant recombination path, 366–72
- effective masses, 90–3
- effective polaron masses, 92
- efficiency ( $\eta$ ) *see also* device  
 characteristics; Shockley-Queisser  
 limit  
 air mass (AM) dependence of, 11–4,  
**12, 13**
- electron probe microanalysis (EPMA), of  
 CZTS single crystal, 142
- electronic structure analysis of defects in  
 CZTS, 319, **320**
- elemental depth profile  
 CZTS thin films, 125–6, **125, 187,**  
**231–2, 232, 339, 342**  
 CZTSe/TiN/MoSe<sub>2</sub>/Mo boundary, **347,**  
**347–8**  
 CZTSSe monograins, 295, **296**

- elemental distribution profile
  - grain boundary of CIGSe thin films, 316–7, **317**
- energy-dispersive X-ray spectroscopy (EDX) *see also* elemental depth profile
  - on CZTSSe devices, **390**
- equilibrium vapor pressures, of elements
  - and binary compounds, **223**
- equivalent circuit of solar cells, **17**
- evaporation flux, control of, 226–7, **226–7**
- evaporation source, **224**, 224–5
- external quantum efficiency (EQE) *see* quantum efficiency
  
- Fermi level pinning, 24, 367, 392
- fill factor (FF), 10, 391 *see also* device characteristics
- first-principles modeling, 77–8, 142, 169, 300, 389
- flux material, for monograin powder growth, 291
  
- grain boundaries
  - carrier recombination at, 314, 319, 321
  - conduction channels arising from, **318**, 318
  - identification techniques for
    - atom probe tomography (APT), 316, **317**
    - cathodoluminescence (CL), 321
    - conductive atomic force microscopy (C-AFM), 321, **323**
    - electron-beam-induced current (EBIC), 326
    - electron energy loss spectroscopy (EELS), 316, **317**
    - energy-dispersive X-ray spectroscopy (EDS), 316
    - scanning Kelvin probe microscopy (SKPM), 314–6, **315–6**, 321–4, **322**, **324**
  - microscopic observation on
    - of CIGSe thin films by various methods, **316**
    - of CIGSe, CZTS, CZTSe and CZTSSe thin films, **322–4**, **327**
    - of high-and low-performance CIGSe thin films, **315**
    - passivation of, 316–26
    - polycrystalline thin-film solar cells and, 314
  
- Hertz–Knudsen equation, 223
- hetero-junction *see also* conduction band offset
  - band diagram of, **20**
- hetero-structure, 20, 28 *see also* hetero-junction
- homogeneity in nanocrystal ink-based process, 246–8
  
- ink coating *see* nanocrystal
- interface recombination, 19, 231–2, 366–7, 370, 372, 407
- interfacial MoS<sub>2</sub> layer, 341, **342**
- interfacial MoSe<sub>2</sub> layer, 262, **345–7**, 345–8
  - TiN diffusion barrier for suppressing MoSe<sub>2</sub> formation, 348
- internal quantum efficiency (IQE), 21, **393**, 398–9
- irreducible representations, 80–90
- IV*, *I-V* and *J-V* characteristics *see* current-voltage characteristics; device characteristics
  
- kesterite decomposition, 114
- kesterite formation, 112–3, 233
  
- leaching solutions, polarographic analysis of, 296, 297
- learning curves, for crystalline Si and CdTe modules, 49, **49**
  
- market development, of thin-film solar modules, 45–8
- market share, of thin-film products, 45, 49–50
- microhardness, of CZTS and related compounds, 157, 158, **158**

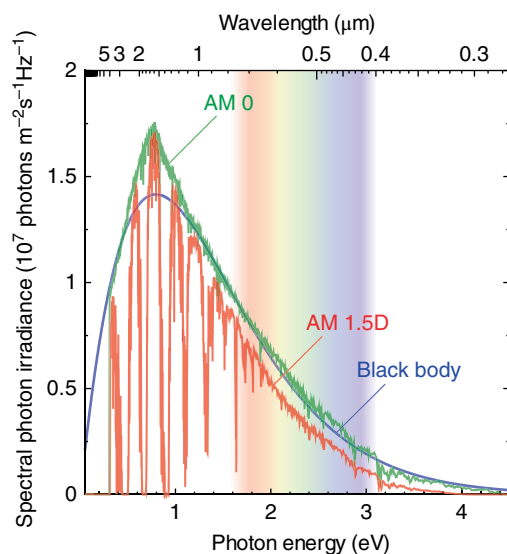
- minority carrier diffusion length, **393**
- minority carrier lifetime *see* carrier lifetime
- Mo back contact *see* Mo electrode
- Mo-coated soda-lime glass (SLG), 27–8, 183, 233, 235, 254, 274, 338, 388  
*see also* substrate
- Mo electrode *see also* interfacial MoS<sub>2</sub> and MoSe<sub>2</sub> layers; Mo-coated soda-lime glass (SLG)  
aqueous solution for preventing erosion of, 274, 277–9
- module production, 43–5
- monograin-layer solar cells *see* device characteristics
- monograin powder growth  
of CZTS, 293–4  
of CZTSe, 294–5
- monomers, nucleation of, 242, 247–8
- morphology of CZTSSe films  
bi-layer, 256, 260–2, **262**  
tri-layer, **262**, 262
- multi-junction (tandem) solar cells, 14, 46–7
- multi-stage process, 232–3 *see also* thin-film growth
- NaF precursor layer, 235
- nanocrystal (nanoparticle)  
of binary/ternary chalcogenide, 245  
characterization techniques for  
atomic absorption spectroscopy (AAS), 251  
electron energy loss spectroscopy (EELS), 250  
energy-dispersive X-ray spectroscopy (STEM-EDX), 250  
inductively coupled plasma mass spectroscopy (ICP-MS), 251  
Raman spectroscopy, **243**, 250  
scanning electron microscopy energy-dispersive  
X-ray spectroscopy (SEM-EDX), 250–1  
transmission electron microscopy (TEM/HRTEM), **243**, 250
- ultraviolet-visible spectroscopy (UV-vis), 251
- X-ray diffraction (XRD), **243**, 250
- X-ray fluorescence (XRF), 251
- X-ray photoelectron spectroscopy (XPS), 251
- CIGS, 240–1
- CIS, 241
- co-injection synthesis of, 243
- CZTGeS, 244, 245–6, **246**
- CZTS, 244  
stacking fault in, 242  
wurtzite, 245
- domain size of, 249
- film, 239–41, **240**
- hot-injection synthesis of, 241–9
- ink, 253–4
- phase purity of, 257–60
- precipitation of  
arrested, 243–4
- size-selective, 247–8
- stability of, 245, 248
- surface ligand on, 251
- synthesis of  
CZTGeS, 245–6  
kesterite/stannite CZTS, 242–4  
wurtzite CZTS, 245
- synthesis of, reaction conditions for  
relative precursor concentrations, 249  
solvent, 244, 247  
surfactant, 244  
temperature, 244, 247–9
- neutron diffraction  
of CZTS powder samples, 64–6, 66, 303  
simulated, of kesterite/stannite CZTS, 71–2, **72**
- non-radiative recombination, probability of, 9
- non-vacuum processing, 239, 272, 284–5  
*see also* solution-based process
- octet rule, 58, 75, 166
- off-stoichiometry (non-stoichiometry)  
in CZTS, **71**, 71, 76, 117, 117, 191

- open-circuit voltage ( $V_{oc}$ ) *see also* device characteristics
  - temperature dependence of, 18, 366, **369**, 395, **396**
- open-circuit voltage against current
  - transport mechanism, 17–8, 366–72
- open-circuit voltage ( $V_{oc}$ ) deficit, 21–2, 350, 364–5, **365**, 390–1, 391
  - chalcopyrite thin-film solar cells, 370, 391
  - CZTS thin-film solar cells, 350
  - CZTSe thin-film solar cells, 357–8, 370
  - CZTSSe thin-film solar cells, 370, 390–7, 404–7
  - ideal solar cells, 21, **365**
- optical properties of CZTS and CZTSe
  - absorption coefficient, **30**, 100–1, **100**, 171–3, **174**, 343–4, **343**
  - complex dielectric function, complex refractive index and normal-incidence reflectivity, 171–3
  - dielectric constant, 97–9, 169–70, 401, **401**
  - theoretical dielectric function, 97–9, **98**
  - Sellmeier equation, 169–70
  - spectroscopic ellipsometry (SE), 150
- optimal band gap for solar cells, 11–3, **12**, **365**, 404–5
  - air mass (AM) dependence of, 13
- parameterized energy band of CZTS and CZTSe, 88–90
- peritectic reaction in CZTS, 134–5, **135**
- phase diagram of CZTS *see also* secondary phases
  - CZTS–Sn pseudobinary system, 137–8, **138**
  - pseudo-ternary diagram of Cu–Zn–Sn–S system, 116–7, **117**
- phonon frequency of CZTSe, 158–9, **159**
- photocurrent density, 366 *see also* short-circuit current density
- photoluminescence (PL)
  - of CIGSSe thin films, 398–9, **399**
  - time-resolved, **398**
  - of CISE thin films, **373**
  - of CZTS monograins, **301**, 301–4, **303**
  - of CZTS thin films, 349–54
    - intensity-dependent, 350, **352**
    - time-resolved, 349–50, **350**, **352**
  - of CZTSe monograins, **301**, 301–3
  - of CZTSe thin films, 354–8, 372–3, **373**
    - spatially resolved, **374**, 374
    - time-resolved, **356**, 357
  - of CZTSSe thin films, 398–9, **399**
    - time-resolved, **398**
  - of near-stoichiometric CZTS monograins, **303**, 303
- photovoltaics, 51, 313
- Planck's formula, 4–5, **5**
- polymorph, 23, 32, 108, 375
- potential fluctuation, 301, 326, 358, 397–9, 406–7
- price of photovoltaic systems, 44
- process curve for reactive sputtering, 205, **206**, 208–9 *see also* thin-film growth
- properties of CZTS thin films *see also* non-vacuum processing
  - dependence on chemical composition, 279–81, **280–1**
  - effect of  $H_2S$  concentration on, 282–4, 282, **283**
- quantum efficiency (QE) *see* device characteristics
- quasi donor-acceptor pair (QDAP), 350–4, **352**, 400
- radiative recombination efficiency, 9
- Raman scattering *see* Raman spectroscopy
- Raman spectroscopy
  - of CZTS, 121, **122–3**, **161**, **302**, **341**
  - of CZTSe, CZTSSe and related compounds, **161**
  - modified random-element-isodisplacement (MREI) model, 161–2
- reactive sputtering of CZTS, 203–15 *see also* thin-film growth

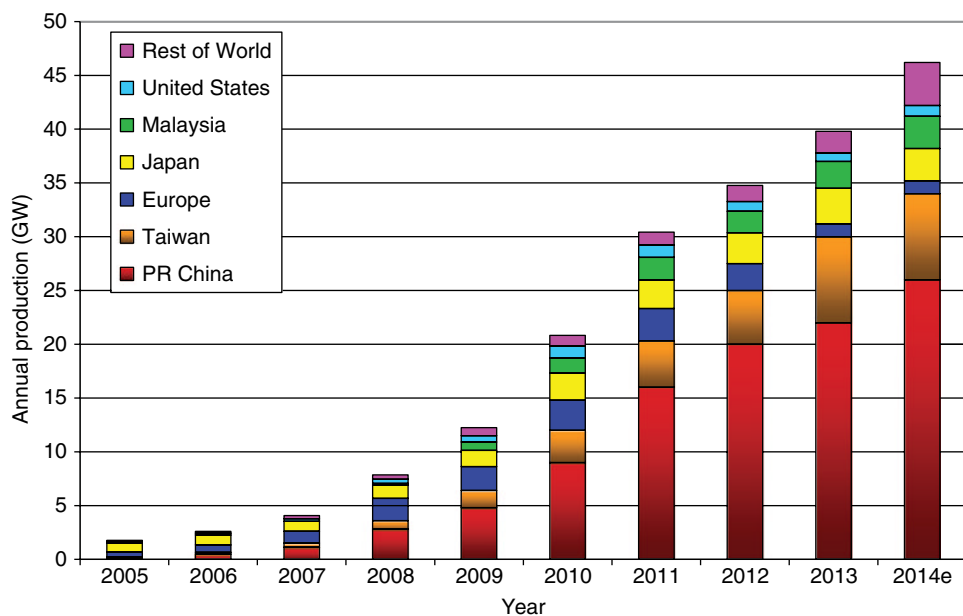
- reflectivity, 398–9
- renewable energy, 3–4, 51
- saturation current density, 230, 366–8, 370, **371**, 379, 391
- secondary phases in CZTS and CZTSe compounds
  - band gap of, 118
  - CTS or  $\text{Cu}_x\text{SnS}_y$ , 125, 342
  - $\text{Cu}_{2-x}\text{S}$ , 118–9, **294**
  - $\text{Cu}_{7/2}\text{S}_4$ , 283–4, **284**
  - $\text{Cu}_{2-x}\text{Se}$ , 257–8
  - etchant for removal of, 126–7, 127, 128
  - identification technique for,
    - atom probe tomography (APT), 125, 380–1, **381**
    - Auger electron spectroscopy (AES), 125–6, **125**
    - Raman spectroscopy, 120–4, 121, **122**, **123**
    - room-temperature
      - photoluminescence (RT-PL), 124
    - scanning electron microscopy (SEM), **123**, 123–4
    - secondary ion mass spectrometry (SIMS), 124
    - transmission electron microscopy (TEM), 124–5
    - X-ray absorption near edge structure (XANES) analysis, **125**, 125–6, 231–2
    - X-ray diffraction (XRD), 118–20, **119**, 120
  - SnS, 118–9, 214–5, 293
  - $\text{SnS}_2$  or  $\text{SnS}_x$ , 118–19, **139**, 293
  - ZnS, 123–6, **294**, **342**, 342
  - ZnSe, 124, 379–81, **381**
  - selenization
    - apparatus for, 254–5, **255**
    - elemental losses during, 257–8
    - of nanocrystal inks, **240**, 252–62
  - series resistance *see* device characteristics
  - Shockley equation, 17–8
  - Shockley–Queisser (SQ) limit, 7–8, **12**, 364–5, **365**, 404
  - Shockley–Read–Hall (SRH) recombination, 10, 372
  - short-circuit current density ( $J_{sc}$ ) *see also* current-voltage characteristics; device characteristics
    - of ideal solar cells, 10, 13, **365**
  - shunt conductance, 372, 402
  - shunt resistance, 16–7 *see also* device characteristics; shunt conductance
  - single crystal growth of CZTS *see* traveling heater method
  - solar cell efficiency *see* efficiency
  - solar constant, 5–7
  - solar radiation, 4–7
  - solution-based method *see* solution-based process
  - solution-based process, 239 *see also* thin-film growth
  - spin-orbit split and crystal-field split, 83, 86, 93–5, 162, **163–4** *see also* band structure
  - sprayed CZTS thin films *see* thin-film growth
  - sputter target for CZTS thin-film growth
    - CuSn alloy and Zn, 203–6
    - Cu, SnS and ZnS, 190–1
    - CZTS compound, 192
  - SQ limit *see* Shockley–Queisser limit
  - stabilizer, 273–4
  - staggered gap hetero-junction, 19–20, **20**
  - straddling gap hetero-junction, 19–20, **20**, 35
  - stress in CZTS thin films, 209–12, 210
  - substrate, for thin-film solar cells
    - soda-lime glass *see* Mo-coated soda-lime glass (SLG)
    - stainless steel, 30
  - sulfurization of precursor layers,
    - conditions for
      - $\text{H}_2\text{S}$  flow, 27–8, 31, 185, 205–6, 275
      - partial pressure of sulfur, 29, 336–8
    - system, 188
    - temperature, 185
  - surface defects of CZTS *see also* defect states
    - density-of-states and, 319–20, **320**

- surface treatment of CZTS thin films
  - with deionized water, 191
  - NaCN treatment, 338
  - with potassium cyanide (KCN), 229–32, **229**
- temperature dependent current-voltage analysis, 366–81, 394–7
- thermal properties of CZTS and related compounds
  - melting point, 152–5, 154, **155**
  - thermal conductivity, 154, 155–7, **155**, 157
  - Wiedemann–Frantz–Lorenz law, 155
- thermal treatment *see also* annealing of CZTS thin films, 338
  - improvement of device performance by *see also under* device characteristics
    - CZTS monograin layer solar cell, 299–300
    - CZTSe monograin layer solar cell, 298–9, **299**
- thin films, densification of, 252–4
- thin films, grain growth of, 196–9, **197**, **199**, **213**, 214, 249, 252–3, 255–60, **256**, 341
- thin-film growth, for absorber layers
  - via coating of CZTGeS nanocrystals and subsequent annealing in selenium vapor, 259–60, **259**, 263–4
  - via coating of CZTS nanocrystals and subsequent annealing in selenium vapor, **256–7**, 257–9, 260–2
  - via coating of oxyhydrate precursor layers by sol-gel method and subsequent annealing in H<sub>2</sub>S, 277–9, **278**, 278
  - via coating of precursor layers by spray pyrolysis and subsequent annealing in H<sub>2</sub>S, 31–2
  - via hydrazine (N<sub>2</sub>H<sub>4</sub>)-based slurry processing and subsequent annealing, 388
  - via multi-stage (two-stage) process
    - coevaporation and subsequent short annealing in sulfur vapor, 338
    - coevaporation of binary and subsequent ternary chalcogenide layers, 233–4, **233–4**
    - coevaporation of Cu-rich and subsequent Cu-poor layers, 234–6, **235**
    - reactive sputtering and subsequent annealing in S/SnS vapor, 214–5
  - via one-stage (single-step) process
    - of atom beam sputtering, 29
    - of coevaporation, 227–32, **229**, **232**
    - of reactive sputtering, 204
  - via physical vapor deposition of precursor layers
    - and subsequent annealing in H<sub>2</sub>S, 20, 27, 183–4, 185
  - via sputter deposition of metallic precursor layers
    - and subsequent sulfo-selenization in sealed ampoule, 32–4
    - and subsequent sulfurization in sealed ampoule, 29
  - via sputter deposition of metallic stacks and subsequent annealing in H<sub>2</sub>S, 27–8
- thin-film solar cells *see also* compound thin-film technology; thin-film growth
  - historical, 25–6, 26
  - technology of, 25, 36–7
- thin-film solar modules
  - CdTe
    - production of, 45–6, **49**
  - chalcopyrite
    - production of, 46–8
- topotactical growth, 233–4
- total energy difference between kesterite and stannite lattices, 81, 82
- transient photocapacitance, of CZTSSe thin-film solar cells, 403–4, **404**
- transmission electron microscopy (TEM) *see also* nanocrystal observation of CZTS thin films by, 338–9, **339**

- transport properties of CZTS and related compounds
  - acceptor band, 145, **145**
  - carrier (hole) concentration, 143
  - conductivity type, 170, 174
  - electrical conductivity, **144**, 156, **157**
  - Hall effect measurement, 142–3
  - hole mobility, 143, 174, 175–6, **176**
  - Mott variable range hopping (M-VRH), 144–5
  - resistivity, 170, 174, **174**
  - thermal activation energy, 145
- traveling heater method (THM), for single crystal growth of CZTS 138–40, **140**
- tunable band gap
  - of CZTS<sub>Se</sub> thin-film absorbers *see* band gap
  - of Ge-alloyed CZTGeSSe thin-film absorbers *see* band gap
- tunneling-induced recombination, 372
- two-stage process *see* thin-film growth
- two-step process, 20, 24, 27, 236, 271–2 *see also* two-stage process
- type I hetero-junction *see* straddling gap hetero-junction
- type II hetero-junction *see* staggered gap hetero-junction
- ultra-thin absorber layer, 256
- Urbach energies, 403
- valence band, 86–90, **87**
- Vegard rule *see* crystallography
- window layers
  - atom-beam-sputter-deposited In<sub>2</sub>O<sub>3</sub> thin films, 27
  - atom-beam-sputter-deposited ZnO thin films, 24, 27
  - epitaxial wurtzite-type CdS layers, 24
  - reactively evaporated indium oxide (In<sub>2</sub>O<sub>3</sub>) thin films, 24, 25
  - RF-sputter-deposited In<sub>2</sub>O<sub>3</sub>:Sn (ITO) thin films, 338
  - RF-sputter-deposited ZnO:Al (AZO) thin films, 184, 290, 338
  - sputter-deposited cadmium-tin oxide thin films, 30
  - ZnO:Al (AZO) thin-films deposited by sol-gel method, 285
  - ZnO/In<sub>2</sub>O<sub>3</sub>:Sn (ITO) bi-layers, 336
- X-ray diffraction (XRD)
  - CZTGeSSe thin films, 259, **259**
  - CZTS single crystals, 141, **141**
  - CZTS thin films, 29, **29**, 192, **193**, 212–4, **213**, 283–4, **284**, 338–40, **340**
  - CZTSe thin films, 345–7, **346**
  - CZTS<sub>Se</sub> thin films, 33, **33**, 256–7, **257**
  - KCN-etched CZTS thin films, 229, **229**
- X-ray powder diffraction, 59 *see also* X-ray diffraction (XRD)
- X-ray fluorescence (XRF) *see* composition

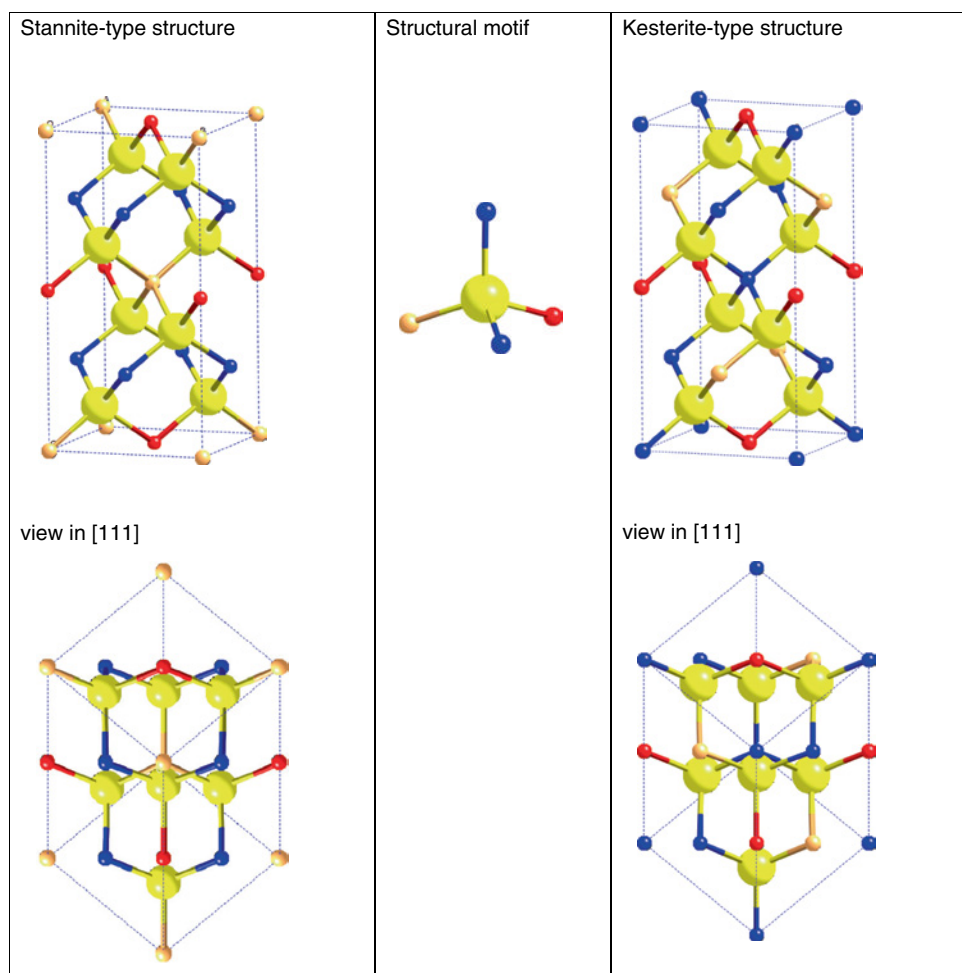


**Figure 1.1** Spectral photon irradiance of AM0, AM1.5D and black body radiation

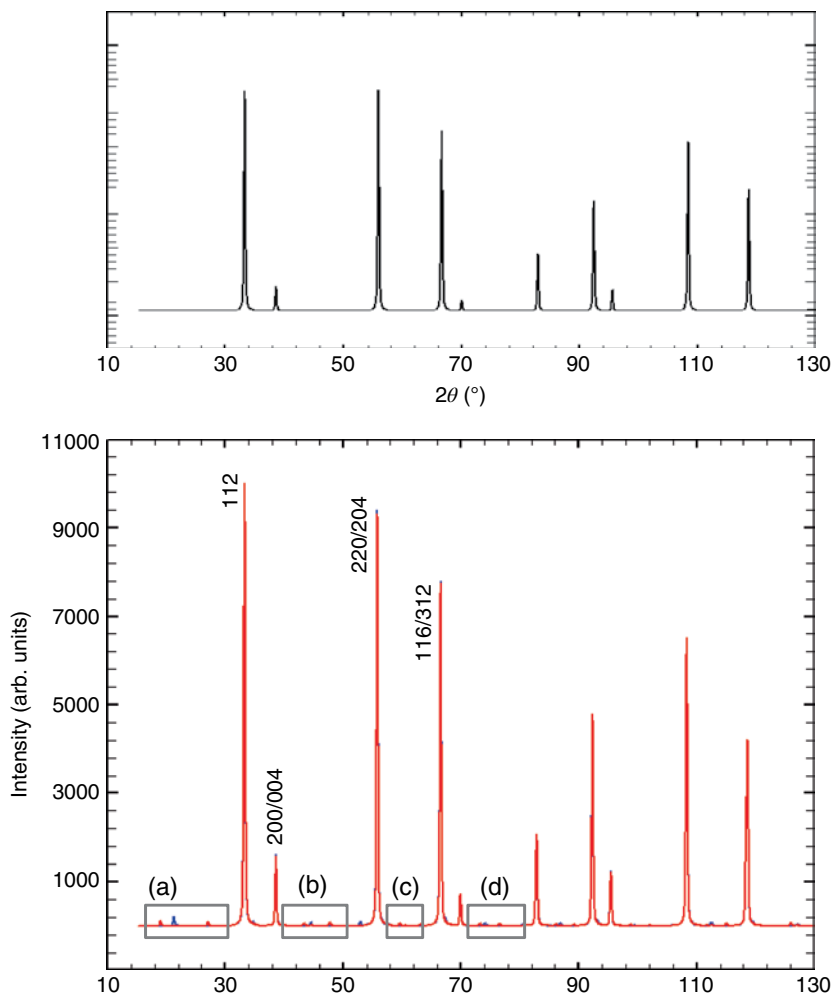


**Figure 2.1** World PV Cell/Module Production from 2005 to 2014 (data source: Photon Magazine, PV Activities in Japan, PV News, and own analysis)

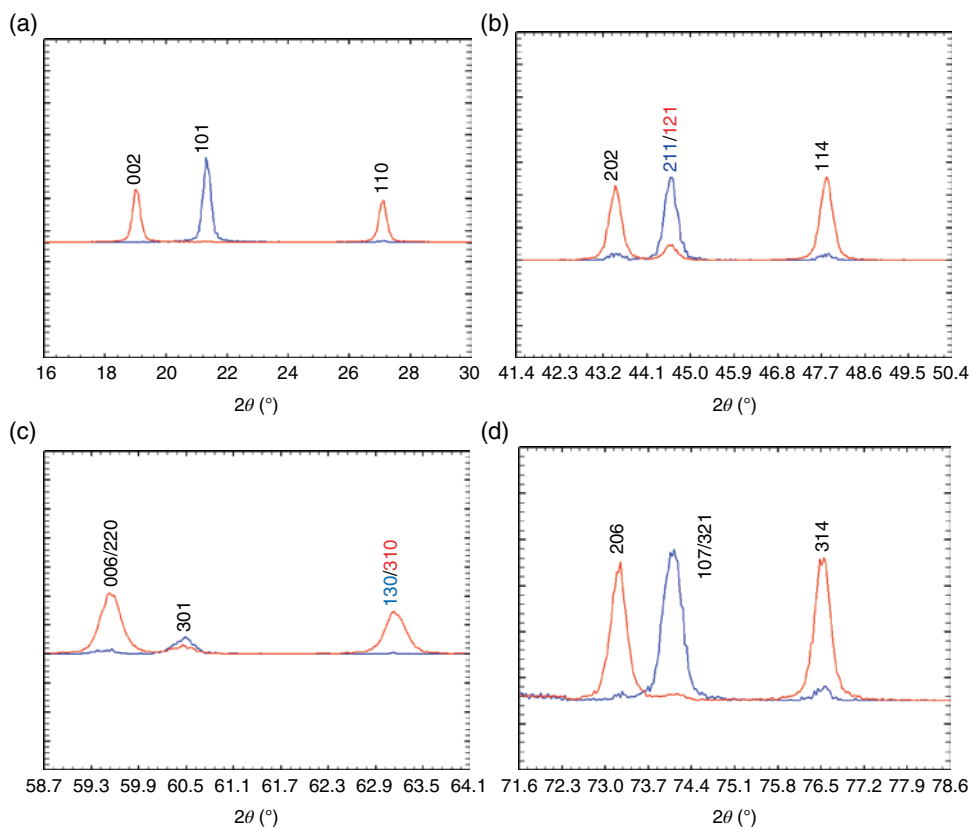




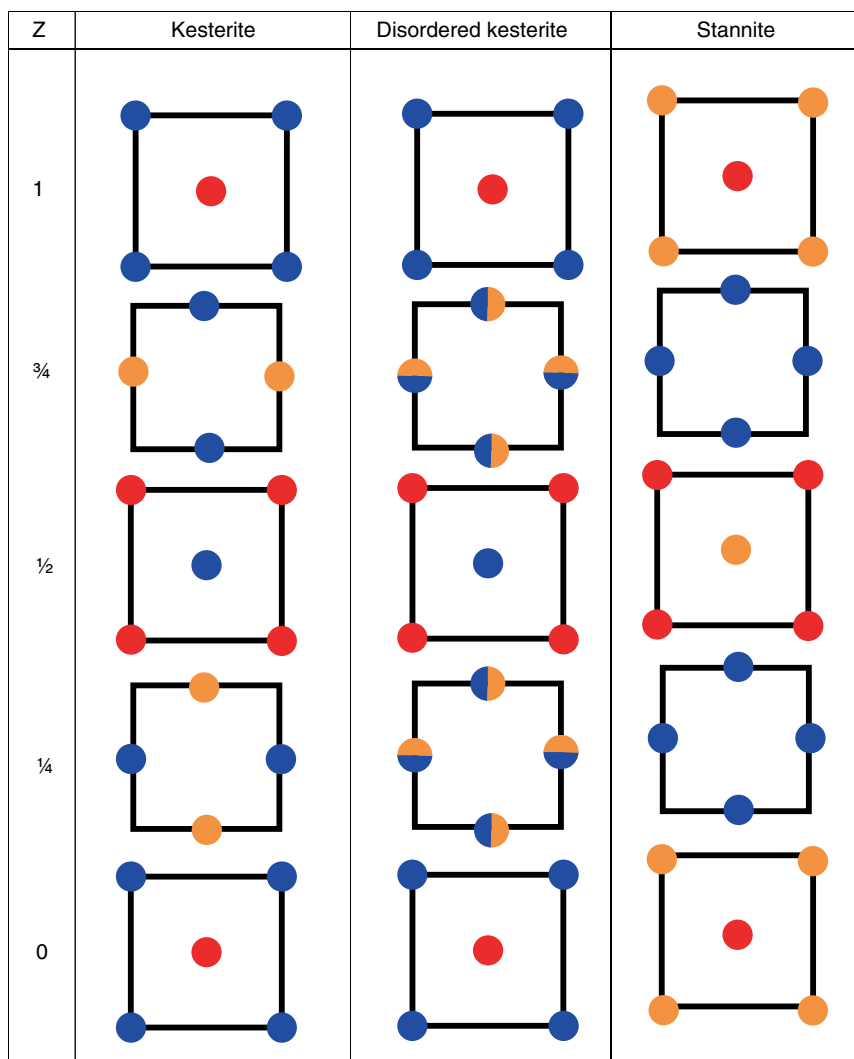
**Figure 3.3** Representations of the stannite and kesterite type structure (blue: Cu, orange: Zn, red: Sn, yellow: S)



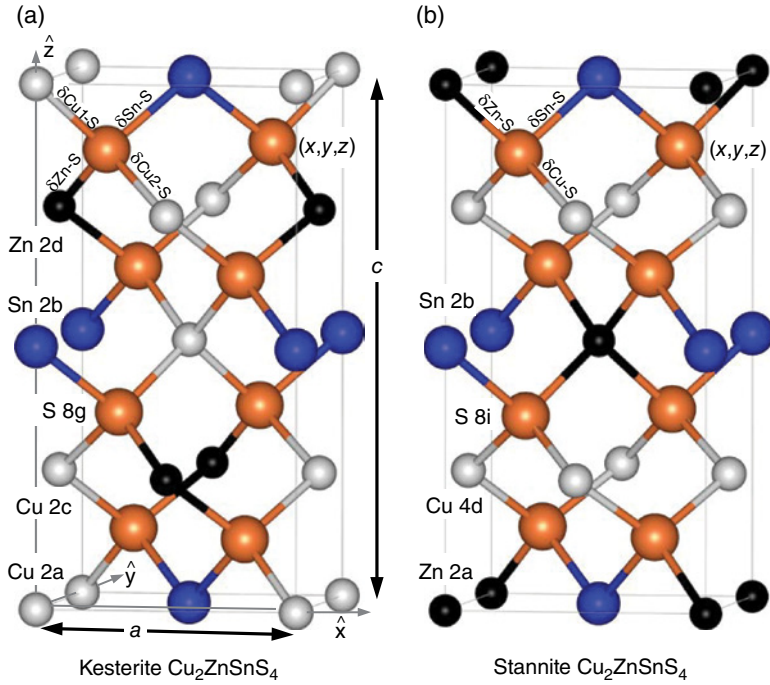
**Figure 3.4** Simulated neutron powder diffraction pattern ( $\lambda=1.79\text{\AA}$ ) for: ZnS (top) and  $\text{Cu}_2\text{ZnSnS}_4$  (middle) in kesterite- (blue) and stannite- (red) type structure. The four regions (a)–(d) marked in the diffraction pattern of  $\text{Cu}_2\text{ZnSnS}_4$ , indicating the small superstructure reflections.



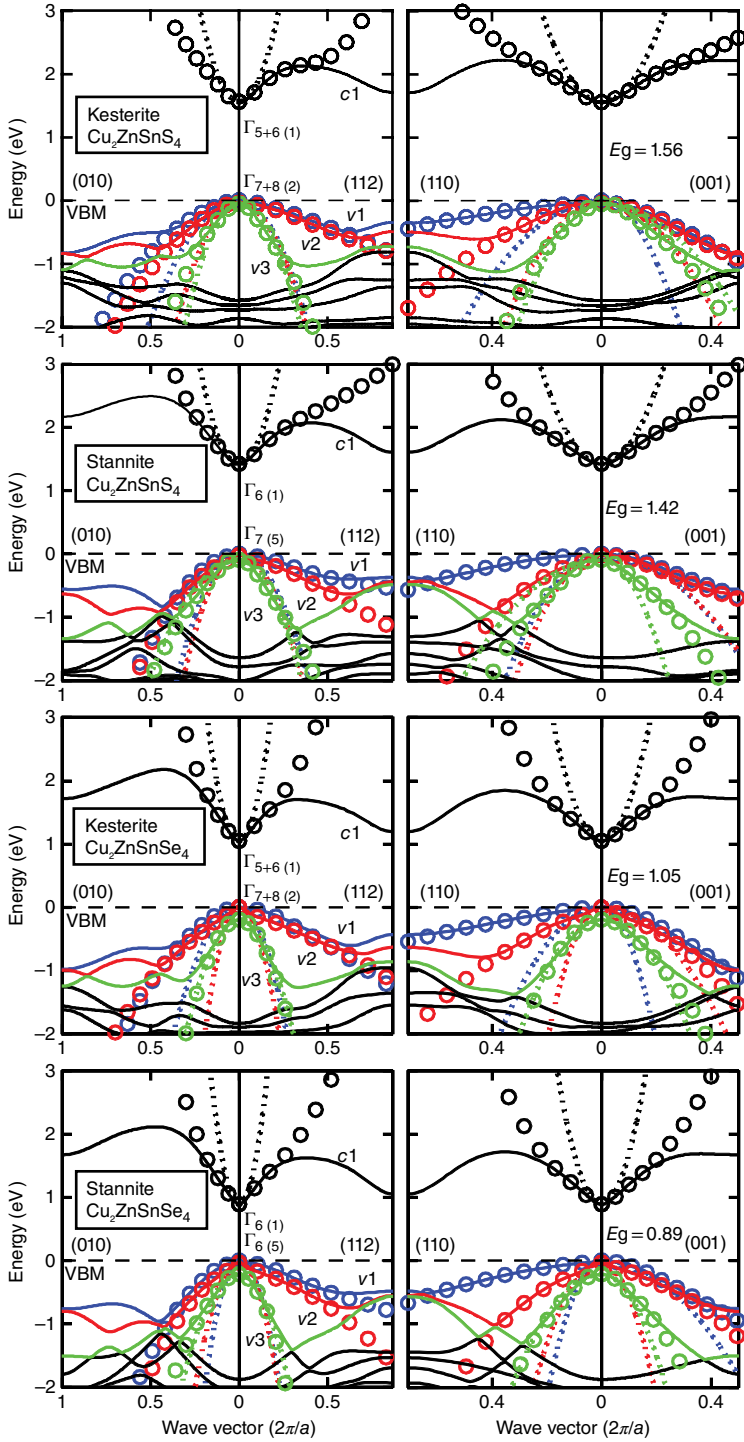
**Figure 3.4** (continued)



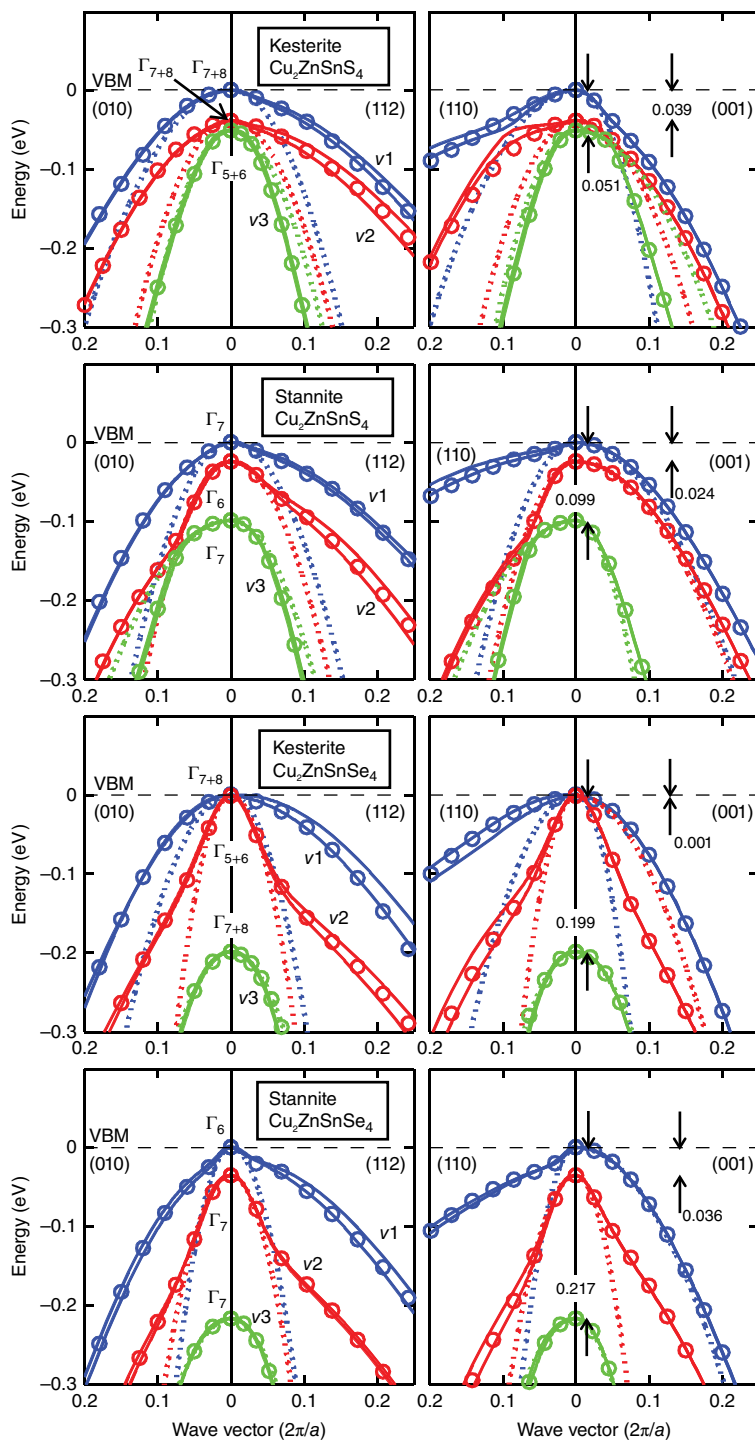
**Figure 3.7** View on the a-b-plane of the kesterite-type and the stannite-type structure as well as the disordered kesterite-type structure. The numbers indicate the z value (with respect to the crystallographic c axis) of the corresponding a-b-plane. The anions planes are not shown (blue: Cu; orange: Zn; red: Sn)



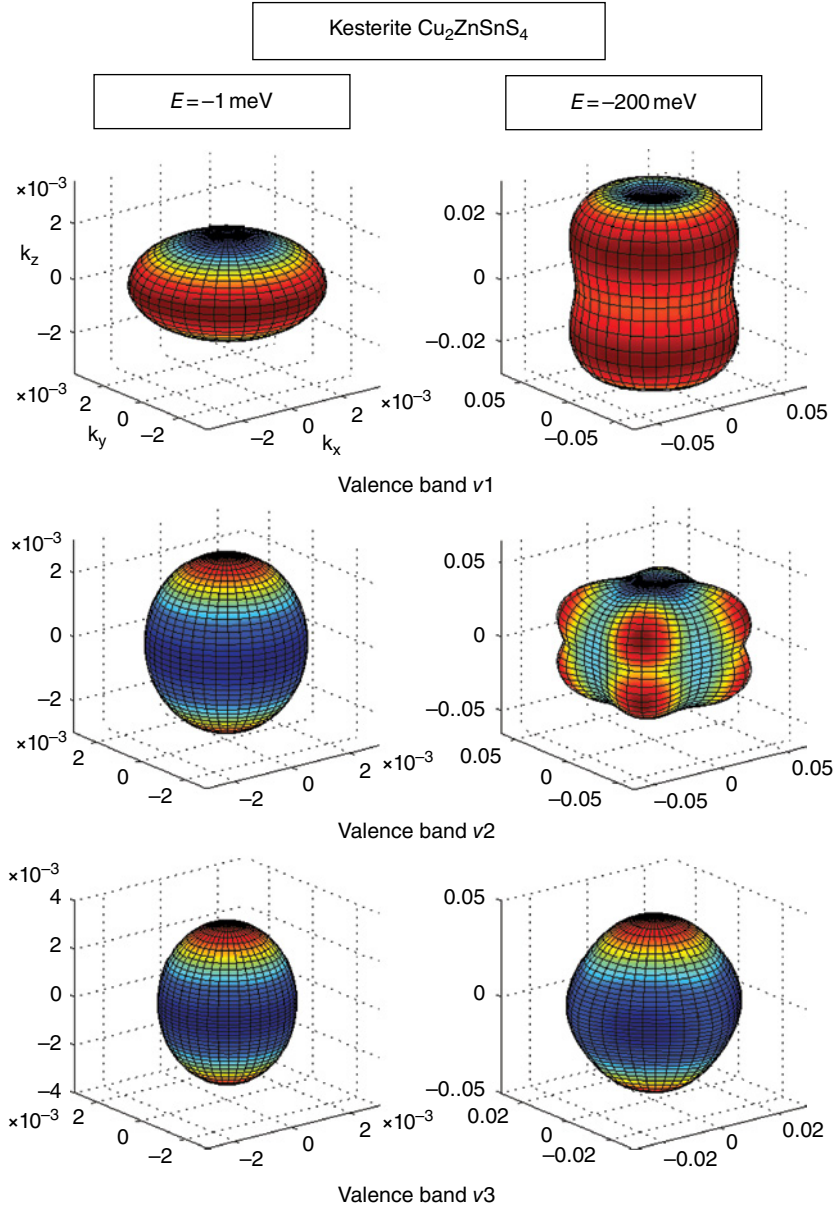
**Figure 4.1** Conventional unit cells of the (a) kesterite and (b) stannite structures of CZTS. The primitive unit cells involve four Cu atoms, two Zn atoms, two Sn atoms, and eight S atoms. For the kesterite  $S_4^2$  phase, the crystal structures are fully defined by the anion 8g Wyckoff position  $(x, y, z)$ , while for the stannite  $D_{2d}^{11}$  phase the structure is defined by the anion 8i position  $(x, y = x, z)$



**Figure 4.2** The electronic band structure  $E_j(\mathbf{k})$  of the kesterite and stannite structures of CZTS and CZTSe along four symmetry directions. The energy refers to the VBM (dashed lines). The spin-orbit interaction is included, but the index of the bands ( $j=v1, v2, v3$ , and  $c1$ ) refers to spin-independent bands where  $c1$  represents the lowest CB and  $v1$  represents the topmost VB. The solid lines are the data from GGA/FP-LAPW calculations, the circles show the results from the full band parameterization, and the dotted lines represent the parabolic band approximation

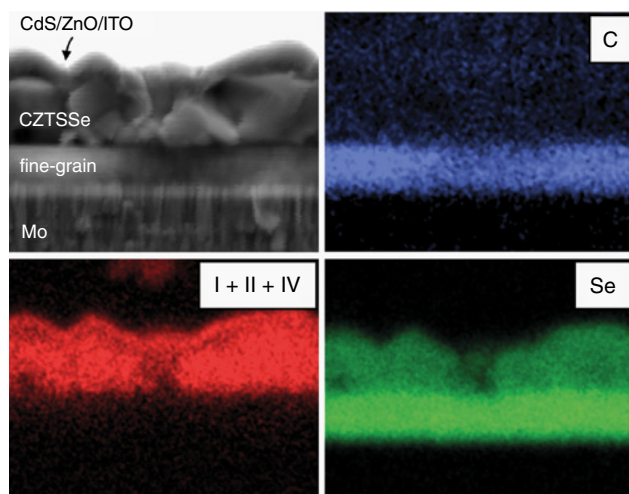


**Figure 4.3** A close-up of Figure 4.2 near the VBM, demonstrating that the uppermost VBs are very non-parabolic

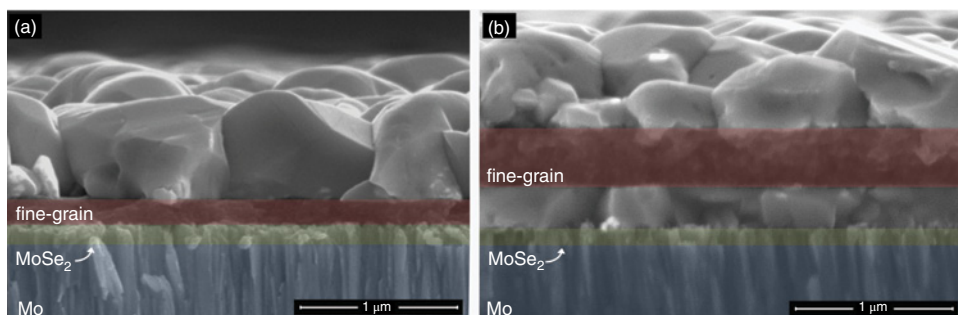


**Figure 4.4** Constant energy surfaces  $S_i(E)$  of kesterite CZTS for the energies  $E = -1 \text{ meV}$  below the VBM (left column) and  $E = -200 \text{ meV}$  (right column). The  $\mathbf{k}$ -mesh is in the unit  $2\pi/a$ . Notice the different scales on the  $\mathbf{k}$ -axis. This figure demonstrates that the three uppermost VBs are very anisotropic away from the  $\Gamma$ -point

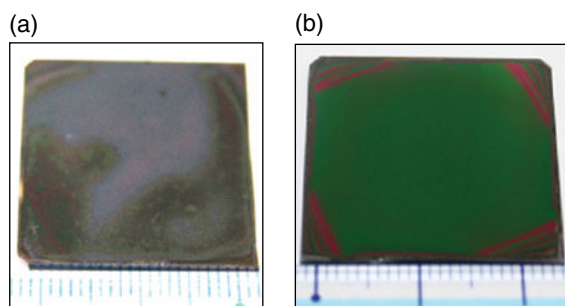




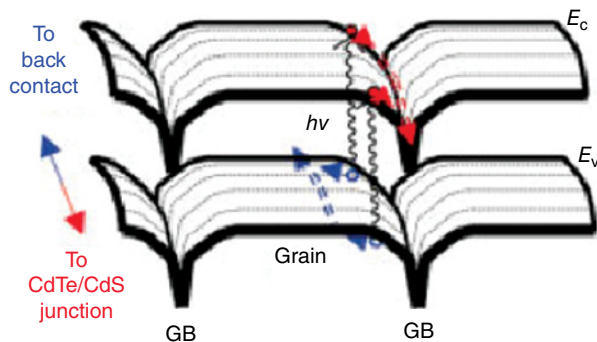
**Figure 11.10** Cross-sectional SEM-EDX mapping demonstrating that the composition of the fine-grain layer resulting from the selenization of a quaternary nanocrystal film mostly comprises Se and C with minimal signal from Cu, Zn, and Sn. The original un-sintered CZTS nanocrystals are therefore absent from the fine-grain layer [23]



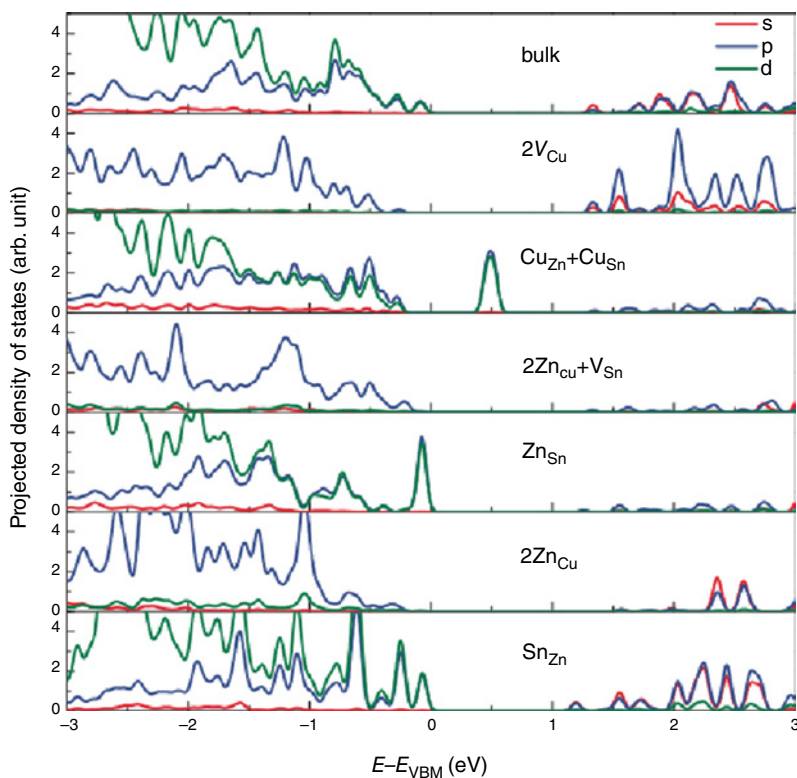
**Figure 11.12** Cross-sectional SEM images illustrating: (a) standard bi-layer morphology typical of high-efficiency devices (annealed in air prior to selenization); and (b) undesirable tri-layer morphology of CZTSSe films following selenization (not annealed prior to selenization)



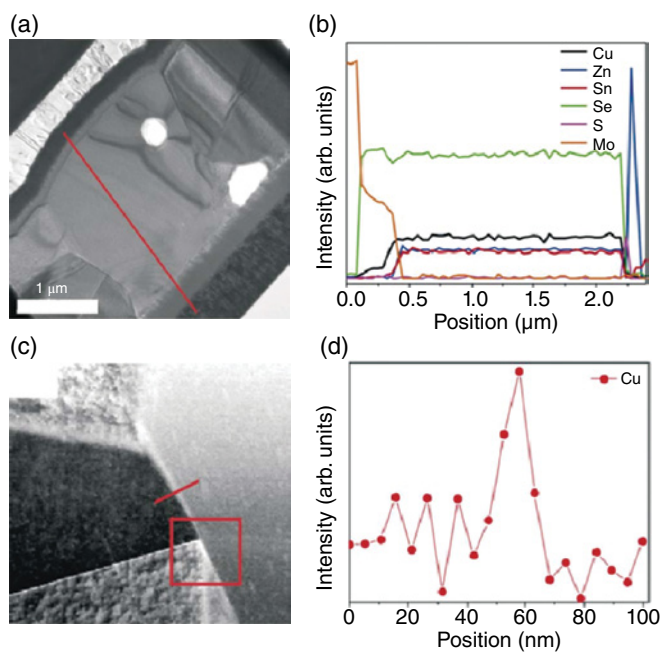
**Figure 12.8** Macroscopic image of the precursor which is deposited from the 1.75 M solution onto the (a) Mo/SLG and (b) 0.35 M solution with ammonium acetate having  $H_2O$ -coated Mo/SLG



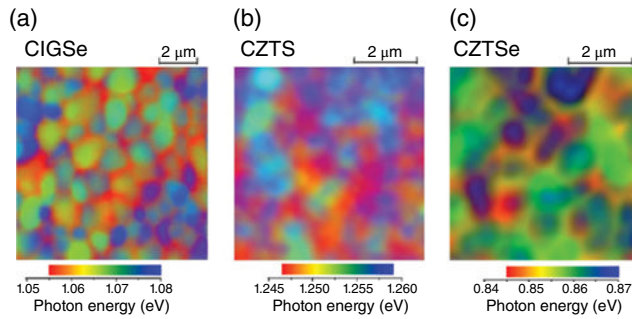
**Figure 14.5** Illustration of band diagram versus spatial coordinate of CdTe grains in the solar cell. Blue and red circles represent hole and electrons, respectively. Blue and red arrows show their direction of movement respectively. Electron-hole pairs are photogenerated near the GB and undergo charge separation due to the GB potential. This is followed by holes travelling within the grain towards the back contact and electrons channeling along the GB core towards the CdTe/CdS junction. Reproduced with permission from [16]. © 2004 WILEY-VCH Verlag GmbH & Co. KGaA, Weinheim



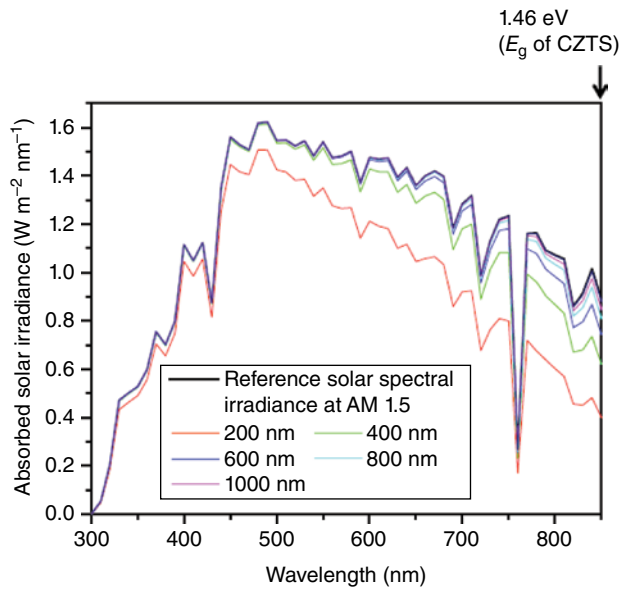
**Figure 14.6** Partial density of states (PDOS) with different surface defects. Reprinted with permission from [88]. Copyright © 2013 by the American Physical Society



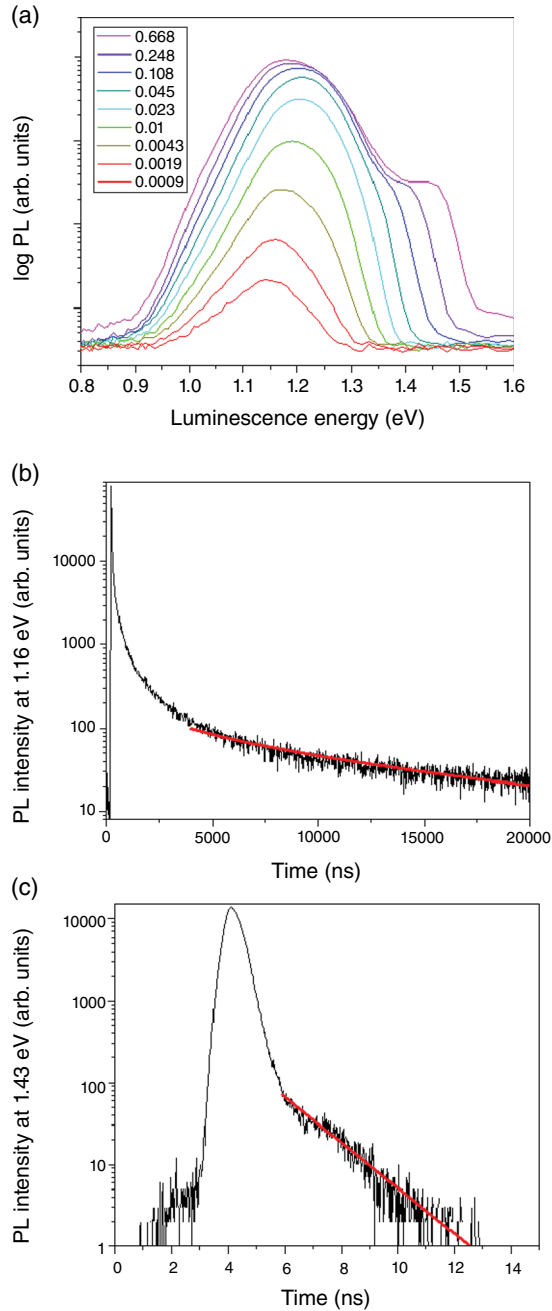
**Figure 14.12** (a) Cross-sectional TEM image and (b) EDS line scan of the low-band-gap champion CZTSe cell. (c) TEM image and (d) EDS line scan of the same cell showing Cu-rich grain boundary. The lines in (a) and (c) indicate the path examined in the EDS line scans of (b) and (d). Reproduced from [66] with permission of The Royal Society of Chemistry



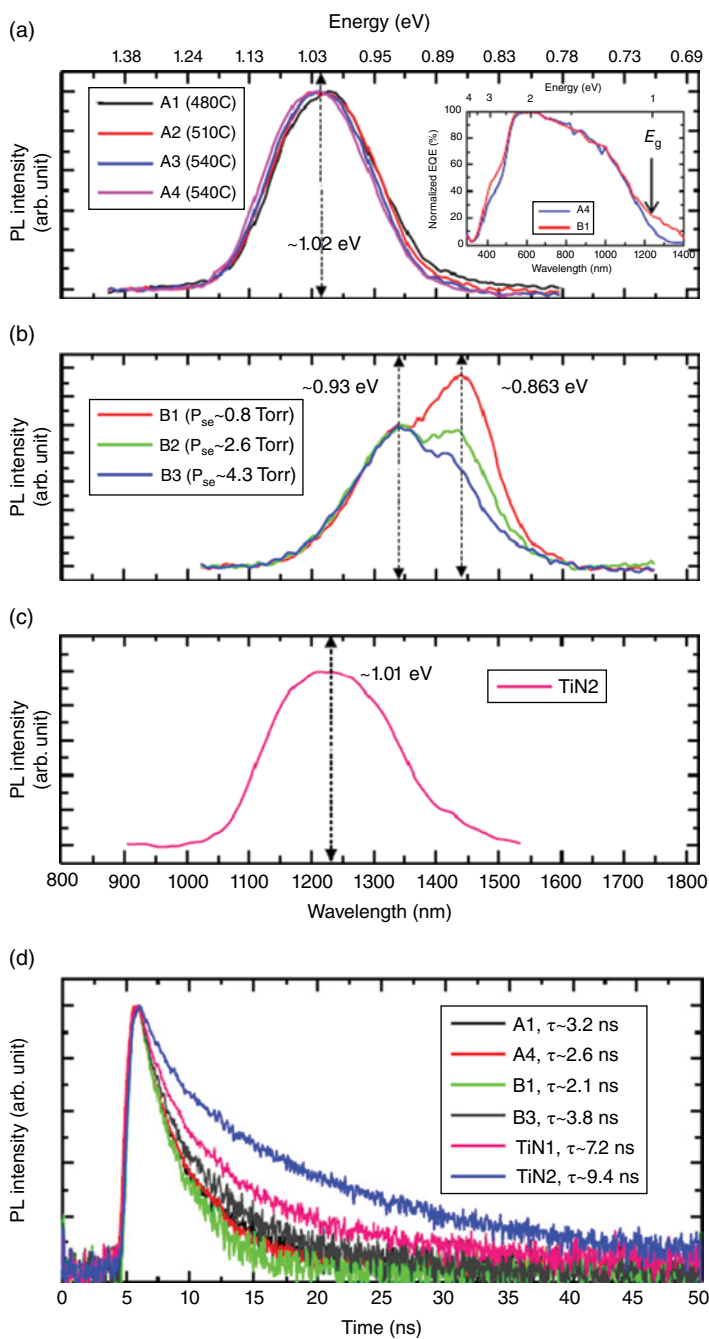
**Figure 14.14** Spectrum imaging of the luminescence from (a) CIGSe; (b) CZTS; and (c) CZTSe. © 2012 IEEE. Reprinted, with permission, from [95]



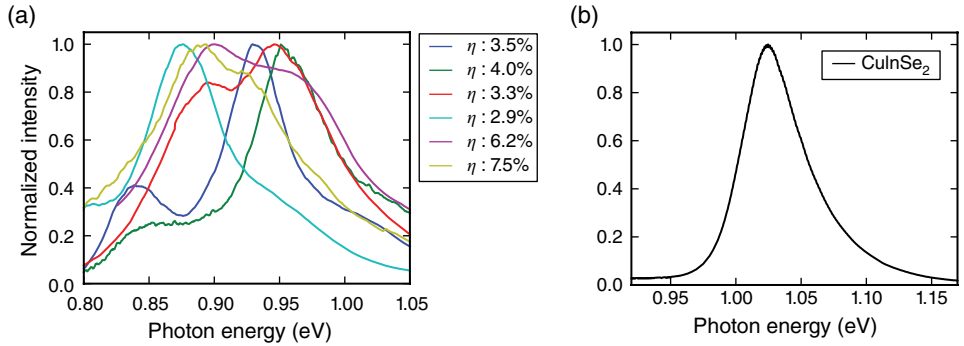
**Figure 15.6** Calculated solar irradiance absorbed by a CZTS of various thicknesses using the measured absorption coefficients shown in Figure 15.5



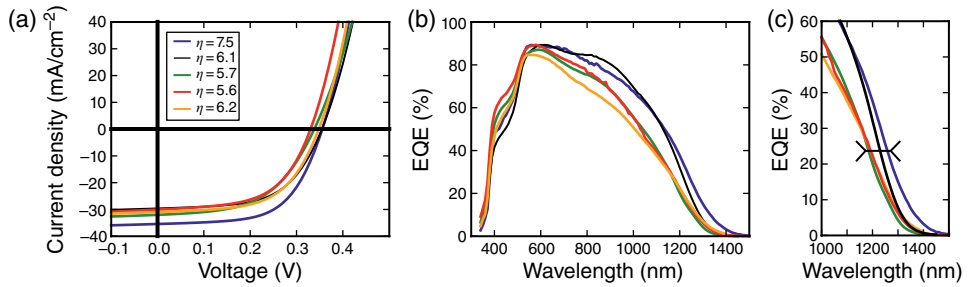
**Figure 15.14** (a) Low-temperature (4K) intensity-dependent PL of a CZTS layer giving an 8.3% efficient device; the numbers in the legend correspond to average  $W\text{ cm}^{-2}$ . PL lifetimes associated with emission at (b) 1.16 eV and (c) 1.43 eV. Measurements were made using an average laser intensity of  $0.668\text{ W cm}^{-2}$ . Reproduced with permission from [53]. Copyright © 2013, AIP Publishing LLC



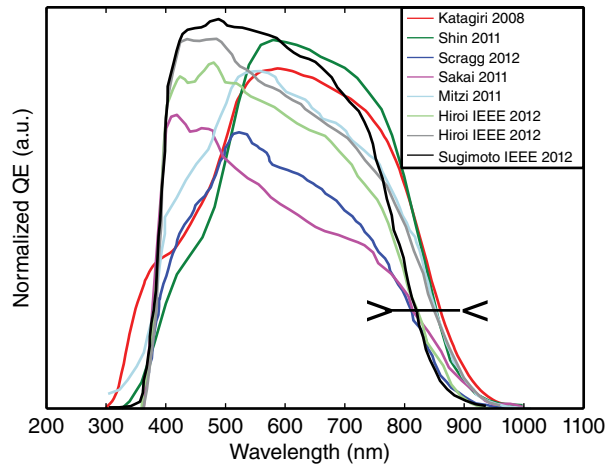
**Figure 15.16** Room-temperature PL spectra of CZTSe samples: (a) samples A1–A4; (b) samples B1–B3; and (c) sample TiN2. EQE of A4 and B1 are shown in the inset of (a). (d) TRPL spectra of some representative samples. Reproduced with permission from [9]. Copyright © 2012, AIP Publishing LLC



**Figure 16.5** (a) Normalized room-temperature photoluminescence spectra of different CZTSe absorber layers which resulted in solar cell devices with efficiencies in the range 2.9–7.5%. (b) For comparison, a typical room-temperature PL spectrum of a polycrystalline  $\text{CuInSe}_2$  absorber with an efficiency of 12.5% and  $V_{oc} = 471$  mV is shown [66]



**Figure 16.7** (a) J–V characteristics of CZTSe solar cell devices and (b, c) the corresponding QE spectra



**Figure 16.8** Reported quantum efficiency data for Se-free devices. The QE data have been normalized and then scaled with the reported  $J_{sc}$  values. A linear extrapolation of the low-energy slopes yield at least 60 meV difference in band gap

# **WILEY END USER LICENSE AGREEMENT**

Go to [www.wiley.com/go/eula](http://www.wiley.com/go/eula) to access Wiley's ebook EULA.